

REPORT DOCUMENTATION PAGE			
1. Recipient's Reference	2. Originator's Reference	3. Further Reference	4. Security Classification of Document
	AGARD-AG-280	ISBN 92-835-1519-6	UNCLASSIFIED
5. Originator	Advisory Group for Aerospace Research and Development North Atlantic Treaty Organization 7 rue Ancelle, 92200 Neuilly sur Seine, France		
6. Title	TURBULENT SHOCK-WAVE/BOUNDARY-LAYER INTERACTION		
7. Presented at			
8. Author(s)/Editor(s)	Various		9. Date
			February 1986
10. Author's/Editor's Address	Various		11. Pages
			224
12. Distribution Statement	This document is distributed in accordance with AGARD policies and regulations, which are outlined on the Outside Back Covers of all AGARD publications.		
13. Keywords/Descriptors	Aerodynamic characteristics Shock waves Boundary layer Transonic flow Supersonic flow Data processing		
14. Abstract	<p>This AGARDograph presents a comprehensive, up-to-date review of the shock-wave boundary-layer interaction problem. A detailed physical description of the phenomena for transonic and supersonic speed regimes is given based on experimental observations, correlations, and theoretical concepts. Approaches for solving the problem are then reviewed in depth. Specifically, these include: global methods developed to predict sudden changes in boundary-layer properties; integral or finite-difference methods developed to predict the continuous evolution of a boundary-layer encountering a pressure field induced by a shock wave; coupling methods to predict entire flow fields; analytical methods such as multi-deck techniques; and finite-difference methods for solving the time-dependent Reynolds-averaged Navier-Stokes equations used to predict the development of entire flow fields. Examples are presented to illustrate the status of the various methods and some discussion is devoted to delineating their advantages and shortcomings. Reference citations for the wide variety of subject material are provided for readers interested in further study.</p>		
<p>This AGARDograph has been produced at the request of the Fluid Dynamics Panel of AGARD.</p>			

LIBRARY
RESEARCH REPORTS DIVISION
NAVAL POSTGRADUATE SCHOOL
MONTEREY, CALIFORNIA 93940

AGARD-AG-280

AGARD-AG-280

AGARD

ADVISORY GROUP FOR AEROSPACE RESEARCH & DEVELOPMENT

7 RUE ANCELLE 92200 NEUILLY SUR SEINE FRANCE

AGARDograph No. 280

Shock-Wave Boundary Layer Interactions

NORTH ATLANTIC TREATY ORGANIZATION



DISTRIBUTION AND AVAILABILITY
ON BACK COVER

NORTH ATLANTIC TREATY ORGANIZATION
ADVISORY GROUP FOR AEROSPACE RESEARCH AND DEVELOPMENT
(ORGANISATION DU TRAITE DE L'ATLANTIQUE NORD)

AGARDograph No.280
SHOCK-WAVE BOUNDARY LAYER INTERACTIONS

by

J.Delery
ONERA
4 rue des Vertugadins
91190 Meudon
France

J.G.Marvin
NASA Ames Research Center
Moffett Field
CA 94035
USA

Edited by

Professor E.Reshotko
Dept. of Mechanical & Aerospace Eng.
Case Western Reserve University
Cleveland
Ohio 44106 — USA

THE MISSION OF AGARD

The mission of AGARD is to bring together the leading personalities of the NATO nations in the fields of science and technology relating to aerospace for the following purposes:

- Exchanging of scientific and technical information;
- Continuously stimulating advances in the aerospace sciences relevant to strengthening the common defence posture;
- Improving the co-operation among member nations in aerospace research and development;
- Providing scientific and technical advice and assistance to the North Atlantic Military Committee in the field of aerospace research and development;
- Rendering scientific and technical assistance, as requested, to other NATO bodies and to member nations in connection with research and development problems in the aerospace field;
- Providing assistance to member nations for the purpose of increasing their scientific and technical potential;
- Recommending effective ways for the member nations to use their research and development capabilities for the common benefit of the NATO community.

The highest authority within AGARD is the National Delegates Board consisting of officially appointed senior representatives from each member nation. The mission of AGARD is carried out through the Panels which are composed of experts appointed by the National Delegates, the Consultant and Exchange Programme and the Aerospace Applications Studies Programme. The results of AGARD work are reported to the member nations and the NATO Authorities through the AGARD series of publications of which this is one.

Participation in AGARD activities is by invitation only and is normally limited to citizens of the NATO nations.

The content of this publication has been reproduced
directly from material supplied by AGARD or the authors.

Published February 1986

Copyright © AGARD 1986
All Rights Reserved

ISBN 92-835-1519-6



*Printed by Specialised Printing Services Limited
40 Chigwell Lane, Loughton, Essex IG10 3TZ*

PREFACE

This AGARDograph presents a comprehensive, up-to-date review of the shock-wave boundary-layer interaction problem. A detailed physical description of the phenomena for transonic and supersonic speed regimes is given based on experimental observations, correlations, and theoretical concepts. Approaches for solving the problem are then reviewed in depth. Specifically, these include: global methods developed to predict sudden changes in boundary-layer properties; integral or finite-difference methods developed to predict the continuous evolution of a boundary-layer encountering a pressure field induced by a shock wave; coupling methods to predict entire flow fields; analytical methods such as multi-deck techniques; and finite-difference methods for solving the time-dependent Reynolds-averaged Navier-Stokes equations used to predict the development of entire flow fields. Examples are presented to illustrate the status of the various methods and some discussion is devoted to delineating their advantages and shortcomings. Reference citations for the wide variety of subject material are provided for readers interested in further study.

* * *

Cet AGARDograph présente une revue d'ensemble et mise à jour des problèmes d'interaction onde de choc/couche limite, en régime turbulent principalement. Dans une première partie, les phénomènes physiques rencontrés aux vitesses transsoniques et supersoniques sont décrits de manière détaillée en s'appuyant sur de nombreuses observations expérimentales, des lois de corrélations et certains concepts théoriques. Dans une seconde partie, les différentes approches utilisées pour modéliser le phénomène sont présentées et discutées en profondeur. Celles-ci comprennent: les méthodes globales dont l'objectif est de calculer le changement brutal que les propriétés de la couche limite subissent au cours de l'interaction; les méthodes intégrales ou aux différences finies qui permettent le calcul continu de l'évolution d'une couche limite rencontrant un champ de pression induit par une onde de choc; les techniques de couplage fluid parfaît-fluide visqueux qui permettent de calculer l'ensemble du champ aérodynamique; les techniques analytiques du type modèle multi-couches, et enfin les méthodes aux différences finies résolvant les équations de Navier-Stokes moyennées en temps qui sont appliquées à l'ensemble de l'écoulement. Des exemples d'application sont brièvement discutés. L'ouvrage contient un grand nombre de références couvrant l'ensemble du sujet et destinées à aider le lecteur intéressé par la recherche d'une plus ample information.

CONTENTS

	Page
PREFACE	iii
INTRODUCTION	1
 <u>PART I: A PHYSICAL DESCRIPTION OF SHOCK-WAVE/BOUNDARY-LAYER INTERACTIONS</u>	
1 GENERAL COMMENTS	3
1.1 Introductory Remarks	3
1.2 The Structure of a Turbulent Boundary-Layer	4
1.3 Upstream Influence	6
1.4 References	7
2 INTERACTION IN TWO-DIMENSIONAL TRANSONIC FLOWS	8
2.1 Some Specific Characteristics of Transonic Flows	8
2.2 Importance of Viscous Effects in Transonic Flows	8
2.3 Phenomenological Description of Transonic Viscous Interaction on an Airfoil	9
2.4 Scaling Effects in Transonic Flows	11
2.5 Basic Experimental Arrangements Used in Transonic Interaction Studies	12
2.6 Transonic Interaction Without Boundary-Layer Separation	14
2.6.1 The General Flow Structure	14
2.6.2 Scaling Laws for the Interaction Domain	16
2.6.3 Development of the Dissipative Layer Properties	20
2.7 Incipient Shock-Induced Separation in Transonic Separation	22
2.7.1 Physical Description of Incipient Separation	22
2.7.2 Prediction of Incipient Shock-Induced Separation	23
2.8 Interaction with Boundary-Layer Separation	28
2.8.1 The Outer Flow Field Structure	28
2.8.2 Correlation Properties of the Wall Pressure Distributions	32
2.8.3 Development of the Dissipative Layer Properties	33
2.9 Examination of Certain Turbulence Properties	40
2.9.1 Introductory Remarks	40
2.9.2 General Structure of the Turbulence Field	41
2.9.3 Specific Characteristics of Turbulence in the Interacting Flow	43
2.9.4 Some Remarks on the Problem of Turbulence Modeling	44
2.10 References	48
3 INTERACTION IN TWO-DIMENSIONAL SUPERSONIC FLOWS	51
3.1 The Four Basic Interactions	51
3.2 The General Flow Field Structure	51
3.2.1 The Compression Ramp Flow	51
3.2.2 The Impinging-Reflecting Oblique Shock	53
3.2.3 Flow Produced by a Forward Facing Step	56
3.2.4 The Reattaching Supersonic Flow	58
3.2.5 Concluding Remarks	58
3.3 Properties of the Wall Pressure Distribution	59
3.4 Some Features of Shock-Wave/Boundary-Layer Interaction in Laminar Flows	61
3.5 Transitional Interactions	63
3.6 The Free Interaction Concept	64
3.7 Scaling Properties of the Supersonic Interaction Streamwise Extent	67
3.7.1 Introductory Remarks	67
3.7.2 The Upstream Interaction Length. General Properties	68
3.7.3 Correlation Laws for the Upstream Interaction Length at High Reynolds Numbers	69
3.7.4 The Upstream Interaction Length in Non-Adiabatic or Axisymmetric Flows	71
3.7.5 The Separation Length	71
3.7.6 Concluding Remarks	73
3.8 Incipient Shock-Induced Separation in Supersonic Flows	73
3.8.1 Introductory Remarks	73
3.8.2 Techniques Used for the Detection of Incipient Separation	73
3.8.3 The Experimental Incipient Separation Limit	75
3.8.4 Simplified Models for Predicting Incipient Separation in Supersonic Flows	76
3.8.5 Concluding Remarks	80
3.9 Development of the Dissipative Layer Properties	80
3.9.1 The Mean Flow Field	80

	Page
3.9.2 The Turbulent Field	82
3.9.3 Concluding Remarks	84
3.10 References	85
4 INTERACTION IN THREE-DIMENSIONAL FLOWS	90
4.1 Introductory Remarks	90
4.2 Separation in Three-Dimensional Flows	90
4.3 Typical Interactions in 3-D Flows	93
4.3.1 Interaction at a Swept Corner	93
4.3.2 The Skewed Shock-Wave Interaction	95
4.3.3 Obstacle Induced Interaction	98
4.3.4 Transonic Flow Over a Swept Wing	100
4.4 Incipient Shock-Induced Separation in 3-D Flows	103
4.5 References	105

PART II: METHODS OF CALCULATION

1 GLOBAL METHODS	109
1.1 Introductory Remarks	109
1.2 Two-Dimensional Interactions	110
1.2.1 Simplified Boundary-Layer Integral Methods	110
1.2.2 Control Volume Methods	115
1.3 Three-Dimensional Interactions	123
1.3.1 General Comments	123
1.3.2 Simplified Boundary-Layer Integral Methods	124
1.3.3 Control Volume Methods	124
1.4 Inviscid Shear Layer Analyses	126
1.5 References	128
2 METHODS FOR THE CALCULATION OF THE CONTINUOUS DEVELOPMENT OF THE BOUNDARY-LAYER	130
2.1 Introductory Remarks – The Inverse Mode of Calculation	130
2.2 Integral Methods	131
2.2.1 Basic Principles and Equations	131
2.2.2 Methods Using the Mean-Flow Kinetic Energy Equation	132
2.2.3 Methods Using the Entrainment Equation	134
2.2.4 Methods Using the Moment of Momentum Equation	136
2.3 Finite-Difference Methods	139
2.3.1 Earlier Inverse Methods	139
2.3.2 Carter's Methods and Derived Methods	140
2.3.3 Ardoneau's Inverse Method	145
2.3.4 Other Inverse Methods	146
2.4 Extension to 3-D Boundary-Layer Flows	146
2.4.1 General Remarks on Boundary-Layer Separation in 3-D Flows	146
2.4.2 Integral Inverse Methods	147
2.4.3 Finite-Difference Inverse Methods	148
2.5 References	150
3 INVISCID-VISCOUS INTERACTIVE METHODS	150
3.1 Basic Principles	153
3.2 The Problem of the Coupling Conditions	153
3.2.1 The Various Forms of the Coupling Equation	153
3.2.2 Subcritical and Supercritical Boundary-Layers	155
3.2.3 Weak and Strong Interactions	157
3.3 The Problem of the Iterative Procedure	158
3.3.1 Entirely Supersonic Interactions	158
3.3.2 Mixed Supersonic-Subsonic Flows	159
3.3.2.1 Direct, Inverse and Semi-Inverse Methods	159
3.3.2.2 Convergence Properties of Direct and Inverse Methods	160
3.3.2.3 Semi-Inverse Methods	161
3.4 Higher Order Methods	165
3.5 Application of Inviscid-Viscous Interactive Methods to Flows Containing Shock-Waves	166
3.6 References	168
4 ANALYTICAL METHODS OR MULTI-DECK MODELS	171
4.1 The Lighthill Multi-Deck Model	171

	Page
4.2 Multi-Deck Theories in Laminar Flows	172
4.2.1 Asymptotic Expansion Methods	172
4.2.1.1 Stewartson and Williams' Theory of Self-Induced Separation in Supersonic Flows	172
4.2.1.2 The Free Interaction Theory in Transonic Flows	172
4.2.2 The Tu and Weinbaum Non Asymptotic Triple-Deck Model	177
4.3 Multi-Deck Theories in Turbulent Flows	178
4.3.1 Asymptotic Expansion Methods	178
4.3.1.1 The Limiting Process in Turbulent Flows	178
4.3.1.2 Melnik and Grossman's Theory for Normal Shock Wave	178
4.3.1.3 Adamson and Messiter's Theory for Normal Shock Wave	178
4.3.1.4 Adamson and Feo's Theory for Oblique Shock-Wave	178
4.3.2 Small Perturbation Methods	185
4.3.2.1 Inger's Theory for Normal Shock-Wave	185
4.3.2.2 Bohning and Zierep's Theory for Normal Shock-Wave	185
4.4 References	191
5 REYNOLDS-AVERAGED NAVIER-STOKES CALCULATIONS METHODS	194
5.1 Introductory Remarks	194
5.2 Governing Equations	194
5.2.1 The Reynolds-Averaged Navier-Stokes Equations	194
5.2.2 The Turbulence Modeling Problem	194
5.2.3 The Equations for Plane Flow	194
5.3 Solution Methods and Turbulence Models	195
5.3.1 Explicit Methods	195
5.3.2 Hybrid Methods	196
5.3.3 Implicit Methods	196
5.3.3.1 Turbulence Models Used in the Implicit Methods	196
5.3.3.2 A Modified Zero-Equation Model	196
5.4 Experimental Requirements	197
5.5 Examples of Navier-Stokes Computations	198
5.5.1 General Comments	198
5.5.2 Impinging Oblique Shock-Waves	199
5.5.3 Supersonic Compression Corner	201
5.5.4 Glancing Shock-Waves	203
5.5.5 Normal-Shock-Wave Interaction	206
5.5.6 Transonic Flows with Shock-Waves	209
5.5.7 Unsteady Flows	210
5.6 Concluding Remarks	211
5.7 References	212
ACKNOWLEDGEMENTS	216

INTRODUCTION

The interactions of a shock-wave with a boundary-layer can have a significant influence on aircraft or missile performance. Drag rise, flow separation, adverse aerodynamic loading, high aerodynamic heating, and poor engine inlet performance are but a few examples of its deleterious influence. Although the problem has received much attention and study, it remains an unresolved fluid mechanics issue. It has been a decade since Hankey and Holden (1975) compiled the last AGARDograph on the subject. Their publication augmented the very comprehensive review by Green (1970) who discussed many of the physical aspects of the problem and some of the methods for predicting its behavior, particularly for the unseparated case (see also the lecture series by Stanewsky, 1973 and by Leblanc, 1976). The 1975 AGARDograph introduced newly emerging theoretical developments on viscous-inviscid coupling, provided a preliminary look into numerical simulations of the Navier-Stokes equations, and extensively reviewed the new experimental work on hypersonic interactions. Since then, rapid developments in computational fluid dynamics and advanced instrumentation provided new opportunities to investigate this important phenomena, especially for the transonic and supersonic speed regimes. And, in those intervening years a certain maturation of the subject has taken place. It is the purpose of this AGARDograph to provide a comprehensive review of the subject in light of these new developments and maturation. Emphasis is therefore placed on high Reynolds number turbulent flows for the transonic and supersonic speed regimes.

The first part of the report presents a physical description of the phenomenon for transonic and supersonic flows based on experimental observations, correlations, and theoretical concepts. The second part presents an in-depth review of various methods used to predict the phenomenon. It begins with methods used to predict the properties of a turbulent boundary-layer encountering a pressure disturbance due to the presence of a shock-wave. There is some overlap in this description with the material covered by Green (1970). However, the authors felt this was necessary to fulfill the requirement of completeness and because of the maturation of some of the concepts. Subsequent discussion deals with coupling methods involving the modeling of viscous and inviscid regions for the purpose of predicting entire flow fields. Then, analytic methods involving multi-deck techniques which provide insight into the physical aspects of the localized phenomena are reviewed. The discussion ends with methods for solving the time-dependent Reynolds-averaged Navier-Stokes equations now being developed to predict entire flow fields. Turbulence modeling necessary for implementing the coupling and Navier-Stokes methods are discussed. Examples are presented throughout the report to support the appropriateness of the various methods and to provide an up-to-date status of their development. The authors have attempted to make the various sections complete and self-consistent in order to facilitate the needs of some readers who may not want to review the complete subject.

References

Green, J.E. (1970): Interactions Between Shock Waves and Turbulent Boundary Layers. Progress in Aerospace Sciences, Vol. 11; edited by D. Küchemann et al, Pergamon Press, Oxford.

Hankey, W.L. and Holden, M.S. (1975): Two Dimensional Shock Wave-Boundary Layer Interactions in High Speed Flows; AGARDograph n° 203, (June 1975).

Leblanc, R. (1976): Recent Progress in Shock Wave Boundary-Layer Interaction. VKI, LS-84 on "Transonic Blade to Blade Flow in Axial Turbomachinery" (Feb. 1976).

Stanewsky, E. (1973): Shock-Boundary Layer Interaction in Transonic and Supersonic Flows. VKI, LS-59 on "Transonic Flow in Turbomachinery" (May 1973).

PART I - A PHYSICAL DESCRIPTION OF SHOCK-WAVE/BOUNDARY-LAYER INTERACTION

1 - GENERAL COMMENTS

1.1 - Introductory Remarks

In analyzing flows past obstacles, both from a theoretical and a phenomenological point of view, it is customary to conceptually divide the field into distinct zones consisting of :

i - regions where viscous effects play a negligible role. There the flow is said to behave like a perfect fluid which means that dissipative effects are (practically) nonexistent. In these regions, the fluid motion can be accurately computed by solving the Euler equations (or a simplified form of these equations if further simplifying assumptions are verified: e.g. irrotationality...). Frequently, the perfect fluid region is called the "outer" or "external" flow field.

ii- regions where viscosity must play a predominant role, namely: boundary-layers, wakes, mixing zones..

Except when the Reynolds number is very low, the viscous or dissipative regions are most often thin when compared to a characteristic dimension of the obstacle (e.g. the chordlength of an airfoil). However, it should be pointed out that even at high Reynolds number, circumstances can be met where the dissipative zones have a thickness comparable to that of the obstacle. This is the case when a boundary-layer separates in a situation leading to the development of a large separated bubble. Such a situation is encountered, for example, when an airfoil is stalled or in a strongly overexpanded nozzle in which the flow separates far upstream of the exit plane.

In this AGARDograph, we will only consider flows with sufficiently high Reynolds number for the classical Prandtl boundary-layer concept to be applicable to the incoming flow which will meet the shock-wave. That means that the yet undisturbed boundary-layer approaching the shock region can be represented in terms of classical boundary-layer concepts. Also, the conditions will be such that the shock structure has a negligible thickness when compared to the various macroscopic scales of the boundary-layer (see Section 1.2 below for more information on the turbulent boundary-layer structure).

Thus, we shall consider the problem of a shock-wave propagating in a transonic or supersonic stream and that "interacts" with the boundary-layer developing on an obstacle. Before going into a detailed examination of the so-called interaction process, it can be useful, for future interpretation of the observed phenomena, to briefly recall the essential features of a boundary-layer flow.

Basically, a boundary-layer is a thin layer across which the flow velocity decreases from the (high) external value to zero at the wall where the no-slip condition must be satisfied. At the same time, the Mach number varies from the outer value M_e to zero. Since the static pressure is transversally constant across it, the boundary-layer can be viewed as a quasi-parallel flow with variable entropy from one streamline to the other, or which is equivalent, as a quasi-parallel rotational flow.

Anticipating forthcoming explanations, it seems reasonable to consider that when a shock-wave propagates through such a dissipative-layer, the viscous forces (resulting both from "true" laminar viscosity and "apparent" turbulent viscosity) have locally a negligible influence over the major part of the flow. This fact will be experimentally and theoretically justified in the forthcoming Sections. However, such behavior can be intuitively understood if it is realized that the shock-wave imparts to the flow such an intense deceleration that - on the macroscopic scale - the viscous forces become temporarily negligible vis à vis the inertial and pressure forces. (In reality, shock-waves are viscous phenomena but on a microscopic scale in most usual situations. Thus, for our purpose, shocks will be considered as perfect discontinuities).

According to the above remarks, for a first and crude schematization of the phenomenon, the shock penetration into a boundary-layer can be viewed as a perfect fluid problem and some general trends can be inferred without consideration of dissipative terms. However, it should be pointed out that a purely inviscid flow model necessarily leads to inconsistencies in the near wall region where viscous terms must be predominant because of the no-slip condition at the wall (this problem will be discussed in detail in Section 4 of Part II). Nevertheless, this so-called "inner viscous layer" is excessively thin, especially in turbulent flows, so that its influence can be assumed of secondary importance.

When a shock-wave propagates through a boundary-layer, it "sees" an upstream flow of lower and lower Mach number as it approaches the wall. The shock must adapt itself to this situation so that it becomes vanishingly weak when it reaches the place where the Mach number is sonic. Moreover, the "pressure signal" carried by the shock is necessarily transmitted in the upstream direction through the subsonic inner part of the boundary-layer. Thus, the pressure rise caused by the shock is "felt" upstream of the point where the shock would meet the surface in the perfect fluid model, i.e., in a flow without boundary-layer. Conversely, the thickening of the boundary-layer subsonic channel, resulting from a rise in pressure, generates compression waves in the adjacent supersonic layer. These waves will in turn weaken the shock wave, according to a mechanism which will be analyzed in more detail in following Sections.

The above simple reasoning shows that a very complex mechanism will take place in such a way that there is a reciprocal influence between the shock-wave and the boundary-layer. This rapid description takes into consideration only one aspect of the various phenomena involved in a shock-wave/boundary-layer interaction. Its purpose is to emphasize the crucial importance of the velocity distribution - and hence the Mach number distribution - of the incoming boundary-layer. Thus, before going into a more thorough examination of shock interaction problems, it is certainly useful to recall some basic properties of a turbulent boundary-layer, since this AGARDograph will be mainly concerned with turbulent flows.

1.2 - The Structure of a Turbulent Boundary-Layer

Experimental observation shows that a "well behaved" or "equilibrium" turbulent boundary-layer has a composite nature. One successively distinguishes, as schematically shown in Fig. 1.1 :

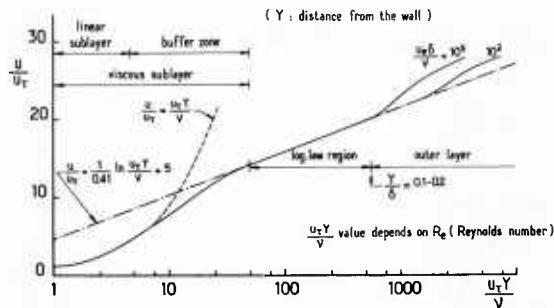


Fig. 1.1 – Structure of a well "behaved" turbulent boundary-layer.

i - a viscous sublayer very close to the wall, in which (molecular) viscosity is essential. This sublayer can be further divided into: a linear sublayer, in contact with the wall, where the velocity is a linear function of the ordinate y , and a buffer layer which insures a smooth transition with the adjacent non-linear region.

ii - a log-law region. With the use of the conventional profile representation : $u/u_T = f(u_T y/\nu)$ - where $u_T = \sqrt{\tau_w/\rho}$ is a scaling velocity (often called the "friction" velocity) - all well behaved boundary-layers collapse into a single curve independent of Reynolds number

iii- an outer region which is a wake-like region, that is independent of the Reynolds number but dependent on the outer flow field, e.g., pressure gradient,

A faithful and widely used analytical representation of the velocity distribution across an incompressible turbulent boundary-layer was given by Coles (1956). It consists in a combination of the law of the wake-law of the wall (logarithmic region) written in the form :

$$(1.1) \quad u/u_T = (1/k) \ln(yu_T/\nu) + c + (\tilde{\pi}/k) w(y/\delta)$$

In this equation, k and C are two constants (usually $k = 0.41$ and $C = 5.1$), $\tilde{\pi}$ is a "form factor" whose value determines the "strength" of the wake-component (for a flat-plate $\tilde{\pi} = 0.55$, it increases when the boundary-layer is submitted to an adverse pressure gradient), and $w(y/\delta)$ is the "wake function".

For our purpose, it is more convenient to express the velocity ratio in terms of u_e , the value of u at the boundary-layer outer edge. Thus, Eq. 1.1 is written in the form :

$$u/u_e = u_T/u_e (1/k) [\ln(yu_T/\nu) + c + (\tilde{\pi}/k) w(y/\delta)]$$

Writing this equation for $y = \delta$, gives :

$$(1.2) \quad 1 = u_T/u_e [(1/k) \ln(\delta u_T/\nu) + c + 2\tilde{\pi}/k]$$

(the function w having been normalized in such a way that its value at $y = \delta$ is 2).

Combining Eqs. 1.1 and 1.2 gives :

$$(1.3) \quad u/u_e = 1 + (1/k) \{ \ln(\delta/\delta^*) + \tilde{\pi} [2 - w(\delta/\delta^*)] \}$$

In terms of more usual boundary-layer parameters, $\tilde{\pi}$ is determined by the equation :

$$(1.4) \quad \tilde{\pi} = k (u_e/u_T) (\delta^*/\delta) - 1$$

where δ is the boundary-layer displacement thickness. Equation 1.3 can also be written in the form :

$$(1.5) \quad u/u_e = 1 + (1/k) (u_T/u_e) \ln(y/\delta) - (\delta^*/\delta - u_T/ku_e) [2 - w(y/\delta)]$$

which eliminates the singularity presents in Eq. 1.3 at the separation point where $\tilde{\pi}$ tends to infinity. According to Coles' formula, at a separation or a reattachment station $u_T = 0$, which suppresses the logarithmic component of the profile representation.

Introducing the Reynolds number $R_\delta = \frac{u_e \delta}{\nu}$ and taking Eq. 1.4 into account, Eq. 1.2 can be written :

$$(1.6) \quad 1. = u_\tau / u_e [(1/k) \ln (R_\delta u_\tau / u_e) + C + 2 (u_e \delta^* / u_\tau \delta - 1/k)]$$

Remembering that from the definition of the friction velocity (in incompressible flow), one has $u_\tau / u_e = (0.5 Cf)^{1/2}$, Eq. 1.6 provides an equation to compute the skin-friction coefficient knowing the Reynolds number R_δ and the profile "shape parameter" δ^* / δ .

According to Coles' hypothesis, $w(y/\delta)$ is a universal function common to all two-dimensional incompressible boundary-layer flows. This function is determined from correlation of experimental data and, for practical purposes, it is frequently represented by the following analytical formula :

$$w(y/\delta) = 1 - \cos(\pi y/\delta)$$

It is to be noticed that Eq. 1.1 (or 1.5) is not valid near the wall since the log term tends to minus-infinity when y approaches zero. However, at usual Reynolds numbers, Eq. 1.1 (or 1.5) can be utilized for very small values of y/δ , with realistic results still being given for $y/\delta = 0.01$. In general, Eq. 1.1 (or 1.5) is sufficient for estimating the boundary-layer global properties. If one needs more accurate information on the velocity distribution and especially on the laminar sublayer, more sophisticated analytical representations are available (see Sections 1 and 2 of Part II).

As shown by Maise and Mc Donald (1967) it is possible to derive a good representation of the velocity distribution in a compressible turbulent boundary-layer by using the Van Driest generalized velocity concept. Thus, in compressible flows, the velocity profile will be given by :

$$(1.7) \quad u/u_e = (1/a) \sin [a (u_\tau / k u_e) \{ \ln (y/\delta) - \frac{\gamma}{\pi} [2 - w(y/\delta)] \} + \sin^{-1} a]$$

where $a = \{0.5r(\gamma-1) M_e^2 / [1+0.5r(\gamma-1) M_e^2]\}^{1/2}$, r being the recovery factor.

However, for an adiabatic wall (i.e., no heat transfer at the wall) and moderate external Mach number M_e ($M_e < 2$), the effect of compressibility on the velocity profile is weak, so that Eq. 1.5 can still be used. The essential difference with an incompressible flow is that the shape parameter will then be defined with the "incompressible" displacement thickness :

$$\delta_i^* = \int_0^\delta (1 - u/u_e) dy$$

and not with the "true" or compressible displacement thickness.

Thus, at a given Mach number, the velocity distribution depends on two-parameters : namely, the skin-friction coefficient and δ_i^*/δ (or $\tilde{\pi}$) ; or (which is equivalent) on the Reynolds number R_δ and δ_i^*/δ .

It is more usual to characterize the shape of the velocity distribution by using the following "incompressible" shape parameter (or form factor) :

$$H_i = \delta_i^*/\theta_i$$

where θ_i is the "incompressible" momentum thickness defined as :

$$\theta_i = \int_0^\delta (u/u_e) (1 - u/u_e) dy$$

As it is a simple matter to deduce H_i from δ_i^*/δ by numerical integrations on the velocity profile, henceforward, we will definitively adopt H_i as shape parameter (the word "incompressible" being omitted). To conclude, one sees that the velocity distribution of a so-called "well behaved" or "equilibrium" turbulent boundary-layer is entirely determined from the knowledge of H_i and R_δ (plus perhaps the Mach number. Furthermore, the flow is assumed adiabatic).

As a matter of fact, H_i and R_δ are not always entirely independent. For a well-behaved flat-plate boundary-layer, H_i is a unique function of the Reynolds number (and of the Mach number). There exist several well-known correlation laws allowing the calculation of H_i from given values of R_δ and M_e . They generally lead to nearly identical results. One of these laws (Clauser, 1954) has been used to compute the variations of H_i with R_δ shown in Fig. 1.2. One notes that for a flat-plate H_i is weakly dependent on the Mach number. An increase in the Reynolds number provokes a decrease of the shape parameter. This decrease in H_i reflects a "filling" of the velocity distribution as the Reynolds number rises.

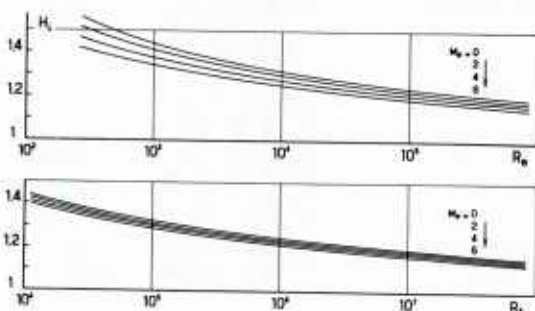


Fig. 1.2 – Flat plate turbulent boundary-layer – Incompressible shape parameter.

For a fixed value of R_δ , H_i can be varied by submitting the boundary-layer to some external constraint : e.g., a pressure gradient, injection or aspiration at the wall or rough-wall effect...

The change in the shape of the velocity profile with varying H_i , at constant Reynolds number, is illustrated in Fig. 1.3 (the drawn profiles have been computed by using Eq. 1.5). The higher H_i the less "filled" is the profile and, consequently, the less the kinetic energy carried. Thus we can already guess that a boundary-layer having a high shape parameter will be more sensible to adverse external agencies. The importance of the boundary-layer shape parameter, specially in transonic interactions, seems to have been pointed out first by Panaras and Inger (1977).

To conclude the present Section, the curves traced in Fig. 1.4 give the skin-friction coefficient of an equilibrium flat-plate boundary-layer. These curves can be helpful for the interpretation of results presented in forthcoming Sections.

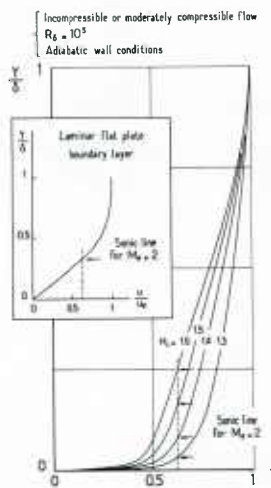


Fig. 1.3 – Velocity distribution in a turbulent boundary-layer (from Coles law of the wall/law of the wake).

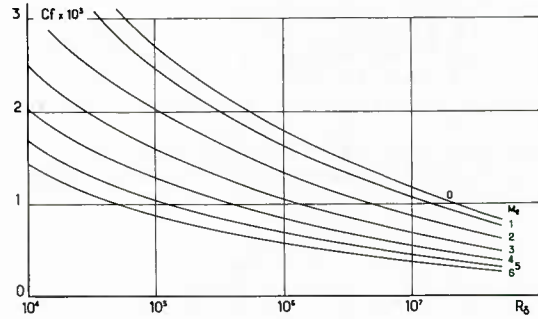


Fig. 1.4 – Flat plate turbulent boundary-layer – Skin friction coefficient

1.3 - Upstream Influence

Let us consider the case of an oblique shock-wave produced in a supersonic flow by a wedge (or compression ramp). For this configuration, it is possible to define unambiguously an upstream interaction length L_o as the distance between the corner which would be the origin of the shock in perfect fluid flow (provided that the deflection angle is not such that the shock is detached) and the point where the existence of the shock is first felt in the real viscous flow.

According to previous remarks, L_o appears as being essentially a function of the height y^* of the subsonic part of the boundary-layer since this part constitutes the "channel" through which the shock effect can be transmitted in the upstream direction. Thus, it can be forecasted that for a given external Mach number, i.e., a given shock-strength, the thicker the subsonic layer, the longer the upstream influence length.

The ordinate y^* depends on the external Mach number, on the velocity and temperature distributions across the boundary-layer as well as on the boundary layer thickness δ (the temperature profile which determines the speed of sound distribution depends mainly on the thermal situation at the wall). Thus, for a turbulent boundary-layer, the normalized ordinate y^*/δ depends on : M_e , R_δ , H_i and on the ratio T_w/T_{te} of the wall temperature to the external stagnation temperature.

In order to give some idea of the value of y^*/δ , Fig. 1.5 shows evolutions of y^*/δ with M_e , H_i and T_w/T_{te} , the Reynolds number being kept constant. Examination of these curves leads to the following remarks :

- i - in a turbulent boundary-layer, the sonic line rapidly approaches the wall as the outer Mach number increases. Hence, it can already be anticipated that the upstream influence length will be much shorter in turbulent flows than in laminar flows (as shown by the insert of Fig. 1.3, the subsonic layer of a laminar flow is far thicker).
- ii - when H_i increases, the velocity profile becomes less filled and, consequently, the subsonic layer is thicker. Hence, in principle, to a greater H_i will correspond a longer upstream influence length. As H_i decreases when R_δ increases for a flat-plate boundary-layer (see Fig. 1.2), we can anticipate a decrease in L_o for increasing Reynolds number. However, this conclusion should be tempered, since the above tendency is not always observed at low Reynolds number.
- iii - cooling the wall ($T_w/T_{te} < 1$) reduces the speed of sound throughout the boundary-layer. Consequently, the Mach number level is raised, especially in the vicinity of the wall: hence, a thinning of the subsonic layer leading to a reduction of the upstream influence length.

A more complete examination of the upstream propagation of shock influence will be presented in the forthcoming Sections, firstly from experimental observations, then by considering theoretical arguments. It will also be seen how the fullness of the initial boundary-layer profile plays a determinant role in the "resistance" of that boundary-layer to Shock Induced Separation. This problem will be thoroughly discussed in Sections devoted to Incipient Separation.

A second parameter of influence is the relative importance of the viscous and inertia forces in the lower part of the boundary-layer. As seen from intuitive arguments and from consideration of the momentum equation, these forces have contrary effects. The above demonstration puts an emphasis on inertia forces in the sense that the "fullness" for the incoming boundary-layer profile is presented as playing the essential role in the interaction mechanism. In fact, this behavior seems to be true only at high Reynolds numbers. At low to moderate Reynolds numbers, the interaction tends to be dominated by viscous effects, in accordance with the Free Interaction Theory presented in Section 3 below. The situation is illustrated by Fig. 1.6 which shows the variation of the sonic layer and viscous layer locations with the Reynolds number for a flat plate turbulent boundary-layer at an outer Mach number of 3 (Settles, 1975). One sees that at low Reynolds number ($R_\delta < 5 \cdot 10^5$), the viscous layer thickness is comparable to that of the sonic layer. But, as the Reynolds number increases, the relative thickness of the viscous layer decreases rapidly and at $R_\delta > 10^7$, it is an order of magnitude thinner than the sonic layer. The consequences of this behavior will be commented on in forthcoming Sections.

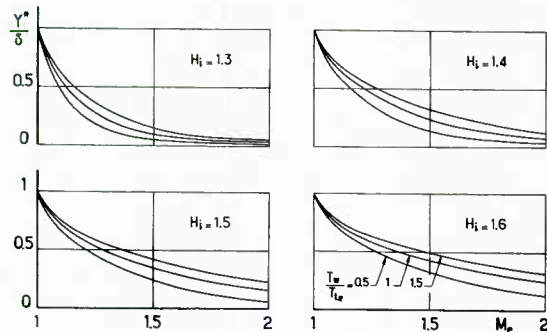


Fig. 1.5 – Location of the sonic line in a turbulent boundary-layer – Wall temperature effect.

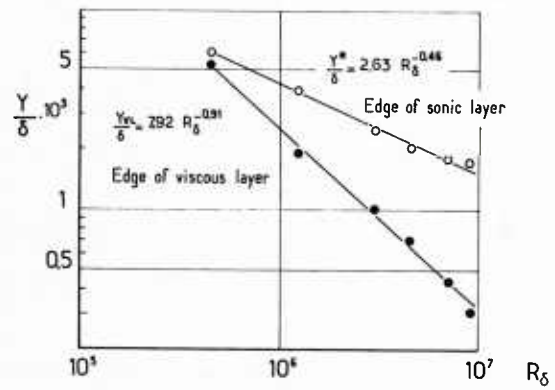


Fig. 1.6 – Flat plate boundary-layer at $M = 3$ – Location of sonic layer and viscous layer edge (Settles, 1975).

1.4 – References

Clauser, F.H. (1954): Turbulent Boundary-Layer in Adverse Pressure Gradient. JAS, Vol. 21, N° 2, pp. 91-108 (Feb. 1954).

Coles, D.E. (1956): The Law of the Wake in Turbulent Boundary-Layer. J. Fluid Mech., Vol. 1, Part 2, pp. 191-226.

Maise, G. and Mc Donald, H. (1967): Mixing Length and Kinetic Eddy Viscosity in a Compressible Boundary-Layer. AIAA Paper N° 67-199; see also AIAA Journal, Vol. 6, N° 1, pp. 73-80 (June 1968).

Panaras and Inger (1977): Transonic Normal Shock/Boundary-Layer Interaction in Pressure Gradient Flows. ASME Paper 77-GT-34.

Settles, G.S. (1975): An Experimental Study of Compressible Turbulent Boundary-Layer at High Reynolds Number. Ph. D. Dissertation, Aerospace and Mechanical Sciences Dept., Princeton University (Sept. 1975).

2 - INTERACTION IN TWO-DIMENSIONAL TRANSONIC FLOWS

2.1 - Some Specific Characteristics of Transonic Flows

Broadly speaking, a flow is said to be transonic when in the outer inviscid stream there exist regions where the Mach number is supersonic and regions where the Mach number is subsonic. This is in contrast to the situation envisaged in Section 3 below where the external stream remains supersonic throughout the region of interest. Hence, the essential characteristics of a transonic flow is that the inviscid part of the fluid is governed by equations of motion which are of the hyperbolic type in some domains - i.e., when the flow is supersonic - and of the elliptic type in other domains - i.e., when the flow is subsonic.

An essential feature of these flows is that the transition from supersonic to subsonic Mach number practically always takes place in an irreversible manner, i.e., by means of a shock-wave (except on shock-free supercritical airfoils which are specially designed to produce an isentropic compression on their upper surface in order to eliminate wave-drag, Whitcomb, 1974; Sobieczky et al., 1979).

An immediate consequence of the ellipticity of part of the outer inviscid flow is that the whole flow depends strongly on conditions prevailing well downstream of the shock interaction region. This fact constitutes a major difference with entirely supersonic outer streams, the flow structure in this later case being essentially determined by the upstream incoming state. Then, the influence of the downstream conditions via the boundary-layer is most often weak, except in the case of large separation.

Another typical feature of the envisaged transonic flows is that the shock-waves they contain are "normal" shock-waves, or more exactly, "quasi-normal" shock-waves. The expression "quasi-normal" means that in most transonic streams, the shocks are strong oblique shock, in the sense of the strong solution of the oblique shock equations (this fact will be established in Section 2.6). As opposed to this situation, in a Supersonic Interaction the shocks encountered are most often weak oblique shocks.

For the two kinds of interaction, however, a situation may exist in which shocks belonging to the other family are also present. For instance, in what is called a transonic lambda shock-system, the leading wave is a weak oblique shock (see section 2.8.1 below).

2.2 - Importance of Viscous Effects in Transonic Flows

Within the concept of Viscous-Inviscid Interaction, the effect of viscous (or dissipative) regions on the external inviscid stream can be interpreted :

- i - either as a change in the effective body-shape, according to the displacement body concept,
- ii - or as a modification of the usual condition enforced on the obstacle, according to the transpiration velocity concept (for more information, see Section 3 of Part II below).

Thus, for a fixed body geometry and unchanged outer boundary conditions at upstream and downstream infinity, local alteration of the boundary conditions "seen" by the outer inviscid stream are due to viscous effects, namely: boundary-layers, wakes....

Hence, considering the fact that in transonic flows, the field contains large elliptic regions, any change -even slight- in the boundary conditions at some specific location may entail dramatic repercussions on the structure of the whole flow field. This is particularly true for the position of a normal shock on an airfoil or in a transonic channel. Consequently, it is to be expected that viscous (we will also say "dissipative") effects, and particularly those taking place when a shock meets a boundary-layer, will be of special importance in transonic flows.

A demonstrative way to illustrate this point is to compare perfect fluid calculations to experiment. Here, we shall give a very limited number of such comparisons, many other examples can be found in the literature.

A dramatic example of the importance of viscous effects on a transonic airfoil is given in Fig. 2.1 (Wai and Yoshihara, 1981b). This case is relative to a supercritical airfoil. Here, experiment is compared to two perfect-fluid calculations: the first one uses the full potential equation, the second, the small disturbance approximation of this equation. Both calculations give a flow in which the shock on the upper surface is located practically at the airfoil trailing-edge; whereas, in reality, the shock occurs at about 30% of the chordlength. Accordingly, on the upper surface, there is a huge difference between the computed and the measured pressure distributions. Neglecting any inaccuracies in applying these inviscid methods where shock Mach numbers are above 1.3, the differences between computation and experiment can be attributed to the neglect of important viscous effects. In the present example, such a large discrepancy is due to the special shape of the airfoil: its upper surface is nearly flat over the major part of the chordlength, with a rear part highly cambered. Hence, any alteration of the airfoil contour in consequence of viscous effects, entails a large displacement of the shock in the perfect fluid calculation. Furthermore, for a highly rear-loaded airfoil, viscous effects are enhanced by the strong compression taking place in the trailing-edge region (see Section 2.3 below). The agreement between computations and experiment is also very poor on the lower surface. This is a consequence of the great change in circulation produced by viscous effects. To conclude, Fig. 2.1 shows a schematic representation of the computed and actual flow fields.

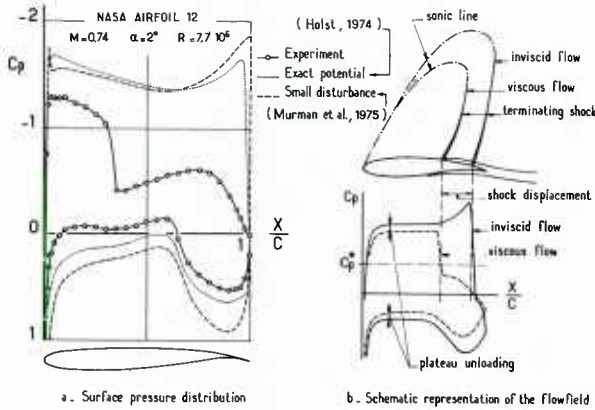


Fig. 2.1 – Importance of viscous effects on a supercritical airfoil.

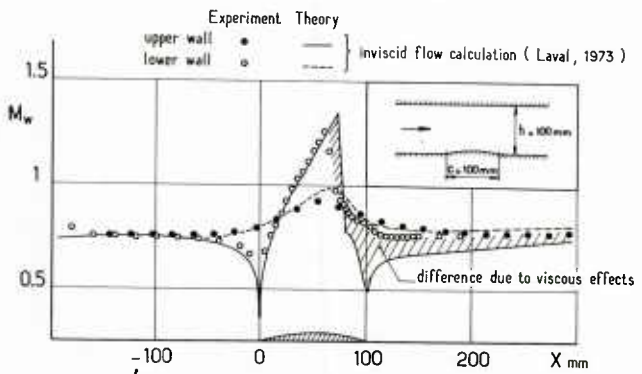


Fig. 2.2 – Example of viscous effects in a channel flow

The second example, shown in Fig. 2.2, is relative to the flow inside a two-dimensional transonic channel (Délery et al., 1973). In this arrangement, a circular half-profile (or bump) is mounted on the channel lower wall, the upper wall being flat (see sketch in Fig. 2.2). The figure shows the "wall" Mach number distributions on the upper and lower walls (the "wall" Mach number M_w is computed from the wall pressure by assuming an isentropic relationship and by considering the stagnation pressure as everywhere constant. Then entropy rise through the shock being here very small, M_w is practically equal to the Mach number at the boundary-layer edge, except in the shock foot region where non-negligible normal pressure gradients may exist).

The bump produces an acceleration of the flow to a velocity which is slightly supersonic near the lower wall. The supersonic pocket which forms is terminated by a shock located at a place where the Mach number is close to 1.25 in the immediate vicinity of the bump. One sees that the channel is not choked, the Mach number near the upper wall remaining subsonic.

The experimental values of M_w are here compared to distributions computed by solving the full Euler equations (Laval, 1973). In the upstream part of the channel, where viscous effects are weak (except in the immediate vicinity of the bump leading edge), agreement between perfect fluid theory and experiment is very good. On the other hand, one observes a large discrepancy between the computed and measured distributions in the downstream part of the bump as well as in the subsequent constant section channel. The origin of the discrepancy is to be found in the "strong" viscous interaction taking place in the shock foot region. This interaction provokes an important thickening of the boundary-layer with a sizeable modification of the channel "effective" geometry as an obvious consequence.

Before proceeding to a detailed local analysis of Transonic Shock-Wave/Boundary-Layer Interaction phenomena, it is useful to provide an overview of viscous interactions on a transonic airfoil, so as to emphasize the crucial role played by phenomena occurring in the shock foot region.

2.3 - Phenomenological Description of Transonic Viscous Interaction on an Airfoil

For an airfoil, viscous effects are of special importance in two regions: in the vicinity of the shock foot and near the trailing edge, the situation at the trailing edge being obviously strongly dependent on the previous history of the boundary-layer, which includes its interaction with the shock.

The phenomenological description of the flow development past an airfoil at transonic speed was given nearly thirty years ago by Pearcey (1955) (see also more recent publications by Pearcey et al., 1968). According to this well-known and now classical work, interactions entailing flow separation (which are of special importance for practical purposes) are classified into Type A and Type B separation patterns.

In Type A flows, a moderately strong shock induces a local thickening of the boundary-layer (see sketch in Fig. 2.3). As the free stream Mach number M_∞ (or incidence) is increased, the shock becomes stronger and a limit is reached where Incipient Separation occurs at the shock foot (see Section 2.7 on Incipient Shock Induced Separation in transonic flows).

Thereafter, a separation bubble forms at the shock foot and any further increase in Mach number (or incidence) beyond that stage results in the growth of the separation bubble. The progressive growth of the bubble is thus a characteristic feature of this type of flow with the separation point fixed at the shock foot and the reattachment point moving progressively downstream toward the trailing edge as the overall strength of the shock increases. According to Pearcey, such a situation does not depend much on the boundary-layer thickness at the shock foot (provided it is fully turbulent). The reason is that Incipient Separation is weakly dependent on the Reynolds number (see section 2.7.2 below). Furthermore, the growth of the separation bubble, in relation to an increase in the shock strength, is so rapid that the flow cannot be strongly influenced by scaling effects in the trailing edge region. In this situation, the rapid divergence of the trailing edge pressure and the correlative change in circulation occur as a consequence of a rapid bubble growth triggered from the shock foot. This kind of interaction, designated as Type A flow, occurs with moderate adverse pressure gradient downstream of the shock.

In Type B flows, a very strong recompression takes place in the rear part of the profile. This situation corresponds to highly rear-loaded airfoils, as is the case with supercritical airfoils (see first example given in the previous Section). The essential difference between this type and Type A is the inclusion of a second separation in the subsonic flow approaching the trailing-edge (see Fig. 2.3). This second separation is the classical subsonic, turbulent, rear-separation occurring in an adverse pressure gradient present on the rear part of an airfoil.

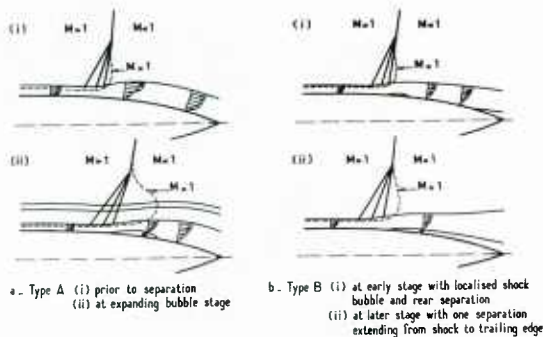


Fig. 2.3 – Transonic Interaction – Schematic representation of shock / turbulent boundary-layer on an airfoil (Pearcey, 1955)

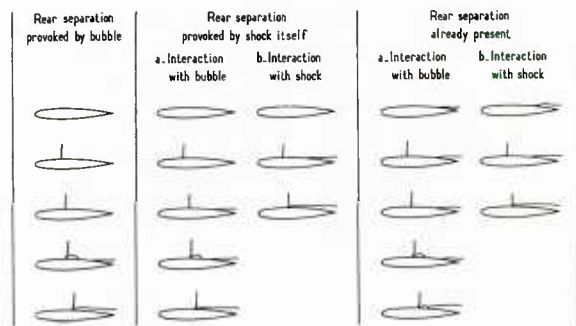


Fig. 2.4 – Transonic interactions – Shock/boundary-layer interaction on an airfoil – Variants of type B (Pearcey et al., 1968).

As is well known, the separation of a boundary-layer primarily depends on the two following factors:

- i - the local adverse pressure gradient imparted to the boundary-layer; or, more exactly, the pressure gradient scaled to the thickness δ of the boundary-layer,
- ii - the velocity distribution across the boundary-layer. A destabilized boundary-layer having a high shape parameter is more likely to separate than one with a low H_i .

The shock effect serves both to thicken the boundary-layer (which increases the intensity of the adverse pressure gradient) and to increase its shape parameter by "emptying" its velocity distribution. Hence, it is clear that the shock interaction will "catalyze" the development of a rear separation that was already either incipient or actually present in the subsonic rear gradients before shock-waves appeared.

In such circumstances, one can expect several variants of the Type B Flow (see Fig. 2.4):

- i - the shock interaction produces a bubble at the shock foot, thus a strong destabilisation of the boundary-layer which thereafter separates near the trailing edge;
- ii - the perturbation produced in an interaction without separation is strong enough to promote rear separation;
- iii - rear separation is already present in subsonic conditions, but the occurrence of a shock at higher Mach numbers worsens the situation by provoking a rapid extension of the rear separation.

For all these circumstances, an increase in the upstream Mach number or in the angle of attack, results in the formation of a large separated zone extending from the shock foot. The formation of this zone can be the consequence of the merging of the bubble present at the shock foot and of the rear separated zone.

A quantitative example of Type B Flow can be found in a paper by Stanewsky and Little (1971). These authors made experiments with a simulated airfoil contour installed near the lower wall of a small transonic wind tunnel (type b test set-up shown in Fig. 2.12). The evolution, with the free stream Mach number M_∞ , of the shock chordwise location and of the extent of the separated regions are shown in Fig. 2.5.

When M_∞ increases, one observes first a displacement of the shock towards the trailing edge. At the same time, the

size of each separated region increases, especially the size of the bubble forming at the shock foot. For M_∞ greater than 0.83, the two separated zones merge and one notices a temporary reversal in the shock motion, probably due to the large change in circulation which occurs when the airfoil is largely separated. This situation is illustrated by the schlieren photograph of Fig. 2.6 (according to Pearcey, 1955) which shows the flow structure past an airfoil with severe separation at the foot of the upper surface shock.

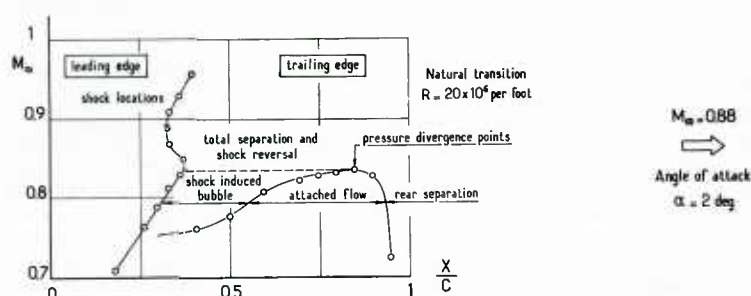


Fig. 2.5 – Example of type B flow – Shock location and development of separated regions on a two-dimensional airfoil contour (Stanewsky and Little, 1971).

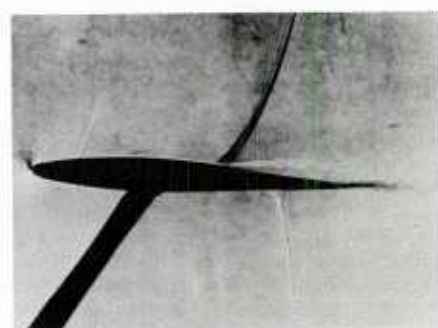


Fig. 2.6 – Transonic interaction on an airfoil schlieren photograph of the flow with severe separation at the foot of the upper-surface shock (Pearcey, 1955).

The progressive evolution from an unseparated to a largely separated situation is illustrated by the sequence of holographic interferograms shown in Fig. 2.7 to 2.9 (according to Johnson and Bachalo, 1978). The sequence corresponds to an increase of the angle of attack α for a symmetrical airfoil (NACA 64A010), the free stream Mach number being kept constant and equal to 0.8. For $\alpha=0$, a shock is already present in the flow, but there is no evidence of separation. For $\alpha=3.5$ deg., one observes an important thickening of the boundary-layer downstream of the shock and it is probable that separation occurs in a small region near the trailing edge. When $\alpha=6.2$ deg., a large separated region emanates from the shock foot. The situation is similar to the one shown in Fig. 2.6. Processing of the interferograms has permitted the tracing of the iso-Mach lines in the inviscid flow which are shown in Figs. 2.7 to 2.9. One notes that the shock induced separation (at $\alpha=6.2$ deg.) corresponds to a situation where the local Mach number at the boundary-layer edge, just upstream of the shock, is close to 1.3. This value is in good agreement with the correlation for Incipient Shock Induced Separation given in Section 2.7.2 below.

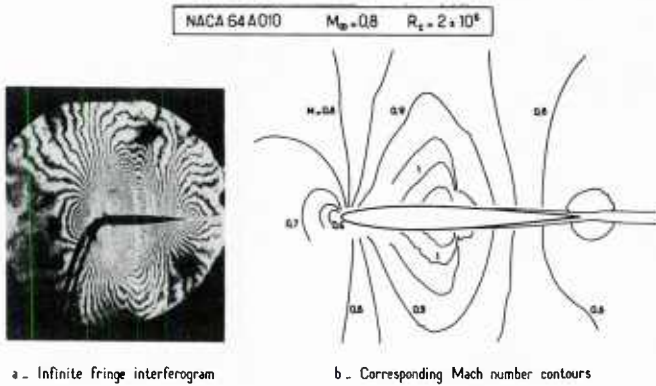


Fig. 2.7 – Transonic flow past an airfoil angle of attack $\alpha = 0$ deg. (Johnson, 1978).

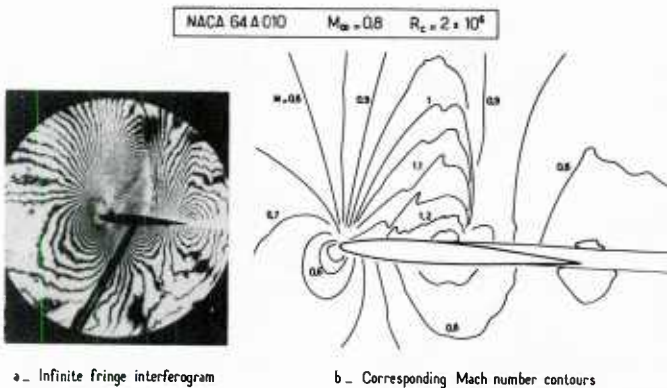


Fig. 2.8 – Transonic flow past an airfoil angle of attack $\alpha = 3.5$ deg. (Johnson, 1978).

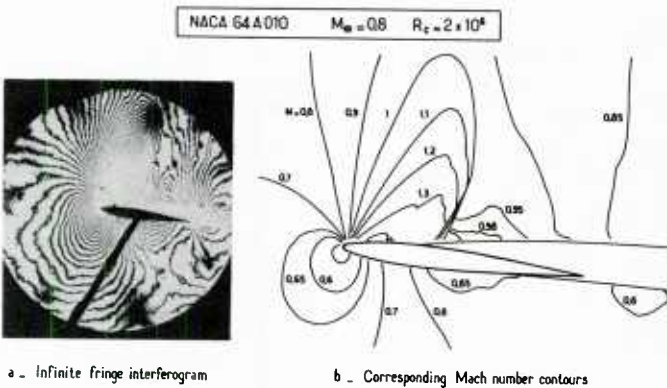


Fig. 2.9 – Transonic flow past an airfoil – Angle of attack $\alpha = 6.2$ deg. – Separation at the shock foot (Johnson, 1978).

2.4 – Scaling Effects in Transonic Flows

Consideration of viscous effects in transonic flows is also essential for the correct interpretation of wind tunnel tests made on small scale models. Differences in Reynolds number and "scaling effects" can lead to dramatic differences between wind tunnel experiments and flight results. This problem has been examined in great detail by Stanewsky (1981). Here, we will give only two examples of these effects in order to illustrate their crucial importance.

The first example is presented in Fig. 2.10 which shows a comparison between flight tests and wind tunnel measurements performed at a Reynolds number ten times smaller (Stanewsky and Little, 1971). In wind tunnel conditions, the boundary-layer on the upper surface is certainly turbulent over the major part of the airfoil. Nevertheless, its relative thickness δ/c (c being the airfoil chordlength) is larger than at higher natural Reynolds numbers (this is particularly true if tripping devices are used to promote transition). Thus, the scaled streamwise pressure gradients (δ/p) (dp/dx) are more intense and, consequently, the viscous effects tend to be more severe in test conditions than for the full scale airfoil: on the small scale model, the shock is farther upstream and the pressure rise in

the rear part of the airfoil is more likely to produce separation. As a consequence, the boundary-layer displacement thickness grows considerably following the jump caused by the shock and the rear separation. On the other hand, at high Reynolds number, the boundary-layer upstream of the shock is thinner. The relative jump in displacement thickness across the shock is greater due to a higher Mach number upstream of the shock and the possible presence of a small separation bubble. However, the increase in boundary-layer displacement thickness down to the trailing edge is more gradual partly due to the absence of rear separation.

Another example of the fundamental importance of scaling effects is relative to an airfoil whose lift coefficient was measured as a function of the free stream Mach number M_∞ , the model being equipped with different transition bands (Pearcey et al., 1968). The corresponding results are shown in Fig. 2.11.

The lower chain-dotted curve in Fig. 2.11 corresponds to a coarse transition band located very near the leading-edge. The upper, full curve, was obtained for a finer band, placed further downstream. In this case, the boundary-layer is certainly thinner than in the first case. One sees that when M_∞ is lower than 0.65, the two curves are very close. They start to diverge for M_∞ greater than 0.65, the lift coefficient measured with the coarse transition band becoming more and more inferior to that obtained for a fine, sparse transition band. Such a divergence is due to the difference in boundary-layer thickness, viscous effects being more severe for the thicker boundary-layer.

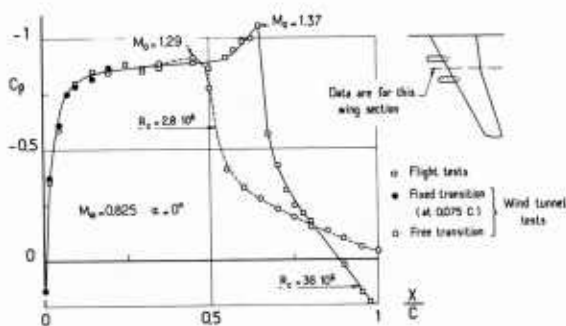


Fig. 2.10 – Transonic interaction – Example of scale effects on C.141 aircraft – Pressure distribution on upper surface (Stanewsky and Little 1971).

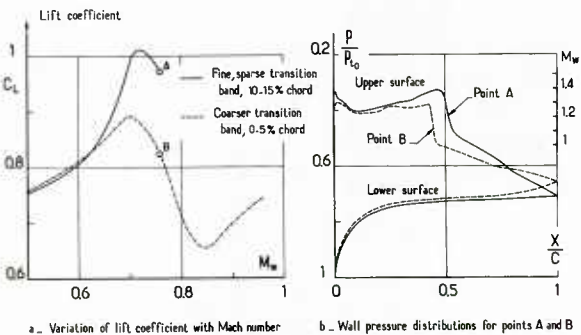


Fig. 2.11 – Transonic interaction on an airfoil – Example of scale effects (Pearcey et al., 1968).

2.5 – Basic Experimental Arrangements Used in Transonic Interaction Studies

The phenomenological discussion of shock-wave/turbulent boundary-layer interaction in transonic flows will be greatly facilitated by a preliminary short presentation of the experimental arrangements most often employed to study these phenomena. Such an Introductory Section allows us to avoid a repetitive description of the various test set-ups utilized to collect the data which will be presented in what follows. As a matter of fact, for transonic flows, it is particularly important to specify the experimental conditions in which the data were obtained since, as will be seen later, a transonic interaction strongly depends on the whole flow field configuration. On the other hand, it can also be of interest to briefly discuss the specific problems encountered in the experimental analysis of transonic interactions.

In this Section, we will consider only two-dimensional test set-ups, since most of the available experimental results were obtained for nominally two-dimensional flows. Also, we will restrict our attention to experimental arrangements aimed at the specific study of viscous interaction and not at the simulation of the transonic flow past an airfoil placed in an unbounded atmosphere. This last problem is extremely difficult to solve. It is the origin of very intensive research programs which are still underway. Its examination would be beyond the scope of the present AGARDograph.

It is clear that the arrangement allowing the most faithful simulation of interactions taking place on an airfoil consists in a model airfoil mounted in the center of the flow field, between the two opposite walls of the wind tunnel test section (Type a test set-up schematically represented in Fig. 2.12). This arrangement has been –and is still– widely used in research aimed at the improvement of airfoil performance or the design of new airfoil shapes. The first phenomenological studies of transonic interactions were made essentially with this type of installation. A frequent drawback of this kind of arrangement is that the Reynolds number is insufficient to insure a fully turbulent boundary-layer at the shock location. To promote transition, it is thus necessary to employ tripping devices that generally provoke an "unnatural" thickening of the boundary-layer. This fact leads to the already mentioned scaling-effects (see Section 2.4 above). Furthermore, the tripped boundary-layer may differ markedly from a well behaved turbulent boundary-layer.

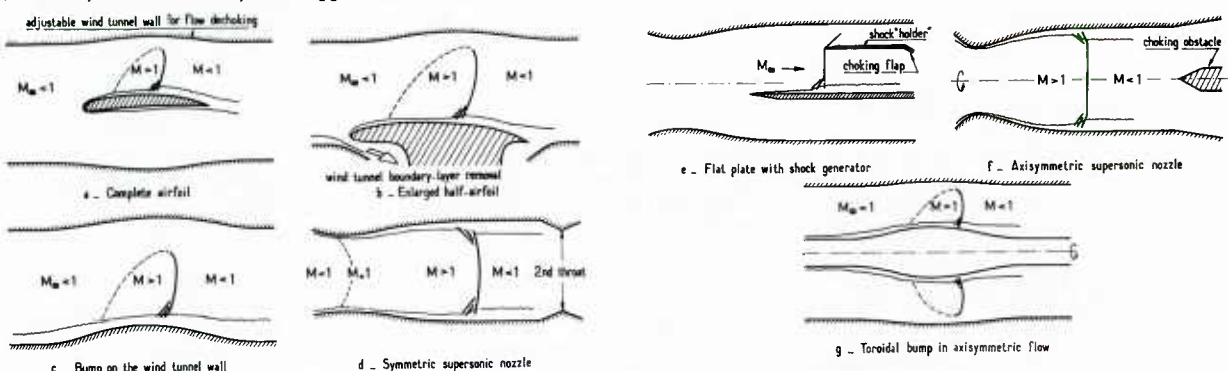


Fig. 2.12 a – Typical experimental arrangements for the study of 2D transonic shock/boundary-layer interaction.

Fig. 2.12 b – Typical experimental arrangements for the study of 2D transonic shock/boundary-layer interaction.

The relatively recent development of pressurized and/or cryogenic wind tunnels tends to overcome this shortcoming by providing unit Reynolds numbers high enough to insure "natural" transition on small scale models. Nevertheless, for basic studies necessitating local flow analysis, other types of model arrangements are often preferred to the complete airfoil so as to have boundary-layers thick enough to be accurately probed by existing techniques. One variant of the complete airfoil model consists in mounting an enlarged half-airfoil model on the floor of the wind tunnel (Type b set-up shown in Fig. 2.12). The wind tunnel floor boundary-layer is removed via a bleed system so that a new boundary-layer will begin at the airfoil leading edge stagnation point. Such an arrangement ensures an airfoil-type flow over the model and makes it easier to implement instrumentation (it is obvious that only the upper-surface flow can be simulated). Furthermore, the boundary-layer is thicker thanks to the realization of greater chordlengths, tunnel blockage being prevented by contouring the facing wall.

A still thicker boundary-layer can be obtained with a bump mounted on a wind-tunnel wall (Type c set-up shown in Fig. 2.12). This arrangement has the disadvantage of the tunnel boundary-layer being superimposed on the model boundary-layer. Furthermore, the wind tunnel boundary-layer has an uncertain origin, so that the Reynolds number and upstream influence are unlike those of an airfoil boundary-layer. This drawback is not very serious if one is mainly concerned with a local analysis of shock interaction phenomena. However, one should be careful to use bumps of sufficiently small relative thickness, otherwise the favorable pressure gradient in the accelerating part of the flow can be so large that the boundary-layer shape parameter H_1 falls to unrealistically small values at the interaction origin (Déleré, 1974). Another disadvantage is that the flow field past the model is rather complex. This fact can lead to serious difficulties in establishing the proper influence of the "basic" parameters acting on the process: namely, the initial Mach number M_∞ , the local Reynolds number, the curvature of the wall, etc... Also, such flows can be hard to model with the presently available theoretical methods.

A simpler "basic" configuration can be obtained by positioning a normal shock-wave in the test section of a supersonic wind tunnel and considering its interaction with the tunnel wall boundary-layer (Type d set-up shown in Fig. 2.12). The initially supersonic flow can be produced either by symmetrical nozzle blocks or by a long bump-like block mounted on one of the tunnel walls. A second throat, of adjustable cross-section, is frequently placed at the test section outlet making it possible to position the shock by choking effects in a continuous and precise manner. A more stable flow is generally obtained by adjusting the second throat in such a way that the shock forms at the end of the diverging part of the nozzle. The presence of a second throat is also recommended in the preceding arrangements in order to isolate the flow under study from pressure disturbances generated in the downstream ducts of the wind tunnel.

The Type e test set-up (see Fig. 2.12) is frequently utilized to study the interaction with a boundary-layer whose origin is well-known and which has developed in a uniform supersonic flow prior to the interaction. This arrangement consists of a flat-plate above which a shock generator is equipped with a choking flap whose aperture is adjusted in such a way that a quasi-normal shock-wave stands in the place containing the shock-holder leading edge.

An intrinsic drawback of all nominally two-dimensional experimental models is that, in reality, they are not free of three-dimensional disturbances produced by side effects, i.e., coming from the interactions taking place with the boundary-layers of the test section side walls. Such disturbances may have considerable influence in transonic flows where a very slight change in the effective tunnel geometry "seen" by that part of the flow considered as inviscid (i.e. the geometry taking into consideration the four wall boundary-layers) can induce dramatic modifications in the flow field and especially in the shock location.

Moderate three-dimensional effects are not really a problem for a phenomenological discussion of shock-wave/boundary-layer interaction focussing on typical trends and characteristic scaling laws. On the other hand, even small side effects affecting a transonic experiment, can render meaningless any comparison with a two-dimensional calculation.

A complete elimination of side-effects in transonic flows is extremely difficult if not impossible to achieve. To overcome this major drawback of two-dimensional installations, without sacrificing the simplicity of flows depending on

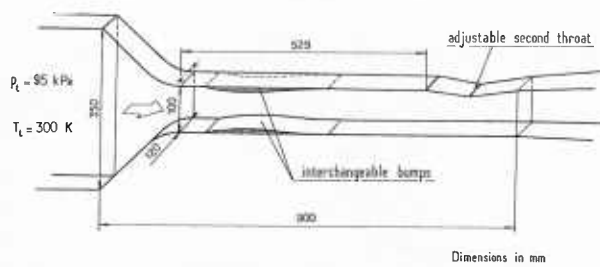


Fig. 2.13 – Schematic of the test section arrangement for investigation of typical transonic interactions.

only two spatial co-ordinates, the best solution is certainly to use an axisymmetric arrangement like the one shown in Fig. 2.12 (Type f test set-up). This arrangement is in fact the axisymmetric counterpart of the 2-D Type d test set-up. It is also possible to employ a toroidal bump mounted on a cylinder placed in a cylindrical transonic channel (Type g test set-up in Fig. 2.12). Then, we would have the axisymmetric counterpart of the bump-on-the-wall arrangement.

A major disadvantage of a totally axisymmetric installation is that it renders both flow visualisation and measurements with non-intrusive optical techniques difficult (e.g. interferometry or Laser Doppler Velocimetry). This constitutes a severe shortcoming since transonic flows are extremely sensitive to disturbances generated by "material" probes.

2.6 - Transonic Interactions Without Boundary-Layer Separation

2.6.1 The General Flow Structure

As will be shown in Section 2.7 on Incipient Shock Induced Separation, this means that the Mach number M_∞ on the upstream face of the shock is less than approximately 1.3. The following analysis will be based on experimental observations made on an arrangement belonging to the Type d test set-up (see Fig. 2.12). These experiments were performed in a small transonic channel whose main dimensions are given in Fig. 2.13. The wind tunnel was continuously supplied with dessicated atmospheric air, the stagnation conditions being $p_t = 95$ kPa for the pressure and $T_t = 300$ K for the temperature (Délery, 1977).

Figure 2.14 shows interferometric photographs of interacting flows obtained with a long bump mounted on the channel lower wall, the upper wall being flat. Before interpreting these photographs, let us recall that, for a two-dimensional flow, the fringes of an interferogram of the kind obtained here -i.e. by using the infinite fringe mode of operation- are lines of constant flow density. Hence, if the flow is isentropic, the fringes are also lines of constant Mach number, constant pressure, etc... This is not true in dissipative or rotational flow regions, such as in boundary-layers or downstream of a curved shock. However, as already pointed out in Section 2.2, for the transonic flows under investigation, the entropy rise across the shock is so small that these flows can be considered as irrotational throughout the field - except of course in the boundary layers.

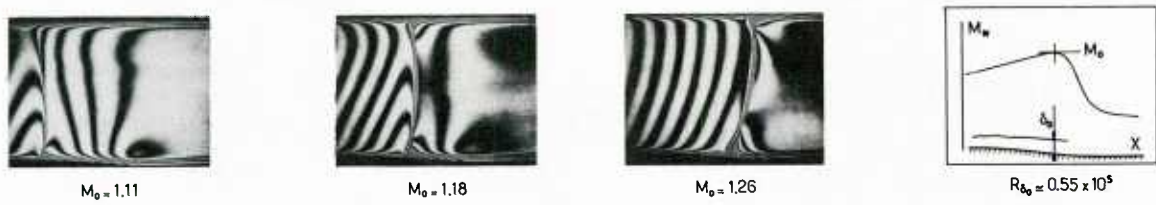


Fig. 2.14 – Transonic interaction without separation
interferogram of flowfields.

On the interferograms, the boundary-layer outer edge coincides with the rapid bending of the fringes visible in the vicinity of the wall. This bending is due to the rapid decrease of density across the boundary-layer. The apparent thickness of the shock in the main field comes from the aforementioned side effects on the test section windows.

In the sequence of photographs shown in Fig. 2.14, the upstream external Mach number M_∞ relative to the interactions taking place on the test section lower wall varies from 1.11 to 1.28. The maximum value nearly corresponds to the limit for Incipient Shock Induced Separation.

A closer examination of the interferograms reveals the following flow features :

- i - when the shock-wave is very weak (Fig. 2.14a), one observes that the discontinuity (which is the trace of the shock in the outer inviscid stream) continues in the boundary-layer. This indicates a deep penetration of the shock inside the boundary-layer. In the present case, the unperturbed incoming boundary-layer is supersonic over approximately half of its thickness in spite of the low external Mach number M_∞ . This is because of the "filling" of the boundary-layer velocity distribution by the strong acceleration taking place in the channel, upstream of the shock (this filling is reflected by a relatively low value for the initial incompressible shape parameter $H_{\delta_0} = 1.3$);
- ii - when the shock strength is increased (Fig. 2.14b and 2.14c), compression waves are seen to form inside the boundary-layer. These waves originate from a region close to the wall and converge to a point from which the quasi-normal shock seems to emanate. There is no special reason for the compression waves to precisely meet at a point. Nevertheless, interferograms show that the focussing of the waves is nearly punctual. The spreading of the compression waves in the vicinity of the wall becomes more and more evident as M_∞ increases. At the same time, one observes an emergence of the shock origin from the interior of the boundary-layer.

A schematic representation of the flow structure in the shock foot region is shown in Fig. 2.15. The rise in pressure produced by the shock propagates upstream through the subsonic part of the boundary-layer. The subsequent deceleration entails a thickening of this subsonic layer. The corresponding bending of the sonic line generates compression waves which propagate in the supersonic part of the flow. Hence, in this region, the shock discontinuity is replaced by a gradual compression.

When the upstream Mach number is very close to unity, the "elliptic leakage" beneath the shock produces a relatively slight thickening of the boundary-layer subsonic channel. Consequently, the compression waves induced in the adjacent supersonic part of the flow are very weak so that the shock is only slightly weakened as it propagates in the boundary-layer. It disappears only upon reaching the sonic line. In the present situation, the observed flow structure rather closely resembles the flow model of asymptotic theories when considering the limiting process in which the boundary-layer sonic line is very close to the wall. Then, according to these theories, the shock penetrates deep into the boundary-layer (for more information on asymptotic theories, see Section 4 of Part II below).

On the other hand, when the incident shock becomes stronger, the thickening of the subsonic layer is more rapid, with subsequent higher local deflection angles. In these circumstances, the induced compression waves are more intense. There results a greater weakening of the shock in the boundary-layer structure.

It should be pointed out that the interaction mechanism cannot be entirely explained in terms of perfect fluid arguments. As a matter of fact, the neglecting of viscous terms (both laminar and turbulent) in the near wall region leads to inconsistencies because of the necessity of satisfying the no-slip condition at the wall. In fact, the upstream influence phenomenon, with the accompanying spreading of the compression at the wall, is a very complex process involving "strong" interaction between the different layers into which the flow can be divided. A correct picture of the phenomenon was developed from rational arguments by Lighthill (1953) and by Stewartson and Williams (1969). Their research led to the so-called "triple-deck" theory which is presented in detail in Section 4 of Part II below. Here, we will only cite its essential conclusion. The flow through an interaction must be considered as consisting of three layers or "decks": the outer potential flow (outer deck), the inviscid rotational flow comprising most of the boundary-layer (main deck) and the thin viscous sublayer in contact with the wall (inner deck). Upstream influence is viewed as the result of a self-induced interaction among these three layers. As a consequence of this process, it may be that viscous-interaction and subsonic forward propagation are mutually responsible for the observed trends (Settles et al., 1981).

A more quantitative picture of the flow in the shock foot region is given in Fig. 2.16 which shows a tracing of iso-Mach lines determined from measurements performed with a two-color Laser Velocimeter in the transonic channel represented in Fig. 2.13.

Before going into a closer examination of the interaction domain, let us briefly consider some properties of the outer inviscid flow. As already seen, the shock tends to be replaced near the wall by a continuous compression wave which extends higher and higher in the inviscid flow field as the upstream Mach number increases. The shock starting from the wave focusing point is generally curved, its structure being that of a "strong" oblique shock.

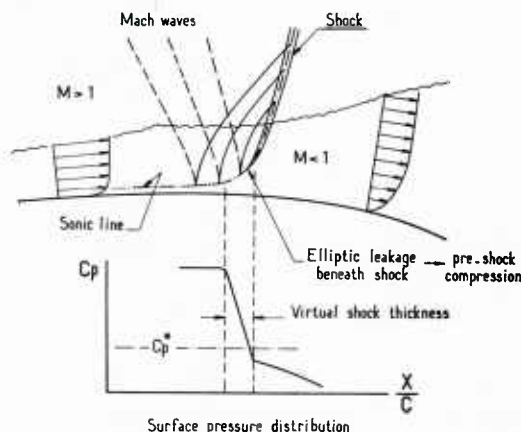


Fig. 2.15 – Schematic representation of the flow in a transonic shock-wave/turbulent boundary-layer interaction without Separation.

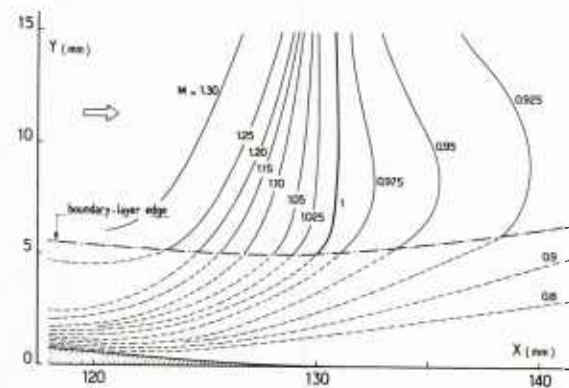


Fig. 2.16 – Transonic interaction – Iso-Mach lines contours in the shock foot region.

Mach number streamwise distributions corresponding to increasing distance from the wall are plotted in Fig. 2.17. They are relative to an interaction whose maximum upstream Mach number is equal to 1.25. One observes a progressive and monotonic decrease in the Mach number for the region closest to the wall. Farther from the wall, the decrease in Mach number occurs through the shock discontinuity, the compression jump being immediately followed by an expansion. Further downstream, the Mach number increases anew before reaching a nearly constant level. The amplitude of the so-called "post shock expansion" increases with the upstream Mach number (see other examples in Section 2.8.1 relative to interactions with shock induced separation). This post shock expansion is a typical feature of the inviscid flow field associated with a transonic shock-wave/boundary-layer interaction. It is also observed in airfoil flows. The phenomenon is due to an apparent wall curvature effect resulting from the rapid growth of the boundary-layer displacement thickness in the interaction region (Gadd, 1961 ; Bohning and Zierep, 1980). Because of this growth, the streamtubes must contract in order to be consistent with the fact that the streamlines are roughly parallel to the wall at a great distance from it and inclined at a positive angle at the boundary-layer edge. There results an expansion of the flow in the subsonic part of the flow field. Upstream of the shock, the influence of the boundary-layer thickening is transmitted along Mach waves and it is thus felt only near the wall.

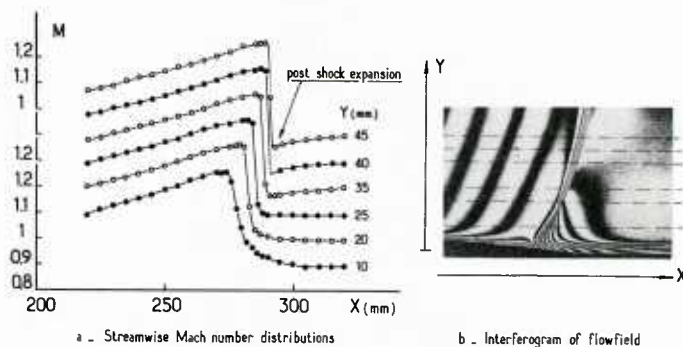


Fig. 2.17 – Transonic interaction – Mach number streamwise distributions in the outer inviscid flowfield.

2.6.2 Scaling Laws for the Interaction Domain

Some experimental evidence. We will now examine some properties exhibited by the wall pressure distributions in a transonic interaction. As typical examples Fig. 2.18 shows "wall" Mach number distributions measured in a wind tunnel allowing large variations of the Reynolds number by adjustment of the stagnation pressure (Laurent, 1977). The experimental arrangement was a bump-on-the-wall type set-up (Type c set-up in Fig. 2.12). The pressure distributions plotted in Fig. 2.18 were measured on the flat wall opposite to the bump (in the curves, the streamwise distance is arbitrarily scaled to the bump chord-length). Figure 2.18a gives results corresponding to a relatively low Reynolds number $R\delta$ (here, $R\delta$ is computed for sonic conditions, the reference length being the boundary-layer thickness just upstream of the shock) and varying initial Mach number M_0 . Results for a Reynolds number approximately twenty times greater are plotted in Fig. 2.18b.

A first obvious consequence of viscous interaction phenomena is a smoothing of the pressure distribution in the shock foot region where a steady rise replaces the discontinuity of perfect fluid theory in the actual flow. This spreading is of course a direct manifestation of the upstream propagation mechanism briefly discussed in the preceding Section.

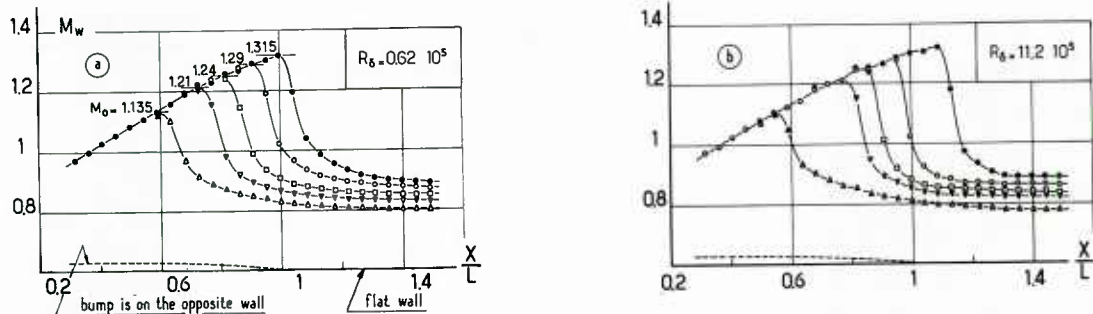


Fig. 2.18 – Transonic interaction in a channel – Influence of Reynolds number on "wall" Mach number distributions.

One also notes that the lower the Reynolds number, the wider the spreading of the pressure distribution. This phenomenon is more clearly shown by plotting on the same graph the wall Mach number distributions relative to different Reynolds numbers $R\delta$, the initial Mach number M_0 and shape parameter H_{10} being the same. An examination of these curves (see Fig. 2.19) reveals the following trends :

- i – the spreading of the wall pressure distribution strongly depends on the local Reynolds number. The streamwise extent of this spreading significantly decreases when the Reynolds number increases. Such a trend is a typical feature of a viscous interaction involving a fully turbulent boundary-layer at high Reynolds number both in transonic and in supersonic flows (see Section 3 below);
- ii – the downstream Mach number level is higher (or, which is equivalent, the pressure level is lower) than the value corresponding to a shock normal to the wall. In the present situation, the downstream, nearly constant, Mach number level would be that of a strong oblique shock producing a deflection $\Delta\phi \approx 5.5$ deg. Here, the pressure rise at the wall falls between the normal shock solution and the level associated with the maximum deflection compatible with an attached oblique shock. In the present case, the pressure rise is noticeably higher than the value for sonic condition behind the shock (see shock polar diagram in Fig. 2.20). In some results, the downstream level nearly corresponds to the sonic conditions after the shock and so some caution should be exercised in defining precise laws for this pressure recovery.

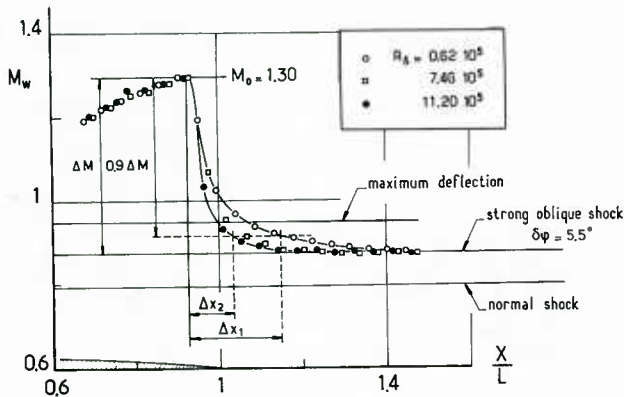


Fig. 2.19 – Transonic interaction – Influence of Reynolds number on interaction extent.

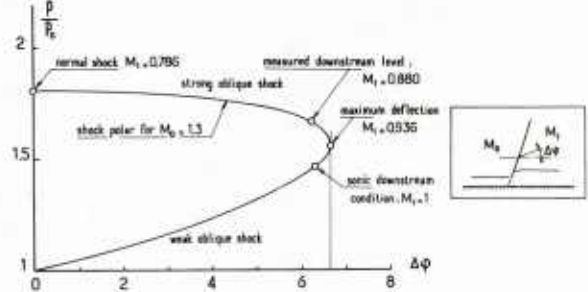


Fig. 2.20 – Transonic interaction – Representation of Fig. 2.19 flow on the shock polar diagram.

Several correlations have been proposed to predict the downstream pressure level (Stanewsky, 1973). For example, Fig. 2.21 shows a plotting of pressure rises measured on airfoils (Leblanc, 1976). In agreement with the above results, the data points lie well below the curve representing the normal shock solution. In the correlation shown in Fig. 2.21, the experimental downstream pressure levels lie between the compression curves respectively relative to the maximum deflection angle $\Delta\phi_{\max}$ and to a sonic downstream state for which the deflection is $\Delta\phi_{\text{sonic}}$.

This kind of correlation is sometimes used in viscous-inviscid coupling methods to model the complex interaction taking place in the shock foot region (Mason et al., 1977 see also Wai and Yoshiharo, 1980a)). One of these models consists in assuming that locally the outer inviscid stream encounters an oblique shock produced by a "viscous wedge" whose angle, function of M_0 , is given by :

$$\Delta\phi_w(M_0) = \frac{1}{2} [\Delta\phi_{\max}(M_0) + \Delta\phi_{\text{sonic}}(M_0)]$$

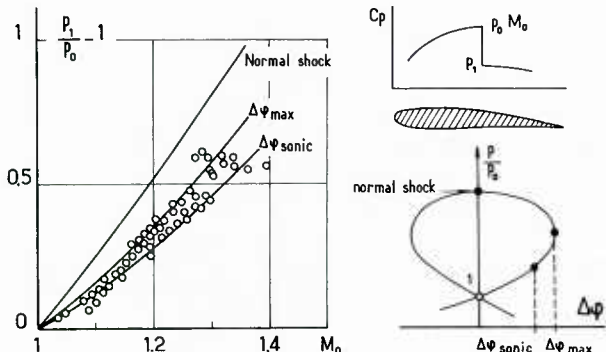


Fig. 2.21 – Correlation for shock pressure rise on an airfoil (Masson et al., 1977).

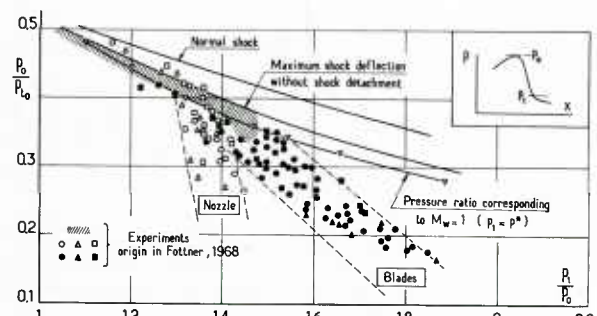


Fig. 2.22 – Correlation for pressure associated with normal shock – Boundary-layer interaction (Fottner, 1968).

Another correlation for the pressure rise p_1/p_0 in a transonic interaction is shown in Fig. 2.22 (Fottner, 1968). Here p_1/p_0 is plotted as a function of the pressure ratio p_0/p_{t_0} relative to the upstream Mach number M_0 (p_{t_0} being the stagnation pressure). The present correlation, which also includes data for cascades and nozzle flows, exhibits a rather large scatter especially when M_0 is greater than approximately 1.2 (p_0/p_{t_0} less than 0.4). For p_0/p_{t_0} smaller than 0.36, one notes a marked modification in the rate of change of p_1/p_0 with increasing upstream Mach number. This phenomenon occurs for M_0 nearly equal to 1.3 and certainly coincides with shock induced separation.

When M_0 is less than 1.3 (p_0/p_{t_0} greater than 0.36), the data points follow (approximately) the curve corresponding to maximum shock deflection. Departure from this curve is observed for interactions strong enough to entail separation. One sees that this takes place when the equivalent wedge deflection angle is roughly equal to 6 deg. This value is close to the criterion for Incipient Shock Induced Separation discussed in Section 2.7.2 below.

Correlations such as those just presented must be considered with caution. In fact, as already pointed out in Section 2.1, the subsonic flow downstream of the shock is highly dependent on the entire flow field. In these conditions, it is doubtful that a correlation involving only the upstream Mach number can be of a general character. Furthermore, a significant "downstream level" cannot always be defined unambiguously, as shown by the data plotted in Fig. 2.23. These results are Mach number distributions measured on a curved bump which imposes a continuous compression downstream of the shock. It is clear that in this case it is no longer possible to properly define a downstream level.

Similar effects can also explain the large scatter of the data points plotted in Fig. 2.22 where it is evident that nozzle data does not correlate with airfoil and blade data. Correlations such as those of Figs. 2.21 and 2.22 apply only to specific situations, namely airfoil flows in the present case.

Domains of a transonic interaction. Actually, the search for scaling laws requires a closer look at the local phenomena taking place in the vicinity of the shock. For this task, interferometric visualisation is a precious tool.

Typical evolutions of the wall pressure distribution for interactions occurring on a bump-on-the-wall configuration are plotted in Fig. 2.24 along with interferometric photographs of the corresponding flow fields. The upstream Mach number of the most intense interaction shown here is equal to 1.4. Thus, this flow must be slightly separated in the shock foot region. However, the flow structure is not profoundly altered as long as the extent of the separated bubble is small. So this configuration is not radically different from a non-separated case.

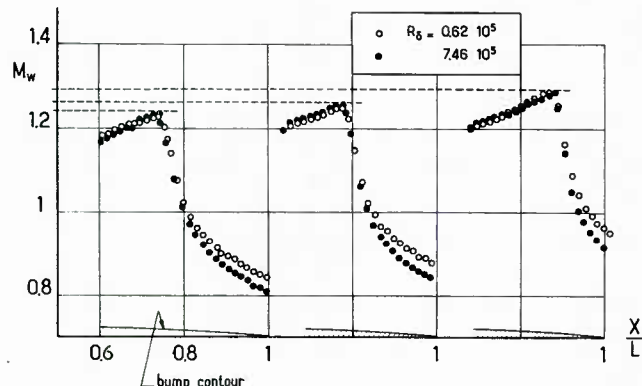


Fig. 2.23 – Transonic interaction – Wall curvature effect downstream of shock-wave.

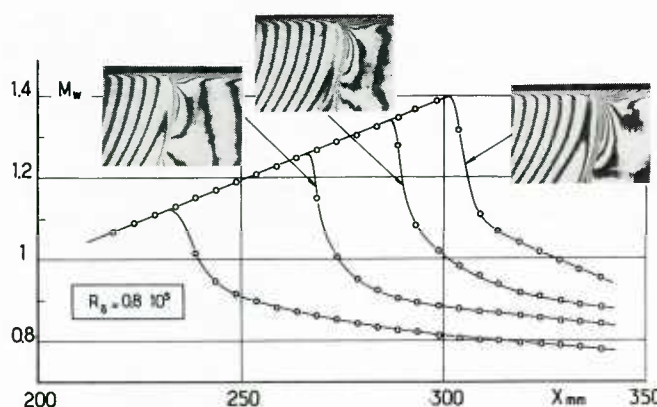


Fig. 2.24 – Transonic interaction – Typical "wall" Mach number distributions in a transonic channel.

The above results have been obtained at a practically constant Reynolds number ($R\delta^* \approx 0.81 \times 10^4$, δ^* being the displacement thickness of the incoming boundary-layer). The pressure distributions were measured on the flat wall facing the bump. As in the preceding examples, the rapid increase through the shock wave is followed by a more gradual compression resulting from flow non-uniformities which are due to the bump curvature adding to the boundary-layer displacement effect.

A more vivid visualisation of the phenomenon is provided by the enlargement of one of the interferometric pictures shown in Fig. 2.25. Interpretation of such a picture was discussed in Section 2.6.1. In addition, this interferogram clearly brings to light the two domains typical of the interaction process :

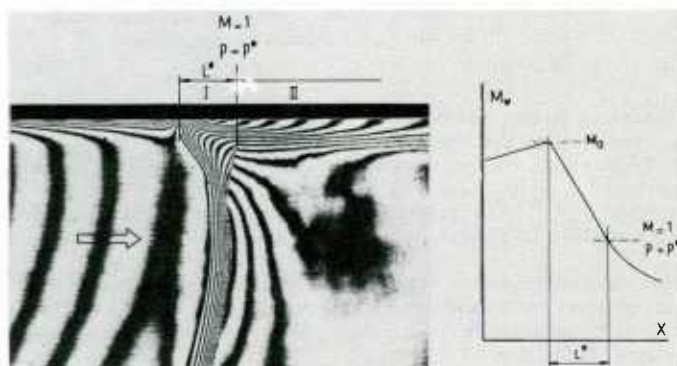


Fig. 2.25 – Transonic interaction – Definition of the supersonic interaction length.

i - on the one hand, in the most upstream part of the interaction, there occurs a continuous and rapid compression of supersonic nature and of nearly simple wave type, up to an almost sonic value of the velocity in the outer inviscid stream. This part of the flow constitutes what we shall call Domain I. One should notice that a truly simple wave evolution implies a supersonic uniform upstream state. This cannot be the case here since, even for a uniform outer flow, the supersonic compression starts inside the boundary-layer where the flow is rotational and hence non-uniform.

ii - on the other hand, downstream of Domain I, the evolution of the velocity field is noticeably less rapid, resulting from a much slower variation of the boundary-layer displacement effect in the absence of separation. This second part of the flow constitutes Domain II.

From these considerations, it is clear that general and specific characteristics of the transonic shock-wave/turbulent boundary-layer interaction phenomena can only be sought within Domain I of supersonic nature. In Domain II, of subsonic nature, the flow structure (and hence the wall pressure distribution) results from both the integration of effects extending far downstream and the taking into account of the entire flow and, in particular, the shape and curvature of the wall.

That is why we shall concentrate on the analysis of phenomena within Domain I and more particularly on the interaction length. Here L^* is defined as the distance between the origin of the interaction (i.e. the point where the pressure at the wall starts to rise) and the x -wise station where the local pressure is equal to the critical value p^* (i.e. corresponds to a "wall" Mach number equal to unity). The interaction length L^* is thus a measure of the extent of the domain of "rapid" interaction.

The measured wall pressure distributions show that the supersonic part of the interaction process corresponds to a very steep rise in pressure, whereas the curves tend to be more gradual downstream of the point where local sonic conditions are reached. This fact was also noticed by Alber et al. (1971) in their experiments made on a bump-on-the-wall type arrangement. They observed that a close examination of their pressure profiles revealed a change in the pressure slope (a kink), downstream of the shock, at a point corresponding to sonic condition. They also concluded that this change in dp/dx indicates a significant modification in the character of the flow from a supersonic interaction type to a subsonic flow typical of a trailing edge situation.

Factors influencing the streamwise extent of the supersonic interaction length. Among the factors likely to influence the domain of rapid (or supersonic) interaction, the most commonly investigated are the initial (or upstream) Mach number M_0 and Reynolds number $R\delta^*$ (here the Reynolds number will be calculated with the displacement thickness δ^* which is better defined than the physical thickness δ).

A thorough analysis of these effects was carried out by Déler (1980b) (see also Sirieix et al., 1981) on a bump-on-the-wall configuration (Type c test set-up of Fig. 2.12). In these experiments, the wall Mach number distributions were practically insensitive to changes in the free stream stagnation pressure, which governed the variations of $R\delta_0^*$. Furthermore, in this kind of arrangement, the effect on the shape parameter of the strongly favorable pressure gradient preceding the shock predominates over that of the Reynolds number. It is thus possible to vary independently the three main parameters M_0 , $R\delta_0^*$ and H_{10} .

The results obtained are presented in Fig. 2.26a in the form of a diagram giving the evolution of the normalized interaction length L^*/δ_0^* as a function of the upstream Mach number M_0 ($1.09 < M_0 < 1.30$) the variation realized for $R\delta_0^*$ being between 0.15×10^4 and 1.08×10^5 and the value of the shape parameter H_{10} for the whole set of results being close to 1.2.

First, one observes an excellent grouping of the experimental data points, with a moderate scatter due for the most part to the difficulty of accurately defining the length L^* from the wall pressure distributions. The influence of the Reynolds number, very marked both on the physical extent L^* and on the thickness δ_0^* , disappears when these two variables are normalized one by the other. Thus, it can be concluded that, for a given value of the shape parameter, the displacement thickness of the incoming boundary-layer is a proper scale for the interaction length L^* . Moreover, it appears that the ratio L^*/δ_0^* is not very sensitive to the effect of the upstream Mach number M_0 . In fact, the scatter observed when M_0 comes close to 1.3 corresponds to a situation very close to separation (see section 2.7.2 below). The quasi-invariance of L^*/δ_0^* with respect to M_0 can be easily understood by referring to the brief analysis presented in Section 1.3. Raising the upstream Mach number increases the strength of the perturbation, and thus its tendency to propagate farther upstream. But, at the same time, the subsonic part of the boundary-layer (which roughly scales the upstream influence mechanism) becomes thinner. So that, by virtue of these two compensating mechanisms, L^* is practically independent of M_0 .

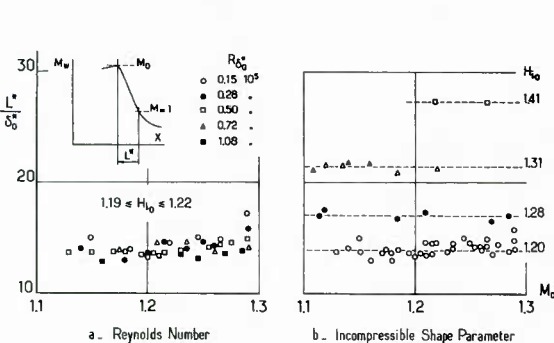


Fig. 2.26 – Transonic interaction – Influence of initial conditions on the supersonic interaction length.

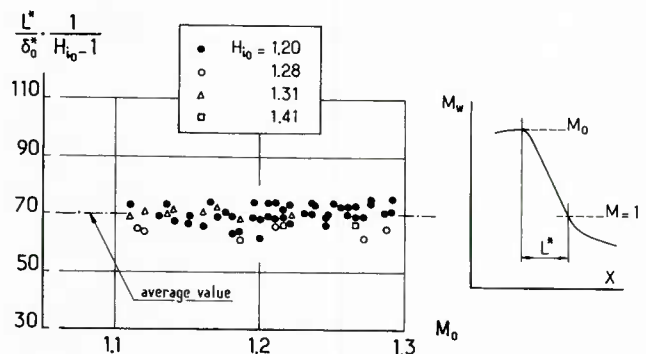


Fig. 2.27 – Transonic interaction – Correlation of supersonic interaction length.

When the normalization L^*/δ_0^* is applied to a more complete set of results obtained in various experimental facilities and which correspond to very different situations as regards the state of the incoming boundary-layer (i.e. very different H_{10}) a pronounced scatter of the data points appears, as shown in fig. 2.26b. However, it is remarkable that the experimental points are regularly spaced as a function of H_{10} . For instance, we observe that L^*/δ_0^* is practically increased twofold when H_{10} passes from 1.2 to 1.4. This increase of L^*/δ_0^* when H_{10} is higher can also be easily understood by considering the arguments developed in Section 1.3. As we know, when H_{10} is high, the boundary-layer is less filled and, consequently, its subsonic part is thicker. Hence, it seems natural that the distance for the propagation of upstream influence be longer.

Considering the above experimental evidence, it could seem rational to scale the interaction length L^* to the height y^* of the boundary-layer subsonic layer. However, attempts to correlate the data points of Fig. 2.26b with y^* failed, in the sense that there is not a proportionality relation between L^* and y^* . The same conclusion was arrived at by Hayakawa and Squire (1982) and by Settles et al. (1981). These authors found that y^* was also and inadequate lengthscale for upstream influence in supersonic shock/turbulent boundary-layer interactions (see Section 3.7.2 below for more complete information).

In order to take the influence of H_{10} into account, a correlation of the results has been looked for within the domain of variation of the parameters involved (namely, $1.15 \leq H_{10} \leq 1.50$; $1.10 \leq M_0 \leq 1.30$). The completely empirical law shown in Fig. 2.27 leads to a rather satisfactory grouping of the results and makes it possible to predict the streamwise extent of the supersonic part of a transonic interaction with reasonable accuracy.

The "viscous ramp" simulation. Following the idea of the "viscous wedge", the correlation law for L^* can be utilized to determine the displacement effect resulting from the strong viscous interaction taking place in the shock foot region. The streamwise evolution $\delta(x)$ between the upstream Mach number M_0 and a locally sonic state defines a "viscous ramp" representing, in a schematic way, the complex phenomena involved in the formation of the shock-wave. In computing this viscous ramp the two following basic assumptions are made :

- i - the outer inviscid flow undergoes a compression from M_0 to the sonic value which is a simple wave process induced by the boundary-layer displacement surface. Hence, the "coupling equation" between the outer flow and the dissipative layer simply writes :

$$(2.1) \quad \frac{d}{dx} \delta^* = \tan [v(M_0) - v(M)] \approx v(M_0) - v(M)$$

where $\psi(M)$ is the Prandtl-Meyer function. We can assume that a simple wave type compression is - a priori - questionable, since as in Section 2.6.2. the compression waves propagate across a rotational layer. However, as experimentally demonstrated by Kooi (1978) a simple wave process is a reasonable assumption (see Fig. 2.28).

ii - the evolution $M(x)$ is linear between M_0 and $M = 1.$, which has also been rather well confirmed by experiment.

Along with the correlation law for L^* , the two above assumptions permit the calculation of the evolution $\delta^*(x)$ over the length L^* . This calculation is performed by integrating Eq. 2.1, initial values δ_0^* , H_{i0} and M_0 being provided by upstream conditions.

Thereafter, knowing $\delta^*(x)$, the momentum thickness evolution $\theta(x)$ can be computed by integrating the von Kármán equation (see Section 2 of Part II) in which the skin-friction coefficient can be assumed equal to zero, its effect being practically negligible in such a rapid interaction process. The knowledge of δ^* at the end of the viscous-ramp, along with that of θ specifies the state of the boundary-layer at the end of the supersonic part of the interaction. These values can be used to continue a "classical" boundary-layer calculation downstream of the shock region.

Figure 2.29 gives the shape of viscous-ramps calculated for several values of the upstream Mach number M_0 , the initial shape parameter H_{i0} being equal to 1.30. This figure also shows the boundary-layer properties at the downstream end of Domain I. It should be said that "jump methods", such as those presented in Section 1 of Part II, also permit the calculation of such viscous-ramps and of the boundary-layer properties at an appropriate station downstream of the shock-wave.

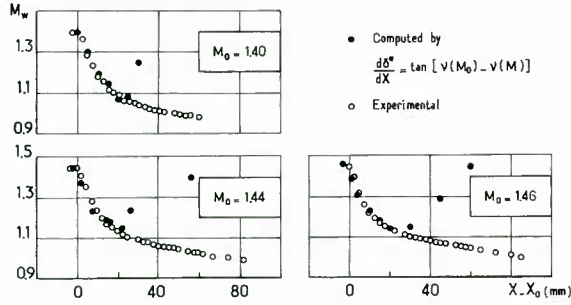


Fig. 2.28 – Transonic interaction – Mach number at the start of interaction computed from the displacement thickness (Kooi, 1978).

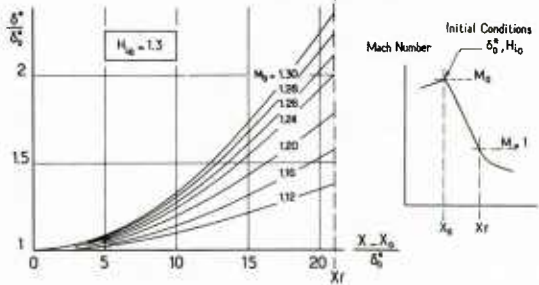


Fig. 2.29 – Transonic interaction – Example of viscous ramp calculations.

Remarks on empirical correlation laws. To conclude this Section on transonic interaction overall properties, we want to emphasize that correlation laws, like those presented above, have a restricted range of validity. Nevertheless, the search for such scaling properties are of interest for at least two reasons :

i- these laws are a great help in understanding the physics of the phenomenon by bringing to light the specific effects of the main influence factors. This fundamental approach of the problem will be also widely utilized in interpreting shock interaction phenomena in entirely supersonic flows;

ii-empirical correlations can be used to devise simplified methods for the modeling of the strong interaction process (e.g. the "viscous wedge" or the "viscous ramp" model). In this respect, they are a valuable substitute for more rigorous calculations calling upon more elaborate flow models, like strong viscous-inviscid coupling methods or analytical methods (see Sections 3 and 4 of Part II). Presently, the quantitative success of these more advanced theories is not always superior, in spite of their higher degree of sophistication. Thus, in many practical situations, semi-empirical methods can be helpful.

2.6.3 Development of the Dissipative Layer Properties

In this Section we will be relatively brief, a more thorough examination of the evolution of the dissipative layer properties during interactions of variable strength - ranging from no separation to large separation - being considered in Section 2.8.3 below.

The effect of a shock-wave of moderate intensity is illustrated by the experimental data given in Figs. 2.30 to 2.32. These figures are relative to an interaction taking place in the transonic channel already depicted in Section 2.6.1 (see Fig. 2.13). In the present case, the maximum upstream Mach number is equal to 1.25; the value of the local Reynolds number at the interaction origin x_0 being $R\delta_0 = 0.72 \times 10^4$. The boundary-layer has been probed by using a LDV system at locations indicated on the "wall" Mach number distribution plotted in Fig. 2.30. One observes that the interaction produces :

i-a distortion of the boundary-layer velocity profiles which is such that - at the beginning of the interaction - the retardation of the flow is larger near the wall than in the outer part of the boundary-layer. This behavior is of course typical of the effect of a strong adverse pressure gradient. The resulting "emptying" of the normalized velocity distribution $\bar{u}/\bar{u}_e = f(y/\delta)$, is reflected by a rapid increase of the shape parameter H_i , as shown in

Fig. 2.31. In the present example, H_i rises to approximately 2, this maximum value being practically reached at Station 3. There, the retardation of the lower part of the boundary-layer flow is at a maximum (see velocity profile 3 in Fig. 2.30). Further downstream, the retardation effect ceases in the region close to the wall, whereas it still continues at the boundary-layer outer edge since the pressure is still rising. This reversal of the tendency is due to the action of turbulent viscous forces which are greatly enhanced by the retardation effect (see Section 2.9.4

below on turbulence properties). As a consequence of this change in the evolution of the profile shape, the shape parameter starts to decrease and, as the boundary-layer "relaxes" towards a new flat-plate situation, H_i tends to a value which is near 1.3 - 1.4 (see Fig. 2.31). In conjunction with the evolution of H_i , the wall shear stress decreases, goes through a minimum and then increases in the downstream part of the interaction.

ii - at the same time, the physical thickness of the boundary-layer δ increases. This growth as well as the rise in H_i results in a rapid increase of the boundary-layer displacement thickness δ^* (see Fig. 2.31). Also, the momentum thickness θ increases but moderately in this case.

The corresponding turbulence intensity profiles of the streamwise component u , are plotted in Fig. 2.32. As a result of the interaction phenomenon, the turbulence level increases. It is noticed that the point of maximum streamwise turbulence intensity moves off progressively from the wall, in accordance with the distortion of the mean velocity profiles. As a matter of fact, the location of the maximum of $T_u = \langle u' \rangle / \bar{u}_e$ nearly coincides with the inflection point of the mean velocity profile, (compare Figs. 2.30 and 2.32) this point being the place where turbulence production is at a maximum.

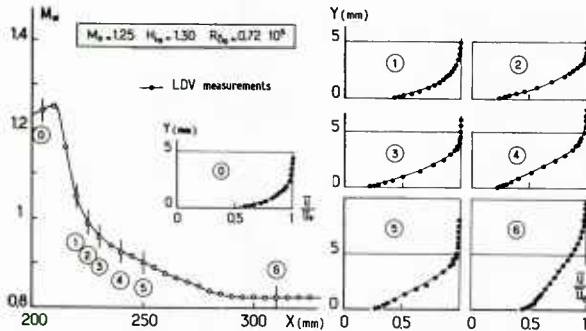


Fig. 2.30 – Transonic interaction without separation – Streamwise mean velocity profiles.

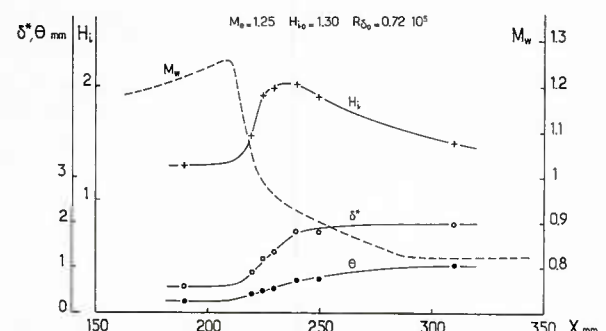


Fig. 2.31 – Transonic interaction without separation – Variation of boundary-layer integral properties.

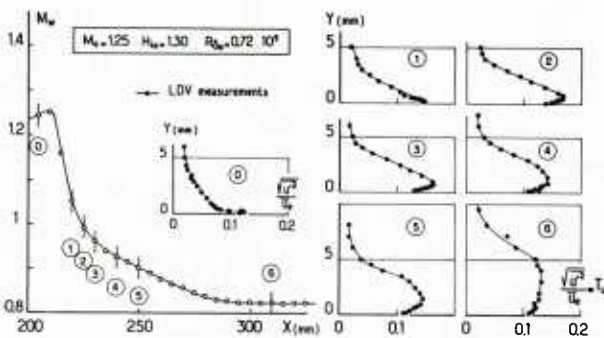


Fig. 2.32 – Transonic interaction without separation – Streamwise turbulence intensity profiles.

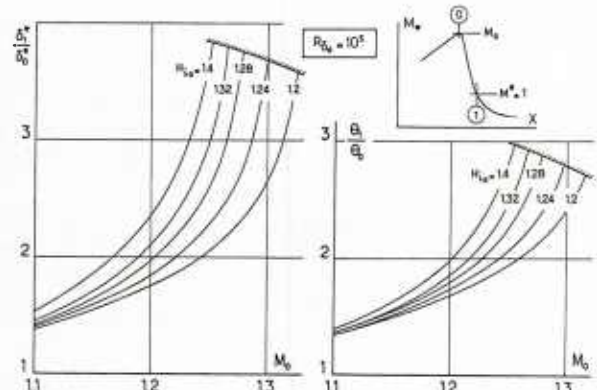


Fig. 2.33 – Transonic interaction – Typical rises in boundary-layer displacement and momentum thicknesses.

In mild interactions – as the one considered here – the growth in turbulence intensity is not very important : in the present example, the highest local value of T_u rises from 0.12 – just upstream of the interaction – to 0.17, before starting to decrease as the boundary-layer relaxes toward a new equilibrium situation. However, the peak value increases very rapidly with the shock strength, especially when separation is approached. For example, $T_u = 0.23$ when $M_0 = 1.30$ (see Fig. 2.37). In Section 2.8.4, it will be seen that T_u reaches values higher than 0.4 in interactions entailing large separation.

Typical rises in the boundary-layer displacement and momentum thicknesses are plotted in Fig. 2.33. The represented quantities are "jumps" of δ^* and θ between the interaction origin and the end of the supersonic part of the interaction domain, i.e., the location where the outer Mach number is sonic (extremity of Domain I defined in Section 2.7.2). These jumps have been computed by using the method discussed in Section 1.2.2 of Part II below. The following general trends are observed :

- i - the amplitude in the jump of integral thicknesses increases with the upstream Mach number M_0 . The growth of the displacement effect becomes quasi "exponential" as Incipient Separation is approached (anticipating the following Section, Incipient Separation occurs when M_0 is near 1.30);
- ii - also, the larger the jump amplitude is, the larger the shape parameter H_{i0} is. This proves that a boundary-layer is more sensitive to "destabilizing" agencies when its shape parameter is higher, i.e., when its velocity profile at the origin of the process is less filled;
- iii - for a fixed value of M_0 , the influence of the Reynolds number R_{δ_0} is weak. In reality, strong Reynolds number effects frequently observed are in fact due to a change in the shape parameter resulting from a variation in R_{δ_0} (see Section 1.2 above).

To conclude, it should be again stressed that "intrinsic" jump correlations for the boundary-layer properties only exist for the supersonic part of the interaction region (Domain I). The evolution downstream of Domain I does not depend anymore on upstream conditions alone. It must be computed by considering the influence of the whole flow field extending - in principle - to downstream infinity.

2.7 - Incipient Shock-Induced Separation in Transonic Flows

2.7.1 Physical Description of Incipient Separation

As we already know (see Section 2.3 above), the phenomenon of boundary-layer separation is of considerable practical importance in transonic flows, since the advent of separation limits the performance of an airfoil, a wing or a cascade... It is thus of great interest to be able to predict separation onset, i.e., to find for known properties of the incoming boundary-layer, the shock strength (or which is equivalent, the upstream Mach number M_0) for which a separated region first forms at the foot of the shock.

By definition, Incipient Separation is the situation in which the minimum of the wall shear stress τ_w in the shock interaction region is exactly equal to zero (see Fig. 2.34). A further increase of the shock strength beyond that point leads to a change in the sign of τ_w , the region where τ_w is negative being termed separated.

The direct measurement of the wall shear stress is still a difficult and inaccurate task within an interaction region characterized by the existence of steep streamwise pressure gradients. For this reason, Incipient Separation is most

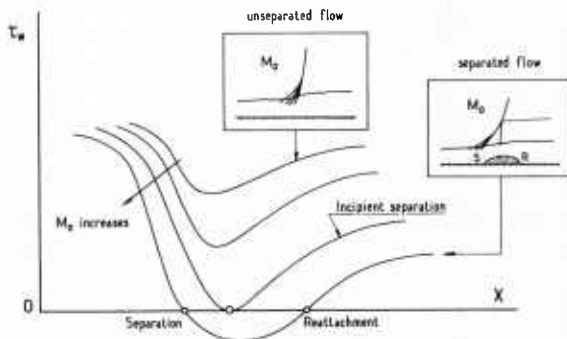


Fig. 2.34 – Definition of incipient separation from wall shear-stress distributions.

often detected from visualisations (surface flow visualisations, schlieren photographs...) or by inspection of the evolution of properties easier to measure than the wall shear stress, namely : wall pressure distributions, boundary-layer mean velocity profiles, etc.

As a matter of fact, the essential properties of a boundary-layer as well as the general flow structure are not greatly affected in the Incipient Separation situation, occurrence of separation being a rather progressive process. However, any further increase of the shock strength or the slight change in outer conditions beyond the Incipient Separation state may provoke a very rapid growth of an initially tiny separation bubble. Such a quasi-explosive increase of the size of the dissipative region considerably affects the whole flow field and generally leads to a catastrophic loss in terms of performance.

The problem of Incipient Separation in itself may seem academic since we have seen that the onset of separation does not entail any really noticeable change in the flow. For this reason, a distinction is frequently made between "true" Incipient Separation (some investigators argue that a microscopic separated zone is always present at the foot of a shock-wave) and "effective" Incipient Separation. The difference will be discussed in what follows and in Section 3.8. In fact, Incipient Separation (or what is detected as the first occurrence of a tiny separated zone) is frequently the immediate precursor of more dramatic events, so that the study of "true" Incipient Separation is not lacking in practical interest. On the other hand, the concept of "effective" Incipient Separation (also termed Significant Separation) is not always clearly and unambiguously defined.

Before going into the presentation and discussion of criteria proposed for predicting Incipient Separation, let us examine the structure of the flow in a situation where separation has just begun to occur. The typical interaction considered here takes place in the transonic channel represented in Fig. 2.13. In the present case, the Mach number immediately upstream of the shock is equal to 1.30. Figure 2.35 shows mean velocity distributions measured across the interacting boundary-layer. By considering these profiles alone, it is difficult to detect the existence of a separated zone which, in this situation, must be extremely thin. A deeper insight into the phenomenon is provided by tracing the curves of equal probability for the instantaneous streamwise velocity component u to take on negative values. For a stream flowing constantly in the downstream direction this probability $P(u \leq 0)$ is equal to zero, whereas it is equal to unity if the u component is always negative.

Usually, a turbulent flow is said to be separated when it contains regions where the mean velocity u (in the sense of Reynolds averaging) is negative (i.e., streams in a direction opposite to that of the external main stream). According to this definition, $P(u \leq 0) = 0.5$ corresponds to a mean velocity equal to zero and the line on which $P(u \leq 0) = 0.5$ coincides with the locus $\bar{u} = 0$. This line necessarily extends from the separation point to the reattachment point.

The lines of constant probability traced in Fig. 2.36 b reveal the existence of a region where \bar{u} is in fact negative (shaded area), so that the flow under consideration is actually slightly separated according to the above definition. However, the size of the so-called separated bubble which is near the limit of spatial resolution of the instrument, appears so small that the present situation practically coincides with Incipient Separation at the shock foot (the reader should note that, in Fig. 2.36b, the distance normal to the wall has been greatly dilated for the sake of clarity).

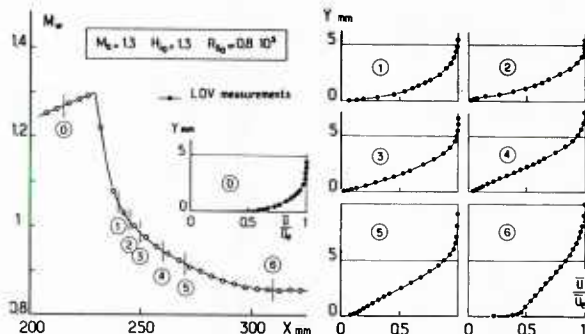


Fig. 2.35 – Transonic interaction – Nearly incipient separation situation – Streamwise mean velocity profiles.

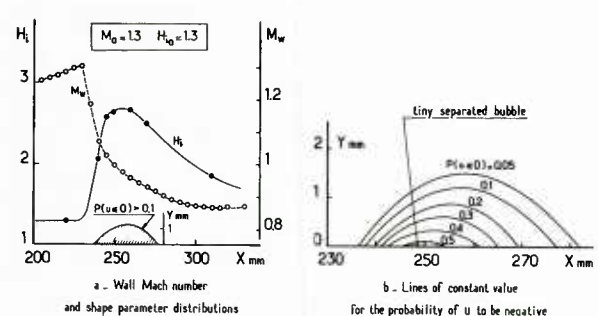


Fig. 2.36 – Transonic interaction – Nearly incipient separation situation.

One will note that instantaneous negative values of u exist in a region where the mean velocity \bar{u} is positive. This means that, in this region, there are instants where the flow near the wall is reversed. This fact may lead to conceptual difficulties in the definition of separation in turbulent flows and more particularly of turbulent Incipient Separation. The problem was discussed in great detail by Simpson et al. (1977; see also Simpson et al., 1981) who have suggested making a distinction between :

- i - fully developed separation (not to be confused with Significant Separation) or time-averaged separation. In this situation, the average wall shear stress changes sign and, accordingly, there exists a region where the mean value \bar{u} is negative ;
- ii - intermittent separation which could be defined as the condition in which $P(u \leq 0)$ reaches the value 0.2 near the wall.

It should also be noticed that the existence of large velocity fluctuations entailing a change of the velocity direction may cause some inaccuracy in the detection of separation by surface flow visualisation techniques.

The corresponding evolution of the shape parameter is plotted in Fig. 2.36a. One sees that H_i reaches a maximum value close to 2.6, which is in fair agreement with the commonly admitted value of 2.5 at a turbulent separation point. Thereafter, H_i decreases rather rapidly and tends to a new flat-plate value.

The streamwise turbulence intensity profiles are plotted in Fig. 2.37. In the present situation, the maximum turbulence intensity is above 0.2, a level significantly higher than for the unseparated flow considered in Section 2.6.3 (see Fig. 2.32). Thus, the advent of separation gives rise to large scale turbulent motions that will be further rapidly amplified if the separation bubble has the opportunity to develop (see Section 2.8.4 below).

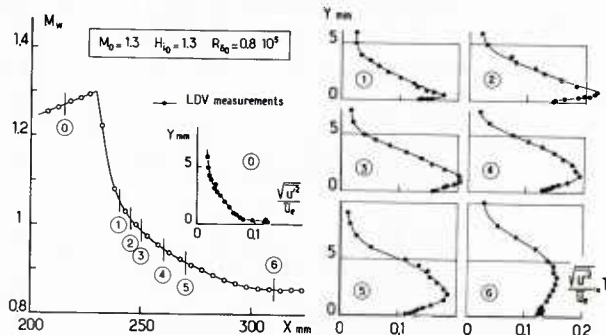


Fig. 2.37 – Transonic interaction – Nearly incipient separation situation – Turbulence intensity profiles.

The above comments on the nature of separation in turbulent flows are certainly instructive from a fundamental point of view. However, they are still of limited interest for most practical situations. Thus, in what follows we will only retain the more usual concept of fully developed separation which we will hereafter term "Separation".

2.7.2 Prediction of Incipient Shock-Induced Separation

Introductory remarks. Most of theoretical methods presented in Part II below are, of course, capable of predicting Incipient Separation since they generally incorporate the calculation of the skin-friction coefficient C_f . We know that Incipient Separation, according to the classical definition of separation, is the situation in which the streamwise distribution $C_f(x)$ has a minimum exactly equal to zero.

However, the availability of more empirical criteria may present some advantages for the following reasons :

- i - as already stated above, the more sophisticated theoretical methods do not always give really good quantitative results, the essential cause of this deficiency being the inadequacy of the presently used turbulence models and hence a law incorporating a greater dose of empirical information has some chance of being more reliable, provided it is applied within the range of parameters covered by the experiments used to establish this law ;
- ii - correlation laws are most often expressed by simple formulae allowing rapid "short-cut" estimation of the occurrence of separation due to strong shock-waves. These shock-waves can be produced either by a back-pressure or by the flow deflection resulting from a corner or a flare encountered by a supersonic flow (see Section 3.8 below for Incipient Separation in supersonic flows).

Consequently, in what follows, we will consider "simple" or global methods based on experimental evidence or experimental correlation laws from which it is possible to deduce practical separation criteria.

Definition of certain separation criteria in transonic flows. In 1955, Pearcey made a rather thorough analysis of flow phenomena associated with separation on an airfoil. From this very complete study, we will only retain the essential conclusions regarding the occurrence of separation.

According to Pearcey, the surface pressure distribution in the vicinity and downstream of separation can be schematically represented as shown in Fig. 2.38 where five characteristic pressure levels are defined, namely :

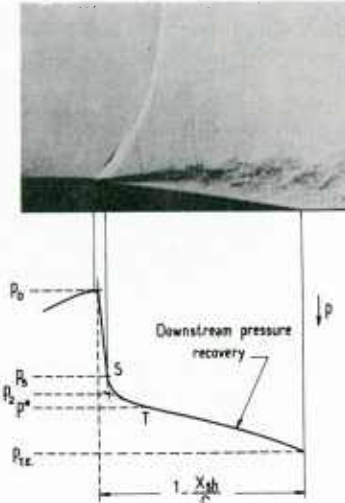


Fig. 2.38 – Transonic interaction on an airfoil – Definition of certain pressures (Pearcey, 1955).

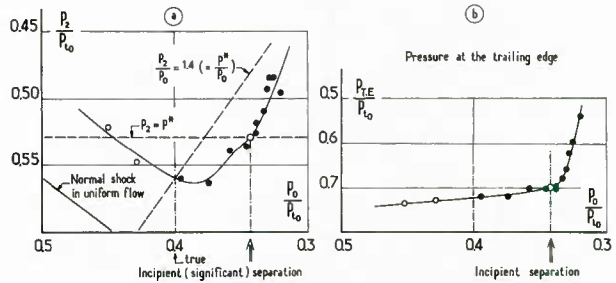


Fig. 2.39 – Transonic interaction – Pearcey's criterion for incipient separation (Pearcey, 1955) (pressure levels are defined in Fig. 2.38).

- 1 - the initial pressure p_0 just before the shock,
- 2 - pressure p_s at the separation point S,
- 3 - pressure p_2 at the "kink" of the pressure distribution, as defined in Fig. 2.38,
- 4 - pressure p^* corresponding to sonic local condition,
- 5 - pressure p_{TE} at the airfoil trailing edge.

Occurrence of separation can be diagnosed by considering the evolution of the normalized pressures p_2/p_0 and p_{TE}/p_0 as functions of p_0/p_0 , i.e. the shock strength (see Fig. 2.39).

Looking at Fig. 2.39a, one sees that p_2/p_0 first increases in the manner expected for a normal shock when the upstream Mach number increases. This rise in p_2/p_0 continues until separation occurs at the shock foot, whereupon p_2/p_0 starts to fall more and more rapidly. At incipient separation, the ratio p_2/p_0 is approximately equal to 1.40 and this value is therefore interpreted as the bare minimum shock strength required to cause separation.

In correlation with the above evolution of the kink pressure p_2 , the pressure at the trailing edge first decreases very slowly as the shock strength increases with no change in the slope of the curve being noticed at incipient separation (see Fig. 2.39b). For a further rise in the upstream Mach number M_0 , an abrupt change in the rate at which p_{TE} decreases is seen to occur for a well defined value of p_0/p_0 . This "divergence" of the pressure at the trailing edge is typical of the development of a large separated bubble. There results a profound modification of the lift coefficient curve which then frequently starts to decrease.

The curves drawn in Fig. 2.39a show that this dramatic change in the flow structure takes place when the kink pressure p_2 is equal to the sonic value p^* . Thereafter, when separation is well established, the ratio p_s/p_0 remains nearly equal to 1.4 which, as seen above, is the value reached by p_2/p_0 at Incipient Separation conditions.

To sum-up, according to Pearcey's analysis, one has to make a distinction between :

- i - true Incipient Shock Induced Separation which is seen to occur for a shock strength such that $p_2/p_0 = 1.4$. In this situation, the flow field is not yet greatly altered by the existence of a separation bubble which is still very small;
- ii - onset of Effective Incipient Separation which is marked by the sudden development of a large separation bubble originating from the foot of the shock. A criterion for the onset of Effective Incipient Separation is that the kink pressure p_2 has become equal to the sonic value p^* . Pearcey (1955) gives a plausible physical explanation of the abrupt change in the size of the separation bubble which takes place when $p_2 = p^*$.

Another way to detect separation on an airfoil has been proposed by Stanewsky (1981). It consists in plotting the variation of the boundary-layer displacement thickness at certain appropriate locations vs. the shock strength, which will be represented here by the upstream Mach number M_0 . Evolutions of this kind are represented in Fig. 2.40 for the three following locations on the airfoil upper surface: upstream of the shock (0), immediately downstream of it (1), and at the trailing edge. The figure also shows the influence of the manner in which boundary-layer transition is induced. In fact, as already mentioned in Section 2.4, boundary-layer tripping mainly affects the thickness of the boundary-layer at the shock location. The large differences between the corresponding variations of δ^* constitute another example of the importance of scaling effects in viscous phenomena on transonic airfoils (see Section 2.4 above).

However, the main point of interest here is the "kink" in the curves $\delta^*(M_0)$ which is observed for a Mach number M_0 slightly greater than 1.3. This kink, which is made more visible by the plotting displayed in Fig. 2.41, can be safely interpreted as an indicator of the fast thickening of a separated region in conjunction with the onset of Effective Incipient Separation. One notices that the kink Mach number M_{ok} depends slightly on the state of the incoming boundary-layer. In fact, the small differences in M_{ok} can be correlated with changes in the shape parameter H_0 . This dependence will be discussed more thoroughly below.

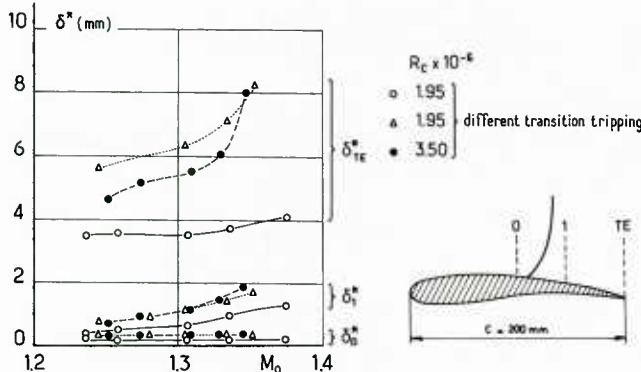


Fig. 2.40 – Displacement thickness variation on a supercritical airfoil (Stanewsky, 1981).

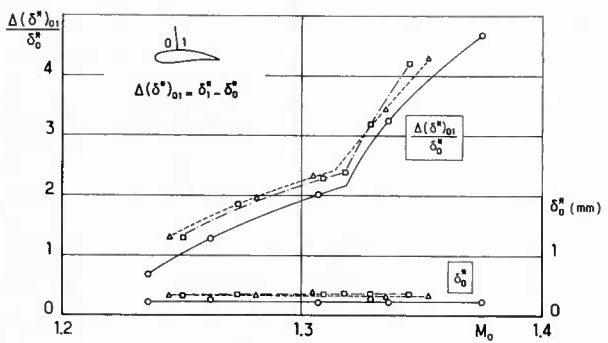


Fig. 2.41 – Incipient separation detection – Kink in the jump of the displacement thickness (Stanewsky, 1981).

A third way to characterize conditions at the onset of separation was derived by Alber et al. (1971). These authors made their experiments on a bump-on-the-wall arrangement (Type c set-up in Fig. 2.12) and used surface flow visualisations to detect separation. Their essential conclusions were derived from a close examination of the wall pressure distributions. In the vicinity of the shock and before separation has occurred, these distributions exhibit a change in slope – a kink – just downstream of the shock. According to Alber and his co-workers, this change in the pressure gradient dP/dx should indicate the passage from a Supersonic Interaction Type Flow (Domain I defined in Section 2.6.2 above) to a subsonic Trailing Edge Type Flow (Domain II). This behavior, confirmed by many other experimental results (Gadd, 1961), is demonstrated by the curve in Fig. 2.42 showing the evolution of the pressure rise at the kink P_2/P_0 vs. the upstream Mach number M_0 . The experimental data points fall exactly on the curve corresponding to $P_2 = p^*$. Furthermore, it can be shown that the turning angle of the inviscid outer flow during the supersonic part of the interaction process (Domain I) cannot exceed 6.6 deg. Once separation has occurred, the turning angle at the separation point station (where the local Mach number is now greater than unity) remains nearly constant

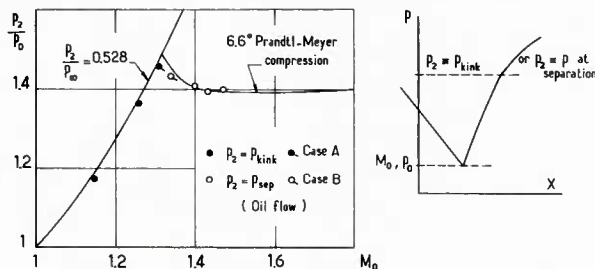


Fig. 2.42 – Transonic flow past a bump – Pressure rise to kink and separation pressure (Alber et al. 1971).

and equal to 6.6 deg. The pressure rise P_2/P_0 calculated from this turning angle by assuming a simple wave type compression agrees remarkably well with experiment (see Fig. 2.42). For M_0 within the range 1.3-2, the value of P_2/P_0 thus calculated stays approximately equal to 1.4, which is consistent with Pearcey's result.

To summarize, Alber et al. have found that Incipient Separation occurs when the Mach number M_0 just before the shock is such that :

$$\nu(M_0) - \nu(M = 1) \approx 6.6 \text{ deg.}$$

which gives $M_0 = 1.32$. Furthermore, it is demonstrated that, in the Incipient Separation situation, the local outer Mach number at the separation point location is sonic. This property, also noticed by Gadd (1961), is utilized in one of the predictive methods explained below.

It can be seen that the separation criterion of Alber et al. does not include a possible influence of the Reynolds number. In reality, we will see that Incipient Separation actually depends on the Reynolds number, although this dependence is weak.

A more thorough experimental program undertaken at ONERA some years ago permitted us to assess more soundly the effect of the main parameters acting on the separation phenomenon. In particular, the influence of the incoming boundary-layer shape parameter was systematically investigated. We already know that H_{10} , which represent the "fullness" of the initial boundary-layer profile, has a great influence on the streamwise spreading of the shock discontinuity.

These experiments were performed in several facilities simulating different flow situations, namely :

- i – an actual profile mounted in the center of the test-section (Type a set-up in Fig. 2.12 ; Rodde, 1980);
- ii – an enlarged profile installed close to the lower wall of the wind-tunnel (Type b set-up ; Gobert et al., 1980);
- iii – a transonic channel of the kind already described in Section 2.6.1 above. In this Type c set-up, high values of H_{10} were obtained by roughening the wall.

Incipient Separation was detected by using a large variety of techniques, including : inspection of the wall pressure distributions, surface flow visualisations, Stanton pressure probe, and boundary-layer probing by conventional probes and also Laser Velocimetry.

The results thus obtained corroborate the fact that Incipient Separation mainly depends on two parameters, namely :

- 1 - the Mach number M_0 on the upstream face of the shock;
- 2 - the shape parameter H_{10} of the incoming boundary-layer.

The often more commonly considered Reynolds number effect is for the greatest part included in the variation of H_{10} . However, one has to be aware that, in principle, these two parameters are not uniquely linked. It is indeed possible to modify H_{10} , at a fixed Reynolds number, by the action of an external agent : e.g., pressure gradient, wall transpiration or suction, wall roughness.

The experimental data points, each representing an Incipient Separation situation, are plotted in the plane (M_0, H_{10}) in Fig. 2.43. One sees that they all nearly collapse on a single curve defining a boundary between interactions without separation and interactions with separation. One notes a rather slow increase in the limit Mach number M_0 when H_{10} is decreasing. This tendency could be anticipated since a lower value of H_{10} means a fuller boundary-layer velocity profile, hence a greater resistance of the boundary-layer to separation (see considerations of Section 1.3 above). However, the effect is not as important as could be conjectured by considering the large influence of the initial shape parameter on the extent of the interaction domain (see Section 2.6.2 above). The reason for this behavior will be exposed below.

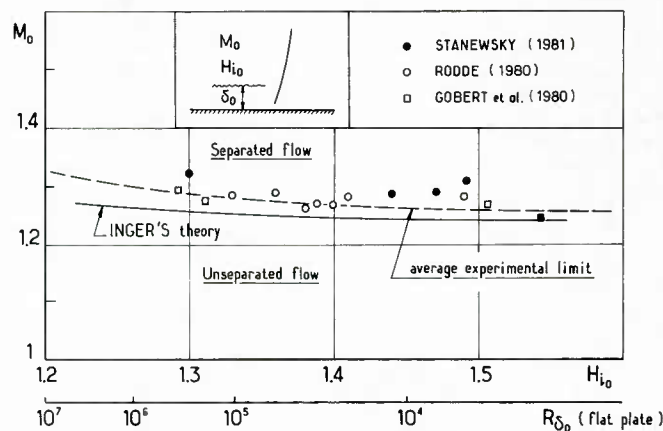


Fig. 2.43 – Experimental shock induced incipient separation limit in transonic flow.

The theoretical limit for Incipient Separation computed by using the simplified analysis presented in Section 1.2.2 of Part II is shown in Fig. 2.44 (full line). One sees that there is a fairly good agreement between experiment and theory. In particular, the relatively weak influence of H_{10} on the shock strength leading to Incipient Separation is well predicted.

This weak influence of the initial shape parameter can be easily understood by considering the following mechanism : as seen in Section 2.6.2, the interaction length L^* increases rapidly when H_{10} increases, i.e., when the boundary-layer velocity profile becomes less filled. Such an increase in L^* reduces the intensity of the streamwise pressure gradient, the supersonic part of the compression being spread over a longer distance. This reduction in the magnitude of the adverse pressure gradient allows separation of the boundary-layer to be avoided, or more precisely, to be postponed, in spite of a less filled velocity profile at the origin of the interaction which, in principle, signals a weaker resistance to separation.

Exactly the same conclusion was arrived at by Squire and Smith (1980) who studied the interaction of a shock-wave with a turbulent boundary-layer disturbed by injection at the wall, with an outer flow entirely supersonic. Also, similar behavior was found by Inger and Zee (1978) in a theoretical analysis applied to transonic flows.

In Fig. 2.44 one also finds the plotting of the Incipient Separation limits given by :

- i - the criterion of Alber et al., which, as we already know, does not include any influence of the shape of the initial velocity distribution ;
- ii - the two criteria applied by Stanewsky (1981), one of them being Pearcey's criterion.

A series of experimental and theoretical studies performed at ONERA tend to substantiate that separation is in fact a purely supersonic process (in the sense that it always takes place in Domain I). Under these conditions, the downstream pressure level p_2 has no real importance on the separation phenomenon itself. Thus, if one accordingly modifies Pearcey's criterion for (true) Incipient Separation by replacing the condition $p_2/p_0 = 1.4$, by $p_s/p_0 = 1.4$, with for Incipient Separation $p_s = p^*$, it is found that the corresponding value of M_0 is equal to 1.27. This value is in relatively good agreement with the other criteria.

If the influence of H_{10} is assumed to be negligible for practical purposes, the above results confirm the well known Nussdorfer criterion according to which separation first occurs when $M_0 \approx 1.3$ (Nussdorfer, 1956).

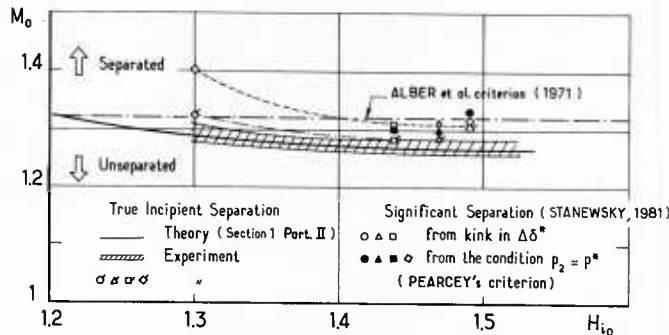


Fig. 2.44 – Shock induced incipient separation in transonic flow – Difference between "true" and "significant" separation.

Comparison with the Incipient Separation limit resulting from Inger's analytical model, presented in Section 4 of Part II, is shown in Fig. 2.43. With this model, it is possible to separately predict the effect of H_{10} and the effect of the Reynolds number. The theoretical prediction of a gradual increase in the Mach number M_0 for Incipient Separation as the Reynolds number $R \delta_0$ increases, is in agreement with the experimental trend. However, the absolute values of M_0 limit predicted by this theory are consistently lower than the average experimental value. According to the authors, this discrepancy is attributable to the combined effect of the linearized inner deck theory (which overpredicts the pressure gradient effect on the skin friction coefficient and hence gives too small an Incipient Separation shock strength) and the assumption of a normal shock-wave when in fact, due to viscous effects, the shock is always oblique near the wall (see Section 2.6.1 above). The theory predicts a small influence of the shape parameter H_{10} which is in agreement with experiment.

To conclude this Section on Shock Induced Incipient Separation in transonic flows, we will briefly comment upon some results relative to the effect of wall curvature and wall temperature.

Figure 2.45a shows this influence as computed from Inger's analytical model (Inger and Sobieszky, 1978 ; Inger, 1981) (δ_0/\mathcal{R} designates the radius of curvature of the wall). According to this theoretical model, wall curvature in the range $0 \leq \delta_0/\mathcal{R} \leq 0.02$ has only a small effect on Incipient Separation. Qualitatively, the effect of curvature is similar to that of increasing the shape parameter H_{10} , the influence of \mathcal{R} being essentially felt as a modification of the skin-friction evolution.

Other calculations incorporating wall curvature effect were made by Bohning and Zierep (1980) (see Section 4 of Part II for more information on this analytical model). Their results are presented in Fig. 2.45b. One sees that with this model, the influence of wall curvature is found to be far more important than with Inger's model. Broadly speaking, the presence of a convex curvature tends to delay separation. The authors explain this behavior by the fact that the post-shock expansion (see Section 2.6.1 above) becomes stronger with increasing wall curvature. This expansion influences the development of the flow in the near-wall region in such a way that it counteracts a possible separation.

A relatively important effect of wall curvature (in the same sense as the one predicted by Bohning and Zierep) was also noticed by Gadd (1961). However, new experiments will be necessary to clearly establish the quantitative effect of wall curvature and to judge the quality of the various analytical models.

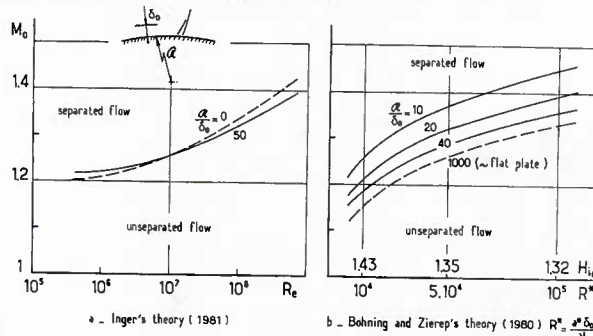


Fig. 2.45 – Transonic interaction – Incipient separation limit – Wall curvature effect.

The influence of wall temperature as predicted by Inger's is shown in Fig. 2.46. In these results, the shape parameter of the incoming boundary-layer is assumed unaffected by the cooling or the heating of the wall (this corresponds to a situation where the wall temperature is changed locally in the interaction domain). One notes that cooling the wall tends to increase the resistance of the boundary-layer to separation. The same trend is observed in supersonic flow (see below).

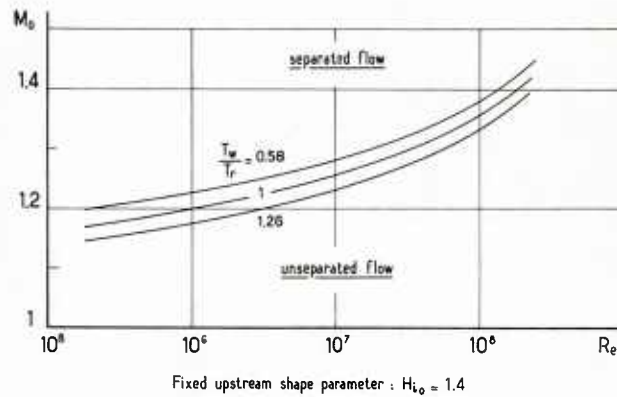


Fig. 2.46 – Transonic interaction – Incipient separation limit – Wall temperature effect (Inger et al. 1983).

2.8 – Interaction With Boundary-Layer Separation

2.8.1 The Outer Inviscid Flow Field Structure

When the upstream Mach number M_0 becomes noticeably greater than 1.3, a sizeable separation bubble forms at the shock foot. This bubble is extremely sensitive to external factors and its streamwise extent can increase dramatically as a consequence of a further rise in M_0 or the action of a downstream adverse pressure gradient, such as the one existing on a highly rear-loaded airfoil.

As the size of the separated region increases, the outer inviscid flow develops a well-defined structure typical of (extended) separation in transonic flows. This structure was originally described by Ackeret et al. (1946). Moreover, much information on the phenomenon was brought to light by the well-known study of Seddon (1960). In fact, it must be kept in mind that this structure emerges progressively from the flow pattern observed in a presumed unseparated configuration (see Section 2.6.1 above) so that there is no real discontinuity between external field structures respectively associated with unseparated and separated flows.

A transonic interaction strong enough to cause a sizeable separation is characterized by the existence in the outer flow of a lambda shock pattern, like the one shown by the interferogram in Fig. 2.47. The flow visualized here was obtained on a Type d experimental set-up (see Fig. 2.12). In the present case, the upstream Mach number is relatively low ($M_0 = 1.37$), nevertheless a large separation bubble forms because of the strong adverse pressure gradient caused by the rapid divergence of the channel downstream of the separation shock. The corresponding wall pressure distribution is plotted in Fig. 2.47b. One sees that the rapid pressure rise associated with separation is followed by a plateau typical of the existence of an extended separated zone.

The interferogram clearly shows the shock system connected to the separated flow as well as the rapid growth of the separated boundary-layer. This flow has been carefully probed by using both interferometry and Laser Velocimetry (Déléry, 1978). The Mach number streamwise distributions in the inviscid field thus obtained are plotted in Fig. 2.48.

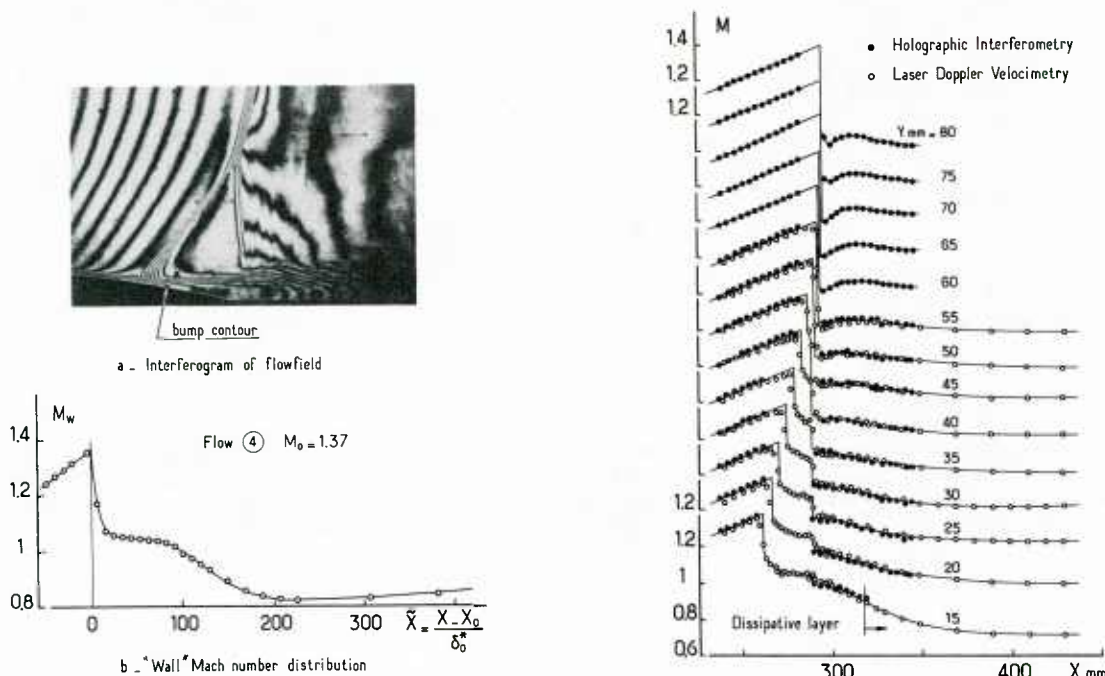


Fig. 2.47 – Extended separation in a transonic channel flow – The lambda shock system.

Fig. 2.48 – Transonic interaction with shock induced separation – Flow 4 streamwise Mach number distributions.

These measurements have permitted the tracing of the iso-Mach lines shown in Fig. 2.49. This tracing reveals that the shock system is composed of :

- i - an oblique shock C_1 produced by the coalescence of the compression waves resulting from the strong adverse pressure gradient at separation ;
- ii - a quasi-normal shock C_2 which meets C_1 at point I ;
- iii - a third shock C_3 , emanating from the triple point I (sometimes called a bifurcation point).

The necessity of this lambda shock pattern comes from the fact that C_1 is a "weak" oblique shock (in the sense of the "weak solution" of the oblique shock theory) whose strength is uniquely a function of the upstream Mach number M_0 and of the incoming boundary-layer properties (see the "Free Interaction" concept developed below in Section 3.6). Thus, when this shock C_1 meets the "strong" quasi-normal shock C_3 present in the far outer field there exist behind C_1 and C_3 two States 1 and 3 with different pressures and velocity inclinations. At the meeting point I of the two shocks, these states are not compatible, as can be seen on the shock polar diagram shown in Fig. 2.50. In order to fulfill the conditions for two adjacent flows to be compatible (i.e. having same pressure and same velocity inclination), a third State 2, having the pressure and the velocity inclination of State 3, must be introduced. This state is reached through a shock-wave C_2 , as shown on the shock polar diagram of Fig. 2.50.

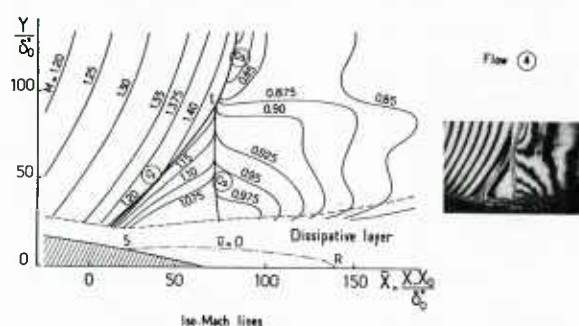


Fig. 2.49 - Extended separation in a transonic channel flow - Inviscid flowfield structure.

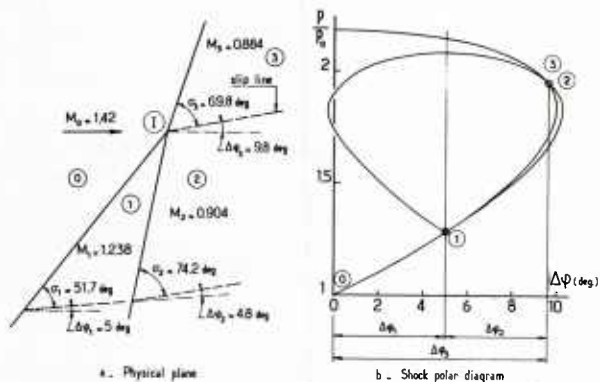


Fig. 2.50 - Situation of the flow at the triple point I - Flow 4 .

Figure 2.51 gives more information on the nature and the strength of the shocks constituting the lambda pattern visible on the interferogram of Fig. 2.47. The various Mach numbers M_0 , M_1 , M_2 and M_3 were directly deduced from field measurements whereas the deflections $\Delta\varphi$ have been computed from oblique shock theory. Due to the non-uniformity of the supersonic incoming stream, conditions on the front face of shocks C_1 and C_2 are not rigorously constant.

It is observed that downstream of C_1 the Mach number of the outer flow remains everywhere supersonic, its value ranging from 1.05 near the boundary-layer edge to 1.15 in the vicinity of the triple point I. Shock C_1 has the structure of a "weak" oblique shock-wave. The Mach number on the downstream face of C_2 decreases from nearly 1 at the edge of the dissipative layer to 0.91 near point I. The deflection $\Delta\varphi$ across C_2 is always other than zero, which shows that C_2 is in fact a "strong" oblique shock-wave. The strength of C_2 is seen to decrease on approaching the wall. This weakening of C_2 is partly due to the varying upstream conditions and partly due to the effect of the compression waves generated by the growth of the boundary-layer displacement effect. As the boundary-layer edge is approached, the rear shock C_2

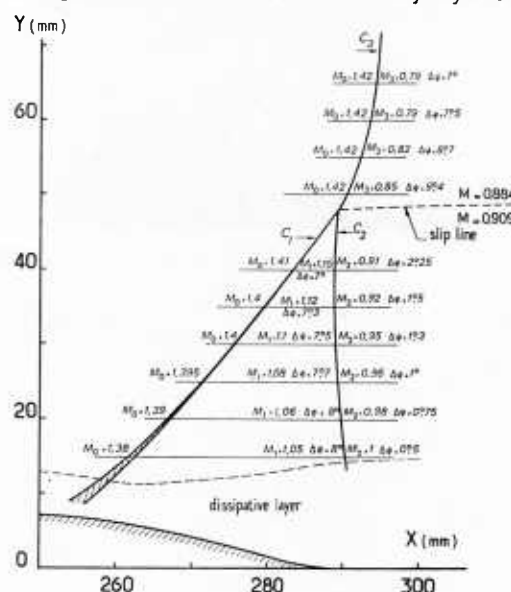


Fig. 2.51 - Details of the lambda shock system - Flow 4
 $M_0 \cong 1.40$

is weakened to such an extent that it causes no disturbance to the wall static pressure distribution (see Fig. 2.47). In the present configuration, the flow is everywhere subsonic downstream of C_2 . This situation is not a general property, but is here due to the fact that the upstream Mach number is not very high ($M_0 = 1.37$). For higher values of M_0 ($M_0 > 1.4$), a locally supersonic zone may exist downstream of C_2 . The extent of this zone (frequently called the supersonic tongue) depends on the particular conditions for the strong coupling process associated with the deviation toward the wall of the reattaching dissipative layer.

The local conditions at the triple point I are given in Fig. 2.50a, the triple shock solution being represented on the shock polar diagram shown in Fig. 2.50b. As a general property of this kind of solution, the flow Mach number after the bifurcated shocks C_1 and C_2 is always greater than the Mach number M_3 downstream of the unique shock C_3 (the total rise in entropy through successive shocks is always less than the rise through a unique shock leading to the same final static pressure). Consequently, the velocity in region 2 is greater than the velocity in region 3, since the stagnation enthalpy does not vary through a shock. This discontinuity in velocity leads to the existence of a slip line originating from the triple point I and which separates flow regions 2 and 3. This slip line is barely visible on the interferogram of Fig. 2.47 (see also Figs. 2.54 and 2.56). The slip line is also called a shear-layer because, in real viscous fluids, the velocity discontinuity allowable in perfect fluid theory is in fact replaced by a thin layer across which the flow properties vary in a continuous manner. The term vortex sheet is sometimes employed.

Flow analysis reveals that the shock C_3 is also a "strong" oblique shock which induces a deflection $\Delta\psi = 10$ deg at the triple point I. In the far field above I, $\Delta\psi$ decreases steadily, as the shock becomes progressively normal. At the same time, its strength increases. The streamwise Mach number distributions plotted in Fig. 2.48 show that C_3 is immediately followed by a post-shock expansion whose amplitude, nearly nonexistent at the triple point I, increases as one goes farther from the wall. This phenomenon, briefly interpreted in Section 2.6.1 above, is met with in every transonic flow involving strong viscous-inviscid interaction (other examples will be presented in what follows).

Another case of a bifurcated shock system associated with large separation in transonic flow is shown in Figs. 2.52 and 2.53. The present experiments were made by Abbiss et al. (1976) on a Type d test set-up (see Fig. 2.12). The field velocity measurements were performed with a Laser Velocimeter. For the flow under investigation, the incoming stream is uniform with a Mach number equal to 1.5. The shock forming at this relatively high Mach number causes a strong interaction with the tunnel wall boundary-layer. However, as the interaction takes place on a flat wall in a channel of constant height, the transverse (vertical) size of the separated bubble is not as large as in the previous example. Here, the test section walls produce a confinement effect which tends to restrict the vertical development of the separated bubble.

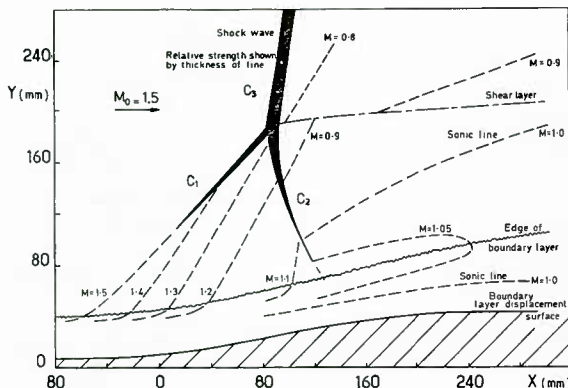
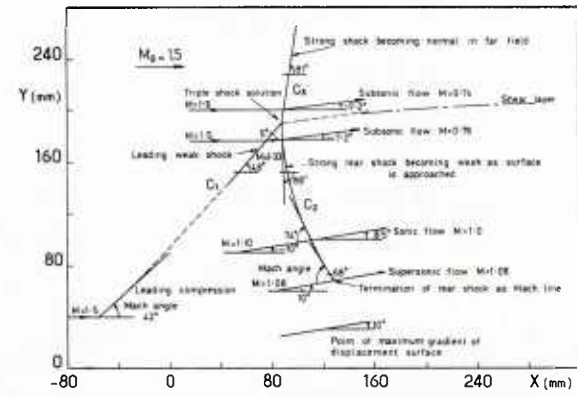


Fig. 2.52 – Transonic interaction with large separation at $M_0 = 1.5$ (Abbiss et al., 1976).



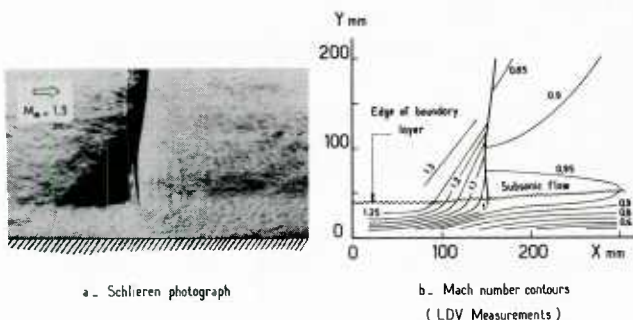


Fig. 2.55 – Transonic interaction – Flow structure for $M_{\infty} = 1.3$ (East, 1976).

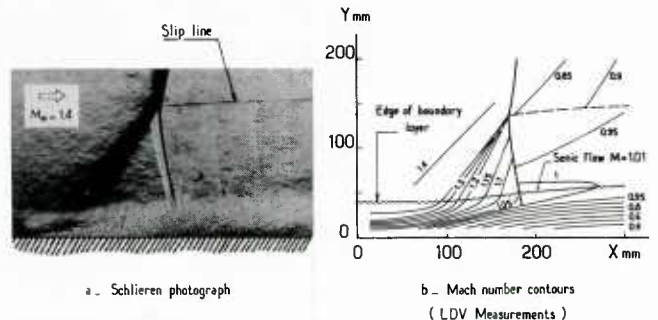
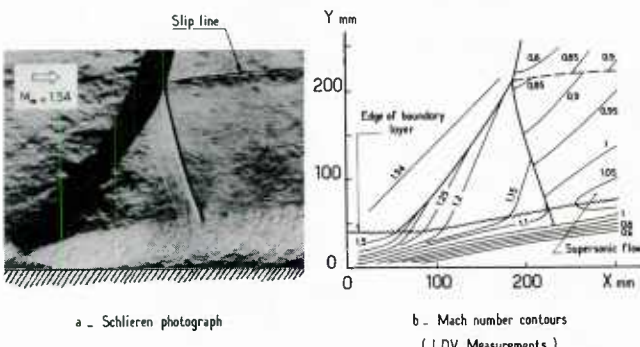


Fig. 2.56 – Transonic interaction – Flow structure for $M_{\infty} = 1.4$ (East, 1976).



a – Schlieren photograph

b – Mach number contours
(LDV Measurements)

Fig. 2.57 – Transonic interaction – Flow structure for $M_{\infty} = 1.4$ (East, 1976).

Nevertheless, the general flow structure is essentially the same as the one of the first example. The main differences come from the higher upstream Mach number (1.4 instead of 1.37). Consequently, the values of the Mach number downstream of the leading shock are higher and one notes the existence of a supersonic region behind shock C_2 , in the vicinity of the boundary-layer edge. Such a region constitutes what Seddon has called the "supersonic tongue". In the present situation the supersonic tongue extends downstream for several boundary-layer thicknesses and the outer edge of the dissipative layer is the last part of the flow to go subsonic. The supersonic compression is apparently achieved without further shock-waves.

Available experimental data show that the supersonic tongue appears for an upstream Mach number slightly less than 1.4. However, its streamwise extension and shape are extremely variable since, for a given value of M_{∞} , the structure of the downstream part of the interaction strongly depends on the viscous-inviscid coupling process and on the conditions prescribed on the boundaries of the subsonic part of the flow field. To illustrate this point, Fig. 2.54 shows a result obtained by Seddon (1960) for an interaction taking place in a Type e experimental set-up (see Fig. 2.12). The uniform incoming stream has a Mach number equal to 1.47 and, in this case, the length of the supersonic tongue is approximately equal to 13 initial boundary-layer thicknesses. Furthermore, the upstream part of the supersonic tongue covers most of the downstream face of shock C_2 . This finding is in disagreement with the results of Abbiss et al. (1976) (as can be seen in Fig. 2.52) and also with those of Kooi (1978) which correspond to nearly the same Mach number ($M_{\infty} = 1.46$, Kooi's results are presented below). In both the flows analyzed by Abbiss and by Kooi, most of the flow downstream of shock C_2 is subsonic. The observed differences can be attributed to far field effects although uncertainties in measurements are not excluded.

The progressive change in the flow field structure accompanying an increase in the upstream Mach number M_{∞} is particularly well illustrated by the experimental results of East (1976). These experiments were performed for three values of the upstream Mach number : 1.3, 1.4 and 1.54, the wind tunnel stagnation pressure being the same for all three tests. As the thickness of the incoming boundary-layer remains practically unchanged, the Reynolds number R_{δ} is nearly the same for the three interactions. The tests were carried out in a Type d experimental set-up, with the flow fields being probed with a Laser Velocimeter. Figures 2.55 to 2.57 show the flow structures as deduced from field measurements along with schlieren photographs of these flows. Due to the very high Reynolds number of the present experiments, the case where $M_{\infty} = 1.3$ corresponds here to a situation preceding Incipient Separation. We see that the compression waves generated by the thickening of the boundary-layer converge and impinge on the quasi-normal shock-wave causing it to curve and reducing it to a sonic Mach line at the outer edge of the boundary-layer. The flow structure observed is very similar to the one displayed by the interferogram of Fig. 2.47 (see Section 2.6.2 above). There is no trace of a supersonic flow behind the shock.

If the upstream Mach number is increased to 1.4, (see Fig. 2.56) then some of the compression waves coalesce into a weak oblique shock (shock C_1) and the lambda pattern arises. No supersonic flow is found downstream of the quasi-normal shock C_2 , but it appears that a narrow region of sonic flow is present at the edge of the boundary-layer.

A further increase in M_{∞} to 1.54 produces a much larger interaction region with an inviscid flow pattern which has become similar to the one analyzed above, except that in the present case a supersonic region exists downstream of shock C_2 (see Fig. 2.57).

We will note that, at the lower Mach number for which separation occurs in East's experiments ($M_{\infty} = 1.4$), the compression waves coalesce outside the boundary-layer to form the leading shock C_1 . At higher Mach number ($M_{\infty}=1.54$), the oblique shock C_1 forms near the boundary-layer edge. A further increase in M_{∞} will entail a penetration of C_1 within the boundary-layer. Also, as the upstream Mach number increases, the triple point moves away from the wall.

2.8.2 Correlation Properties of the Wall Pressure Distributions

Before considering the evolution of the boundary-layer in the course of a transonic interaction entailing separation, let us briefly examine some properties of the wall pressure distribution.

As typical examples, Fig. 2.58 shows the wall pressure distributions corresponding to three values of the upstream Mach number for which separation takes place, namely : $M_0 = 1.40, 1.44$ and 1.46 . These distributions were measured by Kooi (1978) on a Type e experimental arrangement (see Fig. 2.12). Due to the small variation in M_0 , the Reynolds number of these experiments is nearly the same for the three interactions ($R \delta_0 = 2.10^5$). The pressure curves exhibit the following features :

- i - at the start of the interaction, there is a steep rise in pressure, the slope of the curve being practically independent of the upstream Mach number ;
- ii - this rapid rise continues approximately up to the separation point. Thereafter, there is a region of more gradual increase in pressure (the same trend is observed for entirely supersonic interactions, as will be seen in Section 3.3 below) ;
- iii - there are appreciable differences in the shape and in the final level for the three curves, in spite of the rather close values of the upstream Mach number M_0 . As M_0 increases beyond 1.4, an inflection is observed

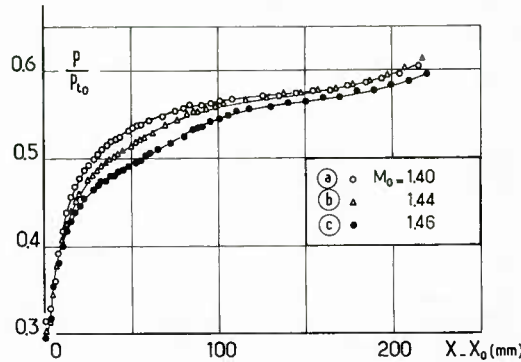


Fig. 2.58 – Transonic interaction – Wall pressure distributions
(Kooi, 1978).

downstream of the separation location. The existence of this inflection is typical of an interaction with a sizeable separated bubble. Such an inflection (sometimes called a "kink", see Section 3.8 below on Incipient Separation in supersonic flows) is in fact the precursor of the pressure plateau associated with extended separated flows. Such an example of large separation was given by the interferogram of Fig. 2.47a, with the corresponding wall pressure distribution plotted in Fig. 2.47b.

- iv - the downstream level is well below the value which would correspond to the pressure rise through a normal shock. A part of the difference comes from the fact that the real shock is curved and bifurcated. However, the greatest part is due to the rapid boundary-layer growth during the interaction. This growth results in an effective converging channel, the effect being clearly demonstrated by the pressure distribution of the case $M_0 = 1.46$. In principle, the downstream level should be the highest for this interaction, whereas it is in fact the lowest because of more intense viscous effects.

Figures 2.59a to 2.59c show the flow structure for the three values of the Mach number M_0 . These contours were deduced from field measurements made with pressure probes (notice that in Fig. 2.59 the horizontal and the vertical scales are different). The features of these flows are similar to those of the flows represented in the preceding Section. For $M_0 = 1.4$, separation occurs, as indicated by surface flow visualisations and skin-friction measurements. However, in this case the separation bubble is too small to be detected by pressure probes. When M_0 is increased, the extent of the separated region grows rapidly. At the same time the displacement effect of the boundary-layer becomes more and more important. This growth explains the rapid concomitant change in the outer flow structure, with in this case the development of a supersonic tongue.

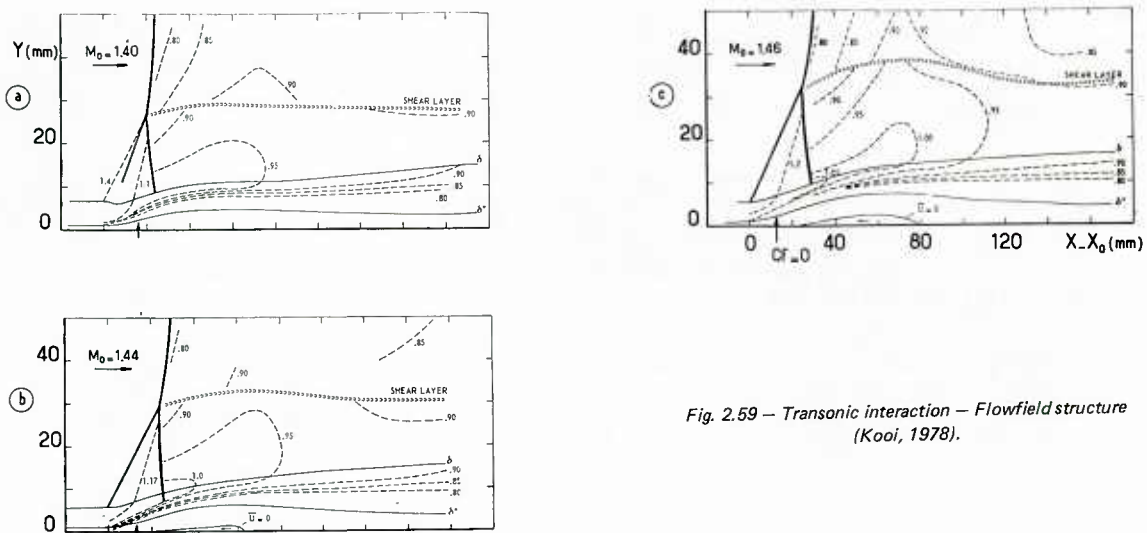


Fig. 2.59 – Transonic interaction – Flowfield structure
(Kooi, 1978).

As already pointed out, it is not possible to define simple and universal scaling laws for the downstream part of the interaction. The flow actually depends too much on external influences, as demonstrated in particular by the experiments of Leblanc et al. (1974).

Thus, just as for interactions without separation (see Section 2.6.2 above), correlation laws can only be searched for in the initial part of the interaction in which the outer inviscid flow remains supersonic.

For interactions with separation, it can be experimentally shown that the supersonic part of the process obeys the Free Interaction concept introduced by Chapman (1957). This concept (which will be more thoroughly discussed in Section 3.6 relative to entirely supersonic flows) states that the separation mechanism depends only on conditions prevailing at the origin of the interaction. According to the Free Interaction theory, the wall pressure distribution should be correlated by the following "universal" function, which is derived in Section 3.6 below :

$$\tilde{F} = \left[\frac{p - p_0}{q_0} \frac{v(\xi) - \bar{v}(\xi)}{C_{fo}} \right]^{1/2}$$

In the above formula, the dynamic pressure q_0 and the skin-friction coefficient C_{fo} are relative to the flow at the start of the interaction. $\bar{v}(\xi)$ is the value of the Prandtl-Meyer function at abscissa ξ in the absence of interaction, $v(\xi)$ being the value of this function when interaction occurs. The scaled streamwise distance ξ is defined in Section 3.6 below.

Figure 2.60 shows a plotting of function \tilde{F} computed first from the already cited Kooi experiments at $M_0 = 1.4$, secondly from the measurements performed by Vidal et al. (1973) (see also Vidal and Kooi, 1976) at very different Reynolds numbers in a large scale Ludwig tube (the Reynolds number R_{ez} indicated in Fig. 2.60 is based on the shock position relative to the leading edge of the flat plate on which the interacting boundary-layer has developed). It is observed that the two experimental distributions closely follow the universal $\tilde{F}(\xi)$ curve given by Carrière (1972).

A similar good agreement was noticed by Délery et al. (1975) for measurements made on a bump-on-the-wall type arrangement, as also shown in Fig. 2.60.

The above results, chosen among many other experimental results, clearly demonstrate that in transonic flows the separation phenomenon is in fact a supersonic process obeying the Free Interaction principle. Specific transonic effects are felt more downstream, when the separated bubble develops and leads to a strong interaction mechanism involving a mixed hyperbolic-elliptic outer flow field.

2.8.3 Development of the Dissipative Layer Properties

Basic interacting transonic flows. Let us now examine the behavior of the turbulent dissipative layer submitted to a strong interaction process involving separation. The following discussion will be essentially based on experimental results obtained by Délery (1981) in a Type d test set-up (see Fig. 2.12). Four different interactions (which can be considered as typical) have been carefully probed by using a two-color Laser Velocimeter. The corresponding wall pressure distributions are plotted in Fig. 2.61, in which the dimensionless streamwise distance x is evaluated from the start of the interaction under consideration, x_0 , and scaled to the displacement thickness δ_0 of the boundary-layer at x_0 . The locations of the transverse explorations made across the dissipative layer are also shown in Fig. 2.61.

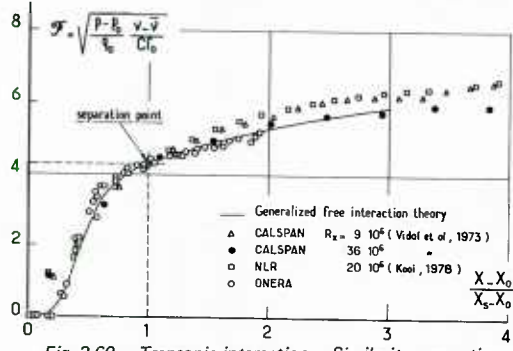


Fig. 2.60 – Transonic interaction – Similarity properties of wall pressure distributions for separated flows.

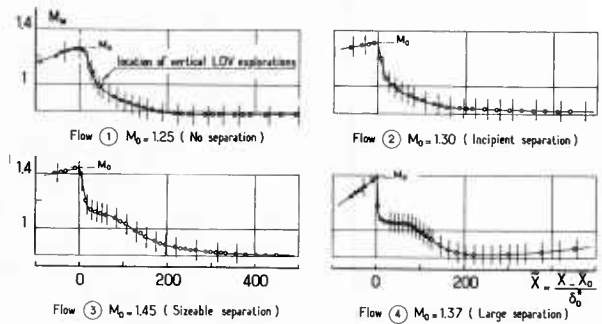


Fig. 2.61 – Transonic interaction with evolution to large separation – "Wall" Mach number distributions.

The four analyzed flows correspond to the following conditions :

- i - Flow 1 - Interaction without separation ($M_0 = 1.25$, No Separation - NS). For this case, the quasi-normal shock-wave is located near the end of the diverging part of a symmetrical nozzle at a station where the initial Mach number is equal to 1.25. This flow case actually does not separate but has been included in this Section in order to show the progressive evolution of the phenomena from an unseparated to a separated situation.
- ii - Flow 2 - Interaction corresponding to Shock Induced Incipient Separation ($M_0 = 1.3$, Incipient Separation - IS). This flow is produced in the same nozzle as Flow 1, but the shock being slightly farther downstream, the upstream Mach number M_0 is now equal to 1.30. Considering the value of the shape parameter of the incoming boundary-layer ($H_{in} = 1.30$), the present situation nearly coincides with Incipient Separation at the shock.
- iii - Flow 3 - Interaction with Sizeable Separation ($M_0 = 1.45$ - SS). Now the interaction occurs in a symmetrical nozzle with a greater maximum area ratio. The shock-wave is at a location where $M_0 = 1.45$, thus a rather large separated bubble forms.
- iv - Flow 4 - Interaction with Large Separation ($M_0 = 1.37$ - LS). This interaction is the one already commented upon in Section 2.8.1 where the discussion was focused on the accompanying inviscid flow structure. It takes place in an asymmetric channel where a bump is mounted on the lower wall of the wind tunnel test section (see Fig. 2.47). In this case, a large separated bubble forms, despite a lower Mach number than for Flow 3. This happens because the bump contour induces a strong adverse pressure gradient.

The table below gives the main boundary-layer properties at the origin of each interaction :

Flow	M_∞	δ_0 (mm)	θ_0 (mm)	H_{θ_0}	$R\theta_0$
1	1.25	0.29	0.15	1.33	2200
2	1.30	0.36	0.14	1.30	2400
3	1.45	0.44	0.18	1.30	2500
4	1.37	0.52	0.27	1.27	3800

The careful experiments of Kooi (1978) and of Alber et al. (1971) already cited will also be used in the following discussion.

The general mean flow structure. Some of the mean streamwise velocity profiles measured across the dissipative layer of Flows 1 to 4 are plotted in fig. 2.62. In the present Section, the mean value of a velocity component will be represented by a barred symbol in order to avoid confusion between mean and instantaneous quantities, the latter being designated by an unbarred symbol. This distinction is introduced here because of the consideration of the flow turbulent properties.

In Fig. 2.62 the location of the wall has been sketched and the profiles extrapolated to the wall by a broken line, which is only a visual aid.

For Flows 1 and 2 - which are not separated - one observes a strong retardation of the profiles in the first part of the interaction. This effect is particularly important in the vicinity of the wall. Yet, negative values for the mean streamwise component were not detected. In the case of Flow 2, if separation occurs it does so close to the wall since it was not detected in the measurements.

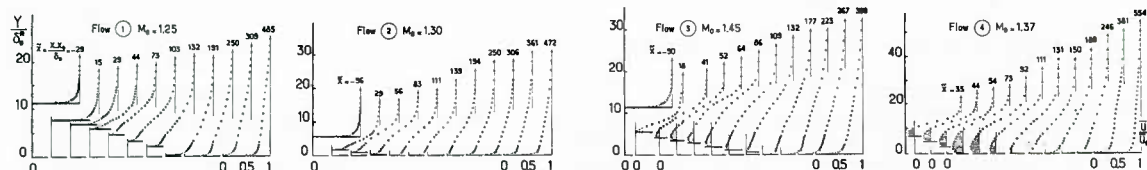


Fig. 2.62 – Mean streamwise velocity distributions
for flows 1 to 4 .

The maximum retardation effect is reached at a certain streamwise location; further downstream, turbulent viscous forces produce a gradual acceleration of the fluid in the inner part of the boundary-layer. During the whole interaction process, the thickness δ of the boundary-layer is seen to increase steadily.

For Flows 3 and 4, a rather large reversed flow region is formed, the thickening of the dissipative layer being now much more important than for Flows 1 and 2. The maximum negative normalized velocity u_m/u_e is equal to -0.12 for Flow 3 and to -0.22 for Flow 4. In both cases, the bubble lengths are comparable, although the bubble vertical extent is much more important for Flow 4 (note the change in vertical scale in Fig. 2.62d). In the case of Flow 4, one observes a dramatic increase in the boundary-layer thickness, δ being practically multiplied tenfold between the origin of interaction and the farthest downstream measuring station.

The structure of the flow within the interacting boundary-layer can be best visualized by the tracing of the mean flow streamlines. It should be pointed out that such streamlines are in fact fictitious since they belong to a mean flow in the sense of statistical turbulence (i.e. Reynolds averaging). As will be seen below the actual flow is highly fluctuating and its instantaneous structure far more complex than the mean organization shown here. However, the streamlines thus constructed are conceptually identical to those which would result from a modeling of the flow with the classical time averaged Navier-Stokes equations.

The streamlines traced in fig. 2.63 have been determined as lines of constant value for the normalized mass flow (per unit span) :

$$m = \int_0^Y (\rho u / \rho_t a_t) dn \quad (\text{in mm})$$

In the above formula, a_t is the sound velocity for stagnation conditions. The density ρ_t was determined either directly from interferometric measurements or computed from the velocity by assuming constant pressure and constant stagnation temperature across the dissipative layer.

The tracing of the streamlines displays the structure of the interacting boundary-layer. When the flow is separated, this layer contains a bubble type region where the streamlines consist of closed curves. The flow which recirculates is bounded by what is called the Dividing Streamline (or DSL). This streamline originates from the separation point S and stagnates at the reattachment point R. Another particular line is the locus of the points where the streamwise velocity

component is equal to zero : this line is the external border of the region in which u is negative. The DSL and the locus $u = 0$ meet at S and R.

The external border of the boundary-layer has been drawn in fig. 2.63a to 2.63d to show the rapid growth of the dissipative part of the flow that takes place during the interaction process. This growth is the consequence of the important entrainment rate along the boundary-layer edge. It is observed that the rate at which the external non-viscous flow feeds the dissipative layer is considerably enhanced by the interaction, especially downstream of the shock system. This rise in entrainment rate is a consequence of the huge turbulence production that takes place in the shock foot region along with the birth of large scale turbulence structures.

The subsequent streamwise evolutions of the mass flow \dot{m} -normalized by its value m_0 at the interaction origin - are represented in Fig. 2.64. One notes the steep increase in m which occurs when the flow is separated.

The entrainment rate is characterized by the entrainment coefficient C_E defined by the relation :

$$C_E = \frac{1}{\rho_e u_e} \frac{dm}{dx}$$

The entrainment coefficient plays a fundamental role in theoretical methods using the Integral Entrainment Equation to compute the boundary-layer development (see Section 2.2.1 of Part II). The streamwise variations of C_E for Flows 1 to 4 are represented in Fig. 2.65. The plotted data show the following tendencies :

- i - at the very beginning of the interaction, the entrainment coefficient starts to decrease and becomes negative, indicating that the mass flow across the boundary-layer actually decreases at first. This tendency is also displayed by the streamlines traced in Fig. 2.63 which show a contraction of the flow in the first part of the interaction ;
- ii- thereafter, the trend is reversed and C_E increases markedly with x -wise distance. A maximum value is reached and its magnitude increases in proportion to the strength of the interaction.
- iii-in the downstream part of the interaction, the entrainment coefficient decreases steadily and tends toward the value representative of a flat plate turbulent boundary-layer.

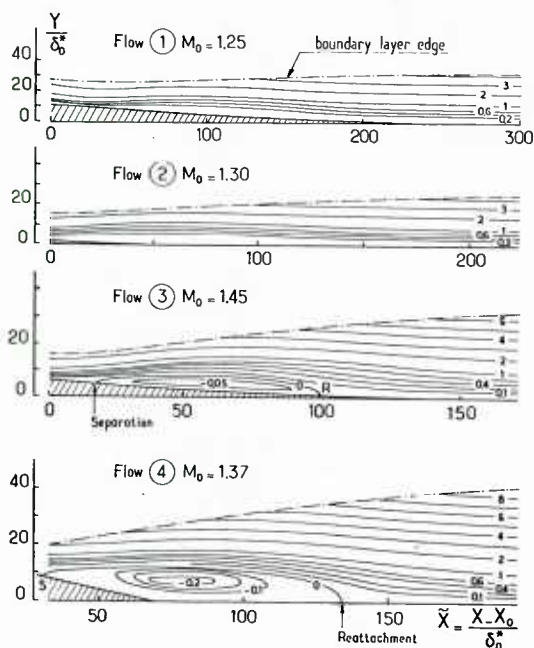


Fig. 2.63 - Mean flow streamlines in the dissipative layer lines of constant $q_m = \int_0^y (\rho/\rho_t \bar{u}/a_t) dy$.

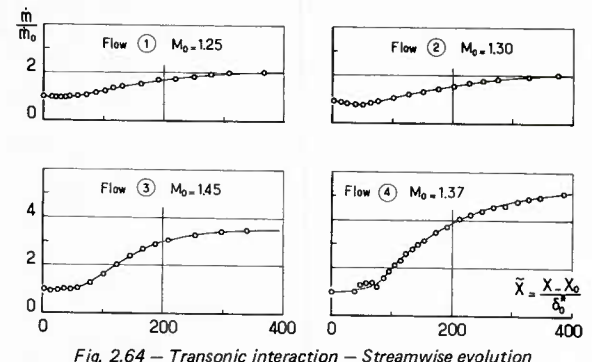


Fig. 2.64 - Transonic interaction - Streamwise evolution of the mass-flow through the dissipative layer.

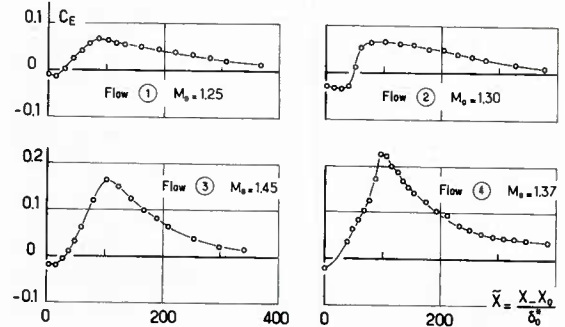


Fig. 2.65 - Transonic interaction - Streamwise evolution of the entrainment coefficient.

The "history" of the entrainment rate during an interaction process can be best represented by plotting C_E against a parameter characterizing the shape of the velocity distribution across the boundary-layer, e.g., the shape parameter H_i or preferably for flows involving large separation $\xi_i = 1 - 1/H_i$.

With this kind of representation, one is led to introduce the concept of "equilibrium" boundary-layers which generalizes the concept of equilibrium flat plate boundary-layer already defined in Section 1.2. Briefly speaking, an interacting boundary-layer will be said to undergo an equilibrium evolution if its properties depend only on the following "main" parameters in the course of the process : a "representative" shape parameter, the local Reynolds number and the outer Mach number (assuming that influences, like heat-transfer at the wall, transpiration or suction effect, are not present). In the case of Flows 1 to 4, compressibility effects are very weak and - for a given interaction - the Reynolds number does not vary much so that its influence (although not negligible) can be considered as secondary. Thus the essential factor is the shape parameter.

The curves plotted in Fig. 2.66 show that the evolution of C_E vs. $\frac{1}{H_i}$ form closed loops. This indicates that there is not a unique correspondence between C_E and $\frac{1}{H_i}$ during the interactions. Such a trend, which will be observed for other flow properties, is typical of evolutions strongly out of equilibrium. This behavior renders the modeling of these strongly interacting flows very difficult, the representation of the non-equilibrium effects being very delicate.

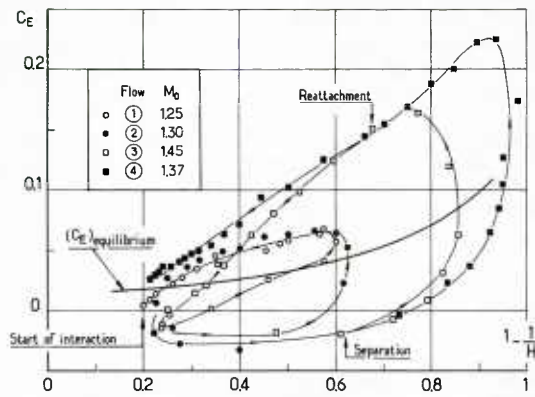


Fig. 2.66 – Transonic interaction – Variation of the entrainment coefficient in the phase plane ($1 - 1/H_i$, C_E) for flows 1 to 4 .

Other typical mean flow patterns associated with transonic interaction have been established by Alber et al. (1971) whose experiments have already been cited. For that study, the velocity field was measured with classical pressure probes. Two interactions were investigated by these authors.

In the first situation, termed Case A, (see Fig. 67a) the shock is not strong enough to induce immediate separation. However, its destabilization effect on the boundary-layer is such that separation occurs at a short distance downstream of it, because of the adverse pressure gradient on the rear part of the bump on which the shock forms (this situation is one of the variants of Pearcey's Flow Model B, see Section 2.3 above).

A very slight increase in the shock strength (the peak Mach number M_0 varies from 1.32 to 1.34) causes the separation point to move from its downstream location to a position just after of the shock foot. This new configuration, called Case B, (see Fig. 67b) corresponds to the Flow Model A of Pearcey.

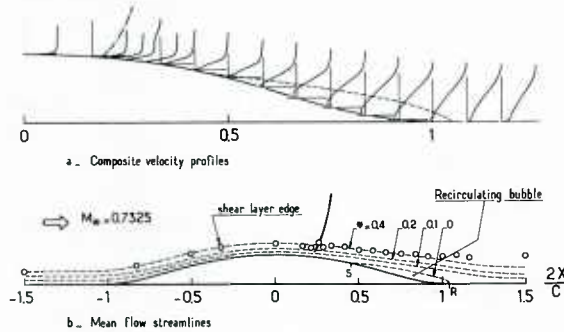


Fig. 2.67 a – Transonic flow past a bump – Trailing edge separation or rear separation – Case A (Alber et al., 1971).

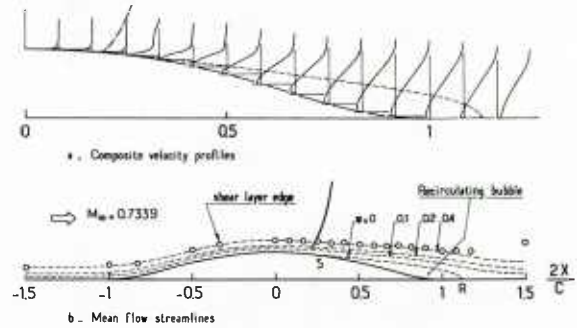


Fig. 2.67 b – Transonic flow past a bump – Shock induced separation or forward separation – Case B (Alber et al., 1971).

The streamwise mean velocity profiles for these two cases, as well as the streamlines in the boundary-layer, are represented in Fig. 2.67. One sees that the shape of these velocity distributions is very similar to that of the profiles measured in Flows 3 and 4.

The dissipative layer integral properties. The streamwise variations of the dissipative layer displacement thickness and incompressible shape parameter for Flows 1 to 4 are shown in fig. 2.68. The variations of the momentum thickness and of the kinetic energy thickness are represented in Fig. 2.69. It is recalled that the kinetic energy thickness θ^* is defined by the formula :

$$\theta^* = \int_0^\delta (\rho u / \rho_e u_e) (1 - u^2 / u_e^2) dy$$

This integral thickness arises in boundary-layer integral methods of calculation employing the Mean Kinetic Energy equation (see Section 2.2.1 of Part II).

The initial intense destabilization of the boundary-layer entails a very fast increase of its displacement effect. The shape parameter H_i is seen to reach its maximum slightly upstream of the maximum of δ^* , this difference being due to the fast growth of the thickness δ .

The rise in δ and H_i is spectacular when separation is present. For Flow 4, H_i reaches a very high value which is uncertain because of the smallness of the incompressible momentum thickness. For this case, such a high value for H_i signifies that the separated flow tends to develop a free-shear layer like structure. This point will be further discussed below.

Considering Flows 3 and 4, one notes a rapid decrease in H_i as the reattachment process begins, up to the reattachment point R. Downstream of R, H_i relaxes more progressively toward a new flat plate value. At the separation station S, H_i is close to 2.6 which is the value commonly admitted at a turbulent separation point. It should be said that an accurate determination of H_i in this region is difficult because of the intense streamwise gradients accompanying a separation phenomenon. At reattachment, H_i is practically equal to 3, this value being known with a better accuracy since the streamwise gradients are here much weaker than at separation. The value $H_i = 3$ at reattachment is also found for (incompressible) flows reattaching behind a rearward facing step (Nguyen, 1971). It seems typical of turbulent reattachment at low to moderate Mach numbers.

The momentum thickness is seen to increase steadily during the whole interaction process. This continuous rise is readily understandable if one considers the Integral Momentum equation (see Section 2.2.1 of Part II). As a matter of fact, in the flows under investigation, the pressure gradient is either zero or positive and, except in the separated regions where its amplitude is always small, the skin-friction coefficient is also positive. Consequently according to Eq. 2.4 of Section 2.2.1 of Part II the derivative d/dx is here always positive. It should be noticed that at separation, the rise in θ is modest, whereas it is much greater during reattachment.

Another example of variations of boundary-layer integral thicknesses is given in Fig. 2.70 which shows results obtained by Kooi in an experimental study already cited. The results demonstrate the rapid increase of the boundary-layer displacement effect as soon as the upstream Mach number goes beyond the Incipient Separation limit.

It should be stressed that the development of the separated boundary-layer depends strongly on the specific flow situation and that no general correlation laws can be derived as pertaining to a "typical" transonic shock-wave/turbulent boundary-layer interaction. This fact becomes obvious if one compares Kooi's results with those of Délery : for nearly the same upstream Mach number $-M_0 = 1.45$ and $M_0 = 1.46$ respectively - very different rises in the displacement thickness were found (see Figs. 2.68 and 2.70). The observed discrepancy is partly due to differences in Reynolds number, but essentially the cause is the use of different test set-ups.

As shown by Fig. 2.71, it is also impossible to correlate the length L_s of the separated zone (L_s is defined here as the x -wise distance between points S and R). The large scatter in the values of L_s/δ_0 found by different experimenters, comes partly from the techniques employed to determine the length of the separated bubble, but also and essentially from the type of conditions prescribed to the outer stream. The only general tendency which can be deduced from the above results is a decrease in L_s/δ_0 with increasing Reynolds number, the upstream Mach number M_0 being kept constant. This trend agrees with the observation already made of a greater resistance to separation at high Reynolds number.

The influence of thermal conditions at the wall on transonic shock induced separation was investigated by Padova et al. (1980). These authors found that the wall pressure distribution was practically insensitive to heat transfer at the wall (see Fig. 2.72). However, it should be pointed out that in these experiments the range of variation of the wall temperature T_w was relatively narrow : $0.85 < T_w/T_{te} < 1.10$ (T_{te} being the external flow stagnation temperature). Concerning the wall shear stress, Padova and his co-workers found that in the fore part of the interaction, the

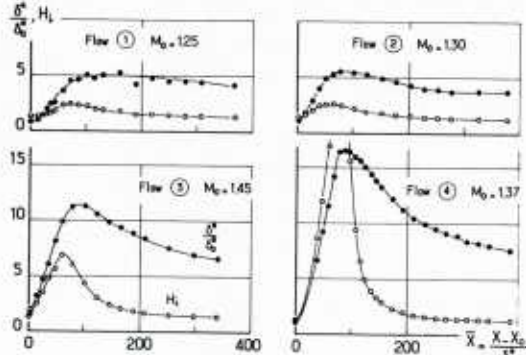


Fig. 2.68 – Streamwise variations of displacement thickness and shape parameter for flows 1 to 4 .

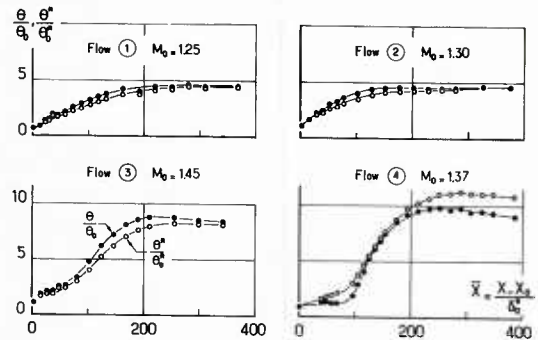


Fig. 2.69 – Streamwise variations of momentum and kinetic energy thickness for flows 1 to 4 .

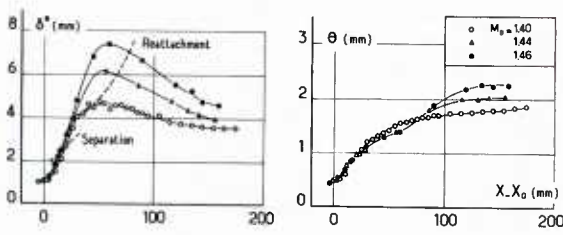


Fig. 2.70 – Variations of displacement and momentum thickness in strong transonic interactions (Kooi, 1978).

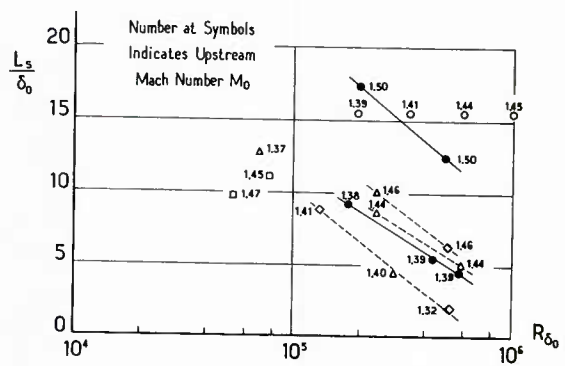


Fig. 2.71 – Transonic interaction – Effect of Reynolds number on the length of separated region (Kooi, 1978).

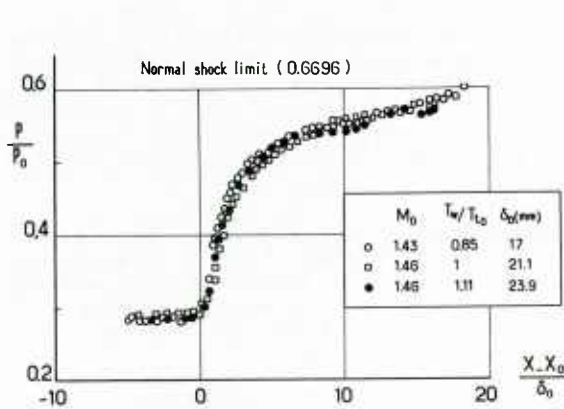


Fig. 2.72 – Transonic interaction – Heat transfer effect on wall pressure distribution – $R_L = 36 \times 10^6$ – (Padova et al., 1980).

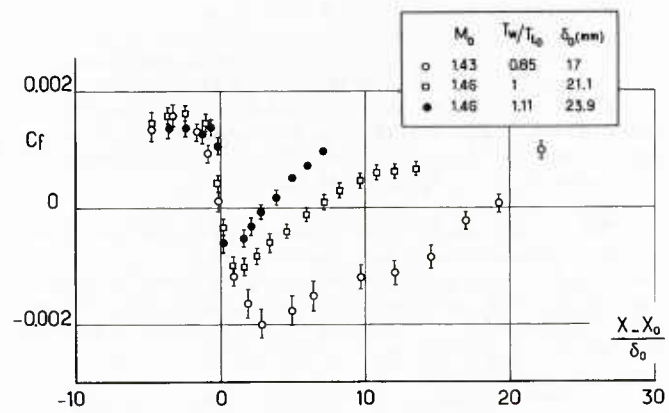


Fig. 2.73 – Transonic interaction – Heat transfer effect on skin friction distribution – $R_L = 36 \times 10^6$ – (Padova et al., 1980).

streamwise distribution of the skin friction coefficient C_f did not depend much on the ratio T_w/T_{te} . But, in the separated zone, $C_f(x)$ was found to be extremely sensitive to heat-transfer effect, a small decrease in T_w/T_{te} producing a large increase in the length of the separated bubble (see Fig. 2.73). This trend is in contradiction with other observations which tend to prove that cooling the wall increases the "stiffness" of the boundary-layer and, accordingly, its resistance to destabilizing effects (see Section 2.7). Thus, the results of Padova et al. should be confirmed by further experiment. The question on wall temperature effect on shock-wave/boundary-layer interaction is discussed in more detail in Section 3.7 devoted to supersonic flows. The conclusion is that cooling the wall always reduces the extent of the interaction domain.

Correlation properties of the boundary-layer velocity profiles. As will be explained in Section 3 of Part II, calculation methods based on the inviscid-viscous coupling approach frequently employ integral methods to compute the development of the boundary-layer. Most often, these methods assume that the dimensionless velocity distribution across the boundary-layer in the form $u/u_e = f(y/\delta)$ depends on a limited number of parameters : namely, the Reynolds number $R\delta_0$, the local Mach number at the boundary-layer edge and a suitable shape parameter such as H_i (only the adiabatic case will be considered, otherwise another parameter representing the wall temperature effect should be added as well as a representation of the temperature profiles).

As already seen in Section 1.3, the velocity distribution of an unseparated turbulent boundary-layer can be accurately represented by Coles' law of the wake/law of the wall formula. In the case of an incompressible flow, the Coles' formula depends on two parameters: the Reynolds number $R\delta_0$ and a shape parameter which can be H_i . For an adiabatic flow (no heat transfer at the wall), the influence of compressibility can be taken into account by employing the Van Driest generalized velocity concept. However, as already mentioned in Section 1.3, the influence of compressibility on the velocity distribution can be neglected if the local edge Mach number is not too high, say $M_e < 2$.

The Coles' formula has been generalized so that separated profiles can be represented by including the possibility of negative skin-friction (for more information see Section 2.2 of Part II). In order to check this new formula, velocity distributions measured in the well-separated flow 4 have been compared to the new Coles' family. This comparison (shown in Fig. 2.74), was made by determining which Coles' profile had the same integral thicknesses δ and θ as the respective distribution. One sees that the Coles' formula generally agrees closely with experiment. The same good correlation is noticed for Flows 1 to 3.

A similarly good agreement was observed by Mathews (1969) for the shock interaction profiles of Seddon (1960).

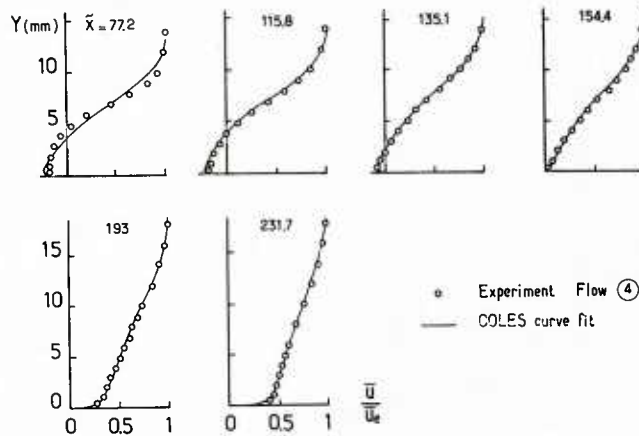


Fig. 2.74 – Velocity profile representation in a separated and reattaching boundary-layer.

The validity of the Coles' formula in the case of shock separated flows was also checked by Alber et al. (1971). They found a very satisfactory correlation with experiment except near the separation point. These authors have also demonstrated that the profiles can be likewise faithfully represented by the Turbulent Similar Solutions of Alber (1971), as shown in Fig. 2.76.

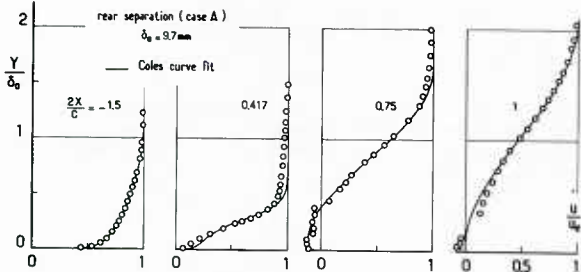


Fig. 2.75 – Transonic interaction – Comparison of the velocity profiles with Coles representation. Rear separation. Case A. Flow of Fig. 2.67 a (Alber et al., 1971).

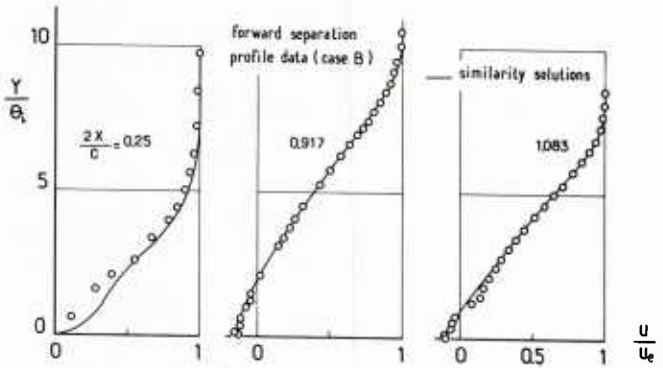


Fig. 2.76 – Transonic interaction – Comparison of the velocity profiles with Alber similarity solutions. Case B. Flow of Fig. 2.67 b (Alber et al., 1971).

As will be seen in Section 2.2 of Part II, most integral methods proposed for computing the interacting boundary-layer utilize, as "second" equation, either the Entrainment Equation or the Mean Kinetic Energy Equation. These methods respectively involve a Mass Flow Shape Factor $Z_i = (\delta_i - \delta_{i-1}) / \delta_i^*$ and a Mechanical Energy Shape Factor $J_i = \theta_i^* / \delta_i^*$ which are defined here with "incompressible" quantities, the compressibility effect being taken into account by the Van Driest generalized velocity concept or by suitable supplementary formulae. (other definitions of the above shape factor may be used ; however, the formulae always involve the three integral thicknesses : δ_i , θ_i and δ_i^*).

The theoretical models must be provided by "closure" relationships expressing the Shape Factors Z_i and J_i as functions of the "basic" shape parameter : H_i (for instance) and of the Reynolds number. As examples, Figs. 2.77a and 2.77b show tracings of J_i and Z_i against the parameter $H_i = 1/H_i$ the curves having been computed with the three Equilibrium Solutions of Michel et al. (1969). These theoretical curves are compared to evaluations of the shape factors made from the experimental profiles of Flows 1 to 4. Concerning the Mechanical Energy Shape Factor, there is very close agreement between experiment and the theoretical curves which nearly coincide. On the other hand, the relatively large scatter observed in the Z_i vs. H_i plot is in great part due to the uncertainty in the definition of the boundary-layer physical thickness δ_i .

Figure 2.78 shows plots of the correlation for the Shape Factor $H_1 = (\delta - \delta^*) / \theta$ vs. H which is frequently utilized in methods based on the Entrainment Equation. The shape parameter H is defined in Section 2.2.3 of Part II. For low Mach number flows, it is practically equal to H_i .

The curves of Fig. 2.78 tend to demonstrate that for the strongly interacting flows under investigation, there is not an unique correlation law between H_1 and H . This is especially true in the first part of the interaction region. A good correlation of the experimental point is only observed downstream of the reattachment station.

To conclude this Section, we will make the following comments on the validity of the generalized Coles' family which is frequently used in interacting boundary-layer calculations. In fact, experiment shows that this family is inadequate under at least two circumstances :

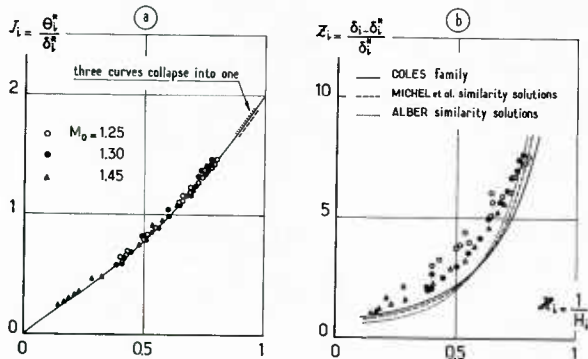


Fig. 2.77 – Correlation of integral properties for flows 1 to 4 .

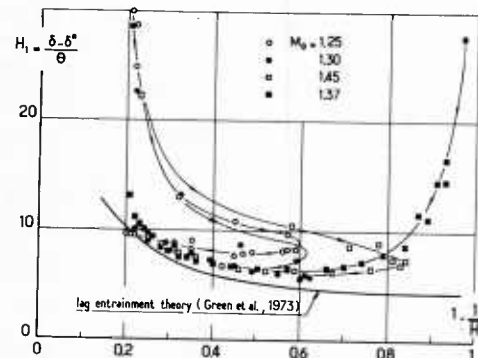


Fig. 2.78 – Variation of the entrainment theory parameter in the phase plane ($1 - 1/H$, H_1) for flows 1 to 4 .

- i - at and in the vicinity of the separation station. As can be seen by inspection of Eq. 1.5 of Section 1.3, the Coles' representation is only composed of the wake-component at a point where the skin-friction vanishes. The corresponding shape parameter H_i is nearly equal to 3, which is substantially higher than the commonly admitted value of 2.6 at a separation point. On the other hand, the Coles' law fits remarkably well the experimental reattachment profile whose shape parameter is precisely equal to 3 (see above).
- ii- when the vertical extension of the separated region becomes large. In this case, the dissipative layer has in fact a free shear-layer like development in its outer part. Consequently, a velocity law depending on only one shape parameter is certainly unable to faithfully represent such a separated flow.

As a matter of fact, when a large separated zone is forming, the streamwise velocity profiles rapidly tend to develop a free shear-layer structure. This behavior is illustrated by plotting the dimensionless velocity (classical in turbulent jet studies) :

$\varphi = (u - u_m)/(u_e - u_m)$, where u_m is the minimum negative velocity against the scaled ordinate $\eta = (y - y_{\varphi=0.5})/b$ and, where b is a conventional mixing zone thickness defined as $b = (y_{\varphi=0.95} - y_{\varphi=0.5})$.

Applied to the separated profiles of Flow 4, this data reduction leads to a very good correlation of the experimental results, as shown by Fig. 2.79. The data points collapse into a single curve practically identical to the well known solution of Görtler for turbulent mixing (Schlichting, 1968). In what follows, we will see that some of the turbulent properties of the separated dissipative layer also exhibit a jet-like (or mixing-like) behavior.

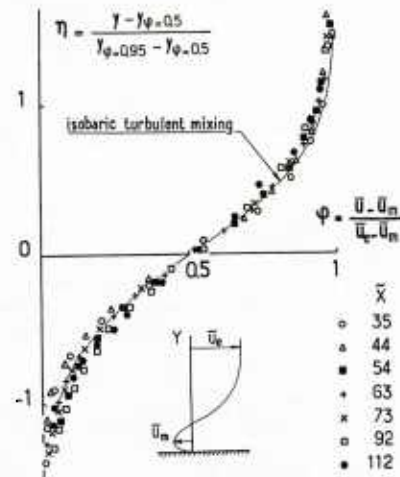


Fig. 2.79 — Similarity properties of the mean streamwise velocity profile in the separated region of flow 4 .

2.9 - Examination of Certain Turbulent Properties

2.9.1 Introductory Remarks

The present Section is devoted to a discussion of certain turbulence properties of the field resulting from the interaction between a shock-wave and a turbulent boundary-layer in transonic flows. In the envisaged situations, the interaction phenomenon will be assumed "steady" in the sense that large scale unsteadiness entailing ample shock motion is absent. Therefore, the following discussion excludes buffeting phenomena. The really unsteady aspects of a transonic shock-wave/turbulent boundary-layer interaction will be briefly examined in Section 5.5.7 of Part II. In the present Section, we will restrict our attention to "classical" turbulence phenomena which are characterized by a more or less random fluctuation of the dissipative field without any significant repercussions on the outer inviscid stream which can be considered as steady. This implies that the shock-wave (or the shock system) does not oscillate appreciably. In reality, in any interaction, a slight vibration of the shock(s) is always noticed. However, for a "stable" interaction, the amplitude of the shock motion remains within the limit of a fraction of the initial boundary-layer thickness. In what follows, the mean and fluctuating components of the velocity field will be defined in the sense of classical statistical turbulence, i.e., Reynolds averaging.

Most turbulence properties discussed in this Section are those of Flows 1 to 4. Let us recall that the measurements were made by using a two-color LDV system. With this kind of device, the statistical quantities are computed from a sample of N couples of instantaneous values u and v recorded at each probing point in the field. Hence, the following expression holds true for :

i - the mean values :

$$\bar{u} = (\sum_{n=1}^N u)/N \quad : \quad \bar{v} = (\sum_{n=1}^N v)/N$$

ii- the normal stresses :

$$\overline{u'^2} = [\sum_{n=1}^N (u - \bar{u})^2]/(N-1) \quad : \quad \overline{v'^2} = [\sum_{n=1}^N (v - \bar{v})^2]/(N-1)$$

iii- the shear stress :

$$\overline{u'v'} = [\sum_{n=1}^N (u - \bar{u})(v - \bar{v})]/N$$

2.9.2 General Structure of the Turbulence Field

The vertical distributions of the turbulence kinetic energy (scaled to the square of the speed of sound a_t for stagnation conditions) relative to Flows 2 and 4 are plotted in Fig. 2.80 (the distributions for Flows 1 and 3, not shown here, exhibit similar trends). The plotted values of the kinetic energy k have been computed by the formula $k = 0.5 (\bar{u}^2 + \bar{v}^2 + \bar{w}^2)$ where the spanwise fluctuation term \bar{w}^2 (in fact, not measured,) has been taken equal to $0.5 (\bar{u}^2 + \bar{v}^2)$, a reasonable estimation of the true value.

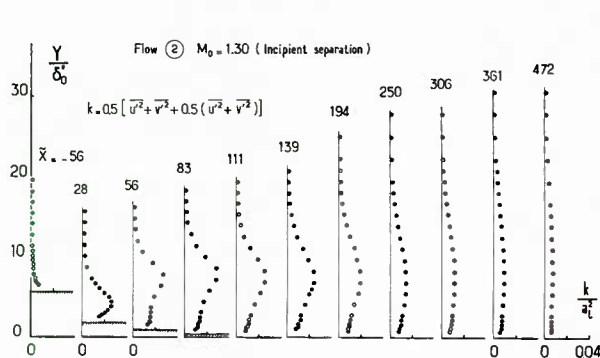


Fig. 2.80 a – Turbulent kinetic energy distributions for flow 2 .

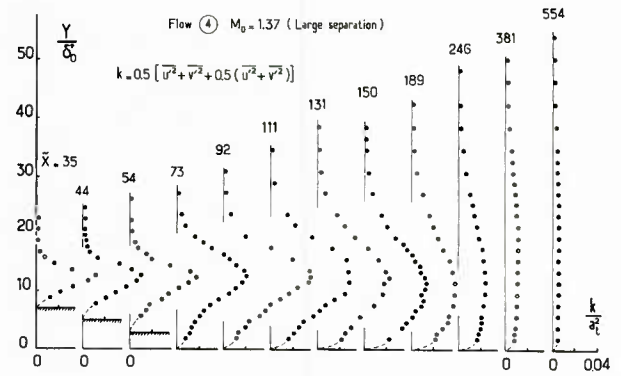


Fig. 2.80 b – Turbulent kinetic energy distributions for flow 4 .

For the two interacting flows considered here, one notes a very large increase in k taking place in the first part of the interaction process, i.e., near the shock foot. In this region, the distributions exhibit a maximum of large amplitude which is well detached from the wall. This behavior is particularly evident for Flow 4 which is the most separated.

Let us consider now the Reynolds shear-stress distributions. For compressible flows, the effective Reynolds shear-stress is given by $\rho \bar{u}' \bar{v}'$ (assuming that the triple correlation $\rho \bar{u}' \bar{v}' \bar{w}'$ is negligible). In the transonic flows under investigation, the change in the mean density ρ across the dissipative layer is small, so that the distribution of $-\bar{u}' \bar{v}' / a_t^2$ is nearly the same as that of $\rho \bar{u}' \bar{v}' / \rho_t a_t^2$. Thus, for practical purposes, $-\bar{u}' \bar{v}' / a_t^2$ can be interpreted as the non-dimensional Reynolds shear-stress.

The distributions of $-\bar{u}' \bar{v}' / a_t^2$ relative to Flows 2 and 4 are plotted in Fig. 2.81. They are also characterized by the existence of a well-defined maximum neatly detached from the wall. For Flow 4 (as also for Flow 3), the maximum values of shear-stress and turbulent kinetic energy generally coincide with the location of maximum mean streamwise velocity gradient $\partial \bar{U} / \partial y$, as shown in Fig. 2.82.

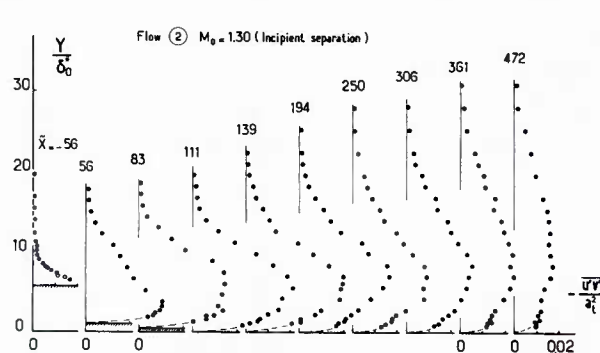


Fig. 2.81 a – Reynolds shear stress distributions for flow 2 .

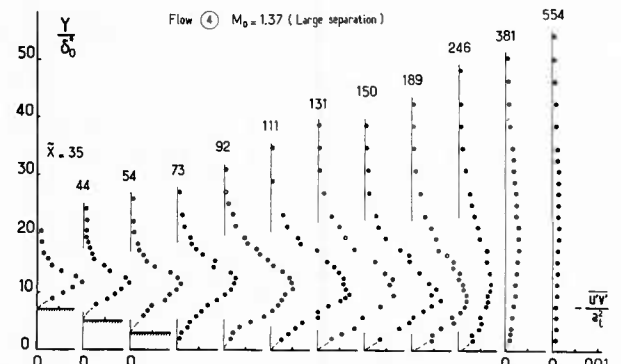


Fig. 2.81 b – Reynolds shear stress distributions for flow 4 .

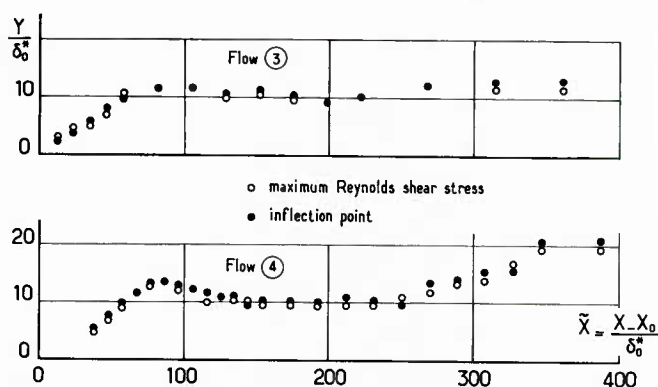


Fig. 2.82 – Coincidence between maximum Reynolds shear stress and inflection point on streamwise mean velocity profiles.

The lines of constant values for the turbulence kinetic energy and the Reynolds shear-stress are traced in Figs. 2.83a and 2.83b. For Flow 4, one observes that the region where k and \overline{uv} are at their maximum is close to the reattachment point and located somewhat above the Discriminating Streamline.

In order to give a more vivid idea of the variations of the turbulent quantities during the interaction process, Fig. 2.84 shows the streamwise evolutions of the maximum turbulence kinetic energy level (k)_M and of the maximum Reynolds shear-stress level (\overline{uv})_M for each vertical distribution.

These plottings demonstrate that there is a very large production of turbulence in the initial part of the phenomenon which is the shock foot region. This production is enhanced when separation occurs : then (k)_M reaches a maximum which is between 8 and 9 times the initial level in the undisturbed boundary-layer. For Flows 3 and 4, (k)_M starts to decrease upstream of the reattachment point R. Downstream of R, the turbulent kinetic energy decreases rather slowly and tends very gradually toward a flat plate level. The shear-stress is seen to grow at a relatively slower pace than k and reaches its highest level downstream of the point where k culminates. In the separated flows, the culmination of (\overline{uv})_M is close to the reattachment point. There, the shear-stress has reached a value which is 10 times the maximum initial level.

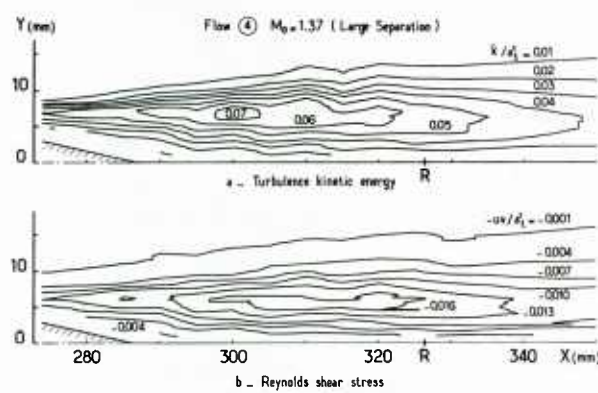


Fig. 2.83 - Lignes of constant value for the turbulence kinetic energy and the Reynolds shear stress.

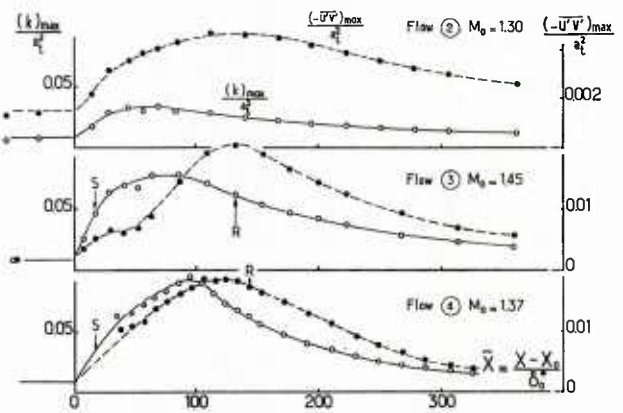


Fig. 2.84 - Streamwise evolution of maximum kinetic energy and shear stress.

The highest turbulent levels are particularly high, since for an incompressible mixing zone, the maximum of T_u and $T(\overline{uv})$ are respectively close to 0.40 and 0.014. The above levels are also significantly higher than the peak values reached in an incompressible separated flow where T_u is near 0.16 - 0.20 (Tani and Iuchi, 1964 ; Solignac 1980).

Similar universal turbulence properties, with comparable fluctuation intensities, were also found by Seegmiller et al.(1978) in a shock induced separation on a thick circular arc airfoil. The distributions of the turbulence quantities, along with the mean streamwise velocity profiles, which were measured by Seegmiller and his colleagues with a two-color LDV system, are plotted in Fig. 2.85. For this flow, it is likewise noticed that the peak values for the shear-stress and the turbulence kinetic energy are located slightly above the Discriminating Streamline and that they generally coincide with the location of the maximum velocity gradient.

Let us now focus our attention on Flow 4 for which the vertical development of the separated dissipative layer is the largest. We will consider the streamwise fluctuating component u' measured in the region where the flow is separated. The distributions of the reduced turbulence intensities $\langle u' \rangle / (\langle u' \rangle_M)$ are plotted against the dimensionless ordinate in Fig. 2.86. One sees that these distributions correlate rather well and are in good agreement with results relative to a turbulent incompressible mixing-zone (Davis et al., 1963).

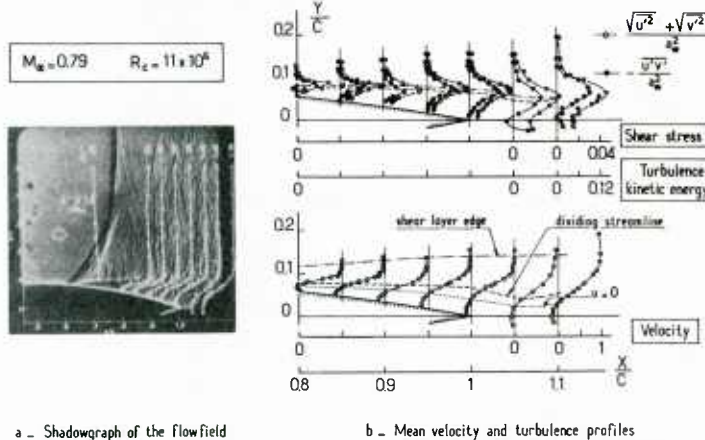


Fig. 2.85 - Transonic interaction - Separation on a biconvex profile (Seegmiller et al., 1978).

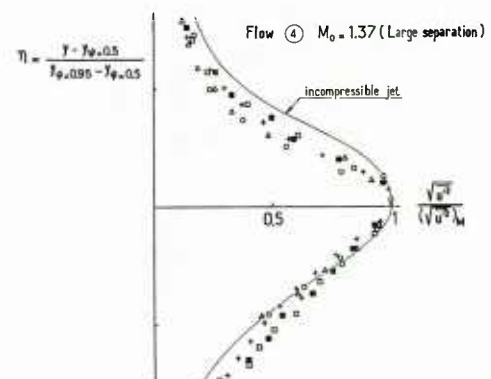


Fig. 2.86 - Correlation properties of normalized streamwise turbulence - Intensity distributions for flow 4 .

The similitude properties of the separated dissipative layer are also displayed by the Skewness Factor S_k and the Flatness Factor F_1 whose distributions are plotted in Fig. 2.87. Over most of their width, the profiles correlate closely with measurements made in an incompressible mixing zone (Wyganski and Fiedler, 1970). The behavior of S_k and F_1 differs from that of a mixing zone only in the vicinity of the wall where conditions imparted to the flow are obviously not the same as those existing at the outer edge of a jet issuing into a quasi-unlimited medium.

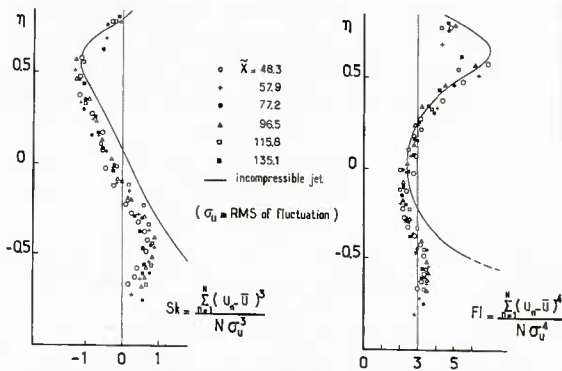


Fig. 2.87 – Similarity properties of the skewness and flatness factors for the streamwise fluctuating component – Flow 4 .

From inspection of these results, it can be concluded that the separated dissipative-layer tends to rapidly develop a mixing-like structure, the influence of the low velocity reversed flow being extremely weak. It may also be inferred that the initial state of the boundary-layer has little influence on the development of the shear layer.

2.9.3 Specific Characteristics of Turbulence in the Interacting Flow

Nevertheless, consideration of the vertical fluctuations shows that the similitude with a mixing layer is far from being complete. The essential differences are made visible, in particular, by considering the x -wise variations of the maximum RMS values $\langle u' \rangle$ and $\langle v' \rangle$, as shown by Fig. 2.88. For the four interactions under investigation, in the most upstream part of the process, the streamwise fluctuations are seen to exceed the vertical fluctuations by more than a factor of 3. This result is in contrast to a mixing layer where $\langle u' \rangle$ is only 30% higher than $\langle v' \rangle$. Similar observations are reported by Johnson and Bachalo (1978) and Johnson et al. (1981).

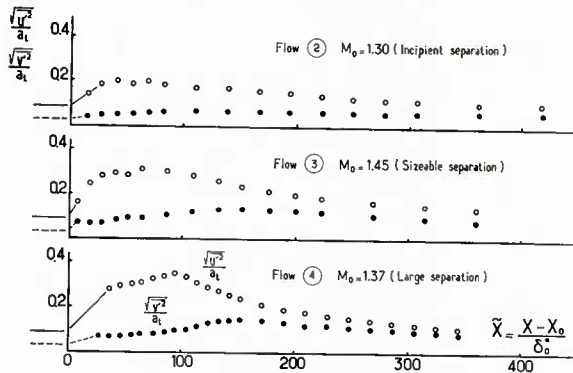


Fig. 2.88 – Streamwise variations of the maximum longitudinal and vertical turbulence intensities for flows 2 3 and 4 .

The initially large increase in $\overline{u'^2}$ is to be expected if one considers the production term of the $\overline{u'^2}$ turbulence transport equation, which will be written here for the case of an incompressible flow for the sake of simplicity. This term P is written as :

$$P = -2\overline{u'v'} \frac{\partial \bar{u}}{\partial y} - 2\overline{u'^2} \frac{\partial \bar{u}}{\partial x}$$

In the first part of the interaction process, the contribution involving the streamwise derivative of \bar{u} is as large as the term involving the strain rate $\partial \bar{u} / \partial y$ (see below). This is a consequence of the strong retardation of the whole dissipative flow. Thus, P is here the sum of two large positive terms.

On the other hand, the production mechanism for $\overline{v'^2}$ is expressed by :

$$P = -2\overline{u'v'} \frac{\partial \bar{v}}{\partial x} - 2\overline{v'^2} \frac{\partial \bar{v}}{\partial y}$$

The derivative $\partial \bar{v} / \partial x$ is everywhere small, $\partial \bar{v} / \partial y$ is equal to $\partial \bar{u} / \partial x$ (nearly equal for a weakly compressible flow), so that the second term tends to decrease $\overline{v'^2}$ production in the first region of the interaction where $\partial \bar{u} / \partial x$ is everywhere negative. Further downstream, a larger and larger part of the viscous layer is accelerated by shear-stress effect. This fact explains the later growth of $\overline{v'^2}$.

Such a strong anisotropy of the flow has two important consequences which must be kept in mind when developing a theoretical flow model :

i - the first point concerns the mechanism of turbulence kinetic energy production. As a matter of fact, for an incompressible flow and if the contribution involving the derivative $\partial \bar{v} / \partial x$ is assumed negligible, the production term of the k transport equation becomes :

$$P = -\bar{u}'\bar{v}' \frac{\partial \bar{u}}{\partial y} - (\bar{u}^2 - \bar{v}^2) \frac{\partial \bar{u}}{\partial x}$$

The first term, representing production by shear-stress, is generally predominant in shear-layer and/or boundary-layer type flows. For this reason, it is frequently the only term retained in most predictive methods.

The two production terms of the above expression have been computed for the aforementioned Flows 2 and 3 ; they are plotted in Fig. 2.89. One sees that production due to normal stress is as high as production due to shear stress over a streamwise distance which is of the order of five times the initial boundary-layer thickness. This region roughly coincides with the region of steepest x-wise pressure gradient where there is a general retardation of the entire flow field. Further downstream, the normal stress contribution becomes rapidly negligible.

ii- the second point is relative to the streamwise momentum equation. In the case of an incompressible flow, the terms of this equation involving Reynolds stress are the following :

$$\frac{\partial}{\partial y} (\bar{u}'\bar{v}') - \frac{\partial}{\partial x} (\bar{u}^2 - \bar{v}^2)$$

The normal distributions of these two terms for Flows 2 and 3 are plotted in Fig. 2.90. In the first part of the interaction, one sees that the x-derivative of the normal stress can be greater than the y-derivative of the shear-stress. Farther downstream, the normal-stress influence is negligible and the "classical" thin shear-layer hypothesis can be applied anew.

Simpson et al. (1977) have made similar observations concerning the importance of normal stress both in the turbulence production mechanism and in the momentum equation in the case of a separating incompressible boundary-layer (see also Viswanath and Brown (1982) who analyzed a separated trailing-edge flow at a transonic Mach number).

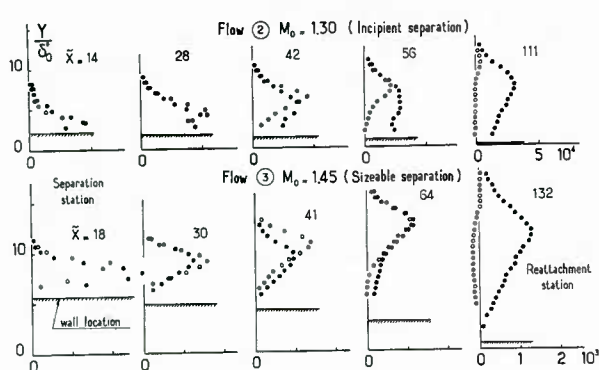


Fig. 2.89 - Distributions of turbulence production terms for flows 2 and 3
 $\bullet - \delta_0^* / \delta_t^2 \bar{u}'\bar{v}' \partial \bar{u} / \partial y$ $\circ - \delta_0^* / \delta_t^2 (\bar{u}^2 - \bar{v}^2) \partial \bar{u} / \partial x$.

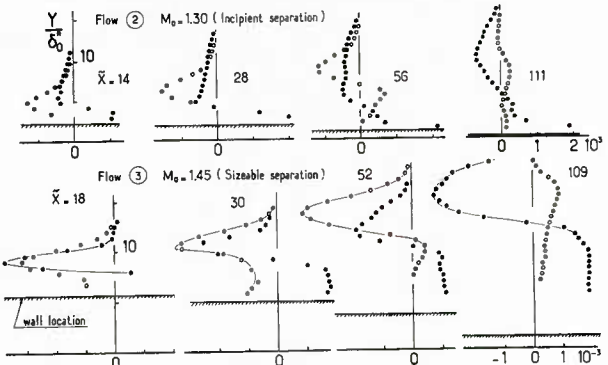


Fig. 2.90 - Distributions of Reynolds stress derivatives for flows 2 and 3
 $\bullet - \delta_0^* / \delta_t^2 \partial (-\bar{u}'\bar{v}') / \partial y$ $\circ - \delta_0^* / \delta_t^2 \partial / \partial x (\bar{u}^2 - \bar{v}^2)$.

2.9.4 Some Remarks on the Problem of Turbulence Modeling

The aforementioned experimental data obtained by Délery and by Seegmiller and his co-workers can be used to guide turbulence model development for use in computer codes that attempt to numerically simulate complicated dissipative flows. Most often, simulations based on the Reynolds averaged Navier-Stokes equations utilize a scalar eddy diffusivity formed from a product of a modeled length scale and velocity.

In the present data processing, the eddy diffusivity was deduced from the measured shear-stress and velocity profiles by using the relation :

$$\nu_t = \frac{-\bar{u}'\bar{v}'}{\partial \bar{u} / \partial y}$$

The distributions of ν_t thus obtained by Seegmiller et al. are represented in Fig. 2.91a. A general observation is that ν_t tends to increase with distance downstream from the separation point and its maximum value tends to diffuse outward through the shear-layer, particularly beyond the trailing edge of the profile used in these experiments. Other eddy diffusivity distributions are plotted in Fig. 2.92. They correspond to Flow 4 which is the most separated (distributions for the other Flows exhibit similar trends). Here the plotted quantity is the eddy diffusivity scaled to the product $u_e \delta$, δ being the local boundary-layer thickness. The same general evolution as in the previous example is observed.

Figure 2.92 also shows a comparison with the following theoretical evaluations of ν_t based on :

i - the models of Alber (1971) and Levy (1978), for the separated flow region ;

ii- the model of Michel et al. (1969) for the reattached boundary-layer (in this case, the two above models give practically identical results, so they are not all plotted).

In certain algebraic turbulence models, the eddy diffusivity is expressed by means of the Prandtl mixing length concept, in the form :

$$\nu_t = l^2 \left| \frac{\partial \bar{u}}{\partial y} \right|$$

Figure 2.93 shows the distributions of the normalized mixing length l/δ computed from the data relative to Flows 2 and 4. One observes that at the beginning of the interaction and in the central part of the dissipative layer, the magnitude of l/δ is much lower than the usual value $l/\delta = 0.09$ adopted in "classical" boundary-layer calculations. Although large errors in the calculation of $\partial \bar{u}/\partial y$ from data points can be expected in the outer region of the dissipative flow where $\partial \bar{u}/\partial y$ tends to zero, l/δ exhibits in this region a distinct tendency to increase. Such an increase was also observed in an incompressible separated flow by Etheridge and Kemp (1978). It could be due to some memory effect in the outer region of the dissipative layer. The inaccuracy of data very near the wall makes it difficult to interpret with assurance the experiments in this region. The high values of l/δ found near the wall at $x = 44$ and $x = 83$ in the case of Flow 4 correspond to the reversed part of the u profile where $\partial \bar{u}/\partial y$ changes signs. The same tendencies for the evolution of l were also noticed by Seegmiller et al., as shown by Fig. 2.91b.

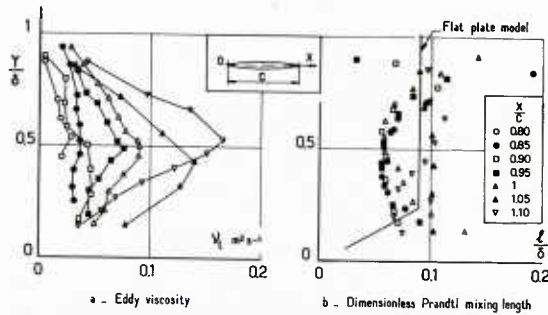


Fig. 2.91 - Separation on a biconvex profile (flow of Fig. 2.85), Eddy viscosity and mixing length distributions (Johnson et al., 1981).

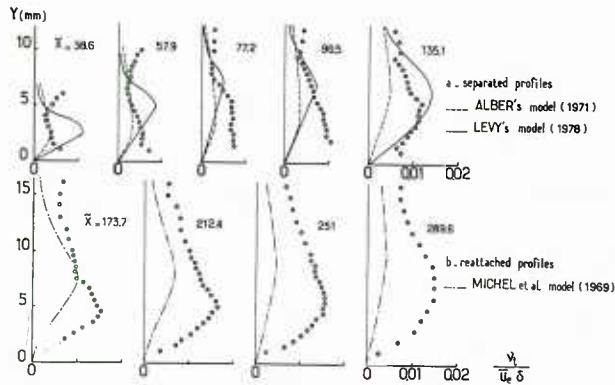


Fig. 2.92 - Distributions of dimensionless eddy viscosity - Flow 4 .

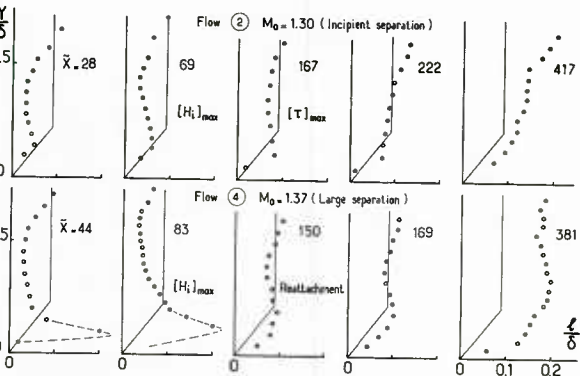


Fig. 2.93 - Distributions of Prandtl's dimensionless mixing length in flows 2 and 4 .

In the core of the layer, l/δ increases steadily with downstream distance and reaches values well in excess of 0.09 for the most downstream probing station. This fact demonstrates that turbulence has a structure different from that of an equilibrium flat plate boundary-layer. The importance of the "memory" effect in the course of the interaction is also illustrated by Fig. 2.94 which shows the distributions of the following quantities \bar{u}/\bar{u}_e , T_u and T_{uv} measured at $\bar{x} = 308$, i.e., far downstream of the reattachment point which is located at $\bar{x} = 150$. These profiles are compared to the well known results of Schubauer and Klebanoff (1951) relative to an incompressible "well behaved" flat-plate boundary-layer. The shape parameters of the two flows are equal to 1.4 and their Reynolds numbers are very close. Consequently, the mean reduced velocity profiles u/u_e are nearly identical. On the other hand, as can be seen in Fig. 2.94, the distributions of turbulent quantities differ appreciably. In particular, the shear-stress profile of the transonic interaction has a wake-like shape over its major part, the high values of shear-stress found in the central part of the boundary-layer being the remnant of the mixing-type structure which developed during separation.

A synthetical overview of the entire history of the interacting boundary-layer, starting from the process onset at x_0 to the far downstream state, can be reflected by considering the evolution in the "phase plane" of the two following variables :

i - the square root of the shear-stress coefficient given by

$$C_T = -2(\rho u' v')_M / \rho e u_e^2$$

where $(\bar{u}' v')_M$ is the maximum shear-stress at each streamwise location,

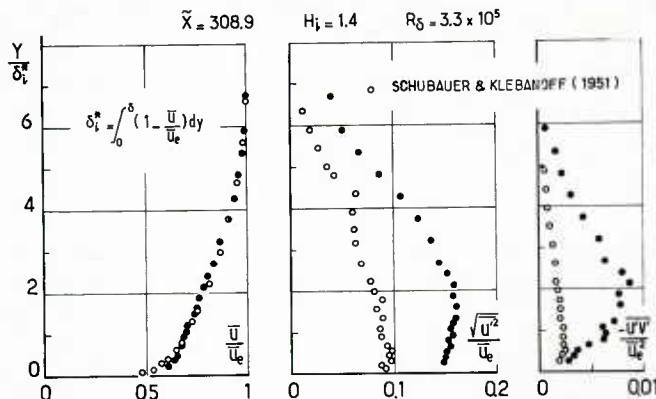


Fig. 2.94 – Boundary-layer properties downstream of reattachment – Comparison with flat plate data at same H_i and R_D (Flow 4 $\tilde{X} = 308.9$).

ii- the "equilibrium shape parameter" J defined as :

$$J = 1 - 1/H_i$$

According to East and Sawyer (1979), one can introduce a function defined by :

$$G = (H_i - 1) / (H_i \sqrt{0.5 C_T}) = J / \sqrt{0.5 C_T} = 6.55$$

which has the ability to remain constant for all equilibrium boundary-layer flows : the value of the constant being that corresponding to a "well behaved" flat-plate boundary-layer. As a matter of fact, G is similar to the Clauser parameter, the difference being that the conventional Clauser parameter involves the skin-friction coefficient. For an equilibrium flat plate boundary-layer there is in fact identity between the two functions since then the shear-stress is maximum at the wall.

Consequently, the equation :

$$J / \sqrt{0.5 C_T} = 6.55$$

specifies the straight line in Fig. 2.95. This line is the locus representative of "equilibrium" boundary-layers, i.e., boundary-layers undergoing specific transformations in which there is an instantaneous adjustment between the distributions of mean velocity and shear-stress. This adjustment is generally only possible for very progressive and slow streamwise evolutions.

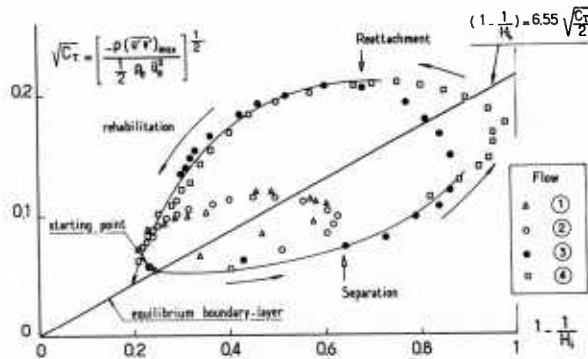


Fig. 2.95 – Transonic interaction – Variation of the normalized maximum Reynolds shear stress in the phase plane $(1 - 1/H_i, \sqrt{C_T})$.

If one plots $\sqrt{C_T}$ against J for Flows 1 to 4 (see Fig. 2.95), the following trends are observed in the course of the interaction :

i - the "trajectories" (or "images") of the four interactions in the phase plane $(J, \sqrt{C_T})$ start from a common point lying close to the equilibrium locus (it is not exactly on the locus because the incoming boundary-layers are slightly out of equilibrium due to the strong acceleration in the first part of the transonic channel). Initially, the trajectories run below the equilibrium locus. This indicates that the boundary-layer undergoes what is called a "Rapid Interaction Process" in the shock foot region. Then, there is a large departure from equilibrium characterized by a "lag" of the shear stress. When the shock is strong enough, separation occurs during this phase of the interaction process.

ii- thereafter, and especially for separated flows, the shear-stress and the shape parameter continue to increase together in a way typical of a free shear-layer development. This mixing-like evolution could continue until $J = 1$. (i.e., until $H_1 = \infty$).

As a matter of fact, during the Rapid Interaction Process, the separating boundary-layer undergoes such an overwhelming perturbation that - as Bradshaw postulated (1972) - the development of the free-shear layer is not significantly influenced by its initial conditions, i.e., the initial boundary-layer properties (provided it is fully turbulent). In that phenomenon, production of turbulence continues in proportion to the growth of the large scale structures which form near the separation location. Such large scale structures can be seen in the short exposure-time interferogram of Fig. 2.96 (Déleray, 1980a).

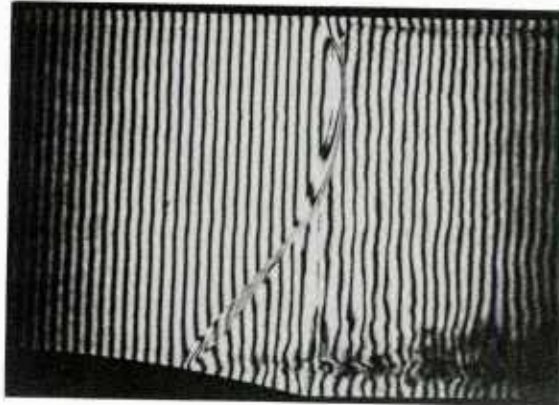


Fig. 2.96 – Short exposure time interferogram of a transonic interaction with separation – Flow 4 .

iii-at some position, the shape parameter culminates and starts to decrease. For separated flows, this reversal means the onset of the Reattachment Process. During this phase of the interaction, the shear-stress level still increases until it reaches a maximum at a streamwise station which nearly coincides with the reattachment point. In the course of the reattachment process, the trajectories in the (J_s/C_T) plane bend and cross the equilibrium locus at a point which is all the farther from the origin as the separated region is larger.

iv- downstream of reattachment (and in the absence of a new destabilizing agency) the trajectories point toward a "final point" located on the equilibrium locus. During this Relaxation Process, the representative points lie above the equilibrium locus and, at some instant, a new situation of maximum departure from equilibrium is reached. Downstream of reattachment, it is to be noticed that the representative points seem to collapse onto a common trajectory tending toward the equilibrium locus.

To end this Section on certain turbulent aspects of transonic interactions and in order to illustrate the highly fluctuating character of these flows, Fig. 2.97 shows tracings of the lines of constant value for the probability of the instantaneous velocity component u being negative. These contour lines are relative to Flows 1 to 4. They have been computed from histograms of u (for the sake of clarity, the vertical co-ordinate has been greatly dilated).

One observes that, even for the presumed unseparated Flows 1 and 2, instantaneous negative values of u occur in regions where the mean velocity u is positive. On the other hand, for Flows 3 and 4, the probability $P(u \leq 0)$ is never equal to 1. in the reversed part of the flow. This means that u is varying continuously from negative to positive values even in the most separated case.

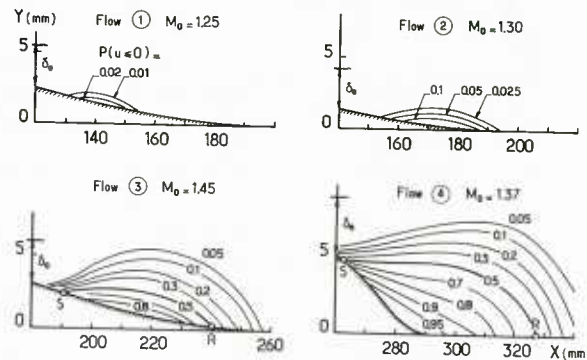


Fig. 2.97 – Lines of constant value for the probability of u to be negative (reversed).

2.10 - References

Abbiss, J.B., East, L.F., Nash, C.R., Parker, P., Pike, E.R. and Sawyer, W.G. (1976): A study of the interaction of a normal shock-wave and a turbulent boundary-layer using a laser anemometer. RAE TR-75 141 (Feb. 1976).

Ackeret, J., Feldmann, F. and Rott, N. (1946): Untersuchungen an Verdichtungsstößen und Grenzschichten in schnell bewegten Gasen. Bericht N° 10 a.d., Inst. für Aerodynamik, ETH, Zürich (1946) ; see also English translation "Investigation of compression shocks and boundary-layers in gases moving at high speed." NACA TM-1113 (Jan. 1947).

Alber, I.E. (1971): Similar solutions for a family of separated turbulent boundary-layer. AIAA Paper n° 71-203 (Jan. 1971).

Alber, I. E., Bacon, J.W., Masson, B.S. and Collins, D.J. (1971): An experimental investigation of turbulent transonic viscous-inviscid interactions. AIAA Paper n° 71-565 (June 1971) ; see also AIAA Journal, Vol. 11, N° 5, pp. 620-627 (May 1973).

Arieli, R. and Murphy, J.D. (1980): Pseudo-direct solution to the boundary-layer equations for separated flows. AIAA Journal, Vol. 18, N° 8, pp. 883-891.

Bohning, R. and Zierep, J. (1980): Normal shock/turbulent boundary-layer interaction at a curved surface. AGARD-CP-291.

Bradshaw, P. and Wong, R.Y.F. (1972): The reattachment and relaxation of a turbulent shear-layer. J. Fluid Mech., Vol. 52, Part 1, pp. 113-135.

Carrière, P. (1972): Aperçu de quelques résultats nouveaux obtenus à l'ONERA sur les phénomènes de décollement et de recollement. ONERA TP-1072.

Cebeci, T., Smith, A.M.O. and Mosinski, G. (1970): Calculation of compressible adiabatic turbulent boundary-layer. AIAA Journal, Vol. 8, N° 11, pp. 1974-1982 (Nov. 1970).

Chapman, D. R., Kuehn, D.M. and Larson, H.K. (1957): Investigation of separated flows in supersonic and subsonic streams with emphasis on the effect of transition. NACA TN-3869 (March 1957).

Davies, P.O.A.L., Fisher, M.J. and Baratt, M.J. (1963): The characteristics of the turbulence in the mixing region of a round jet. J. Fluid Mech., Vol. 15, Part 3 (March 1963).

Délery, J., Laval, P. and Chattot, J.-J. (1973): Etude expérimentale et théorique de l'écoulement transsonique autour d'un demi-profil. 10ème Colloque d'Aérodynamique Appliquée de l'AAAF, Lille (France), 7-9 Nov. 1973.

Délery, J. (1974): Recherches sur les phénomènes d'interaction et de décollement dans les grilles d'aubes. ONERA RSF-13/7078AY (Jan. 1974).

Délery, J., Chattot, J.-J and Le Balleur, J.-C. (1975): Interaction visqueuse avec décollement en écoulement transsonique. AGARD-CP-168.

Délery, J., (1977): Recherches sur l'interaction onde de choc-couche limite turbulente. La Recherche Aérospatiale, N° 1977-6, pp. 337-348 (Nov.-Dec. 1977).

Délery, J., (1979): Analyse du décollement résultant d'une interaction choc-couche limite turbulente en transsonique. La Recherche Aérospatiale, N° 1978-6, pp. 305-320 (Nov. 1978) ; English Translation ESA-TT 560.

Délery, J. (1980a): Some features of transonic shock-wave/turbulent boundary-layer interaction. VKI LS 1980-8 on "Shock-Boundary Layer Interaction in Turbomachines. (June 1980).

Délery, J. (1980b): Interaction onde de choc-couche limite turbulente en transsonique. (Recherches en 1978-1979). ONERA RSF-36/7078AY (July 1980).

Délery, J. (1981): Investigation of strong shock/turbulent boundary-layer interaction in 2D transonic flows with emphasis on turbulence phenomena. AIAA Paper N° 81-1245 (June 1981) ; see also AIAA Journal, Vol. 21, N° 2, pp. 180-185 (Feb. 1983).

Délery, J. (1984): L'interaction onde de choc-couche limite et son contrôle. AGARD-CP-365 ; see also ONERA-TP N° 1984-27.

East, L.F. (1976) : The application of a laser anemometer to the investigation of shock-wave/boundary-layer interactions. RAE Tech. Memo. AERO 1666 (Feb. 1976) ; see also AGARD-CP-193.

East, L.F. and Sawyer, W.G. (1979): An investigation of the structure of equilibrium turbulent boundary-layers. AGARD CP-271.

Etheridge, D.W. and Kemp, P.H. (1978): Measurements of turbulent flow downstream of a rearward-facing step. J. Fluid Mech., Vol. 86, Part 3, pp. 545-566.

Fottner, L., (1968): A semi-empirical approach of the transonic flow past cascades, including shock and viscous effects. AGARD CP-34.

Gadd, G.E. (1961): Interaction between normal shock-waves and turbulent boundary-layers. ARC R & M n° 3262 (1961).

Gobert, J.L., Seraudie, A. and Mignosi, A., (1980): Etude de l'interaction onde de choc-couche limite sur profil LC-100D de 400 mm de corde dans la soufflerie T2. ONERA RT-38/7078AYD.

Green, J.E., Weeks, D.J. and Brooman, J.W.F. (1973) : Prediction of turbulent boundary-layers and wakes in compressible flow by a lag-entrainment equation. RAE-TR-72 231.

Hiyotaka Hayakawa and Squire, L.C., (1982): The effect of the upstream boundary-layer state on the shock interaction at a compression corner. *J. Fluid Mech.*, Vol. 122, pp. 369-394.

Holst, T.L. (1979): An implicit algorithm for the conservative, transonic full potential equation using an arbitrary mesh. *AIAA Journal*, Vol. 17, N° 10, pp. 1038-1056 (Oct. 1979).

Inger, G.R. and Zee, S. (1978): Transonic shock-wave/turbulent boundary-layer interaction with suction or blowing. *Journal of Aircraft*, Vol. 15, N° 11, pp. 750-754 (Nov. 1978).

Inger, G.R. and Sobieszky, H. (1978): Normal shock interaction with a turbulent boundary-layer on a curved wall. VPI Aero-088 (Oct. 1978).

Inger, G.R. (1981): Transonic shock-turbulent boundary-layer interaction and incipient separation on curved surface. *AIAA Paper N° 81-1244* (June 1981).

Inger, G.R., Lynch, F.T. and Fancher, M.F. (1983) : A theoretical and experimental study of non-adiabatic wall effects on transonic shock/boundary-layer interaction. *AIAA Paper N° 83-1421* (June 1983).

Johnson, D.A. and Bachalo, W.D. (1978): Transonic flow about a two-dimensional airfoil. Inviscid and turbulent flow properties. *AIAA Paper n° 78-1117* (July 1978); see also ; *AIAA Journal*, Vol. 18, N° 1, pp. 16-24 (Jan. 1980).

Johnson, D.A., Bachalo, W.D. and Owen, F.K. (1981): Transonic flow past a symmetrical airfoil at high angle of attack. *Journal of Aircraft*, Vol. 18, n° 1, pp. 7-14 (Jan. 1981).

Kooi, J.W. (1978): Influence of the free-stream Mach number on transonic shock-wave/boundary-layer interactions. *NLR MP-78013 U* (May 1978).

Laurent, J. (1977): Interaction onde de choc-couche limite à grands nombres de Reynolds. Mesures sur la paroi plane. *ONERA PV-25/7078AY* (Dec. 1977).

Laval, P. (1973): Méthodes instationnaires de calcul des effets d'interaction de paroi en écoulement bidimensionnel supercritique. *Congrès Français de Mécanique*, Poitiers (France), Sept. 1973; see also: *La Recherche Aérospatiale*, N° 1973-5, pp. 275-288 (Sept.-Oct. 1973).

Leblanc, R., Mercier, V., Crosmier, J.C., Roulaud, R. and Goethals, R. (1974): Etude du phénomène d'interaction onde de choc normale-couche limite turbulente en vue des applications aux turbomachines transsoniques. *CEAT Report*, Poitiers University, Poitiers, France (Oct. 1974).

Leblanc, R. (1976): Recent progress in shock-wave/boundary-layer interaction. VKI LS-84 on "Transonic Blade to Blade Flow in Axial Turbomachinery". (Feb. 1976).

Levy, Jr., L.L. (1978): Experimental and computational steady and unsteady transonic flow about a thick airfoil. *AIAA Journal*, Vol. 16, N° 6, pp. 564-572 (June 1978).

Lighthill, M.J. (1953): On boundary-layer upstream influence. II Supersonic flows without separation. *Proc. Roy. Soc., Ser. A217*, pp. 478-507.

Mason, W., Ballhaus, W., Mackenzie, C., Frick, J. and Stern, M. (1977) : An automated procedure for computing three-dimensional transonic flow over wing-body combinations, including viscous effects. *AFFDL TR-122 Vol. 1* (Feb. 1977).

Mathews, D.G. (1969): Shock-wave/boundary-layer interactions in two-dimensional and axially-symmetric flows, including the influence of suction. *Ph. D. Thesis*, University of Washington (Nov. 1969).

Mateer, G.G., Brosh, A. and Viegas, J.R., (1976): A normal shock-wave turbulent boundary-layer interaction at transonic speeds. *AIAA Paper N° 76-161* (Jan. 1976).

Michel, R., Quémard, C. and Durant, R. (1969): Application d'un schéma de longueur de mélange amélioré à l'étude des couches limites d'équilibre. *ONERA NT-154*.

Murman, E., Bailey, F.R. and Johnson, M.L. (1975): TSFOIL - a computer code for two-dimensional transonic calculations, including wind tunnel wall effects and wave drag evaluation. *NASA SP-347*, Conference Proceedings for Aerodynamic Analysis Requiring Advance Computers, March 4-6, 1975.

Nguyen Van Noi (1971): Etude théorique et expérimentale du recollement subsonique incompressible d'un écoulement plan turbulent à sa frontière. *Thèse de Docteur Ingénieur*, Université de Paris.

Nussdorfer, T.J. (1956): Some observations of shock-induced turbulent separation in supersonic diffusors. *NACA RM1L26* (May 1956).

Padova, C., Falk, T.J. and Wittliff, C.E. (1980): Experimental investigation of similitude parameters governing transonic shock-boundary layer interaction. *AIAA Paper N° 80-0158* (Jan. 1980).

Pearcey, H.H. (1955): Some effects of shock-induced separation of turbulent boundary-layer in transonic flow past aerofoils. *ARC R & M N° 3108*.

Pearcey, H.H. (1961): Shock induced separation and its prevention by design and boundary-layer control. in *Boundary-Layer and Flow Control*, Vol. 2, G.V. Lachman Editor, Pergamon Press.

Pearcey, H.H., Osborne, J. and Haines, A.B. (1968): The interaction between local effects at the shock and rear separation - A source of significant scale effect in wind-tunnel tests on aerofoils and wings. AGARD CP-35.

Rodde, A.-M. (1980): Détermination des conditions d'apparition du décollement au pied du choc sur le profil LC-100D à bord de fuite modifié. ONERA RSF-45/1685AY (June 1980).

Schlichting, H. (1968): Boundary-Layer Theory, Mc Graw-Hill.

Schubauer, G.B. and Klebanoff, P.S. (1951): Investigation of separation of the turbulent boundary-layer. NACA Report N° 1030.

Seddon, J. (1960): The flow produced by interaction of a turbulent boundary-layer with a normal shock-wave of strength sufficient to cause separation. ARC R & M N° 3502 (March 1960).

Seegmiller, H.L., Marvin, J.G. and Levy Jr., L.L. (1978): Steady and unsteady transonic flow. AIAA Paper N° 78-160 (Jan. 1978); see also AIAA Journal, Vol. 16, N° 12, pp. 1262-1270 (Dec. 1978).

Settles, G.S., Perkins, J.J. and Bogdonoff, S.M. (1981): Upstream influence scaling of 2D and 3D shock/turbulent boundary-layer interaction at compression corners. AIAA Paper N° 81-0334 (Jan. 1981); see also: AIAA Journal, Vol. 20, N° 6, pp. 782-789 (June 1982).

Simpson, R.L., Chew, Y.-T. and Shivaprasad, B.G. (1981): The structure of a separating turbulent boundary-layer. Part I: Mean flow and Reynolds stresses. J. Fluid Mech., Vol. 113, pp. 23-51.

Simpson, R.L., Strickland, J. H. and Barr, P.W. (1977): Features of separating turbulent boundary-layer in the vicinity of separation. J. Fluid Mech., Vol. 52, Part I, pp. 553-594.

Sinnott, C.S. and Osborne, J. (1958): Review and extension of transonic aerofoil theory. ARC R & M N° 3156 (Oct. 1958).

Sirieix, M., Déléry, J. and Stanewsky, E., (1981): High Reynolds number boundary-layer/shock-wave interactions in transonic flow. Lecture Notes in Physics 148, Springer Verlag.

Sobieczky, H., Yu, N.-J., Fung, K.-Y and Seebass, A.R. (1979): New method for designing shock-free transonic configurations. AIAA Journal, Vol. 17, N° 7, pp. 722-729 (July 1979).

Solignac, J.-L. (1980): Etude expérimentale du décollement au bord de fuite d'un arrière-corps de révolution profilé. La Recherche Aérospatiale N° 1980-3, pp. 205-211 (May-June 1980).

Squire, L.C. and Smith, M.J. (1980): Interaction of a shock-wave with a turbulent boundary-layer disturbed by injection. The Aeronautical Quarterly, Vol. 31, Part 2, pp. 85-112 (May 1980).

Stanewsky, E. and Little, B.H. (1971): Studies of separation and reattachment in transonic flow. Journal of Aircraft, Vol. 8, N° 12, pp. 952-958 (Dec. 1971).

Stanewsky, E. (1973): Shock-boundary layer interaction in transonic and supersonic flows. VKI LS-59 on "Transonic Flows in Turbomachinery" (May 1973).

Stanewsky, E. and Zimmer, H. (1974): Entwicklung und Windkanalerprobung von drei überkritischen Tragflügelprofilen für Verkehrsflugzeuge. 7 Jahrestagung der DGLR, Kiel (W.-Germany), 17-19 Sept. 1974, Vortrags Nr. 74-100.

Stanewsky, E. (1981): Wechselwirkung zwischen Außenströmung und Grenzschicht an transsonischen Profilen, Doctor-Engineer Dissertation, D 83, Berlin (May 1981).

Stewartson, K. and Williams, P.G. (1969): Self-induced separation. Proc. Roy. Soc., Ser. A312, pp. 181-206.

Tani, I. and Iuchi, M. (1964): Experimental investigation of flow separation associated with a step or a groove. Aeronautical Research Institute, University of Tokyo, Report n° 364 (April 1964).

Vidal, R.J. and Kooi, J.W. (1976): Comparison of data from two shock-wave/turbulent boundary-layer interaction experiments. NLR AC-76-02 (Jan. 1976).

Vidal, R.J., Wittliff, G.E., Catlin, P.A. and Sheen, B.H. (1973): Reynolds number effects on the shock-wave/turbulent boundary-layer interaction at transonic speeds. AIAA Paper N° 73-661 (June 1973).

Viswanath, P.R. and Brown, J.L. (1982): Separated trailing-edge flow at transonic Mach number. AIAA Paper N° 82-0348 (Jan. 1982), see also: AIAA Journal, Vol. 21, N° 6, pp. 801-807 (June 1983).

Wai, J.-C. and Yoshihara, H. (1980a): Planar transonic airfoil computations with viscous interactions. AGARD-CP-291.

Wai, J.-C. and Yoshihara, H. (1981b): Viscous transonic flow over airfoils. Lecture Notes in Physics, Springer Verlag, pp. 417-422.

Whitcomb, R.T. (1974): Review of NASA supercritical airfoil. 9th International Congress on Aeronautical Sciences, Haifa, Israël.

Wygnanski, I. and Fiedler, H.E. (1970): The two-dimensional mixing region. Boeing Scientific Research Laboratories, Document D1-82-0951 (Feb. 1970).

3 - INTERACTION IN TWO-DIMENSIONAL SUPERSONIC FLOWS

3.1 - The Four Basic Interactions.

What can be considered as the four basic configurations involving interaction between a shock-wave and a boundary-layer in supersonic flows are schematically represented in Fig. 3.1. In what follows, the incoming outer flow will be assumed an uniform flow streaming along a flat surface for the sake of simplicity.

- i - the first and most conceptually simple configuration is the wedge (or ramp) flow. Here, a discontinuity in the wall direction is the origin of a shock-wave (C_1) through which the supersonic incoming flow undergoes a deflection equal to the corner angle α :
- ii- the second type of flow is associated with the impingement on the wall of an incident oblique shock (C_1). The incoming flow undergoes a deflection $\Delta\psi_1$ through (C_1) and the necessity for the downstream flow to be again parallel to the wall entails the formation of a reflected shock (C_2) issuing from the impingement point I of (C_1). The deflection $\Delta\psi_2$ produced by (C_2) must be such that $\Delta\psi_2 = -\Delta\psi_1$. The pressure jumps p_1/p_0 and p_2/p_1 through each shock are not equal, though not very different ;
- iii-the third flow is induced by a step of height h facing the incoming flow. Such an obstacle provokes the separation of the flow at a point S. The very rapid pressure rise accompanying separation, especially in turbulent flows, gives rise to a shock-wave (C_1) emanating from a place very close to the separation point S. Downstream of S, a separated zone develops ; it is characterized by the existence of a bubble of recirculating flow in contact with the step. In fact, there is some similarity between wedge flow and flow produced by a forward facing step. In the latter case, the separated region is "felt" by the outer inviscid stream as a corner whose angle is determined by the displacement effect of the dissipative zone ;
- iv- the fourth situation corresponds to the reattachment downstream of a rearward facing step. The incoming flow separates at the base shoulder S undergoing an expansion with a (negative) downward deflection. Further downstream, the flow reattaches on the wall. The resulting positive deviation generates compression waves which coalesce into the so-called "reattachment shock". In contact with the wall, a recirculating bubble is trapped, inside which the flow is reversed.

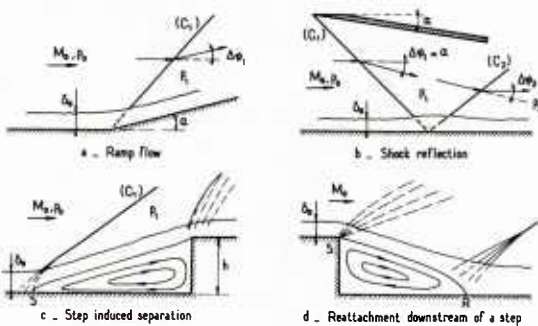


Fig. 3.1 – Basic shock/boundary-layer interactions in supersonic flow.

Now we will examine in more detail the general structure of the flow fields resulting from these interactions.

3.2 - The General Flow Field Structure

3.2.1 - The Compression Ramp Flow

Let us first consider the flow structure associated with a compression ramp. Figure 3.2 shows a sequence of microsecond spark shadowgraphs visualizing this type of flow for an upstream Mach number equal to 2.85 and a Reynolds number (based on the thickness of the incoming boundary-layer) equal to 1.7×10^6 (Settles et al., 1978). The four pictures correspond to different values of the corner angle ranging from 8 to 24 deg. (The appearance of a second ramp in some of the photos is due to optical interference and is not affecting the flow development).

In the 8 deg. case, a distinct shock-wave is seen to arise from the corner location. This shock-wave forms well within the boundary-layer and - as already pointed out in the Section devoted to Transonic Flows - most of the boundary-layer behaves like an inviscid (rotational) fluid, viscous forces being negligible compared to pressure and inertia forces throughout the major part of the boundary-layer. Furthermore, at the high Reynolds number value of the present experiment, the velocity profile of the incoming boundary-layer is very "filled" so that the Mach number slowly decreases over the major part of the boundary-layer thickness (see Section 1.1 above). The transition to zero velocity at the wall takes place over a very short normal distance and, accordingly, the subsonic layer is extremely thin. These features explain why the shock originates from a region very close to the wall.

From above, the shock is first seen to be curved, the curvature being due to its propagation through a rotational layer in which the entropy changes from one streamline to the other. Outside the boundary-layer, the shock is rectilinear, since the incoming flow is here uniform.

For $\alpha = 8$ deg., the upstream influence is very small, since shock emanates practically from the corner angle. On the other hand, for $\alpha = 16$ and 20 deg., the shadowgraphs reveal a substantial increase of the upstream influence length due to an intensifying of the perturbing agency, namely the shock strength. This phenomenon will be studied in more detail below. Also, the spreading of the shock near the wall becomes clearly visible. As for transonic flows, the shock is seen to result from the coalescence of compression waves induced by the thickening of the low velocity portion of the boundary-layer.

For $\alpha = 24$ deg., the pressure rise is strong enough to provoke significant separation. The shadowgraph shows the

following typical features (part of this shadowgraph is obscured by the aerodynamic fences which were necessary to insure flow field two-dimensionality) :

- i - the corner upstream influence has considerably increased ;
- ii- a first shock forms well upstream of the corner. This shock results from an initial turn of the flow at separation;
- iii-an additional compression fan at reattachment merges with the separation shock and reinforces it.

For flow conditions different from those of the present example, the compression waves at reattachment may coalesce into a shock before reaching the separation shock. In this situation, the two shocks meet at a bifurcation point I (also called a triple point) and the inviscid flow structure is similar to a double-wedge configuration with a first wedge corresponding to the initial turn at separation and a second wedge to the final turn at reattachment (see Fig. 3.3a). This inviscid flow structure can also be conceived as a double shock system produced by a still air region at a pressure superior to that of the incoming flow. The free boundary of this still air region starts from the "separation" point S_T and hits the ramp at the "reattachment" point R_T , S_T and R_T not being coincidental with the physical separation and reattachment points since the real flow field is more complex than the above perfect fluid model (see Fig. 3.2). The model of the second kind is utilized in certain multi-component methods developed to compute large separated zones in turbulent flows (Déleray and Masure, 1969). Consideration of these methods would be beyond the scope of the present AGARDograph.

The shock polar construction in Fig. 3.3b shows the local flow situation at point I. In order for the two-flows downstream of I be compatible (i.e., have same pressure and same direction), an intermediate state 2' must be introduced between the final states 2 and 3. According to the relative position of the shock polars Γ_1 and Γ_2 , the wave connecting 2 and 2' is either a shock (most often very weak) or a centered expansion.

The occurrence of the double-shock system is illustrated in Fig. 3.4 by a plotting of the shock-wave angles θ_1 and θ_2 against the corner angle α (Spaid and Frishett, 1972). At low α , only one shock -(C₁)- of angle θ_1 , is now visible. At high α , in addition to the main shock (C₁) (which continues above the bifurcation point I), a second shock (C₂) of angle θ_2 , is now visible. In the present example, this separation shock appears for $\alpha=16$ deg. When α increases, θ_2 first increases slightly, then it rapidly tends to a nearly constant value. The constancy of θ_2 indicates that the strength of the separation shock does not depend on downstream conditions, namely the corner angle in this case. In fact, (C₂) is entirely determined by flow conditions prevailing upstream of separation. Thus, the supersonic separation process is perceived to manifest a behavior typical of a flow which Chapman et al. (1957), called a Free-Interaction.

As will be seen in Section 3.8.2 the appearance of a double-shock system is sometimes used as a detector of Incipient Separation.

The weak influence of viscosity in this kind of flow, when the ramp angle is moderate, is demonstrated by the theoretical result shown in Fig. 3.5 (Roshko and Thomke, 1969). This calculation was performed by considering the boundary-layer as a rotational inviscid flow and by applying the rotational Method of Characteristics to determine the shock shape and the flow over the ramp. To make such a calculation possible, the inner part of the incoming boundary-layer must be ignored, the "cut" being chosen in such a way that the Mach number behind the shock remain supersonic. This kind of calculation belongs to what will be termed "Inviscid Shear Layer Analyses" in Section 1.4 of Part II.

One sees in Fig. 3.5 that there is very good agreement between the wall pressure distribution thus computed and experiment. In the present case, this is because the low velocity portion of the boundary-layer has a quasi negligible influence on the flow field, the inner subsonic layer being excessively thin.

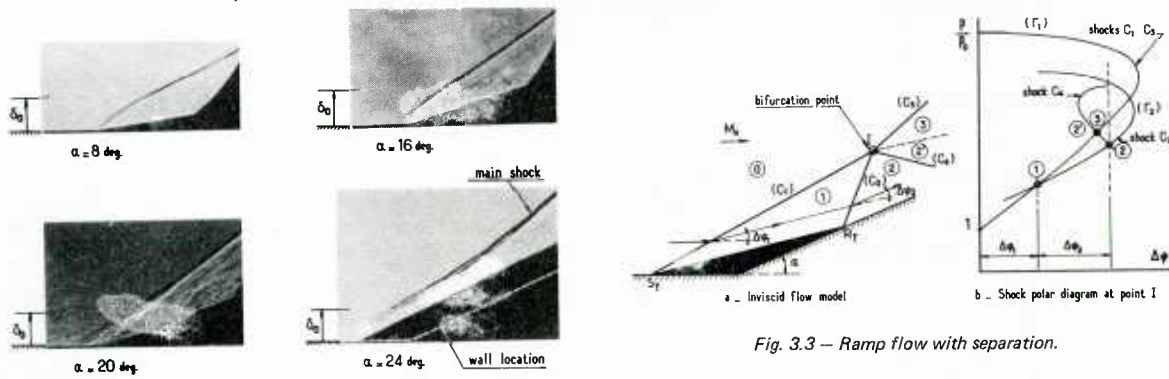


Fig. 3.2 - Ramp flow - Flowfield shadowgraphs - $M_\infty = 2.85$, $R\delta_0 = 1.7 \times 10^6$ (Settles et al., 1979).

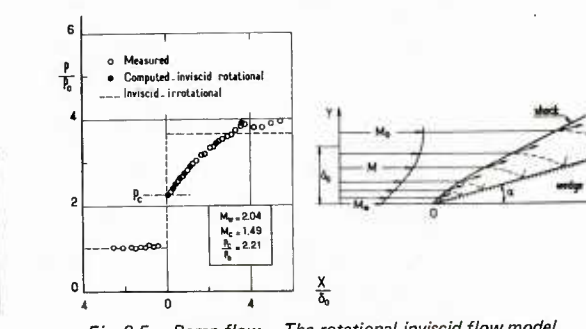
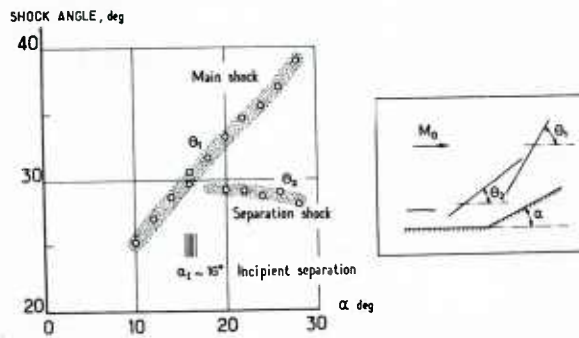


Fig. 3.4 - Ramp flow - Shock wave angles - $M_\infty = 2.85$, $R\delta_0 = 1.7 \times 10^6$.

Fig. 3.5 - Ramp flow - The rotational inviscid flow model (Roshko and Thomke, 1969).

3.2.2 - The Impinging-Reflecting Oblique Shock

In the present configuration, a shock-wave is generated by a "shock-generator" made up of a flat-plate, with sharp leading-edge, inclined at an angle α relative to the uniform incoming flow. The planar oblique shock originating from the plate leading-edge impinges on a straight wall facing the shock generator.

The sequence of schlieren photographs shown in Fig. 3.6 (Délery, 1970) visualizes the shock reflection phenomenon for increasing values of the primary deflection $\Delta\varphi = \alpha$ through the incident shock-wave. In the present example, the incoming flow Mach number is equal to 1.93 and the Reynolds number R_{δ_0} to 0.75×10^4 . The apparent thickness of the shock on the photographs is the manifestation of side effects on the test-section windows. The following schlieren photographs interpretation closely resembles the schematic flow representations given by Bogdonoff and Kepler (1954) more than thirty years ago.

When the incident shock is weak (as in the first photograph in Fig. 3.6), the general flow structure does not differ much from the perfect fluid model. However, a closer look at the picture reveals that complex phenomena take place inside the boundary-layer. A schematic sketch of the observed wave-field is represented in Fig. 3.7.

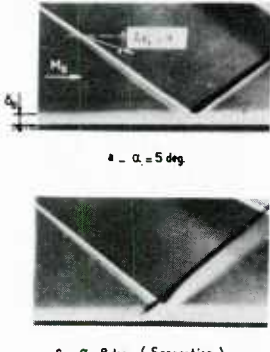


Fig. 3.6 – Incident reflecting shock – Flowfield Schlieren photographs
 $M_0 = 1.93$, $R_{\delta_0} = 0.75 \times 10^4$.

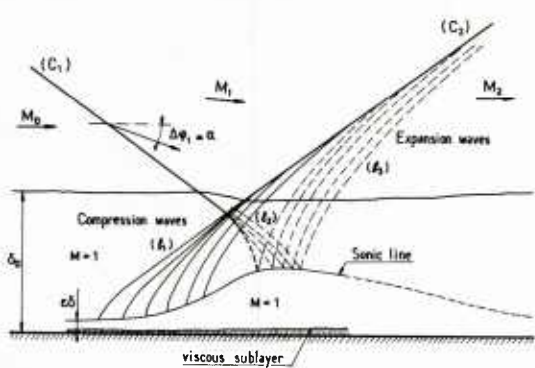
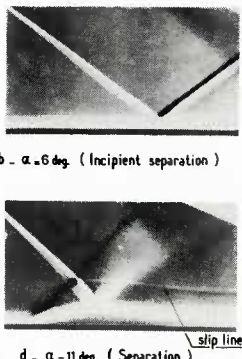


Fig. 3.7 – Shock reflection without boundary-layer separation – Schematic representation of the flowfield.

The incident shock (C_1) progressively curves in as it penetrates the boundary-layer because of the decrease in local Mach number. Correlatively, its intensity weakens and becomes vanishingly small when the shock reaches the sonic line. On the other hand, the pressure rise through (C_1) tends to propagate upstream in the subsonic region $\epsilon \delta_0$ of the boundary-layer, causing this part to thicken.

As we already know, the thickening of the boundary-layer subsonic channel generates outgoing compression waves (l_1) that rapidly coalesce to form the reflected shock (C_2). The refraction of these waves – like that of the incident shocks – as they propagate through the rotational quasi-inviscid layer $(1 - \epsilon) \delta_0$, induces the secondary wave system (l_2). These last waves are reflected by the sonic line as expansion waves (l_3) which are clearly visible, just behind shock (C_2), on the schlieren picture.

For very weak incident shocks, the upstream interaction distance is extremely short, so that the above flow pattern is embedded well within the boundary-layer. Thus, at the outer flow scale, the only reflected wave is a shock (C_2) with a deflection angle $\Delta\varphi$ equal – but with opposite sign – to that of the incident shock (C_1). In this case, the reflection of the shock is said to be "a weak interaction process" in the sense that the (real) viscous flow closely resembles the inviscid flow solution. This resemblance is also evident when considering the wall pressure distributions plotted in Fig. 3.8.

A very thorough theoretical description of the wave-system resulting from the propagation of a shock in a boundary-layer was given by Henderson (1967). In the chosen approach, the shock reflection is reinterpreted as a process of shock refraction by a rotational inviscid layer. A large variety of wave patterns was constructed by Henderson. For weak interactions, these patterns are generally in good agreement with experimental observations (see examples of Henderson's results in Fig. 3.9). However, they start to differ markedly from experiment as soon as the incident shock strength is increased.

Let us now consider the case of an incident shock strong enough to separate the boundary-layer. The resulting typical wave pattern is visualized by the two last photographs in Fig. 3.6. A very schematic representation of the observed flow field is sketched in Fig. 3.10.

The boundary-layer separates at point S, located well upstream of the point where the shock would meet the surface if the fluid were inviscid. The rapid pressure rise at separation takes place as a result of compression waves propagating at first in the supersonic part of the boundary-layer, then in the outer inviscid stream. These waves coalesce to constitute what can be interpreted as the leading reflected shock (C_2) through which the outer inviscid stream is turned upward from the wall. Shock (C_2) intersects the incident shock (C_1) at point H from which emanate the two refracted shocks (C_3) and (C_4). As the entropy rise through (C_1) plus (C_4) is generally different from the entropy rise through (C_2) plus (C_3), H is the origin of a slip-line well visible on the last photograph. A shock-polar representation of the situation at point H is schematically represented in Fig. 3.11. If one increases the intensity of the incident shock, a situation can be reached where the two shock polars representing the refracted shock-waves (C_3) and (C_4) do not intersect anymore (see sketch in Fig. 3.12a). Then a Mach stem phenomenon appears with the formation of a quasi-normal shock inside the flow field as shown by the flow visualisation of Fig. 3.12b.

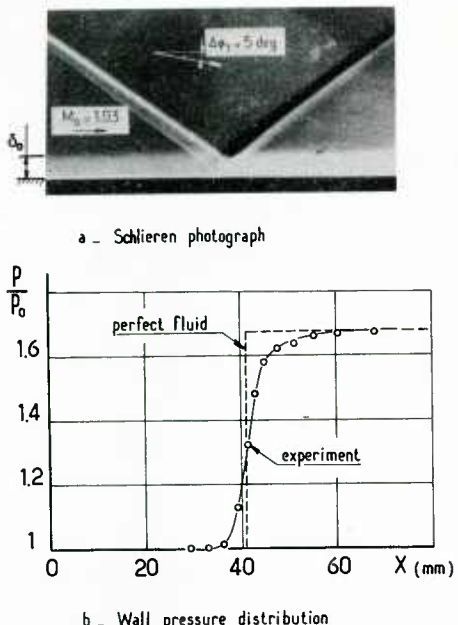


Fig. 3.8 - Shock reflection without separation - An example of weak viscous interaction - $M_0 = 1.93$, $R\delta_0 = 0.75 \times 10^5$.

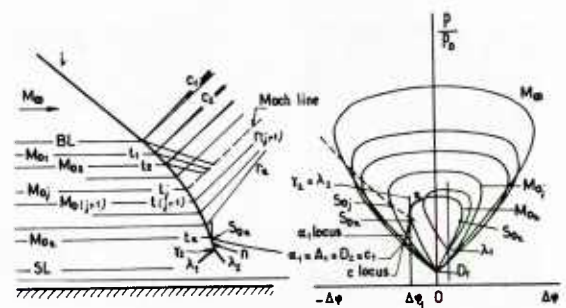
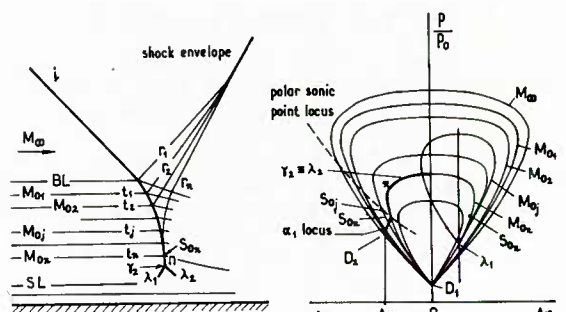


Fig. 3.9 - Examples of rotational inviscid flows models, by Henderson (1967).

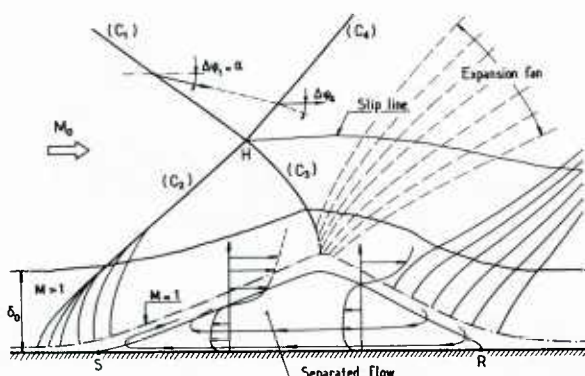


Fig. 3.10 - Shock reflection with boundary-layer separation - Schematic representation of the flowfield.

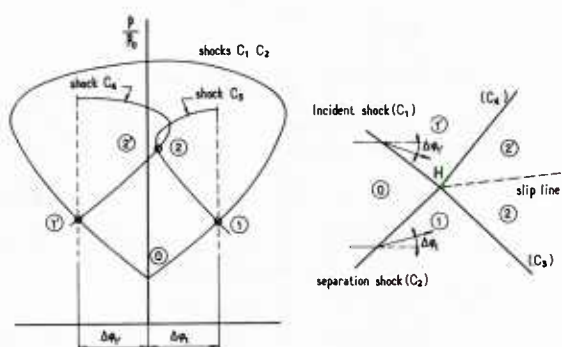


Fig. 3.11 - Shock polar representation of situation at point H (see Fig. 3.10).

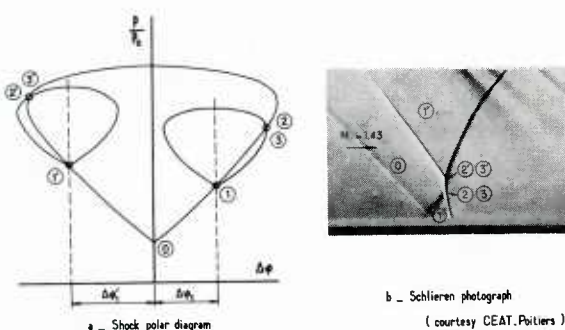


Fig. 3.12 - Shock reflection with occurrence of a Mach stem phenomenon.

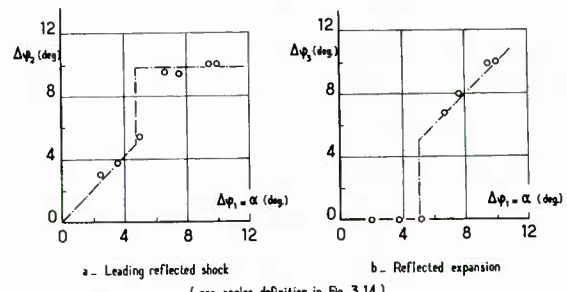


Fig. 3.13 - Incident reflecting shock - Deflection through principal reflected waves - $M_0 = 2.5$, $R\delta_0 = 4 \times 10^5$ (Green, 1970).

After intersection with (C_2), shock (C_1) is bent because of the entropy gradient downstream of (C_2) and the compression waves generated by the thickening of the boundary-layer (see Fig. 3.10). Afterwards, (C_1) enters into the separated dissipative layer from which it is reflected into an expansion wave. Thus the impingement of (C_1) on the boundary-layer is seen to be similar to a shock reflection at a constant pressure free-boundary, as is the case of the outer boundary of a large separated region.

Field measurements made by Green (1970) in a shock reflection taking place at $M_\infty = 2.5$ have shown that the incident shock and reflected expansion turn the flow toward the wall at an angle twice as large as the deflection through the incident shock alone. As this total downward turning is greater than the upward turning through the separation shock (see below and Fig. 3.14), downstream of the expansion fan, the outer stream flows toward the surface. At the same time, the thickness of the dissipative layer decreases. Afterwards, the external stream is progressively turned of an angle $\Delta\varphi_4$ to become parallel to the wall. Simultaneously, the boundary-layer reattaches at point R. The deviation accompanying the reattachment process is far more progressive than the deflection at separation. The resulting compression waves are barely visible on the schlieren photographs of Fig. 3.6.

As was suggested by Green (1970), occurrence of separation at a shock reflection can be detected by plotting the deflections $\Delta\varphi_2$ and $\Delta\varphi_3$ through the leading reflected shock and the expansion, respectively, against the primary deflection $\Delta\varphi_1$. The plottings of Fig. 3.13, which are due to Green, show the following trends :

- i - when $\Delta\varphi_1$ is small ($\Delta\varphi_1 < 5$ deg.), $\Delta\varphi_2$ is nearly equal to $\Delta\varphi_1$ and the reflection is close to the inviscid flow model ;
- ii- for $\Delta\varphi_1$ nearly equal to 5 deg., one observes a jump in $\Delta\varphi_2$ to a value which thereafter is independent of $\Delta\varphi_1$.

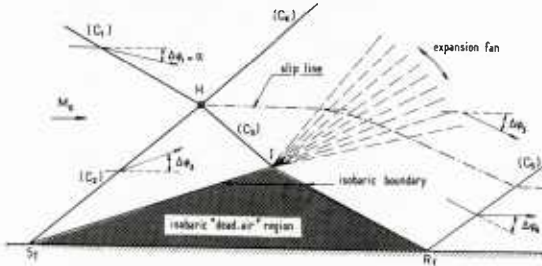


Fig. 3.14 - Shock-reflection with separation –
Inviscid flow model.

- iii- for $\Delta\varphi_1 = 5$ deg., $\Delta\varphi_3$ jumps from zero (no reflected expansion visible) to a finite value approximately equal to $\Delta\varphi_1$. Thereafter, $\Delta\varphi_3$ increases as $\Delta\varphi_1$.

The observed jumps in $\Delta\varphi_2$ and $\Delta\varphi_3$ were seen to coincide with the occurrence of separation as determined from surface oil flows. The existence of a reflected expansion seems to be typical of shock-reflection induced separation, the expansion appearing suddenly with Incipient Separation. Such an Incipient Separation situation is shown by photograph b in Fig. 3.6.

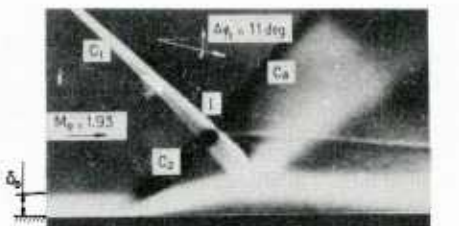
Furthermore, the constancy of $\Delta\varphi_2$, once separation has occurred, indicates that the separation shock strength is independent of the strength of the incident shock-wave that causes separation. Such behavior is also typical of a Free-Interaction process.

In the same nature as the double-wedge (or free boundary) inviscid flow model for a separated wedge flow, one can also imagine a similar model schematizing the reflected-shock separated flow (see Fig. 3.14). It consists in a still-air (or "dead-air") region at constant pressure whose free-boundary starts from the "separation" point S_T . The incident shock (C_1) hits the free-boundary at point I which is the origin of an expansion fan cancelling the shock pressure jump to insure continuity of pressure. There results an abrupt deviation of the free-boundary which runs toward the wall downstream of I and meets it at the "reattachment" point R_T .

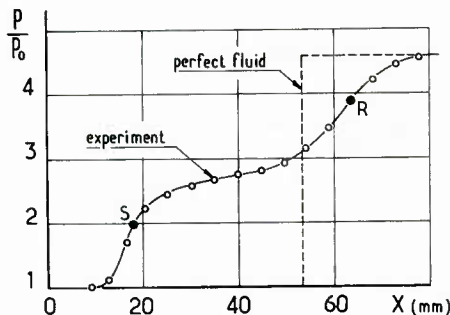
As pointed out by Green (1969), the wave system produced by an incident oblique shock can be thought of as a variant of the separated corner flow pattern. In the two cases, there is first a strong interaction with outward deflection of the outer flow at separation. Further downstream, both for the wedge flow and for the shock impingement, the interacting boundary-layer "feels" an abrupt change of the external flow direction relative to the local wall direction : for the wedge flow, it is the wall that turns of an angle α , for the incident shock it is the outer flow that turns of an angle $\Delta\varphi_1 + \Delta\varphi_2 + \Delta\varphi_3$ (see remark above). Thereafter, for the two flows, a similar reattachment process takes place. During this process, the outer flow is progressively turned to become approximately parallel to the wall. It is a fact that the theoretical methods using the classical viscous-inviscid coupling concept do not distinguish essentially between the two cases.

Furthermore, for the shock impingement, the net angular deflection of the outer stream is zero (provided that the wall is flat). Thus one has $\Delta\varphi_1 + \Delta\varphi_2 + \Delta\varphi_3 + \Delta\varphi_4 = 0$; hence $(\Delta\varphi_1 + \Delta\varphi_4) = -(\Delta\varphi_2 + \Delta\varphi_3) \approx -2\Delta\varphi = 2\alpha$. It is seen that the total deflection through outgoing compression waves is nearly equal to twice the primary deflection through the incident shock. Thus, a compression corner of angle 2α and an incident shock of deflection α reflecting at a plane surface give rise to two successive compressive interactions (at separation and reattachment) the total strength of which is the same. It will be seen in Section 3.3 that for these two flows, the wall pressure distributions are nearly identical if the overall pressure rises are equal.

When shock reflection induces separation, there is a large difference between the perfect fluid solution and the real (viscous) flow. This difference is obvious from the schlieren photographs ; it is also evident if one compares the inviscid and real wall pressure distributions plotted in Fig. 3.15. Such a flow will be termed a "strong interaction process", in the sense that the purely inviscid solution is now far from portraying the true flow field.



a - Schlieren photograph



b - Wall pressure distribution

Fig. 3.15 - Shock reflection with separation -
An example of strong viscous interaction
 $M_0 = 1.93, R\delta_0 = 0.75 \times 10^5$.

3.2.3 - Flow Produced by a Forward Facing Step

The case of flow separation in front of a forward facing step is illustrated by the schlieren photographs in Fig. 3.16 (Délery and Le Balleur, 1972). They correspond to the same upstream conditions as for the shock reflection example, namely : $M_0 = 1.93$ and $R\delta_0 = 0.75 \times 10^4$. The photographs are relative to three different heights of the step provoking separation of the flow. The most visible features on these photographs are : the incoming boundary-layer, the shear-layer that develops along the border of the separated region, the separation shock and the expansion wave originating from the reattachment at the step shoulder. The flow, schematically represented by the sketch in Fig. 3.16, is characterized by the existence of a large recirculation bubble the size of which is roughly proportional to the step height.

We will not consider here, the complex phenomena at the step shoulder, such a discussion being beyond the scope of the present AGARDograph. We will restrict our attention to the separation region. As shown by the photographs, the structure of the flow in the vicinity of the separation shock is similar to what has been observed in the preceding examples. The essential difference is that the extent of the separated region can be greatly amplified in the present situation.

Perhaps the most striking feature of this kind of flow is the independence of the separation shock angle as well as of the direction of the supersonic flow bordering the shear-layer with respect to the step height (see also Zukoski, 1967). This constancy (for fixed upstream conditions) demonstrates clearly that the separation process does not actually depend on downstream conditions and, particularly, on the obstacle at the origin of the separation of the boundary-layer.

In fact, as will be seen in Section 3.6 below, the separation process (in supersonic flows) is independent of the cause that provoked the phenomenon : the separation process itself is thus identical for ramp induced, impinging-shock induced or step induced separation. It depends only on the flow properties at the onset of the phenomenon : hence, the expression "Free-Interaction" introduced by Chapman to designate this kind of interacting flow.

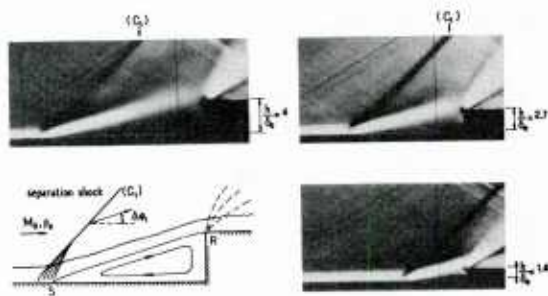


Fig. 3.16 - Supersonic separation in front of a forward facing step
Influence of the step height $M_0 = 1.93, R\delta_0 = 0.75 \times 10^5$.

The above separation experiments were also used to analyze in detail the flowfield structure in the shock foot region. In particular, wall pressure distributions and streamwise velocity profiles were measured (Délery and Le Balleur, 1973). These data have been used to compute the development of the separating boundary-layer by the rotational Method of Characteristics, i.e., by assuming the flow inviscid. A starting characteristic, originating inside the boundary-layer at the point where the local Mach number is equal to 1.05, was first determined from the velocity distribution on the iso-Mach line $M = 1.05$ which was chosen as lower boundary of the flow region assumed inviscid (Carrière et al., 1975).

The computed characteristics network is drawn in Fig. 3.17. One sees that there is good agreement between the calculated and the experimental location of the line on which $M = 1.05$. As shown in Fig. 3.18, the computed velocity distributions agree also closely with experimental data.

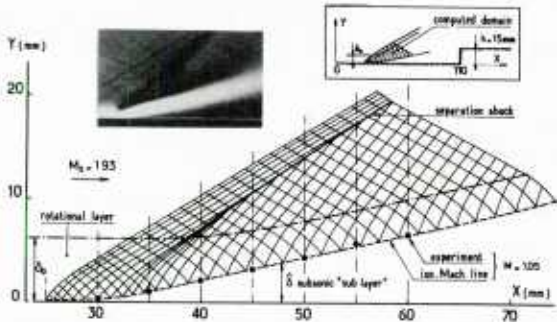


Fig. 3.17 – Separation in front of a step – Perfect fluid calculation.
Characteristics network – $M_0 = 1.93$, $R_{\delta_0} = 0.75 \times 10^5$.

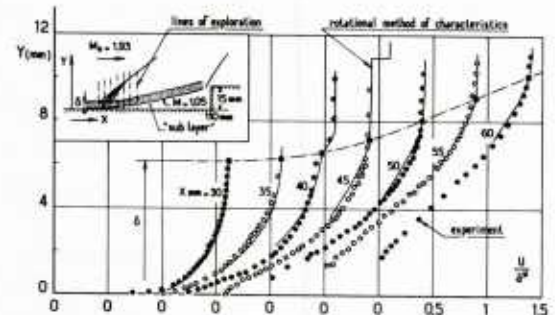


Fig. 3.18 – Separation in front of a step – Perfect fluid calculation:
streamwise velocity profiles – $M_0 = 1.93$, $R_{\delta_0} = 0.75 \times 10^5$.

In addition, the computed normal pressure distributions, represented in Fig. 3.19, show that large y -wise variations of pressure exist within the boundary-layer in the region where the separation shock forms. Further downstream, as the free shear layer develops, the pressure tends to become transversally constant throughout the dissipative region. The same tendencies were noted by Behrens (1971) in a similar flow.

To sum up, the above calculation, supported by many other observations, clearly establishes the following typical features of the separation phenomenon in supersonic flow :

- i - in this "rapid interaction" process, most of the boundary-layer behaves like an inviscid fluid. This finding corroborates observations already made in preceding Sections;
- ii- because of the no-slip condition at the wall, viscous forces must be necessarily predominant in the vicinity of the surface. However, in turbulent flows, this viscous "inner layer" is very thin;
- iii-large axial and normal pressure gradients are both present within the separating boundary-layer, except in the "inner layer" where the classical first-order boundary-layer approximation may certainly apply.

Such behavior is observed each time the streamwise extent of a strong interaction is of the order of the thickness of the incoming boundary-layer. It allows simplifications of the equations of motion leading to the already mentioned Inviscid Shear Layer analyses (see Section 1.4 of Part II). This simplified approach has also received a more rational justification within the framework of the "multi-deck" theories presented in Section 4 of Part II. The essential conclusions of these theories are already apparent in the above flow description.

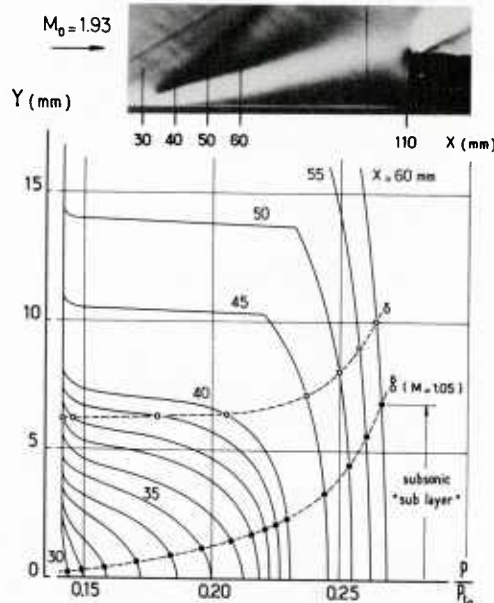


Fig. 3.19 – Separation in front of a step – Perfect fluid calculation – Transverse static pressure distributions
 $M_0 = 1.93$, $R_{\delta_0} = 0.75 \times 10^5$.

3.2.4 - The Reattaching Supersonic Flow

Figure 3.20 shows a schematic representation of a supersonic flow reattaching behind a rearward facing step. In this AGARDograph, we do not intend to give a thorough description of the reattachment process, the subject being marginal to our main topic. Surveys of the supersonic reattachment problem and of the accompanying base-flow problem can be found elsewhere (Délery and Sirieix, 1979 ; Délery, 1983). In the present Section, only the essential features of the flowfield will be briefly reviewed with a view to helping in the understanding of the structure of shock separated flows.

Broadly speaking, the turbulent dissipative flow can be divided into five regions (see Fig. 3.20) :

- i - the first region I is located in the vicinity of the base shoulder S where the incoming boundary-layer separates. In the portrayed situation, the boundary-layer undergoes at I a Prandtl-Meyer expansion. In other circumstances, such as in ramp induced or shock induced separation, the boundary-layer at S is submitted to a compression ;
- ii- downstream of S, in region II, a quasi-isobaric turbulent mixing-layer develops ;
- iii-region II is followed by a first compression zone III extending to the reattachment point R ;
- iv- the compression continues downstream of R in region IV until some constant downstream level is reached ;
- v - in contact with the wall, a recirculating bubble V is trapped. Inside this bubble, the flow is reversed, feeding the mixing-layer.

The conservation of the fluid mass contained in what is called the "dead-air" region requires the streamline (j) issuing from the separation point S to end up at the reattachment point R. Any streamline above (j) must continue beyond R and any streamline below (j) should fold back toward the dead-air due to the existence of the adverse pressure gradient in the vicinity of R. Streamline (j) will be called the Dividing StreamLine or DSL.

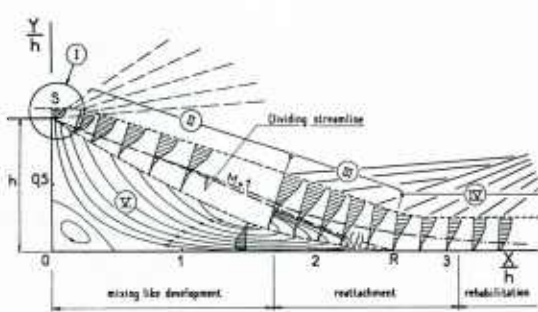


Fig. 3.20 – Supersonic reattachment downstream of rearward facing step – Schematic representation of the flowfield.

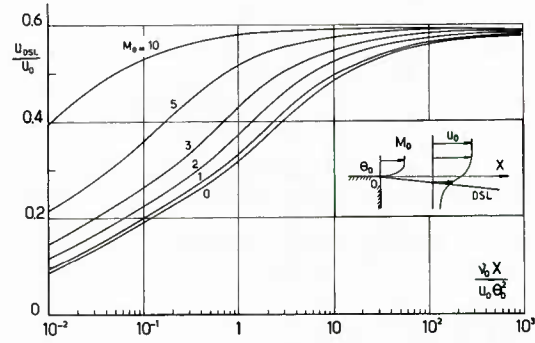


Fig. 3.21 – Two-dimensional free shear layer – Variation of velocity on the dividing streamline (Carpenter and Tabakoff, 1971).

As the separated shear layer develops, the velocity u_j on the DSL progressively increases from zero at the separation point. This increase, which is due to the action of shear-stress, continues until an asymptotic value is reached when the length of the free shear-layer has become very large compared to the initial boundary-layer thickness (see Fig. 3.21 giving evolutions of u_j computed by Carpenter and Tabakoff, 1971). When the reattachment process begins, i.e., when the pressure at the wall starts to rise, the whole flow is decelerated. The velocity on the DSL decreases progressively until stagnation at the reattachment point.

As can be intuitively understood, reattachment depends essentially on the pressure rise that the mixing-layer can handle when the external flow turns to become parallel to the wall. Intuitively, this pressure rise is a function of the kinetic energy gained by the mixing-layer and, more precisely, of the velocity level reached on the DSL when the reattachment process starts. Most of the so-called "component methods" developed to predict separation are based on some adequate criterion modeling the flow deceleration on the DSL. In particular, it is frequently assumed that this deceleration takes place isentropically on each streamline (Chapman et al., 1957; Korst 1956). As these theories will not be reviewed here we will only summarize the main conclusions pertaining to reattachment :

- i - for fixed initial conditions, i.e., for a given pressure in the dead-air region, the higher the pressure rise at reattachment, the greater must be the velocity u_j on the Dividing Streamline ;
- ii- for fixed initial conditions the greater the velocity u_j , the longer must be the mixing layer, i.e., the separated zone ;
- iii-as already noticed in the case of transonic flows, the compression at reattachment is more progressive than at separation. Consequently, the reattachment shock, resulting from the coalescence of compression waves, generally forms farther from the wall.

3.2.5 - Concluding Remarks

We have seen that there is a close similitude between wedge-flow and shock impingement flow. Of course differences exist in the details of the phenomena since they correspond to rather distinct situations. Nonetheless, the resemblance concerns the main flow features the analysis of which is of the greatest importance for a clear understanding of the physics of the phenomenon.

On the other hand, separation in front of a step and reattachment behind a downward facing step constitute two

"basic component flows" into which a shock separated flow can be divided. The main point of this distinction is to emphasize specific characteristics which are sometimes hidden when the two phenomena are closely connected in a more complex configuration.

Consequently, in the forthcoming Sections we will no longer make a strict distinction between the different situations which have been envisaged up to here.

3.3 - Properties of the Wall Pressure Distribution

The main properties of the wall pressure distributions measured in a supersonic shock-wave/turbulent boundary-layer interaction will now be examined by considering typical experimental data.

i - the first example is a wedge flow at an upstream Mach number $M_0 = 2.95$ and a Reynolds number $R_{\delta_0} = 0.78 \times 10^6$ which was investigated in considerable detail by Settles (1975). The data plotted in Fig. 3.2.2 show that the pressure at the wall starts to rise upstream of the corner by virtue of the upstream propagation mechanism already discussed. The correlation properties of the so-called Upstream Influence Length - or Upstream Interaction Length - as defined from the wall pressure distribution will be examined in Section 3.7 ;

ii- as we already know, when the corner angle α is small, the difference between the inviscid solution and the real flow is small. This situation corresponds to what was termed a weak interaction ;

iii-for the highest values of α , the pressure curves clearly exhibit three inflection points. This shape is typical of an interaction involving a noticeable separation of the boundary-layer. The three inflection points are respectively associated with separation, the onset of reattachment and the reattachment compression. Now, as we already know, the fully inviscid solution differs considerably from the real flow and such a situation is called a strong interaction ;

iv- in fact, as demonstrated in Fig. 3.23 by results relative to an impinging shock at $M_0 = 1.93$ and $R_{\delta_0} = 0.75 \times 10^5$ (see the corresponding schlieren photographs of this flow in Fig. 3.6), a separated bubble is present before the occurrence of the three inflection points (Déleray and Le Balleur, 1972). In fact, as shown by experiment, such a "kink" in the wall pressure distribution becomes apparent once the separated region has already attained a noticeable size. This behavior may lead to difficulty in the detection of supersonic Incipient Separation from inspection of wall pressure distributions (see Section 3.8.2 below) ;

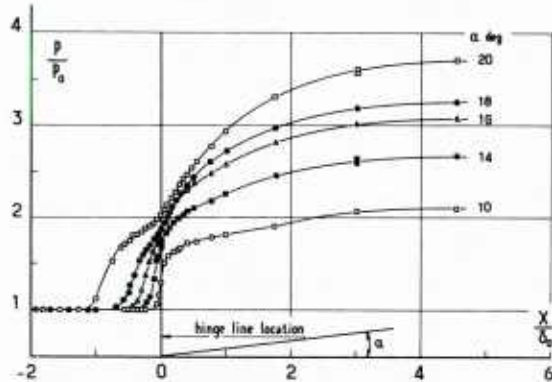


Fig. 3.22 - Ramp flow - Wall pressure distributions –
 $M_0 = 2.95$, $R_{\delta_0} = 0.78 \times 10^6$ (Settles, 1975).

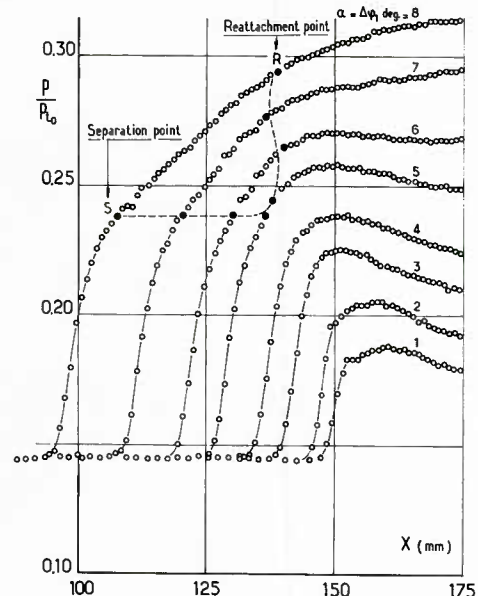


Fig. 3.23 - Shock reflection - Wall pressure distributions – $M_0 = 1.93$, $R_{\delta_0} = 0.75 \times 10^5$.

v - let us consider the same example of an impinging shock. Examination of the pressure distributions plotted in Fig. 3.23 reveals that - for small values of the deflection $\Delta\varphi_1$ through the incident shock - the curves exhibit an overshoot to values superior to the level corresponding to the theoretical pressure jump. The amplitude of this overshoot progressively shrinks as $\Delta\varphi_1$ increases and, in the present case, it is null for $\Delta\varphi_1 = 6$ deg. As shown by the data plotted in Fig. 3.24, the same phenomenon is observed for a wedge flow in the conditions $M_0 = 1.95$ and $R_{\delta_0} = 1.89 \times 10^6$ (Roshko and Thomke, 1969). Broadly speaking, the overshoot only exists at moderate Mach numbers ; it disappears when M_0 is approximately greater than 2.5 ;

vi- the data plotted in Fig. 3.25 were published by Shang et al. (1976). They are relative to a compression ramp and to an impinging shock giving the same overall pressure rise as the ramp. The initial conditions are identical in the two cases, namely : $M_0 = 2.96$ and $R_{\delta_0} \approx 10^5$. The left part of the figure shows lines of constant density determined from interferometric measurements. Although the structures of the two flows are very different, one sees that the two families of wall pressure distributions plotted on the same figure are nearly coincident. This observation corroborates Green's statement on the close similarity between the ramp flow and the reflected shock flow (see above).

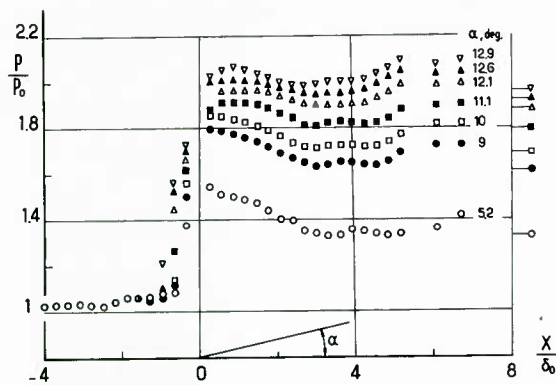


Fig. 3.24 — Ramp flow — Example of pressure overshoot at small angle — $M_\infty = 1.95$, $R\delta_0 = 1.89 \times 10^6$ (Roshko and Thomke, 1969).

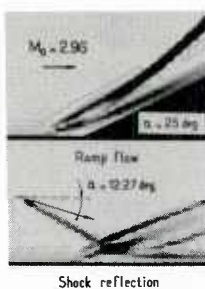


Fig. 3.25 – Comparison of ramp flow and shock reflection flow
 $M_\infty = 2.96$, $R_E = 1 \times 10^7$ (Shang et al., 1976).

vii-figure 3.26 shows plotings of wall pressure distributions for the same incoming flow separating in front of steps of different heights (the corresponding schlieren photographs are shown in Fig. 3.15). For the highest step, the pressure curve exhibits the "plateau" typical of an extended separated zone. If these distributions are re-plotted in such a way that the origins of the interactions coincide - as is done in Fig. 3.27 - one observes a close correlation of the curves on the whole. Also, as demonstrated by Fig. 3.27, a similarly good correlation exists between step-induced and shock-induced compressions. Such a coincidence was noticed by Chapman et al. (1957), Gadd et al. (1954) and also by Bogdonoff and Keppler (1954). It is a new argument in favor of the Free Interaction theory which will be presented in section 3.6.

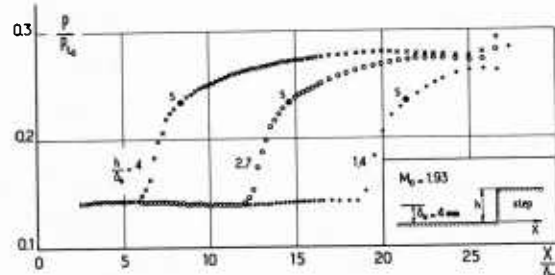


Fig. 3.26 — Separation in front of a step — Influence of the step height on the wall pressure distribution — $M_\infty = 1.93$, $R\delta_0 = 0.75 \times 10^5$.

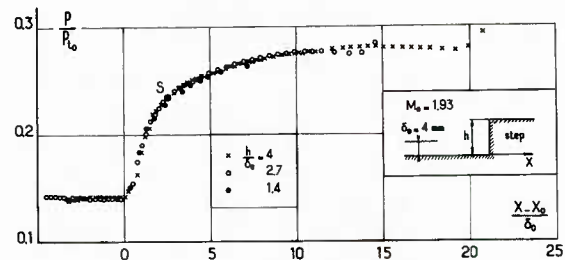


Fig. 3.27 – Separation in front of a step – Correlation of wall pressure distributions.

viii- wall pressure distributions resulting from flare-induced separation at $M_\infty = 3.96$ and high Reynolds number (Roshko and Thomke, 1974) are plotted in Fig. 3.28. These results tend to show that the extent of the pressure plateau region increases with the flare angle, i.e., with the overall pressure jump $[\Delta p]_T$. As seen in vii, the pressure rise to separation does not depend on downstream conditions and is, thus, entirely determined by the flow situation at the interaction onset. Consequently, an increase in the overall pressure rise necessarily entails a higher pressure rise at reattachment. As seen in Section 3.2.5, this can only be achieved by an increase in the

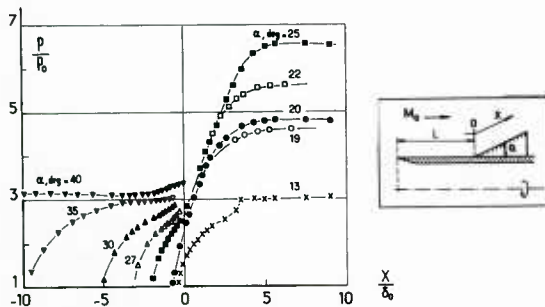


Fig. 3.28 – Flare induced separation – Wall pressure distributions
 $M_\infty = 3.96$, $R_L = 30 \times 10^6$ (Roshko and Thomke, 1974).

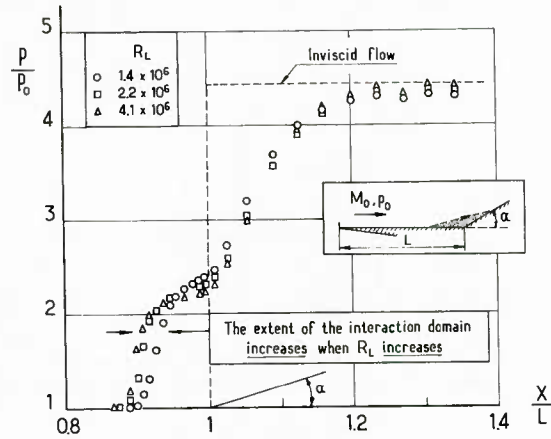


Fig. 3.29 – Ramp flow – Reynolds number effect at low to moderate Reynolds numbers – $M_0 = 2.7$ (Chapman et al., 1957).

velocity on the Discriminating Streamline of the separated bubble. Hence, the length of the separated shear-layer must be longer in order to permit a greater acceleration on the DSL before reattachment begins;

ix - the pressure distributions plotted in Fig. 3.29 were measured in a compression corner at $M_\infty = 2.7$ and for relatively low Reynolds numbers R_x varying in the range 1.4×10^6 to 4×10^6 (Chapman et al., 1957). According to these results, there is clearly a visible increase in the streamwise extent of the interaction when the Reynolds number increases. On the other hand, as shown in Fig. 3.30, in experiments performed at high Reynolds number (R_x of the order of 10^9 , Roshko and Thomke, 1969), there is an obvious decrease in the interaction extent with increasing Reynolds number. This reversal in trend will be further commented in the forthcoming Sections;

x - this last typical feature of a turbulent shock-wave/boundary-layer interaction is observed at very high Mach numbers. As shown by the curves of Fig. 3.31 which correspond to wedge induced separation at $M_\infty = 9.22$, (Elfstrom, 1971), a hypersonic interaction is characterized by the existence of a large pressure overshoot that follows reattachment. A plausible explanation of this phenomenon can be found by resorting to the double wedge inviscid model for ramp induced separation given in Section 3.2.1 above. An inviscid flow of this type was theoretically investigated by Sullivan (1963) for hypersonic free stream Mach numbers. In this case, the three-shock configuration with its bifurcation point I is very close to the wall (most often, in the real viscous flow, the shock system itself is embedded within the boundary-layer). Consequently, the reflected wave starting from I strikes the wall at a small distance downstream of the reattachment region. Since, in hypersonic flows, this wave is a rather intense expansion wave, its trace on the wall results in a steep decrease of the pressure immediately following the rise at reattachment.

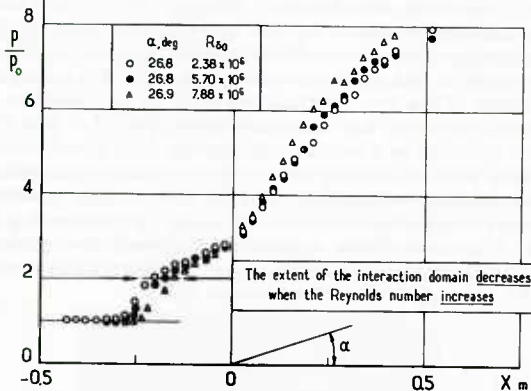


Fig. 3.30 - Ramp flow - Reynolds number effect at high Reynolds numbers - $M_\infty = 3.93$ (Roshko and Thomke, 1969).

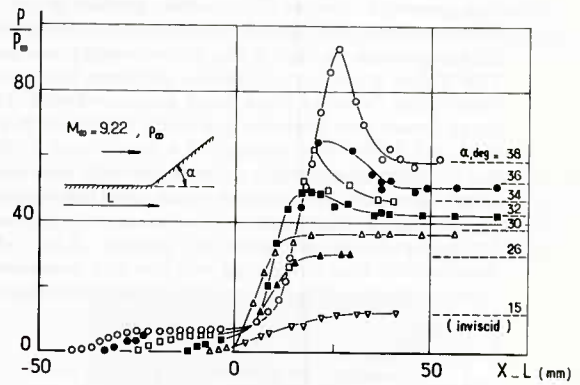


Fig. 3.31 - Downstream overshoot at high Mach number $M_\infty = 9.22$ (Elfstrom, 1971).

3.4 - Some Features of Shock-Wave Boundary-Layer Interaction in laminar Flows

As already stated in the Introduction this AGARDograph is essentially concerned with turbulent flows and thus we do not intend to give ample information on the laminar régime. The aim of this Section is simply to emphasize the main differences between turbulent and laminar interacting flows.

Such differences were already noticed and carefully discussed nearly forty years ago by Liepmann (1946) for the case of a transonic flow past a circular arc profile. His experiments demonstrated that a change from laminar to turbulent boundary-layer - at a given free stream Mach number - considerably alters the whole flowfield if shock-waves are present in this flow.

In this Section, we will restrict our attention to a limited number of typical examples relative to entirely supersonic interactions.

Figure 3.32 shows a comparison between a laminar and a turbulent interaction having nearly the same upstream Mach number (Chapman et al., 1957). The wall pressure distributions clearly exhibit a greater spreading of the discontinuity in the case of the laminar boundary-layer. This greater x-wise extension is far beyond the scaling by the incoming boundary-layer thickness. Also, the various characteristic pressure rises, in particular the pressure at separation, are far less important in laminar flows than in turbulent flows.

The above differences in the flow behaviors have at least two immediate consequences :

i - the pressure rise required to separate a laminar boundary-layer is much lower than the pressure rise inducing separation of a turbulent boundary-layer. A direct quantitative comparison of the respective sensitivity of the two flows to shock-induced separation is difficult, since such a comparison should be made by varying the pressure rise while keeping the same Reynolds number for the two flows. However, some information can be inferred from the Free Interaction Theory developed in Section 3.6 below. This theory establishes the fact that the normalized pressure rise at separation - which can be identified with the pressure ratio necessary for Incipient Separation - is nearly five times smaller in laminar flow than in turbulent flow (see Section 3.6 below);

i - the x-wise scale of the reattachment domain has considerably shrunk ;

ii- the associated pressure rise, along with the accompanying pressure gradient, have been greatly amplified.

The various situations encountered when transition moves in the interaction domain have been thoroughly discussed by Gadd et al. (1954). These authors have suggested the various possible configurations schematically portrayed in Fig. 3.40. In the sequence of sketches, the transition "point" T moves upstream as the strength of the incident shock increases. The figure also shows a schematic representation of the corresponding wall pressure distributions.

Of the same nature, the effect of shock impingement on boundary-layer transition was investigated by Le Balleur and Délery (1973). These experiments were performed in a two-dimensional test set-up at an upstream Mach number equal to 1.95. The transition location was located by inspection of short-exposure time schlieren photographs. These authors found that transition could be moved considerably upstream of its "natural" location by the impact of a relatively weak incident shock-wave. Such a displacement is illustrated by the sequence of schlieren photographs of Fig. 3.41. It was demonstrated that the upstream displacement of transition is a function of the shock intensity and of the Reynolds number. The results obtained are represented in Fig. 3.42 which shows the variation of the extent of the laminar portion downstream of the shock impingement point I as a function of the Reynolds number computed with the boundary-layer momentum thickness at I, with the pressure jump through the incident plus reflected shock as parameter. It is seen that independently of the Reynolds number, transition positions itself at the impact point as soon as the total pressure ratio is greater than 1.4.

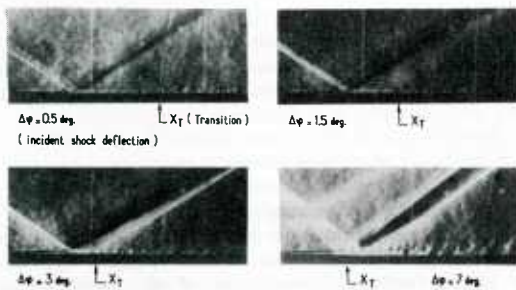


Fig. 3.41 – Effect of shock impingement on boundary-layer transition – Short exposure time shadowgraphs.

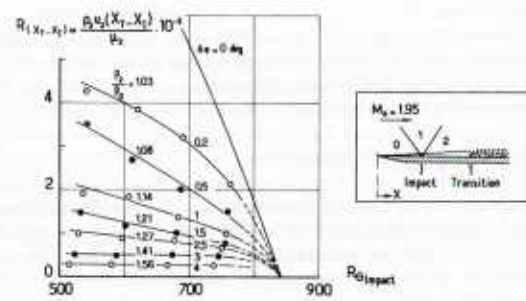


Fig. 3.42 – Laminar distance downstream of the shock impingement point.

3.6 - The Free Interaction Concept

Some of the experimental results presented in the above Sections tend to demonstrate that the major part of a supersonic interacting flow evolving toward separation does not (appreciably) depend on the agency at the origin of separation, this agency being either a solid obstacle or an incident shock-wave. That part of the flow independent of the downstream situation comprises the compression at separation as well as the development of the pressure plateau for largely separated flows. Everything happens as if the flow were entirely determined by its properties at the onset of interaction.

Such flows that are (to a first approximation) free from direct influence of downstream geometry were termed by Chapman "Free Interactions". Later, a more rational definition of this concept was given within the framework of asymptotic theories (see Section 4 of Part II below) and inviscid-viscous interacting methods (see Section 3 of Part II below). As a matter of fact, as will be seen below, the interacting flow can be modeled by a coupling approach which consists in making compatible two flow regions which are respectively represented by boundary-layer equations and Euler equations. For a supersonic outer inviscid flow, and within the classical first order boundary-layer concept, the solution can be looked for by a purely downstream marching procedure. In this approach, the role of downstream conditions - i.e., the perturbing agency - is simply to fix the origin of the interaction.

The Free Interaction concept permits the derivation of correlation laws explicitly displaying the dependence of the phenomenon on such basic parameters as the Mach number and the Reynolds number. Although the character of generality of these laws is now questioned (see Section 3.7 below), the Free Interaction Theory is still of important historical interest since it is at the origin of ideas having led to decisive progress in the modeling of interacting flows. For these reasons, we will present it in some detail.

The analysis that follows is in fact attributable to Erdos and Pallone (1962), but it was directly inspired from the original work of Chapman et al. published in 1957.

The incoming flow will be assumed adiabatic (no heat transfer at the wall) and initially the outer inviscid stream is assumed to be a uniform planar two-dimensional flow. The correlation laws are established by utilizing two basic equations, namely :

i - the boundary-layer momentum equation written at the wall :

$$(3.1) \quad dp/dx = (\partial \tau / \partial y)_w$$

An x -wise integration of Eq. 3.1 from the beginning x_0 of the interaction domain, along with the introduction of normalized variables, leads to the following equation :

$$(3.2) \quad (p - p_0)/q_0 = (\tau_{w0} L / \delta_0^* q_0) \int_{x_0/L}^{x/L} (\partial \tau / \partial y)_w (\delta_0^* / \tau_{w0}) dy = (\tau_{w0} L / \delta_0^* q_0) f_1(x - x_0/L)$$

τ_{w0} is the wall shear-stress at the origin of the interaction, L a still undetermined x -wise length scale and f_1 a dimensionless function of the scaled variable $(x - x_0)/L$.

ii- the second equation is the coupling equation written on the boundary-layer displacement surface (see Section 3 of Part II below for more information on coupling equations in inviscid-viscous interactive methods). In the present analysis, the pressure variation induced in the outer inviscid flow is expressed via the linearized simple wave equation. Thus, the coupling equation is written here :

$$0.5 (M_0^2 - 1)^{1/2} (p - p_0)/q_0 = d\delta^*/dx$$

Hence, after introduction of normalized quantities :

$$(3.3) \quad (p - p_0)/q_0 = 2(M_0^2 - 1)^{-1/2} (\delta_0^*/L) d(\delta^*/\delta_0^*)/d(x/L) = 2(M_0^2 - 1)^{-1/2} (\delta_0^*/L) f_2(x - x_0/L)$$

where f_2 is a new dimensionless function.

A multiplication of Eq. 3.2 by Eq. 3.3 leads to the following correlation law for the pressure at the wall :

$$(3.4) \quad \begin{aligned} (p - p_0)/q_0 &= \mathcal{F}(x - x_0/L) (2C_{f_0})^{1/2} (M_0^2 - 1)^{-1/4} \\ L/\delta_0^* &= k \mathcal{C}_{f_0}^{-1/2} (M_0^2 - 1)^{-1/4} \end{aligned}$$

where $\mathcal{F} = f_1 f_2$ is assumed to be a universal correlation function, independent of Mach and Reynolds numbers. This function has to be determined from experiment.

Figure 3.43 shows the functions \mathcal{F}_L and \mathcal{F}_T respectively obtained for laminar and turbulent flows by Erdos and Pallone. In the representation of Fig. 3.45, the x -wise length scale is the distance from the origin x_0 of the station at which \mathcal{F} reaches the value corresponding to the pressure plateau of an extended separated flow. The following particular values of \mathcal{F} are found :

i - at the separation point :

$$\begin{aligned} \mathcal{F}_s &= 0.81 \text{ for laminar flow} \\ &= 4.22 \text{ for turbulent flow} \end{aligned}$$

ii- for the pressure plateau :

$$\begin{aligned} \mathcal{F}_s &= 1.47 \text{ for laminar flow} \\ &= 6.00 \text{ for turbulent flow} \end{aligned}$$

The above values reflect the fact that pressure rises in a turbulent separation are far more important than in a laminar separation.

A correlation law for the streamwise scale of separation is obtained by the division of Eq. 3.2 by Eq. 3.3. This gives an equation of the form :

$$L/\delta_0^* = k \mathcal{C}_{f_0}^{-1/2} (M_0^2 - 1)^{-1/4}$$

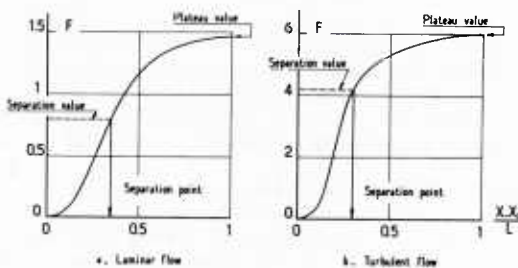


Fig. 3.43 – Free interaction theory – Wall pressure correlation functions (Erdos and Pallone, 1962).

where the constant k must be determined experimentally. Its value depends on the manner in which a representative streamwise scale is defined. The two most adopted scales L are the one used by Erdos and Pallone and the distance between the separation point and the origin of the interaction domain.

The above analysis has been generalized by Carrière et al. (1968) and Carrière (1973) in order to take into account non-uniformities in the incoming outer flow as well as wall curvature effect in the interaction region. These authors have shown that in the most general case, the universal correlation function takes the form :

$$(3.5) \quad \{[(p-p_0)/a_0][\bar{v}(x) - v(x)]/C_{F_0}\}^{1/2} = \tilde{\mathcal{F}}(x-x_0/L)$$

where v is the Prandtl-Meyer function for the actual pressure at x and \bar{v} the value that v would take at the same x in the absence of separation.

At low to moderate Reynolds number (say $R_{\delta_0} < 10^5$), Eqs. 3.4 or 3.5 most often correlate very well experimental wall pressure distributions measured for greatly different situations. Examples of such correlations have already been given in Section 2.9.2 relative to transonic flows. Here, we will only give two further examples concerning supersonic separation :

i - the first example is made up of the separated flows considered in Section 3.2. These flows are produced either by an upstream facing sep or by a shock reflection. In the present application, the streamwise length scale L is the distance $x_s - x_0$, the separation point location being conventionally defined as the abscissa where $\tilde{\mathcal{F}} = 4.22$. Figure 3.44 shows that the function $\tilde{\mathcal{F}}$ permits an excellent correlation of these different separated flows. For practical purposes, $\tilde{\mathcal{F}}$ can be accurately computed by the following analytical expression :

$$\tilde{\mathcal{F}}(\xi) = \sum a_n \xi^n + (b_0 + b_1 \xi) \exp(-k\xi) \quad \text{with } \xi = (x-x_0)/(x_s-x_0)$$

The coefficients a_n , b_0 , b_1 and k are given in Fig. 3.45.

On the other hand, as shown in Fig. 3.46, the correlation for the length scale is less satisfactory, presumably because of the difficulty of accurately determining the separation distance $L = x_s - x_0$ which is always very short in turbulent flows (see also Erdos and Pallone, 1962).

ii- the second example, shown in Fig. 3.47, is relative to separation in strongly overexpanded axisymmetric supersonic nozzles. In this case, the flow before separation is non-uniform and the generalized universal function $\tilde{\mathcal{F}}$ alone is capable of correlating the experimental data.

The Free Interaction Theory has frequently been used as a guide-line for establishing other correlation laws. Among these laws, we can cite the correlation of Popinski and Ehrlich (1966) which expresses the plateau pressure coefficient C_{PP} in the form :

$$(C_{PP}) R_x^{1/10} = 1.91 (M_\infty^2 - 1)^{-0.309}$$

Knowing this, the above equation is, for a flat-plate turbulent boundary-layer, in fact nearly the same as the one of Erdos and Pallone. The Popinski and Ehrlich correlation law is compared to various experimental data in Fig. 3.48. Other examples of application of the Free Interaction concept will be given in the forthcoming Sections.

To briefly summarize this part of the text, the Free Interaction Theory predicts that the pressure levels in a separation (including the pressure at the separation point and the pressure plateau) :

i - increase with the upstream Mach number ; this tendency has been well confirmed by experiment ;

ii- decrease when the Reynolds number increases since the skin-friction coefficient decreases when the Reynolds number increases (see Fig. 1.4) for a flat-plate situation before separation.

This second tendency is certainly true in laminar flow where it has been corroborated both by experiment and more advanced theoretical models. In turbulent flow, it has also been verified by experiment at low to moderate Reynolds numbers.

However, at high Reynolds number ($R_{\delta} > 10^5$), several investigators have found that the pressure rises to separation and/or to the plateau tend to become independent of the Reynolds number and even to slightly increase with it. This change in the Reynolds number dependence was clearly established by the experiments of Zukoski (1967), Roshko and Thomke (1974) and those of Settles (1975). To illustrate this point, Fig. 3.49 shows experimental data and correlations for the pressure plateau which depend on the upstream Mach number M_∞ only (Zukoski, 1967; Werlé, 1968).

The Free Interaction Theory also predicts that the separation length $L = (x_s - x_0)$ (or any other characteristic streamwise length scale) must increase with the Reynolds number. Although the experimental determination of L is delicate, there is strong evidence that for a turbulent flow at high Reynolds number, L actually decreases with increasing Reynolds number. This tendency has already been noticed in Section 2.7.2. Consideration of Fig. 3.30 obviously demonstrates that the streamwise extent of the interaction is smaller as the Reynolds number is higher. Many experimental results on Incipient Separation of a turbulent boundary-layer at high Reynolds numbers tend also to prove that the "stiffness" of the boundary-layer increases with R_{δ_0} . Experimental results on Incipient Separation in transonic flows also led to the same conclusion (see Section 2.8 above).

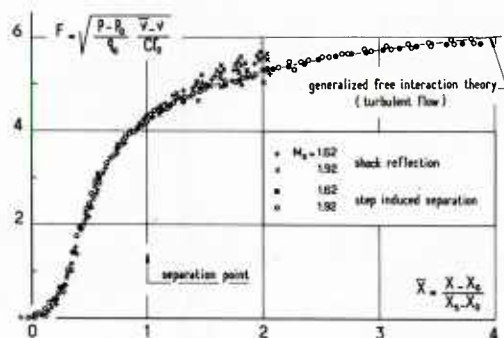


Fig. 3.44 – The free interaction theory – Correlation of wall pressure measurements – Uniform incoming flow.

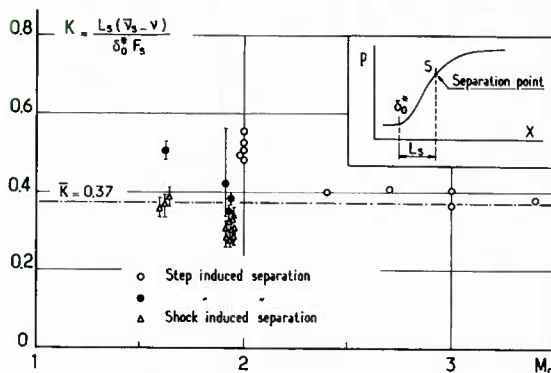


Fig. 3.46 – The free interaction theory – Correlation for the streamwise scale of the interaction domain.

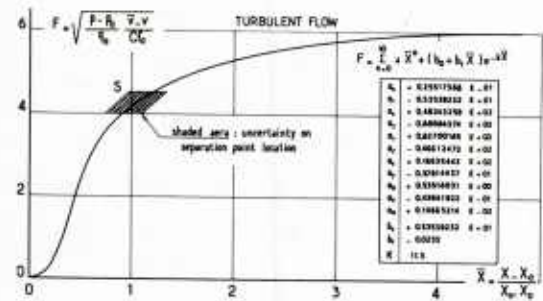


Fig. 3.45 – The free interaction theory – "standard" representation of the generalized wall pressure correlation function.

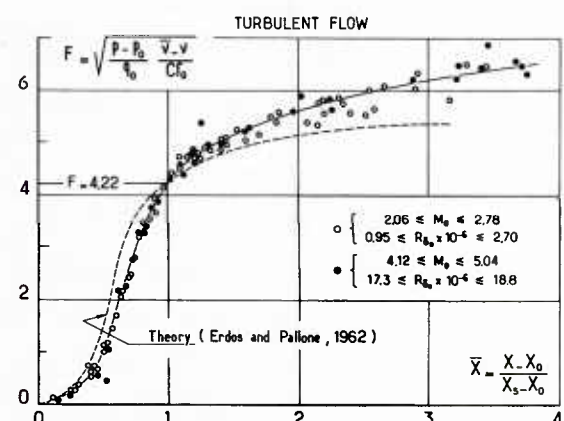


Fig. 3.47 – The free interaction theory – Correlation of wall pressure distributions – Non uniform incoming flow (Carrière et al. 1968).

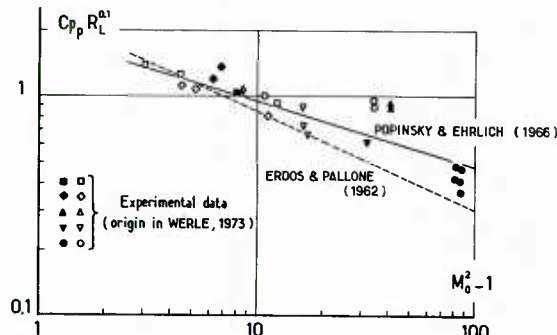


Fig. 3.48 – Free interaction type – Correlation for the plateau pressure coefficient (Werle, 1973)

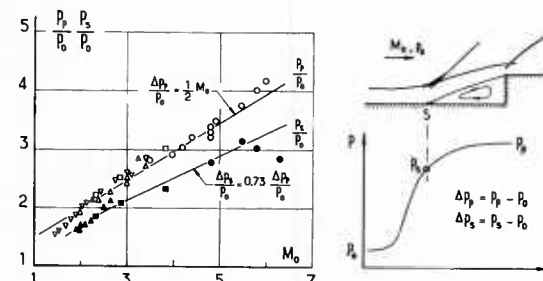


Fig. 3.49 – Separation in front of a forward-facing step – Correlations for plateau and separation pressure (Zukosky, 1967)

This trend reversal, which occurs when the Reynolds number is sufficiently high, has not yet been completely understood. It will be more thoroughly discussed in the following Sections concerned with streamwise scaling laws and Incipient Separation in supersonic interactions.

3.7 - Scaling Properties of the Supersonic Interaction Streamwise Extent

3.7.1 - Introductory Remarks

The "intensity" of a shock-wave/boundary-layer interaction can also be characterized by its upstream influence, i.e., the distance at which the interaction - or the shock presence - is first felt. This distance is most often measured from the wedge corner or from the point where an incident shock would impinge on the wall in the absence of a boundary-layer.

A second point of interest is the separation length which is conventionally defined as the distance of the separation

point from a suitably chosen origin, for example, the start of the interaction.

As in transonic flows, the basic question is : what are the appropriate scaling laws for these characteristic lengths? The answer to this question is important, not only for practical purposes, but also for the physical understanding of the phenomenon. In particular, clear and accurate information on this subject is of great interest to help in the modeling of the phenomenon, especially in turbulent flows where one has still to rely heavily on experiment.

3.7.2 - The Upstream Interaction Length. General Properties

Essentially we will consider scaling properties for the upstream interaction length L_0 in the case of wedge-flows. The main reason for this choice is that most known results concern this type of flow in which L_0 is relatively easier to measure than in a shock reflection. However, it should be emphasized that general tendencies observed in wedge-flows are also similar to shock reflections, since in the inviscid sense there is no essential difference between these two kinds of flow as was seen in Section 3.3 (see also section 3.8 below on Incipient Separation).

The upstream interaction length is most often defined from inspection of the wall pressure distribution. Theoretically, the origin of the interaction is at the point where the wall pressure starts to rise. Some investigators have adopted this definition (Spaid and Frishett, 1972). Unfortunately, the experimental localization of the true interaction origin is difficult and hence inaccurate. For this reason, most investigators have chosen a conventional origin obtained by extrapolating to the wall the quasi-linear pressure rise at separation, as is shown in Fig. 3.50 (Settles and Bogdonoff, 1973; Roshko and Thomke, 1974; Settles, 1975; Hayakawa and Squire, 1982).

According to Green (1969), the main parameters likely to influence the extent of a shock-wave/boundary-layer interaction are :

- i - the upstream Mach number M_∞ ;
- ii- the Reynolds number $R\delta_\infty$;
- iii-the wedge angle α (or incident shock intensity) ;
- iv- the thickness of the incoming boundary-layer δ_∞ .

If one considers any typical streamwise length L_0 scaled to the incoming boundary-layer physical thickness δ_∞ , or displacement thickness δ_∞ , there remain the three following influence parameters : M_∞ , $R\delta_\infty$ and α (or shock strength). If we now focus our attention on the dimensionless length L_0/δ_∞ , it is generally agreed that - for a fixed value of $R\delta_\infty$ -:

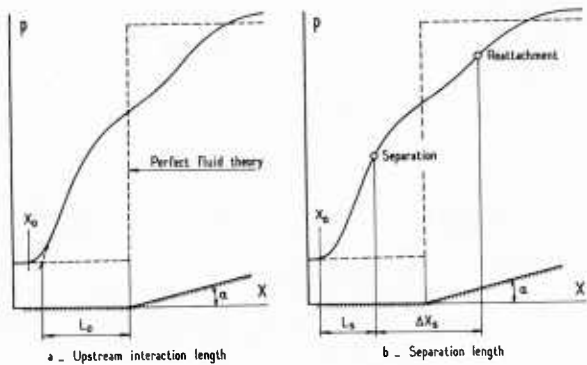


Fig. 3.50 - Characteristic lengths of a supersonic interaction.

- i - L_0/δ_∞ increases with α for a fixed Mach number M_∞ ;

- ii- L_0/δ_∞ decreases when M_∞ increases for a fixed angle α

However, there is some controversy over the influence of the Reynolds number.

On the one hand, there are the experiments made by several investigators (Kuehn, 1959 ; Elfstrom, 1971; Batham, 1972 ; Spaid and Frishett, 1972) at low or moderate Reynolds number ($R\delta_\infty < 10^5$), both with tripped and untripped boundary-layer. These experiments indubitably show that L_0/δ_∞ increases with the Reynolds number $R\delta_\infty$. Such a tendency is in agreement with the Free Interaction Theory.

On the other hand, experiments performed at high Reynolds number manifestly show a reversal of this trend, L_0/δ_∞ decreasing with increasing Reynolds number (Hammitt and Hight, 1959 ; Roshko and Thomke, 1974 ; Settles, 1975; Settles et al., 1975). The same tendency was observed in transonic flows (see Section 2.7.2 above) ; it was then interpreted as resulting from a "filling" of the initial boundary-layer profile which is a consequence of a rise in the Reynolds number.

In what follows, we will present various laws proposed to correlate the upstream influence length at high Reynolds number, the case of low Reynolds number being satisfactorily represented by the Free Interaction theory.

3.7.3 - Correlation Laws for the Upstream Interaction Length at High Reynolds Numbers

A systematic survey of the influence of M_∞ , R_{δ_0} and α on the interaction length L_o was made by Roshko and Thomke (1974) for wedge flows in the Reynolds number range $10^5 < R_{\delta_0} < 10^6$. Some of the results that they obtained are plotted in Fig. 3.51 where L_o is arbitrarily scaled to the distance of the corner from the leading edge of the plate on which the incoming boundary-layer develops. A rapid examination of these results leads to the following remarks :

- i - for fixed Reynolds number R_C (R_C is computed for free stream conditions and with the distance of the wedge corner to the plate leading edge) and Mach number M_∞ , the upstream interaction length increases with α , i.e., with the intensity of the perturbation. It is now clear that the increase in L_o with the shock intensity has to do with the fact that a higher back pressure must feed farther upstream through the subsonic part of the boundary-layer ;
- ii- for fixed R_C and α , L_o decreases when M_∞ increases. This trend can certainly be explained by the reduction of the relative subsonic layer y^*/δ_0 when M_∞ is higher.

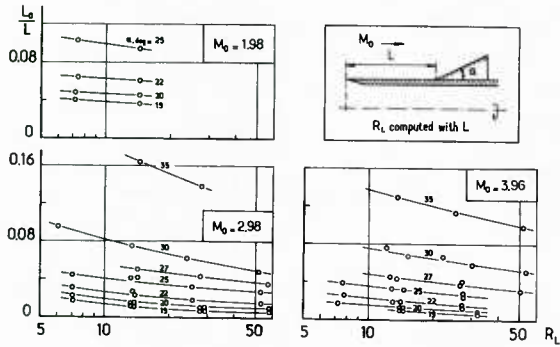


Fig. 3.51 - Upstream interaction length - Influence of Mach number, Reynolds number and corner angle (Roshko and Thomke, 1974).

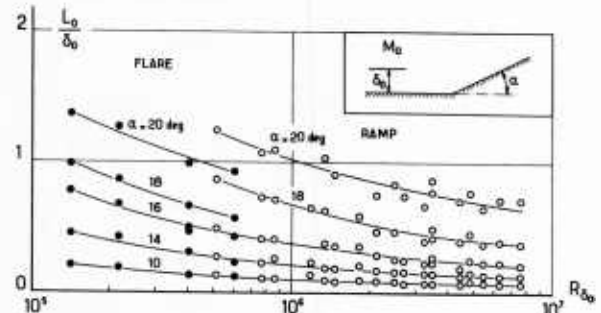


Fig. 3.52 - Upstream interaction length - Influence of deflection angle and Reynolds number - $2.84 \leq M_\infty \leq 2.95$ (Settles, 1975).

- iii- for fixed M_∞ and α , L_o decreases where the Reynolds number increases. As already stated, this tendency can also result from a thinning of the subsonic layer.

It should be noticed that the above tendencies are still observed when L_o is scaled to the physical thickness of the boundary-layer δ_o (or to its displacement thickness δ_o^*). This fact proves that δ_o (or δ_o^*) alone cannot be the scale of the interaction. The same behavior was observed in transonic flows (see Section 2.7.2 above).

Roshko and Thomke (1974) have proposed the following completely empirical correlation law for the normalized upstream interaction length L_o/δ_o :

$$(3.6) \quad L_o/\delta_o = (\alpha/18.25)^{2.81} [10^3 C_{fo} - 1 + (\alpha/29)^2]$$

It is recalled that C_{fo} is the skin-friction coefficient at the start of interaction and α the wedge angle. This equation correlates experimental data in the range :

$$1.98 < M_\infty < 4.45$$

$$10^5 < R_{\delta_0} < 10^6$$

Conclusions similar to those of Roshko and Thomke were arrived at by Settles (1975) (see also Settles et al. 1975), who performed experiments on corner flows at high Reynolds number ($0.5 \times 10^6 < R_{\delta_0} < 7.6 \times 10^6$). These experiments were made at a nearly constant upstream Mach number ($2.84 < M_\infty < 2.95$) both with a (two-dimensional) ramp model and an axisymmetric flare model. Figure 3.52 shows the influence of the Reynolds number R_{δ_0} on L_o/δ_o for both models. From this figure a consistent trend of decreasing upstream influence with increasing Reynolds number is apparent. The data corresponding to the ramp flow are cross-plotted as L_o/δ_o vs. α with the Reynolds number as parameter in Fig. 3.53. These cross-plottings show that, for a given value of R_{δ_0} , L_o/δ_o is a very regular function of α (similar behavior is observed for the flare). The strictly empirical formula below has been proposed by Settles for L_o/δ_o

$$(3.7) \quad L_o/\delta_o = 0.0092 R_{\delta_0}^{-0.36} \exp(-0.29 \alpha) + 0.03$$

(This equation is only valid for $M_\infty \geq 3$).

A few years ago, Settles et al. (1981) published a more rational discussion of scaling laws for the upstream interaction length. A Reynolds number dependence was looked for by a logarithmic plotting of L_o/δ_o against R_{δ_0} . The quasi-linear curves thus obtained (see Fig. 3.54) demonstrate that the correlation for L_o must be of the form :

$$(L_o/\delta_o) R_{\delta_0}^{1/3} = \text{constant (for fixed } M_\infty, \alpha).$$

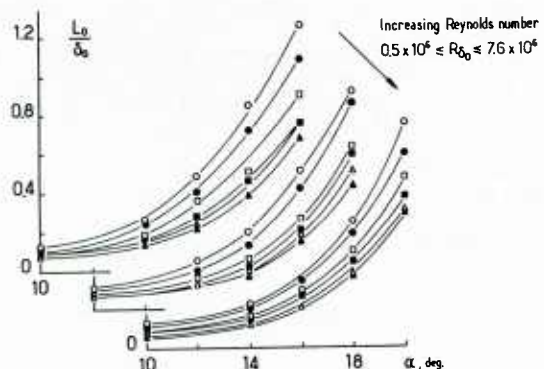


Fig. 3.53 – Upstream interaction length vs ramp angle with Reynolds number as parameter $2.84 \leq M_o \leq 2.95$ (Settles, 1975).

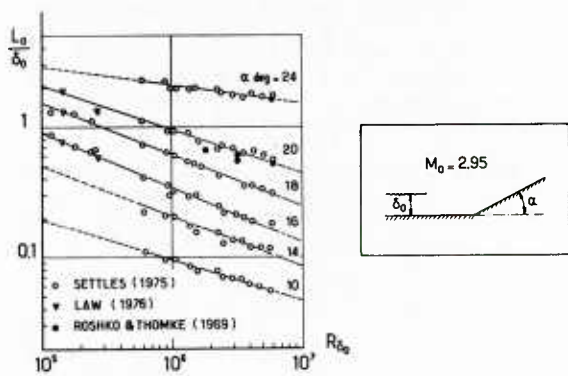


Fig. 3.54 – Upstream interaction length for ramp flow – Reynolds number effect (Settles et al. 1981).

The above equation is valid for $M_o \sqrt{3}$ and may not apply outside the range of α and R_{δ_0} considered by the authors. Its main interest is to show clearly and definitively that, if the upstream influence length is scaled to δ_0 , then a R_{δ_0} "residual remains".

The effect of the ramp angle can also be taken into account by the more general formula, nearly identical to Eq. 3.7 above :

$$(3.8) \quad (L_o / \delta_0) R_{\delta_0}^{1/3} = 0.9 \exp(0.23\alpha)$$

which, as shown in Fig. 3.55, gives an acceptable correlation of the data.

Thereafter, the same authors examined the ability of the following lengths to appropriately scale L_o :

- i - the displacement and momentum thicknesses of the incoming boundary-layer ;
- ii- the height Y_{LSL} of the laminar sublayer ;
- iii- the height y^* of the sonic layer.

As shown in Fig. 3.56, none of these thicknesses exhibits a Reynolds number dependence in the form $\propto R_{\delta_0}^{-1/3}$.

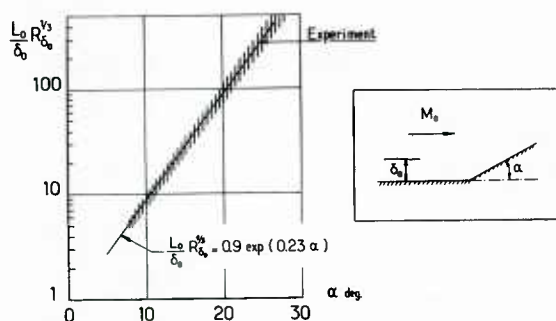


Fig. 3.55 – Correlation law for ramp upstream interaction length – $M_o \sim 3$ $10^5 \leq R_{\delta_0} \leq 10^7$ $10 \leq \alpha \text{ deg} \leq 20$ (Settles et al., 1981).

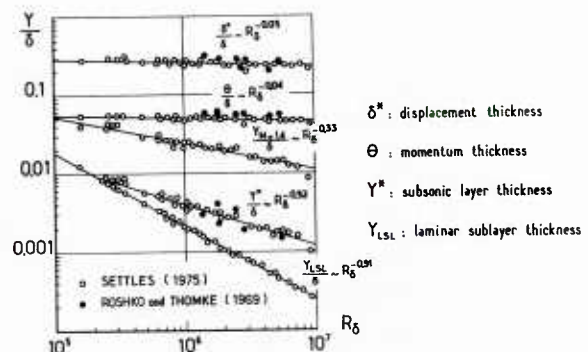


Fig. 3.56 – Reynolds number effect on some scales of the incoming boundary-layer at $M_o = 3$ (Settles et al., 1981).

which would be necessary to correlate L_o . In particular, the sonic layer thickness is not the appropriate scale, although its dependence on R_{δ_0} is close to that of L_o . Several other investigators also found that y^* was not a representative length scale for the upstream interaction length (see Hayakawa and Squire (1982) for supersonic flows and, for transonic flows, the work of Déleré commented in Section 2.7.2 above).

The correlation laws given by Eqs. 3.6, 3.7 and 3.8 are only valid for corner flows in which the incoming boundary-layer is practically always a flat plate boundary-layer. But, experiments in transonic flows have demonstrated that a fundamental factor of influence is in fact the shape of the velocity distribution of the incoming boundary-layer ; this shape being characterized by the "incompressible" shape parameter H_{δ_0} . As we know, for a flat-plate situation, at a given Mach number and for a well behaved undisturbed turbulent boundary-layer in adiabatic flow there is a unique relationship between H_{δ_0} and $R\delta_0$ (see Section 1). Consequently, a variation in $R\delta_0$ is equivalent to a variation in H_{δ_0} . However, if prior to the interaction the boundary-layer has been submitted to a favorable or adverse pressure gradient, its profile at the onset of interaction is no longer determined solely by the Reynolds number $R\delta_0$. In this situation, the above correlations are certainly not valid.

The effect of a change in the shape parameter, independent of the Reynolds number, was examined by Hayakawa and Squire (1982). To this end, they disturbed the boundary-layer upstream of the corner by an injection of air through a wall made of a porous material. In this case, the boundary-layer profiles have many similarities with the profiles of a boundary-layer having undergone an adverse pressure gradient (in the two situations, H_{δ_0} increases).

In their experiments, Hayakawa and Squire found that the increase in the upstream interaction length due to injection was more rapid than the subsequent thickening of the boundary-layer, i.e., L_0/δ_0 increased with the injection rate or - which is equivalent - with the shape parameter H_{δ_0} . Furthermore, in the present situation L_0/δ_0 increases although wall-injection has provoked a decrease of the skin-friction coefficient. Such a trend is in (apparent) contradiction with the restricted correlation laws given by Eqs. 3.6, 3.7 and 3.8. The behavior noticed by Hayakawa and Squire fully confirms the fact that a fuller initial velocity profile entails a greater "stiffness" of the boundary-layer which thus will become more resistant to separation, as will be seen in Section 3.8.

All the above experimental studies seem to prove that, at high Reynolds number, the wall-shear in itself is of secondary importance in strong interaction phenomena. Its role in certain correlation laws is in fact to represent shape parameter effect though the relation linking $C_f 0$, H_{δ_0} and $R\delta_0$ for a flat-plate boundary-layer. This finding is in contradiction with the Free Interaction Theory in which the skin-friction coefficient reflects the crucial role played by the conditions at the wall, according to this model.

3.7.4 - The Upstream Interaction Length in Non-Adiabatic or Axisymmetric Flows

The effect of wall temperature on L_0 was carefully investigated by Frishett (1971) (see also Spaid and Frishett, 1972). This author found that cooling the wall can considerably reduce the upstream interaction length as well as the separation length. This point will be further discussed in the next Section.

Concerning the action of geometrical factors, such as axisymmetry, Fig. 3.57 shows a comparison between upstream influence lengths obtained respectively for wedge and flare. For a deflection $\alpha < 14$ deg., the values of L_0 for wedge and flare are practically identical. They start to diverge when α rises beyond 14 deg. Thus, for the axisymmetric model, reattachment takes place on the flare at a location which is more and more distant from the symmetry axis. So, the separating-reattaching process becomes a mixed two-dimensional and conical process which significantly departs from a planar two-dimensional flow. This departure comes from the very important axisymmetry effect both on the shear-layer development and on the reattachment mechanism (Délery, 1983).

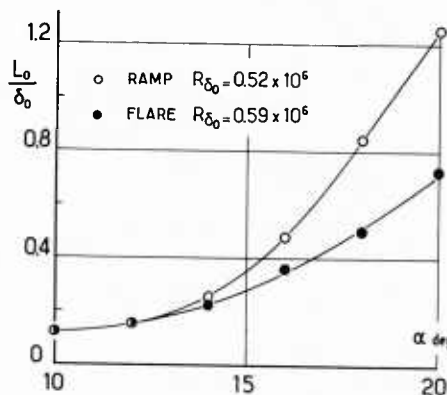


Fig. 3.57 – Comparison of ramp and flare – Upstream interaction length (Settles, 1975).

3.7.5 - The Separation Length

Another length which is of interest for characterizing the streamwise extent of the interaction is the separation length - or separation distance -. For wedge flows, L_s is defined as the distance between the corner hinge and the separation point S (see Fig. 3.50). The experimental determination of L_s is more delicate than that of the upstream interaction length, because it necessitates the accurate location of the separation point. The various techniques employed to this end being thoroughly commented in Section 3.82 below, we will just present here some basic properties of the separation length.

As for the upstream interaction length, experiments performed at low or moderate Reynolds number tend to prove that L_s increases with the Reynolds number. This tendency is illustrated by the results of Spaid and Frishett (1972) shown in Fig. 3.58. In these experiments, $R\delta_0$ varies in the range $3 \times 10^4 - 6 \times 10^4$. A similar trend was also observed by Batham (1972). Such an increase of L_s with the Reynolds number is of course in agreement with the Free Interaction Theory.

Spaid and Frishett also found that cooling the wall reduces the separation distance, as was the case for the upstream interaction length. The cooling effect is shown in Figs. 3.58 and 3.59. In the second figure \hat{L}_s represents the

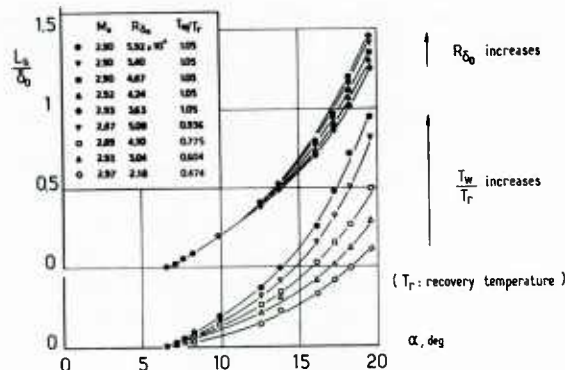


Fig. 3.58 – Separation length – Influence of Reynolds number and heat transfer at low to moderate Reynolds number (Spaid and Frishett, 1972).

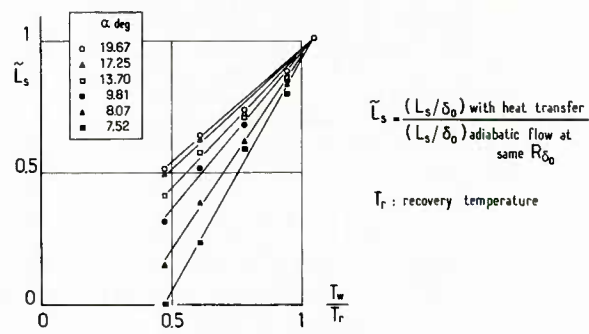


Fig. 3.59 – Influence of heat transfer on normalized separation length (Spaid and Frishett, 1972).

value of L_s/δ_0 measured when heat-transfer is present, normalized by the value of L_s/δ_0 in adiabatic flow and evaluated at the same R_{δ_0} . The decrease in L_s with wall temperature can be interpreted :

i - either within the framework of the Free Interaction theory, since a decrease of the ratio T_w/T_r (T_r being the wall recovery temperature) provokes an increase of the skin-friction coefficient. As a matter of fact, a scaling of L_s by the grouping $\lambda = \delta_0^* C_f (M_\infty^2 - 1)^{1/4}$, which directly results from the Free Interaction theory, provides a good correlation of the data (Frishett, 1971).

ii- or by an overall contraction of the interaction domain resulting from a thinning of the subsonic layer due to a lower temperature level near the wall (see Section 1.3 above).

The effect of wall temperature on the separation length was also investigated by Kilburg and Kotansky (1969), Elfstrom (1971), Holden (1982) and by Back and Cuffel (1976). All these investigators also reached the conclusion that wall cooling reduces the streamwise extent of the interaction region. This effect is particularly well illustrated by the wall pressure distribution plotted in Fig. 3.60. These distributions were measured in a shock reflection at $M_\infty = 3.18$. In Fig. 3.60a the wall is adiabatic and one notes an important extension of the interaction, the real flow-field being nearly distinct from the perfect fluid model. Particularly, the upstream interaction length is specially important. On the other hand, as shown by Fig. 3.60b, cooling the wall shrinks considerably the interaction domain so that the real flow becomes close to the inviscid flow model in which at the wall the shock is a perfect discontinuity. Conversely, surfact heating increases the size of the separated region, as demonstrated by the tracing of mean flow streamlines shown in fig. 3.61.

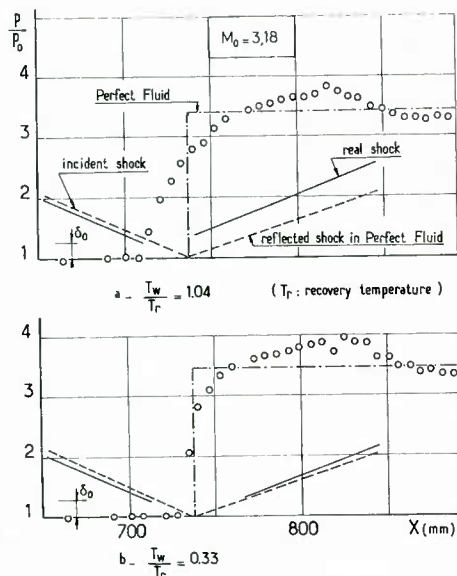


Fig. 3.60 – Effect of wall cooling on incident shock reflection – Wall pressure distribution (Kilburg and Kotansky, 1969).

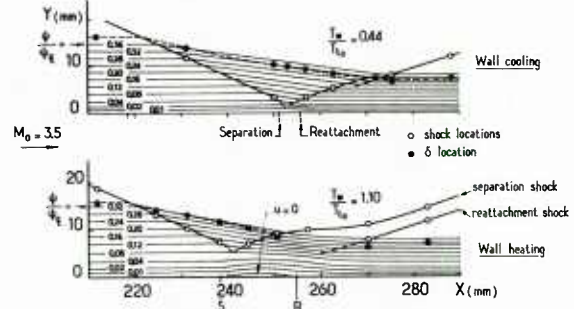


Fig. 3.61 – Effect of wall cooling and wall heating on incident shock reflection – Streamlines pattern (Back and Cuffel, 1976).

Now let us consider adiabatic flow again, but at high Reynolds number. As observed by many investigators (Kessler et al., 1970 ; Settles and Bogdonoff, 1973 ; Law, 1974 ; Roshko and Thomke, 1974 ; Settles, 1975) there is a clear decrease in the separation length L_s with increasing Reynolds number, in a way similar to what has been observed for the upstream interaction length. This fact is clearly demonstrated by the wall pressure distributions plotted in Fig. 3.30. From these data (which were obtained for values of R_{δ_0} greater than 10^6), the decrease in the streamwise extent of the interaction domain with increasing Reynolds number is obvious.

The influence of the Reynolds number as well as of the ramp angle on the separation length was thoroughly studied by Settles for an upstream Mach number close to 3. The evolutions of L_s/δ_0 measured by this author are represented in Fig. 3.62 vs. the Reynolds number with the ramp angle as parameter. Examination of these plottings leads to the following observations :

i - the decrease of L_s/δ_0 with increasing Reynolds number is fully confirmed in the range of variation $5 \times 10^6 < R_{\delta_0} < 7.6 \times 10^6$.

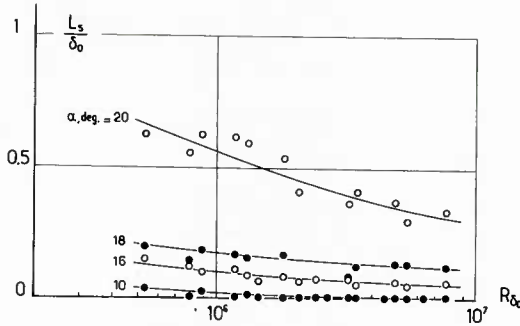


Fig. 3.62 – Separation length – Influence of ramp angle and Reynolds number at high Reynolds number – $M_\infty \cong 3$ (Settles, 1975).

ii- the curves seem to asymptote toward zero separation at zero corner angle. This behavior would prove that separation is in fact always present at the corner, the size of the separation bubble being initially very small at low values of α . Such an observation tends to confirm Kuehn's suggestion that there is always some separation at a wedge, even for vanishingly small ramp angles. However, according to Law (1974), care should be taken in interpreting surface flow visualisations at very small ramp angles. In fact the oil flow technique (like the one used by Settles) should only give the approximate location of the separation points as the streamwise location of some small value (but not equal to zero) of skin friction.

iii-as a consequence of point ii), separation is seen to be a very progressive phenomenon. This leads to conceptual difficulties in the definition of what is commonly called Incipient Separation. And, as was the case in transonic flows, a distinction should be made before "true" Incipient Separation and "effective" Incipient Separation (see Section 3.8.1 below).

To conclude the present Section, it can be said that overall tendencies observed for the upstream interaction length are still valid for the separation distance.

3.7.6 – Concluding Remarks

To briefly summarize the question of the streamwise scaling of a supersonic interaction, it should be again emphasized that the subsonic inner layer certainly plays a major role in the upstream propagation of upstream influence. This fact explains the strong dependence of the upstream interaction length (as well as the separation distance) on the Mach number distribution across the initial boundary-layer.

Nevertheless, the actual propagation mechanism involves a complex coupling between the different "decks" composing the interacting boundary-layer. Thus, it is highly probable that inviscid-viscous interaction between these decks and the subsonic forward propagation are mutually responsible for the observed trends.

At low Reynolds number, and for a turbulent boundary-layer, the viscous sublayer represents a greater part of the total boundary-layer. In these conditions, the interaction must be dominated by viscous phenomena in the near wall region, hence the Free Interaction Theory is more likely to prevail. On the other hand, at high Reynolds number, the viscous sublayer becomes exponentially thin. Therefore, interaction tends to be controlled by inertia and pressure forces, the influence of viscosity being minimized. Furthermore, at high Reynolds number, the subsonic layer is far thicker than the laminar sublayer. As a consequence of these two facts, pressure propagation is now essentially an inviscid mechanism.

3.8 - Incipient Separation in Turbulent Supersonic Flows

3.8.1 - Introductory Remarks

As in transonic flows, the knowledge of Incipient Separation conditions is of great practical interest in supersonic and/or hypersonic flows. It is recalled that Incipient Separation is traditionally defined as the condition in which the shear-stress becomes vanishingly small at some point on the wall, while remaining positive elsewhere. However, as will be seen below, this definition can be inadequate for practical purposes in circumstances where a tiny separated zone seems to be always present, even for very weak shocks. As already mentioned, Kuehn (1961) was the first to suggest this for a compression ramp geometry case : at the scale of the subsonic inner part of the boundary-layer, the wedge shape of the wall should inevitably provoke a local separation. Consequently, as for transonic flows (see Section 2.8 above), we will be faced with the necessity of distinguishing between "true" Incipient Separation and "effective" (or significant) Incipient Separation, the last situation alone being of real significance for practical applications since it corresponds to the onset of most dramatic change in the flow field.

As we already know, detection of Incipient Separation is a very delicate task. This difficulty partly explains the often large discrepancy in the separation limits given by different authors. Thus, before examining the various separation criteria published to this day, it can be useful to describe the techniques most often utilized to determine Incipient Separation. The majority of these techniques can only be used to detect separation induced by a ramp (or a flare) because they call upon some adequate criterion based either on the upstream interaction length or on the separation length measured from the hinge of the ramp. Only a rather limited number of these techniques can be applied to diagnose separation induced by a shock reflection. In spite of this disparity, in what follows we will not make a real distinction between wedge induced and shock induced separation since the Incipient Separation mechanism is basically the same in both cases, as will be seen.

3.8.2 - Techniques Used for the Detection of Incipient Separation

In principle, direct measurement of wall shear-stress is the best way to detect the existence of a separated region as also to locate unambiguously the separation and the reattachment points. In particular this technique has been used in

hypersonic flows by Holden (1972). The drawback of this approach is that accurate determination of the wall shear-stress is a very delicate task in regions of vanishingly small wall shear-stress where strong pressure gradients exist in addition. For this reason, direct measurement of skin friction has rarely been utilized to detect Incipient Separation.

Many investigators working on this problem have preferred a detector based on inspection of wall pressure distributions, pressure at the wall being a quantity easy to measure and generally known with high accuracy. In particular a popular detection technique is based on the occurrence of a "kink" - or triple inflection point - in the wall pressure distribution (Drougge, 1953 ; Kuehn, 1961 ; Kessler, 1972 ; Rose et al., 1973 ; Law, 1974 ; Settles et al., 1975; Hayakawa and Squire, 1982). An example of this technique is shown in Fig. 3.63. Since the occurrence of the kink may be difficult to detect, more "objective" variants of this technique have been proposed in particular by Law (1974) and by Settles et al. (1975). Several investigators (Spaid and Frishett, 1972 ; Settles et al., 1981) have shown that the separated region has to reach a certain minimum size before a kink in the pressure distribution appears. Hence, the method does not detect "true" Incipient Separation but the conditions corresponding to the onset of "effective" Incipient Separation.

Another possibility to define the limit ramp angle corresponding to Incipient Separation is to look for a break or inflection in curves of pressure near the corner vs. corner angle α as shown in Fig. 3.64 (Thomke and Roshko, 1969 ; Elfstrom, 1971 ; Spaid and Frishett, 1972 ; Settles and Bogdonoff, 1983 ; Coleman and Stollery, 1974 ; Hayakawa and Squire, 1982).

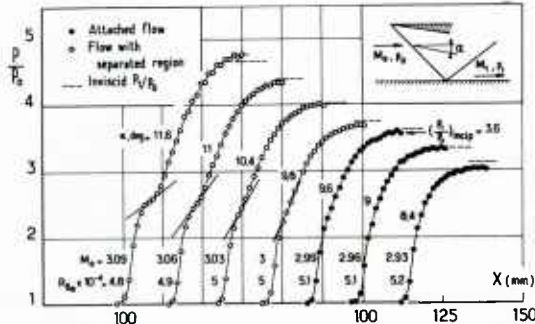


Fig. 3.63 – Incipient separation detection – Occurrence of a triple inflection ("kink") in the wall pressure distribution (Kuehn, 1959).

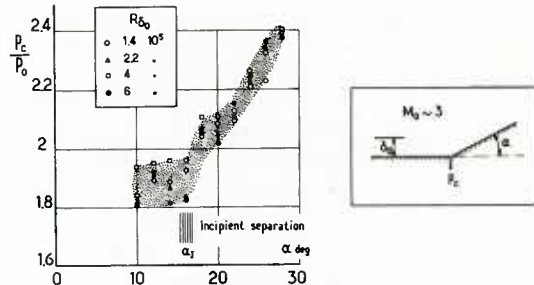


Fig. 3.64 – Incipient separation detection – Ramp flow – Plot of corner pressure vs ramp angle (Settles et al., 1975).

The limit ramp angle α_I can also be determined by considering the variation with α of the normalized upstream interaction length L_0/δ_0 already studied in Section 3.7.2. As shown in Fig. 3.65, Incipient Separation is identified with the sharp change in the curves L_0/δ_0 vs. α (Kessler et al., 1970 ; Settles and Bogdonoff, 1973 ; Hayakawa and Squire, 1982).

Other techniques based on pressure measurements have been developed to detect separation. Among them, we can cite the "orifice dam" arrangement allowing the reading of the surface flow direction by means of small obstacles placed on the wall (Roshko and Thomke, 1969 ; Reda and Page, 1969 ; Rose, 1973). The existence of a separated region has also been looked for by Pitot pressure probing (Drougge, 1953 ; Bogdonoff et al., 1953 ; Seabaugh, 1968 ; Grande, 1971; Appels, 1975 ; Délery and Lacharme, 1978).

Incipient Separation has also been detected by means of surface flow visualisation techniques consisting in the use of a light coating of oil on the surface. Then one observes whether ridges of accumulation are present that could be associated with the stagnation points of separation and reattachment (Reda and Page, 1969 ; Spaid and Frishett, 1972 ;

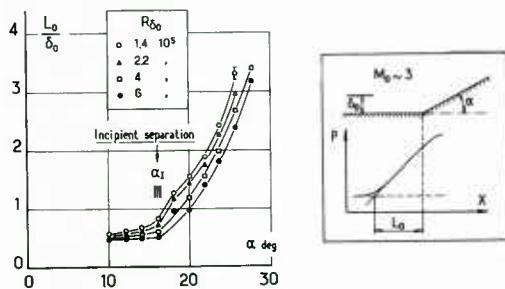


Fig. 3.65 – Incipient separation detection – Ramp flow – Inspection of upstream interaction length (Settles et al., 1975).

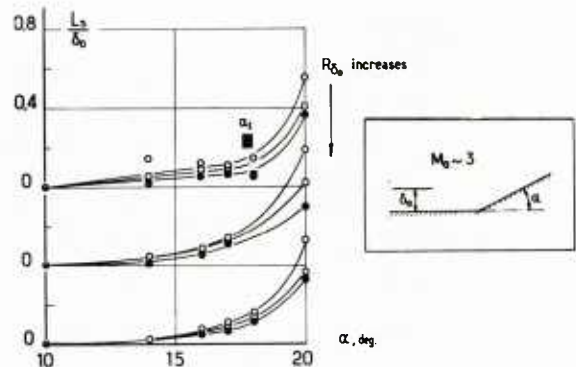


Fig. 3.66 – Incipient separation detection – Ramp flow – Inspection of separation length (Settles et al., 1975).

Délery and Le Balleur, 1972 ; Rose et al., 1973 ; Law, 1974 ; Appels, 1975 ; Hayakawa and Squire, 1982). From surface flow visualisation, one can plot the separation distance L_s/δ_0 against the ramp angle α . Such plottings (already analyzed in Section 3.7.5) generally show that separation is present even for very small values of α . In these conditions, "effective" Incipient Separation can be identified with the occurrence of the rapid rise in the curves plotted in Fig. 3.66. Nevertheless, there remains some uncertainty in the definition of α_I , since the separation curves are without sharp break.

It is also possible to detect separation by a careful processing of flow field pictures obtained by optical methods (namely, schlieren and shadowgraph pictures, holographic interferometry). The detection techniques consist in examining the change in the shock waves pattern associated with occurrence of separation as discussed in Section 3.4 above (Drouge, 1953 ; Roshko and Thomke, 1969 ; Spaid and Frishett, 1972 ; Batham, 1972 ; Settles and Bogdonoff, 1973 ; Coleman and Stollery, 1974 ; Holden, 1974 ; Appels, 1975 ; Law, 1976; Hayakawa and Squire, 1982).

To conclude, it is to be noticed that most investigators working on the problem of Incipient Separation have jointly used several of the above techniques in order to confirm their data. They have generally found good agreement between results obtained by optical methods, surface flow visualisations and inspection of wall pressure distributions. However, for future work in this field, we should recommend the use of more advanced non-intrusive techniques like Laser Doppler Velocimetry which allows very fine and very instructive information on the separation phenomenon (see Section 2.7.1 above and Simpson et al., 1981).

3.8.3 - The Experimental Incipient Separation Limit

Adiabatic, planar two-dimensional flows. In what follows, the limit for Incipient Separation will be given in the classical form $\alpha_I = f(R\delta_0)$ for varying upstream Mach number M_0 , the flow being a planar two-dimensional adiabatic flow. The effects of heat-transfer at the wall and axisymmetry will be considered in separate Sections.

This representation implies that the phenomenon depends essentially on only three parameters, namely : the upstream Mach number, the shock strength and the Reynolds number. As seen in the above Sections, the reality is probably more subtle. For example, the incompressible shape parameter H_{10} of the incoming boundary-layer is also an important factor of influence whose effect is not always taken into account by the Reynolds number. Unfortunately, the paucity of data on the specific influence of H_{10} makes a proper correlation of the dependence of Incipient Separation on H_{10} very difficult. It is for this reason that we will adopt the traditional form, it being understood that the results are restricted to a flat-plate incoming boundary-layer.

In the case of separation induced by a shock reflection, α_I will represent the equivalent ramp angle producing the same overall pressure rise as the two successive compressions through the incident and the reflected shock-waves. Experiments made by Holden (1972) and by Law (1976) have clearly shown that by considering this effective ramp angle, there is no essential difference between ramp-induced and incident shock-induced separation. As a matter of fact, the pressure rise to Incipient Separation is almost the same in both situations.

As a brief recall of comments made above, experiment clearly shows that - like for transonic flows - a distinction must be made between :

- i - "true" Incipient Separation which would correspond to the first appearance of a tiny separation bubble. This situation is detected only by the most subtle techniques like surface flow visualisations and/or careful schlieren photograph processing. For a corner flow case, existence of this limit has been questioned by some investigators (Settles et al., 1975) who argue that separation onset is basically a smooth and gradual transition between "attached" and "separated" flow rather than an abrupt change. Seen from this view-point, the lower limit of the phenomenon is practically impossible to detect and "true" Incipient Separation would be a purely academic problem ;
- ii- "effective" Incipient Separation or Significant Separation which is observed when the separated bubble has reached a size large enough to produce "significant" change in the flow field. As has already been said, this state is the immediate precursor of more spectacular events caused by the rapid growth of the separated flow region. "Effective" Incipient Separation is in fact the most important for practical applications. It is the situation detected by the less sensitive methods.

Figure 3.67 shows a plotting in the $(R\delta_0, \alpha_I)$ plane of the limits for "true" and "effective" Incipient Separation for the same flow (Rose et al., 1973). One sees that the difference between these two values of α_I can be very large.

Because of its great practical importance and also because most available results are relative to this limit, in what follows we will mainly consider "effective" Incipient Separation and the term "effective" will be henceforth dropped.

Most of the published data have been plotted in Fig. 3.67. In spite of an important scatter, the following trends can be discerned :

- i - the angle α_I (or the pressure jump p_f/p_0) increases when the upstream Mach number M_0 increases ;
- ii- at low Reynolds number, α_I decreases as $R\delta_0$ increases. Such a trend is in agreement with the Free Interaction theory.
- iii at high Reynolds number, most investigators have noticed a reversal in the Reynolds number influence ; i.e., the angle α_I increases with $R\delta_0$; the variation being rather slow ;
- iv- according to other investigators (Settles and Bogdonoff, 1973 ; Settles et al., 1981), the separation angle would in fact be independent of the Reynolds number.

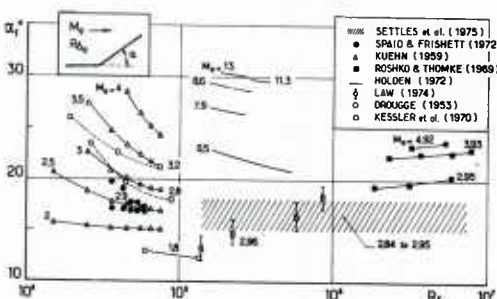


Fig. 3.67 - Shock induced incipient separation
in supersonic flow.

It is difficult to be absolutely conclusive about the above tendencies since there is frequently a large uncertainty in the experimental determination of the angle α_i . Furthermore, some experiments were performed in "uncommon" situations. For instance, Kuehn's very careful measurements, as well as those of Kessler et al. (1970), could have been compromised by the use of tripped incoming boundary-layers. Thus, these results do not correspond to "normal" turbulent boundary-layer. Also, the high Reynolds number experiments of Roshko and Thomke (1969) have utilized the tunnel wall boundary-layer and some argue that such a boundary-layer may differ from an equilibrium turbulent boundary-layer since it was submitted to a highly favorable pressure gradient prior to the interaction (Holden, 1972). Further comments on the observed behavior are included in the next Section.

To close this Section, we will give some information on the effect of heat transfer at the wall and on Incipient Separation in axisymmetric flows.

Effect of Heat-Transfer at the Wall. Experiments performed by Spaid and Frishett (1972) and by Elfstrom (1971) clearly show that cooling the wall increases the resistance to separation. For example, Spaid and Frishett found that at $M_0 = 2.9$, the Incipient Separation angle increased from 6.5 to 7.5 degrees as the ratio of wall temperature to recovery temperature was lowered from 1.05 to 0.47. However, in this field, experimental results are too scarce to provide really useable correlation curves. The greater resistance to separation can be interpreted in the same terms as the decrease in separation length occurring when the wall temperature is lowered, i.e., cooling the wall reduces the thickness of the boundary-layer subsonic part (see Section 3.7.5 above and also Elfstrom's flow model presented in the next Section. This model provides a way to predict wall temperature effect which agrees reasonably well with the few available experimental results).

Incipient Separation in Axisymmetric Flows. According to an observation made by Kuehn (1961) and also by Colemen and Stollery (1974), the Incipient Separation angle should be slightly higher for axisymmetric external flow than for planar two-dimensional flow.

In fact, Incipient Separation being a local phenomenon involving the boundary-layer properties in the vicinity of the wall, it can be safely conjectured that this process is certainly not very sensitive to axisymmetrical effect and, in most cases, the separation limit is identical to that found in planar two-dimensional flows (see also conclusions about the separation distance in Section 3.7.4 above).

Nevertheless, a sizeable influence can be felt if the upstream development of the boundary-layer has been significantly influenced by three-dimensional effects. This is the case if the thickness of the incoming boundary-layer is not small when compared to the distance of the wall to the symmetry axis. Then, the velocity distribution across the boundary-layer can be affected in such a way that the interaction process appreciably departs from a purely two-dimensional flow.

For axisymmetric internal flow (like the flow inside a nozzle), Rose and al. (1973) found a very low Incipient Separation pressure rise (see fig. 3.68). However, these authors employed a technique which actually detects the "true" Incipient Separation limit. This limit is known to be considerably lower than for "effective" Incipient Separation. So, no conclusion can be drawn about a possible (but highly improbable) lower resistance of axisymmetric internal flows to separation, except may be for flows with very thick boundary-layers.

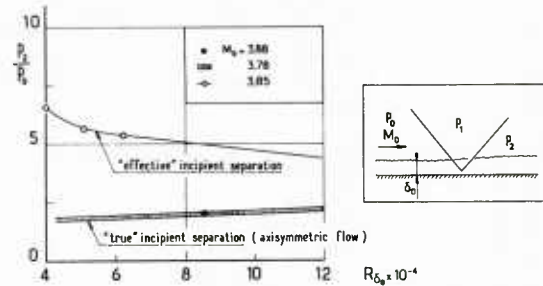


Fig. 3.68 – Difference between "true" and "effective" incipient separation (Rose et al., 1973).

3.8.4 - Simplified Models for Predicting Incipient Separation in Supersonic Flows

Introductory Remarks. For reasons already given in Section 2.8.2 dealing with Incipient Separation in transonic flows, we will now present a short review of some correlations or "simple" methods aimed at the prediction of Incipient Separation in supersonic flows. In this review, we do not intend to be exhaustive since a great number of such methods have been proposed. We will limit our attention to the most typical and the most instructive (for a review containing other separation criteria see Hahn et al. 1973).

Criteria Derived from Boundary-Layer Type Analysis or from Fully Empirical Laws. One of the oldest and maybe the simplest separation criterion can be derived from the analysis of Reshotko and Tucker (1955) for the effect of a pressure discontinuity on a turbulent boundary-layer (see Section 1.2.1 of Part II below). This criterion is simply obtained by stating that separation first occurs when, downstream of the discontinuity (which is a compression jump in

the present case), the transformed shape parameter \bar{H} introduced by Reshotko and Tucker (\bar{H} differs slightly from the "true" shape parameter H_1) reaches the value representative of the velocity profile at separation, namely : $H = 2.2$.

For a given initial shape parameter H_{10} (or \bar{H}_{10}), this situation arises for a well defined value of the ratio M_1/M_0 of the Mach numbers on each side of the discontinuity. Hence the separation criterion is expressed by the simple relation :

$$M_1/M_0 = C$$

where C is a function of H_{10} . For "usual" flat-plate turbulent boundary-layer (i.e., $H_{10} \approx 1.3$), Reshotko and Tucker have suggested $C = 0.762$. The Mach number ratio can easily be converted into pressure ratio or deflection angle by using shock tables. The present criterion predicts an increase in the pressure ratio p_1/p_0 when the upstream Mach number M_0 increases, which is in agreement with experiment.

Although the Reshotko and Tucker criterion does not display explicitly the influence of the Reynolds number (viscous terms are neglected in their analysis), this influence is actually taken into account via the dependence of H_{10} on the Reynolds number (see Section 1 above).

Seeing that for a well-behaved (or equilibrium) flat plate boundary-layer H_{10} decreases when $R\delta_0$ increases, the present criterion predicts greater resistance to separation as the Reynolds number is higher. The pressure rise for Incipient Separation calculated by using the analysis of Reshotko and Tucker is given in Fig. 3.69 as a function of $R\delta_0$ with the upstream Mach number M_0 as parameter. To execute these calculations the equilibrium flat-plate relation between H_{10} and $R\delta_0$ has been utilized.

Todisco and Reeves (1969) also deduced a separation criterion from a theoretical analysis similar in nature to that of Reshotko and Tucker. Their criterion likewise predicts a slight increase with Reynolds number of the shock strength for Incipient Separation. Another separation criterion was proposed by Gadd (1953) from his momentum integral analysis (see Section 1.2.1 of Part II below). This criterion shows no influence of the Reynolds number.

A separation criterion can also be established from the purely empirical curve proposed by Zukoski for the separation pressure (see Section 3.2.4 above and Fig. 3.70). It consists in equating the pressure ratio p_1/p_0 with the ratio p_s/p_0 where p_s is the pressure at the separation point. It would also be possible to identify p_1/p_0 with the ratio p_p/p_0 corresponding to the plateau pressure. These two procedures define two separation limits which are represented in Fig. 3.70. One sees that the curve obtained by equating p_1 and p_p leads to a higher pressure rise for Incipient

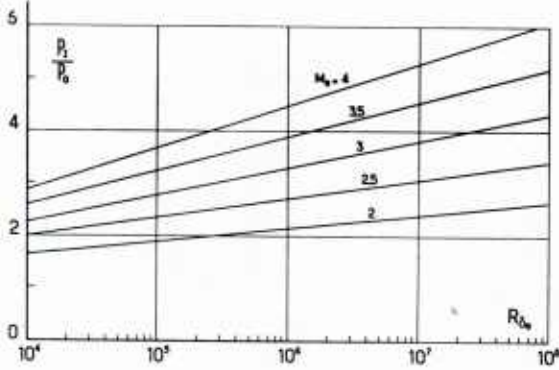


Fig. 3.69 – Incipient separation criterion deduced from Reshotko and Tucker – Discontinuity analysis.

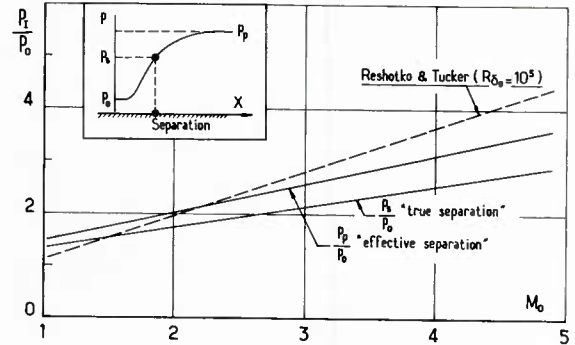


Fig. 3.70 – Incipient separation criterion deduced from Zukoski's correlation.

Separation which is in close agreement with the limit given by the Reshotko and Tucker analysis if the value $C = 0.762$ is adopted. Although no experimental justification of this fact can be provided, the lower pressure rise in which p_1 is equated to the separation pressure could be identified with the limit for "true" Incipient Separation : whereas the pressure ratio p_1/p_0 in which p_1 is equated to the plateau pressure could correspond to the limit for "effective" Incipient Separation. It is clear that Zukoski's results do not contain any influence of the Reynolds number. Therefore, the Incipient Separation curves given in Fig. 3.70 are in fact valid for a "standard" incoming boundary-layer whose shape parameter is close to 1.3

It must be pointed out that the above Incipient Separation criteria have been experimentally confirmed for high Reynolds numbers (say $R\delta_0$ greater than 10^5) and for upstream Mach numbers that are not too high (say M_0 lower than 4).

Another completely empirical separation criterion was proposed by Roshko and Thomke (1974) from their correlation law for the normalized upstream interaction length (see Eq. 3.6 in Section 3.7.3 above). Examination of the variation of L_0/δ_0 vs. α led these two authors to postulate that separation at a corner occurs when the upstream interaction length is such that $L_0/\delta_0 = 0.55$, independent of Mach and Reynolds numbers. This assumption provides an equation to compute α_I as a function of the skin-friction coefficient C_f . From the well known formulae expressing C_f as a function of the Mach and Reynolds numbers, it is an easy matter to draw Incipient Separation curves according to the traditional plotting $\alpha_I = f(R\delta_0)$. As shown in Fig. 3.71, at high Reynolds number, the correlation with most of the experimental data seems to be at least as good as the agreement among the different data. However, this correlation, as well as the previous ones, are unable to predict the decrease of α_I for increasing $R\delta_0$ at low Reynolds number. The criterion $L_0/\delta_0 = 0.55$ should give "effective" Incipient Separation, and "true" Incipient Separation, as detected by surface flow technique would correspond to $L_0/\delta_0 = 0.05$.

Korkegi (1975) has proposed a completely empirical Incipient Separation criterion valid only for moderate to high Reynolds numbers. This criterion which is given in Section 4.4 relative to three-dimensional Incipient Separation, assumes that there is no influence of the Reynolds number, this influence being in fact questionable as seen above. Thus, Korkegi's criterion is simply a curve in the plane $(R\delta_0, \alpha_I)$ or $(R\delta_0, p_I/p_0)$.

Criteria base on the Free Interaction theory. Several separation criteria have been derived from Chapman's analysis (see Section 3.6 above). Basically, the pressure rise can be obtained by postulating that separation first occurs when the pressure jump through the shock at the corner (or through the incident plus reflected shock) is such that :

$$\frac{p_I - p_0}{q_0} = 4.22 (2 C_{fo})^{1/2} (M_0^2 - 1)^{-1/4}$$

The constant 4.22 is the value at the separation point of the universal correlation function F introduced by Erdos and Pallone (see Section 3.6 above). In other criteria, the value 4.22 is replaced by 6, which corresponds to the plateau pressure reached in extended separation. The Incipient Separation pressure rises deduced from the Free Interaction Theory are represented in Fig. 3.72. The two families of curves correspond respectively to the values 4.22 and 6. Such criteria should not be used at high Reynolds number and Mach numbers that are too high ($M_0 < 5$).

Several variants of the above criteria have been proposed to try to improve agreement with experimental results.

Thus, Roshko and Thomke (1966) (see also Holden (1972)) obtained a correlation law from the classical balance between the inertial and viscous forces at the wall. In the spirit of Chapman's analysis, this relation is roughly approximated by :

$$\frac{p_I - p_0}{L} \propto \frac{\tau_{w0}}{\delta_0}$$

At high Mach number, the interaction length scale can be estimated as $L \propto M_0 \delta_0$. Hence, a correlation law of the form :

$$\frac{p_I - p_0}{p_0} \propto M_0^3 C_{fo} \text{ is obtained.}$$

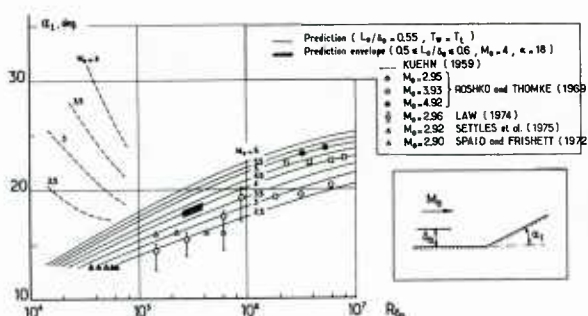


Fig. 3.71 – Incipient separation prediction at high Reynolds number by Roshko and Thomke (1969).

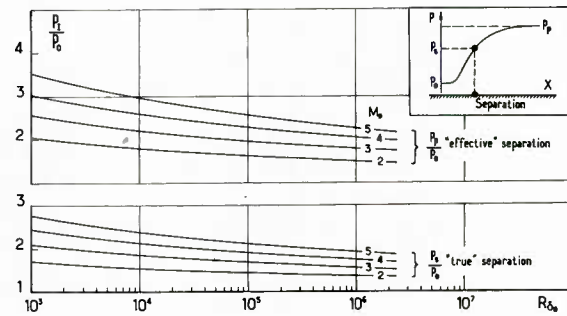


Fig. 3.72 – Incipient separation criterion deduced from the "free interaction theory".

A completely empirical improvement of the above law was proposed by Elfstrom (1971) who has plotted the ratio $(p_I - p_0)/p_0$ as a function of $C_{fo}^{1/2} M_0^{5/2}$.

For hypersonic flows also, Needham and Stollery (1966) deduced a correlation law by considering the quantity $M_0 \alpha_I$ and the hypersonic viscous interaction parameter $X = M_0^3 C^*/R_x$ (C^* is the constant of the Chapman-Rubesin viscosity law). It is to be noticed that $M_0 \alpha_I$ is the hypersonic limit for the pressure jump given by the linearized Prandtl-Meyer law. Also, in laminar flows $X \propto M_0 C_f$, so that this correlation is similar to the law of Roshko and Thomke. Having found that correlation of experimental data leads to a relation of the form $M_0 \alpha_I \propto X^{1/2}$, Needham and Stollery finally proposed a correlation in which the parameter $\alpha_I/M_0^{1/2}$ is plotted against the Reynolds number R_x .

The correlation laws more or less inspired by the Free Interaction theory are represented in Figs. 3.73 and 3.74. They generally correlate data at low to moderate Reynolds number ; in this range they all predict less resistance to separation at increasing Reynolds number. We already know that this tendency is in contradiction with experiment at high Reynolds number.

Furthermore, the above separation criteria predict in fact "effective" Incipient Separation. On the other hand, the correlation theory proposed by Appels (1973) is aimed at predicting the limit for "true" Incipient Separation. Appel's theory also uses arguments belonging to the Free Interaction concept, but, as true Incipient Separation is identified with the birth of a tiny separation bubble, it is assumed that the flow reversal initially occurs in the laminar sublayer. Consequently, the phenomenon only involves parameters - or quantities - relative to this sublayer.

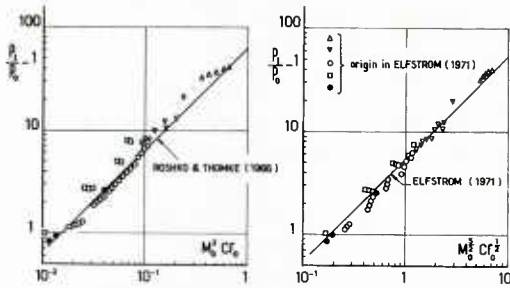


Fig. 3.73 – Correlation law for incipient separation –
Turbulent flow at moderate Reynolds number (Elfstrom, 1971).

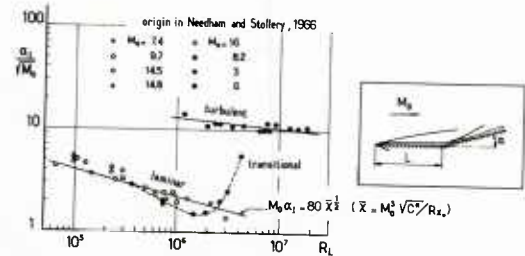


Fig. 3.74 – Correlation law for incipient separation – Laminar
and turbulent flow at moderate Reynolds number (Needham
and Stollery, 1966).

This analysis, can be seen as a very simplified version of more sophisticated multi-deck theories. Its agreement with measured Incipient Separation is relatively good, although the Reynolds number effect is apparently not correctly represented.

The inviscid flow model of Elfstrom. In 1971, Elfstrom proposed an attractive flow model for predicting Incipient Separation. His method is based on the Inviscid Shear Layer type of approach described in Section 1.4 of Part II below. According to this approach, the interacting corner flow (in fact the method can also be applied to shock reflection), is considered as essentially inviscid, the major part of the boundary-layer behaving like an inviscid rotational flow. In order for the calculation of such a flow to be possible, the viscous sublayer must be ignored. Furthermore, the outer part of the velocity profile (which in fact comprises most of the boundary-layer flow) is extrapolated in its lower part in such a way that a (fictitious) slip velocity exists at the wall. The extrapolated profile is

the continuation of the so-called "inviscid" portion of the boundary-layer, i.e., the region where the turbulent stress form the greatest part of the total shear-stress (broadly speaking, this corresponds to the logarithmic and the wake regions, see Section 1 above).

Given the properties of the incoming flow (outer Mach number, Reynolds number, boundary-layer shape parameter, wall-to-external temperature ratio...), the initial Mach number distribution can be computed by utilizing one of the available representations of the velocity distribution across a turbulent boundary-layer. In his calculations, Elfstrom has used a family of turbulent velocity profiles attributable to Green.

Thereafter, the corner flow is computed by assuming that the entire flow passes through an oblique shock upon turning parallel to the ramp. Although an exact calculation of this flow would be possible by using the rotational Method of Characteristics, Elfstrom has chosen a simplified and more rapid version of this method which is very accurate at high Mach numbers.

Of course, such an analysis can only be applied if the flow on the ramp remains supersonic. This restriction is not in fact overly severe since the subsonic part of a turbulent boundary-layer becomes excessively thin as soon as the outer Mach number is greater than three (especially at high Reynolds number). Wall pressure distributions computed with this method are generally in good agreement with experiment.

Elfstrom has postulated that Incipient Separation conditions correspond to the highest ramp angle for which the wall pressure distribution still appears to represent a fully attached flow. This condition is identified as the ramp angle at which the oblique shock becomes detached at the wall in the inviscid flow model. Hence, prediction of Incipient Separation is rather straightforward. The "wall" or "slip" Mach number M_w is first determined from the incoming velocity profile as explained above. Then, the turning angle α which produces a detached shock for the Mach number M_w is identified with the Incipient Separation angle α_I .

Curves $\alpha_I = f(R\delta_0)$ calculated by this method for adiabatic wall conditions are represented in Fig. 3.75. Agreement with experiment can be considered as remarkable. In particular, the change in the trend with increasing Reynolds number is accurately predicted. According to Elfstrom, this reversal in the α_I trend with $R\delta_0$ closely follows the development of the wake component in the velocity profile. A stronger developed wake results in a more energetic boundary-layer which is thus more resistant to separation. The profile being fuller, M_w is higher, hence a higher detached shock limit. As reported by Appels, studies in turbulent boundary-layers (Johnson and Bushnell, 1970) show that close to transition the "strength" of the wake component first decreases with increasing Reynolds number, hence a decrease in α_I in virtue of Elfstrom's model. For higher Reynolds number, the wake component becomes stronger and

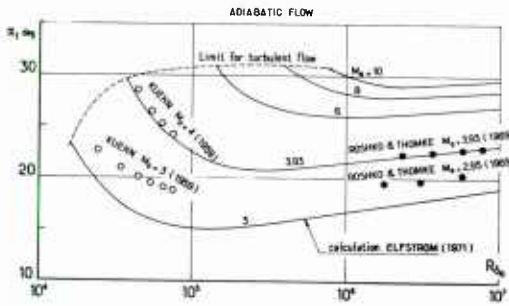


Fig. 3.75 – Incipient separation in turbulent flow –
Prediction by Elfstrom's flow model.

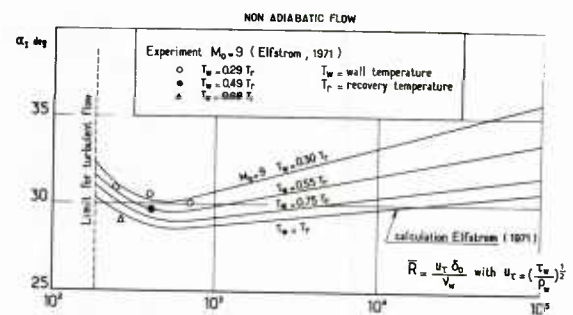


Fig. 3.76 – Incipient separation in turbulent flow –
Prediction by Elfstrom's flow model.

the resistance to separation increases. The Elfstrom flow model also permits the prediction of wall temperature effect, as shown in Fig. 3.76.

3.8.5 - Concluding Remarks

As briefly explained the interaction between a shock-wave and a boundary-layer is a very complex phenomenon involving a delicate balance between inertia forces and viscous forces, especially in the near wall region.

Perfect fluid models, like those of Elfstrom or Reshotko and Tucker (see also Rose et al., 1968), favor the contribution of the inertia and pressure terms. Thus, according to these models, Incipient Separation (as well as upstream influence), is essentially controlled by the more or less important filling of the incoming boundary-layer velocity and Mach number distributions. This fact explains why increasing the Reynolds number (which fills the velocity profile), or lowering the wall temperature (with increases the Mach number near the wall) tend to augment the resistance to separation. This interpretation is certainly valid at high Reynolds number where significant viscous effects are confined within an exponentially thin sublayer. In this situation, the interaction is controlled by a wall interaction layer which is considerably thicker than the viscous sublayer and penetrates some distance into the supersonic portion (see Roshko and Thomke, 1974).

On the other hand, Free Interaction type theories privilege the situation at the wall, i.e., the role played by the viscous forces which are dominant in the wall sublayer. Thus, these theories are more likely to give a fair representation of reality at (relatively) low Reynolds numbers where the viscous sublayer thickness is a few (up to ten) percent of the total boundary-layer thickness. Furthermore, Free Interaction type theories seem more suitable for predicting "true" Incipient Separation which is a phenomenon confined to the very near wall region. To conclude this still open question of the reversal in trend with increasing Reynolds number, it should be said that Free Interaction analyses apply the classical boundary-layer equations to the entire interacting dissipative layer. This model is certainly questionable when the shock-wave penetrates deep into the boundary-layer, as is the case at high Mach number in particular.

3.9 - Development of the Dissipative Layer Properties

3.9.1 - The Mean Flow Field

This Section will be brief since the evolution of the dissipative layer during a supersonic interaction is very similar to the evolution observed in transonic flow, the latter having been examined in detail in Sections 2.7.3 and 2.9.3.

To begin with, let us consider the behavior of the mean properties. For this purpose, we will first examine experimental results obtained by Rose (1973) in an axisymmetric facility in order to avoid three-dimensional effects due to the side wall interactions present in nominally two-dimensional facilities. His experimental arrangement is constituted of an axisymmetric nozzle producing a uniform flow whose Mach number is equal to 3.88. A conical incident shock-wave is generated by a cone of a 9 deg. half-angle mounted at zero incidence along the nozzle centerline. The interaction under study occurs on the nozzle and test-section wall. The strength of the incident shock corresponds nearly to Incipient Shock-Induced Separation. The initial Reynolds number $R\delta_0$ is equal to 0.87×10^6 . The interacting flow was carefully probed by means of pressure and hot-wire probes.

The experimentally deduced flow field is represented in Fig. 3.77. The corresponding streamwise evolutions of the displacement thickness δ^* and of the boundary-layer mass-flow m relative to its initial value m_0 are plotted in Fig. 3.78. These results display trends typical of supersonic interactions :

- i - the boundary-layer thickness δ decreases markedly in the course of the interaction. Here, the relative "jump" $\Delta \delta / \delta_0$ between two stations located respectively downstream and upstream of the shock impingement region is equal to -0.35 ;
- ii- also, the displacement thickness decreases ; in the present case $\Delta \delta^* / \delta_0^* = -0.35$;
- iii-by contrast, the boundary-layer mass flow increases sharply. It is clear that the entrainment rate dm/dx is about an order of magnitude greater downstream of the interaction than upstream.

The important rise in dm/dx during the interaction was also noticed in transonic interactions (see Section 2.9.3 above). It results from the amplification of the turbulent mixing process, especially at the boundary-layer edge. Thus a larger amount of fluid is transferred from the outer flow into the boundary-layer.

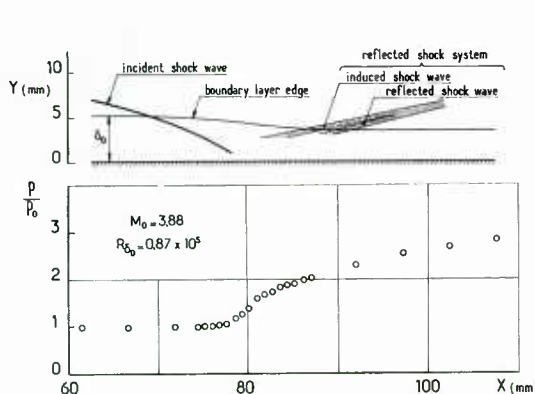


Fig. 3.77 – Shock reflection – Flowfield main features and wall pressure distribution (Rose, 1973).

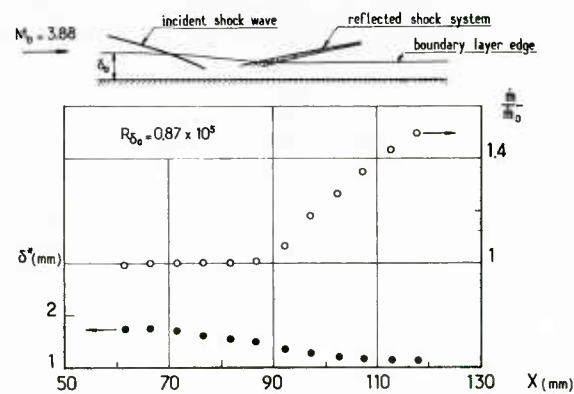


Fig. 3.78 – Shock reflection – Evolution of boundary layer – Displacement thickness and boundary layer mass flow (Rose, 1973).

On the other hand, the decrease in δ and δ^* observed in the present shock reflection is in contradiction with the tendencies observed in transonic and/or moderately supersonic flows (see Section 2.9.3 above and shadowgraph pictures in fig. 2.20). As a matter of fact, the "jump" in δ and δ^* can be explained by considering the following expression of the mass-flow of a boundary-layer :

$$\dot{m} = \rho_e u_e (\delta - \delta^*)$$

where ρ_e and u_e are relative to local conditions at the boundary-layer outer edge. Hence :

$$\delta = \delta^* + \frac{\dot{m}}{\rho_e u_e}$$

As just seen, \dot{m} rises steeply during the interaction. But at the same time, due to the decrease in the outer Mach number M_∞ , $(\rho_e u_e)$ also increases, the increase in $(\rho_e u_e)$ being more pronounced as the initial Mach number is higher. Thus when M_∞ is raised, a situation can be reached in which the increase in $(\rho_e u_e)$ outbalances that of \dot{m} leading to a thinning of the boundary-layer. The decrease of δ^* is a consequence of that of δ if the interaction is not strong enough to sufficiently "empty" the boundary-layer velocity profile. However, it is clear that there is no general rule to decide if an interaction will entail a thinning or a thickening of the boundary-layer since the phenomenon depends on many more parameters than the initial Mach number alone.

Information on a separating boundary-layer in supersonic conditions is provided by experiments carried out by Behrens (1971). This author analyzed with great care the flow produced by a forward facing step placed in a two-dimensional uniform supersonic flow (see Fig. 3.16 and Section 3.2.3 above). The initial conditions were as follows : $M_\infty = 4$, and $R_{\delta_0} = 1.12 \times 10^5$. The flow was investigated by means of pressure probes. Moreover, some fluctuation measurements were performed by using hot-wires. Some of the streamwise velocity profiles located downstream of the separation point are plotted in Fig. 3.79. In this representation, h is the step height and x the distance from the step, positive values being upstream distances. The profiles exhibit a region of reversed flow and their shape is similar to that of the profiles found in transonic interactions. The x -wise evolution of the following quantities is plotted in Figs. 3.80 and 3.81. :

i - the maximum reversed flow velocity

ii - the reversed mass-flow, i.e. the mass-flow between the wall and the ordinate y_0 at which the streamwise component crosses zero.

One observes that the reversed flow region is fed by the flow which moves down the step and is sharply turned in the upstream direction. This flow is quickly accelerated to a velocity $|u_m|/u_e = 0.37$. Thereafter the maximum back-flow velocity decreases slowly to zero at the separation point. At the same time, the reversed mass flow decreases steadily in magnitude because of the aspiration or entrainment effect of the forward flow along the $u = 0$ line (see sketch in Fig. 3.80). Behrens indeed found that the profiles above the $u = 0$ line compare very well with boundary-layer profiles disturbed by large wall injection, if the injection rate at the wall is identical to the entrainment rate along the $u = 0$ line.

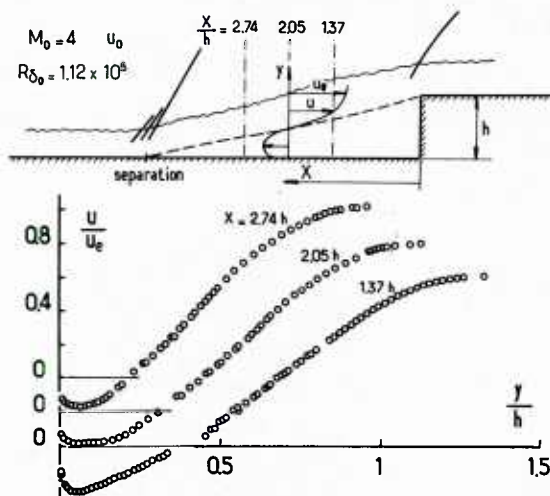


Fig. 3.79 – Separation in front of a forward facing step – Velocity profiles in the separated region (Behrens, 1971).

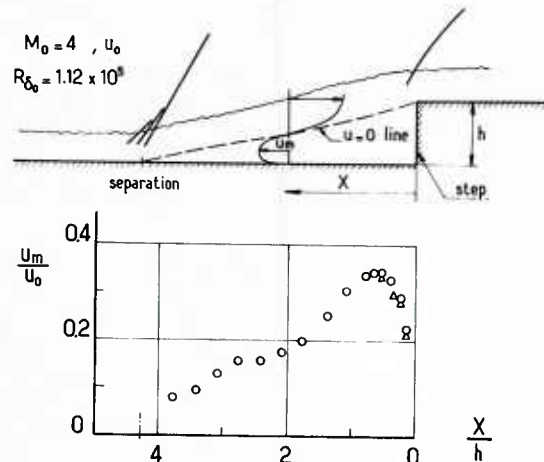


Fig. 3.80 – Separation in front of a forward facing step – Maximum reversed flow velocity (Behrens, 1971).

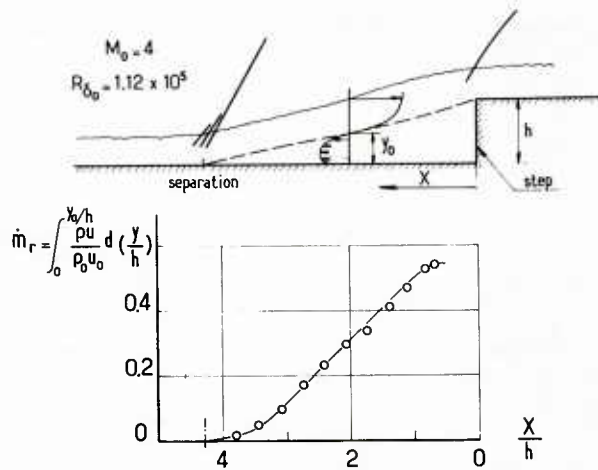


Fig. 3.81 – Separation in front of a forward facing step – Reversed mass flow (Behrens, 1971).

3.9.2 – The Turbulent Field

Accurate information on turbulence behavior in a supersonic interaction is provided by the experiments of Ardoneau (1981) (see also Ardoneau et al., 1980). These tests were carried out on a ramp flow with the initial conditions : $M_0 = 2.25$ and $R_{\delta_0} = 0.90 \times 10^5$. Three ramp angles were considered : $\alpha = 8, 13$ and 18 deg. The measurements were performed by using both hot-wire and laser velocimetry. The wall pressure distributions for the three ramp angles are plotted in Fig. 3.82 and the corresponding mean streamwise velocity profiles in Fig. 3.83. The case $\alpha = 13$ deg. is on the verge of separation and for $\alpha = 18$ deg., a separated region is clearly seen. These velocity distributions exhibit the same general trends as those observed in transonic flows (see Section 2.9.3 above). In particular, downstream of reattachment (case $\alpha = 18$ deg.), the flow is highly accelerated near the wall, which results in characteristic profiles including two inflection points. This feature will be interpreted shortly hereafter.

The profiles of the RMS values of the streamwise and vertical velocity fluctuations are plotted in Figs. 3.84 and 3.85. Like in transonic flows, the $\sqrt{u'^2}$ distributions reveal the existence of a very intense maximum of velocity fluctuations which is more and more detached from the wall as the interaction becomes stronger (i.e., α increases). As we already know, the interaction with the shock entails a large increase in the fluctuation level, the production of turbulence being higher when the flow is separated. The increase in $\sqrt{v'^2}$ is far less important which leads to the development of a strong anisotropy, as was already observed in transonic flows. According to Ardoneau et al. (1980), this situation can be explained by the fact that the turbulent kinetic energy is essentially produced on the u'^2 component (see Section 2.9.3.4 above) and redistributed on the v'^2 and w'^2 components mainly through the pressure-strain correlation. Due to the very short streamwise extent of the interaction, the tendency to isotropy cannot balance the large u'^2 production and values of u'^2/v'^2 greater than 16 are obtained in some regions.

The large increase in the anisotropy which is a typical feature of this kind of interacting flows was also noticed by Rose and Johnson (1985) who investigated a shock reflection for the conditions : $M_0 = 2.9$ and $R_{\delta_0} = 1.4 \times 10^5$, the deflection through the primary incident shock being equal to 7 deg. The measurements were also performed by using both hot-wire and laser velocimetry. No sizeable separation bubble was observed, the incident shock not being strong enough to induce large separation. However, it was found that $\sqrt{u'^2}$ increased very much, while the transverse fluctuation component $\sqrt{v'^2}$ remained nearly unchanged during the interaction (see Fig. 3.86).

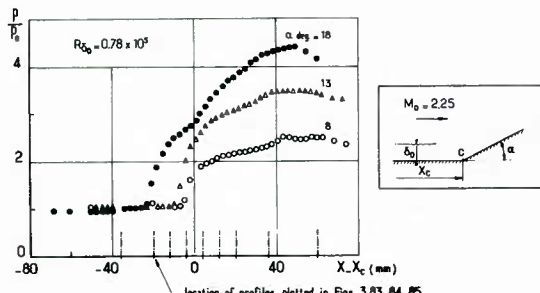


Fig. 3.82 – Ramp flow – Wall pressure distribution (Ardoneau et al., 1980).

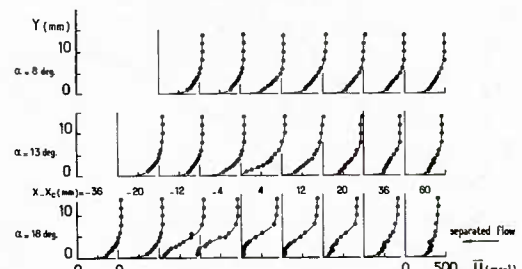


Fig. 3.83 – Ramp flow – Mean streamwise velocity distributions (Ardoneau et al., 1980).

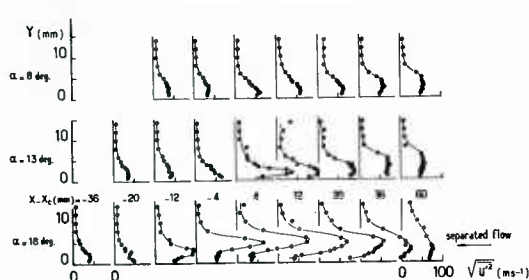


Fig. 3.84 – Ramp flow – Streamwise fluctuation distributions (Ardoneau et al., 1980).

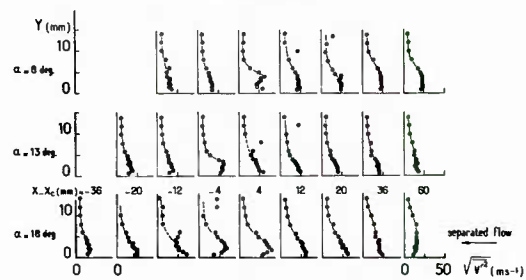


Fig. 3.85 – Ramp flow – Vertical fluctuation distributions (Ardoneau et al., 1980).

The evolution of the Reynolds shear-stress $\bar{u}'\bar{v}'$ has been investigated by several authors, among them :

i - Rose and Johnson (1975) for the flow situation just described ;

ii- Marvin et al. (1975) who considered a shock reflection in an axisymmetric flow. The experimental arrangement was made up of a long cone-ogive -cylinder whose axis was aligned with the free stream flow. The incident shock-wave was produced by an annular shock-wave generator concentric with the cylinder. The free stream Mach number M_∞ was equal to 7.2 and the Reynolds number R_{δ_0} close to 0.2×10^5 . In the cited study, the Reynolds shear-stress was evaluated indirectly by the use of mean quantity $(\bar{u}, \bar{v}, \bar{p}, \rho)$ distributions to solve boundary-layer type equations for the interacting dissipative flow. Direct measurements of $\bar{u}'\bar{v}'$ were later performed on the same arrangement by Mikulla and Horstman (1976) who employed hot-wire techniques;

iii-also Rose (1973) (see also Rose and Childs, 1974) performed Reynolds shear-stress measurements with hot-wires on the shock-reflection flow already considered in the present Section.

The essential features revealed by these investigations will now be briefly summarized. They are in fact similar to those found in transonic flows (see Section 2.9.3.4 above).

i - as a result of the shock-wave/boundary-layer interaction, the shear-stress level is substantially increased (see the results of Rose and Johnson plotted in Fig. 3.87) ;

ii- non-equilibrium effects are especially important throughout the interaction and persist far downstream of the interaction region. Importance of these effects is illustrated by the dimensionless mixing-length distributions plotted in Fig. 3.88. It is clear that for this kind of flow there is not a unique relationship between the shear-stress and the mean velocity gradient. This is obvious for the outer mixing length level (see fig. 3.88). Marvin et al. (1975) demonstrated that the distribution is also modified in the near wall region ;

iii-the Reynolds normal stress terms, normally neglected in boundary-layer analyses, are important within and just downstream of the interaction.

A consequence of the large increase of the turbulent mixing rate (or Reynolds shear-stress) during the interaction is that the momentum added to the flow near the wall is particularly important. This mechanism explains the rapid acceleration of the flow field which occurs in the downstream part of the interaction (see the results of Ardoneau above and also those obtained in transonic flows). So that (according to Rose) if another shock-wave/boundary-layer interaction follows closely downstream of the first one, the boundary-layer could sustain a larger pressure rise than the initial boundary-layer without separating.

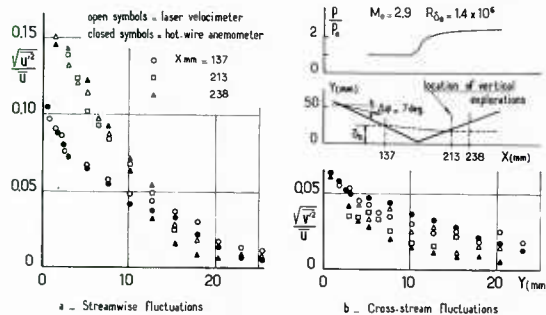


Fig. 3.86 - Effect of shock reflection on velocity fluctuations (Rose and Johnson, 1975).

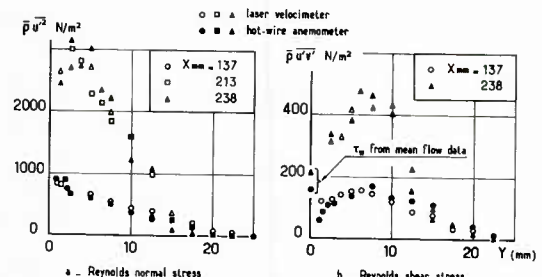


Fig. 3.87 - Shock reflection - Flow situation of Fig. 3.86 - Reynolds stress distributions (Rose and Johnson, 1975).

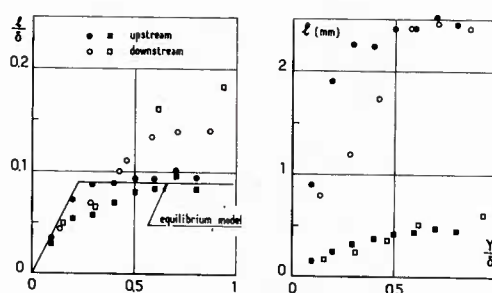


Fig. 3.88 - Shock reflection - Flow situation of Fig. 3.86 - Mixing length distributions (Rose and Johnson, 1975).

3.9.3 - Concluding Remarks

To conclude this Section, it must be pointed out that the interaction between a shock-wave and a boundary-layer raises many other questions on turbulence behavior and involves a large number of complex phenomena. In fact, this very difficult subject belongs to the domain of research on fundamental turbulence. Therefore, a close examination of this problem would entail long developments that would be beyond the scope of the present AGARDograph. Furthermore, the modeling of turbulence in such complicated flows is still far from having received a complete and satisfactory solution. Among the problems unsolved we can mention those relative to :

i- the importance of bulk dilation :

ii- the role of temperature - or density - fluctuations and the correlative problem of modeling of the terms involving these fluctuations in the turbulence transport equations. For a thorough discussion of this question see also Rose (1973) for experimental results on temperature fluctuations in a shock-wave/boundary-layer interaction ;

iii- the theoretical treatment of the near wall region is still in great part conjectural due to the lack of experimental information on this region.

In addition, for supersonic and hypersonic flows where the shock penetrates deep into the boundary-layer, a crucial problem is that of the effect of a discontinuity on a turbulence field. The first theoretical results on this essential question have been obtained by Debiève (1980) (see also Debiève, Gouin and Gaviglio (1981)). This author developed a discontinuity type analysis allowing the calculation of the jump through the shock wave of all the Reynolds tensor components. His analysis leads to simple algebraic expressions relating the Reynolds stress values on each side of the shock-wave. This model has been compared with measurements made on a two-dimensional ramp model of an angle $\alpha = 6$ deg., the upstream Mach number being equal to 2.3. Thus, Fig. 3.89 shows a comparison between the computed and the measured distributions of $\sqrt{u'^2}/U$ for this case. The calculation is seen to be in close agreement with experiment.

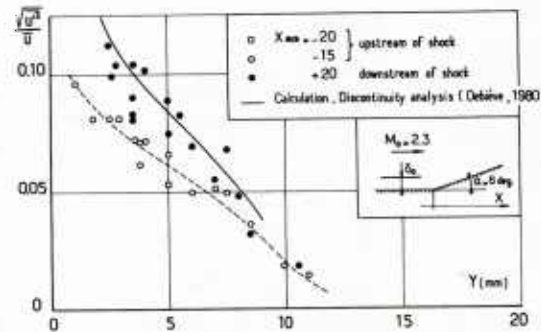


Fig. 3.89 – Ramp flow – Jump in $\sqrt{u'^2}$ through the shock-wave (Debiève et al., 1981).

3.10 - Références

Appels, C. (1973): Turbulent boundary-layer separation at Mach 12. VKI, TN 90 (Sept. 1973).

Appels, C. (1974): Incipient separation of a compressible turbulent boundary-layer. VKI, TN-99 (April 1974); see also AGARD CP-168 (1975).

Ardonceau, P., Lee, D.H., Alziary de Roquefort, T. and Goethals, R. (1980): Turbulence behavior in a shock-wave/boundary-layer interaction. AGARD CP-271, Paper N° 8.

Ardonceau, P. (1981): Etude de l'interaction onde de choc-couche limite supersonique. Thèse de Docteur ès Sciences Physiques, Université de Poitiers, France (July 1981).

Back, L.H. and Cuffel, R.F. (1976): Shock-wave/ turbulent boundary-layer interactions with and without surface cooling. AIAA Journal, Vol. 14, N° 4, pp. 526-532 (April 1976).

Batham, J.P.(1972): An experimental study of turbulent separating and reattaching flows at a high Mach number. J. Fluid Mech., Vol. 52, Part 3, pp. 425-435.

Behrens, W. (1971): Separation of a supersonic turbulent boundary-layer by a forward facing step. AIAA Paper N° 71-127 (Jan. 1971).

Bogdonoff, S.M., Keppler, E.C. and Sanlorenzo, E. (1953): A study of shock-wave/turbulent boundary-layer interaction at M=3. Princeton University, Dept. of Aero. Eng., Report N° 222.

Bogdonoff, S.M. and Keppler, E.C. (1954): Separation of a supersonic turbulent boundary-layer. Princeton University, Dept. of Aero. Eng., Report 249 (Jan. 1954).

Carpenter, P. and Tabakoff, W. (1971): The initial development of the non-isoenergetic compressible free shear layer. NASA CR-1828, (Oct. 1971).

Carrière, P., Sirieix, M. and Solignac, J.-L. (1968): Propriétés de similitude des phénomènes de décollement laminaires ou turbulents en écoulement supersonique non uniforme. 12th International Congress of Applied Mech., Stanford University, (Aug. 1968) and ONERA TP N° 659F (1968).

Carrière, P. (1973): Aperçu de quelques résultats nouveaux obtenus à l'ONERA sur les phénomènes de décollement et de recollement. ZAMM 53, T3 - T14.

Carrière, P., Sirieix. M. and Délery, J. (1975): Méthodes de calcul des écoulements turbulents décollés en supersonique. Progress in Aerospace Sciences, Pergamon Press, Vol. 16, N° 4, pp. 385-429.

Chapman, D.R., Kuehn, D.M. and Larson, H.K. (1957): Investigation of separated flow in supersonic and subsonic streams with emphasis on the effect of transition. NACA TN-3869.

Coleman, G.T. and Stollery, J.L. (1974): Incipient separation of axially symmetric hypersonic turbulent boundary-layers. AIAA Journal, Vol. 12, N° 1, pp. 119-120 (Jan. 1974).

Curle, N. (1961): The effect of heat transfer on laminar boundary-layer separation in supersonic flow. Aero. Quarterly, Vol. 12 (Nov. 1961).

Debièvre, J.-F. (1980): Bilan des tensions de Reynolds dans une interaction onde de choc turbulence. C.R. Acad. Sc. Paris, t. 291, Série B, pp. 133-136 (Oct. 1980).

Debièvre, J.-F., Gouin, H. and Gaviglio, J. (1981): Momentum and temperature fluxes in a shock-wave turbulence interaction. Proceedings of the ICHMT/IUTAM Symposium on the Structure of Turbulence and Heat and Mass Transfer, Dubrovnik, Yugoslavia - Hemisphere Publishing Co., Washington.

Délery, J. and Masure, B. (1969): Action d'une variation brusque de pression sur une couche limite turbulente et application aux prises d'air hypersoniques. La Recherche Aérospatiale, N° 129, pp. 3-12.

Délery, J. (1970): Examen des phénomènes d'interaction choc-couche limite dans un canal interaubes. ONERA NT-2-7078AY (Feb. 1970).

Délery, J. and Le Balleur, J.-C. (1972): Résultats sur l'interaction choc-couche limite à des nombres de Mach modérément supersoniques. AGARD AG-164 on "Boundary Layer Effects in Turbomachines".

Délery, J. and Le Balleur, J.-C. (1972): Interaction choc-couche limite turbulente à $M_\infty = 1.92$ at 1.62. Synthèse des résultats obtenus. ONERA NT-8/7078AY (Feb. 1972).

Délery, J. and Le Balleur, J.-C. (1973): Recherches sur l'interaction choc-couche limite turbulente. ONERA NT-21/2247AN (April 1973).

Délery, J. and Lacharme, J.-P. (1978): Interaction onde de choc-couche limite en écoulement transsonique stationnaire. ONERA RSF-31/7078AY (April 1978).

Délery, J. and Sirieix, M. (1979): Ecoulements de culot. AGARD LS-98 on Missile Aerodynamics (March 1979), English translation "Base flows behind missiles". ONERA TP N° 1979-14E.

Délery, J. (1983): ONERA Research on afterbody viscous/inviscid interactions with special emphasis on base flow problems. Symposium on Rocket/Plume Fluid Dynamics Interactions, Huntsville, Ala., 5-7 April 1983 and ONERA TP N° 1983-26.

Don Gray, J. (1967): Investigation of the effect of flare and ramp angle on the upstream influence of laminar and transitional reattaching flows from Mach 3 to 7. AEDC-TR-66-190 (Jan. 1967).

Drougge, G. (1953): An experimental investigation of the influence of strong adverse pressure gradients on turbulent boundary-layers at supersonic speeds. FFA Report 47.

Dussauge, J.-P. (1982): Evolution des transferts turbulents dans une détente rapide en écoulement supersonique. Thèse de Docteur ès Sciences Physiques, Université de Provence, Marseille, France.

Elfstrom, G.M. (1971): Turbulent separation in hypersonic flow. Imperial College of Sciences and Technology, I.C. Aero Report 71-16 (Sept. 1971); see also : Turbulent hypersonic flow at a wedge compression corner. J. Fluid Mech., Vol. 53, Part 1, pp. 113-127 (1972).

Erdos, J. and Pallone, A. (1962): Shock/boundary-layer interaction and flow separation. Heat Transfer and Fluid Mechanics Institute Procs., Stanford University Press.

Frishett, J.C. (1971): Incipient separation of a supersonic turbulent boundary-layer including effects of heat transfer. Ph. D. Dissertation, University of California, Los Angeles.

Gadd, G. E. (1953): Interaction between wholly laminar or wholly turbulent boundary-layers and shock-waves strong enough to cause separation. JAS, Vol. 20, N° 11 (Nov. 1953).

Gadd, G. E., Holder, D. W. and Regan, J. D. (1954): An experimental investigation of the interaction between shock-waves and boundary-layers. Proc. Roy. Soc., Ser. A, Vol. 226, pp. 227-253.

Grande, E. (1971): An investigation of the unsteady flow properties of the interaction between a shock-wave and a turbulent boundary-layer in two-dimensional internal flow. Ph. D. Thesis, University of Washington.

Green, J.E. (1969): Interaction between shock-waves and turbulent boundary-layers. RAE TR-69098 (May 1969); see also Progress in Aerospace Sciences, Pergamon Press, Vol. 11, pp. 235-340 (1970).

Green, J. E. (1970): Reflexion of an oblique shock-wave by a turbulent boundary-layer. J. Fluid Mech., Vol. 40, Part 1, pp. 81-95.

Hahn, M., Rubbert, P.E. and Mahal, A.S. (1973): Evaluation of separation criteria and their application to separated flow analysis. AFFDL-TR-72 145 (Jan. 1973).

Hakkinen, R. J., Greber, I., Trilling, L. and Abarbanel, S. S. (1959): The interaction of an oblique shock-wave with a laminar boundary-layer. NASA Memo 2-18-59W (March 1959).

Hammitt, A. G. and Hight, S. (1959): Scale effects in turbulent shock-wave/boundary-layer interactions. AFOSR TN 60-82, Procs. 6th Midwestern Conf. on Fluid Mechanics.

Henderson, L. F. (1967): The reflexion of a shock-wave at a rigid wall in the presence of a boundary-layer. J. Fluid Mech., Vol. 30, Part 4, pp. 699-722.

Holden, M. S. (1972): Shock-wave/turbulent boundary-layer interaction in hypersonic flow. AIAA Paper N° 72-74 (Jan. 1972).

Holden, M. S. (1974): Experimental studies of shock-wave/boundary-layer interactions. VKI, LS-62 (Jan. 1974).

Johnson, C. B. and Bushnell, D. M. (1970): Power law velocity profile exponent variations with Reynolds number, wall cooling and Mach number in a turbulent boundary-layer. NASA TN-D-5753 (April 1970).

Kessler, W. C., Reilly, J. F. and Mockapetris, L. J. (1970): Supersonic turbulent boundary-layer interaction with an expansion ramp and a compression corner. Mc Donnell Douglas, Report MDC E 0264 (Dec. 1970).

Kilburg, R. F. and Kotansky, D. R. (1969): Experimental investigation of the interaction of a plane oblique incident-reflecting shock-wave with a turbulent boundary-layer on a cooled surface. NASA CR-66-841.

Kiyotaka Hayakawa and Squire, L. C. (1982): The effect of the upstream boundary-layer state on the shock interaction at a compression corner. J. Fluid Mech., Vol. 122, pp. 369-394.

Korkegi, R.H. (1975): Comparison of shock-induced two- and three-dimensional incipient turbulent separation. AIAA Journal, Vol. 13, N° 4, pp. 534-535 (April 1975).

Korst, H. H. (1956): A theory for base pressure in transonic and supersonic flow. J. Appl. Mech., Vol. 23, pp. 593-600.

Kuehn, D. M. (1959): Experimental investigation of the pressure rise required for the incipient separation of turbulent boundary-layers in two dimensional supersonic flow. NASA Memo 1-21-59 A (Feb. 1959).

Kuehn, D. M. (1961): Turbulent boundary-layer separation induced by flares on cylinders at zero angle of attack. NASA TR-R117.

Law, C. H. (1974): Supersonic, turbulent boundary-layer separation. AIAA Journal, Vol. 12, N° 6, pp. 794-797 (June 1974).

Law, C. H. (1976): Supersonic shock-wave/turbulent boundary-layer interactions. AIAA Journal, Vol. 14, N° 6, pp. 730-734 (June 1976).

Le Balleur, J.-C. and Délery, J. (1973): Etude expérimentale de l'effet de la réflexion d'une onde de choc sur la transition de la couche-limite. Congrès Français de Mécanique, Poitiers (France), 17-20 Sept. 1973; see also La Recherche Aérospatiale, N° 1974-3, pp. 165-173 (May-June 1974).

Lewis, J. E., Kubota, T. and Lees, L. (1967): Experimental investigation of supersonic laminar two-dimensional boundary-layer separation in a compression corner with and without cooling. AIAA Paper, N° 67-191 (Jan. 1967); see also AIAA Journal, Vol. 6, N° 1, pp. 7-14 (Jan. 1968).

Liepmann, H. W. (1946): The interaction between boundary-layer and shock-waves in transonic flow. JAS, Vol. 13, N° 12, pp. 623-638 (Dec. 1946).

Marvin, J. G., Horstman, C.C., Rubesin, M. W., Coakley, T.J. and Kussoy, M.I. (1975): An experimental and numerical investigation of shock-wave induced turbulent boundary-layer separation at hypersonic speeds. AGARD CP-168, Paper N° 25.

Mikulla, V. and Horstman, C.C. (1976): Turbulence measurements in hypersonic shock-wave interaction flows. AIAA Paper N° 76-162 (Jan. 1976).

Needham, D. A. and Stollery, J. L. (1966): Boundary-layer separation in hypersonic flow. AIAA Paper N° 66-455 (June 1966).

Popinski, Z. and Ehrlich, C. F. (1966): Development design methods for predicting hypersonic aerodynamic control characteristics. AFFDL - TR - 66 - 85 (Sept. 1966).

Reda, D. C. and Page, R. H. (1969): Supersonic turbulent flow reattachment downstream of a two-dimensional backstep. AFOSR 69-1592 TR.

Reshotko, E. and Tucker, M. (1955): Effect of a discontinuity on turbulent boundary-layer thickness parameters with application to shock induced separation. NACA TN-3454.

Rose, W. C., Murphy, J. D. and Watson, E. C. (1968): Interaction of an oblique shock-wave with a turbulent boundary-layer. AIAA Journal, Vol. 6, N° 9, pp. 1792-1793 (Sept. 1968).

Rose, W. C. (1973): Turbulence measurements in a compressible boundary-layer subjected to a shock-wave-induced adverse pressure gradient. AIAA Paper N° 73-167 (Jan. 1973).

Rose, W. C. (1973): The behavior of a compressible turbulent boundary-layer in a shock-wave induced adverse pressure gradient. NASA TN-D-7092 (March 1973).

Rose, W. C., Page, R. J. and Childs, M. E. (1973): Incipient separation pressure rise for a Mach 3.8 turbulent boundary-layer. AIAA Journal, Vol. 11, N° 5, pp. 761-763 (May 1973).

Rose, W. C. and Childs, M. E. (1974): Reynolds shear-stress measurements in a compressible boundary-layer within a shock-wave-induced adverse pressure gradient. J. Fluid Mech., Vol. 65, Part 1, pp. 177-188.

Rose, W. C. and Johnson, D. A. (1975): Turbulence in shock-wave boundary-layer interaction. AIAA Journal, Vol. 13, N° 7, pp. 884-889 (July 1975).

Roshko, A. and Thomke, G. J. (1966): Correlations for incipient separation pressure. Douglas Aircraft Co., DAC-59800.

Roshko, A. and Thomke, G. J. (1966): Observations of turbulent reattachment behind an axisymmetric downstream-facing step in supersonic flow. AIAA Journal, Vol. 4, N° 6, pp. 975-980 (June 1966).

Roshko, A. and Thomke, G. J. (1969): Supersonic turbulent boundary-layer interaction with a compression corner at very high Reynolds number. Mc Donnell Douglas, Paper 10163 (May 1969).

Roshko, A. and Thomke, G. J. (1974): Flare induced interaction lengths in supersonic, turbulent boundary-layers. Mc Donnell Douglas, MDAC Paper WD 2416 (Dec. 1974); see also AIAA Journal, Vol. 14, N° 7, pp. 873-879 (July 1976).

Seebaugh, W. R. (1968): An investigation of the interaction of a shock-wave and a turbulent boundary-layer in axially symmetric internal flow including the effect of mass bleed. Ph. D. Thesis, University of Washington.

Settles, G. S. and Bogdonoff, S. M. (1973): Separation of a supersonic turbulent boundary-layer at moderate to high Reynolds numbers. AIAA Paper N° 73-666 (July 1973).

Settles, G. S. (1975): An experimental study of compressible turbulent boundary-layer separation at high Reynolds number. Ph. D. Dissertation, Aerospace and Mechanical Sciences Dept., Princeton University (Sept. 1975).

Settles, G.S., Bogdonoff, S.M. and Vas, I.E. (1975): Incipient separation of a supersonic turbulent boundary-layer at moderate to high Reynolds numbers. AIAA Paper N° 75-7 (Jan. 1975); see also AIAA Journal, Vol. 14, N° 1, pp. 50-56 (Jan. 1976).

Settles, G. S., Fitzpatrick, T. J. and Bogdonoff, S. M. (1978): A detailed study of attached and separated compression corner flowfields in high Reynolds number supersonic flow. AIAA Paper N° 78-1167 (July 1978); see also AIAA Journal, Vol. 17, N° 6, pp. 579-585 (June 1979).

Settles, G. S., Perkins J. J. and Bogdonoff, S. M. (1981): Upstream influence scaling of 2D and 3D shock/turbulent boundary-layer interactions at compression corners. AIAA Paper N° 81-0334 (Jan. 1981).

Sfeir, A. A. (1969): Supersonic laminar boundary-layer separation near a compression corner. University of California, Berkeley, Aeronautical Sciences Division, Report N° AS-69-6 (March 1969).

Shang, J. S., Hankey Jr., W. L. and Law, C. H. (1976): Numerical simulation of shock-wave/turbulent boundary-layer interaction. AIAA Journal, Vol. 14, N° 10, pp. 1451-1457 (Oct. 1976).

Simpson, R. L., Chew, Y.-T. and Shivaprasad, B. G. (1981): The structure of a separating turbulent boundary-layer. Part 1: Mean flow and Reynolds stresses. *J. Fluid Mech.*, Vol. 113, pp. 23-51.

Spaid, F. W. and Frishett, J. C. (1972): Incipient separation of a supersonic, turbulent boundary-layer, including effects of heat transfer. AIAA Paper N° 72-114 (Jan. 1972); see also *AIAA Journal*, Vol. 10, N° 7, pp. 915-922 (July 1972).

Sullivan, P. A. (1963): Hypersonic flow over slender double wedges. *AIAA Journal*, Vol. 1, N° 8, p. 1927 (Aug. 1963).

Thomke, G. J. and Roshko, A. (1969): Incipient separation of a turbulent boundary-layer at high Reynolds number in two-dimensional supersonic flow over a compression corner. *Mc Donnell Douglas, Report DAC 59819*.

Todisco, A. and Reeves, B. L. (1969): Turbulent boundary-layer separation and reattachment at supersonic and hypersonic speeds. Paper presented at Symposium on "Viscous Interaction Phenomena in Supersonic and Hypersonic Flow", Hypersonic Research Laboratory, USAF ARL, Ohio.

Werle, M.J. (1968): A critical review of analytical methods for estimating control forces produced by secondary injection. *U.S. Naval Ordnance Laboratory, NOLTR 68-5* (Jan. 1968).

Zukoski, E.E. (1967): Turbulent boundary-layer separation in front of a forward-facing step. *AIAA Journal*, Vol. 5, N° 10, pp. 1746-1753, (Oct. 1967).

4 - INTERACTION IN THREE-DIMENSIONAL FLOWS

4.1 - Introductory Remarks

In reality, as most flows of practical interest are three-dimensional, the two-dimensional case - about which a large amount of information is available - may appear as somewhat academic. In fact, as pointed out by Green (1969), in Aeronautics, real two-dimensional shock-wave/boundary-layer interactions are in practice confined largely to axisymmetric flows, e.g., in axisymmetric air-intakes and nozzles and on the flare of launch vehicles or missiles.

It is only for obvious reasons of simplicity that the majority of theoretical studies on shock/boundary-layer interaction are restricted to planar or axisymmetric flows. On the other hand, in the experimental domain, the complexity of 3-D flows, especially when separation occurs, renders extremely difficult and costly investigations as refined as those performed on 2-D interactions. The probing of a 3-D flowfield is still far from being a routine task in spite of the efforts accomplished to develop 3-D instrumentation and to improve the efficiency of the probing techniques.

However, the continuous progress of both computer technology and numerical methods, should permit the calculation of more and more complex flows in the near future. As a matter of fact, very promising results have already been obtained in the prediction of 3-D shock-separated turbulent flows (Hung and Mc Cormick, 1978 ; Kussoy et al., 1980, Anderson and Benson, 1983 see also section 5 of Part II). This fast development of computational methods renders particularly urgent the accompanying execution of detailed experimental investigations. The aim of these tests is to establish a clear physical picture of 3-D interacting flows - the organisation of which is still far from being entirely understood - and to provide data with which to assess the theoretical methods.

In spite of the great practical importance of the subject, the Section concerned with 3-D interactions will be relatively brief for the following main reasons :

- i - rather complete information on 3-D shock-wave/boundary-layer interactions can be found in a relatively recent AGARDograph devoted to 3-D separated flows prepared by Peake and Tobak (1980);
- ii - the number of detailed and fundamental analyses on 3-D interactions is still limited ;
- iii - the general structure and the physical properties of these flows are not yet completely understood.

The subject will be presented by describing the main features of typical 3-D shock-wave/boundary-layer interactions, the turbulent regime alone being considered. These flows are :

- i - the swept wedge flow ;
- ii - the skewed (or glancing) oblique shock-wave ;
- iii - the blunt fin or cylindrical obstacle ;
- iv - transonic flow over a swept wing.

However, before going into the physical description of the above flows, it can be helpful to briefly introduce some concepts and definitions pertinent to the separation phenomenon in 3-D flows. The reader interested in more complete information on this subject is referred to the already cited AGARDograph of Peake and Tobak.

4.2 - Separation in Three-Dimensional Flows

Let us first briefly recall the main characteristics of a three-dimensional boundary-layer and define basic concepts which will be used in the forthcoming discussion. It is customary to resolve the 3-D boundary-layer in a streamline co-ordinates system that is based on the geometry of the external inviscid flow. In this system the first family of co-ordinates curves is the projection of the external streamline on the surface of the body and the second family consists of the orthogonal trajectories in the surface of the first family. Thus, as shown in Fig. 4.1a, the velocity vector in the boundary-layer is resolved into a streamwise component u along the external streamline and a transverse component w constituting the crossflow along the orthogonal trajectories.

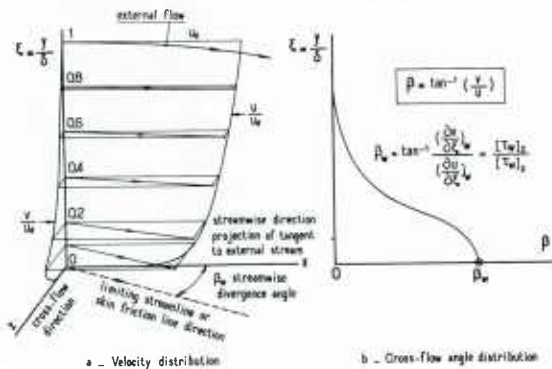


Fig. 4.1 - Main features of a three-dimensional boundary-layer.

In contrast with 2-D and axisymmetric boundary-layer flows in which the velocity vector remains in the same plane, the distinctive feature of 3-D flows is the ability to develop such a crossflow under the influence of a pressure gradient acting in the transverse direction. Thus the velocity vector in the boundary-layer can be progressively rotated resulting in a "skewing" of the viscous flow characterized by the crossflow angle β defined in Fig. 4.1b. This angle measures the deflection between the local streamline and the external streamline. When the distance y from the surface tends to zero, the velocity vector reaches a limiting direction which is colinear to the skin-friction vector \vec{T}_w . At the same time, the streamlines tend to a limit position, the so-called "limiting streamline" which is also a trajectory of the skin-friction vector field. For this reason, limiting streamlines are also called skin-friction lines. As it will be seen below, the skewing of a 3-D boundary-layer can be very important, especially when separation occurs. In that case, the angle θ_w between the skin-friction line and the external streamline can be close to 90 deg.

The separation phenomenon has been extensively studied in two-dimensional flows, incompressible as well as compressible. But, in the three-dimensional case, what is commonly called "separation" becomes much more difficult to characterize and even to define. In fact, there is still some controversy about what separation means in 3-D flows.

In a 2-D steady stream, it is generally recognized that separation occurs when the wall shear-stress (or equivalently, the skin-friction coefficient) vanishes at a certain point - the so-called separation point. Beyond that point, the wall shear-stress τ_w is negative, the velocity distribution along a direction normal to the surface having a portion close to the wall where the streamwise component u streams opposite to that of the outer main flow.

In most 3-D flows, such a definition becomes insufficient and useless because, on general 3-D surfaces, there is no privileged direction along which the sign of the wall shear-stress has an intrinsic significance (except in very special situations, such as a plane of symmetry or the case of an infinite swept wing).

The first attempt to give a rational and universal definition of 3-D separation can probably be ascribed to Maskell (1955). However, the most decisive progress in this field was brought about by the cogitations of Legendre (1952, 1977) and of Lighthill (1963).

Legendre has shown that nearly all the observed surface flow patterns belonging to what are called separated flows can be interpreted in a rational and simple way by introducing a very limited number of elementary singularities into the family of skin-friction lines of an isolated obstacle.

The singularities envisioned are isolated singular points on the surface where both the skin-friction vector and the surface vorticity vanish. These singular points are of two kinds : nodal points and saddle points. Among the nodal points (or nodes), one is led to distinguish between :

- i - nodes of attachment or separation where all the skin-friction lines - except one - have a common tangent (see Fig. 4.2a). In some circumstances - for example at the stagnation point of an axisymmetric body at zero angle of attack - the nodal point becomes an isotropic node (see Fig. 4.2b);
- ii - focus (of attachment or separation) where there is no longer a common tangent line. An infinity of streamlines spiral around such a point (see Fig. 4.2c).



Fig. 4.2 -- Three-dimensional separation -- Singular point in skin friction lines pattern.

Only two skin-friction lines can run through a saddle-point (see Fig. 4.2d) : all the other skin-friction lines "avoid" the singular point. After bending, the skin-friction lines tend to take the direction of the two particular skin-friction lines. These two lines act as barriers in the field of skin-friction lines, making one set of these lines inaccessible to the adjacent set.

Simple topological rules dictate the number of nodes and saddle points that can exist on the surface of the same obstacle. The difference between the number of nodes and the number of saddle points is necessarily equal to two. In these conditions, a flow will be said separated if its skin-friction line pattern contains more than two nodes. Since the skin-friction lines coming from two nodes of the same nature (attachment or separation) cannot cross, a singular point - which is necessarily a saddle point - must be placed somewhere between these two points. Hence, it is concluded that any separated three-dimensional flow has at least one saddle point through which run two particular skin-friction lines. One of these lines is the separation line. Thus the so-called separation line delimits two domains on the surface flow. The skin-friction lines belonging to each of these domains run asymptotically into the separation line. This means that they never cross the separation line and that they have no contact with it.

From this standpoint, the two dimensional case represents a very particular situation. It would correspond to a 3-D separated flow in which the separation line is rectilinear and is the locus of an infinite number of saddle points. The separation point would be the trace of this separation line on the plane perpendicular to it that contains the 2-D flow. As a matter of fact, careful surface flow visualizations of nominally 2-D flows reveal that in the vicinity of separation or reattachment, the structure of the surface flow is very complex. This is illustrated by the experimentally determined surface patterns shown in Figs. 4.3 and 4.4. The first example is relative to ramp-induced separation in a 2-D supersonic flow (Settles et al, 1978) ; the second to supersonic reattachment behind an axisymmetric downstream facing step (Roshko and Thomke, 1965 ; see also the experiments of Ginoux, 1962). In both cases, the surface flow exhibits a repetitive pattern looking like a succession of saddle-points regularly distributed on the separation or reattachment line. Such observations tend to prove that two-dimensionality is in fact an abstraction without real existence in the actual 3-D world.

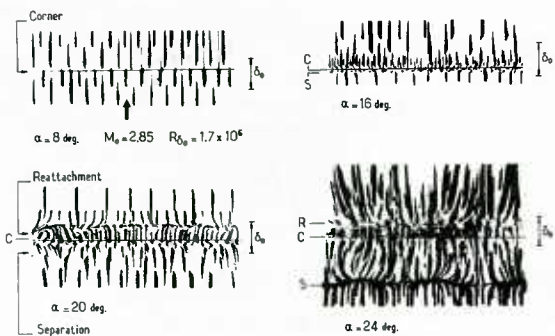


Fig. 4.3 - Two-dimensional ramp flow – Surface flow pattern
(Settles et al., 1978).

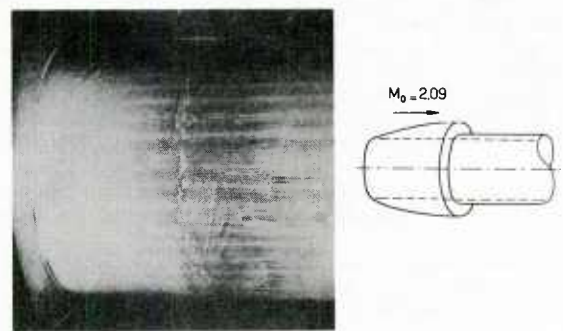


Fig. 4.4 – Reattachment behind an axisymmetric downstream facing step surface flow pattern (Roshko and Thomke, 1965).

Recently, Tobak and Peake (1981) suggested a modification to the above definition of 3-D separation in order to take into account some experimental observations that seem to contradict the original definition. These authors have proposed making a distinction between :

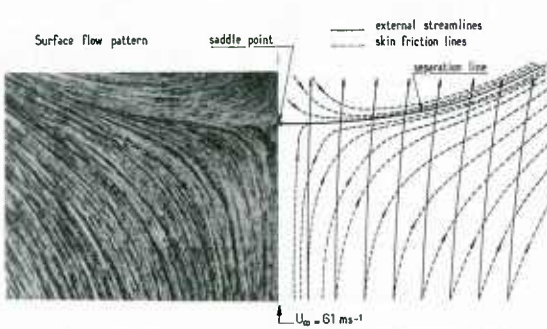
- i - global separation which corresponds to the existence of a saddle point through which runs what they call a global separation line,
- ii - and local separation where the separation line has its origin at a nodal point of attachment, for instance.

Nevertheless, in both cases, the separation phenomenon is characterized by the existence of a particular skin-friction line – the separation line – that "separates" the skin-friction lines into two sets.

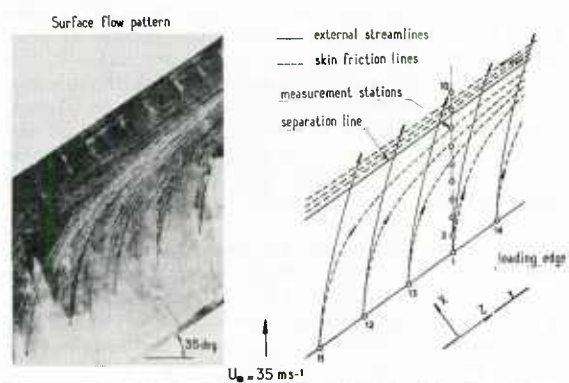
In a separation phenomenon, the skin-friction lines converge asymptotically towards the separation line from either side of this line. A reattachment process can be defined in the same terms, but now the skin-friction lines diverge from the reattachment line.

In spite of this relatively clear definition, there is still some controversy about the origin of separation in 3-D flows. For example, some investigators claim that a separation line can form without necessarily originating from a singular point where the wall shear-stress vanishes (see Wang, 1983 and Hornung, 1983). Here, we will not enter into this dispute, but we will retain the following fact that is now commonly recognized : the system of singular points (nodes and saddle points) actually constitutes what Peake and Tobak have called a "flow grammar whose finite number of elements can be combined in myriad ways to describe, understand, and connect the properties common to all three-dimensional viscous flows".

In order to illustrate the above considerations, Figs. 4.5 to 4.7 give examples of skin-friction line patterns for 3-D separated flows. The first example (see Fig. 4.5) is a separation produced in a subsonic flow by a cylindrical obstacle mounted perpendicularly to a flat plate, (similar separation will be considered in Section 4.3.3 for a supersonic incoming flow). The left-hand part of the figure shows the surface flow pattern determined experimentally by East and Hoxey (1971); its right-hand part shows the same pattern as computed by the inverse 3-D boundary-layer method presented in Section 2.4.3 of Part II (Délery and Formery, 1983). The two surface flow patterns clearly exhibit the formation of a saddle-point contained in the plane of symmetry of this flow. The separation line originates from this point and appears evidently as an asymptote to the skin-friction lines. The second example (see Fig. 4.6) shows the occurrence of separation on a wing-like surface under infinite swept wing conditions. In this case, the flow is invariant along a particular direction which is here parallel to the wing leading edge. Flows of this kind are said to possess a cylindrical symmetry along a direction z . This property is expressed mathematically by stating that the derivatives along z are equal to zero. Cylindrical symmetry leads to considerable simplifications in the equations of motion which take a quasi two-dimensional form, although the solution may retain a strongly three-dimensional character, as will be shown in the forthcoming examples. For this reason, the assumption of cylindrical symmetry is frequently made in predictive methods. The experimental results shown in Fig. 4.6 were obtained by Van den Berg and Elsenaar (1972); they also correspond to an incompressible flow. In the case of cylindrical symmetry, the separation line is rectilinear and parallel to the direction z , the saddle-point singularity being in effect at negative infinity.



Experiment (East and Hoxey, 1971) Computation (Délery and Formery, 1983)



Experiment (Van den Berg and Elsenaar, 1972) Computation (Délery and Formery, 1983)

Fig. 4.5 – Three-dimensional separation in front of a cylindrical obstacle in incompressible flow.

Fig. 4.6 – Three-dimensional separation on an infinite swept wing in incompressible flow.

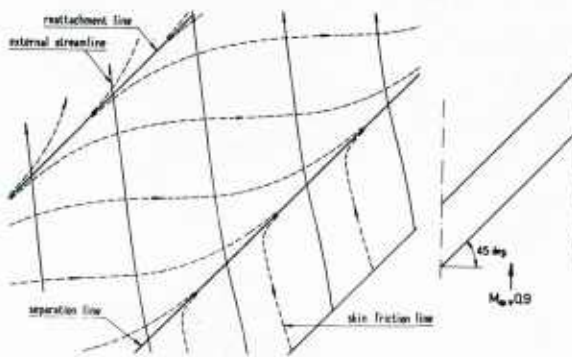


Fig. 4.7 – Computed flow pattern over an infinite swept wing in transonic flow.

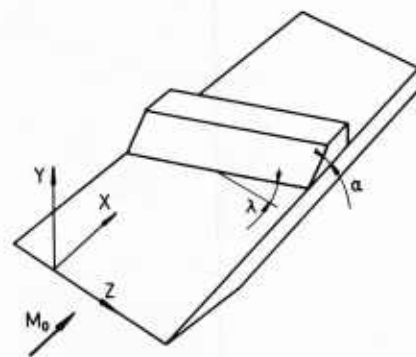


Fig. 4.8 – The swept corner configuration.

The last example (see Fig. 4.7) is purely numerical. The calculation simulates separation on an infinite swept wing in transonic flow, the boundary-layer being turbulent. This calculation was made by using the already cited inverse boundary-layer method. It shows a case of separation followed by reattachment in what can be called a bubble-type 3-D separation.

The above examples exhibit trends typical of separation in 3-D turbulent flows which will be observed in the 3-D shock-wave/boundary-layer interactions examined in what follows. To summarize, these features are the following :

- i - in the separated region, the external streamlines (i.e., the streamlines at the boundary-layer edge) are only slightly deflected (see Fig. 4.5 to 4.7), whereas the skin-friction lines turn abruptly on approaching the separation line. Thus, the surface flow pattern could give a misleading impression that the entire flowfield is highly skewed from the streamwise direction, which is not the case. In fact, the major part of the boundary-layer flow has not yet been strongly affected in the separation region. It continues to stream in a direction differing slightly from that of the incoming flow. Most of the flow turning takes place over a thin region of low energy fluid close to the wall.
- ii - in a 3-D separation, the wall shear-stress - or more exactly the modulus of the wall shear-stress vector $|\tau_w|$ - generally does not vanish on a separation line, except of course at a node or a saddle-point. Thus it is clear that the vanishing of the wall shear-stress cannot be used as a criterion - or even a definition - for separation in 3-D flows. The only property identifiable with separation seems to be the passage of $|\tau_w|$ through a minimum. However, this property is a frequently made observation which has no rational justification. The unique feature of the wall shear-stress at a separation line is that the component of τ_w normal to the separation line vanishes, but this property results simply from the definition of a separation line. It is of no help in identifying separation from wall shear-stress measurements.
- iii - the separation phenomenon is characterized by a very rapid turning of the skin-friction lines when they approach the separation line from upstream. This could give the impression that they are tangent to the separation line. On the other hand, the tendency towards the separation line from downstream as well as the tendency towards a reattachment line is far more progressive.

To conclude, it should be said that the consideration of the surface-flow pattern plays an important role in the experimental investigation of 3-D separated flows. Surface flow patterns are of the greatest help in understanding the structure of these flows. At supersonic velocities, they play a role comparable to that of optical methods (schlieren or shadowgraph pictures) in the study of two-dimensional interactions.

4.3 - Typical Interactions in 3-D Flows.

4.3.1 - Interaction at a Swept Corner

This first flow is produced by a corner (or ramp) of angle α swept at an angle λ in relation to the incoming supersonic flow, which is assumed uniform for the sake of simplicity (see Fig. 4.8). It is clear that $\lambda = 0$. corresponds to the 2-D interaction considered in some detail in Section 3 above. Thus, with the present configuration, by progressively increasing the sweep angle λ from zero, it is possible to create a flow situation in which there is a continuous transition from a two-dimensional interaction to interactions where 3D effects become more and more pronounced.

The corresponding change in the surface flow pattern is illustrated by the photographs shown in Fig. 4.9. These experiments were carried out by Settles and Perkins (1979) at an upstream Mach number of 3 and for a Reynolds number range between $R\delta_0 = 1.86 \times 10^6$ and 6.23×10^6 . The flow patterns presented here are relative to an angle $\alpha = 24$ deg. Also, a case where $\alpha = 16$ deg. and $\lambda = 30$ deg. is presented. When the corner is swept, the surface flow pattern reveals the existence of a separation line and of a reattachment line originating both from the corner apex. Except in the apex region, this pattern has a close resemblance to the computed pattern of Fig. 4.7. Its essential features are schematically represented in Fig. 4.10. Their examination reveals the following properties :

- i - broadly speaking, the flow can be divided into two regions. Near the apex, the flow tends to develop a conical structure ; the distance separating the separation line from the reattachment line increases progressively with the distance ξ from the apex. Figure 4.11 a shows a very schematic representation of the projected streamlines in a vertical plane perpendicular to the corner hinge. Due to the spreading of the separated flow, the lateral outflow within the recirculation increases with ξ in such a way that an extra fluid is drawn into the recirculation. The reattachment stream surface thus passes over the surface springing from the separation line (the reverse situation would be observed if the extent of the separation were decreasing).

At a certain distance ξ_c from the apex, the flow develops a cylindrical pattern, in the sense that it is invariant along directions parallel to the corner hinge line (the flow possesses a cylindrical symmetry). The length required for the inception of a cylindrical flow increases with the sweep angle λ (all other parameters being kept fixed). Also, at a given λ , ξ_c increases when α is increased. Obviously, the cylindrical symmetry is not always observed for such flows. Its establishment necessitates a sufficient spanwise size of the experimental arrangement. As we already know, for a cylindrical flow, all derivatives parallel to the corner are zero. In particular, the lateral flow within the separation bubble is constant. Thus, the projected streamlines constitute a closed "recirculation bubble" (see Fig. 4.11b).

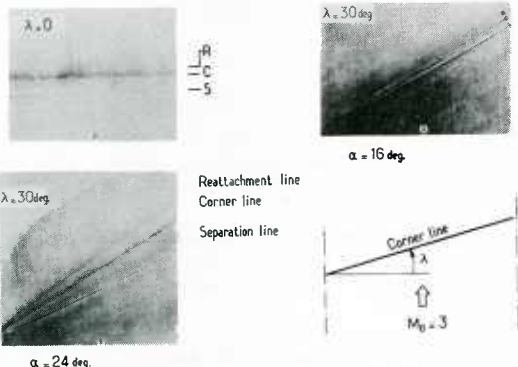


Fig. 4.9 – Swept corner flow – Surface flow patterns
(Settles and Perkins, 1979).

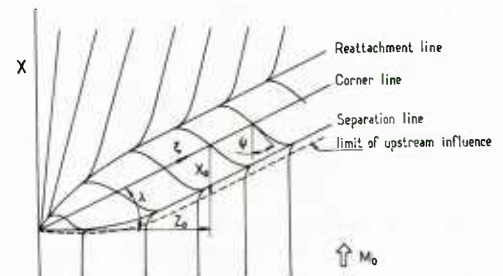


Fig. 4.10 – Swept corner flow – Schematic representation of the skin friction line pattern (Settles and Perkins, 1979).

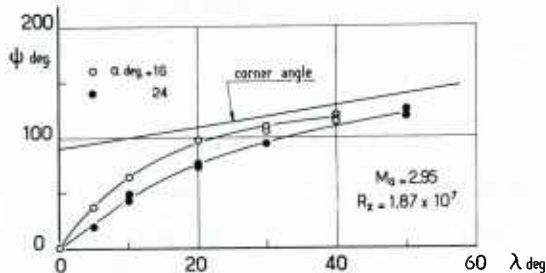


Fig. 4.12 – Swept corner flow – Deviation of skin friction line in the separated region – ψ defined in Fig. 4.10

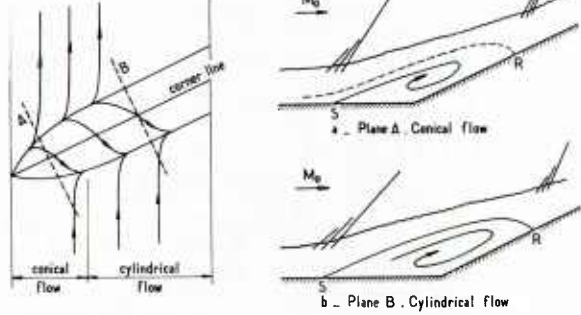


Fig. 4.11 – Swept corner flow – Schematic representation of the projected streamlines in plane perpendicular to the corner hinge.

- ii - as shown in Fig. 4.10, let us define the angle ψ as the deflection of the skin-friction lines in the central part of the separated region (also called the secondary flow region). As shown by the experimental data points plotted in Fig. 4.12, ψ starts immediately to deviate from pure flow reversal ($\psi = 0$ deg.), as soon as a small amount of corner sweep is added to the initially 2-D interaction. In the present case, the skin-friction lines of the secondary flow appear to approach asymptotically a situation in which they are inclined at 10 deg. to the corner line at the higher sweep angles.
- iii - the wall pressure distributions measured along a line $z = \text{constant}$ (see Fig. 4.8) for $\alpha = 16$ deg. and varying sweep angle λ are plotted in Fig. 4.13. A striking feature of the interaction is that the pressure distribution does not change at all from the 2-D case for sweep angles up to 10 deg., although, at the same time, the flow in the vicinity of the wall is strongly affected, as shown by the rapid variation of ψ (see Fig. 4.12). When λ is greater than 10 deg., the pressure rise at the wall starts to spread progressively both in the upstream and in the downstream directions.

Let us now consider scaling properties of the upstream influence. In the present situation, the interaction propagates both in the x streamwise and in the spanwise directions, so that one must consider the two interactions lengths x_0 and z_0 defined in Fig. 4.10. It is clear that the interaction length scales must necessarily come from the incoming flow since the corner geometry has no significant dimension. However, the appropriate scales will, in principle, depend also on the two angles λ and α . The 2-D analysis of Settles et al (1981) (see Section 3.7.2 above), can be extended to 3-D interactions for which it leads to a very good correlation for the lengths x_0 and z_0 , as shown in Fig. 4.14. It is to be noticed that, for the corner angle $\alpha = 10$ deg. cylindrical symmetry is reached within the test section only for λ less than 50 deg. and if $\alpha = 24$ deg. for λ less than 40 deg. The problem of the spanwise propagation of the swept-corner influence in the apex region has been analytically investigated by Stalker (1960, 1982). By using the small perturbation approach of the Lighthill triple deck model (see Section 4.1 of Part II), this author found that this influence propagates at an angle (relative to the corner hinge line) determined by the sweep angle, the properties of the boundary-layer (namely its velocity profile) and the upstream Mach number. It does not however depend on the boundary-layer thickness. This theory is restricted to weak disturbances and to non-separated flows.

As we know, when cylindrical symmetry exists, the interacting flow is in fact a quasi 2-D flow. Then, purely 2-D correlation properties can frequently be applied by considering the flow quantities normal to the sweep angle (see, for example Stalker, 1960). Thus, Settles and his co-workers have found that the Roshko and Thomke (1974) correlation given in Section 3.7.2 above, works satisfactorily well when the normal components of the Mach number, the Reynolds number and δ_0 are used. This kind of transposition is also applied in order to derive 3-D Incipient Shock-Induced Separation criteria (see Section 4.4 below).

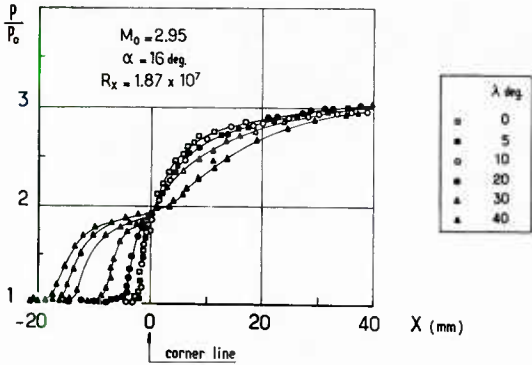


Fig. 4.13 – Swept corner flow – Wall pressure distributions (Settles and Perkins, 1979).

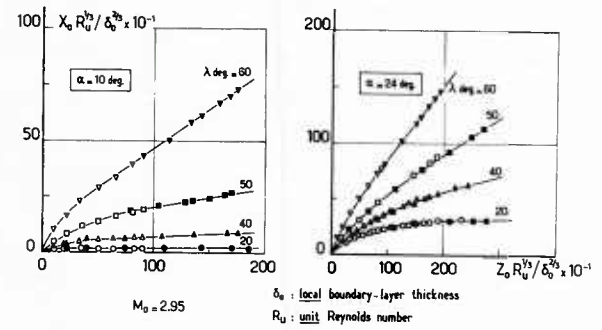


Fig. 4.14 – Swept corner flow – Streamwise and spanwise scaling of upstream influence lengths (Settles et al., 1981).

Interaction with separation at a swept corner was also investigated by Bachalo and Holt (1975). These authors used a symmetric model formed by making two oblique, symmetric cuts in a plane compression corner. Their experiments, which include boundary-layer surveys, were carried out both in laminar and turbulent flows.

4.3.2 - The Skewed Shock-Wave Interaction

This kind of flow is schematically represented in Fig. 4.15. A planar shock-wave is generated by a plate with a sharp leading-edge set at an angle of attack α_G . In variants of this arrangement, the shock is generated by a ramp.

In the present situation, one considers the shock-wave/boundary-layer interaction taking place on an adjacent flat plate perpendicular to the shock generator. This kind of flow is also termed "Glancing Shock-Wave/Boundary-Layer Interaction" and is identical to the so-called "Sharp Fin-Induced Shock/Boundary-Layer Interaction". In practice, such phenomena occur, for example, on the side plate of supersonic two-dimensional mixed or external compression inlets or on the wing surfaces of aircraft with highly swept wings in supersonic flight.

This type of 3-D interaction has been more intensively studied than the other types ; presumably because of its greater practical importance... and also because it is amenable to relatively simple analyses. Most of these analyses, discussed in Section 1.3 of Part II, assume that the flow is cylindrical in a direction parallel to the freestream shock. This assumption permits a rather straightforward extension of purely 2-D theories.

Let us first examine the skin-friction pattern resulting from an interaction of this kind. For this purpose, we will use experiments performed by Oskam et al. (1976). Many other experimental results can be found in the literature (Stanbrook, 1960 ; Lowrie, 1965 ; West and Korgogi, 1972 ; Law, 1975 ; Peake and Rainbird, 1975 ; Cousteix and Houdeville, 1976 ; Oskam et al., 1977 ; Degrez and Ginoux, 1983). In the present case, the incoming turbulent flow has an outer Mach number equal to 2.95. Figures 4.16a and 4.16b show photographs of oil flow patterns obtained for two values of the shock generator angle α_G . One observes that for the lower value of α_G ($\alpha_G = 4$ deg.), the skin-friction lines start to be deflected well upstream of the calculated shock position (from inviscid flow theory) which nearly coincides with the shock location in the outer inviscid stream. The maximum deflection angle of the skin-friction lines is approximately equal to 10 deg., which is about twice the shock generator angle but is well below the shock wave angle θ . In fact, the present surface flow pattern is typical of a 3-D boundary-layer undergoing a moderate compression. The adverse pressure gradient causes the slower moving fluid in the bottom part of the boundary-layer to deflect to larger angles than the faster moving fluid in the outer portion of the boundary-layer.

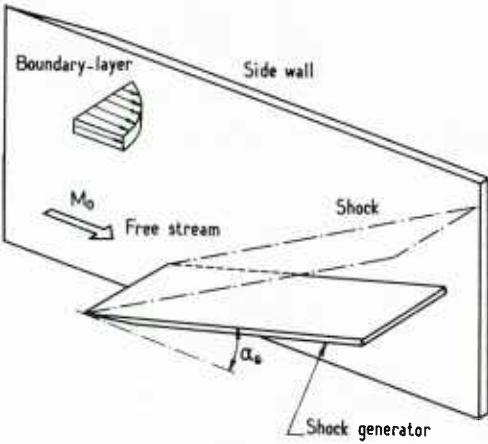


Fig. 4.15 – The skewed shock wave (or glancing shock) configuration.

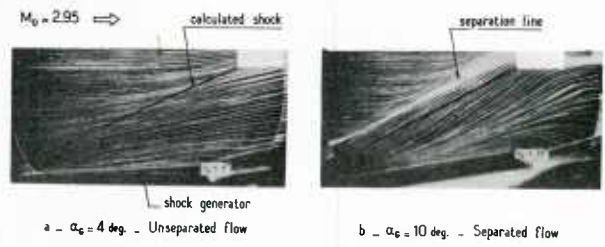


Fig. 4.16 – Skewed shock wave – Surface flow patterns on side wall (Oskam et al., 1976).

When the shock generator is set at an angle $\alpha_G = 10$ deg., the surface flow pattern is radically different. In this case, the skin-friction lines coming from upstream infinity are abruptly turned well upstream of the outer shock location and they run asymptotically into a line (S) which is roughly parallel to the shock. Farther downstream, the skin-friction lines are deflected to angles substantially larger than the shock angle. In this part of the flow, the surface flow streams from the apex of the shock generator and the streamwise component of this motion (i.e., the component in the direction of the still unperturbed incoming flow) is opposite that of the outer stream. These downstream skin-friction lines also run asymptotically into the line (S) which thus has the character of a separation line.

The surface flow pattern also reveals the existence of a reattachment line (R) close to the trace of the shock generator. In the present situation, the two lines (S) and (R) originate from a region very close to the shock generator leading edge. In this region, the size of the surface phenomena is too small to be resolved by the oil technique, so that the singular point(s) at the origin of the separation and reattachment lines cannot be observed.

A tentative representation of this kind of interacting flow was postulated by Kubota and Stollery (1980). In this model, (see Figs 4.17a and 4.17b) a first corner vortex forms. Also, the inner part of the shock generator boundary-layer is pushed under the sidewall boundary-layer. When separation occurs (see sketch in Fig. 4.17b), the skin-friction lines of this flow constitute the pattern observed downstream of (S). A separation sheet emanates from (S) where the two families of skin-friction lines meet. Then the sheet rolls up into a vortex.

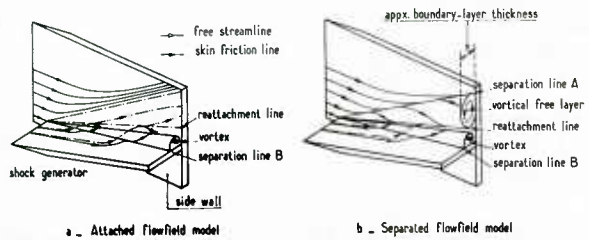


Fig. 4.17 – Skewed shock wave – Schematic representations of the flowfield (Kubota and Stollery, 1980).

Wall pressure distributions measured by Oskam and his colleagues are plotted in Fig. 4.18. These distributions were measured along the x_s direction defined by the sketch in Fig. 4.18. The different curves correspond to increasing values of the shock generator angle α_G (the distance x_s is normalized by the boundary-layer thickness δ_0 at the beginning of the pressure rise). A key feature of the plotted distributions is that the upstream extent of the interaction measured from the shock location ($x_s = 0$) and along the chosen direction is largely independent of the shock strength. However, a careful reconsideration of the problem of upstream influence by Dolling and Bogdonoff (1981) has shown that with this kind of plotting, the influence of shock strength is masked. This fact is demonstrated by the correlation curves represented in Fig. 4.19. Here, the streamwise influence length x_0 is plotted against the distance ξ for different shock strengths (ξ is the distance from the shock generator leading edge measured along the free stream shock-wave).

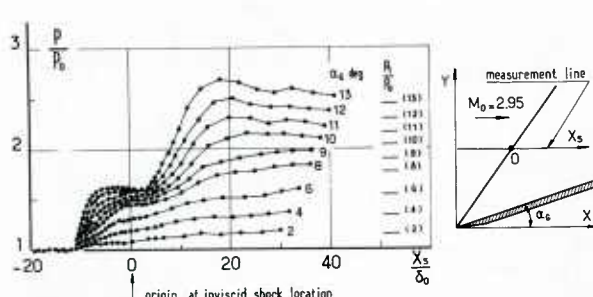


Fig. 4.18 – Skewed shock wave – Wall pressure distributions along a line Y -constant (Oskam et al., 1976).

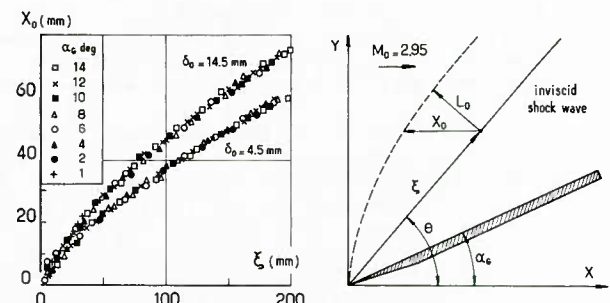


Fig. 4.19 – Skewed shock wave – Streamwise upstream interaction length (Dolling and Bogdonoff, 1981).

In fact, the length x_0 has no particular physical significance. A more correct scaling of the phenomenon is obtained by considering the distance L_0 normal to the free stream shock. Now, with L_0 , the influence of the shock strength is clearly visible as shown by the data points plotted in Fig. 4.20. Furthermore, a good correlation of the shock strength effect can be obtained by normalizing the normal distance L_0 with a "normal Mach number function" M_R defined as the ratio of the normal Mach number $M_{no} = M_0 \sin \theta$ to a "reference" normal Mach number (here, the value of M_{no} corresponding to $\alpha_G = 2$ deg.). As shown in Fig. 4.21, the collapse of the data for various α_G on a single curve demonstrates the essential role played by the normal flow in the determination of certain basic properties of this kind of interaction.

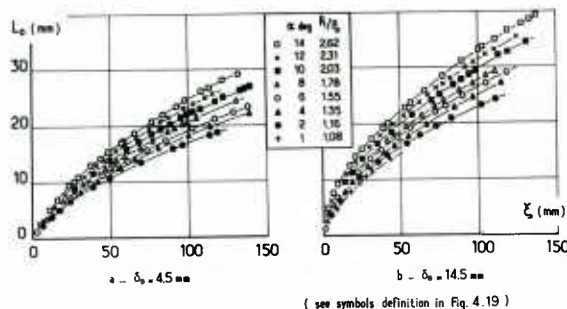


Fig. 4.20 – Skewed shock wave – Normal upstream interaction length (Dolling and Bogdonoff, 1981).

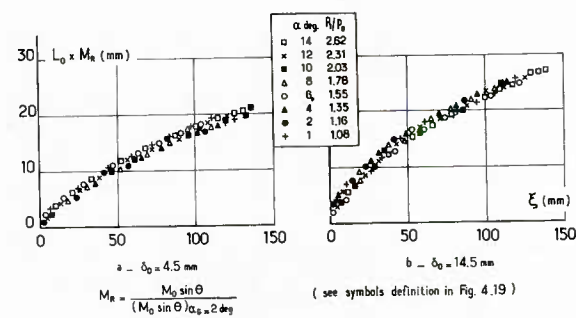


Fig. 4.21 – Skewed shock wave – Normal upstream interaction length scaled to "normal Mach number function" (Dolling and Bogdonoff, 1981).

Similar to the case of the swept ramp, a typical feature of the skewed shock/boundary-layer interaction is the large extent of upstream influence, even for very weak shock-waves. This behavior is clearly demonstrated by the variation of L_o with α_G plotted in Fig. 4.22. One observes the three following tendencies :

- i - the normal interaction length L_o becomes important as soon as α_G is different from zero ;
- ii - the increase of L_o with α_G is moderate ;
- iii - the upstream interaction length is typically an order of magnitude or more greater than that occurring in 2-D interactions (with the same incoming flow conditions).

Also, Dolling and Bogdonoff (1981) found that the functional dependence of L_o on the Reynolds number and the incoming boundary-layer thickness is the same as that observed in both unswept and swept compression corners.

Lu and Settles (1983) have examined the similarity properties of the interaction produced by a fin swept at an angle λ (see sketch in Fig. 4.23). As demonstrated by data plotted in Fig. 4.23, this flow obeys a conical similarity principle irrespective of fin sweepback or angle of attack. Also, scaling laws for Reynolds number and normal Mach number effects already mentioned (see Figs. 4.14 and 4.21) are seen to apply well to the present interaction.

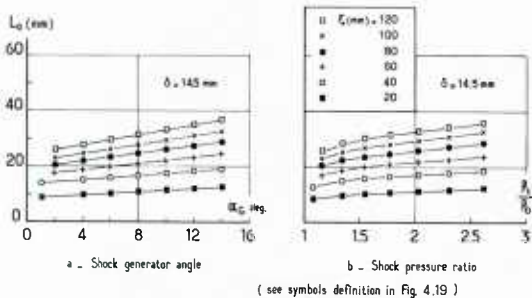


Fig. 4.22 – Skewed shock wave – Normal interaction length as function of shock wave strength (Dolling and Bogdonoff, 1981).

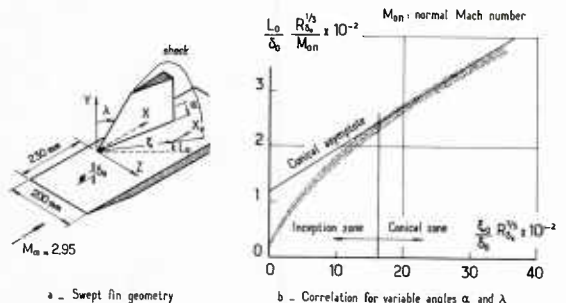


Fig. 4.23 – Skewed shock wave produced by a swept fin – Scaling of normal upstream interaction length (Lu and Settles, 1983).

The structure of three-dimensional separation produced by a skewed shock-wave was also investigated by Korkegi (1976) who gave a detailed description of the flow region between the interaction origin and the shock generator. Thus, for increasing shock strength, Korkegi proposed the sequence of flow patterns represented in Fig. 4.24 :

- i - sketches a and b correspond to the situations already analyzed. In a, the shock strength is not sufficient to induce separation ; in b separation occurs.
- ii - as the separated region grows in size due to a progressively stronger shock, the "reverse flow" can also separate. Then, a secondary separation region develops within the primary one (see Fig. 4.24c). In the sketch, (S) and (R) are respectively the primary separation and reattachment lines and (S₁) and (R₁), the secondary ones.

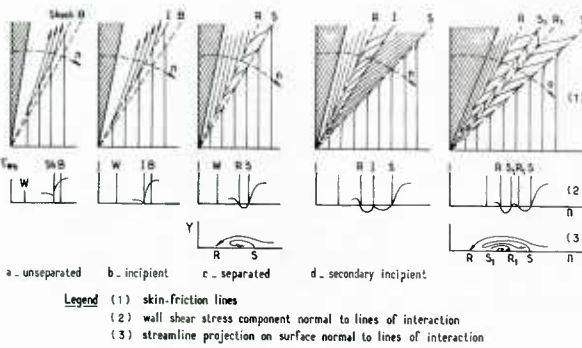


Fig. 4.24 – Skewed shock wave – Schematic representation of the flowfield (Korkegi, 1976).

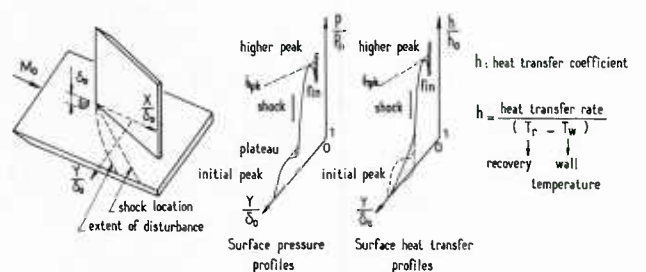


Fig. 4.25 – Skewed shock wave – Typical surface pressure and surface heating profiles.

The figure also shows (very schematically) the wall shear-stress component τ_{wn} normal to the lines of interaction defined in the sketch. As these lines have practically the direction of the separation and reattachment lines (the flow being assumed conical), τ_{wn} changes sign on (S), (R) and (S₁), (R₁). Also, the streamlines projected on the surface normal to lines of interaction are represented.

The above region is the siege, not only of high pressure rises, but also of high heating rates in non-adiabatic flow conditions (for example, in the case of a reentry vehicle flying at hypersonic Mach numbers). Typical surface pressure and surface heating distributions along a spanwise direction are schematically represented in Fig. 4.25. As the free stream enters the interaction region, it is compressed through a first pressure rise. This increase may result in an initial pressure peak or plateau. The first compression is generally followed by a much higher pressure peak occurring between the shock-wave and the shock generator (see the curves of Fig. 4.18 corresponding to high angles α_G). The surface heating distribution increases more slowly and reaches a peak value located also between the shock-wave and the shock generator.

Several empirical correlations have been proposed for predicting the main features of the above pressure and heating distributions. For instance, Neumann and Hayes (1977) gave the following formulae to represent peak pressure (second highest peak p_{pk}) and peak heating h_{pk} (see Fig. 4.25)

$$\frac{p_{pk}}{p_0} = (M_\infty \sin\theta)^{np}, \quad \frac{ST_{pk}}{ST_0} = (M_\infty \sin\theta - 1) NST + 0.75$$

where ST_{pk} is the Stanton number, ST_0 being the value of ST at the origin of interaction. The exponent np and the coefficient NST are functions of X/δ_0 given in Figs. 4.26a and 4.26b. Similar empirical laws have been proposed by Scuderi (1978). For the problem of kinetic heating due to skewed shock-wave/turbulent boundary-layer interaction, see also Degrez (1981).

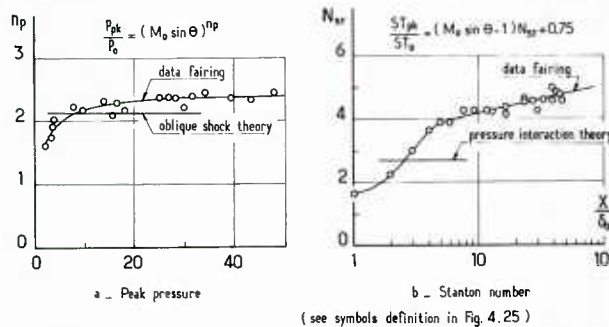


Fig. 4.26 – Skewed shock wave – Correlations for higher peak pressure and peak heat transfer (Neumann and Hayes, 1977).

4.3.3 – Obstacle – Induced Interaction

The third configuration envisaged consists of a blunt cylindrical obstacle – which can be a fin with rounded leading edge – mounted perpendicularly to a flat plate on which a turbulent boundary-layer develops. For the sake of simplicity, the incoming flow will be assumed uniform. The flow resulting from an obstacle-induced shock-wave/boundary-layer interaction is the supersonic counterpart of the well known incompressible 3-D separating flow analyzed in great detail by East and Hoxey (1971). Part of the surface flow pattern is shown in Fig. 4.5.

When the obstacle is sufficiently tall and the flow supersonic, very high values of pressure, pressure gradients and heat transfer are measured both on the obstacle and in its vicinity on the flat plate. Such high values are not found for small protuberances, but in this case, the disturbance caused by the obstacle can persist for hundreds of protuberance heights downstream. Thus, this kind of flow is of great practical importance and has been the object of several specific investigations (Price and Stallings, 1967 ; Westkaemper, 1968 ; Korgegi, 1971 ; Winkelmann, 1972 ; Kaufman et al., 1972 ; Dolling et al., 1979).

The present 3-D flow is excessively complex and depends on a large number of parameters : the dimensions (three lengths), shape and orientation (sweep) of the obstacle, free stream Mach number and Reynolds number, the undisturbed velocity profile of the incoming boundary-layer and its thickness δ_0 . Because of this complexity, detailed information on such interactions is still scarce and fragmentary. Therefore, the structure of the flow, as well as its general properties, are still far from being completely elucidated. Thus, the present Section is restricted to a brief presentation of the most typical flow features.

The overall structure of the outer flow ahead of a fin with circular leading-edge is revealed by the shadowgraph of Fig. 4.27a. The present experiments were carried out by Dolling et al. (1979) at an upstream Mach number $M_\infty = 3$ and at high Reynolds number. The shadowgraph visualizes the trace in the symmetry plane of the shock system at the foot of the fin. This system consists essentially of a bow shock and of a separation shock originating in the inner part of the boundary-layer well ahead of the fin. The interaction between the bow shock and the separation shock results in a complex system made more visible by the sketch in Fig. 4.27b. The represented schema of the shock structure was designated Type IV by Edney (1968). This structure includes a triple point I, a Mach stem and also a supersonic jet embedded in a subsonic region. At high Mach number, the peak impact pressure of this jet can be extremely high, as can be the local heat transfer. The structure represented in Fig. 4.27b is not proper to all fin induced flows but corresponds to particular conditions. However, its main components – the bow shock, the separation shock and the Mach stem – are encountered in every such flow.

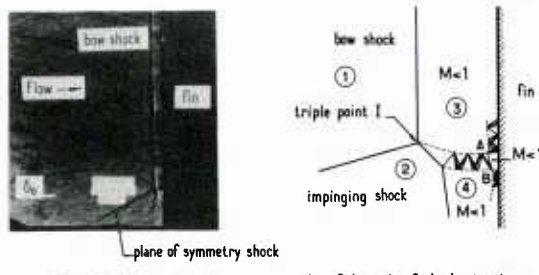


Fig. 4.27 – Obstacle induced flow – Shock structure ahead of the obstacle (Dolling et al., 1979).

An example of surface flow pattern is shown in Fig. 4.28. It was obtained by Sedney and Kitchens (1977) at $M_\infty = 2.5$. In this experiment, the obstacle is a circular cylinder with a height equal to 2.67 times its diameter. The most visible features of the pattern are :

- i - the saddle-point singularity S constituting the "separation point" in the plane of symmetry. One sees very clearly the pattern of skin-friction lines that tend asymptotically into the separation line passing through S ;
- ii - the reattachment point and the corresponding reattachment line close to the obstacle (these features, of a much smaller scale, are barely visible on the photograph) ;
- iii - two oil accumulation dots, downstream of the cylinder. They are the traces on the surface of two tornado-like vortices. These vortices spring from focus-type singular points in the skin-friction lines pattern, then bend over into the free stream direction and continue as the trailing edge pair.
- iv - the photograph also shows the traces of the bow shock and of the Mach stem.

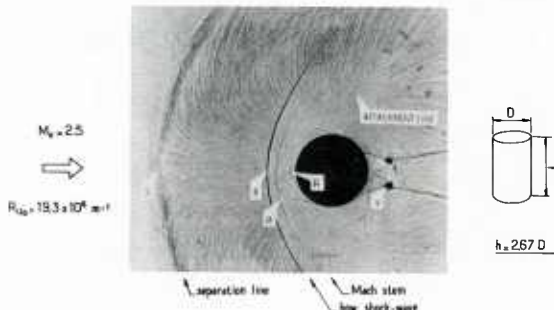


Fig. 4.28 – Obstacle induced flow – Surface flow pattern of a two-vortex configuration (Sedney and Kitchens, 1975).

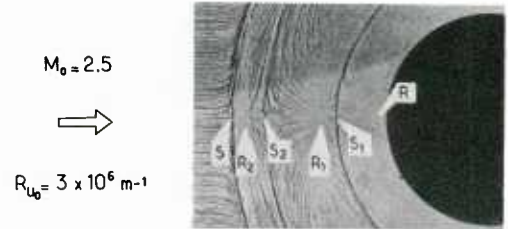


Fig. 4.29 – Obstacle induced flow – Surface flow pattern of a six-vortex configuration (Sedney and Kitchens, 1975).

The present case is an example of flow with two horseshoe vortices that surround the front part of the obstacle and then continue downstream in a direction parallel to that of the free stream. Here, the streamwise extent of the large vortex is about 25 times that of the small one. For a given cylinder geometry, at fixed Mach number M_∞ , the number of such vortices may change considerably with the Reynolds number. Thus, Fig. 4.29 shows the surface flow pattern of a six-vortex configuration. On the photograph, (S) is the primary separation line, (S_1) and (S_2) the secondary separation lines, (R), (R_1) and (R_2) being the corresponding reattachment lines. Also, flows with four vortices were observed by Sedney and Kitchens. In each case, (S) and (R) are always present, but the structure between them changes. The change in the flow structure occurs for rather small variations in Reynolds number and are perfectly repeatable. According to Sedney and Kitchens, this suggests that there may be a delicate balance in the flow which is upset by changing the Reynolds number so that one structure easily changes to another. Tentative representations of the flow off the surface in the symmetry plane are shown in Fig. 4.30. The sketches correspond to a two-vortex and to a six-vortex flow in the case of a small obstacle (then, there is no attachment on the obstacle). They are not to scale and the streamwise dimensions are magnified compared to vertical dimensions for clarity. For the same reason, the traces of the shocks are omitted. Because of symmetry, there is no flow across a symmetry plane, but there is flow out of or into it, so that streamlines being tangent to it can appear to end in a side view of this plane.

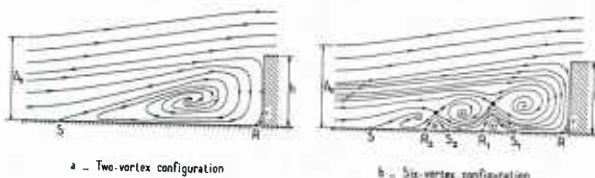


Fig. 4.30 – Obstacle induced flow – Schematic representation of flow off the surface in the symmetry plane (Sedney and Kitchens, 1977).

Similar observations are reported by Ozcan (1982) who made most of his experiments in laminar flow. He noticed that the number of separation lines dropped from 3 to 2 and from 2 to 1 with increasing Reynolds number. However, at high Reynolds number, several separation lines can be observed again.

Let us examine some scaling properties of the obstacle induced interaction. This question has been studied by several investigators (Westkaemper, 1968 ; Winkelmann, 1972 ; Dolling et al., 1979 ; Sedney and Kitchens, 1977 ; Lucas, 1971 ; Uselton, 1967). Here, we will only briefly summarize their essential findings. The developments that follow were for the most part directly inspired by a paper of Dolling (1982) who made a careful comparison between sharp and blunt fin-induced shock-wave/turbulent boundary-layer interactions. In particular, Dolling has shown that in the case of a blunt fin, a distinction must be made between two regions :

- i - close to the fin (or the obstacle), there is what he calls an inner region where the flowfield can be described as leading edge dominated. Within this region, the flow properties depend primarily on the leading edge diameter D and are only slightly affected by changes in the incoming boundary-layer thickness. This property is demonstrated by Fig. 4.31 which shows wall pressure distributions in the symmetry plane ahead of the fin. These distributions were measured for five different values of δ_0/D . One observes that the distributions do not differ much even for ratios δ_0/D varying from 0.26 to 5.3. In particular, the upstream influence length - defined as the distance between the obstacle and the beginning of the pressure rise - is slightly affected by the large changes in δ_0/D . Upstream influence is predominantly a function of D, practically independent of δ_0 and of the freestream Mach number. This strong dependence on geometric parameters tends to prove that this kind of interaction has an essentially inviscid character. It is thus radically different from separation in front of a two-dimensional step in spite of the resemblance of wall pressure distributions. For a two-dimensional step, the thickness of the incoming boundary-layer is the primary streamwise scale of the separation process (see the Free Interaction Theory in Section 3.6 above).

Sedney and Kitchens also showed that for cylindrical obstacles, the primary separation distance L_s - i.e., the distance between the obstacle leading edge and primary separation point S (see above) - depends mainly on D, on the obstacle height h and on the free stream Mach number M_∞ ; but it only depends very weakly on the thickness δ_o (see the correlation curves in Fig. 4.32). This result also raises the question of the distinction between "small" and "large" protuberances. More precisely, a protuberance will be considered as "large" if it produces the "asymptotic results", a condition occurring when further increases in the height of the protuberance do not change the extent of the disturbance field. The two situations are sketched in Fig. 4.33. In particular, when the "asymptotic height" $h = h_a$ is reached, the upstream influence length, the primary separation distance and the height h_T of the triple point location no longer depend on h . Experimental observations show that the "shock root" and in particular the location of the triple point are independent of h provided that $h \geq h_T$. The question of the scaling of the asymptotic height was carefully discussed by Dolling and Bogdonoff (1981) who arrived at the conclusion that the proper scale for h_a is the diameter D of the obstacle.

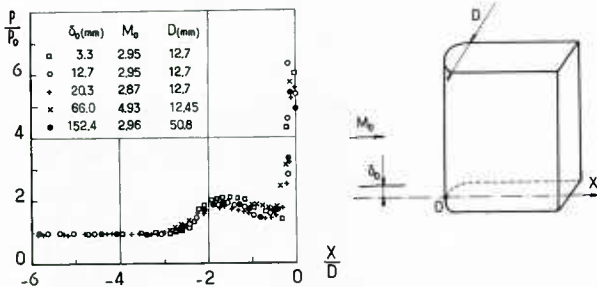


*Fig. 4.31 — Obstacle induced flow
Wall pressure distribution on the plane of symmetry
(Dolling and al , 1979)*

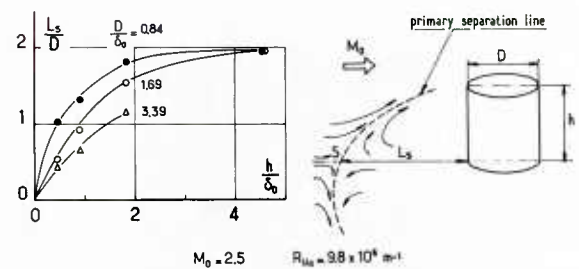


Fig. 4.32 – Obstacle induced flow – Variation of primary separation distance (Sedney and Kitchens, 1977).

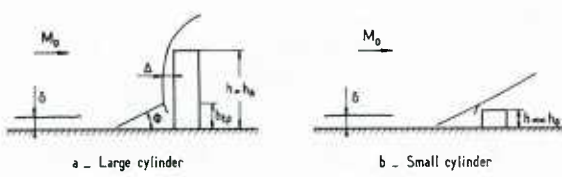


Fig. 4.33 – Obstacle induced flow – Schematic of shock structure for a) "large" and b) "small" cylinders (Dolling and Bogdonoff, 1981).

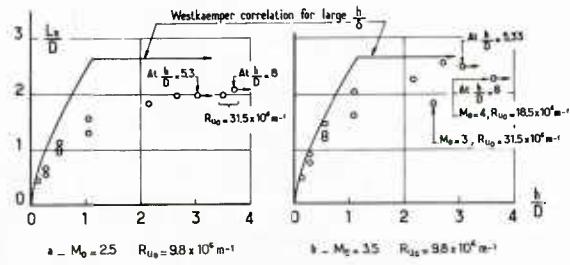


Fig. 4.34 – Obstacle induced flow – Correlation for the primary separation distance (Sedney and Kitchens, 1977).

Similar behavior was noticed by Sedney and Kitchens (1977). This property is a direct consequence of the character of the flow in the so-called "inner region" where it is found that the influence of the free stream boundary-layer is of second order. In principle, a universal value for h_a , only function of D , cannot be specified, since h_a depends also on the Mach and Reynolds numbers. However, the correlation curves of Sedney and Kitchens given in Fig. 4.34 show a relatively small variation of the ratio h_a/D with M_0 and the Reynolds number. The value of h_a/D is close to 2.5 for the two cases considered. Furthermore, for the same cases, the normalized "asymptotic" primary separation distance L_s/D is nearly equal to 2.2-2.3, this level being practically independent of the Reynolds number, provided that the regime be fully turbulent. The above value of L_s/D has been confirmed by several other investigators (Stanbrook, 1960 ; Voitenko et al., 1966 ; Young et al., 1968). On the other hand, in laminar and transitional flows, Ozcan found that L_s depends strongly on the Reynolds number. In laminar flow regime, L_s increases when the Reynolds number increases, whereas in transitional flow regime, the trend is reversed. We have seen that the same tendency is observed in two-dimensional flows (see Section 3.7 above) ;

- ii - at a large spanwise distance from the fin, there is an outer region in which the properties of the interaction are independent of leading edge blunting. As shown by Dolling (1982), in this region the scaling laws of the phenomenon are identical to those of the sharp fin (see previous Section)), i.e., depend primarily on the incoming boundary-layer properties.

In reality, the flowfield in the vicinity of the obstacle leading edge is characterized by a highly unsteady shock wave structure, as found both by Dolling and Bogdonoff (1981) in turbulent flow regime, and by Ozcan (1982) at low Reynolds number. This is not the place to discuss in detail this aspect of the phenomenon which is not yet well known. However, it should be kept in mind that the above considerations pertain in fact to a mean flow which has no real existence.

4.3.4 - Transonic Flow Over a Swept Wing

The flow past a swept wing at transonic speed can be extremely complex, especially when separation occurs. This flow depends on many parameters : the freestream Mach number M_∞ , the Reynolds number, the shape and size of the wing, its angle of attack α and its sweep angle γ . A thorough description of such a complex flow would be beyond the scope of the present AGARDograph. The interested reader can find detailed information on this subject in the existing literature (Rogers and Hall, 1960 ; Squire et al., 1961 ; Monnier and Charpin, 1975). In what follows, we will restrict ourselves to a rapid description of the shock system which forms on the wing upper surface at high subsonic Mach numbers.

The wing configuration considered for this description has been studied in great detail by Schmitt and Manie (1979). It is a rectangular wing equipped with a symmetrical profile having a relative thickness of 0.105. The sweep angle γ of this wing can be varied continuously from 0 deg. to 60 deg., thus allowing a complete examination of the flow phenomena over a large range of sweep angles. The present tests were all carried out for a Reynolds number $R_C = 2.5 \times 10^6$ (geometrical quantities are defined in Fig. 4.35).

Let us first consider flow evolution with the sweep angle at fixed freestream Mach number - $M_\infty = 0.84$ - and angle of attack - $\alpha = 4$ deg. The wall pressure distributions measured at two spanwise stations for different values of γ are plotted in Fig. 4.35. The rapid pressure rises on these distributions indicate the shock-wave locations.

At $\gamma = 0$ (no sweep), a quasi-normal shock stands approximately at mid-chord. In this case, the flow can be considered as two-dimensional over the major part of the wing, three-dimensional effects being important only near the wing tip and the wing root. For $\gamma = 30$ deg., one observes at the spanwise station $Y/b = 0.45$ a double compression, the flow remaining supersonic behind the first compression. Only one shock is observed in the most outboard section at $Y/b = 0.75$. Surface flow visualizations do not show separation. For $\gamma = 40, 50$ and 60 deg., only one shock is visible. This shock is just about parallel to the wing leading-edge and it moves upstream as the sweep angle is increased. At the same time, the Mach number peak value decreases so that the shock weakens. The traces of the shocks on the wing surface, as determined from pressure measurements, are shown in Fig. 4.35. At $\gamma = 30$ deg., the shock system exhibits a typical lambda pattern. Then, in the inboard part of the wing, two shocks form. Through the first shock - or forward shock - the flow undergoes a supersonic-supersonic compression, whereas it becomes subsonic behind the second - or rear - shock.

Now, let us examine the flow evolution with the freestream Mach number M_∞ , at fixed sweep angle and angle of attack ($\alpha = 4$ deg.). The first evolution, reflected by the wall pressure distributions plotted in Fig. 4.36, corresponds to $\gamma = 0$ deg. For the section located nearly at mid span ($Y/b = 0.60$), the evolution is similar to that of a two-dimensional airfoil, with a progressive displacement of the shock towards the trailing edge as the freestream Mach number is raised. At the same time, the shock becomes stronger and induces separation, as indicated by the rapid change of the trailing edge pressure. On the other hand, near the wing tip ($Y/b = 0.95$), a two-shock system is observed due to the locally strong three-dimensional effects. For $\gamma = 50$ deg. (see Fig. 4.36b), the flow downstream of the shock is supersonic only beyond $M_\infty = 0.92$. Then, a lambda shock pattern forms, like for $\gamma = 30$ deg., $M_\infty = 0.84$. In this case, separation does not occur, as can be deduced from the constancy of the trailing-edge pressure.

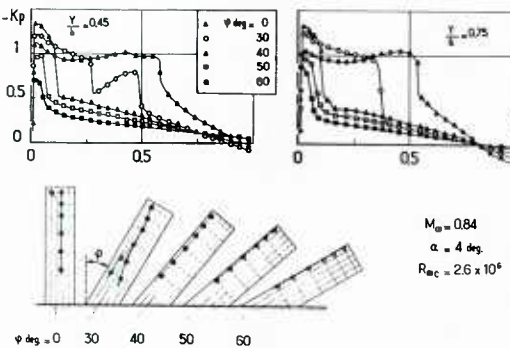


Fig. 4.35 - Swept wing in transonic flow - Chordwise pressure distribution on upper surface - Sweep angle effect (Schmitt and Manie, 1979).

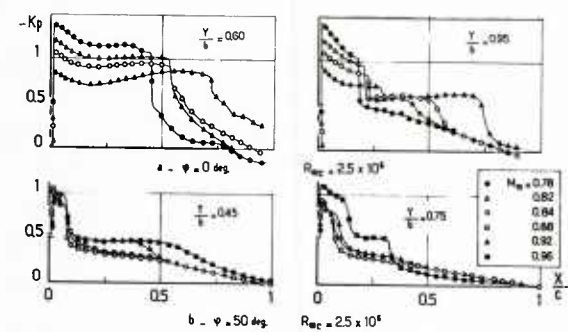


Fig. 4.36 - Swept wing in transonic flow - Chordwise pressure distribution on upper surface - Free stream Mach number effect (Schmitt and Manie, 1979).

To conclude, the last example of results illustrates the changes in the flowfield for variable angle of attack, M_∞ and γ being kept fixed. The corresponding wall pressure distributions are plotted in Fig. 4.37 and the shock locations on the wing planform are represented in Fig. 4.38. When α is increased, the shock moves towards the trailing edge and becomes stronger. The lambda pattern appears as soon as $\alpha = 2$ deg. Thereafter, the intersection point of the two shocks moves progressively inboard as α is increased. Simultaneously, the forward shock strengthens and induces separation in the outboard part of the wing as soon as $\alpha = 7$ deg.

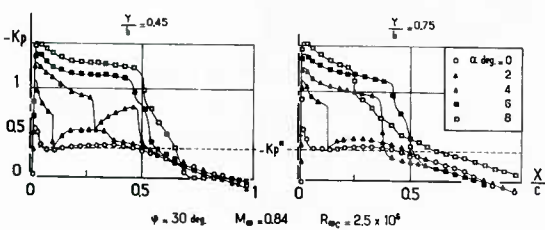


Fig. 4.37 - Swept wing in transonic flow - Chordwise pressure distribution on upper surface - Angle of attack effect (Schmitt and Manie, 1979).

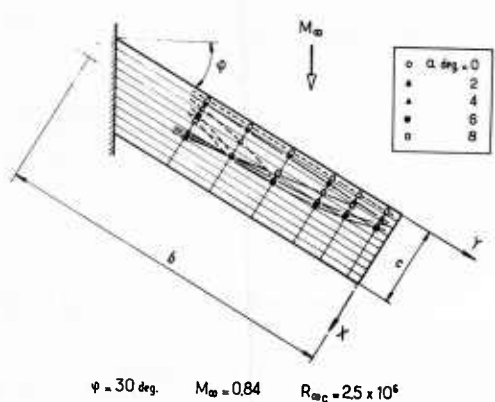


Fig. 4.38 - Swept wing in transonic flow - Upper surface shock pattern (Schmitt and Manie, 1979).

After this rapid overview, we will now examine some properties of the shock-wave/boundary-layer interactions that occur on such wings. The experimental results chosen for this purpose were obtained in a pressurized transonic wind-tunnel on a wing similar to the one used above to analyze the overall flow structure. The experimental arrangement is schematically represented in Fig. 4.39. The cylindrical wing, mounted on one of the tunnel side walls, can be set at variable sweep angles. It is equipped with a supercritical profile. Pressure orifices are located along three sections of the wing, as indicated in Fig. 4.39. The present experiments (Mignosi et al., 1980 ; Dor and Seraudie, 1982) were carried out at a freestream Mach number $M_\infty = 0.90$. Boundary-layer transition is promoted by a tripping band located at the chordwise station $X/C = 0.05$. In these conditions, a shock-wave nearly parallel to the wing leading edge forms at $X/C \approx 0.15$.

We will focus our attention on the region close to the wing tip where row N° 3 of pressure taps is located (see Fig. 4.39). Let us first examine surface flow patterns forming in this region, slightly downstream of the leading edge. The first photograph of Fig. 4.40 shows the pattern obtained when the angle of attack α is equal to 2 deg. One observes that the skin-friction lines, which tend to become perpendicular to the leading edge in the most upstream part of the flow, are strongly deflected in the shock foot region. They continue downstream of the shock and tend progressively to adopt the direction of the outer flow. Let us now consider the surface flow pattern obtained when $\alpha = 4$ deg. In this case, it is clearly visible that the skin-friction lines coming from the leading-edge region do not "cross" the shock anymore. In the shock foot region, these lines are abruptly bent and converge into a separation line (S). Downstream of (S), the skin-friction lines also converge asymptotically into the separation line. Along (S), the surface flow streams toward the wing tip. A reattachment line is also visible. Downstream of it, the surface flow is progressively deflected in the direction of the trailing edge. The computed pattern represented in Fig. 4.7 closely resembles the present observation. In particular, it clearly shows that the outer flow, at the boundary-layer edge, is weakly deflected by the shock, whereas the surface flow is highly skewed. For greater clarity, the experimental skin-friction line patterns are schematically represented in Fig. 4.40.

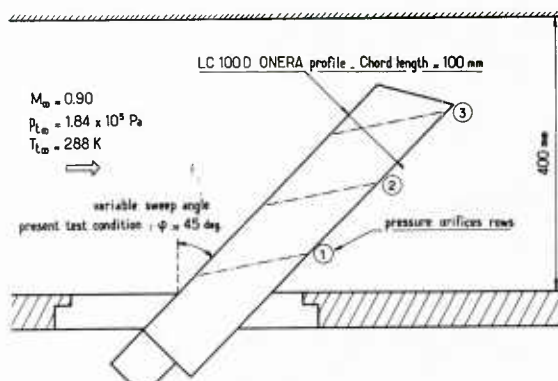
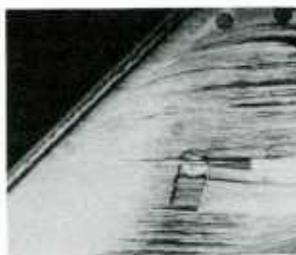
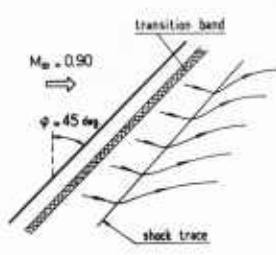


Fig. 4.39 – Transonic interaction on a swept wing – Wing installation in the tunnel test-section (Mignosi et al., 1980).



$\alpha = 2$ deg. – Interaction without separation

Fig. 4.40 a – Transonic interaction on a swept wing – Surface flow pattern (Mignosi et al., 1980).



$\alpha = 4$ deg. – Interaction with separation

Fig. 4.40 b – Transonic interaction on a swept wing – Surface flow pattern (Mignosi et al., 1980).

The "wall" Mach number distributions along row N° 3 are plotted in Fig. 4.41. The Mach number M_0 immediately upstream of the shock increases steadily with the angle of attack. In the present cases, the downstream level is always supersonic. The shock-wave is nearly planar and practically normal to the wing, so that it is possible to define a "normal" Mach number. This property will be utilized to deduce a criterion for Incipient Shock-Induced Separation in the following Section. Chordwise evolutions of the boundary-layer global properties (displacement and momentum thicknesses, incompressible shape-parameter) are represented in Figs. 4.42 and 4.43 for a sweep angle of 30 deg. They correspond to the cases of a non-separated and of a separated boundary-layer at the shock foot. In the first case, the normal Mach number is equal to 1.28, in the second case it is equal to 1.36. The integral quantities have been computed with the total velocity. In fact, except in the separated bubble, the skewing of the flow is small so that the boundary-layer is nearly two-dimensional. The present evolutions of δ^* , θ and h_i are very similar to those observed in purely two-dimensional flows.

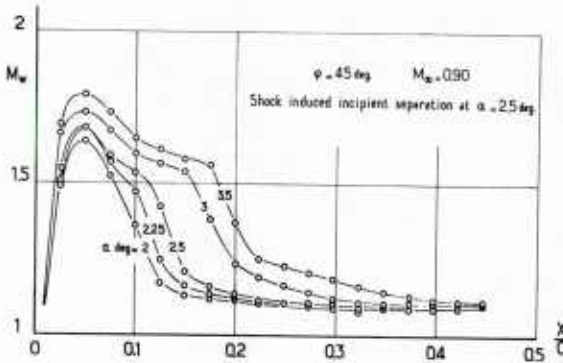


Fig. 4.41 — Transonic interaction on a swept wing — "Wall" Mach number distribution along row 3 (see Fig. 4.39).

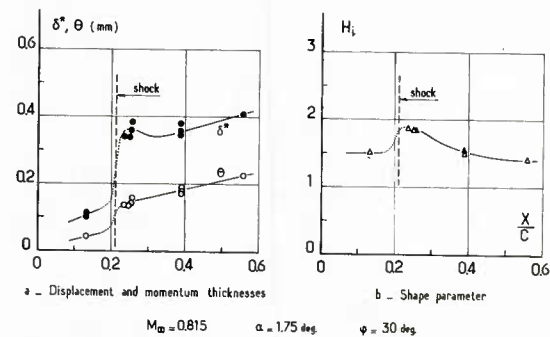


Fig. 4.42 — Transonic interaction on a swept wing — Variation of boundary-layer integral properties — Unseparated flow (Mignosi et al., 1980).

4.4 - Incipient Shock-Induced Separation in 3-D Flows.

Information on Incipient Shock-Induced Separation in three-dimensional flows is still very scarce when compared to the abundance of results on two-dimensional flows (see Section 3.8 above). This scarcity is certainly due to the complexity of 3-D separated flows and also to the difficulty in defining 3-D Incipient Separation.

Three-dimensional separation is detected experimentally by inspection of the skin-friction lines pattern. In practice, this pattern is obtained by oil flow pictures but which are often difficult to interpret. The oil pattern is determined by many forces, including surface tension, gravity and buoyancy, as well as wall shear-stress and pressure gradient. The response of the oil film itself depends on the oil physical properties : viscosity, density, ... The difficulties of interpretation explain in part the large scatter of the experimental results. Furthermore, there is still some controversy over the way of defining separation from inspection of a skin-friction lines pattern (see Section 4.2 above). This fact also contributes to the discrepancy in the Incipient Separation limits published by different authors.

What follows is restricted to separation induced by a skewed shock-wave on a side wall normal to it. Result on other types of interaction are practically non-existent.

To our knowledge, one of the first Incipient Separation criteria for three-dimensional flows was proposed by Mc Cabe (1966). This author assumed that Incipient Separation occurred when the skin-friction lines turned parallel to the inviscid shock direction. Then by applying his simple theoretical model for the 3-D shock/boundary-layer interaction, Mc Cabe was able to compute the conditions leading to Incipient Separation (see Section 1.3.3 of Part II for a brief presentation of Mc Cabe's theory).

Korkegi (1973) showed that at high Mach number - and for $\gamma = 1.4$ - Mc Cabe's separation limit could be approximated by the very simple equation :

$$(4.1) \quad M_0 \alpha_{GI} = 0.364 \text{ (in radians)}$$

where M_0 is the Mach number of the undisturbed incoming flow and α_{GI} the angle of the shock generator in the Incipient Separation condition on the side plate. However, Korkegi found thereafter that a better agreement with experiment was obtained by changing the constant to 0.3, thus the criterion becomes :

$$(4.2) \quad M_0 \alpha_{GI} = 0.3 \text{ (in radians)}$$

At the same time, Korkegi (1975) proposed a correlation for 2-D Incipient Separation that takes into account most of the available experimental results presented in Section 3.8.3 above. This correlation, given here for purposes of comparison with the 3-D case, holds true only for high values of the Reynolds number $R\delta_0$. Furthermore, it is assumed that if $R\delta_0$ is sufficiently high, its influence on Incipient Separation is practically negligible. This assumption is not really in contradiction with experiment, the influence of the Reynolds number at high $R\delta_0$ not being obvious - and even controversial - due to the large experimental scatter. Thus, Korkegi's correlation is a unique curve in the (M_0, α_{GI}) plane which is traced in Fig. 4.44a. It is assumed valid for the range $10^5 \leq R\delta_0 \leq 10^7$. The pressure rise for Incipient Separation corresponding to Fig. 4.44a is shown in Fig. 4.44b along with two empirical formulae adequate for rough estimates in adiabatic flow conditions.

The two 3-D Incipient Separation criteria proposed by Mc Cabe (Eq.4.1) and by Korkegi (Eq. 4.2) are represented in Fig. 4.45a. They are in good agreement with the experimental results of Kubota and Stollery (1980) and those of Neumann and Token (1974). To Eq. 4.2 corresponds the pressure rise across the shock $p_1/p_0 = 1.5$, independent of M_0 (see Fig. 4.45b).

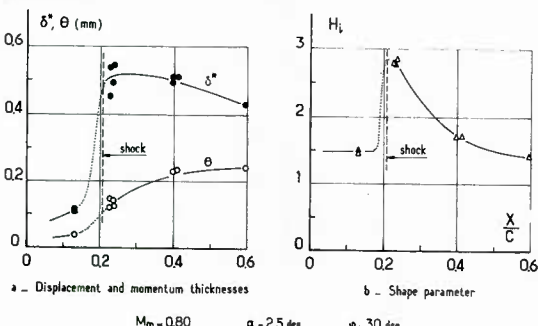


Fig. 4.43 — Transonic interaction on a swept wing — Variation of boundary-layer integral properties — Separated flow (Mignosi et al., 1980).

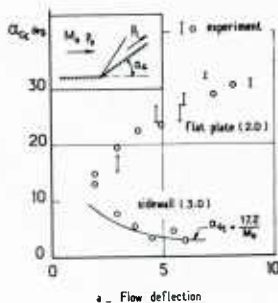


Fig. 4.44 – Shock induced incipient separation –
Korkegi's criteria for 2-D and 3-D flows (Korkegi, 1975).

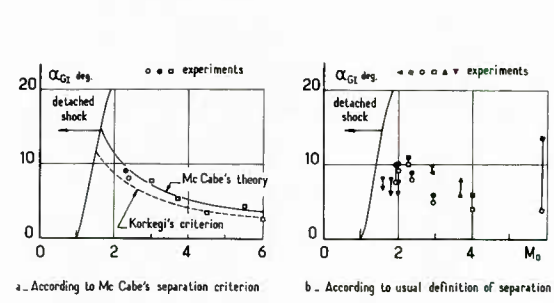


Fig. 4.45 – Incipient separation limit for a skewed shock wave
(Kubota and Stollery, 1980).

According to Kubota and Stollery, the Incipient Separation definition adopted by Mc Cabe (and by Korkegi) would be inadequate since there are experiments which show that the surface flow can be deflected through angles exceeding the shock-wave angle before the formation of a true separation line. Thus, as explained above, true Incipient Separation actually occurs when the skin-friction lines converge and merge asymptotically into a separation line or what Kubota and Stollery call a "convergence line". In fact there is no contradiction with the definition of Mc Cabe : the difference comes from the observation that the true separation line is not necessarily parallel to the inviscid shock, as postulated by Mc Cabe.

The Incipient Separation conditions detected by using this second definition are plotted in Fig. 4.45b (this compilation was made by Kubota and Stollery). Since the turning angle of the surface flow can be higher than the shock angle before a separation line is formed, this definition – in principle more exact – leads to values of the limit angle α_{GI} significantly higher than those given by Mc Cabe's criterion. The presently available experimental results show no influence of the Reynolds number. For well established turbulent flow regime, this influence – if it exists – is certainly weak and well within the scatter of the data points.

Goldberg (1969) has proposed an approximate criterion for 3-D Incipient Separation induced by a glancing shock wave which consists in applying the 2-D criterion with the Mach number normal to the inviscid shock. Consideration of the results plotted in Fig. 4.45 suggests a still simpler criterion consisting in adopting for α_{GI} the value $\alpha_{GI} = 8$ deg., independent of the Mach number and Reynolds number.

Whatever the definition adopted, the above results show that the pressure rise for 3-D Incipient Separation by a skewed shock-wave is far less important than for 2-D ramp (or shock reflection) induced separation and the gap widens with increasing Mach number. This greater sensitivity of 3-D flows was also noticed by Myring (1977) as a result of his simplified analysis presented in Section 1.3.3 of Part II. Thus, as pointed out by Korkegi (1975) as well as by Goldberg (1969), it is the skewed shock-wave interaction with the side wall turbulent boundary-layer in rectangular diffusors or inlets that first leads to separation and to possible flow breakdown for compression angles (or pressure rises) which may be well below the incipient values for the two-dimensional case.

It should also be emphasized that Incipient Separation in 3-D flows depends certainly on the kind of interaction considered (see Myring and Goldberg). Thus the above results are, in principle, applicable only to a skewed shock-wave normal to a flat plate. For other types of interacting flows – like swept corner or oblique skewed shock – the Incipient Separation conditions should be different.

Now we will give some information on Incipient Separation on a swept wing in transonic flows. This problem was carefully studied by Dor and Plazanet (1982) on the experimental arrangement shown in Fig. 4.39. In their investigations, the Incipient Separation situation was detected by interpretation of surface flow patterns and inspection of wall pressure distributions. They arrived at the conclusion that Incipient Separation occurred when the Mach number normal to the shock was equal to 1.33. No noticeable influence of the Reynolds number or of the shape parameter of the incoming boundary-layer was noticed, mainly because of the limitations of the test set-up. The value 1.33 for the normal Mach number is close to the value of the Mach number for Incipient Separation in 2-D transonic flows (see Section 2.7 above).

4.5 – Références

Anderson, B.H. and Benson, T.J. (1983): Numerical solution to the glancing sidewall oblique shock-wave/turbulent boundary-layer interaction in three dimension. AIAA Paper N° 83-0136 (Jan. 1983); see also NASA TM-83056 (1983).

Bachalo, W.D. and Holt, M. (1975): Three-dimensional boundary-layer separation in supersonic flow. AGARD CP - 168, Paper N° 35.

Cousteix, J. and Houdeville, R. (1976): Epaississement et séparation d'une couche limite turbulente soumise à une interaction tridimensionnelle avec un choc oblique. La Recherche Aérospatiale, N° 1976-1, pp. 1-11 (Jan. 1976).

Degrez, G. (1981): Kinetic heating due to a skewed shock-wave/turbulent boundary-layer interaction. VKI TN-138 (Jan. 1981).

Degrez, G. and Ginoux, J.J. (1983): Three-dimensional skewed shock-wave laminar boundary-layer interaction at Mach 2.25. AIAA Paper N° 83-1755 (July 1983).

Déléry, J.M. and Formery, M.J. (1983): A finite difference method for inverse solutions of 3-D turbulent boundary-layer flow. AIAA Paper N° 83-0301 (Jan. 1983).

Dolling, D.S., Cosad, C.D. and Bogdonoff, S.M. (1979): An examination of blunt fin-induced shock-wave turbulent boundary-layer interactions. AIAA Paper N° 79-0068 (Jan. 1979).

Dolling, D.S. and Bogdonoff, S.M. (1981): Upstream influence scaling of sharp fin-induced shock-wave turbulent boundary-layer interactions. AIAA Paper N° 81-0336 (Jan. 1981).

Dolling, D.S. and Bogdonoff, S.M. (1981): Scaling of interactions of cylinders with supersonic turbulent boundary-layers. AIAA Journal, Vol. 19, N° 5, pp. 655-657 (May 1981).

Dolling, D.S. and Bogdonoff, S.M. (1981): An experimental investigation of the unsteady behavior of blunt fin-induced shock-wave/turbulent boundary-layer interactions. AIAA Paper N° 81-1287 (June 1981).

Dolling, D.S. (1982): Comparison of sharp and blunt fin-induced shock-wave/turbulent boundary-layer interactions. AIAA Journal, Vol. 20, N° 10, pp. 1385-1391 (Oct. 1982).

Dor, J.B. and Seraudie A. (1982): Etude de l'interaction onde choc-couche limite sur une aile à 45° de flèche. ONERA PV OA N° 53/7078 AND (April 1982).

Dor, J.B. and Plazanet, M. (1982): Approfondissement de l'étude expérimentale sur aile en flèche de profil LC 100 D. ONERA RT OA N° 58/7078 AND (Dec. 1982).

East, L.F. and Hoxey, R.P. (1971): Low-speed three-dimensional turbulent boundary-layer data. Part 1-2. RAE R. & M. N° 3653.

Edney, B. (1968): Anomalous heat-transfer and pressure distributions on blunt bodies at hypersonic speeds in the presence of an impinging shock. Aeronautical Research Institute of Sweden, Report 115 (Feb. 1968).

Freeman, L.M. and Korkegi, R.H. (1975): Experiments on the interaction with a turbulent boundary-layer of a skewed shock-wave of variable strength at Mach 2.5. ARL-TR-75-0182.

Ginoux, J. (1962) : On the existence of cross flows in a separated supersonic stream. TECA TN-6.

Goldberg, T.J. (1973): Three-dimensional separation for interaction of shock-waves with turbulent boundary-layers. AIAA Journal, Vol. 11, N° 11, pp. 1573-1574 (Nov. 1973).

Green, J.E. (1970): Interaction between shock-waves and turbulent boundary-layers. RAE TR-69098 (May 1969) ; see also Progress in Aerospace Sciences, Pergamon Press, Vol. 11, pp. 235-340.

Hornung, H.G. (1983): The vortex skeleton model for three- dimensional steady flows. AGARD CP-342, Paper N° 2 (1983).

Hung, C.M. and Mc Cormack, R.W. (1978): Numerical solution of three-dimensional shock-wave and turbulent boundary-layer interaction. AIAA Paper N° 78-161 (Jan. 1978).

Kaufman, L.G. II, Korkegi, R.H. and Morton, L.G. (1972): Shock impingement caused by boundary-layer separation ahead of blunt fins. ARL 72-0118, Aerospace Research Laboratories, (Aug. 1972); see also AIAA Journal, Vol. 11, N° 10, pp. 1363-1364 (Oct. 1973).

Korkegi, R.H. (1971): Survey of viscous interactions associated with high Mach number flight. AIAA Journal, Vol. 9, N° 5, pp. 771-784 (May 1971).

Korkegi, R.H. (1973): A simple correlation for incipient turbulent boundary-layer separation due to a skewed shock-wave. AIAA Journal, Vol. 11, N° 11, pp. 1578-1579 (Nov. 1973).

Korkegi, R.H. (1975): Comparison of shock-induced two- and three- dimensional incipient turbulent separation. AIAA Journal, Vol. 13, N° 4, pp. 534-535 (April 1975).

Korkegi, R.H. (1976): On the structure of three-dimensional shock-induced separated flow regions. AIAA Journal, Vol. 14, N° 5, pp. 597-600 (May 1976).

Kubota, H. and Stollery, J.L. (1980): An experimental investigation of the interaction between a glancing shock-wave and a turbulent boundary-layer. ICAS - 80 - 14-1, pp. 563-574.

Kussoy, M.I., Viegas, J.R. and Horstman, C.C. (1980): An experimental and numerical investigation of a 3-D shock separated turbulent boundary-layer. AIAA Paper N° 80-0002 (Jan. 1980); see also AIAA Journal, Vol. 18, N° 12, pp. 1477-1484 (Dec. 1980).

Law, C.H. (1975): Three-dimensional shock-wave/turbulent boundary-layer interactions at Mach 6. ARL-TR-75-0191 (1975).

Legendre, R. (1952): Ecoulement au voisinage de la pointe avant d'une aile à forte flèche aux incidences moyennes. La Recherche Aéronautique, N° 30, pp. 3-8 (Nov. - Dec. 1952).

Legendre, R. (1977): Lignes de courant d'un écoulement permanent. Décollement et séparation. La Recherche Aérospatiale, N° 1977-6, pp. 327-335 (Déc. 1977).

Lightill, M.J. (1963): Attachment and separation in three dimensional flow. In Laminar Boundary Layers, Section II 2-6, pp. 72-82, L. Rosenhead, Oxford Univ. Press (1963).

Lowrie, B.W. (1965): Cross flows produced by the interaction of a swept shock-wave with a turbulent boundary-layer. Ph. D. Thesis, University of Cambridge.

Lu, F.K. and Settles, G.S. (1983): Conical similarity of shock/boundary-layer interactions generated by swept fins. AIAA Paper N° 83-1756 (July 1983).

Lucas, E.J. (1971): Investigation of blunt fin-induced flow separation on a flat plate at Mach number 2.5 to 4.0. AEDC-TR-70-265 (Jan. 1971).

Mc Cabe, A. (1966): The three-dimensional interaction of a shock-wave with a turbulent boundary-layer. The Aeronautical Quarterly, Vol. 17, Part 2, pp. 231-252.

Maskell, E.C. (1955): Flow separation in three dimensions. RAE Aero Report 2565 (Nov. 1955).

Mignosi, A., Gobert, J.-L. and Seraudie, A. (1980): Etude préliminaire de l'interaction onde de choc couche-limite sur une aile à flèche variable. ONERA RT OA N° 43/7078 AYD (Oct. 1980).

Monnerie, B. and Charpin, F. (1975): Essais de tremblement ("Buffeting") d'une aile en flèche en transonique. L'Aéronautique et l'Astronautique N° 50, pp. 3-16 (1975) ; see also ONERA TP-1975-11.

Myring, D.F. (1977): The effect of sweep on conditions at separation in turbulent boundary-layer/shock-wave interactions. The Aeronautical Quarterly, Vol. 28, Part 2, pp. 111-122 (May 1977).

Neumann, R.D. and Token, K.H. (1974): Prediction of surface phenomena induced by three-dimensional interactions on planar turbulent boundary-layers. Paper 74-058, International Astronautical Federation XXV Congress, Amsterdam, The Netherlands (Oct. 1974).

Neumann, R.D. and Hayers, J.R. (1977): Prediction techniques for three-dimensional shock-wave/turbulent boundary-layer interactions. AIAA Journal, Vol. 15, N° 10, pp. 1469-1473 (Oct. 1977).

Oskam, B., Vas, I.E. and Bogdonoff, S.M. (1976): Mach 3 oblique shock-wave/turbulent boundary-layer interactions in three dimensions. AIAA Paper N° 76-336 (July 1976).

Oskam, B., Vas, I.E. and Bogdonoff, S.M. (1977): An experimental study of three-dimensional flowfields in an axial corner at Mach 3. AIAA Paper N° 77-689 (June 1977).

Ozcan, O. (1982): An experimental investigation of three-dimensional boundary-layer separation in supersonic flow past a circular cylinder on a flat plate. Ph. D. Thesis, University of California, Berkeley (March 1982).

Peake, D.J. and Rainbird, W.J. (1975): The three-dimensional separation of a turbulent boundary-layer by a skewed shock-wave; and its control by the use of tangential injection. AGARD CP-168, Paper N° 40.

Peake, D.J. and Tobak, M. (1980): Three-dimensional interactions and vortical flows with emphasis on high speeds. AGARDograph N° 252 (July 1980).

Price, E.A. and Stallings, R.L. (1967): Investigation of turbulent separated flows in the vicinity of fin-induced protuberances at supersonic Mach numbers. NASA TN-D-3804 (Feb. 1967).

Rogers, E.W.E. and Hall, I.M. (1960): An introduction to the flow about plane swept-back wings at transonic speeds. The Journal of the Royal Aeronautical Society, Vol. 64, N° 596.

Roshko, A. and Thomke, G.J. (1965): Observations of turbulent reattachment behind an axisymmetric downstream-facing step in supersonic flow. Douglas Report SM-4 3069 (April 1965).

Roshko, A. and Thomke, G.J. (1974): Flare-induced interaction lengths in supersonic, turbulent boundary-layers. Mc Donnell Douglas, MDAC Paper WD 2416 (Dec. 1974); see also AIAA Journal, Vol. 14, N° 7, pp. 873-879 (July 1976).

Schmitt, V. and Manie, F. (1979): Ecoulements subsoniques et transsoniques sur une aile à flèche variable. La Recherche Aérospatiale, N° 1979-4, pp. 219-237 (July-Aug. 1979).

Scuderi, L.F. (1978): Expressions for predicting 3-D shock-wave/turbulent boundary-layer interaction pressures and heating rates. AIAA Paper N° 78-162 (Jan. 1978).

Sedney, R. and Kitchens, C.W. Jr. (1977): Separation ahead of protuberances in supersonic turbulent boundary-layers. BRL Report N° 1958 (Feb. 1977); see also AIAA Journal, Vol. 15, N° 4, pp. 546-552 (April 1977).

Settles, G.S., Fitzpatrick, T.J. and Bogdonoff, S.M. (1978): A detailed study of attached and separated compression corner flowfields in high Reynolds number supersonic flow. AIAA Paper N° 78-1167 (July 1978); see also AIAA Journal, Vol. 17, N° 6, pp. 579-585 (June 1979).

Settles, G.S. and Perkins, J.J. (1979): Investigation of three-dimensional shock/boundary-layer interactions at swept compression corners. AIAA Paper N° 79-1498 (July 1979); see also Settles, G.S., Perkins, J.J. and Bogdonoff, S.M. same content in AIAA Journal, Vol. 18, N° 7, pp. 779-785 (July 1980).

Settles, G.S., Perkins, J.J. and Bogdonoff, S.M. (1981): Upstream influence scaling of 2-D and 3-D shock/turbulent boundary-layer interactions at compression corners. AIAA Paper N° 81-0334 (Jan. 1981).

Squire, L.C., Jones, J.G. and Stanbrook, A. (1961): An experimental investigation of the characteristics of some plane and cambered 65° delta wings at Mach numbers from 0.7 to 2. RAE Report N° Aero 2655.

Stalker, R.J. (1960): Sweep back effects in turbulent boundary-layer/shock-wave interaction. JAS, Vol. 27, pp. 348-356 (May 1960).

Stalker, R.J. (1982): Spanwise propagation of disturbances in swept shock-wave/boundary-layer interactions. AIAA Paper N° 82-0988 (June 1982).

Stanbrook, A. (1960): An experimental study of the glancing interaction between a shock-wave and a turbulent boundary-layer. ARC CP 55 (July 1960).

Tobak, M. and Peake, D.J. (1981): Topological structure of three-dimensional separated flows. AIAA Paper N° 81-1260 (June 1981).

Uselton, J.C. (1967): Fin shock-boundary-layer interaction tests on a flat plate with blunted fins at M=3 and 5. AEDC-TR-67-113 (June 1967).

Van den Berg, B. and Elsenaar, A. (1972): Measurements in a three-dimensional incompressible turbulent boundary-layer in an adverse pressure gradient under infinite swept wing condition. NLR TR-72092 U (Aug. 1972).

Voitenko, D.M., Zubkov, A.E. and Panov, Y.A. (1966): Supersonic gas flow past a cylindrical obstacle on a plate. Mekhanika Zhidkosti i Gaza, Vol. 1, N° 1, pp. 121-125 ; see also Journal of Fluid Dynamics, Vol. 1, N° 1, pp. 84-88.

Wang, K.C. (1983): On the dispute about open separation. AIAA Paper N° 83-0296 (Jan. 1983).

West, J.E. and Korkegi, R.H. (1972): Supersonic interaction in the corner of intersecting wedges at high Reynolds numbers. AIAA Journal, Vol. 10, N° 5, pp. 652-656 (May 1972).

Westkaemper, J.C. (1968): Turbulent boundary-layer separation ahead of cylinders. AIAA Journal, Vol. 6, N° 7, pp. 1352-1355 (July 1968).

Winkelmann, A.E. (1972): Experimental investigations of a fin protuberance partially immersed in a turbulent boundary-layer at Mach 5. NOLTR-72-33 (Jan. 1972).

Young, F.L., Kaufman, L.G. and Korkegi, R.H. (1968): Experimental investigation of interaction between blunt fin shock waves and adjacent boundary-layers at Mach numbers 3 and 5. ARL 68-0214, Aerospace Research Laboratories.

PART II. — METHODS OF CALCULATION

1. — GLOBAL METHODS

1.1. — Introductory Remarks

With very few exceptions, the main purpose of the methods considered in this Section is the prediction of the change in the boundary-layer properties (integral thicknesses, shape parameter) across a shock-wave of insufficient strength to induce separation. The case of a separated flow is only considered by Hammitt (see Section 2.2.2) and by Baker (see Section 2.2.6). For most of the methods, the limit of validity coincides with incipient separation, the prediction of this limit being a secondary, but important, objective of these approximate theories.

The interaction problem is generally formulated in the following terms:

- an initial state is given at a Station 1 which coincides with the beginning of the interaction domain. Thus, Station 1 is located at the point where the wall static pressure starts to rise or at the point where an incident oblique shock-wave meets the boundary-layer edge. At Station 1, the following quantities are known: inviscid flowfield properties (i.e. Mach number $M_{\infty 1}$, pressure p_1 , density $\rho_{\infty 1}$, etc.) and boundary-layer characteristics. These characteristics may consist of the full velocity distribution, if it is available, or more frequently of global quantities like momentum and displacement thicknesses, shape parameter and, eventually, skin-friction coefficient. These quantities generally result from a “classical” boundary-layer calculation which has been performed in the region upstream of the shock location. Very frequently, this calculation is made by one of the many available integral techniques which are very popular owing to their rapidity and practicality;
- a downstream Station 2 is defined at the end of the interaction domain where the *inviscid flow properties are prescribed* (i.e. Mach number $M_{\infty 2}$, pressure p_2 , density $\rho_{\infty 2}$, etc.). These quantities may result from an inviscid flow calculation or be given by experimental correlations. Definition of the final state at Station 2 is often less obvious than the choice of the initial conditions. As a matter of fact, if there is generally no ambiguity involved in defining the start of interaction, especially in turbulent flows, the end of the process is often far from being unambiguously defined. Thus, the fixing of the downstream Station 2 can sometimes be arbitrary. This is more particularly true in transonic shock-wave/boundary-layer interactions;
- the problem is to compute the boundary-layer properties at Station 2, i.e., the distorted profile or more global quantities: momentum and displacement thicknesses as well as a parameter characteristic of the shape of the velocity distribution, etc. This information could then be used as input for a new classical boundary-layer calculation downstream of the interaction region. Other quantities like the streamwise extent of the interaction domain are also of interest.

Many of the approximate methods developed to predict the downstream boundary-layer properties rely on *discontinuity analysis*. According to this approach, the interaction process is considered as a “black-box” with State 1 as input and State 2 as output. The details of the phenomenon are ignored or crudely represented.

The rather simple flow model on which these methods are constructed is inspired by experimental evidence and incorporate more or less empirical information. This fact explains the relatively good quantitative success of discontinuity analyses together with the very “rapid” character of the interaction process which allows drastic simplifications (mainly the neglecting of viscous effects). The counterpart of this kind of approach is a rather limited range of validity, so that the method to be used depends on the flow situation to be treated: oblique shock reflection or quasi-normal shock-wave, transonic, supersonic or hypersonic conditions, etc.

The approximate methods founded on a discontinuity analysis belong to one or the other of the following two families, which are, in fact, closely related:

- *boundary-layer integral methods*;
- *control volume methods*.

We will now present some of the existing analyses by first considering two-dimensional flows (Section 1.2), then three-dimensional flows (Section 1.3).

In Section 1.4, we will envisage a rather different approach which was termed by Green (1969) “the inviscid shear-layer analysis”. In this approach, the *local* flow properties are computed by considering the interacting boundary-layer flow as a wholly inviscid stream.

This presentation is essentially concerned with turbulent boundary-layers. In principle, it would be possible to apply certain of the following methods to laminar situations by making appropriate changes (velocity profile representation, entrainment rate, skin friction law, etc.) However, use of such analyses in laminar flows is questionable for several reasons:

- some assumptions valid in turbulent flows do not hold true for laminar flows: for instance (as seen in Section 3.4 of Part I) interaction length is far more important in laminar than in turbulent, and as a consequence, the neglecting of viscous forces, which is frequently made in turbulent, is not always justifiable;
- except in very low Reynolds number flows, or for very weak shocks, interaction with a shock-wave generally provokes separation of the laminar boundary-layer and simultaneously induces transition. This phenomenon is difficult to model within the framework of a discontinuity analysis;
- there exist reliable and more exact methods for computing a purely laminar interaction [(solution of the full Navier-Stokes equations (see Section 5), viscous-inviscid coupling techniques (see Section 3)], so that the use of discontinuity analyses is of no real interest.

In order to simplify the presentation of the different methods, the flow will be assumed *adiabatic* (no heat transfer at the wall). In principle, these analyses could be generalized to non-adiabatic flows by addition of the energy equation. However, this extension has rarely been carried out and will not be discussed here. In fact, it leads to difficult problems for properly taking into account heat transfer at the wall.

For adiabatic flows at moderate Mach numbers (say $M_e \lesssim 4$), it is frequently assumed that stagnation enthalpy is everywhere constant (isoenergetic flow). This hypothesis leads to some simplifications of the calculation without affecting appreciably the accuracy of methods which involve more "severe" simplifying assumptions.

1.2. — Two Dimensional Interaction

1.2.1. — Simplified Boundary-Layer Integral Methods

General comments. — A first way to devise an approximate analysis treating the interaction between a shock-wave and a turbulent boundary-layer is to use a simplified form of the Prandtl equations. The key hypothesis of this approach is to assume that viscous forces have no time to play an appreciable role during the rapid interaction process which is essentially controlled by pressure and inertia forces. Of course, such an assumption is not true very close to the wall, however in a turbulent boundary-layer the "viscous-layer" is so thin that it appears legitimate to consider that the whole process is only weakly affected by viscosity. This conclusion certainly does not hold true for laminar flows, as has already been pointed out in the introductory remarks. The resolution of the simplified version of the boundary-layer equations is made by *considering an integral form* of these equations since the use of the local partial differential equations would require a special treatment of the wall region in order to satisfy the no-slip condition (see Section 1.4 below on Inviscid Shear Layer analyses and Section 4 on Multi-Deck theories). Practically all the existing boundary-layer integral methods can be modified in order to give a global description of the shock/boundary-layer interaction. Nevertheless, we will here consider only three methods which are the most popular and have been specifically designed to treat the interaction problem.

For all these theories, the approaching boundary-layer is considered as an input to the problem (this means that we know its integral properties which are most often: the momentum thickness θ , the displacement thickness δ^* and the "incompressible" shape parameter H_1). The Mach number M_{e1} at the boundary-layer edge just upstream of the shock as well as the downstream value M_{e2} are also given. The problem is to compute the downstream state (i.e., θ_2 , δ_2^* , H_{12} , etc.) for a boundary-layer that has been submitted to a "rapid" pressure change from p_1 to p_2 (rapid meaning that the interaction length, or the distance between Station 1 and 2, is of the order of a few δ_1). It is to be noticed that the sign of the pressure change ($p_2 - p_1$) does not matter and thus the boundary-layer methods may also be applied to a concentrated expansion resulting, for example, from a change in the slope of a wall or from separation at a base shoulder, the flows being of course supersonic. For an adiabatic flow, the problem has three unknown quantities: two integral thicknesses and a shape parameter (other quantities of interest, like the skin friction coefficient, may generally be deduced from the previous quantities by appropriate relations). Thus, one needs *three equations*. In all the methods, two of these equations are integral forms of Prandtl's equations, the first one being as always the well known Von Kármán equation (with the wall shear stress omitted). The third relation (or "closure" assumption) is obtained by assuming that the velocity distributions in the boundary-layer belong to a *one parameter family*, i.e., are fully specified by the knowledge of only one shape parameter. Thus, the various methods differ one from the other by the use of a different *second integral equation* and a different *velocity profile family*.

These basic principles of calculation also underlie methods which compute the details of the phenomenon by a continuous streamwise integration of integral boundary-layer equations (see Section 2).

Reshotko and Tucker's method (1955). — This analysis being among the oldest methods (Tyler and Shapiro, 1953; Crocco and Probstein, 1954; Mayer, 1955), it is nevertheless still widely used to predict boundary-layer change resulting from the action of a concentrated pressure gradient (compression as well as expansion).

The authors start from the following boundary-layer equations where the shear stress term is omitted:

— continuity:

$$\frac{\partial(\rho u)}{\partial x} + \frac{\partial(\rho v)}{\partial y} = 0, \quad (1.1)$$

— momentum:

$$\rho u \frac{\partial u}{\partial x} + \rho v \frac{\partial u}{\partial y} = - \frac{dp}{dx}. \quad (1.2)$$

It is assumed that the total enthalpy h_t is constant throughout the dissipative region, which implies adiabatic conditions (no heat transfer at the wall) and an external Mach number M_e which is not too high (up to 4 approximately; for this value the change in h_t is nearly equal to 4%). With the assumption $h_t = \text{Const.}$, the energy equation is not needed.

Equations 1.1 and 1.2 are first cast into an "incompressible" form by using a Stewartson type transformation:

$$dX = \frac{\rho_e a_e}{\rho_{te} a_{te}} dx,$$

$$\frac{\partial Y}{\partial y} = \frac{\rho a_e}{\rho_{te} a_{te}},$$

where a is the speed of sound, e designates the situation at the boundary-layer edge and t , the stagnation conditions.

Thus, one obtains:

$$\frac{\partial U}{\partial X} + \frac{\partial V}{\partial Y} = 0, \quad (1.3)$$

$$U \frac{\partial U}{\partial X} + V \frac{\partial U}{\partial Y} = U_e \frac{dU_e}{dX}. \quad (1.4)$$

The "compressible" and the "incompressible" quantities (capital letters) are related in the following way:

— velocity:

$$u = \frac{a_e}{a_{te}} U.$$

— Mach number:

$$M_e = \frac{U}{a_{te}},$$

— momentum thickness:

$$\theta = \frac{\rho_{te} a_{te}}{\rho_e a_e} \Theta, \quad (1.5)$$

— shape parameter:

$$H = \bar{H} + \frac{\gamma-1}{2} M_e^2 (\bar{H} + 1). \quad (1.6)$$

It is to be noticed that the shape parameter \bar{H} , computed with the transformed thicknesses, differs from the usual "incompressible" shape parameter H_i defined by:

$$H_i = \int_0^\delta \left(1 - \frac{u}{u_e}\right) dy / \int_0^\delta \frac{u}{u_e} \left(1 - \frac{u}{u_e}\right) dy.$$

Thereafter, two integral equations are deduced from the transformed equations 1.3 and 1.4.

The first is the Von Kármán equation without the skin friction term:

$$\frac{d\Theta}{dX} + \Theta \frac{2 + \bar{H}}{U_e} \frac{dU_e}{dX} = 0 \quad (1.7)$$

The second, following the general integral formulation developed by Teterin and Chia Chiao Lin (1951) is obtained by multiplying 1.4 by the normal co-ordinate Y before integration between $Y=0$ and $Y=\delta$. Furthermore, if a *power-law velocity profile family* is assumed, one obtains the equation:

$$\frac{d\bar{H}}{dX} = - \frac{\bar{H}(\bar{H}^2 - 1)(\bar{H} - 1)}{2} \frac{1}{U_e} \frac{dU_e}{dX}. \quad (1.8)$$

Knowing that $U_e = a_{te} M_e$, Eqs. 1.7 and 1.8 can be formally integrated to give the following relations which link the values after (2) and before (1) the pressure discontinuity:

$$\frac{M_{e2}}{M_{e1}} = \frac{f(\bar{H}_2)}{f(\bar{H}_1)}, \quad (1.9)$$

$$\frac{\Theta_2}{\Theta_1} = \frac{g(\bar{H}_2)}{g(\bar{H}_1)}, \quad (1.10)$$

where $f(\bar{H})$ and $g(\bar{H})$ are the functions:

$$f(\bar{H}) = \frac{\bar{H}^2 \exp[1/(\bar{H}+1)]}{(\bar{H}^2 - 1)^{1/2} (\bar{H} + 1)},$$

$$g(\bar{H}) = \{(\bar{H}^2 - 1)^{3/2} (\bar{H} + 1) \exp[-1/(\bar{H} + 1)]\} / \bar{H}^4.$$

Application of this method is straightforward and very rapid since the solution is explicit and expressed by analytic forms: initial values H_1 , θ_1 being given, along with the Mach number M_{e1} , one computes first \bar{H}_1 and Θ_1 by 1.5 and 1.6. Then, knowing the downstream Mach number M_{e2} ; \bar{H}_2 and Θ_2 are deduced from 1.9 and 1.10. Finally, formulae 1.5 and 1.6 give the "compressible", or true downstream quantities H_2 and θ_2 .

Since viscous terms are entirely neglected, the method does not indicate any direct influence of the Reynolds number, except via the value of the incompressible shape parameter H_{i1} which, indeed, is a function of the local Reynolds number (see Section 1, in Part I).

The authors applied their analysis to predict the shock-induced separation limit by simply letting the limit value for \bar{H}_2 , corresponding to incipient separation, be equal to 2.2. Thus, for a given upstream shape parameter \bar{H}_1 , it is possible by using Eq. 1.9 to compute the Mach number ratio M_{e2}/M_{e1} , which leads to separation. For a form factor $\bar{H}_1 = 1.286$, which corresponds to a *transformed* seventh-power law velocity profile, it has been found that $M_{e2}/M_{e1} = 0.762$. In fact, as has already been pointed out, \bar{H} does not coincide with the "true" shape parameter H_p . Thus a more rigorous application of the method should take this fact into account in order to predict separation. Nevertheless, the conclusion drawn by the authors remains valid: the lower the form factor H_p , the greater must be the pressure rise capable of provoking separation. This tendency has been wholly confirmed by experiments at sufficiently high Reynolds numbers (see Section 3.8 of Part I).

Applications of Reshotko and Tucker's analysis are presented in Figures 1.1 and 1.2. They deal with oblique shock reflection for varying primary deflection angle $\Delta\phi$ at a constant upstream Mach number $M_0 = 1.92$. The "jumps" in the boundary-layer momentum thickness θ (Fig. 1.1) and shape parameter H_i (Fig. 1.2) are well predicted as long as the incident shock intensity is not too high. The example of $\Delta\phi = 6.3$ deg. nearly corresponds to Incipient Separation. In this situation, the present model underestimates the change in the boundary-layer properties. Also, in Figure 1.2, an empirical formula is given to represent the "relaxation" of H_i downstream of the shock impingement. Another example of application of Reshotko and Tucker's analysis is given in Section 3.8.5 of Part I as curves giving the Incipient Separation limit in supersonic flows.

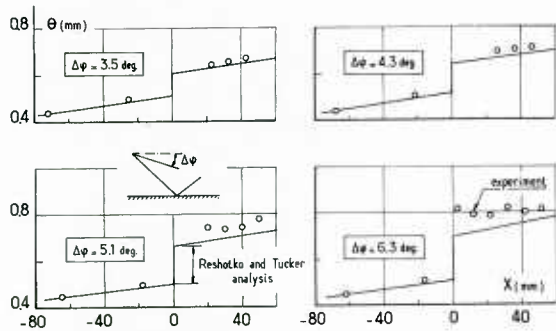


Fig. 1.1 — Prediction of boundary-layer momentum thickness variation in a shock reflection — $M_0 = 1.92$; $R_{\delta_0} = 0.85 \times 10^5$.

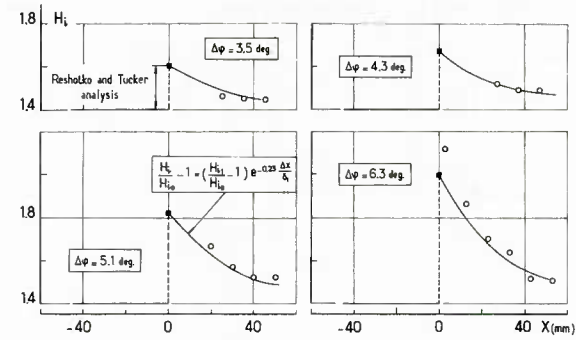


Fig. 1.2 — Prediction of boundary-layer shape parameter variation in a shock reflection — $M_0 = 1.92$; $R_{\delta_0} = 0.85 \times 10^5$.

Gadd's method (1961). — In 1961, Gadd proposed quite a thorough analysis of the shock turbulent boundary-layer interaction problem in transonic flows. In fact, this analysis pertains also to coupling methods or to analytical methods since its aim is to compute both the boundary-layer and the external inviscid flow according to an interactive technique. However, we have decided to present it in this section because one of its essential merits was to propose a simple method for calculating the effects of the sharp adverse pressure gradient on the velocity profile of a turbulent boundary-layer.

We will be very brief concerning the calculation of the part of the flow considered to be inviscid since much more sophisticated methods are now available. In Gadd's very simplified analysis, the interaction domain is divided into an upstream region and a downstream region. The upstream part extends from the undisturbed initial state to the shock position. There, the boundary-layer thickening induces compression waves which propagate into the supersonic flow. This compression wave region is of the simple-wave type, with the Mach waves emanating from the edge of the boundary-layer intersecting the shock-wave and being terminated by it (see Fig. 1.3). This terminating shock is vanishingly weak at the edge of the boundary-layer, so that the latter is not called upon to support any discontinuous jump of pressure.

The downstream part of the interaction extends from behind the shock to downstream infinity. The two inviscid flowfields are computed by making crude simplifying assumptions in order to obtain rather simple equations which will not be given here.

The interacting dissipative layer is computed by assuming that the static pressure is transversally constant. Following the basic principles of other analyses, two equations are used. The first one is obtained by assuming that *the rate of entrainment of fluid into the boundary-layer from the external flow is the same as just upstream of the region of interaction* (this rate is assumed to be equal to zero in the upstream part of the interaction, which is the zero-entrainment hypothesis of many global analyses.)

The second equation is *the Mean Flow Kinetic energy equation* (see Section 2.2.1 below) written under the assumption that the non-dimensional shear-work integral $\int_0^\delta \frac{\tau}{\rho_e u_e^2} \frac{\partial}{\partial y} \left(\frac{u}{u_e} \right) dy$ remains constant in the interaction region.

The problem is "closed" by supposing that the boundary-layer velocity distributions can be represented by *power-law profiles* throughout the interaction domain.

Thus, for a prescribed distribution of Mach number at the boundary-layer edge, the problem has two unknown quantities (the power-law exponent n and the boundary-layer thickness δ) which can be computed by solving the above two equations.

The skin friction coefficient (the knowledge of which is of interest for predicting, incipient separation) is computed by using the boundary-layer momentum integral equation.

The simultaneous solving of these boundary-layer equations and of the inviscid flow equations, along with a matching condition written at δ , enables Gadd to compute the whole interaction process. In particular, he could deduce from his calculations a limit for Incipient Shock Induced Separation.

This theory is not in very good quantitative agreement with experiment, mainly because of the rather crude simplifications involved in the transonic inviscid flow calculation. However, it has played an important role in the development of ideas which led to the much more advanced analytical methods which are presently used to compute transonic shock-wave/turbulent boundary-layer interaction (see Section 4 below).

Green's method (1969). — This author does not employ a compressibility transformation but solves the problem in natural co-ordinates.

A first relation is derived from the Von Kármán integral equation written with a skin friction coefficient C_f equal to zero:

$$\frac{d\theta}{dx} = -\frac{\theta}{u_e} (H+2) \frac{du_e}{dx} - \frac{\theta}{\rho_e} \frac{dp_e}{dx}.$$

This may be rearranged:

$$d(\ln \rho_e u_e \theta) = -(H+1) d(\ln u_e). \quad (1.11)$$

A second equation is obtained by assuming that *the boundary-layer mass flow remains unchanged* during the interaction process (zero entrainment hypothesis). This is simply expressed by:

$$\frac{d}{dx} \left(\int_0^\delta \rho u dy \right) = 0. \quad (1.12)$$

Introducing the new "shape parameter" H_1 defined by:

$$H_1 = \frac{1}{\theta} \int_0^\delta \frac{\rho u}{\rho_e u_e} dy = \frac{\delta - \delta^*}{\theta}$$

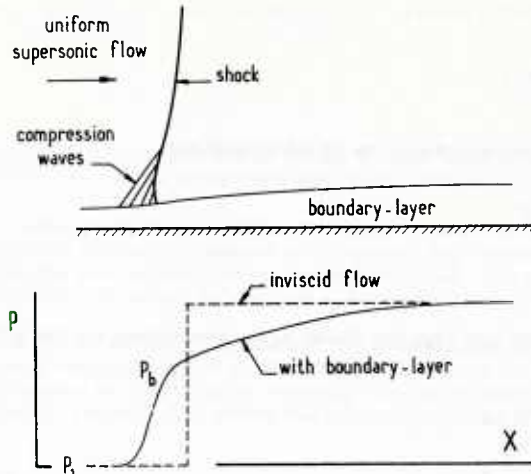


Fig. 1.3 – Gadd's theory – Flow pattern and pressure distribution.

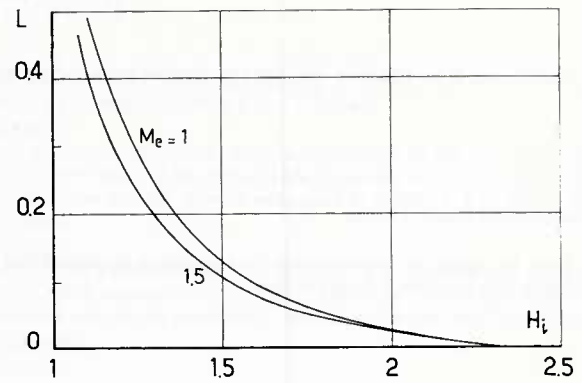


Fig. 1.4 – Panaras' theory – Shape factor L variation.

and taking 1.11 into account, 1.12 is written:

$$d(\ln H_1) = (H+1) d(\ln u_e). \quad (1.13)$$

The conventional shape-parameter $H = \delta^*/\theta$ which appears in equations 1.11 and 1.13 is not really representative of the shape of the velocity profile (contrary to H_i), since it is a strong function of the Mach number M_e .

A more convenient parameter, which depends only slightly on the Mach number, is the transformed shape parameter:

$$H^* = \left(H - \frac{\gamma-1}{2} M_e^2 \right) / \left(1 + \frac{\gamma-1}{2} M_e^2 \right).$$

For flows with constant stagnation temperature, H^* is identical to Reshotko and Tucker's "incompressible" shape parameter \bar{H} (see above).

Finally, equations 1.11 and 1.13 take the following forms:

$$\begin{cases} d(\ln \rho_e u_e \theta) = -(H^* + 1) d(\ln M_e), \\ d(\ln H_1) = (H^* + 1) d(\ln M_e). \end{cases} \quad (1.14)$$

This system can be solved for the downstream values θ_2 and H_2^* provided that a law $H_1 = H_1(H^*, M_e)$ is available. Such a law can be empirical or computed from velocity profiles belonging to a one parameter family (Coles, 1956; Mellor and Gibson, 1966; Michel et al., 1969; Alber, 1971). In fact, experimental results as well as calculations using power-law profiles, have shown that H_1 varies only slightly with the Mach number, so that, for a first approximation, H_1 may be taken as a unique function of H^* . If this simplification holds true, integration of system 1.14 between State 1 and final State 2 leads to relations of the form:

$$\begin{aligned} H_2^* &= h\left(\frac{M_{e2}}{M_{e1}}, H_1^*\right), \\ \left(\frac{\rho_e u_e \theta}\right)_2 &= k\left(\frac{M_{e2}}{M_{e1}}, H_1^*\right). \end{aligned}$$

Panaras' method (1976, 1980, 1981). — More recently, a method was proposed by Panaras which uses the following simplified integral equations:

- momentum; or Von Kármán equation;
- Mean Flow Kinetic Energy equation (see Section 2.1 below)

$$\frac{d\theta^*}{dx} + \theta^* \left(\frac{3}{u_e} \frac{du_e}{dx} + \frac{1}{\rho_e} \frac{d\rho_e}{dx} \right) + 2 \frac{\theta^{**}}{u_e} \frac{du_e}{dx} = 0, \quad (1.15)$$

where:

$$\theta^* = \int_0^\delta \frac{\rho u}{\rho_e u_e} \left(1 - \frac{u^2}{u_e^2} \right) dy,$$

is the boundary-layer energy thickness and:

$$\theta^{**} = \int_0^\delta \frac{\rho u}{\rho_e u_e} \left(\frac{h}{h_e} - 1 \right) dy$$

is the enthalpy thickness.

Pinckney's method for oblique shock-wave (1965). — This method, as well as the next one, were devised essentially to compute the effects resulting from the reflection of an oblique shock-wave for conditions entirely supersonic. In fact, Pinckney's method does not use a control volume approach. Nevertheless, we think that it is more suitable to consider it in the present Section than among boundary-layer analyses.

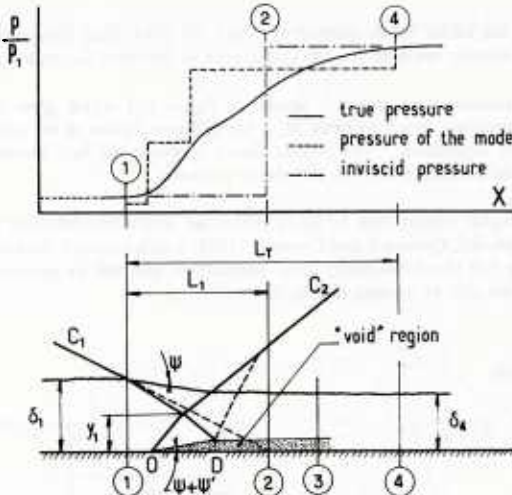


Fig. 1.7 — Pinckney's model for oblique shock reflection.

The aim of this method is to introduce a simplified shock pattern which resembles the one observed on schlieren photographs and to treat the boundary-layer as a one-dimensional supersonic stream in a manner similar to Hammitt's analysis. Figure 1.7 is a typical schematic flowfield. The incident shock C_1 enters the boundary-layer at Station 1. There, the true horizontal velocity distribution is replaced by a *power law profile* whose exponent n is determined in such a way that the approximate distribution yields the same mass flow as the real one (the thickness δ_1 and the Mach number M_{e1} being identical). Then the boundary-layer flow (whose velocity distribution is now depicted by a power-law profile) is represented by a one-dimensional stream which has the same thickness δ_1 and the same mass, momentum and energy than the real flow. If E designates quantities pertaining to the one-dimensional stream, we must have the following relations:

$$\rho_E u_E = \int_0^1 \rho u d\left(\frac{y}{\delta}\right) = m, \quad (1.21)$$

for the mass;

$$p_E + \rho_E u_E^2 = p_e + \int_0^1 \rho u^2 d\left(\frac{y}{\delta}\right) = p_e + \varphi, \quad (1.22)$$

for the momentum;

$$\rho_E u_E C_p T_{t_E} = \int_0^1 \rho u h d\left(\frac{y}{\delta}\right) + \frac{1}{2} \int_0^1 \rho u^3 d\left(\frac{y}{\delta}\right), \quad (1.23)$$

for the energy.

It is to be noticed, that:

$$\frac{m}{m_e} = \int_0^1 \frac{\rho u}{\rho_e u_e} d\left(\frac{y}{\delta}\right); \quad \frac{\varphi}{\varphi_e} = \int_0^1 \frac{\rho u^2}{\rho_e u_e^2} d\left(\frac{y}{\delta}\right); \quad \frac{\eta}{\eta_e} = \int_0^1 \frac{\rho u^3}{\rho_e u_e^3} d\left(\frac{y}{\delta}\right),$$

can be computed once for all as functions of the exponent n and of the external Mach number M_e , if the wall is adiabatic (a modified Crocco's law is then used). Solving 1.21 to 1.23 we can compute the equivalent Mach number M_E which is given implicitly by:

$$f(M_E) = \frac{M_e (m/m_e)^{1/2} (n/(n+1) + (\gamma-1)/2 M_e^2 \eta/\eta_e)^{1/2}}{(1 + \gamma M_e^2 \varphi/\varphi_e)}, \quad (1.24)$$

where:

$$f(M_E) = M_E \left(1 + \frac{\gamma-1}{2} M_E^2 \right)^{1/2} / (1 + \gamma M_E^2).$$

The pressure p_E is then calculated by:

$$\frac{p_E}{p_e} = (1 + \gamma M_e^2 \varphi/\varphi_e) / (1 + \gamma M_E^2). \quad (1.25)$$

The fictitious pressure p_E differs from the real pressure p_e , but in fact, the difference is generally small.

Knowing the properties of the incoming one-dimensional stream, we can then proceed to the construction of the shock pattern.

For a given value of the deflection ψ_e induced in the free stream by the incident shock C_1 , one chooses a value ψ of the deflection provoked by C_1 in the boundary-layer (ψ will be determined by a trial and error method). The reflected shock C_2 springs from the wall at point 0 which is upstream of the point where C_1 would impinge against the wall in the case of an inviscid flow. The deflection across C_2 is put equal to $\psi + \psi'$ where ψ' is an angle introduced to take into account the entrainment effects at the boundary-layer edge. Experimental data show that ψ' can be approximated by:

$$\begin{aligned}\psi' &= 2^\circ \quad \text{if } \psi \geq 3^\circ, \\ \psi' &= \frac{2}{3}\psi \quad \text{if } \psi < 3^\circ\end{aligned}$$

The origin 0 of shock C_2 is positioned so that the incident and the reflected shocks intersect at a point I whose height Y_1 has a well determined value. The crux of the treatment is an empirical correlation giving Y_1 by a relation of the form $Y_1/L_1 = f(\Delta p/q_{e1})$ where:

- Δp is the total pressure jump associated with the reflection;
- q_{e1} the dynamic pressure of the upstream flow;
- L_1 a length defined on Figure 1.7.

Now, it is supposed that downstream of I the flows which were previously above and below I have undergone identical deflections. If these flows have the same Mach number (as is supposed), then their direction must be ψ' . Thus, it is necessary to impose at D , an expansion of angle ψ' in order to make the flow parallel to the wall. (In fact, the difference ψ' is small and is an empirical refinement of the flow model; the expansion ψ' is a geometric requirement and not the constant pressure reflection of the incident shock.)

It appears that the geometric construction which has been made implies the existence of a void region downstream of 0.

After the shock interaction, the pressure in the one-dimensional equivalent flow is assumed constant, and the pressure p_{e3} in a Section 3, sufficiently far downstream is given by:

$$\frac{p_{e3}}{p_{e1}} = \frac{p_{e1} p_{e3} p_{e3}}{p_{e1} p_{e1} p_{e3}}. \quad (1.26)$$

The ratio $\frac{p_{e3}}{p_{e1}}$ results from shock calculation, and $\frac{p_{e1}}{p_{e1}}$ and $\frac{p_{e3}}{p_{e3}}$ are computed by relation 1.25

The right ψ deflection is obtained when the pressure p_{e3} given by 1.26 equals the pressure corresponding to the reflection of shock C_1 in the absence of boundary-layer. Thus, it is postulated that the pressure downstream of the interaction tends towards the perfect fluid solution.

When the solution has been converged, the boundary-layer downstream characteristics are computed at a Station 4 whose distance L_T results from an empirical correlation: $L_T/\delta_1 = f(M_{e1}, \psi)$. There, it is supposed that the one-dimensional mass flow is equal to the mass flow at D through a section including the height of a void region, which leads to the relation:

$$(p_E u_E)_D \delta_D = (p_E u_E)_4 \delta_4. \quad (1.27)$$

Knowing $M_{e4} = M_{e3}$, $p_{e4} = p_{e3}$ and M_{e4} , p_{e4} (given by the perfect fluid calculation) equation 1.24 allows the calculation of n ; that is to say, defines the shape of the velocity distribution. The thickness δ_4 is given by equation 1.27.

Seebaugh, Paynter and Childs' method for oblique shock-wave. (1968). — In 1968, Seebaugh *et al.* proposed a rather simple model for predicting shock reflection in supersonic flows. In contrast with the previous analysis, their method relies completely on control volume arguments. Its objective is to predict the change in boundary-layer properties during the shock reflection, including the effect of boundary-layer bleed. Originally, velocity distributions were represented by power-law profiles and a Dorodnitsyn-Howarth transformation was used in order to simplify the equations by reducing their density dependence. And in fact, the analysis led to simple algebraic equations which could be easily solved.

In a subsequent analysis, Mathews (1969) used a law of the wall/law of the wake profile to replace the power-law profile. Mathews also allowed for boundary-layer mass entrainment in the interaction region. More recently Sun and Childs (1974, 1976), further improved the method by introducing a more refined wall-wake velocity profile for turbulent isoenergetic compressible boundary-layer flow. These authors have treated axisymmetric as well as two dimensional flows. They have also considered the case of successive oblique shock-wave/turbulent boundary-layer interactions. Such interactions may occur, for example, in engine inlets of supersonic aircraft.

Here we will present only the most recent version of Seebaugh's method, but, for the sake of simplicity, we will restrict ourselves to the two-dimensional case, extension to an axisymmetric situation being rather straightforward. The flow model used in the analysis is shown in Figure 1.8. The incoming shock C_1 meets the boundary-layer edge at the Station 1 where all the conditions are assumed to be known. The reflected shock C_2 emerges from the boundary-layer at the Station labelled 3. Surface 2 is the stream surface of the inviscid flowfield which passes through the intersection of C_2 with the boundary-layer edge at Station 3. Note that Surface 2 intersects the incident shock-wave outside the boundary-layer edge. The distance Δ_E is introduced to allow for mass entrainment into the boundary-layer during the course of interaction.

Considering the control volume drawn in Figure 1.8, the equation for the conservation of mass may be expressed in the form:

$$\int_0^{\delta_3} \rho u dy = \int_0^{\delta_1 + \Delta_E} \rho u dy + \dot{m}_B, \quad (1.28)$$

while the x -momentum equation may be written:

$$\int_0^{\delta_3} \rho u^2 dy = \int_0^{\delta_1 + \Delta_E} \rho u^2 dy + p_1 (\delta_1 + \Delta_E) - p_3 \delta_3 - \int_{\delta_1 + \Delta_E}^{\delta_3} p_2 dy - L \bar{\tau}_w + I_{Bx}, \quad (1.29)$$

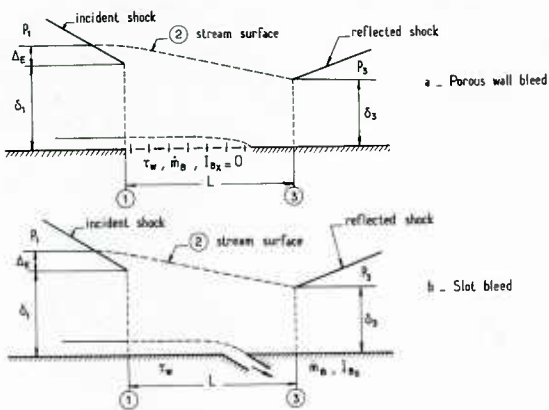


Fig. 1.8 – Seebaugh et al.'s model for oblique shock reflection.

where $\bar{\tau}_w$ is the average wall shear stress between Stations 1 and 3 ($\bar{\tau}_w = \frac{1}{2}(\tau_{w1} + \tau_{w3})$), \dot{m}_B the boundary-layer mass bleed rate, I_{Bx} the x -momentum of the bleed flow and L the shock-wave/boundary-layer interaction length. The pressure terms are determined from the inviscid flow calculation; p_1 and p_3 are assumed constant but p_2 may vary along the stream surface 2 if the flow is not uniform. The distance Δ_E is determined by assuming an entrainment rate equal to that for the flow upstream of the interaction. It is to be noticed that the introducing of Δ_E makes it necessary to use an iterative process to construct the stream surface 2.

The velocity distributions at Stations 1 and 3 are given by a wall-wake velocity profile expressed in the form (Sun and Childs, 1973):

$$\frac{u}{u_e} = \frac{1}{\sqrt{\sigma}} \sin \left\{ \arcsin \sqrt{\sigma} \left[1 + \frac{1}{k} \left(\frac{u_r}{u_e^*} \ln \frac{y}{\delta} + 2 \left(1 - \frac{y}{\delta} \right)^{1/2} - 2 \ln \left(1 + \left(1 - \frac{y}{\delta} \right)^{1/2} \right) - \frac{\Pi}{k} \frac{u_r}{u_e^*} \left(1 + \cos \frac{\pi y}{\delta} \right) \right] \right\}, \quad (1.30)$$

where:

$$\Pi/k = \frac{1}{2} \left\{ \left(u_e^*/u_r \right) - \left(1/k \right) \ln \left(\delta u_r / v_w \right) - 5.1 + 0.614/k \right\}.$$

In these expressions:

$$\sigma = \frac{\gamma - 1}{2} M_e^2 \left(1 + \frac{\gamma - 1}{2} M_e^2 \right);$$

$k = 0.4$ (Von Kármán constant);

u_e^* = van Driest's generalized velocity;

v = kinematic viscosity;

u_r = friction velocity;

Π = coefficient of the Coles wake function.

For a given external Mach number M_e , the profile defined by equations 1.30 is a function of two parameters: the Reynolds number and a "shape parameter" which can be u_r/u_e^* , for example.

The first step of the method consists in finding the best representation of the given boundary-layer distribution at Station 1 by means of equation 1.30. This is done by a least-squares fit and yields τ_{w1} .

Then, knowing the mass bleed rate \dot{m}_B , and with a suitable representation of the magnitude of I_{Bx} , equations 1.28 and 1.29 constitute a system for the two unknowns δ_3 and τ_{w3} (which define the shape of the profile at Station 3). This system is solved by a suitable iterative method. It is obvious that the x -momentum of the bleed flow depends on the manner in which the bleed flow is accomplished. The analysis has been applied to three bleed models: porous wall suction, slot suction and scoop suction (see Fig. 1.8).

For the porous wall model, the x -momentum of the bleed flow I_{Bx} is neglected. With slot suction, I_{Bx} is assumed equal to the momentum of the extracted fluid when it enters the control volume, i.e.:

$$I_{Bx} = \int_0^{\delta_B} \rho u^2 dy,$$

where δ_B is determined from:

$$\dot{m}_B = \int_0^{\delta_B} \rho u dy.$$

For scoop suction, the control volume encloses only that part of the boundary-layer which passes downstream.

The method has been generalized in order to compute successive oblique shock reflections according to the model shown in Figure 1.9. Regions extending from Station 1 to Station 3 and from Station 5 to 7 are computed by using the control volume analysis; between 3 and 5, a "classical" boundary-layer calculation is made. The wall static pressure distribution needed for this calculation is provided by an inviscid flow solution which is obtained in such a way as to allow for the effects of the first shock/boundary-layer interaction.

An example of application of Sun and Childs' method is given in Figure 1.10. It corresponds to two successive interactions provoked by the impingements of two oblique shock-waves generated by a double cone centerbody, the flow being axisymmetric. For this case, the predicted boundary-layer properties are in good agreement with the experimental values.

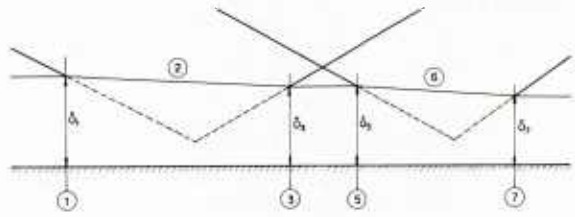


Fig. 1.9 – Sun and Childs flow model for successive oblique shock reflections.

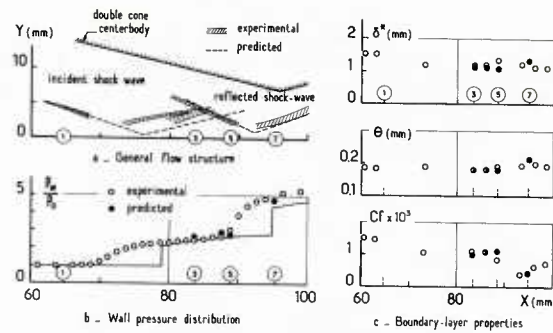


Fig. 1.10 — Successive oblique shock-wave interactions
Sun and Childs flow model.

Délery's method for transonic interaction (1977). — The two former control volume methods are in fact applicable to entirely supersonic situations where an oblique shock meets a turbulent boundary-layer. At sufficiently high Mach number, in the absence of extended separation, and with the condition that no shock detachment or Mach stem phenomena occur, it is a rather simple task to construct a realistic inviscid shock system associated with the interaction. Furthermore, the initial and the downstream states may generally be defined unambiguously.

In transonic flows, the situation is not so clear: the inviscid shock structure depends strongly on viscous interaction effects and the scheme of a shock wave normal to the wall (as it would be in perfect fluid flow) is far from reflecting the reality. In fact (see Section 2 of Part I), the quasi normal shock forms at a certain distance from the wall. Near the surface, the viscous displacement effect entails a progressive compression through converging supersonic compression waves which coalesce into the transonic shock.

The location of the initial station of a jump method is always well defined, since it is generally taken at the point where the wall static pressure starts to rise. By contrast, the choice of the downstream station is not so obvious. Indeed, the wall pressure distribution generally shows a continuous and rather slow increase after the very steep compression associated with the supersonic part of the interaction (i.e. the evolution from the initial supersonic state, of Mach number M_{e1} , to a locally sonic situation where $M=1$; see Section 2.7.2 of Part I on scaling laws in transonic interactions). Downstream of the point where $M=1$, the flow has an elliptic character and consequently depends strongly on conditions far from the interaction domain (trailing edge flow for an airfoil, width to length ratio in the case of a channel flow, etc.). Thus it doesn't seem feasible to construct a general "a priori" model of transonic interactions extending to downstream subsonic conditions. Adoption of a final subsonic state necessarily leads to specific flow situations.

The simplified boundary-layer integral methods may be applied to interactions in transonic flows. They generally give good quantitative results as long as the shock is not too strong. But when the upstream Mach number goes beyond 1.2, they systematically underpredict the rapid boundary-layer growth which occurs between $M_{e1}=1.2$ and the Mach number leading to Incipient Shock Induced Separation.

The method presented here has been developed in order to improve the prediction in the Mach number range extending from $M_{e1}=1.2$ to Incipient Separation, this domain being of great interest for practical applications.

In this method, one considers:

- an upstream State 1 corresponding to the flow situation in front of the shock;
- a downstream State 2 defined somewhere behind the shock and which will be specified later.

Let $M_{e1}, p_1, \rho_{e1}, u_{e1}$ be the conditions at boundary-layer edge in 1 and $M_{e2}, p_2, \rho_{e2}, u_{e2}$ corresponding values in 2.

Applying conservation relations between 1 and 2 one obtains:

- for the mass:

$$\int_0^{\delta_2} \rho u dy = \int_0^{\delta_1} \rho u dy + K_m \rho_{e1} u_{e1} (1) (\delta_2 - \delta_1), \quad (1.31)$$

- for the x -momentum (the effect of wall shear stress is neglected):

$$\int_0^{\delta_2} \rho u^2 dy = \int_0^{\delta_1} \rho u^2 dy + K_m \rho_{e1} u_{e1}^2 (2) (\delta_2 - \delta_1) - \delta_2 (p_2 - p_1). \quad (1.32)$$

The terms labelled 1 and 2 represent an overall mass entrainment effect taking place during the interaction process. K_m is an empirically determined coefficient.

Equations 1.31 and 1.32 with $K_m=1$ are identical to the first two equations used by Klineberg (1968) to compute the supercritical-subcritical jump of his viscous-inviscid interaction theory. Equation 1.31 written with $K_m=0$ corresponds to the zero entrainment hypothesis.

In fact, the mass flux does not remain constant during the interaction process. This is demonstrated by Figure 1.11 which shows measured evolutions of transonic shock-wave/boundary-layer interactions of various strength. One generally observes a substantial increase of the mass except in the case of very weak shocks. A careful processing of these experimental data (obtained by using holographic interferometry, thus without perturbation of the flow fields) allowed the determination of K_m . The values obtained for K_m are plotted in Figure 1.12 as functions of the Mach numbers ratio M_{e2}/M_{e1} . They exhibit a rather large scatter, mainly due to the difficulty of defining the physical thickness δ of the boundary-layer. A constant average value $K_m=0.5$ is proposed. It corresponds to an incompressible shape parameter $H_i=1.24$. In fact, application of this jump method has shown that K_m is a function of H_i . This dependence may be taken into account by the simple formula:

$$K_m = 0.5 H_i / 1.24$$

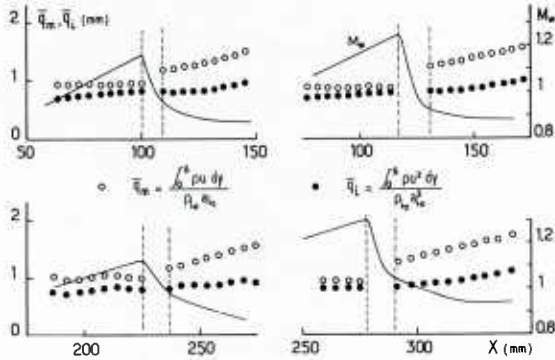


Fig. 1.11 – Mass flux and momentum flux variation during a transonic shock/boundary-layer interaction.

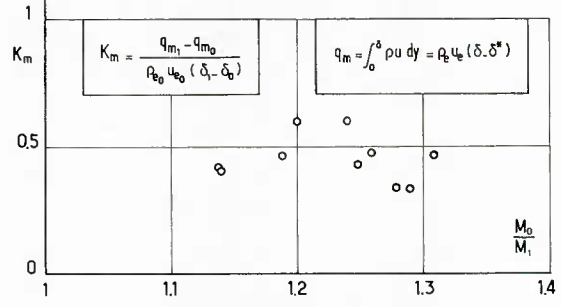


Fig. 1.12 - global entrainment coefficient in a transonic interaction without separation.

For numerical solution, equations 1.31-1.32 are more conveniently written in the following forms:

$$\rho_{e2} u_{e2} (\delta_2 - \delta_2^*) = \rho_{e1} u_{e1} (\delta_1 - \delta_1^*) + K_m \rho_{e1} u_{e1} (\delta_2 - \delta_1), \quad (1.33)$$

$$\rho_{e2} u_{e2}^2 (\delta_2 - \delta_2^* - \theta_2) = \rho_{e1} u_{e1}^2 (\delta_1 - \delta_1^* - \theta_1) + K_m \rho_{e1} u_{e1}^2 (\delta_2 - \delta_1) - \delta_2 (p_2 - p_1). \quad (1.34)$$

If the values of the external Mach numbers M_{e1} and M_{e2} are specified, equations 1.33-1.34 which contain three unknown quantities (δ_2 , δ_2^* , θ_2) may be solved, provided that the boundary-layer velocity profiles belong to a family depending on only one shape parameter. The adopted family is represented by an equation similar to Coles (1956) law-of-the-wall/law-of-the-wake (for more details, see Section 1.1 of Part I). It is supposed that there is no Mach number effect on velocity profile shape, which is well verified in the transonic domain and even for Mach numbers ranging up to 2. This fact is demonstrated by Figure 1.13 which shows a comparison between adopted profiles and velocity distributions measured downstream of a transonic shock wave.

In the application of the present discontinuity analysis, the downstream state (2) is defined as the location where the *sonic condition* is reached, i.e. $M_{e2}=1$. This choice is dictated by the fact that only the supersonic part of the interaction obeys similitude rules of the “free interaction” type, as defined by Chapman (1958) (see Section 3.6 of Part I).

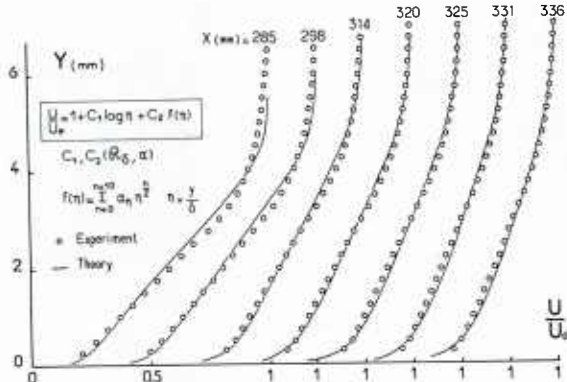


Fig. 1.13 – Velocity profiles representation in a transonic interaction without separation.

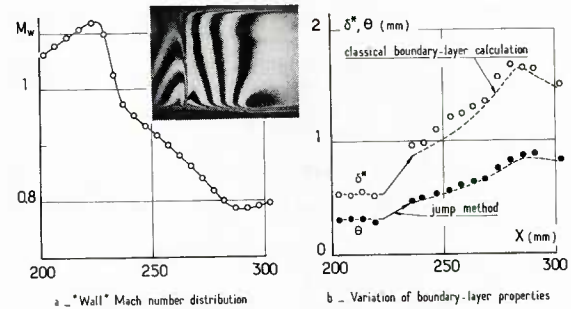


Fig. 1.14 – Transonic interaction

Examples of application of Delery's jump method.

The input of the calculation is: the Mach number M_{e1} and the boundary-layer properties at Station 1 (usually the thicknesses δ_1^* and θ_1 plus the shape parameter H_{i1}).

The downstream Mach number M_{e2} being given, equations 1.33-1.34 are solved taking the velocity profile equation into account to obtain the boundary-layer conditions at Station 2 (displacement and momentum thickness, shape parameter, skin-friction). These conditions can be used to initiate a “classical” boundary-layer calculation downstream of the shock quasi-discontinuity.

The length L^* of the interaction region, i.e. the stream-wise distance between Stations 1 and 2, may be obtained from the empirical correlation law (see Section 2.7.2 of Part I):

$$L^* = 70 (H_{i1} - 1) \delta_1^*.$$

Some applications of the above method have already been given in Section 2.7.3 of Part I to illustrate the jump in the boundary-layer momentum and displacement thicknesses throughout transonic interaction. Further examples relative to interactions occurring in a transonic channel are presented in Figure 1.14. Downstream of the jump region, the boundary-layer has been computed by an integral method using the Mean Flow Kinetic Energy Equation (see Déler's method in Section 2.2 below).

The existence of a correlation law for the supersonic interaction length L^* makes it possible to develop a simplified theory for predicting *Incipient Separation in transonic flows*. This theory will be presented in this section, although it is not exactly a control volume type analysis.

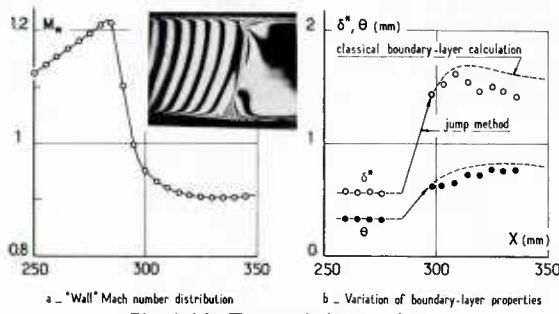


Fig. 1.14 - Transonic interaction
Examples of application of Delery's jump method

The present theory rests on the following basic assumptions :

- the point of Incipient Separation necessarily appears at the end of the supersonic part of the compression; i.e. coincides with an outer state locally sonic. The separation limit is thus defined by the conditions of coincidence of the points where the wall shear-stress τ_w vanishes and where $M=1$. This very heuristic approach is based on a number of experimental observations (see Section 2.7 of Part I).
- the evolution of the dissipative layer submitted to the compression from M_{e1} to $M=1$ is represented by means of the classical first order boundary-layer equations;
- in these equations, the Reynolds shear-stress is computed by an algebraic turbulence model calling upon the mixing-length concept (Michel et al., 1969).

The principle of the method is as follows. For given initial conditions H_{i1} and M_{e1} , the above correlation law for L^* provides the dimensionless extent L^*/δ_1^* of the interaction domain. Hence it is possible to deduce the Mach number distribution $M(X/\delta_1^*)$ in the supersonic part of the interaction this distribution being approximated by a linear law linking M_{e1} and $M=1$. Thereafter, starting from a suitable initial velocity profile at the origin of the interaction, the boundary-layer equations are integrated by using a finite difference method with the above Mach number distribution prescribed as the outer boundary condition along the boundary-layer edge. Due to the proximity of separation, this calculation must be made according to an *inverse procedure* in which the prescribed quantity is the wall shear stress streamwise distribution $\tau_w(X)$ (see Section 2.3 below). With this kind of procedure, the outer Mach number is the result of the calculation, thus in order to satisfy the given distribution $M(X/\delta_1^*)$, one must at each x -wise integration step iterate on τ_w until the outer Mach number resulting from the boundary-layer calculation coincides with the assigned value.

The shape factor H_{i1} and the Reynolds number R_{δ_1} being kept constant, a second iteration loop on the initial Mach number M_{e1} has to be made until assumption (i) above is verified.

The value of M_{e1} thus found gives the transonic shock strength leading to Incipient Separation. This theory is compared to experiment in Section 2.7.2 of Part I.

Baker's method for transonic interaction (1980). — This method has been specifically designed to predict turbulent boundary-layer development throughout a normal shock wave interaction. It has many points in common with Délery's analysis but incorporates refinements which allow, in particular, the prediction of the interaction length which is no longer an empirical input. It also claims to be able to predict boundary-layer characteristics at the end of a separated region.

Two kinds of control volume are used (see Fig. 1.15): one — CV1 — to model unseparated flow; the other — CV2 — to model the separated part of the flow.

The control volume CV1 is made up of two regions: an upstream region, of length l_1 , which originates at Station 1 where the wall pressure distribution starts to rise. It ends at Station 1' located at the intersection of the initial boundary-layer edge with the leading Mach wave of the compression wave system. In this part of the interaction domain, the thickness δ is assumed constant. The downstream region, of length l_2 , extends from Station 1' to Station 2. For flows without separation, Station 2 is at the point where the Mach number at the edge of the boundary-layer is equal to 1. If separation occurs, Station 2 is fixed at the separation point, and has to be determined in an iterative manner until the skin friction at Station 2 vanishes. Between Stations 1 and 2, the boundary-layer will be assumed to grow linearly with distance. Then, a further control volume — CV2 — is drawn between Station 2 and a downstream Station 3 which is made to coincide with the reattachment point. Between Stations 2 and 3, the boundary-layer is also presumed to grow linearly.

We will now present the analysis for CV1. Its application to CV2 entails only minor modifications which will be indicated later.

The following conservation equations are written:

— for mass:

$$\int_0^{\delta_2} \rho u dy = \int_0^{\delta_1} \rho u dy + \bar{\rho}_e \bar{u}_e \bar{C}_E l, \quad (1.35)$$

— for x-momentum:

$$\int_0^{\delta_2} \rho u^2 dy = \int_0^{\delta_1} \rho u^2 dy + p_1 \delta_1 - p_2 \delta_2 + \frac{1}{2} (p_1 + p_2) (\delta_2 - \delta_1) + \bar{\rho}_e \bar{u}_e^2 C_E l - \frac{1}{2} \bar{\rho}_e \bar{u}_e^2 \bar{C}_f, \quad (1.36)$$

In these equations: $l = l_1 + l_2$; $\bar{\rho}_e$ and \bar{u}_e are respectively average density and average velocity at boundary-layer edge; \bar{C}_E an average entrainment coefficient between Stations 1 and 2; and \bar{C}_f an average skin friction coefficient. Pressures p_1 and p_2 are assumed transversally constant and equal to the edge values. Coefficients \bar{C}_E and \bar{C}_f are approximated by the following formulae:

$$\bar{C}_E = \left[C_{E1} l_1 + \frac{1}{2} (C_{E1} + C_{E2}) l_2 \right] / l,$$

$$\bar{C}_f = \frac{1}{2} (C_{f1} + C_{f2}),$$

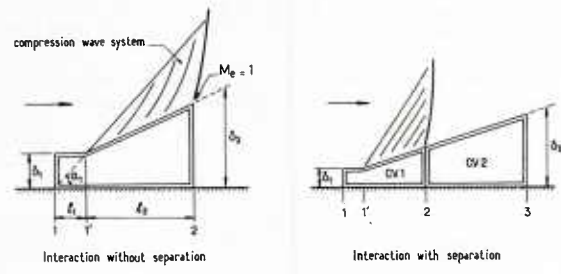


Fig. 1.15 – Baker's model for transonic shock-wave/boundary-layer interaction.

$\bar{\rho}_e$ and \bar{u}_e are defined like \bar{C}_e . Therefore, \bar{C}_e , $\bar{\rho}_e$, \bar{u}_e are weighted averages of their respective values between Stations 1 and 1', and their average values between Stations 1' and 2. (The inviscid flow is assumed to remain unchanged between Stations 1 and 1'.)

A geometric relation, necessary to compute l , is obtained by applying the *free interaction principle*. That is, the inviscid flow undergoes a simple wave compression along the boundary-layer displacement surface between Stations 1 and 2. Thus we have:

$$\frac{d\delta^*}{dx} = \tan(v_{e1} - v_e). \quad (1.37)$$

where v is the well known Prandtl-Meyer angle.

On a first approximation, equation 1.37 may be written:

$$\frac{\delta_2^* - \delta_1^*}{l_2} = \frac{1}{2} \tan(v_{e1} - v_{e2}), \quad (1.38)$$

Finally, the length l_1 will be given by:

$$l_1 = \delta_1 / \tan \alpha_1 \quad \text{where } \alpha_1 = \sin^{-1}(1/M_{e1}).$$

The system of equations 1.35-1.36 is "closed" by making the following assumptions:

- the boundary-layer velocity profiles are assumed to be of the *power-law* form;
- density throughout the boundary-layer is computed by using the Crocco relation between temperature and velocity;
- the formula of Green (1972) is used to specify the entrainment coefficient;
- the skin friction coefficient is determined from the Winter and Gaudet (1970) skin friction relations as modified by Green *et al.* (1973). However, an empirical correction had to be introduced to obtain better agreement with experiment in the "free interaction" region.

For a given initial state (upstream Mach number M_{e1} , boundary-layer velocity profile at Station 1) it is now possible to compute flow conditions at Station 2 and interaction length l .

If the skin friction at Station 2 is found negative, Station 2 is no longer determined by the condition $M_{e2}=1$, but has to be defined in an iterative manner until $C_{f2}=0$.

Afterwards, the previous analysis is applied to CV 2 (separated region) with the following adaptations:

- for CV 2 the "free interaction" principle does not apply. Thus, in order to compute the interaction length, it is necessary to prescribe the pressure distribution;
- the position of Station 3 is found in an iterative manner until the skin friction C_{f3} falls to zero; i.e., Station 3 becomes the reattachment position and the boundary-layer parameters are known at this point.

This analysis can be easily modified to represent effect of mass bleed at the wall (injection or suction). If the fluid is injected (extracted) perpendicular to the surface, equation 1.36 remains the same since there is then no streamwise change in the momentum flux. It is only necessary to add an extra term in the equation of conservation of mass 1.35 which will represent mass bleed rate (*see* Seebaugh *et al's* method above).

The author has also included in his analysis extra terms for modeling the outflow of mass and momentum from the sides of the control volume. Such an outflow would result from three dimensional effects. These correction terms are added in order to make more significant comparisons with experimental data distorted by three dimensional parasitic effects. The latter are due, in the main, to the interaction between the channel side wall boundary-layers and the shock system.

The present method relies on sound physical evidence for the modeling of the supersonic (or non-separated) part of the interaction. So it can be considered as a reliable and rather simple tool for predicting the overall flow properties in this region. Introduction of the skin friction is not essential for the calculation of the boundary-layer thickness at Station 2 since the contribution of C_f to the x -momentum balance is practically negligible. The main interest of knowing C_{f2} is to be able to predict Shock Induced Separation. However C_{f2} does not result from equation 1.36 but is deduced from the shape of the velocity distribution at Station 2.

Perhaps the weakest point of this method is the use of simple power-law profiles which seem inappropriate for representing highly retarded or separated boundary-layer flows.

The modeling of the separated flow (control volume CV 2) is much more tentative and far too coarse to give a realistic description of the flow phenomena.

Two applications of Baker's analysis are shown in Figure 1.16. They concern transonic interactions experimentally studied by Kooi (1978) (*see* Section 2.9 of Part I). The momentum thickness as well as the skin-friction coefficient are relatively well predicted but agreement for the thickness ratio $H=\delta^*/\theta$ is less satisfactory.

To conclude this Section on two-dimensional flows, Figure 1.17 shows a comparison of some of the above analyses. As suggested by Green (1969), the ratio $(\rho_e u_e \theta)_1 / (\rho_e u_e \theta)_2$ is plotted vs. the ratio of the upstream Mach number to the downstream Mach number M_{e1}/M_{e2} . Except for Panaras'method which overpredicts the shock effect, the various analyses are in close agreement with experiment for M_{e1}/M_{e2} less than 1.3. As the shock becomes stronger, they all tend to underpredict its effect, especially when the situation is close to Shock-Induced Incipient Separation. It should be said that the results plotted in Figure 1.17 do not display any influence of the initial shape parameter H_{i1} , which as we know plays a considerable role. Thus the present results are representative of an "average" value of H_{i1} close to 1.4.

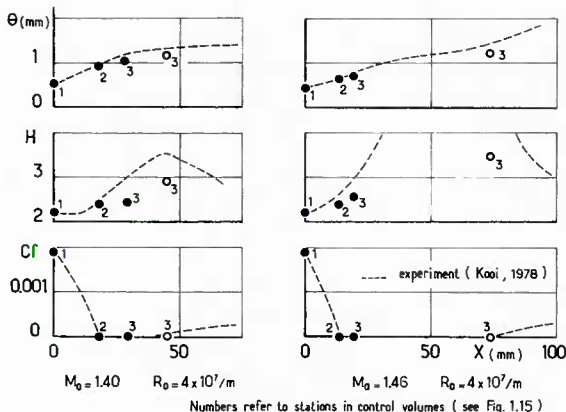


Fig. 1.16 – Transonic interaction – Examples of application of Baker's jump method.

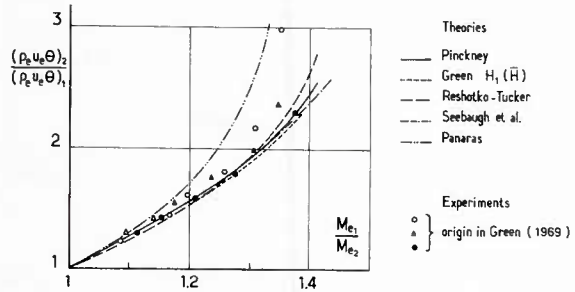


Fig. 1.17 – Comparison of different "jump" methods to predict the rise in boundary-layer momentum thickness.

1.3. – Three Dimensional Interactions

1.3.1. – General Comments

As we know, for 2-D boundary-layer the essential and more useful features of the flow are determined by the knowledge of 3 "integral" thicknesses; namely δ , δ^* and θ (other quantities of interest, like the skin-friction coefficient may be deduced from these thicknesses by *ad-hoc* relations). An assumption concerning the shape of the velocity distribution provides a link between δ , δ^* and θ so that for adiabatic flow, only two equations are needed to solve the problem.

In a 3-D isoenergetic boundary-layer flow, one generally considers the following integral thicknesses:

$$\begin{aligned}\delta_1^* &= \int_0^\delta \left(1 - \frac{\rho U}{\rho_e U_e} \right) dy, & \delta_2^* &= \int_0^\delta - \frac{\rho W}{\rho_e W_e} dy, \\ \theta_{11} &= \int_0^\delta \frac{\rho U}{\rho_e U_e} \left(1 - \frac{U}{U_e} \right) dy, & \theta_{22} &= \int_0^\delta - \frac{\rho W^2}{\rho_e U_e^2} dy, \\ \theta_{21} &= \int_0^\delta - \frac{\rho W U}{\rho_e U_e^2} dy, & \theta_{12} &= \int_0^\delta \frac{\rho W}{\rho_e U_e} \left(1 - \frac{U}{U_e} \right) dy,\end{aligned}$$

where U and W are respectively the streamwise and crosswise boundary-layer velocity components (i.e., U is the component in the direction of the local external velocity vector at the boundary-layer edge, W being directly perpendicular to U).

Thus the problem possesses 7 unknown quantities: the 6 above integral thicknesses, plus δ . (The skin-friction coefficients are supposed to be expressed as functions of the previous quantities by appropriate formulae.)

In the most usual approaches, integral as well as control volume, the number of unknown quantities is reduced to *three* by assuming that streamwise and crosswise velocity distributions are each defined by only one shape-parameter: one for the U component and one for the W component. In this manner, only three equations are needed to determine the remaining unknown quantities which are: one thickness and the two shape parameters. Most often, these equations are the streamwise and crosswise integral momentum equations plus the integral form of the continuity equation, also called the *entrainment equation* (see Section 2.4.2 below).

We have retained here three discontinuity analyses which have been proposed for treating 3-D shock-wave/turbulent boundary-layer interactions. The first two are simplified boundary-layer integral methods; the third is a control volume analysis.

These three methods share the following assumptions:

- (i) a velocity component in a direction parallel to the shock is assumed to exist, but the flow properties in a direction parallel to the incident shock are considered as constant (the flow is said to be *cylindrically symmetric*);
- (ii) the downstream inviscid flow properties are known from oblique shock theory;
- (ii) the flow is assumed *isoenergetic* (this assumption is not essential, it simply makes it possible to avoid considering the energy equation);
- (iv) viscous forces and mass entrainment have negligible effects.

Thus these methods differ from each other essentially by the velocity profile families adopted in order to derive the "closure" relationships.

In what follows, we consider the rectangular cartesian axes x and z as lying in the body surface, the z -axis being parallel to the *shock which is assumed to be rectilinear*. The y -axis is normal to the body surface. According to assumption (i), the formulations will be restricted to the case of cylindrically symmetric shock interactions, i.e., *conditions along the z-axis are assumed invariant*.

1.3.2. — Simplified Boundary-Layer Integral Methods

Cousteix and Houdeville's method (1976). — This method belongs to the class of simplified boundary-layer integral methods. Taking into consideration assumptions (i) to (iv) above, the boundary-layer integral equations take the following forms:

- momentum integral equation for the x -direction:

$$d(\rho_e U_e^2 \theta_{11}) + \delta_1^* \rho_e U_e dU_e = 0, \quad (1.39)$$

- momentum integral equation for the z -direction:

$$d(\rho_e U_e^2 \theta_{21}) = 0, \quad (1.40)$$

- entrainment equation:

$$d[\rho_e U_e (\delta - \delta_1^*)] = 0. \quad (1.41)$$

As a consequence of the cylindrically symmetry assumption, thicknesses δ_2^* , θ_{22} and θ_{12} do not appear in the integral equations.

Equations 1.39 to 1.41 have to be integrated between Station 1 where the velocity U_{e1} and the boundary-layer characteristics are known, and Station 2 where the velocity U_{e2} is prescribed by oblique shock theory. These three equations, which contain 4 unknown quantities (namely δ , δ_1^* , θ_{11} and θ_{21}), must be completed by closure assumptions. *Cousteix and Houdeville* have obtained the closure relations by using “self similar” solutions of the 3-D boundary-layer partial differential equations (Cousteix and Houdeville, 1976, see Section 2.4.2 below).

To derive these solutions, the following basic assumption is made: the turbulent shear stress is supposed to be parallel to the mean velocity gradient and is thus represented by introducing an *isotropic eddy viscosity*. This viscosity is expressed by a mixing length model.

The self similar solutions make it possible to express the various thickness ratios as well as the skin-friction and entrainment coefficients as functions of:

- two shape parameters;
- the external Mach number M_e ;
- the local Reynolds number R_s .

Thus, for known initial conditions at Station 1, solution of equations (1.39-41) gives the boundary-layer properties at Station 2, the downstream Mach number M_{e2} being prescribed.

Myring's method (1975, 1977). — This method is similar to Cousteix and Houdeville's analysis. The difference lies in the closure relations employed.

For streamwise velocity profiles, Myring uses semi-empirical relations which correlate the “shape parameters” H_1 and H^* involved in his formulation (see Green's method in Section 1.2.1).

For crossflow velocity profiles, he uses the two-layer triangular model developed by Johnston (1957). This representation involves the cross flow angle β , which is the angle between the external streamline and the skin-friction line. In order to evaluate β , values of the streamwise skin-friction coefficient C_f are needed. At the start of interaction, C_f is determined by the well known Ludwig-Tillmann skin-friction law evaluated at the Eckert reference temperature. In the region of a strong adverse pressure gradient, Myring uses a special law deduced from his experiments (1967).

Although this analysis could be applied to compute the change in the boundary-layer integral properties, the author seems to have developed it essentially with a view to predicting the effects of sweep on condition at separation.

In this analysis, the separation line is defined as the skin-friction line which runs parallel to the line of the shock (for more details on three dimensional shock-wave/boundary-layer interaction (see Section 4 of Part I). This condition fixes the angle β at separation, i.e., fixes one of the parameters used to describe the boundary-layer. It is thus possible to determine the external velocity (or, the pressure coefficient which is equivalent) at the position of the separation line (this type of resolution is similar in nature to Inverse Methods presented in Section 2).

1.3.3. — Control Volume Methods

Paynter's method (1980). — This method, which is a control volume analysis, has been proposed for computing the change in boundary-layer properties across a weak glancing shock/boundary-layer interaction (GSBLI). This phenomenon occurs, for example, on the sideplates of supersonic two-dimensional mixed or external compression inlets or on the wing surfaces of aircraft with highly swept wings in supersonic flight. GSBLI arises when oblique shock generated by a deflection imparted to the flow meets the boundary-layer of a wall approximately normal to the shock generating surface. The proposed analysis is restricted to *weak GSBLI*; i.e., interactions in which there is no coalescence of the skin-friction lines towards a separation line (Peake, 1976). In this case, the skin-friction lines (or streamlines very near the wall) undergo a deviation which begins upstream of the oblique shock front. Their final turning angle is generally greater than that of the streamlines at the boundary-layer edge. (See Section 4 of Part I for a phenomenological discussion of 3-D shock-wave/turbulent boundary-layer interaction.)

In the present method, it is supposed that the incoming boundary-layer is two-dimensional. The downstream boundary-layer properties are computed by performing a control volume analysis which generalizes the 2-D method of Seebauch *et al.* (See above).

The basic assumptions made are listed above in Section 1.3.1 (in particular, the flow is assumed *cylindrically symmetric*).

The closure relations are provided here by considering that the velocity components normal and tangential to the shock, both upstream and downstream of the interaction region, are represented by *power-law profiles*. It is also assumed that the static pressure downstream of the interaction region, at Station 2 of the control volume, is constant normal to the wall.

The control volume is shown in Figure 1.18. The view AA is in a plane normal to the wall and to the shock. With the notations already used, we can write the following balance equations:

- continuity (zero entrainment assumption):

$$\int_0^{\delta_2} \rho u dy = \int_0^{\delta_1} \rho u dy, \quad (1.42)$$

- x-momentum:

$$\int_0^{\delta_2} \rho u^2 dy = \int_0^{\delta_1} \rho u^2 dy + p_1 \delta_1 - p_2 \delta_2 + \bar{p}(\delta_2 - \delta_1), \quad (1.43)$$

- z-momentum:

$$\int_0^{\delta_2} \rho w u dy = \int_0^{\delta_1} \rho w u dy. \quad (1.44)$$

The term \bar{p} which appears in equation 1.43 is the average pressure acting on the upper surface of the control volume. It is computed by representing rather crudely the true pressure distribution in the interaction domain. This analysis is made in plane AA, normal both to the wall and to the shock.

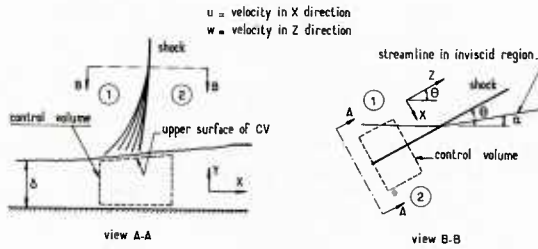


Fig. 1.18 — Paynter's model for glancing shock/boundary-layer interaction.

One considers:

- first, a supersonic compression from the upstream State 1 to locally sonic conditions. This process is supposed to be isentropic;
- second, a subsonic compression from the sonic state p^* to the final pressure p_2 (p_2 results from oblique shock relations).

In addition, it is supposed that there is no thickening of the boundary-layer during the course of the supersonic part of the process (i.e., the "free interaction" domain) and that compression from p^* to p_2 occurs in such a way that the shape of the curve $p(x/l)$ (l being the interaction length) is parabolic. Thus \bar{p}/p_1 is given by:

$$\frac{\bar{p}}{p_1} = 0.67 \frac{p_2}{p_1} + 0.33 \left[\frac{1 + (\gamma - 1)/2 \cdot M_{e1}^2 \sin^2 \theta}{1 + (\gamma - 1)/2} \right]^{\gamma/(\gamma - 1)}.$$

By combining equations 1.42 and 1.43 and expressing $\rho_e u_e$ in terms of Mach number and pressure, one arrives at:

$$\frac{p_2 M_{e2}}{p_1 M_{e1}} \left[\frac{1 + (\gamma - 1)/2 M_{e2}^2}{1 + (\gamma - 1)/2 M_{e1}^2} \right]^{1/2} \frac{\sin(\theta - \alpha)}{\sin \theta} \left[\frac{\int_0^1 \rho u / \rho_e u_e d(y/\delta)}{\int_0^1 \rho u / \rho_e u_e d(y/\delta)} \right]_2 - \left\{ \frac{p_2/p_1 - \bar{p}/p_1 + p_2/p_1 [\gamma M_{e2}^2 \sin^2(\theta - \alpha)]}{1 - \bar{p}/p_1 + \gamma M_{e1}^2 \sin^2 \theta} \left[\frac{\int_0^1 \rho u^2 / \rho_e u_e^2 d(y/\delta)}{\int_0^1 \rho u^2 / \rho_e u_e^2 d(y/\delta)} \right]_2 \right\} = 0. \quad (1.45)$$

Combining equations 1.42 and 1.44 yields:

$$\left[\frac{1 + (\gamma - 1)/2 M_{e2}^2}{1 + (\gamma - 1)/2 M_{e1}^2} \right]^{1/2} \left[\frac{\int_0^1 \rho u / \rho_e u_e d(y/\delta)}{\int_0^1 \rho u / \rho_e u_e d(y/\delta)} \right]_2 - \frac{M_{e2} \cos(\theta - \alpha)}{M_{e1} \cos \theta} \left[\frac{\int_0^1 \rho w / \rho_e u_e w_e d(y/\delta)}{\int_0^1 \rho w / \rho_e u_e w_e d(y/\delta)} \right]_2 = 0. \quad (1.46)$$

Assumption concerning the velocity profiles leads to the following representations:

- normal velocity:

$$\frac{u}{u_e} = \left(\frac{y}{\delta} \right)^{1/n_1 x},$$

- tangential velocity:

$$\frac{w}{w_e} = \left(\frac{y}{\delta} \right)^{1/n_2 x},$$

where $x=1$ indicates that the profile is upstream of the shock and $x=2$ indicates that the profile is downstream of the shock.

Finally equations 1.45 and 1.46 constitute a system for the two unknown n_{12} and n_{22} ; this system is solved iteratively. Thereafter, equation 1.42 may be used to compute δ_2 .

The previous analysis can be successively applied to cope with multiple GSBLI consisting of shocks of opposite families or shocks of the same family (Paynter, 1981).

McCabe's theory for the prediction of Incipient Separation (1966). — In 1966 McCabe proposed a rather simple theory for predicting the onset of separation in a situation where an oblique shock-wave interacts with the boundary-layer formed on a surface which is normal to the plane of the shock. This theory applies to turbulent flows and is largely inspired by experimental evidence. In a 3-D interaction taking place on a flat plate, there exists a transverse pressure gradient in a direction perpendicular to the incoming parallel stream. This pressure gradient will deflect the slower moving layers of the boundary-layer at a larger angle than the faster moving layers. Consequently, in the shock foot region, the direction of the flow changes continuously throughout the boundary-layer: the inner streamlines are more deflected than the outer streamlines. This may be described as a "twist" of the boundary-layer. Now, following Myring's idea (see Section 1.3.3 above), it is postulated that separation first occurs when the streamline direction at the surface is parallel to the shock-wave. The flow direction close to the surface is computed by resorting to vorticity transport arguments. The basis of the theory is to assume that all vorticity in the boundary-layer upstream of the shock is convected with the free stream velocity. Furthermore, it is assumed that viscosity has no effect during the (rapid) interaction process. Henceforth, it is not necessary to stipulate zero slip velocity at the wall. The wall streamline direction is determined by considering the calculation around a circuit moving with the fluid from upstream to downstream of the shock. The fact that this circulation does not alter with time, plus oblique shock equations and appropriate simplifications allow the author to compute the change in flow direction across the boundary-layer. Hence, an Incipient Separation limit can be determined as a function of the upstream Mach number and shock sweep angle. The shape of the incoming velocity profile is not taken into account, which constitutes a drawback to this kind of theory.

A comparison with experiment of the Incipient Separation limit predicted by McCabe's analysis is given in Section 4 of Part I devoted to the physical description of shock-wave/boundary-layer interaction in three-dimensional flows.

1.4. — Inviscid shear layer analyses

As we know, viscous forces often play a negligible role in the largest part of a turbulent dissipative layer undergoing a rapid interaction involving either compression or expansion. The phenomenon is controlled essentially by pressure and inertia forces. Thus the key hypothesis in Inviscid Shear Layer analyses is the constancy of entropy on each streamline: the interacting boundary-layer is considered as a *rotational inviscid stream*. This assumption leads to two different methods of calculation.

The first method pertains more or less to discontinuity analysis, since it consists in computing a downstream state 2 from a known initial velocity distribution at Station 1 and prescribed static pressures p_1 and p_2 . Flow evolution between Stations 1 and 2 is ignored. The basic principle of the method is to divide the shear layer into N streamtubes of thickness Δy_n (this thickness may vary from one streamtube to the other) over which the flow properties are considered as constant. By assuming that each streamtube undergoes an *isentropic* compression (or expansion) between Stations 1 and 2 and making use of the continuity relation (conservation of mass), one may construct the downstream velocity distribution at 2 (provided that the static pressure is transversally constant at Stations 1 and 2).

No restrictive assumption has to be introduced concerning the shape of the velocity profiles and this technique is rather general, in the sense that no boundary-layer approximations are made. However the calculation requires that the total pressure of the streamtube exceed the static pressure p_2 or at least be equal to it. For a compression, this condition is not fulfilled near the wall and a way is therefore needed to deal with the inner part of the initial boundary-layer in which total pressure is less than the final static pressure. This difficulty can be circumvented if suction is performed at the wall in such a manner as to insure that the low energy fluid be continuously sucked away (for more details on this special but interesting case, see Green, 1969).

No problem of this kind exists for a rapid expansion where p_2 is lower than p_1 . Indeed, the method gives very good results in the prediction of boundary-layer change across a centered expansion wave (Murthy and Hammitt, 1958; Kirk, 1959; Carrière and Sirieix, 1960; Nash, 1962; Weinbaum, 1966; Délery and Masure, 1969).

The second approach consists in performing an *exact calculation* of the rotational shear layer throughout the interaction zone. Calculation of this kind can be made without any special difficulty if most of the shear flow remains supersonic. Then the equations of motion are of hyperbolic nature and can be solved by a downstream marching process. The Method of Characteristics is very well suited for such calculation.

Naturally, there is a problem with the subsonic part of the boundary-layer. Nonetheless, if the Mach number of the external inviscid stream is high enough (say greater than 2), the subsonic region of a turbulent boundary-layer is very thin compared to its total thickness δ (see Section 1 of Part I), so that the influence of the subsonic inner layer can be neglected in a first level approximation.

This kind of analysis has been used with very good quantitative success for expansion occurring at a sharp corner or at a base shoulder. In these circumstances, the subsonic layer is laminated so that its influence actually decreases.

One of the first applications of the inviscid rotational approach to shock-wave/turbulent boundary-layer interaction was made by Thomke and Roshko (1969). The inviscid model was applied to the compression over a wedge, the initial external Mach number being approximately equal to 4. In this model, a small, inner portion of the boundary-layer profile was ignored and the outer portion was considered simply as a supersonic, rotational stream that interacts inviscidly with the ramp (see Fig. 1.19). The lower edge of this layer is defined by a Mach number $M_w > 1$ and is taken to be at the wall itself. Calculations were performed by using a rotational Method of Characteristics code. This implies that the Mach number M_w on the lower boundary-layer be high enough (or the wedge angle sufficiently small) to preserve supersonic flow on the ramp. The starting conditions were provided by the measured incoming boundary-layer profile where the "cut" Mach number was determined from empirical considerations. The computed wall pressure distribution agreed very well with the measured one as can be seen in Figure 3.5 of Section 3.2.1, Part I. Other examples of this kind of computation can be found in Section 3.2 of Part I.

This kind of calculation was later improved by Rosen, Roshko and Pavish (1980) in order to take account of the influence of the inner layer and to deduce a rational basis for determining the Mach number M_w . The basic principle of this improved method consists in applying to the inner layer a control volume analysis similar in nature to those presented above (see Section 1.2.2). The chosen control volume is shown in Figure 1.20. The static pressure is assumed constant across the inner layer, and the entrainment as well as the viscous forces are assumed negligible at its outer edge.

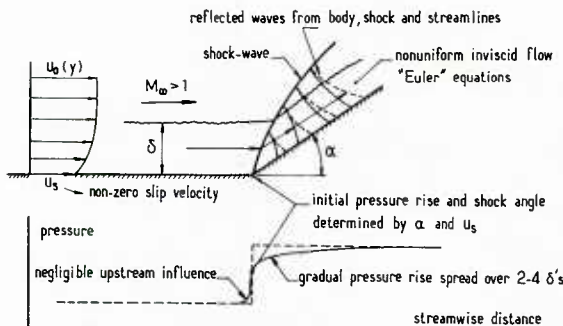


Fig. 1.19 – Roshko and Thomke's inviscid rotational flow model.

Three equations are obtained by writing conservation of mass, of momentum is the direction of the initial flow and of momentum in the direction normal to the incoming flow. This basic system is supplemented by the assumption that the velocity distributions belong to a family of profiles depending essentially on only one shape parameter. In this analysis, the thickness δ_1 of the incoming inner layer as well as the streamwise extent Δx (see in Fig. 1.20) are unknown. Thus, two additional relations are required; they are obtained from matching pressure and velocity at the interface between the two layers.

Examples of application of this improved analysis are presented in Figure 1.21. The two computed cases are relative to ramp flows at the same upstream Mach number of 3.93 but with different ramp angles. Agreement with the experiments of Roshko and Thomke (1969), is very good except for the downstream part of the wall pressure distribution which is, in fact, affected by disturbances coming from the external flow.

Rose, Murphy and Watson (1968), have also used the rotational inviscid approach to compute the interaction between an oblique shock and a turbulent boundary-layer in hypersonic flows. Here, the lower edge of the outer portion of the layer was defined by a characteristic break in the measured initial Mach number profile. The inviscid part of the flow was computed by the Method of Characteristics. In a first version of their method, the authors made the assumption that the thickness of the viscous (and partly subsonic) inner layer remains unchanged during the shock reflection (i.e., no interaction effect between the two layers was considered). In an improved version (Rose, 1970; Rose et al., 1972), a more refined two-layer model was used. It incorporated a very simplified interaction mechanism between an inner laminar viscous sublayer and the outer inviscid flow.

Examples of such calculations are given in Figure 1.22. They concern shock reflections in hypersonic flows for a laminar case and for a turbulent case (Watson et al., 1967). Agreement with experiment is good, especially in the laminar case. The laminar interaction has also been computed by Goodwin et al. (1977) by using a method belonging to the category of viscous-inviscid interactive methods (see Section 3 below).

A similar analysis was developed by Elfstrom (1971), but without any interactive effect between the two layers. This theory was essentially applied to predict wall pressure distribution over a wedge-compression corner in hypersonic turbulent flow. It was also used to derive a criterion for Incipient Separation at the wedge corner. As seen in Section 3.8 of Part I devoted to Incipient Separation in two-dimensional supersonic flows, Elfstrom's model gives results which are in close agreement with experiment provided that the free stream Mach number be high enough (say M_{∞} greater than 4).

The ideas underlying Inviscid Shear Layer analyses result in great part from experimental observations. This demonstrates the quasi negligible effect of viscous forces in turbulent flows submitted to rapid interaction.

Of course, viscous forces *must* necessarily play a dominant role in the immediate vicinity of the wall in order for the no slip condition to be satisfied. For this reason, the use of an entirely inviscid model leads inevitably to inconsistencies which cannot always be ignored. A more realistic solution of the problem necessitates that one resort to a more refined theoretical examination of the flow structure. This is precisely the object of the *multi-deck theories* which are presented in Section 4.

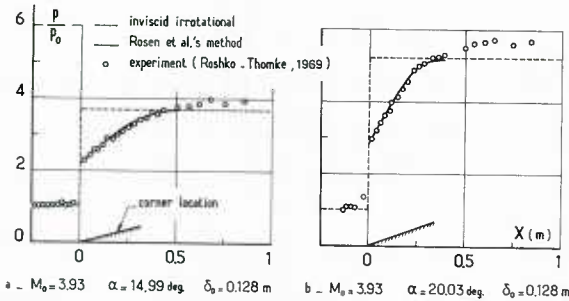


Fig. 1.21 – Ramp flow – Calculations by the free shear layer analysis of Rosen, Roshko and Pavish (1980).

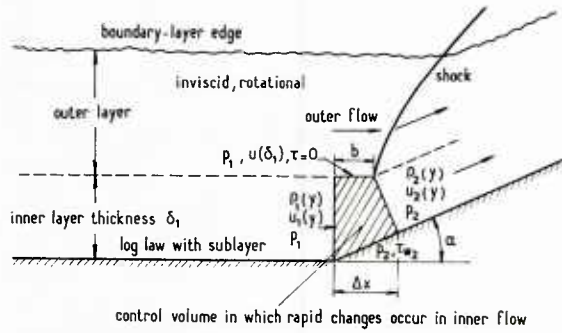


Fig. 1.20 – Rosen et al.'s flow model – Control volume for inner layer determination.

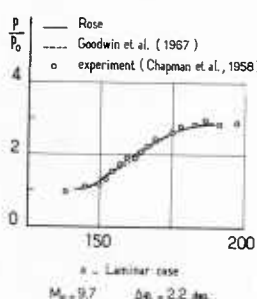
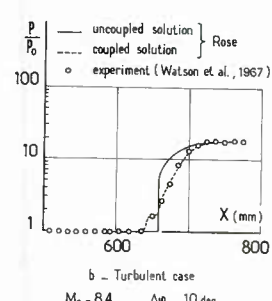


Fig. 1.22 – Shock reflection – Calculations by the flow model of Rose.



1.5. — *References*

Alber, I. E. (1971): Similar Solution for a Family of Separated Turbulent Boundary-Layers. AIAA Paper 71-203.

Alber, I. E.; Bacon, J. W.; Masson, B. S. and Collins, D. J. (1971): An Experimental Investigation of Turbulent Transonic Viscous-Inviscid Interactions. AIAA Paper 71-565 (1971); see also AIAA Journal, Vol. 11, No. 5, pp. 620-627 (May 1973).

Baker, C. J. (1980): The Prediction of Boundary-Layer Development Through a Normal Shock-Wave/Turbulent Boundary-Layer Interaction. Cambridge University, Engineering Department, A-Aero, TR 10.

Carrière, P. and Sirieix, M. (1960): Facteurs d'influence du recollement d'un écoulement supersonique. 10^e Congrès International de Mécanique Appliquée, Stresa, Italy.

Chapman, D.R.; Kuehn, D. M. and Larson, H. K. (1958): Investigation on Separated Flows in Supersonic and Subsonic Streams with Emphasis on the Effect of Transition. NACA TR 1356.

Coles, D. E. (1956). The Law of the Wake in Turbulent Boundary-Layer. J. Fluid Mech., Vol. 1, Part 2, pp. 191-226.

Cousteix, J. (1974): Analyse théorique et moyens de prévision de la couche limite turbulente tridimensionnelle. Publication ONERA No. 157.

Cousteix, J. and Houdeville, R. (1976): Épaississement et séparation d'une couche limite turbulente soumise à une interaction tridimensionnelle avec un choc oblique. La Recherche Aérospatiale, No. 1976-1, pp. 1-11, (Jan. 1976).

Crocco, L. and Lees, L. (1952): A Mixing Theory for the Interaction Between Dissipative Flows and Nearly Isentropic Streams. JAS, Vol. 19, No. 10, pp. 649-676 (oct. 1952).

Crocco, L. and Probstein, R. F. (1954): The Peak Pressure Rise Across an Oblique Shock Emerging from a Turbulent Boundary-Layer over a Plane Surface. Rep. No. 254, Dept. Aero. Eng.; Princeton Univ.

Délery, J. and Masure, B. (1969): Action d'une variation brusque de pression sur une couche limite turbulente et application aux prises d'air hypersoniques. La Recherche Aérospatiale, No. 129, pp. 3-12.

Délery, J. (1977): Recherches sur l'interaction onde de choc-couche limite turbulente. La Recherche Aérospatiale, No. 1977-6, pp. 337-348 (Dec. 1977).

Elfstrom, G. M. (1971): Turbulent Separation in Hypersonic Flow. Imperial College of Science and Technology, Department of Aeronautics, Aero. Report No. 71-16.

Gadd, G. E. (1961): Interactions Between Normal Shock-Waves and Turbulent Boundary-Layers. ARC, R. & M. No. 3262.

Goodwin, F. K.; Nielsen, J. N. and Lynes, L. L. (1967): Calculation of Laminar Boundary-Layer Shock-Wave Interaction by the Method of Integral Relations. NEAR Rep. TR 2, Nielsen Engineering and Research Inc. (July 1967).

Green, J. E. (1969): Interaction Between Shock-Wave and Turbulent Boundary-Layers. RAE-TR 69 098.

Green, J. E. (1972): Application of Head's Entrainment Method to the Prediction of Turbulent Boundary-Layers and Wakes in Compressible Flows. RAE, TR-72079.

Green, J. E.; Weeks, D. J. and Brooman, J. W. F. (1973): Prediction of Turbulent Boundary-Layers and Wakes in Compressible Flow by a Lag-Entrainment Method. RAE TR 72231.

Hammitt, A. G. (1958): The Interaction of Shock-Waves and Turbulent Boundary-Layers. JAS, Vol. 25, No. 6, pp. 345-356 (June 1958).

Johnston, J. P. (1957). Three-Dimensional Turbulent Boundary-Layer. Massachusetts Institute of Technology, MIT Gas Turbine Laboratory Report 39.

Kirk, F. N. (1959): An Approximate Theory of Base Pressure in Two-Dimensional Flow at Supersonic Speeds. RAE TN Aero 2377.

Klineberg, J. M. (1968): Theory of Laminar Viscous-Inviscid Interactions in Supersonic Flow. Ph. D. Thesis, California Institute of Technology.

Kooi, J. W. (1978): Influence of Free Stream Mach Number on Transonic Shock-Wave/Boundary-Layer Interactions. NLR-MP-78-013 U.

McCabe, A. (1966): The Three-Dimensional Interaction of a Shock-Wave with a Turbulent Boundary-Layer. The Aeronautical Quarterly, Vol. 17, Part. 2, pp. 231-252.

Mager, A. (1955): Prediction of Shock-Induced Turbulent Boundary-Layer Separation. JAS, Vol. 22, No. 3, pp. 201-202.

Mathews, D. C. (1969): Shock-Wave/Boundary-Layer Interactions in Two-Dimensional and Axially Symmetric Flows Including the Influence of Suction. Ph. D. Thesis, Dept. of Mechanical Engineering, University of Washington, Seattle, Wash.

Mellor, G. L. and Gibson, D. M. (1966): Equilibrium Turbulent Boundary-Layers. J. Fluid Mech., Vol. 24, Part 2, pp. 225-253.

Michel, R.; Quémard, C. and Durant, R. (1969): Application d'un schéma de longueur de mélange amélioré à l'étude des couches limites turbulentes d'équilibre. ONERA-NT No. 154.

Michel, R.; Quémard, C. and Cousteix, J. (1972): Méthodes pratiques de prévision des couches limites turbulentes bi et tridimensionnelles. La Recherche Aérospatiale, No. 1972-1, pp. 1-14.

Murthy, K. R. and Hammitt, A. G. (1958): Investigation of the Interaction of a Turbulent Boundary-Layer with Prandtl-Meyer Expansion Fan at $M=1.88$. Princeton University, AFOSR TN 58-839, Report No. 434.

Paynter, G. C. (1979): Analysis of Weak Glancing Shock/Boundary-Layer Interactions. AIAA Paper 79-0144, *see also Journal of Aircraft*, Vol. 77, No. 3, pp. 160-166 (March 1980).

Paynter, G. C. (1981): Analysis of Multiple Weak Glancing Shock/Boundary-Layer Interaction. AIAA Paper 80-0196 R, *see also AIAA Journal*, Vol. 19, No. 1, pp. 72-78 (Jan. 1981).

Peake, D. J. (1976): Three-Dimensional Swept Shock/Turbulent Boundary-Layer Separation with Control by Air Injection. National Research Council of Canada, Aero. Report LR-592.

Pinckney, S. Z. (1965): Semi Empirical Method for Predicting Effects of Incident-Reflecting Shocks on the Turbulent Boundary-Layer. NASA TN D-3029.

Reshotko, E and Tucker, M. (1955): Effect of a Discontinuity on Turbulent Boundary-Layer Thickness Parameters with Application to Shock-Induced Separation. NACA TN 3454.

Rose, W. C.; Murphy, J. D. and Watson, E. C. (1968): Interaction of an Oblique Shock-Wave with a Turbulent Boundary-Layer. AIAA Journal, Vol. 6, No. 9, pp. 1792-1793 (Sept. 1968).

Rose, W. C. (1970) A Method for Analyzing the Interaction of an Oblique Shock-Wave with a Boundary-Layer. NASA TN D 6083.

Rose, W. C.; Nielsen, H. L. and Watson, E. C. (1972): Shock-Wave/Turbulent Boundary-Layer Interaction on a Blunted Compression Surface. *Journal of Spacecraft and Rockets*, Vol. 9, No. 4, pp. 278-280 (April 1972).

Rosen, R.; Roshko, A. and Pavish, D. L. (1980): A Two-Layer Calculation for the Initial Interaction Region of an Unseparated Supersonic Turbulent Boundary-Layer with a Ramp. AIAA Paper 80-0135.

Roshko, A. and Thomke, G. J. (1969): Supersonic Turbulent Boundary-Layer Interaction with a Compression Corner at Very High Reynolds Number. Proc. of the Symposium on Viscous Interaction Phenomena in Supersonic-Hypersonic Flow, University of Dayton Press, pp. 109-138 (May 1969).

Seebaugh, W. R.; Paynter, G. C. and Childs, M. E. (1968): Shock-Wave Reflection from a Turbulent Boundary-Layer with Mass Bleed. *Journal of Aircraft*, Vol. 5, No. 5, pp. 461-469 (May 1968).

Sun, C. C. and Childs, M. E. (1973): A Modified Wall-Wake Velocity Profile for Turbulent Compressible Boundary-Layers. *Journal of Aircraft*, Vol. 10, No. 6, pp. 381-383 (June 1973).

Myring, D. F. (1967): Boundary-Layers in Supersonic Flow and the Effect of Shock-Wave Interaction. Ph. D. Thesis, University of London.

Myring, D. F. (1975): Pressure Rise to Separation in Cylindrically Symmetric Shock-Wave/Turbulent Boundary-Layer Interaction. AGARD CP No. 168 on Flow Separation.

Myring, D. F. (1977): The Effect of Sweep on Conditions at Separation in Turbulent Boundary-Layer/Shock-Wave Interaction. *The Aeronautical Quarterly*, Vol. 28, Part. 2, pp. 111-122.

Nash, J. (1962): An Analysis of Two-Dimensional Turbulent Base Flow Including the Effect of the Approaching Boundary-Layer. NPL Aero Report No. 1036.

Panaras, A. G. (1976): Calculation of Boundary-Layer Interacting with a Normal Shock by a Discontinuity Analysis. VKI TN 121.

Panaras, A. G. (1980): Separation Pressure of a Turbulent Boundary-Layer in Transonic Interactions. AIAA Journal, Vol. 18, No. 7, pp. 852-854 (July 1980).

Panaras, A. G. (1981): The Transonic Interaction of a Normal Shock with a Nonseparating Turbulent Boundary-Layer. Z. Flugwiss. Weltraumforsch. 5, Heft 6, pp. 382-389.

Sun, C. C. and Childs, M. E. (1974): Flowfield Analysis for Successive Oblique Shock-Wave/Turbulent Boundary-Layer Interactions. *Journal of Aircraft*, Vol. 11, No. 1, pp. 54-59 (Jan. 1974).

Sun, C. C. and Childs, M. E. (1976): Flowfield Analysis for Successive Oblique Shock-Wave/Turbulent Boundary-Layer Interactions. NASA CR-2656.

Tetervin, N. and Lin, C. C. (1951): A General Integral Form of the Boundary-Layer Equations for Incompressible Flow with an Application to the Calculation of the Separation Point of Turbulent Boundary-Layers. NACA Rep. 1046.

Thomke, G. J. and Roshko, A. (1969): Incipient Separation of a Turbulent Boundary-Layer at High Reynolds Number in Two-Dimensional Supersonic Flow Over a Compression Corner. NASA CR 73-308.

Tyler, R. D. and Shapiro, A. H. (1953): Pressure Rise Required for Separation in Interaction Between Turbulent Boundary-Layer and Shock-Wave JAS, Vol. 20, No. 12, pp. 858-860.

Watson, E. C.; Murphy, J. D. and Rose, W. C. (1967): Shock-Wave/Boundary-Layer Interactions in Hypersonic Inlets. Conference on Hypersonic Aircraft Technology, NASA-SP-148.

Weinbaum, S. (1966): Rapid Expansion of a Supersonic Boundary-Layer and its Application to the Near Wake. AIAA Journal, Vol. 4, No. 2, pp. 217-226 (Feb. 1966).

Winter, K. G. and Gaudet, L. (1970): Turbulent Boundary-Layer Studies at High Reynolds Number and Mach Number Between 0.2 and 2.8. ARC, R. & M. 3712.

2. — METHODS FOR THE CALCULATION OF THE CONTINUOUS DEVELOPMENT OF THE BOUNDARY-LAYER

2.1. — Introductory Remarks. The Inverse Mode of Calculation

The present Section is concerned with the use of Prandtl's equations to compute the *continuous evolution* of the boundary-layer in the course of interaction with a shock-wave.

Application of the classical boundary-layer concept is in fact not feasible for this situation since the purely inviscid solution leads to a discontinuity in the wall pressure distribution. The existence of such a discontinuity implies an infinite pressure gradient which would provoke the breakdown of the boundary-layer calculation even for a vanishingly weak shock. Consequently, a trouble free boundary-layer calculation necessitates a "smoothing" of the wall pressure discontinuity. In reality as explained in Part I, this smoothing results from the shock-wave/boundary-layer interaction phenomenon itself. Therefore, a complete and real prediction of the interaction within the framework of the boundary-layer concept requires the use of a coupling (or matching) technique. In this kind of technique, the boundary-layer and the flow considered as inviscid are computed simultaneously and made compatible by satisfying appropriate "matching conditions". Such methods of calculation, which pertain to the *weak interaction* and *strong interaction* concepts, will be presented in the next Section.

Before considering interactive analyses, we will first discuss the ability of boundary-layer methods to properly predict flow evolution during an interaction. Within this limited perspective, the shock is considered as a rapid but *continuous* process. The input of the boundary-layer calculation is a smoothed wall pressure distribution (as long as the boundary-layer does not separate [see below]) which may result from measurements or be provided by an inviscid flow calculation using a shock capturing technique which produces an artificial smearing of discontinuities.

If the shock-wave is of insufficient strength to induce separation, any boundary-layer method can be used in conjunction with the properly smoothed pressure distribution. There exists a large number of such methods (finite difference as well as integral methods); it would be out of place to mention them here. They generally give acceptable results as long as the shock-wave is not too strong. A difficulty with this kind of calculation is the correct smoothing of (or filling in the blanks if the data points are too sparse) the pressure distribution in the shock foot region. If the shock is weak enough (say $M_0 \leq 1.2$ in transonic flows), the final result (i.e., boundary-layer quantities downstream of the shock region) is not very sensitive to the shape of a "reasonably" smoothed curve. However, if the shock strength is increased, the pressure gradient becomes steeper and the boundary-layer calculation is more sensitive to the shape of the adopted pressure distribution. A badly defined compression may lead to the breakdown of the calculation announcing a separation which does not actually occur. One of the merits of the Discontinuity Analyses (see Section 1 above) as well as of the Multi-Deck theories (see Section 4 below) is to avoid this problem by providing a local treatment for the shock foot region. Furthermore, Discontinuity Analyses can incorporate empirical refinements rather simply which improves the prediction in circumstances where "classical" boundary-layer methods can deviate markedly from experiment (for example, in the case of interactions just before Incipient Separation conditions in transonic flows).

If separation occurs (or is likely to occur) in the course of the interaction, some adjustment of the classical boundary-layer methods is required in order to avoid the breakdown of the calculation in the vicinity of the separation point. Some improvements of the physical model also have to be introduced in order to adequately represent the highly destabilized boundary-layer.

In what follows, attention will be focused on boundary-layer methods which incorporate such adaptations and which are commonly used in calculations of shock-wave/turbulent boundary-layer interactions by interactive techniques. The distinctive feature of these methods is their ability to compute *unseparated* as well as *separated* boundary-layer flows and to work either in the *direct mode* or in the *inverse mode*. This capacity allows them to continuously join a separated state to an unseparated state and vice versa.

In the *classical, or direct, formulation* of the boundary-layer problem, Prandtl's equations have to satisfy initial conditions (i.e., initial velocity and temperature distributions) and a *prescribed streamwise pressure distribution* (if the flow is non-adiabatic, the wall temperature must also be imposed). For the sake of simplicity, only the adiabatic case will be considered in what follows). The solution of these equations (by finite difference or integral methods) provides the streamwise evolution of the boundary-layer. The main quantities of practical interest are most often the displacement and momentum thicknesses, a representative shape-parameter and the skin-friction coefficient.

In the *inverse mode*, one prescribes the *streamwise variation of a quantity pertaining to the boundary-layer development*; for instance, the skin friction coefficient or the displacement thickness (other quantities can also be chosen). In this case, one of the results of the calculation is the pressure distribution imparted to the boundary-layer.

For many years the inverse mode was used for "design" purposes. In this case, the aim of the inverse calculation is to furnish a pressure distribution $p(x)$ leading to the maximum pressure recovery which can be sustained by the boundary-layer without separating. Thereafter, an inverse inviscid flow calculation (i.e., a calculation with the pressure distribution $p(x)$ imposed as boundary condition) gives the shape of the object (airfoil, turbomachine blade or diffusor wall, etc.).

However, an essential merit of the inverse mode is to render possible the use of the boundary-layer equations in separated flow situations by avoiding the *separation point singularity* encountered in direct mode calculations.

As is now well known, in 2-D steady flows, computation of a boundary-layer (laminar or turbulent) satisfying a prescribed distribution of pressure $p(x)$ [or external velocity $u_e(x)$] is not generally possible if law $p(x)$ results in separation of the boundary-layer. The numerical difficulties which are then encountered on approaching separation are linked to the existence of a singularity of Prandtl's equations at the point where the wall shear stress vanishes. This singularity manifests itself when the pressure p is imposed as boundary condition. For laminar flows, the nature and the origin of this singular behavior have been extensively analyzed by Goldstein (1948), Stewartson (1958) and Brown (1965). To our knowledge, such a local analysis has not yet been carried out for turbulent flows.

Singularity at separation in the direct mode is also met when using integral methods of calculation. Here, the singularity manifests itself in the vanishing of the principal determinant made up of the coefficients of the system of ordinary differential equations governing the boundary-layer development (most often two equations are used, see Section 2.2.1 below).

The impossibility to perform a conventional boundary-layer calculation until separation and to continue it beyond that point is not attributable (as was originally thought) to the failure of the boundary-layer concept. In fact, this impossibility denotes the establishment of a "*strong interaction*" régime between the boundary-layer and that part of the flow considered as inviscid. Consequently, the pressure distribution $p(x)$ can no longer be independently prescribed, as is the case for "*weak interaction*" régime. In this case $p(x)$ results from the *strong coupling mechanism* between the viscous layer and the outer inviscid flow. Such a mechanism establishes itself when the boundary-layer undergoes a strong destabilization, like in a shock-wave/boundary-layer interaction. The notion of strong coupling was originally introduced by Crocco and Lees (1952). It permits the determination of an inviscid external flow and of the accompanying boundary-layer in such a way that the distribution $p(x)$ resulting from the calculation ensures a smooth passage of the solution through the separation (and/or reattachment) point.

In a more restricted perspective, the calculation of a 2-D boundary-layer including a separated bubble can be performed without encountering any singularity at separation (or reattachment) by use of the inverse mode, as has already been pointed out. The capacity to compute separated boundary-layers by means of an inverse technique has at least a double advantage (besides the "design" purpose):

- on the one hand, it permits the application of coupling methods to subsonic and *transonic* flows. In these cases, due to the ellipticity of the inviscid stream, the boundary-layer and the external flow must be calculated independently and made compatible by overall successive iterations. The situation is different for entirely supersonic external streams; for then it is possible to satisfy the compatibility conditions at each step of a purely downstream marching process, provided the boundary-layer calculation is made entirely parabolic in the downstream direction (see Section 2.3 on Finite Difference Methods and Section 3 on Coupling Methods);

- on the other hand, when compared to the solving of the full Navier-Stokes equations, it may provide an effective and economical computational tool for defining and criticising models of turbulence applicable to strongly interacting flows.

In what follows, we will present boundary-layer type methods which are used in transonic and/or supersonic flows where separation resulting from the interaction with a shock-wave is likely to occur (or actually occurs). Only methods working for *turbulent flows* will be considered, since the turbulent régime is the most likely to exist in shock/boundary-layer interactions. Most of the existing methods are restricted to 2-D flows as only a very limited number of methods are available for treat 3-D boundary-layer flows.

We will first consider *integral methods* (Section 2.2) which are often used in coupling algorithms because of their rapidity. Then *finite difference methods* (Section 2.3) will be presented. These last methods allow a more local description of the flow and the use of more sophisticated turbulence models, even though it be at the cost of longer computing times, of course.

2.2. — Integral Methods

2.2.1. — Basic Principles and Equations

The basic principle underlying nearly all existing integral methods is to describe the boundary-layer development by means of *two* integral equations. It is thus possible to compute the streamwise variation of *two* characteristic quantities, namely:

- a *length scale* measuring the boundary-layer thickness. The most often retained thicknesses are: either the displacement thickness or the momentum thickness;
- a *shape-factor* which represents the shape of the boundary-layer velocity profiles. The knowledge of this shape factor (also called form-factor or form parameter) allows the determination of all the other integral thicknesses when only one of them is known (of course the external Mach number as well as thermal conditions at the wall must also be known).

The resolution of the system of ordinary differential equations necessitates additional or "closure" relationships which consist of:

- an appropriate velocity profile family;
- a turbulence model or *ad-hoc* formulae to evaluate the viscous terms.

Thus the two-equation integral methods permit the prediction of two quantities of main interest, namely: the *skin friction* or *momentum loss* due to viscous forces, and the *displacement effect* which is at the origin of the viscous-inviscid interaction mechanism.

The taking into account of thermal effects would require, in principle, an integral form of the energy equation. However, most of the methods employed to compute shock-wave/boundary-layer interaction make use of Crocco's integral to relate the temperature and the velocity profiles. Moreover, it is also frequently assumed that the stagnation enthalpy is constant across the boundary-layer. This assumption does not entail large errors provided the flow is adiabatic (absence of heat transfer at the wall) and the Mach number M_e at the boundary-layer edge is moderate (the variation of stagnation enthalpy across an adiabatic boundary-layer is approximately equal to 4% when $M_e=2$). In what follows we will not consider the energy equation.

Let us consider the turbulent boundary-layer equations of a 2-D compressible steady flow assumed adiabatic:

- continuity:

$$\frac{\partial(\rho u)}{\partial x} + \frac{\partial(\rho v)}{\partial y} = 0 \quad (2.1)$$

- streamwise momentum:

$$\rho u \frac{\partial u}{\partial x} + \rho v \frac{\partial u}{\partial y} = - \frac{dp}{dx} + \frac{\partial}{\partial y} \left[(\mu + \mu_t) \frac{\partial u}{\partial y} \right]. \quad (2.2)$$

In these equations all the symbols are relative to mean quantities (Reynolds' averaging) and μ_t is the turbulent eddy viscosity defined by:

$$\mu_t \frac{\partial u}{\partial y} = - \rho \overline{u' v'}$$

As already stated, the energy equation is replaced by Crocco's integral which for adiabatic flows is written:

$$\frac{T}{T_e} = 1 + r \frac{\gamma-1}{2} M_e^2 \left(1 - \frac{u^2}{u_e^2} \right) \quad (r: \text{recovery factor}). \quad (2.3)$$

The most widely used integral equations are the following.

The first one is the *Von Kármán momentum equation* which can be written:

$$\frac{d\theta}{dx} + \theta \left[\left(2 + \frac{\delta^*}{\theta} \right) \frac{1}{u_e} \frac{du_e}{dx} + \frac{1}{\rho_e} \frac{dp_e}{dx} \right] = \frac{C_f}{2}, \quad (2.4)$$

or, if the flow at the boundary-layer edge is isentropic:

$$\frac{d\theta}{dx} + \left(2 + \frac{\delta^*}{\theta} - M_e^2 \right) \frac{\theta}{u_e} \frac{du_e}{dx} = \frac{C_f}{2}.$$

The second (or complementary) equation differs according to the author's preference. Three kinds of equations are commonly used.

(i) The *Mean-Flow Kinetic Energy Equation* also called the *Mechanical Energy Equation*.

This equation is obtained by multiplication of equation 2.2 by u prior to integration in the y direction, which gives:

$$\frac{d\theta^*}{dx} + \theta^* \left(\frac{3}{u_e} \frac{du_e}{dx} + \frac{1}{\rho_e} \frac{dp_e}{dx} \right) + \frac{2\theta^{**}}{u_e} \frac{du_e}{dx} = D, \quad (2.5)$$

or, for an isentropic external flow:

$$\frac{d\theta^*}{dx} + \left(3 + 2 \frac{\theta^{**}}{\theta^*} - M_e^2 \right) \frac{\theta^*}{u_e} \frac{du_e}{dx} = D$$

Thicknesses θ^* and θ^{**} as well as the Shear-Work Integral D are defined in Section 1.2.1 above (D is also termed the dissipation integral).

(ii) *Integral Continuity Equation* also called the *Entrainment Equation*.

This equation results from integration of the continuity equation between $y=0$ and $y=\delta$, which gives:

$$\frac{d(\delta - \delta^*)}{dx} - (\delta - \delta^*) \frac{d(\rho_e u_e)}{dx} = \frac{d\delta}{dx} - \frac{v_e}{u_e} = C_E, \quad (2.6)$$

or for an isentropic external stream:

$$\frac{d(\delta - \delta^*)}{dx} - (\delta - \delta^*)(1 - M_e^2) \frac{1}{u_e} \frac{du_e}{dx} = \frac{d\delta}{dx} - \frac{v_e}{u_e} = C_E.$$

The coefficient C_E represents the rate at which the external flow enters the boundary-layer. It is sometimes called Head's entrainment coefficient (1958). It has been demonstrated by Michel *et al.* (1969):

$$\frac{d\delta}{dx} - \frac{v_e}{u_e} = - \frac{1}{\rho_e u_e} \left(\frac{\partial \tau}{\partial u} \right)_{y=\delta}, \quad (2.7)$$

which clearly shows that the entrainment coefficient is strongly related to turbulence properties at boundary-layer edge.

(iii) *The Moment of Momentum Equation*.

It is obtained by multiplication of equation 2.2 by y prior to integration from $y=0$ to $y=\delta$, which leads to the following equation:

$$\int_0^\delta \left\{ \rho u \frac{\partial u}{\partial x} - \frac{\partial u}{\partial x} \int_0^y \frac{\partial(\rho u)}{\partial x} d\eta - \rho_e u_e \frac{du_e}{dx} \right\} y dy = - \int_0^\delta \tau dy. \quad (2.8)$$

The Moment of Momentum Equation may prove superior to the Mean-Flow Kinetic Energy Equation due to difficulties in evaluating numerically the Shear-Work Integral in the latter.

In what follows, the retained methods are classified according to the second equation they use (all of them employ the Von Kármán equation). In this review, only the distinguishing features of the methods are presented, i.e.:

- the velocity profile family (if any) used to evaluate the different thickness ratios;
- the essential formulae giving the viscous terms.

2.2.2. — Methods Using the Mean-Flow Kinetic Energy Equation

It seems that the first integral method especially devised to compute separated flows at transonic speed should be accredited to Klineberg and Steger (1972). The method was restricted to laminar flow so we will not consider it in much detail here. It also incorporated the calculation of the airfoil wake which could be either laminar or turbulent. In this method, the basic integral equations were transformed into an equivalent incompressible form. The various profile quantities, as well as the skin friction coefficient and the shear-work integral, were deduced from boundary-layer and wake-like similarity solutions (Klineberg 1968; Klineberg and Lees (1969)).

The method proposed by *Délery* (1975) to compute a separated turbulent boundary-layer is formulated directly in the compressible (physical) plane. The velocity profiles belong to a family derived from *Cole's law-of-the-wall/law-of-the-wake* formula, which is here written in the form:

$$\frac{u}{U_e} = 1 + \frac{U_t}{0.41 U_e} \ln \frac{y}{\delta} - 2.24 \left(\frac{\delta^*}{\delta} - \frac{U_t}{0.41 U_e} \right) f \left(\frac{y}{\delta} \right), \quad (2.9)$$

where $\frac{U_t}{U_e} = \frac{C_{f_i}}{C_{f_i}} \sqrt{\frac{1}{2} |C_{f_i}|}$ is defined with an *incompressible* skin friction coefficient and can be negative to accommodate separated flows. The ratio δ^*/δ involving the "incompressible" displacement thickness: $\delta^* = \int_0^\delta \left(1 - \frac{u}{u_e} \right) dy$ can be considered as a shape-factor. The "wake" function $f(y/\delta)$ is a polynomial function of $(y/\delta)^{1/2}$ defined from a correlation of turbulent velocity profiles measured in the separated and reattaching zone behind a downstream facing step (Noi, 1971). Reasoning for the (fictional) incompressible state, U_t is a function of δ^*/δ and of the Reynolds number R_δ . However by fitting equation 2.9 with the well known law-of-the-wall, it is possible to derive the following relation between these three parameters:

$$\frac{\delta^*}{\delta} = \frac{1}{2.24} \left\{ - \frac{U_t}{U_e} \left[\frac{1}{0.41} \ln \left(R_\delta \frac{|U_t|}{U_e} \right) + 5. - \frac{2.24}{0.41} \right] + 1. \right\}. \quad (2.10)$$

Thus the profiles depend essentially on only one parameter: the shape-factor δ^*/δ . The Reynolds number is a secondary parameter since it is a function of δ and u_e (plus the fixed stagnation conditions). The effect of compressibility on the shape of the dimensionless velocity profiles u/u_e was assumed negligible. This assumption has been well verified experimentally for adiabatic flows, the external Mach number of which is not too high ($M_e \lesssim 3$). Thus equation 2.9 is assumed valid for compressible boundary-layer at moderate Mach numbers. The true or "compressible" skin friction coefficient is deduced from C_{f_i} by using the relation:

$$C_f = C_{f_i} \left(1 + r \frac{\gamma-1}{2} M_e^2 \right)^{-1/2},$$

which gives a good correlation for the compressibility effect if the flow is iso-energetic. It is to be noticed that equation 2.9 is not valid in the immediate vicinity of the wall since the logarithmic term tends to infinity when $y \rightarrow 0$. Nevertheless, equation 2.9 can be applied very close to the wall, down to $y/\delta = 0.01$. The part of the profile below this ordinate is approximated by a linear evolution.

The above velocity profile representation is sufficient to compute the various thickness ratios involved in the formulation. However, formula 2.9 is not accurate enough to permit a realistic calculation of the shear-work integral from an eddy viscosity model and the slope $\partial u / \partial y$ evaluated by differentiating equation 2.9. It is more appropriate to compute D with an equation given independently of the velocity profile representation. Initially, D was deduced from Alber's turbulent similarity solutions (1971). In a subsequent version of the method, D was evaluated with a more accurate and more convenient expression derived by Le Balleur (see Section 2.2.3 below). This expression gives the shear-work integral coefficient C_D in the form:

$$C_D = \frac{D}{\rho_e u_e^3} = [|C_f| |u_p| + 0.018 (1-u_p)^3] \frac{1}{1 + 0.53(\gamma-1)/2 M_e^2}.$$

Here the "wake velocity" u_p is simply:

$$u_p = 1. - 2.24 \frac{\delta^*}{\delta}.$$

(The wake velocity is the velocity which would exist at the wall if U_t were set equal to zero in equation 2.9. It corresponds to a slip velocity in the absence of the logarithmic component.)

More recently, *Whitfield, Swafford and Jacocks* (1981) have proposed a method which uses a very sophisticated boundary-layer velocity family. This family is represented, in incompressible flow by (see also Whitfield, 1979 and Swafford, 1981):

$$\frac{u}{u_e} = \frac{u_t}{u_e} \frac{S}{0.09} \tan^{-1}(0.09 Y^+) + \left[1 - \frac{u_t}{u_e} \frac{S \pi}{0.18} \right] \tanh^{1/2}[a(Y/\theta)^b], \quad (2.11)$$

where:

$$S = \text{sgn}(C_{f_i}), \quad \frac{u_t}{u_e} = \sqrt{\left| \frac{C_{f_i}}{2} \right|} \quad \text{and} \quad Y^+ = \frac{yu_t}{v} = \frac{[R_{\theta}]_i y}{u_e / u_t \theta}.$$

The profiles defined by equation 2.11 depend on three quantities: H_i , C_{f_i} and $[R_\theta]_i$ (a and b can be evaluated if the three previous parameters are known). In fact, the number of parameters is reduced to two by adopting a correlation law giving C_{f_i} as a function of H_i and $[R_\theta]_i$.

In compressible flows, the profiles are still represented by equation 2.11 with "incompressible" values related to compressible ones by the following relationships:

$$C_f = C_{f_i} \left(1 + \frac{\gamma-1}{2} M_e^2 \right)^{-1/2},$$

$$R_\theta = [R_\theta]_i \left(1 + \frac{\gamma-1}{2} M_e^2 \right)^{1/2}.$$

For the purpose of defining integral thicknesses at high Reynolds number, equation 2.11 can be conveniently replaced by the following formula:

$$\frac{u}{u_e} = \frac{(u_i)_\infty}{u_e} + \left[1 - \frac{(u_i)_\infty}{u_e} \right] \tanh^{1/2} [a(Y/\theta)^b], \quad (2.12)$$

in which $(u_i)_\infty/u_e$ is a fictitious "slip velocity" representing the outer limit of the first term of equation 2.11 (i.e., the limit of this term when $Y^+ \rightarrow \infty$). For separated flows, the second representation has an advantage in that $(u_i)_\infty$ represents the maximum reverse flow velocity which can be correlated more easily than the skin-friction, which for separated flows is very small and difficult to measure. Thus, a correlation is provided which gives $(u_i)_\infty/u_e$ as a function of H_b .

Also, a correlation is given to compute the energy integral thickness parameter θ^*/θ_i as a function of H_b , although such a correlation is not strictly necessary since θ^*/θ_i can be computed from equation 2.11 (or 2.12). Such a correlation is only useful for saving computer time.

The shear-work integral D is evaluated by using the Cebeci-Smith (1974) two-layer eddy viscosity turbulence model and the analytical velocity expression for $\partial u / \partial y$. However, the numerical results thus obtained can be reproduced very closely by a two-term approximation of D as the sum of an inner and of an outer contribution. The integral thus becomes:

$$D = D_i + D_0.$$

In the inner region (contribution D_i), the shear is assumed constant and equal to the wall value; in the outer region (contribution D_0), it is computed by using Clauser's eddy viscosity model (1954). The shear-work integral coefficient thus computed can be approximated as:

$$C_D = C_{D_i} + C_{D_0} = 2 \left| \frac{C_f}{2} \right|^{3/2} \frac{\pi}{0.18} + 2K \left(\frac{2H_i - 1}{3H_i} \right)^3 \frac{\pi^2}{2} \quad \text{with } K = 0.0168. \quad (2.13)$$

The above expression is an excellent correlation law for boundary-layer flows evolving in near equilibrium conditions. It is inadequate for flows undergoing a rapid interaction process, as is the case of a shock-wave/boundary-layer interaction. We know that in this case non-equilibrium effects are particularly important (see Sections 2.9 and 3.9.2 of Part I). So, in a more recent version of this method, Whitfield and Thomas (1983) proposed modeling these effects by means of a relaxation-type equation for the outer contribution D_0 . This equation, which is derived from arguments similar to those employed by Green *et al.* in their "Lag Entrainment Method" (see below), is written:

$$\frac{\delta}{C_{D_0}} \frac{d(C_{D_0})}{dx} = \lambda [(C_{D_0})_{EQ}^{1/3} - (C_{D_0})^{1/3}],$$

where the term $(C_{D_0})_{EQ}$ is given by equation 2.13. λ is a known function of the shape-parameter. The authors assume that the near wall region responds much more rapidly than the outer region so that its contribution D_i to the shear-work integral can be computed by the equilibrium expression 2.13.

The above method is applied to compressible flows by relating compressible integral thicknesses to their incompressible counter-parts by means of suitable velocity-temperature relations.

In the method proposed by Thiede (1976) for computing *separated* turbulent boundary-layer a correspondence is first established between physical (or compressible) thicknesses and incompressible thicknesses. This transformation makes use of Crocco's relation to link the temperature and the velocity profiles (see equation 2.3 above). The closure relations are thus deduced from a one parameter incompressible profile family. This family is made up of the "lower branch" turbulent similar solutions of Alber (1971) i.e., velocity distributions including a reversed flow region. The shear-work integral coefficient (in the incompressible plane) is given by an equation which contains an empirical term representing non-equilibrium effects:

$$C_D = (C_D)_{EQ} + \Delta C_D (\Pi - \Pi_{EQ}).$$

In the above formula Equilibrium Quantities are relative to similar solutions; Π is the pressure gradient parameter defined as:

$$\Pi = \frac{1}{U_e} \frac{dU_e}{dx} \int_0^\delta \left(1 - \frac{U}{U_e} \right) dY.$$

and $(C_D)_{EQ}$ is a function of the "incompressible" shape-parameter \bar{H} resulting from the transformation (it is recalled that \bar{H} differs from the "true" incompressible shape-parameter H_b , see Section 1.2.1 above).

2.2.3. — Methods Using the Entrainment Equation

A very sophisticated and popular integral method using Head's entrainment concept has been proposed by Green, Weeks and Broaman (1972). This method was developed to compute (turbulent) compressible boundary-layers submitted to a rapid evolution involving strong out-of-equilibrium effects. In this method the entrainment equation is written in the form:

$$\theta \frac{d\bar{H}}{dx} = \frac{d\bar{H}}{dH_1} \left[C_E - H_1 \left\{ \frac{C_f}{2} - (H+1) \frac{\theta}{u_e} \frac{du_e}{dx} \right\} \right]. \quad (2.14)$$

where:

$\bar{H} = \frac{1}{\theta} \int_0^\delta \frac{\rho}{\rho_e} \left(1 - \frac{u}{u_e} \right) dy$ is a pseudo incompressible shape-factor which is a weak function of the Mach number (see also Section 1.2.1 above) and:

$$H_1 = \frac{1}{\theta} \int_0^\delta \frac{\rho u}{\rho_e u_e} dy = \frac{\delta - \delta^*}{\theta}.$$

The entrainment coefficient C_E is given by a differential equation representing "lag" effects which are likely to occur in a rapid compression (or expansion). This equation is written:

$$\theta \frac{dC_E}{dx} = F \left[\frac{2.8}{H+H_1} \{ (C_v)_{EQ}^{1/2} - C_r^{1/2} \} + \left(\frac{\theta}{u_e} \frac{du_e}{dx} \right)_{EQ} - f(M_e) \frac{\theta}{u_e} \frac{du_e}{dx} \right],$$

where $f(M_e)$ is a known function of the Mach number M_e , $H = \frac{\delta^*}{\theta}$ and C_r is the skin-friction coefficient computed with the shear-stress τ at a conventional value of y/δ in the boundary-layer. The above equation for C_E is developed from the equation for the shear-stress that Bradshaw *et al.* (1967) derived from the turbulence kinetic energy equation. Quantities $(C_v)_{EQ}$ and $\left(\frac{\theta}{u_e} \frac{du_e}{dx} \right)_{EQ}$ are relative to equilibrium flows.

These flows are defined as flows in which the shape of the velocity and shear-stress profiles do not vary with the streamwise distance x . The other closure formulae are obtained from the following considerations:

- appropriate relations are provided to express H_1 and H as functions of H ;
- the skin-friction coefficient is determined from H and R_θ by a relation involving a flat plate skin friction C_{f0} given by the correlation of Winter and Gaudet (1970);
- the equilibrium values $(C_v)_{EQ}$ and $\left(\frac{\theta}{u_e} \frac{du_e}{dx} \right)_{EQ}$ are deduced from results concerning equilibrium flows and by applying equations 2.4 and 2.14 to an equilibrium boundary-layer for which $dH/dx=0$. These operations provide algebraic relations allowing the calculation of equilibrium quantities from the knowledge of C_f , H , H , H_1 and the external Mach number M_e .

The method also incorporates factors representing extraneous influences on the turbulence structure: longitudinal curvature, lateral strain, dilatation, momentum imbalance due to departure from two-dimensional flow.

Modifications of the method concerning essentially the shape parameter relations have been introduced by East, Smith and Merryman (1977) to improve the prediction in highly separated flows.

In the method developed by Michel, Quémard and Cousteix (1977) the closure relationships are deduced from "self-similar" solutions of the compressible turbulent boundary-layer equations. These solutions are obtained via a procedure analogous to Alber's approach. This procedure consists in making restrictive assumptions regarding the streamwise evolution of the boundary-layer. Then the partial differential equations reduce to ordinary differential equations, the solutions of which constitute a family of velocity profiles depending on a limited number of parameters. In the present case, the similar solutions are derived by using a mixing length model to express the turbulent shear stress:

$$\tau = \mu \frac{\partial u}{\partial y} + \rho F^2 l^2 \left| \frac{\partial u}{\partial y} \right| \frac{\partial u}{\partial y}.$$

In the above relation l/δ is taken to be a universal function of y/δ which is of the form:

$$\frac{l}{\delta} = 0.085 \tanh \left(\frac{0.41 y}{0.085 \delta} \right).$$

The viscous sub-layer correction function F is a modified form of the Van Driest damping function. It is written:

$$F = 1 - \exp \left[- \frac{l}{26 k \mu} \sqrt{\tau \rho} \right] \quad (\text{here } k = 0.41).$$

In compressible flows, the self-similarity hypothesis consists basically in saying that the dimensionless profile u/u_e depends only on y/δ ; i.e.:

$$\frac{u}{u_e} = f \left(\frac{y}{\delta} \right).$$

Then the boundary-layer equations are reduced to ordinary differential equations with y/δ as independent variable. Their solutions depend on three parameters: the Mach number M_e , the Reynolds number R_θ and a pressure gradient parameter. In the integral method, the profiles are "unhooked" from the actual pressure gradient and characterized in fact by Clauser's shape parameter:

$$G = (H_i - 1) / [H_i \sqrt{C_{f/2}}]$$

Consequently, the various thickness ratios intervening in the integral formulation, as well as the skin friction and entrainment coefficients are computed from the self-similar solutions and expressed as functions of M_e , R_θ and G .

The method has been extended to take into account three-dimensionality (see Section 1.3 about "jump" methods for 3-D shock-wave/turbulent boundary-layer interaction), wall curvature and free stream turbulence. These extensions are made by a suitable generalization of the mixing-length model (Cousteix *et al.*, 1974; Cousteix and Houdeville, 1977).

The method developed by Le Balleur (1981) applies to laminar, transitional and turbulent flows. Here, we will consider only the turbulent case since this régime is the most likely to occur in shock-wave/boundary-layer interactions met in most practical situations.

The turbulent version of the method uses the momentum and the entrainment equations which are integrated directly in the compressible (physical) plane. In addition to the assumption of a constant stagnation enthalpy, it is assumed that compressibility has no effect on the shape of the dimensionless velocity distributions. These distributions are represented by a formula similar to equation 2.9 (see Section 2.2.2 above). However the present method introduces two improvements in the representation of the profiles:

- the wake component of the Coles' law is given by the formula:

$$f \left(\frac{y}{\delta} \right) = \left[\left(\frac{y}{\delta} \right)^{3/2} - 1 \right]^2,$$

which coincides with the asymptotic far wake solution if the turbulent eddy viscosity is modeled by using a mixing length relation (Quémard and Archambaud, 1976). Thus the method can also be applied in a rather continuous manner and with only minor changes to the turbulent wake which follows turbulent boundary-layer separating at a trailing edge;

— an adaptation of the wake component is introduced to extend Coles' relation to *largely separated boundary-layers*. In fact, it can be shown that equation 2.9 together with the usual forms of the wake component lead to unbounded negative velocities when H_i becomes very large. To avoid this unphysical behavior, the wake function, designated here by \tilde{f} , takes the following form:

$$\begin{aligned} 0 < y < y^*, \quad \tilde{f}\left(\frac{y}{\delta}\right) &= 1. \\ y^* < y < \delta, \quad \tilde{f}\left(\frac{y}{\delta}\right) &= f\left(\frac{y-y^*}{\delta-y^*}\right). \end{aligned}$$

This means that the velocity distribution includes a zone of constant return velocity below $y=y^*$ and has the usual wakelike shape above $y=y^*$. The reduced ordinate y^*/δ is a prescribed function of the shape-factor δ_i^*/δ . This function is empirically defined to generate realistic profiles for a continuous variation of H_i (or δ_i^*/δ) from the attached flat plate value (or the wake value) to the value corresponding to the turbulent isobaric mixing, i.e., a largely separated boundary-layer.

The skin-friction coefficient results from the adjustment of the velocity distribution (see equation 2.10 in Section 2.2.2 above) with the wall law when H_i is greater than 1.6. The compressibility effect on C_f is represented by the relation given by Michel *et al.* (1972). For H_i smaller than 1.6 the Michel *et al.* law is preferred because of its superior accuracy.

Non equilibrium effects are taken into account by expressing the entrainment coefficient in the form:

$$C_E = \lambda(x)(C_E)_{EQ}.$$

The equilibrium value $(C_E)_{EQ}$ is deduced from known equilibrium turbulent boundary-layer properties; whereas $\lambda(x)$, which characterizes departure from equilibrium, is a function of the streamwise distance x . This function is computed by integrating simplified turbulence transport equations.

At high Reynolds number $(C_E)_{EQ}$ is given by the following relations:

— if $H_i \geq 1.6$,

$$(C_E)_{EQ} = 0.053 \left(1 - \frac{u_B}{u_e}\right) - 0.182 \frac{C_f}{\sqrt{|C_f|}},$$

where the reduced “wake-velocity” u_B/u_e is related to the shape-factor δ_i^*/δ by:

$$\frac{u_B}{u_e} = 1 - \frac{2.22 \delta_i^*/\delta}{1 + 1.22 y^*/\delta},$$

— if $H_i < 1.6$, the Michel *et al.* formula is employed, i.e.:

$$(C_E)_{EQ} = 0.074 \frac{H_i - 1}{H_i} - 0.548 \frac{H_i}{H_i - 1} C_f.$$

The departure from equilibrium, represented by the “one-dimensional” function $\lambda(x)$, is computed by first assuming that the velocity profiles representation remains unaffected. Then, from the definition of the entrainment coefficient and the relation 2.7 of Section 2.2.1 above, we get:

$$\frac{\tau(x, y)}{[\tau(x, y)]_{EQ}} = \frac{C_E(x)}{[C_E(x)]_{EQ}} = \lambda(x).$$

The following additional approximation is introduced:

$$\frac{\tau(x, y)}{[\tau(x, y)]_{EQ}} \approx \frac{\tilde{\tau}(x)}{[\tilde{\tau}(x)]_{EQ}},$$

where $\tilde{\tau}(x)$ is a turbulent shear-stress level depending on x alone and characterizing an “average” turbulent state of the boundary-layer at station x . This “one-dimensional” shear-stress is computed by using very simplified transport equations for an average turbulence kinetic energy \tilde{k} , an average dissipation rate $\tilde{\epsilon}$ and $\tilde{\tau}$. These equations are derived from Launder and Hanjalic's transport equations (1972) by making simplifications which reduce them to ordinary differential equations for the “one-dimensional” turbulent variables $\tilde{k}(x)$, $\tilde{\epsilon}(x)$ and $\tilde{\tau}(x)$. This approach bears some similarity to Green's lag entrainment method (see above).

2.2.4. — Methods Using the Moment of Momentum Equation

In the method of Kuhn and Nielsen (1973), a Stewartson transformation is first applied to reduce the equation of the compressible boundary-layer to those of an incompressible boundary-layer. Thus the velocity profiles found to be valid for incompressible flows can also be used to compute compressible flows. The adopted velocity profiles are represented by a function which is a modification of Coles' family with a laminar sublayer added and the wake function approximated by a cosine. This formula, which involves incompressible values, is written:

$$\frac{U}{U_e} = \frac{U_s}{U_e} [2.5 \ln(1 + Y^+) + 5.1 - (3.39 Y^+ + 5.1) \exp(-0.37 Y^+)] + \frac{1}{2} \frac{U_B}{U_e} \left[1 - \cos\left(\pi \frac{Y}{\delta}\right) \right], \quad (2.15)$$

where $Y^+ = |U_t| Y/v$. The friction velocity U_t is modified to accomodate separated flows and can be positive or negative (see equation 2.9 in Section 2.2.2 above). U_β is the wake-velocity (see Section 2.2.2 above). The exponential term and the additional unit in the logarithmic term provide a smooth transition from the turbulent flow to the wall through a laminar sublayer. There are three parameters involved in equation 2.15: U_e , U_β and δ . However, U_β can be eliminated by evaluating equation 2.15 at $Y=\delta$ which gives an equation similar to equation 2.10, but here unlike other methods, U_β is eliminated instead of U_t .

The shear-work integral is computed by using equation 2.15 for $\partial U/\partial Y$ and an eddy viscosity model which is an extension of the two-layer model used by Kuhn (1971). In the inner layer of *attached flows*, the eddy viscosity parameter $\beta=1+v_t/v$ is represented by an exponential expression based on the law-of-the-wall. In the outer layer, v_t is represented by Clauser's expression along with an intermittency function :

$$v_t = k \gamma U_e \delta^*.$$

The Klebanoff intermittency function γ is approximated by:

$$\gamma = \left[1 + 5.5 \left(\frac{Y}{\delta} \right)^6 \right]^{-1}.$$

In order to represent the decrease of the "constant" k noticed in strongly retarded flows, k is calculated by:

$$k = 0.013 + 0.0038 \exp(-P/15),$$

where P is the dimensionless pressure gradient parameter:

$$P = \frac{\delta^* dp}{\tau_w dx}.$$

For *separated flows*, the value of k at separation is retained, but the length scale of the eddy viscosity is changed. In accordance with Alber's analysis, the conventional displacement thickness is replaced by the displacement thickness based on the profile above the $U=0$ line:

$$\tilde{\delta} = \int_{Y(u=0)}^{\delta} \left(1 - \frac{U}{U_e} \right) dY.$$

Substitution of equation 2.15 into the two basic integral equations expressed in their incompressible form leads to the following system:

– momentum equation:

$$A_{11} \frac{dU_t}{dx} + A_{12} \frac{d\delta}{dx} + A_{13} \frac{dU_e}{dx} = -U_t |U_t| / U_e \delta,$$

– moment of momentum equation:

$$A_{21} \frac{dU_t}{dx} + A_{22} \frac{d\delta}{dx} + A_{23} \frac{dU_e}{dx} = -\frac{v}{U_e \delta^2} \int_0^\delta \beta \frac{\partial U}{\partial Y} dY.$$

Thus the easier way to use Kuhn and Nielsen's method in an inverse calculation is to prescribe the friction velocity U_t which is in fact equivalent to prescribing the skin-friction coefficient. However the method of integration can be modified without difficulty to introduce the displacement thickness δ^* as a working variable (δ^* being a known function which can be expressed in terms of U_t , δ and U_e). The use of δ^* is generally more convenient for viscous-inviscid calculations. In such calculations, the displacement thickness plays a key role in the various coupling (matching) equations which can be written (see Section 3.2.1 below).

The authors have extended the method to compressible axisymmetric flows by making use of the Probstein-Elliott transformation in order to give the boundary-layer equations an almost two-dimensional form before applying the compressible-incompressible transformation (Kuhn and Nielsen, 1975).

More recently, Gerhart (1979) proposed a method which is formulated in the physical plane. The velocity profiles are also represented by a modified form of Coles' law which allows for compressibility and possible reversed flow (Alber and Coats, 1969; Mathews *et al.*, 1973):

$$\frac{u}{u_e} = \frac{1}{a} \sin \left\{ \frac{a \lambda}{0.41} [\ln(1+y^+) + 5 - (1.5y^+ + 5) \exp(-0.18y^+)] + au_\beta \sin^2 \left(\frac{\pi y}{2\delta} \right) \right\} \quad (2.16)$$

where:

$$a = \frac{r(\gamma-1)/2 M_e^2}{1+r(\gamma-1)/2 M_e^2}, \quad \lambda = \frac{C_f}{\sqrt{|C_f|}} \quad \text{and} \quad y^+ = \frac{y |U_t|}{v_w}.$$

The main profile parameters are λ and u_β . However, following the now classical procedure, equation 2.16 written at $y=\delta$ results in a relation between λ and u_β . Thus, the profiles in fact depend essentially on only one parameter, like in the preceding methods.

The shear-work integral D is evaluated by differentiation of 2.16 and by using a mixing length expression for the turbulent eddy viscosity. The total (laminar plus turbulent) shear-stress is thus written:

$$\tau = \left(\mu + \rho l^2 F^2 \left| \frac{\partial u}{\partial y} \right| \right) \frac{\partial u}{\partial y},$$

which allows for negative shear in regions of reversed flow. A continuous distribution of mixing length l identical to the Michel *et al.* expression is used (see Section 2.2.3 above).

The Van Driest exponential damping term is expressed by:

$$F = 1 - \exp \left[-\frac{y}{26v} \left(\frac{|\tau_w|}{\rho} + \frac{1}{\rho} \frac{dp}{dx} y \right)^{1/2} \right],$$

which avoids the singular behavior at the separation point of the original Van Driest formula in which $F=0$ everywhere if $\tau_w=0$. When the boundary-layer separates, the damping effect of the wall is removed and a different formulation of the mixing length is adopted:

- above the zero velocity point ($y \geq y_0$); i.e., the outer edge of the reversed flow region:

$$l = l_\infty = \left(\frac{l_\infty}{\delta} \right) \delta,$$

- while below the zero velocity point ($y < y_0$),

$$l = l_\infty y / y_0.$$

For an equilibrium attached boundary-layer, the value of l_∞/δ is rather well determined as: $l_\infty/\delta=0.09$. However, for a boundary-layer undergoing a strongly out of equilibrium evolution like in a shock-wave/boundary-layer interaction the ratio l_∞/δ does not remain constant but decreases markedly (Simpson *et al.*, 1981; Délery, 1981) ((see Section 2.9 of Part I)). The author proposes different possibilities to model this evolution.

The first and simplest way is to use an algebraic formulation, following the approach of Alber (1968). The relation adopted for l_∞/δ has a form similar to Kuhn and Nielsen's formula (Kuhn and Nielsen, 1975) :

$$\frac{l_\infty}{\delta} = 0.055 + 0.035 \exp(-\beta/5). \quad (2.17)$$

The parameter β is related to the local "equilibrium" shape-factor and is not taken to be equal to the reduced pressure gradient, according to its original definition. Thus β is calculated from:

$$G = 6.1 \sqrt{\beta + 1.81} - 1.7.$$

where G is the Clauser defect shape-factor defined above (see Section 2.3.2).

Another possibility is to use a differential equation (see Green's lag entrainment method as well as Le Balleur's method in Section 2.2.3 above) which can be derived from the turbulence kinetic energy equation. In the integral form this equation is:

$$\frac{1}{2} \int_0^\delta \frac{\partial}{\partial x} (\rho u k) dy = \int_0^\delta \left[\tau_i \frac{\partial u}{\partial y} - (\bar{u}^2 - \bar{v}^2) \frac{\partial u}{\partial x} \right] dy - \int_0^\delta \rho \epsilon dy, \quad (2.18)$$

where k is the turbulence kinetic energy and ϵ the turbulence dissipation rate. Following results of McDonald and Camarata (1968), Bradshaw *et al.* (1967), and Collins and Simpson (1976), the different terms involved in equation 2.18 can be modeled and expressed as functions of M_∞ , λ , δ , u_∞ , l_∞/δ provided that a formula is available to compute the length scale L for the dissipation.

The following expressions were used by Gerhart:

- for attached boundary-layers:

$$\frac{L}{\delta} = \frac{L_\infty}{\delta} \tanh \left(\frac{0.41 y}{L_\infty/\delta \delta} \right) \left[1 + 5.5 \left(\frac{y}{\delta} \right)^6 \right]^{-1},$$

- for separated boundary-layers:

$$\frac{L}{\delta} = \frac{L_\infty}{\delta} (\delta - y_0)$$

For a non-equilibrium situation, L_∞/δ cannot be considered as constant and a formulation of the form:

$$\frac{L_\infty}{\delta} = 0.05 + 0.04 \exp(-\beta/4),$$

is proposed.

According to the author's conclusion, equation 2.18 does not give better results than the much simpler algebraic expression.

2.3. — Finite Difference Methods

2.3.1. — Earlier Inverse Methods

To our knowledge, the first inverse method using a finite difference technique to solve the boundary-layer equations was published by Catherall and Mangler in 1966. The method was applied to an incompressible two-dimensional laminar boundary-layer and the case of a *prescribed displacement thickness* was considered. The equations are written in terms of a stream function and the vorticity. A transformation is introduced in which the independent variables are simply connected to the *inviscid* stream function and velocity potential. The stream function ψ is expressed as the sum of two functions: one representing the inviscid solution, the other — H — the viscous modification to the inviscid flow; so that if H is made to decay as we move from the body into the main stream, the solution will merge into the external potential flow solution. This function H is directly related to the displacement thickness δ^* . Thus the method incorporates two important features of inverse formulations that were developed afterwards:

- elimination of the unknown pressure gradient by introducing the *vorticity* ω ;
- use of a modified stream function which allows the *prescribed displacement thickness to figure explicitly in the equations to be solved as well as in the boundary conditions.*

These two essential features will be presented in more detail below.

Catherall and Mangler presented applications which showed that it is indeed possible to compute a boundary-layer past the point of vanishing skin friction and also past the point of reattachment.

The numerical method was carried out by using an entirely parabolic procedure marching always in the downstream direction. Consequently, numerical difficulties were encountered in the reversed flow region where the calculation developed instabilities. Nevertheless, the integration was continued by decreasing the convergence criterion at each station. As the authors pointed out, this difficulty is to be expected, because the region of reversed flow should actually be integrated in the *upstream direction* with boundary conditions provided from downstream. This problem will be discussed in more detail below:

The case of a *prescribed wall shear* was treated in 1972 by Keller and Cebeci for an incompressible laminar boundary-layer. The equations are reduced to the familiar dimensionless form:

$$\frac{\partial^3 f}{\partial \eta^3} + f \frac{\partial^2 f}{\partial \eta^2} + \beta(\xi) \left[1 - \left(\frac{\partial f}{\partial \eta} \right)^2 \right] = 2\xi \left(\frac{\partial f}{\partial \eta} \frac{\partial^2 f}{\partial \xi \partial \eta} - \frac{\partial^2 f}{\partial \eta^2} \frac{\partial f}{\partial \xi} \right), \quad (2.19)$$

where $f(\eta, \xi)$ is proportional to a stream function, $\xi \geq 0$ is a transformed streamwise variable, $\eta \geq 0$ measures distances normal to the wall and $\beta(\xi)$ is the pressure gradient parameter. When the ξ -derivatives are put equal to zero this equation reduces to the well known Falkner-Skan equation.

The inverse problem results from requiring that the wall shear be specified, meaning:

$$\frac{\partial^2 f}{\partial \eta^2}(\xi, 0) = S(\xi). \quad (2.20)$$

Specification of both $\beta(\xi)$ and $S(\xi)$ would result in an over-determined problem: thus, a solution is obtained by solving equation 2.19 (with appropriate and classical boundary conditions) where $\beta(\xi)$ is considered as an "eigenvalue" which is determined so that 2.20 can be satisfied. In brief, the procedure consists in treating the unknown distribution as an "eigenvalue" which is approximated by a Newton iteration scheme based on satisfying equation 2.20. For iteration, a standard boundary-layer flow problem is solved which may lead to severe difficulties if separation occurs. The numerical scheme uses a two-point finite difference method (Keller and Cebeci, 1977 a and b) plus Newton linearization. The linear system is then solved by the block elimination method.

In 1976, Cebeci extended this method to compressible and turbulent boundary-layer, although the method was still restricted to non-separated flow (see Section 2.3.4 below).

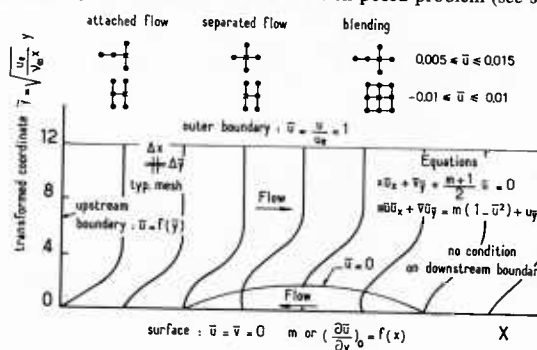
A more elaborate analysis capable of properly accounting for negative wall shear was proposed in 1974 by Klineberg and Steger. As it was restricted to laminar incompressible flows, we will not consider it in much detail. We will only comment on some of its essential features which have been incorporated in future methods.

The problem is here formulated in *primitive variables* (u, v, p) with a transformation that keeps the boundary-layer nearly uniform in thickness in the computation domain.

The boundary-layer equations are solved subject to the following boundary conditions (in the inverse mode):

$$y=0, \quad u, v=0, \quad \frac{\partial u}{\partial y} = h(x); \quad y \rightarrow \infty, \quad u \rightarrow u_e.$$

Here, $h(x)$ is a prescribed function and u_e must be determined as part of the solution process. The pressure gradient is deduced from the momentum equation evaluated at the surface. The computational domain may contain a zone of reversed flow. But the boundary-layer has to be attached both in the *entrance* and in the *outgoing* section in order to have a well posed problem (see sketch below).



One of the essential features of the method is the use of differencing schemes which allow the information to propagate in accordance with the local flow direction. Thus, in the part of the boundary-layer where the stream flows in the downstream direction, a backward difference scheme is used, whereas a centered scheme is employed in reversed flow regions. A blending formula is employed in the intermediate zone to enhance the iteration process. This formula is not otherwise fundamental.

The possible existence of a reversed flow where the scheme is centered precludes-in principle-the use of a simple forward marching procedure, but necessitates an iterative method consisting of successive sweeps of the computational domain until convergence is reached. For this purpose, both point and line Successive Underrelaxation were used. The relaxation procedure was initiated by assuming a Blasius profile everywhere.

The major result of this study was to demonstrate that regular solutions of the boundary-layer equations in separated regions could be found by the inverse technique provided the reversed flow region is correctly treated in order to avoid the numerical difficulties met by Catherall and Mangler. The authors have also developed a local analysis which proves that regular flows are characterized by an integrable saddle-point type singularity that makes it difficult to obtain numerical solutions which pass continuously into the separated region. This singularity is removed by specifying the wall shear-stress distribution and computing the pressure gradient as part of the solution.

However, numerical applications made by Klineberg and Steger [and also by Carter (1975)] have shown that discontinuous solutions may be found for highly separated flows. Then the computed value of the pressure gradient tends to become discontinuous at a point located downstream of separation. Correspondingly, the normal velocity increases rapidly. This phenomenon is certainly not an indication of a possible breakdown of the boundary-layer equations since highly separated flows are computed without any discontinuity by methods in which the displacement thickness is prescribed. It is more probably due to possible branching phenomena associated with the existence of two reversed flow solutions having the same wall shear-stress but corresponding to different pressure gradients. These two solutions are found when solving the Falkner-Skan equation (Stewartson, 1954).

2.3.2. — Carter's Method and Derived Methods

We will now expose in more detail a method which works for compressible and turbulent boundary-layer flows and which is commonly used in transonic flow calculations. This method, proposed by Carter was first formulated for laminar incompressible flows (Carter and Wornom, 1975). Then it was extended to incompressible turbulent flows (Carter, 1978) and later to compressible turbulent flows. It is basically designed to make inverse calculations with prescribed displacement thickness. However, it can be applied to the case of specified wall shear stress distribution at the cost of minor changes. Two versions of the method have been successively proposed by Carter:

- the first uses as dependent variables the stream function ψ and the vorticity ω (more exactly the pseudo vorticity $\omega = \partial u / \partial y$);
- the second method employs primitive variables.

Formulation with Variables (ω, ψ). For the sake of simplicity, the basic principles of the method will be exposed by considering an incompressible turbulent boundary-layer. Extension to compressible flow is rather straightforward and will be considered thereafter.

Starting from the boundary-layer equations, the unknown pressure p (or edge velocity u_e) is first eliminated by taking the y -derivative of the momentum equation. Introducing the vorticity $\omega = \partial u / \partial y$ and taking the continuity equation into account, the ω transport equation is obtained:

$$u \frac{\partial \omega}{\partial x} + v \frac{\partial \omega}{\partial y} = \frac{\partial^2}{\partial y^2} [(v + v_t) \omega]. \quad (2.21)$$

The turbulent shear-stress has been modeled with the eddy viscosity concept (this is not essential, more sophisticated modeling can be envisaged); thus:

$$-\overline{u'v'} = v_t \frac{\partial u}{\partial y} = v_t \omega$$

In order to eliminate the edge velocity from the outer boundary condition it is convenient to introduce the stream function ψ so that:

$$u = \frac{\partial \psi}{\partial y}, \quad v = -\frac{\partial \psi}{\partial x}.$$

Equation 2.21 is now written :

$$u \frac{\partial \omega}{\partial x} - \frac{\partial \psi}{\partial x} \frac{\partial \omega}{\partial y} = \frac{\partial^2}{\partial y^2} [(v + v_t) \omega]. \quad (2.22)$$

A "modified stream function" $\tilde{\psi}$ is defined by letting ($\tilde{\psi}$ is also called the "perturbation stream function"):

$$\tilde{\psi} = \psi - u(y - \delta^*). \quad (2.23)$$

Considering the definition of the displacement thickness δ^* , it can be easily verified that $\tilde{\psi} \rightarrow 0$ when $y \rightarrow \infty$. Thus, introduction of $\tilde{\psi}$ has a double advantage:

- first, the prescribed displacement thickness figures explicitly in the equations. Consequently, there is no need for an iterative or shooting technique as would be required by a "classical" formulation;

- second, $\tilde{\psi}$ has "convenient" boundary conditions, since $\tilde{\psi}$ is zero both for $y=0$ and $y \rightarrow \infty$.

Differentiating 2.23 with respect to y gives:

$$\frac{\partial \tilde{\psi}}{\partial y} = \omega(\delta^* - y). \quad (2.24)$$

Thus, the inverse problem consists in solving equations 2.22-23 along with the boundary-conditions:

$$\begin{aligned} u(x, 0) &= \tilde{\psi}(x, 0) = 0, \\ \omega(x, y), \tilde{\psi}(x, y) &\rightarrow 0 \quad \text{for } y \rightarrow \infty, \end{aligned} \quad (2.25)$$

the distribution of δ^* being prescribed.

When the wall shear-stress is imposed the condition is simply:

$$\omega(x, 0) = \omega_w(x) \quad (\text{a given function of } x).$$

Applications in compressible flow. — In order to extend the above formulation to compressible flows with a minimum change in the numerical treatment, Délery (1980) has applied a compressible-incompressible transformation similar to Stewartson's transformation. The new independent variables X and Y are defined in such a way that:

$$dX = \frac{a_e \rho_e}{a_0 \rho_0} dx, \quad \frac{\partial Y}{\partial y} = \frac{a_e \rho}{a_0 \rho_0},$$

where a_0 (sound velocity) and ρ_0 are relative to a constant reference state. Letting:

$$\rho u = \rho_0 \frac{\partial \psi}{\partial y}, \quad \rho v = -\rho_0 \frac{\partial \psi}{\partial x}$$

and making the assumption that the *stagnation enthalpy remains constant throughout the flowfield* (iso-energetic flow), one obtains the following quasi-incompressible form for the two governing equations:

$$\begin{aligned} U \frac{\partial U}{\partial X} + V \frac{\partial U}{\partial Y} &= U_e \frac{dU_e}{dX} + \frac{1}{\rho_e} \frac{\partial}{\partial Y} \left[(\mu + \mu_r) \frac{\rho}{\rho_0} \frac{\partial U}{\partial Y} \right], \\ \tilde{\psi} &= \psi - U(Y - \Delta^*) \quad \text{with} \quad \psi(X, Y) \equiv \psi(x, y), \end{aligned} \quad (2.26)$$

where the compressible (physical) and incompressible (transformed) quantities are related by the relations:

$$u = \frac{a_e}{a_0} U, \quad v = \frac{\rho_0}{\rho} \left(\frac{a_e \rho_e}{a_0 \rho_0} V - \frac{\partial Y}{\partial x} U \right)$$

and:

$$M_e = \frac{u_e}{a_e} = \frac{U_e}{a_0}.$$

The "incompressible" displacement thickness Δ^* is defined as:

$$\Delta^* = \int_0^\infty \left(1 - \frac{U}{U_e} \right) dY$$

and we have the following relation between Δ^* and the physical displacement thickness δ^* :

$$\Delta^* = \frac{a_e \rho_e}{a_0 \rho_0} \delta^* - \frac{\gamma - 1}{2} M_e^2 \int_0^\infty \left(1 - \frac{U^2}{U_e^2} \right) dY. \quad (2.27)$$

Introducing the transformed vorticity $\Omega = \frac{\partial U}{\partial Y}$, the equations to be solved are:

$$\begin{aligned} U \frac{\partial \Omega}{\partial X} - \frac{\partial \psi}{\partial X} \frac{\partial \Omega}{\partial Y} &= \frac{1}{\rho_e} \frac{\partial^2}{\partial Y^2} \left[(\mu + \mu_r) \frac{\rho}{\rho_0} \Omega \right], \\ \frac{\partial \psi}{\partial Y} &= (\Delta^* - Y) \Omega, \end{aligned}$$

along with the usual boundary conditions 2.25.

The transformed vorticity equation is not entirely "incompressible" since density and viscosity remain in the Right Hand Side. Total elimination of ρ and μ would require very restrictive assumptions concerning the compressibility effect on the turbulent eddy viscosity. Such a restriction is not recommended if one wishes to use realistic turbulence models. The essential merit of the transformation is to give equations in which there is only one term involving density.

One should note that Δ^* must be determined iteratively from 2.27, since the input of the calculation is in fact δ^* . In practice this iteration is included in the iterative cycle of the calculation procedure (see below).

It is also possible (as was done by Kawai, 1977), to perform the calculation directly in the compressible (physical) plane. Then differentiating with respect to y , the x -momentum equation yields:

$$u \frac{\partial \rho}{\partial y} \frac{\partial u}{\partial x} + \rho u \frac{\partial \omega}{\partial x} - \frac{\partial \psi}{\partial x} \frac{\partial \omega}{\partial y} - u \frac{\partial \rho}{\partial x} \omega = \frac{\partial^2}{\partial y^2} [(\mu + \mu_r) \omega], \quad (2.28)$$

where:

$$\omega = \frac{\partial u}{\partial y}$$

The equation for the modified stream function is now written:

$$\frac{\partial \tilde{\psi}}{\partial y} = (\delta^* - y) \left(\rho \omega + u \frac{\partial \rho}{\partial y} \right) \quad \text{from} \quad \tilde{\psi} = \psi - \rho u (y - \delta^*), \quad (2.29)$$

The above system has to be supplemented by the energy equation which will not be written here since its solution does not need any special procedure. Furthermore, in transonic adiabatic flows, the stagnation enthalpy can be assumed constant. This avoids the solving of the energy equation.

Method of Numerical Solution. — In his first publication (1975), which concerned only laminar boundary-layer, Carter envisaged two computational schemes:

- for a *prescribed displacement thickness*, a Crank-Nicolson scheme is employed in the forward flow region and a centered scheme in the reversed flow region;
- for *prescribed wall shear*, the computational molecules are similar to those used by Klineberg and Steger (see above).

In a further extension of the method to turbulent flows, Carter considered only the second kind of computational scheme which is employed both for prescribed displacement thickness and prescribed wall shear. In fact use of the Crank-Nicolson scheme in this case leads to oscillations of the numerical solution.

Thus, the two following computational molecules have to be considered for calculating turbulent boundary-layer:



The discretization is most often established for a variable step size in the y -direction to allow for mesh refinement near the wall as is essential when calculating turbulent flows. Generally, the grid is varied at a constant rate $\Delta y_n = K \Delta y_{n-1}$ where K is close to unity in order to maintain second order accuracy (usually $K=1.04$ to 1.09). About 60 to 80 points are distributed across the boundary-layer in such a way that several points lie in the viscous sublayer. More recently, Carter *et al.* (1982) proposed a composite y -transformation which allows the simultaneous capture of the two turbulent length scales: i.e., boundary-layer total thickness and wall layer thickness. Basically, the transformation consists in the addition of two co-ordinates: an inner co-ordinate N_i based on the approximate analytical velocity representation proposed by Whitfield (1979) and an outer co-ordinate N_o deduced from an approximate fit to the Clauser correlation. There results an adaptative grid procedure which enlarges the inner region, therefore permitting a uniform mesh to be used in the computation plane.

Linearization and discretization of the ω transport equation 2.22 at point (m, n) leads to the linear equation:

$$A_n \omega_{m,n-1} + B_n \omega_{m,n} + C_n \omega_{m,n+1} = D_n, \quad (2.30)$$

where A_n , B_n , C_n and D_n are coefficients which due to the non-linear character of the problem depend on the solution.

The equation for $\tilde{\Psi}$ (equation 2.23) is discretized at the middle point between n and $(n+1)$. This gives a relation of the form:

$$\tilde{\Psi}_{m,n} = \tilde{\Psi}_{m,n+1} + E_n (\omega_{m,n+1} - \omega_{m,n}). \quad (2.31)$$

The velocity component u is computed from ω by using the trapezoidal rule.

Repeated application of equation 2.30 across the boundary-layer results in a tridiagonal system which is conveniently solved by Thomas' algorithm. A recurrence formula of the form:

$$\omega_{m,n} = D'_n + C'_n \omega_{m,n-1}, \quad (2.32)$$

is obtained at each streamwise station m .

In a similar way equation 2.31 can be combined with equation 2.32 to obtain a recurrence relation for the stream function:

$$\tilde{\Psi}_{m,n} = K_n + L_n \omega_{m,n-1}.$$

The coefficients D'_n and C'_n , which are a combination of A_n , B_n , C_n and D_n are computed recursively from the outer boundary to the wall, with the outer boundary condition $\omega(x, \infty) = 0$ imposed by setting $D'_N = C'_N = 0$ (N denotes the grid point at the outer edge).

Equation 2.32 is then used to compute all the $\omega_{m,n}$ provided that the starting value at the wall $\omega_{m,-1}$ is known. This value is deduced from an implicit procedure consisting in a combination of equation 2.32 written for $n=2$ with equation 2.31 evaluated for $n=2$ and in which the boundary condition $\psi(x, 0) = 0$ is imposed. Proceeding in a similar way, K_n and L_n are computed from the outer edge to the wall with the boundary condition $\omega(x, \infty) = \tilde{\Psi}(x, \infty) = 0$ imposed by setting $K_N = L_N = 0$.

Due to the non-linearities of the governing equations, the above procedure has to be iterated at each station m until a convergence criterion is satisfied. A slight underrelaxation has generally to be applied.

In a relaxation or successive sweeps procedure, as the one used by Klineberg and Steger (see above), starting (initial) values of ω and $\tilde{\Psi}$ are guessed at each point of the computational domain. At the upstream border, the y distributions of ω and $\tilde{\Psi}$ are prescribed. At the downstream boundary, the flow is assumed attached; hence it is unnecessary to impose any conditions here. The columns ($m = \text{const.}$) are computed successively beginning at the upstream boundary and continuing to some point downstream of reattachment. Since there exists a region of separated flow, this sweep procedure must be repeated iteratively until satisfaction of a convergence criterion.

When the amplitude of the negative velocity in the reversed flow region is small, it is possible to use a *forward-marching procedure* everywhere without too much loss of accuracy. As is well known, such a method of calculation leads to instabilities when the integration proceeds in a direction opposite to that of the local flow. Nevertheless, the calculation can be stabilized by setting the convection term $u \partial u / \partial x$ (or $u \partial \omega / \partial x$) in the x -momentum equation equal to zero when u is less than zero. This approximation is often called the FLARE approximation from Flügge-Lotz and Reyhner who introduced it for the first time (1968). The FLARE approximation permits a substantial reduction in computer time and storage capacity. This time-gain is of great interest for coupling methods where many successive inviscid flow/boundary-layer calculations are often necessary, especially when separation occurs (Carter and Wornom, 1975).

We will say only a few words about Kawai's method, since his numerical procedure is very similar to the one employed by Carter. Equations 2.28 and 2.29 are linearized in the form:

$$\left[u \frac{\partial \rho}{\partial y} \right] \frac{\partial u}{\partial x} + [\rho u] \frac{\partial \omega}{\partial x} - \left[\frac{\partial \Psi}{\partial x} \right] \frac{\partial \omega}{\partial y} - \left[u \frac{\partial \rho}{\partial x} \right] \omega = \frac{\partial^2}{\partial y^2} \{ (\mu + \mu_e) \omega \}, \quad \frac{\partial \Psi}{\partial y} = (\delta^* - y) \left\{ \left[\frac{\partial \rho}{\partial y} \right] u + [\rho] \omega \right\},$$

where the bracketed terms are considered as the constant coefficients. A modified Thomas algorithm is used in order to treat implicitly the $\partial u / \partial x$ derivative. The recurrence formulae are now:

$$\begin{aligned} \omega_{m,n} &= d_n + a_n \omega_{m,n-1} + b_n u_{m,n-1}, \\ \tilde{\Psi}_{m,n} &= K_n + L_n \omega_{m,n-1} + M_n u_{m,n-1}. \end{aligned}$$

Coefficients a_n , b_n , d_n , K_n , L_n and M_n are computed recursively starting from the boundary-layer outer edge.

This method was applied by Kawai to laminar flows, but it can be extended without difficulty to turbulent flows as was done by Dély. In this case, second order backward difference schemes are recommended. Kawai's method leads to more complicated algebra than methods using compressible-incompressible transformation. However, the overall computing time is comparable since it does not entail repeated exchanges between the incompressible and the physical planes.

Formulation with Primitive Variables. Carter (1978) has extended his inverse method to compressible flow through the use of the Levy-Lees compressibility transformation.

The following new independent variables are introduced:

$$\begin{aligned} \xi &= \int_0^x \rho_e u_e \mu_e dx, \\ \eta &= \frac{\rho_e u_e}{\sqrt{2\xi}} \int_0^y \frac{\rho}{\rho_e} dy. \end{aligned} \tag{2.33}$$

(In reality, the transformation used by Carter also includes a factor allowing the mapping of an axisymmetric flow into a two-dimensional flow: for the sake of simplicity, this factor has been discarded here.)

The transformed continuity and x -momentum equations are written:

$$\begin{aligned} 2\xi \frac{\partial F}{\partial \xi} + F + \frac{\partial V}{\partial \eta} &= 0, \\ 2\xi F \frac{\partial F}{\partial \xi} + V \frac{\partial F}{\partial \eta} &= \beta(\theta - F^2) + \frac{\partial}{\partial \eta} \left[l \left(1 + \frac{\mu_e}{\mu} \right) \frac{\partial F}{\partial \eta} \right] \end{aligned} \tag{2.34}$$

where:

$$F = \frac{u}{u_e}, \quad \theta = \frac{T}{T_e}, \quad l = \frac{\rho \mu}{\rho_e \mu_e}, \quad \beta = \frac{2\xi}{u_e} \frac{du_e}{d\xi}$$

and:

$$V = \frac{2\xi}{\rho_e u_e \mu_e} \left(F \frac{\partial \eta}{\partial x} + \frac{\rho v}{\sqrt{2\xi}} \right).$$

(Carter's formulation also takes into consideration the energy equation which will not be considered here for reasons exposed above.)

In the transformed plane, the relation between the stream function f and the perturbation stream function \tilde{f} becomes:

$$\tilde{f} = f - F \left(\int_0^\infty \theta d\eta - \frac{\rho_e u_e \delta^*}{\sqrt{2\xi}} \right).$$

The stream function \tilde{f} satisfies the boundary conditions:

$$\tilde{f}(\xi, 0) = f(\xi, \infty) = 0.$$

Finally a second change of variables is introduced:

$$\bar{\eta} = \frac{\sqrt{2\xi}}{\bar{m}} \eta \quad \text{or} \quad \bar{\eta} = \left(\int_0^y \frac{\rho}{\rho_e} dy \right) / \delta^*,$$

where $\bar{m} = \rho_e u_e \delta^*$ is the “perturbation mass flow”, i.e., the loss of mass flow in the *inviscid stream* resulting from the existence of the boundary-layer. With the new variables, the perturbation stream function is written:

$$\tilde{f} = f - \frac{F \bar{m}}{\sqrt{2\xi}} (\bar{\eta} - 1 + h), \quad (2.35)$$

where:

$$h = \int_0^\infty (\theta - 1) d\bar{\eta}.$$

This relation is similar to the above relation 2.27 which can also be written:

$$\tilde{\Psi} = \Psi - U \left(Y - \frac{a_e \rho_e}{a_0 \rho_0} \delta^* + h \right)$$

the only difference being in the scaling of the y co-ordinate.

This similarity is to be expected since the crux of all compressible-incompressible transformation methods lies in the correspondence:

$$y \rightarrow Y \propto \int_0^y \frac{\rho}{\rho_e} dy.$$

The final equation to be solved is equation 2.34 and the relation obtained by differentiating equation 2.33 with respect to y (plus the energy equation in Carter's publication). These equations are:

$$\begin{aligned} \frac{\partial \tilde{f}}{\partial \bar{\eta}} &= \frac{\bar{m}}{\sqrt{2\xi}} (1 - \bar{\eta} - h) \frac{\partial F}{\partial \bar{\eta}}, \\ \bar{m}^2 F \frac{\partial F}{\partial \xi} - \bar{m} \frac{\partial}{\partial \xi} [\sqrt{2\xi} \tilde{f} + \bar{m} F (\bar{\eta} - 1 + h)] \frac{\partial F}{\partial \bar{\eta}} &= \bar{m}^2 \beta (\theta - F^2) + \frac{\partial}{\partial \bar{\eta}} \left[l \left(1 + \frac{\mu_e}{\mu} \right) \frac{\partial F}{\partial \bar{\eta}} \right]. \end{aligned}$$

Carter solves the inverse problem for a *prescribed perturbation mass flow* $\bar{m}(x)$ instead of the displacement thickness. This choice [which is particularly convenient since the grouping $\rho_e u_e \delta^*$ appears in the definition of the perturbation stream function (equation 2.35)] presents, in fact, more essential advantages when the inverse calculation is used in a viscous-inviscid coupling method (see Section 3.2.1).

Method of Numerical Solution. — The governing equations are solved by using the Crank-Nicolson finite difference scheme with Newton linearization. In the present formulation, Newton linearization is used on non-linear terms to accelerate the convergence of the iterative process at each streamwise location. In the reversed flow region, the FLARE approximation is introduced to prevent instability while preserving the usual rapid forward-marching scheme (see above).

In order to facilitate comparison with the numerical method employed in the $(\omega, \tilde{\Psi})$ formulation, let us designate by δu , $\delta \tilde{\Psi}$ and $\delta \beta$ the change in the dependent variables at a given point between two successive column iterations; that is:

$$\delta u_{m,n} = u_{m,n}^{q+1} - u_{m,n}^q,$$

where q is the iteration index (it is recalled that β represents the unknown pressure gradient parameter: $\beta = u_e \frac{du_e}{dx}$).

The linearized finite difference form of the governing equations are written as:

$$\delta \tilde{\Psi}_{m,n} - \delta \tilde{\Psi}_{m,n-1} + P_n (\delta u_{m,n} - \delta u_{m,n-1}) = Q_n \quad (2.36)$$

and:

$$A_n \delta u_{m,n-1} + B_n \delta u_{m,n} + C_n \delta u_{m,n+1} + D_n \tilde{\Psi}_{m,n} = E_n + H_n \delta \beta. \quad (2.37)$$

Repeated application of equations 2.36 and 2.37 across the boundary-layer results in a system of block tridiagonal linear system which is solved by the following recurrence formulae:

$$\delta u_{m,n} = E'_n - H'_n \delta \beta - A'_n \delta u_{m,n+1}, \quad (2.38)$$

$$\delta \tilde{\Psi}_{m,n} = Q'_n - S'_n \delta \beta - R'_n \delta u_{m,n+1}. \quad (2.39)$$

The recurrence coefficients are computed from the wall where $\delta u_{m,1} = \delta \tilde{\Psi}_{m,1} = 0$ to the boundary-layer edge. In the *inverse mode*, the perturbation in the edge velocity $\delta u_{m,N}$ and in the pressure gradient parameter $\delta \beta$ are computed from formulae and relations derived from:

- equation 2.39 where the boundary condition $\delta \tilde{\Psi}_{m,N} = 0$ is imposed;
- equation resulting from the x -momentum equation written at the outer edge where the y -derivatives must cancel out, thus:

$$u \frac{\partial u}{\partial x} = \beta.$$

Hence the four relations:

$$\begin{aligned} \delta u_{m,N-1} &= E'_{N-1} - H'_{N-1} \delta \beta - A'_{N-1} \delta u_{m,N}, \\ \delta \tilde{\Psi}_{m,N-1} &= Q'_{N-1} - S'_{N-1} \delta \beta - R'_{N-1} \delta u_{m,N}, \\ B_N \delta u_{m,N} &= E_N + H_N \delta \beta, \\ \delta \tilde{\Psi}_{m,N-1} &= P_N (\delta u_{m,N} - \delta u_{m,N-1}) - Q_N, \end{aligned}$$

which permit the determination of $\delta u_{m, N}$ and $\delta \beta$. These edge values allow the starting of the recurrence formulae 2.38 and 2.39 which are swept from the boundary-layer edge to the wall.

It is to be noticed that in this method the unknown pressure gradient parameter β is treated implicitly in the numerical procedure. This treatment avoids the numerical difficulties which are met at the separation (or reattachment) point by other methods also using primitive variables in which β is determined explicitly by a shooting technique (see Keller and Cebeci's method above as well as Arieli and Murphy's method below).

Remarks. — Formulation of the direct and/or inverse boundary-layer problem in primitive variables may present some advantages:

- the possibility of a resolution either in the direct mode or in the inverse mode is far easier than for the $(\omega, \tilde{\psi})$ formulation. In a direct calculation, u_e and β are known, thus $\delta u_{m, N} = \delta \beta = 0$ and the back substitution process begins by using equations 2.38 and 2.39. The ability of a boundary-layer calculation to easily switch from the direct to the inverse mode and vice versa is essential for coupling techniques.

As a matter of fact, it is preferable to treat *weak* interaction regions in *direct mode*, whereas *strong* interaction regions *must* be computed in the *inverse mode* (for more detail, see Section 3):

- the use of primitive variables avoids the complication of solving for the unknown surface vorticity as is required by the $(\omega, \tilde{\psi})$ formulation.

In some applications (Carter, 1979, 1981), especially when large separated zones form or for very rapid compressions (as in shock-wave/boundary-layer interactions), the Crank-Nicolson scheme produces streamwise oscillations of the solution. Then it is advantageous to employ a fully implicit backward difference scheme. This of course does not change the basic principles of the method.

2.3.3. — Ardoneau's Inverse Method

A different way of solving the inverse problem in primitive variables was proposed in 1981 by Ardoneau. His method is quite general since it applies both to laminar and compressible turbulent flows. The problem is formulated in the compressible plane with primitive variables and can deal with a large variety of prescribed quantities:

- pressure $p(x)$ (direct mode);
- displacement thickness $\delta^*(x)$;
- skin friction coefficient $C_f(x)$;
- perturbation mass flow $\bar{m}(x)$;
- edge normal mass flow: $\rho_e v_e(x)$.

The x -momentum and energy equations are discretized by using a second order centered difference scheme to represent the y -derivatives. This scheme allows for a variable y -step in the case of turbulent flows. When the flow is attached, the x -derivatives are approximated by a second order backward difference scheme. For separated flows, a global iteration procedure similar to the one of Klineberg and Steger (see above) is employed but with a more refined discretization of the form:

$$\frac{\partial u}{\partial x} = \frac{F+1}{2} \frac{\partial u}{\partial x}\Big|_b + \frac{F-1}{2} \frac{\partial u}{\partial x}\Big|_f,$$

with:

$$\begin{aligned} \frac{\partial u}{\partial x}\Big|_b &= \frac{3u_{m,n} - 4u_{m-1,n} + u_{m-2,n}}{2\Delta x}, \\ \frac{\partial u}{\partial x}\Big|_f &= \frac{-3u_{m,n} + 4u_{m+1,n} - u_{m+2,n}}{2\Delta x}. \end{aligned}$$

The function F which insures a blending between the forward and backward schemes is defined as:

$$F_{m,n} = \frac{u_{m,n}}{|u_{m,n}|} \left[1 - \exp\left(\frac{|u_{m,n}|}{u_M}\right) \right].$$

This progressive transition between the two schemes avoids oscillations of the line $u(x, y)=0$ during the iteration on the non-linear terms. The reference velocity u_M is chosen sufficiently small so as not to allow downstream influence on well attached profiles.

The discretized x -momentum and energy equations results in a block (2×2) tridiagonal matrix of dimension $N \times N$ (N being the number of grid points in the boundary-layer) plus:

- one column containing the discretized *unknown edge gradient*: $\rho_e u_e \frac{du_e}{dx}$;
- one row which expresses the *prescribed boundary-condition* in a discretized form.

In this formulation, the boundary condition (prescribed quantity) is treated implicitly (like in Carter's method) thus avoiding numerical difficulties at separation (or reattachment).

The resolution of the above matrix is made by a substitution algorithm derived from Thomas' algorithm. The velocity v -component is given by the continuity equation integrated from the wall to the outer edge by means of a Crank-Nicolson scheme. As in the above methods, an iteration is made at each streamwise step in order to cope with the non-linearities of the problem.

2.3.4. — Other Inverse Methods

In 1974, Horton proposed an inverse method for a separating *laminar* boundary-layer with *prescribed wall shear* (see also Horton, 1975). The boundary-layer equation in the form 2.19 is used (see Section 2.3.1 above). The method of solution consists in replacing the ξ derivatives by 3- or 4-point Lagrange backward difference formulae. This results in an ordinary differential equation for $\partial f/\partial \eta$ at each ξ . The inverse problem is solved with condition 2.20 prescribed at the wall. The solution procedure uses a *shooting technique* on β with Newton's method to enhance convergence. The author was able to compute separation and reattachment with *non evidence* of any singular behavior and found no numerical instabilities in the reversed flow region although the forward marching procedure was used everywhere without, seemingly, the FLARE approximation. This result is in contradiction with calculations made by other authors.

In 1972 Klemp and Acrivos presented an original method for integrating the boundary-layer equations through a region of reversed flow. Their basic idea consists in dividing the flow into two-domains: a region I in which the flow is reversed and a region II where u is everywhere positive. Along the line $y=\Gamma(x)$ separating I and II $u=0$. For a given boundary location $\Gamma(x)$, the boundary-layer equations are integrated separately in I and II in the *appropriate flow direction* by using standard numerical techniques. The solution is obtained by iteration on $\Gamma(x)$ until the slopes $\partial u/\partial y$ along $\Gamma(x)$ become identical in flows I and II. The authors applied this technique to the problem of the flow over a finite stationary flat plate, the surface of which moves at a constant velocity in the opposite direction of the free stream. The pressure gradient being assumed to be zero the method was in fact worked in the direct mode and, consequently, the singularity at separation (and reattachment) was not avoided. In spite of this limited and non-conclusive calculation, Klemp and Acrivos' method is to be retained. It has received an interesting application by Cebeci *et al.* (see below).

As already mentioned, in 1976, Cebeci published an inverse technique for *compressible* laminar and *turbulent* boundary-layers. His method applied to prescribed wall shear as well as to prescribed displacement thickness but it was restricted to non-separated flows. The method was formulated in primitive variables with the unknown pressure gradient kept in the x-momentum equation. The boundary-layer equations are solved by using at two-point finite difference method (Keller, 1970). The unknown pressure gradient is determined explicitly at each streamwise station by an outer iteration loop using Newton's method.

In 1979 Cebeci, Keller and Williams (1979) extended the above method to separating boundary-layer flows (their formulation is restricted to incompressible laminar flows but it could be easily transposed to compressible turbulent flows). The method, which is worked out for a prescribed displacement thickness, employs the Box Scheme along with the FLARE approximation in separated regions. The equations being written with primitive variables, the inverse problem is treated as a non-linear "eigenvalue" problem for the pressure gradient. Although the FLARE approximation allows a fully forward marching procedure, the approximate reversed flow thus computed is corrected by a downstream-upstream iteration similar in nature to the one introduced by Klemp and Acrivos (see above).

In 1980 Arieli and Murphy proposed an inverse method which solves the compressible laminar and turbulent boundary-layer equations written in *primitive variables*. A Levy-Lees transformation (see equations 2.33 in Section 2.3.2 above) is applied mainly to permit the computational domain to grow in the streamwise direction following to some extent the growth of the boundary-layer. A stream function f is introduced so that an equation similar to equation 2.19 is obtained (differences arise from the presence of the turbulent eddy viscosity). The total enthalpy is assumed constant (the energy equation is not solved). The partial differential equation is integrated by using the generalized Galerkin's method (for details see Murphy, 1973). In the present case, the stream function f , the velocity $\partial f/\partial \eta$ and the shear $\partial^2 f/\partial \eta^2$ are approximated by Taylor's series between adjacent mesh points in the η direction assuming a constant fourth derivative $\partial^4 f/\partial \eta^4$ across the interval (η_n, η_{n+1}) . The streamwise derivatives are approximated by:

- backward difference at nodal points where: $\frac{\partial f}{\partial \eta} = \frac{u}{u_e} \geq 0.01$;
- central difference near the zero-velocity line; i.e., at nodal points where: $-0.01 \leq \partial f/\partial \eta \leq 0.01$;
- forward difference when the flow is reversed and $\frac{\partial f}{\partial \eta} < -0.01$.

Iterative sweeping is used so that convection in the region of backflow can be properly taken into account.

The inverse mode is solved with *prescribed wall shear* or *prescribed wake centerline velocity* if the method is applied to compute a wake flow.

In reality, this method is a pseudo-inverse method in the sense that it incorporates an iterative procedure on the prescribed quantity which is varied until the computed pressure distribution coincides with the pressure distribution imparted to the boundary-layer. Thus the present method is in fact a direct technique which uses the inverse mode to avoid (in a manner which is not clear) the singularity at separation (or reattachment). Basically, the iterative process employs a Newton-Raphson iteration procedure in which the "sensitivity" functions are evaluated by solving a set of perturbation equations.

2.4. — Extension to 3-D Boundary-Layer Flows

2.4.1. — General Remarks on Boundary-Layer Separation in 3-D Flows

Like for 2-D flows, any boundary-layer method (integral as well as finite difference method) can be used in 3-D transonic or supersonic shock-wave/boundary-layer interaction as long as the compression is not too intense. It must also be sufficiently spread out to maintain local conditions far from the onset of separation. This is not the place to cite these methods. As in 2-D flows, we will restrict our attention to methods which incorporate special procedures enabling them to work in situations where separation occurs or is likely to occur. Such situations generally correspond to the breakdown of classical methods.

As we already know, the calculation of a 2-D boundary-layer which undergoes an interaction leading to separation or to a nearly separated state is not possible in the direct mode (except in the very improbable situation where the prescribed pressure distribution would satisfy regularity conditions ensuring a smooth passage of the solution through the separation point). In 3-D boundary-layer calculations, numerical difficulties are also met when the *prescribed external flowfield* entails a destabilization of the boundary-layer towards a state where the 3-D separation phenomenon is likely to occur. Physically, this situation is evidenced by a rapid deviation of the wall streamlines (also called skin friction lines) which tend to become asymptotic to what is called the *separation line* (for more information on separation in 3-D flows see Section 4 of Part I). A local mathematical analysis of boundary-layer equations is far more complicated in 3-D flows than it is in 2-D flows. To our knowledge, no analysis similar to Goldstein's study has been undertaken for 3-D boundary-layers.

Nonetheless, very instructive results were obtained by Cousteix and Houdeville within the context of an integral method of solution (1981). They showed that singularities appear as a consequence of the focusing of the skin friction lines. These lines form in fact a family of characteristic lines of the quasi-linear system of first order partial differential (integral) equations applied to the boundary-layer. Such a focusing occurs in the vicinity of a separation line but must not be confused with the separation phenomenon itself. In direct mode calculations, the approach of the singularity leads to quasi unbounded and unrealistic growth of the boundary-layer thickness. In fact, this unphysical behavior can be avoided by extending the inverse concept to 3-D boundary-layer flows. In three dimensions, two quantities must be prescribed since now the inverse problem involves two unknown quantities, namely the two external velocity components in the surface. The prescribed quantities may be:

- either the streamwise and crosswise displacement thicknesses (which is the more convenient choice for coupling methods of calculation);
- or the wall shear-stress components.

Indeed the 3-D inverse concept has been successfully worked out within the context of integral methods. Applications for incompressible flows have been presented by Cousteix and Houdeville (1981), Stock (1980) and Blaise (1982). These computations have shown that it is possible to extend the use of the boundary-layer equations to the immediate neighbourhood of a separation line and even beyond it.

2.4.2. — Integral Inverse Methods

To our knowledge, applications of 3-D inverse boundary-layer calculations using an integral formulation have been restricted to *incompressible flows*. The essential reason for this restriction is probably the lack of accurate experimental data on 3-D separated compressible flows, these data being necessary to test an inverse method. Nevertheless, it should be worthwhile to briefly present the existing methods since their extension to compressible flow would be generally straight-forward. The three methods cited above which apply to turbulent flow use the *two global momentum equations* plus the *entrainment equation*. These equations are written below in streamline co-ordinates. The x -axis coincides with the projection on the surface of the external streamline. The z -axis is orthogonal to the streamline in a plane tangent to the surface, the y -axis being normal to the surface.

In the equations, $\partial/\partial s$ and $\partial/\partial n$ represent $(1/h_1)(\partial/\partial x)$ and $(1/h_2)(\partial/\partial z)$; h_1 and h_2 are the metric coefficients of the employed co-ordinate system. K_1 and K_2 are the geodesic curvatures of the x and z lines; they are related to the metric coefficients by the formulae:

$$K_1 = -\frac{1}{h_1 h_2} \frac{\partial h_2}{\partial x}, \quad K_2 = -\frac{1}{h_1 h_2} \frac{\partial h_1}{\partial z},$$

- streamwise momentum:

$$\frac{\partial \theta_{11}}{\partial s} + \theta_{11} \left(\frac{H+2}{U_e} \frac{\partial U_e}{\partial s} - K_1 \right) + \frac{\partial \theta_{12}}{\partial n} + \theta_{12} \left(\frac{2}{U_e} \frac{\partial U_e}{\partial n} - 2K_2 \right) + \delta_1^* \left(\frac{1}{U_e} \frac{\partial U_e}{\partial n} - K_2 \right) + K_1 \theta_{22} = C_{f_s}/2,$$

- crosswise momentum:

$$\frac{\partial \theta_{21}}{\partial s} + \theta_{21} \left(\frac{2}{U_e} \frac{\partial U_e}{\partial s} - 2K_1 \right) + K_2 \theta_{11} (H+1) + \frac{\partial \theta_{22}}{\partial n} + \theta_{22} \left(\frac{2}{U_e} \frac{\partial U_e}{\partial n} - K_2 \right) = C_{f_n}/2,$$

- entrainment:

$$\frac{\partial(\delta - \delta_1^*)}{\partial s} + (\delta - \delta_1^*) \left(\frac{1}{U_e} \frac{\partial U_e}{\partial s} - K_1 \right) - \frac{\partial \delta_2^*}{\partial n} - \delta_2^* \left(\frac{1}{U_e} \frac{\partial U_e}{\partial n} - K_2 \right) = \frac{\partial \delta}{\partial s} - \frac{V_e}{U_e} = C_E.$$

The integral thicknesses figuring in the above equations have been defined in Section 1.3 (for an incompressible flow $\rho/\rho_e=1$). The thickness ratio H is defined as $H=\delta_1^*/\theta_{11}$. Generally speaking, the above system possesses ten unknowns. In the direct mode, these unknowns are the six integral thicknesses, the two skin-friction coefficients and the entrainment coefficient. In the inverse mode, the two external velocity components are unknown so that two quantities pertaining to the boundary-layer development must be prescribed. In the cited methods, these input quantities are the two displacement thicknesses δ_1^* and δ_2^* . But it is obvious that other quantities can be prescribed, for example the skin friction coefficients.

Classically, the above system of three equations must be supplemented with “closure” relationships to express thickness ratios as well as the skin-friction and entrainment coefficients.

In Cousteix and Houdeville’s method, the closure relations are deduced from *similarity solutions* of the 3-D boundary-layer partial differential equations (Michel *et al.*, 1972; Cousteix and Houdeville, 1981). These solutions are obtained by using an isotropic eddy viscosity model such that:

$$\tau_x = \mu \frac{\partial U}{\partial y} - \rho \bar{U}' \bar{V}' = (\mu + \mu_t) \frac{\partial U}{\partial y}; \quad \tau_z = \mu \frac{\partial W}{\partial y} - \rho \bar{W}' \bar{V}' = (\mu + \mu_t) \frac{\partial W}{\partial y},$$

where the turbulent eddy viscosity is expressed with the mixing length concept:

$$\mu_t = \rho F^2 l^2 \sqrt{\left(\frac{\partial U}{\partial y} \right)^2 + \left(\frac{\partial W}{\partial y} \right)^2} \quad \text{with} \quad \frac{l}{\delta} = 0.085 \tanh \left(\frac{0.41 y}{0.085 \delta} \right)$$

and incorporates a damping function of the form:

$$F = 1 - \exp \left[-\frac{1}{26 \times 0.41 \times \mu} \sqrt{\tau \rho} \right] \quad \text{with} \quad \tau = (\tau_x^2 + \tau_z^2)^{1/2}.$$

The use of the similarity solutions permits the expression of the closure relations as functions of the three parameters:

$$G = \frac{H-1}{H \sqrt{C_{f_s}/2}}, \quad R_{\theta_{11}} = \frac{\rho_e U_e \theta_{11}}{\mu_e}, \quad T = -\frac{\delta_2^*/\delta}{K_2 \delta},$$

thus reducing the number of unknowns to three.

In the method proposed by Stock (1980), the closure relations are deduced by considering two velocity profile representations:

- the streamwise velocity distributions are represented by the Coles family extended to flows describing separated profiles (see above);
- the method being restricted to *infinite swept wing conditions*, (or cylindrical flow) it is assumed that the velocity profile in the spanwise direction can be represented by a *flat plate* velocity profile. Knowing the angle α between the chordwise direction and the external velocity vector at the same time as the streamwise velocity profile, the crossflow profile can be computed from a simple geometric construction.

The entrainment coefficient is evaluated with the lag-entrainment formulation (see Section 2.3 above).

2.4.3. – Finite Difference Methods

The finite difference inverse method developed by Formery (1981; see also Formery and Délery, 1981; Délery and Formery, 1983) extends to 3-D flows the basic principles underlying Carter's method (see Section 2.3.2 above). In order to simplify the presentation, we will restrict ourselves to the case of a 3-D boundary-layer developing on a *flat plate*. It will also be assumed that the Reynolds shear-stresses can be expressed in terms of an *isotropic eddy viscosity* μ_t . This assumption is not essential, more sophisticated turbulence modeling can be envisaged. Let us consider a cartesian co-ordinate system $Oxyz$ set up in such that axes Ox , Oz are in the surface and Oy is perpendicular to the surface. The 3-D turbulent boundary-layer equations relative to the mean motion (Reynolds' averaging) are written:

- continuity:

$$\frac{\partial(\rho u)}{\partial x} + \frac{\partial(\rho v)}{\partial y} + \frac{\partial(\rho w)}{\partial z} = 0,$$

- streamwise momentum:

$$\rho u \frac{\partial u}{\partial x} + \rho v \frac{\partial u}{\partial y} + \rho w \frac{\partial u}{\partial z} = - \frac{\partial p}{\partial x} + \frac{\partial}{\partial y} \left[(\mu + \mu_t) \frac{\partial u}{\partial y} \right] \quad (2.40)$$

- crosswise momentum:

$$\rho u \frac{\partial w}{\partial x} + \rho v \frac{\partial w}{\partial y} + \rho w \frac{\partial w}{\partial z} = - \frac{\partial p}{\partial z} + \frac{\partial}{\partial y} \left[(\mu + \mu_t) \frac{\partial w}{\partial y} \right]. \quad (2.41)$$

The energy equation will be replaced here by the assumption that the stagnation enthalpy is constant throughout the flowfield. As we know (see Section 2.2.1 above), this assumption does not entail large errors provided the flow is adiabatic and the Mach number M_e at the boundary-layer edge moderately supersonic. However, consideration of the energy equation would not modify the basic principles of the method.

One introduces vectors Ω and A defined as:

$$\Omega = \text{curl } V, \quad \rho V = \text{curl } A.$$

The components of Ω and A along the axes Oy , Ox , Oz are designated respectively by Ω_1 , Ω_2 , Ω_3 and A_1 , A_2 , A_3 . Introduction of the potential vector A automatically satisfies the continuity equation. Without loss of generality (except for possibility of mass injection at the wall) vector A – which is defined to within an arbitrary gradient – is chosen in such a way that:

$$A_1(x, y, z) \equiv 0, \quad A_2(x, 0, z) = A_3(x, 0, z) = 0.$$

Within the boundary-layer approximations the following relations hold true:

$$\begin{aligned} \Omega_1 &= \frac{\partial w}{\partial x} - \frac{\partial u}{\partial z}, & \Omega_2 &= - \frac{\partial w}{\partial y}, & \Omega_3 &= \frac{\partial u}{\partial y}, \\ \rho u &= - \frac{\partial A_3}{\partial y}, & \rho v &= \frac{\partial A_3}{\partial x} - \frac{\partial A_2}{\partial z}, & \rho w &= \frac{\partial A_2}{\partial y}. \end{aligned}$$

By taking the y -derivative of equations 2.40-2.41 in order to eliminate the unknown pressure p , one obtains the new system:

$$\rho u \frac{\partial \Omega_2}{\partial x} + \rho v \frac{\partial \Omega_2}{\partial y} + \rho w \frac{\partial \Omega_2}{\partial z} - \rho \Omega_2 \frac{\partial u}{\partial x} - \rho \Omega_3 \frac{\partial w}{\partial x} - \left(u \frac{\partial \rho}{\partial x} + w \frac{\partial \rho}{\partial z} \right) \Omega_2 - u \frac{\partial \rho}{\partial y} \frac{\partial w}{\partial x} - w \frac{\partial \rho}{\partial y} \frac{\partial w}{\partial z} = \frac{\partial^2}{\partial y^2} [(\mu + \mu_t) \Omega_2] \quad (2.42)$$

$$\rho u \frac{\partial \Omega_3}{\partial x} + \rho v \frac{\partial \Omega_3}{\partial y} + \rho w \frac{\partial \Omega_3}{\partial z} - \rho \Omega_2 \frac{\partial u}{\partial z} - \rho \Omega_3 \frac{\partial w}{\partial z} - \left(u \frac{\partial \rho}{\partial x} + w \frac{\partial \rho}{\partial z} \right) \Omega_3 - u \frac{\partial \rho}{\partial y} \frac{\partial u}{\partial x} - w \frac{\partial \rho}{\partial y} \frac{\partial u}{\partial z} = \frac{\partial^2}{\partial y^2} [(\mu + \mu_t) \Omega_3] \quad (2.43)$$

By definition, the streamwise and crosswise displacement thicknesses Δ_1 and Δ_2 are expressed by the following relations in the computation reference system (the displacement thicknesses expressed in the external streamlines co-ordinate system are defined in Section 1.3 above):

$$\Delta_1 = \int_0^\infty \left(\frac{u_e}{V_e} - \frac{\rho u}{\rho_e V_e} \right) dy = \int_0^\infty \frac{1}{\rho_e V_e} \left(\rho_e u_e + \frac{\partial A_3}{\partial y} \right) dy,$$

$$\Delta_2 = \int_0^\infty \left(\frac{w_e}{V_e} - \frac{\rho w}{\rho_e V_e} \right) dy = \int_0^\infty \frac{1}{\rho_e V_e} \left(\rho_e w_e - \frac{\partial A_2}{\partial y} \right) dy,$$

where V_e represents the velocity modulus at the boundary-layer edge. It can be readily shown that the "modified stream functions" \tilde{A}_2 and \tilde{A}_3 defined by relations:

$$\tilde{A}_2 = A_2 + \rho u \Delta_2 \cos \alpha - \rho w (y - \Delta_2 \sin \alpha), \quad (2.44)$$

$$\tilde{A}_3 = A_3 + \rho u (y - \Delta_1 \cos \alpha) - \rho w \Delta_1 \sin \alpha, \quad (2.45)$$

where α is the angle between the external velocity V_e and axis Ox satisfy the boundary conditions:

$$\begin{aligned} \tilde{A}_2 &= \tilde{A}_3 = 0 && \text{when } y = 0, \\ \tilde{A}_2, \tilde{A}_3 &\rightarrow 0 && \text{when } y \rightarrow \infty. \end{aligned}$$

Thus, the use of \tilde{A}_2 and \tilde{A}_3 permits the generalising to the 3-D case of the modified stream function $\tilde{\Psi}$ of Carter's 2-D inverse method (see Section 2.3.2 above). By taking the y -derivative of equations 2.44 and 2.45, one obtains:

$$\frac{\partial \tilde{A}_2}{\partial y} = \rho \Omega_2 (y - \Delta_2 \sin \alpha) + \rho \Omega_3 \Delta_2 \cos \alpha + \Delta_2 u \frac{\partial \rho}{\partial y} \cos \alpha - w (y - \Delta_2 \sin \alpha) \frac{\partial \rho}{\partial y} \quad (2.46)$$

$$\frac{\partial \tilde{A}_3}{\partial y} = \rho \Omega_2 \Delta_1 \sin \alpha + \rho \Omega_3 (y - \Delta_1 \cos \alpha) + u (y - \Delta_1 \cos \alpha) \frac{\partial \rho}{\partial y} - \Delta_1 w \sin \alpha \frac{\partial \rho}{\partial y}. \quad (2.47)$$

The inverse problem consists in solving equations 2.42-43-46-47, the unknown functions of which are Ω_2 , Ω_3 , \tilde{A}_2 and \tilde{A}_3 . The boundary conditions of the problem are:

— at the wall:

$$y = 0; \quad \tilde{A}_2 = \tilde{A}_3 = 0, \quad u = v = w = 0,$$

— at the external boundary:

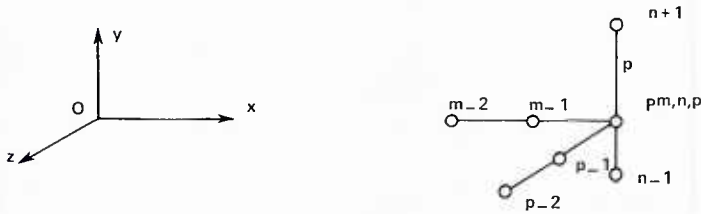
$$y \rightarrow \infty; \quad \Omega_2 = \Omega_3 = \tilde{A}_2 = \tilde{A}_3 = 0.$$

Components u , v , w of velocity are easily computed from Ω_2 , Ω_3 , \tilde{A}_2 and \tilde{A}_3 .

In the proposed method, the inverse problem can be solved according to one or the other of the following sets of prescribed quantities:

- displacement thicknesses δ_1^* and δ_2^* (Δ_1 and Δ_2 are immediately deduced from δ_1^* and δ_2^*);
- components of the skin friction vector; or which is equivalent, the skin-friction coefficients C_{fx} and C_{fr} .

For the numerical resolution, equations 2.42-43-46-47 are linearized and discretized according to the computational molecule shown below:



The mesh has a variable step size in the y -direction to permit mesh refinement in the vicinity of the wall. The x and z -derivatives are evaluated by second order forward difference schemes. The y -derivatives are computed by a centered scheme.

Discretization of equations 2.42 and 2.43 at point $P^{m,n,p}$ and of equations 2.46 and 2.47 at P' of co-ordinates $(m \Delta x, y_{n+(1/2)}, p \Delta z)$ along with the use of the trapezoidal rule to express the velocity components u and w lead to a linear system of algebraic equations which is solved at each computation station (m, p) by using a generalization of Thomas' algorithm [for detail, see Formery, 1981]. When the displacement thicknesses are prescribed, a special procedure must be used to compute the components of vorticity at the wall in order to start the recurrence calculation. The adopted method is an implicit procedure which generalizes to 3-D flows the method briefly described in Section 2.3.2 above. The procedure leads to a linear system of two equations allowing the computation of Ω_2 and Ω_3 for $y=0$. When the skin-friction vector is prescribed the computation is a bit more simple since then Ω_2 and Ω_3 at the wall are practically equal to the prescribed quantities.

The computation is stabilized in the region where u and w change sign thanks to the FLARE approximation.

Another finite difference method was proposed more recently by Radwan and Lekoudis (1983). In this method, the primitive momentum equations are solved directly, i.e., without prior differentiation with respect to y . But, in a manner similar to that employed in the previous technique of solution, a two component vector potential is introduced. The solution procedure is based on the Keller box scheme with use of the FLARE approximation in reversed flow regions. Calculations were performed with the displacement thicknesses prescribed, an algebraic eddy viscosity model being used. Since application was restricted to incompressible cylindrical flows, we will not give any further details on this method.

Applications of the Formery-Délery method are given in Section 4.2 of Part I. One of them concerns a transonic interaction under infinite swept wing conditions due to the lack of experimental data relative to compressible 3-D interactions (in fact the method works in truly 3-D flows). The example clearly shows the ability of the inverse mode to compute a separated zone including a separation and a reattachment line.

2.5. — References

Alber, I. E. (1968): Application of an Exact Expression for the Equilibrium Dissipation Integral to the Calculation of Turbulent Non-Equilibrium Flows. *Computation of Turbulent Boundary-Layers*, Stanford Press.

Alber, I. E. and Coats, D. E. (1969): Analytical Investigation of Equilibrium and Non-Equilibrium Turbulent Boundary-Layer. AIAA Paper 69-689.

Alber, I. E. (1971): Similar Solutions for a Family of Separated Turbulent Boundary-Layers. AIAA Paper 71-203.

Arieli, R. and Murphy, J. D. (1980): Pseudo-Direct Solution to the Boundary-Layer Equations for Separated Flows. AIAA Journal, Vol. 18, No. 8, pp. 883-891 (Aug. 1980).

Ardonceau, P. (1981): Étude de l'interaction onde de choc-couche limite supersonique. Thèse de Docteur ès Sciences Physiques, Université de Poitiers.

Blaise, P. (1982): Mise en œuvre et développement d'une méthode de couplage fort pour le calcul d'écoulements autour d'ailes en flèche infinies. Thèse de 3^e cycle, Université de Lille-1.

Bradshaw, P.; Ferris, D. and Atwell, N. (1967): Calculations of Boundary-Layer Development Using the Turbulent Energy Equation. *J. Fluid. Mech.*, Vol. 28, Part. 3, pp. 593-616.

Brown, S. N. (1965): Singularities Associated with Separating Boundary-Layers. *Philosophical Transactions of the Royal Society*, Vol. 257, A 1084, pp. 409-444.

Carter, J. E. (1975): Inverse Solutions for Laminar Boundary-Layer Flows with Separation and Reattachment. NASA TR R 447.

Carter, J. E. and Wornom, S. F. (1975): Forward Marching Procedure for Separated Boundary-Layer Flows. AIAA Journal, Vol. 13, No. 8, pp. 1101-1103 (Aug. 1975).

Carter, J. E. and Wornom, S. F. (1975): Solutions for Incompressible Separated Boundary-Layers Including Viscous-Inviscid Interaction. NASA SP 347, pp. 125-150.

Carter, J. E. (1978): Inverse Boundary-Layer Theory and Comparison with Experiment. NASA TP 1208.

Carter, J. E. (1979): A New Boundary-Layer Inviscid Iteration Technique for Separated Flow. AIAA Paper 79-1450.

Carter, J. E. (1981): Viscous-Inviscid Interaction Analysis of Transonic Turbulent Separated Flow. AIAA Paper 81-1241.

Carter, J. E.; Edwards, D. E. and Werle, M. J. (1982): Co-ordinate Transformation for Laminar and Turbulent Boundary-Layers. AIAA Journal, Vol. 20, No. 2, pp. 282-284 (Feb. 1982).

Catherall, D. and Mangler, K. W. (1961): The Integration of the Two-Dimensional Laminar Boundary-Layer Equations Past the Point of Vanishing Skin-Friction. *J. Fluid Mech.*, Vol. 26, Part 1, pp. 163-182.

Cebeci, T. and Smith, A. M. O. (1974): *Analysis of Turbulent Boundary-Layers*. Academic Press, New York.

Cebeci, T. (1976): An Inverse Boundary-Layer Method for Compressible Laminar and Turbulent Boundary-Layers. *Journal of Aircraft*, Vol. 13, No. 9, pp. 709-717 (Sept. 1976).

Cebeci, T.; Keller, H. B. and Williams, P. G. (1979): Separating Boundary-Layer Flow Calculations. *J. of Computational Physics*, Vol. 31, pp. 363-378.

Clauser, F. H. (1954): Turbulent Boundary-Layer in Adverse Pressure Gradient. *JAS*, Vol. 21, No. 2, pp. 91-108 (Feb. 1954).

Collins, M. and Simpson, R. L. (1976): Flowfield Prediction for Separating Turbulent Boundary-Layers. Southern Methodist University, Report WT-4.

Cousteix, J.; Houdeville, R. and Michel, R. (1974): Couches limites turbulentes avec transfert de chaleur. La Recherche Aérospatiale, No. 1974-6, pp. 327-338, (Nov.-Dec. 1974).

Cousteix, J. and Houdeville, R. (1977): Méthode intégrale de calcul d'une couche limite turbulente sur une paroi courbée longitudinalement. La Recherche Aérospatiale, No. 1977-1, pp. 1-13 (Jan.-Feb. 1977).

Cousteix, J. and Houdeville, R. (1981): Singularities in Three-Dimensional Boundary-Layer Calculations and Separation Phenomena. AIAA Journal, Vol. 19, No. 8, pp. 176-185 (Aug. 1981).

Crocco, L. and Lees, L.: A Mixing Theory for the Interaction Between Dissipative Flows and Nearly Isentropic Streams. *JAS*, Vol. 19, No. 10, pp. 649-676.

Délery, J.; Chattot, J. J. and Le Balleur, J. C. (1975): Interaction visqueuse avec décollement en écoulement transsonique. AGARD-CP-168.

Délery, J. and Le Balleur, J. C. (1980): Interaction et couplage entre écoulement de fluide parfait et écoulement visqueux. ONERA RSF No. 4/3073.

Délery, J. M. (1981): Investigation of Strong Shock-Wave/Turbulent Boundary-Layer Interaction in 2-D Transonic Flows with Emphasis on Turbulence Phenomena. AIAA Paper 81-1245; see also AIAA Journal, Vol. 21, No. 2, pp. 180-185 (Feb. 1983).

Délery, J. and Formery, M. (1983): A Finite Difference Method for Inverse Solution of 3-D Turbulent Boundary-Layer Flow. AIAA Paper 83-0301.

East, L. F.; Smith, P. D. and Merryman, P. (1977): Prediction of the Development of Separated Turbulent Boundary-Layers by the Lag-Entrainment Method. RAE, TR 77046.

Formery, M. and Délery, J. (1981): Méthode aux différences finies pour le calcul en mode inverse de la couche limite turbulente tridimensionnelle. La Recherche Aérospatiale, No. 1981-5, pp. 303-313.

Formery, M. (1982) : Méthode aux différences finies pour le calcul en modes inverses de la couche limite turbulente tridimensionnelle. Thèse de Docteur-Ingénieur, Université Pierre-et-Marie-Curie, Paris-6.

Gerhart, P. M. (1979) An Integral Method for Predicting Subsonic Turbulent Separating Boundary-Layer with Specified Free Stream Input. Proc. Symposium ASME/CSME on "Turbulent Boundary Layers", Niagara Falls, (June 18-20, 1978).

Goldstein S. (1948): On Laminar Boundary-Layer Flow Near a Position of Separation. The Quarterly Journal of Mechanics and Applied Mathematics, Vol. 1, Part 1, pp. 43-69.

Green, J. E.; Weeks, D. J. and Brooman, J. W. F. (1972): Prediction of Turbulent Boundary-Layers and Wakes in Compressible Flow by a Lag-Entrainment Method. RAE, TR 72231.

Hanjalic, K. and Launder, B. E. (1972): A Reynolds Stress Model of Turbulence and its Application to Thin Shear Flows. J. Fluid Mech., Vol. 52, Part 4, pp. 609-638.

Head, M. R. (1958): Entrainment in the Turbulent Boundary-Layer. A.R.C.-R. & M. 3152.

Horton, H. P. (1974): Separating Laminar Boundary-Layers with Prescribed Wall Shear. AIAA Journal, Vol. 12, No. 12, pp. 1772-1774 (Dec. 1974).

Horton, H. P. (1975): Numerical Investigation of Regular Laminar Boundary-Layer Separation. AGARD-CP-168.

Kawai, N. (1977): Inverse Technique for Compressible Boundary-Layers with Separation and its Application to Interacting Supersonic Boundary-Layer Flows. 12th Int. Symp. on Space Technology and Science, Tokyo, Proc. pp. 147-152.

Keller, H. B. (1970): A New Difference Scheme for Parabolic Problems. *Numerical Solution of Partial Differential Equations*, edited by J. Bramble, Vol. II, Academic Press, New York.

Keller, H. B. and Cebeci, T. (1971): Accurate Numerical Methods for Boundary-Layer Flow, I: Two-Dimensional Laminar Flows. Proceedings of the Second International Conference on Numerical Methods in Fluid Mechanics, *Lecture Notes in Physics*, Springer-Verlag.

Keller, H. B. and Cebeci, T. (1971): Accurate Numerical Methods for Boundary-Layer Flows, II: Two-dimensional Turbulent Flows. AIAA Paper 71-164.

Keller, H. B. and Cebeci, T. (1972): An Inverse Problem in Boundary-Layer Flows: Numerical Determination of Pressure Gradient for a Given Wall Shear. J. of Computational Physics, Vol. 10, pp. 151-161.

Klemp, J. B. and Acrivos, A. (1972): A Method for Integrating the Boundary-Layer Equations Through a Region of Reverse Flow. J. Fluid Mech., Vol. 53, Part 1, pp. 177-191.

Klineberg, J. M. (1968): Theory of Laminar Viscous-Inviscid Interactions in Supersonic Flows. Ph. D. Thesis, Cal. Inst. of Techn.

Klineberg, J. M. and Lees, L. (1969): Theory of Laminar Viscous-Inviscid Interactions in Supersonic Flows. AIAA Journal, Vol. 7, No. 12, pp. 2211-2222 (Dec. 1969).

Klineberg, J. M. and Steger, J. L. (1972): Calculation of Separated Flows at Subsonic and Transonic Speeds. Proceedings of the Third International Conference on Numerical Methods in Fluid Mechanics, *Lecture Notes in Physics* No. 19, Springer Verlag.

Klineberg, J. M. and Steger, J. L. (1974): On Laminar Boundary-Layer Separation. AIAA Paper 74-94.

Kuhn, G. D. (1971): Calculation of Compressible, Non-Adiabatic Boundary-Layers in Laminar, Transitional and Turbulent Flow by the Method of Integral Relations. NASA-CR-1797.

Kuhn, G. D. and Nielsen, J. N. (1973): Prediction of Turbulent Separated Boundary-Layers. AIAA Paper 73-663.

Kuhn, G. D. and Nielsen, J. N. (1975): Prediction of Turbulent Separated Flow at Subsonic and Transonic Speeds Including Unsteady Effects. AGARD-CP-168.

Le Balleur, J. C. (1981): Calcul par couplage fort des écoulements visqueux transsoniques incluant sillages et décollements. Profils d'ailes portants. La Recherche Aérospatiale, No. 1981-3, pp. 161-185.

Mc Donald, H. and Camarata, F. (1968): An Extended Mixing Length Approach for Computing the Turbulent Boundary-Layer Development. *Computation of Turbulent Boundary-Layers*, Stanford Press.

Mathews, D.; Childs, M. and Paynter, G. (1970): Use of Coles' Universal Wake Function for Compressible Turbulent Boundary-Layers. Journal of Aircraft, Vol. 7, No. 2, pp. 137-140 (March-April 1970).

Michel, R.; Quémard, C. and Durant, R. (1969): Application d'un schéma de longueur de mélange amélioré à l'étude des couches limites d'équilibre. ONERA N.T. No. 154.

Michel, R.; Quémard, C. and Cousteix, J. (1972): Méthodes pratiques de prévision des couches limites turbulentes bi et tridimensionnelles. La Recherche Aérospatiale, No. 1972-1, pp. 1-14.

Murphy, J. D. (1973): Application of the Generalized Galerkin Method to the Computation of Fluid Flows. Proceedings of the AIAA Computational Fluid Dynamics Conference, Palm-Spring, Calif., pp. 63-68 (July 19-20, 1973).

Noi, Nguyen Van (1971): Étude théorique et expérimentale du recollement subsonique incompressible d'un écoulement plan turbulent à sa frontière. Thèse d'Ingénieur-Docteur, Faculté des Sciences de l'Université de Paris.

Quémard, C. and Archambaud, J. P. (1976): Méthode intégrale de calcul d'un sillage avec gradient de pression longitudinal. Note Technique DERAT (ONERA), No. 1/508.

Radwan, S. and Lekoudis S. G. (1983): Boundary-Layer Calculations in the Inverse Mode for Incompressible Flows Over Infinite Swept Wings. AIAA Paper 83-0454.

Reyhner, T. A. and Flügge-Lotz, I. (1968): The Interaction of a Shock-Wave with a Laminar Boundary-Layer. Int. Journal of Non-Linear Mech., Vol. 3, No. 2, pp. 173-199.

Simpson, R. L.; Chew, Y-T and Shivaprasad, B. G. (1981): The Structure of Separating Turbulent Boundary-Layer. Part 1: Mean Flow and Reynolds Stresses. J. Fluid Mech., Vol. 113, pp. 23-51.

Stewartson, K. (1954): Further Solutions of the Falkner-Skan Equation. Proc. Cambridge Phil. Soc., Vol. 50, pp. 454-465.

Stewartson, K. (1958): On Goldstein's Theory of Laminar Separation. The Quarterly Journal of Mechanics and Applied Mathematics, Vol. 11, p. 399.

Stock, H. W. (1980): Computation of the Boundary-Layer and Separation Lines on Inclined Ellipsoids and of Separated Flows on Infinite Swept Wings. AIAA Paper 80-1442.

Swafford, T. W. (1981): Analytical Approximation of Two-Dimensional Separated Turbulent Boundary-Layer Velocity Profiles. Arnold Air Force Station, Tenn., AEDC-TR-79-99.

Thiede, P. (1976): Prediction Method for Steady Aerodynamics Loading on Airfoils with Separated Transonic Flow. AGARD-CP-204.

Whitfield, D. L. (1979): Analytical Description of the Complete Turbulent Boundary-Layer Velocity Profile. AIAA Journal, Vol. 17, No. 10, pp. 1145-1147 (Oct. 1979).

Whitfield, D. L.; Swafford, T. W. and Jacocks, J. L. (1981): Calculation of Turbulent Boundary-Layers with Separation and Viscous-Inviscid Interaction. AIAA Journal, Vol. 19, No. 10, pp. 1315-1322 (Oct. 1981).

Whitfield, D. L. and Thomas, J. L. (1983): Transonic Viscous-Inviscid Interaction Using Euler and Inverse Boundary-Layer Equations. *Viscous Flow Computational Methods in Recent Advances in Numerical Methods in Fluids*, W. G. Habashi Editor, Pineridge Press, U.K.

Winter, K. G. and Gaudet, L. (1970): Turbulent Boundary-Layer Studies at High Reynolds Number at Mach Numbers Between 0.2 and 2.8. A.R.C.-R. & M. 3712.

3. – INVISCID-VISCOUS INTERACTIVE METHODS

3.1. – Basic Principles

The basic idea of most Inviscid Viscous Interactive (IVI) methods (also called coupling methods) consists in splitting the flowfield into:

- an external or outer region where viscous forces (laminar as well as turbulent stresses) are assumed to play a negligible role;
- one or several inner region(s) in which the dissipative effects are essential. These regions are boundary-layers, wakes, mixing zones, etc.

The usual coupling approach is a substitute for the solving of the full time-averaged Navier-Stokes equations for flows in which dissipative effects are confined within regions small in size when compared to a characteristic length scale of the problem (chord length of an airfoil, blade to blade distance of a cascade, etc.).

Thus, in the coupling approach, the external flow has to satisfy the much simpler *Euler equations* (which are frequently replaced by the potential equation if the inviscid flow is, or is assumed to be, irrotational); whereas the dissipative zones are modeled according to various approaches differing in their level of sophistication:

- the full Navier-Stokes equations can be applied to the whole inner region, as is done in what is called the multi-domain approach (see Section 5);
- analytical methods based on asymptotic expansion or perturbation techniques are sometimes employed (see Section 4);
- the most popular models, however, make use of the Prandtl equations which are solved either by finite difference techniques or, more frequently, by integral methods (see Section 2).

Mixed procedures can in fact be envisaged: for instance, boundary-layer equations are applied to the major part of the viscous flow, except in small regions where the validity of these equations is questionable (shock foot region, trailing edge flow, largely separated zone, etc.). These sub-domains are represented by more refined analyses using either analytical techniques or numerical solution of the full Navier-Stokes equations.

In what follows, we will only consider viscous-inviscid coupling methods using the *classical Prandtl equations* to represent the boundary-layer flow. More refined approaches, still in the development stage, will be briefly evoked in Section 3.4. This presentation will also be restricted to *isoenergetic* and *steady* flows. Neither do we intend to discuss viscous-inviscid coupling methods in general. These methods involve many problems, the consideration of which is beyond the scope of the present AGARDograph. Thorough examination of the coupling approach can be found elsewhere (Le Balleur, 1978, 1980; Lock and Firmin, 1981). The present review will concentrate on points which are of critical importance when applying coupling methods to shock-wave/boundary-layer interaction problems, with emphasis being put on turbulent régime.

Briefly speaking, development of a viscous-inviscid interactive technique requires the following elements:

- (1) an *accurate* and *fast* solver of the inviscid flow equations. These qualities are especially important when computing shock-wave/boundary-layer interactions since a meaningful “capturing” of the interaction necessitates local mesh sizes smaller than the thickness of the incoming boundary-layer;
- (2) an *accurate* (i.e., physically realistic) method with which to compute dissipative flow regions;
- (3) *representative* and *convenient* compatibility relations between the outer and the inner flow regions. The compatibility generally results in a *coupling equation*, the form of which may lead to difficult problems in transonic and/or supersonic flows.
- (4) an *efficient iterative procedure* to insure a fast convergence of the interactive calculations between the two flow regions.

Point 1 is a very broad domain, the examination of which would be beyond the scope of the present AGARDograph. Point 2 has been developed in Section 2. Points 3 and 4 will be discussed in what follows.

3.2. – The Problem of the Coupling Conditions

3.2.1. – The Various Forms of the Coupling Equation

Basically, the inviscid-viscous coupling problem consists in the calculation of two flows, described by *different equations*, which must satisfy boundary conditions (at infinity and on the body surface) and be “compatible” along their common free boundary $\delta(x)$. Conditions to be satisfied on $\delta(x)$ are *continuity of pressure and flow direction*. It is usual to choose as free boundary δ some conventional outer edge of the boundary-layer.

In what follows, we will neglect wall curvature effects and consider the classical boundary-layer system of co-ordinates where axis Ox is in the surface.

Integration along y of the boundary-layer *continuity equation* gives the flow deviation $[\theta]_{BL}$ induced at δ by the boundary-layer, viz.:

$$[\theta]_{BL} \# \frac{v_e}{u_e} = \frac{d\delta^*}{dx} - \frac{(\delta - \delta^*)}{\rho_e u_e} \frac{d(\rho_e u_e)}{dx} \quad (3.1)$$

In this above equation, δ^* is the conventional boundary-layer displacement thickness (more sophisticated viscous-inviscid models involving “defect formulation” will be briefly presented in Section 3.4).

Thus, the two flows must satisfy, at each streamwise distance x , the following conditions:

$$[\bar{p}(x)]_{\delta} = [p(x)]_{\delta} \quad (\text{the } \bar{\cdot} \text{ designates perfect fluid quantities}) \quad (3.2)$$

and:

$$[\bar{\theta}_{\delta}] = [\theta_{\delta}]_{BL}. \quad (3.3)$$

Equation 3.1 constitutes what is called the *coupling relation*. Other forms of this equation are often preferred. To facilitate the inviscid calculation, an analytical approximate report of condition 3.1 at some distance of the free boundary is carried out. As demonstrated by Lighthill (1958), this is done by considering a *continuation of the external inviscid flow* into the region occupied by the boundary-layer. By making a Taylor expansion in the vicinity of δ while, neglecting second order terms and assuming that \bar{p} and \bar{u} for this fictitious flow can be regarded as constant across the boundary-layer and equal to their outer edge values (which is consistent with the standard boundary-layer approximations), one arrives at:

$$\rho_e \bar{v}(y) = \rho_e \bar{v}_e + (\delta - y) \frac{d(\bar{\rho}_e \bar{u}_e)}{dx}.$$

Since it is assumed $\rho_e = \bar{\rho}_e$ and $u_e = \bar{u}_e$, combining this relation with equation 3.1 yields:

$$\theta_y = \left[\frac{\bar{v}}{\bar{u}_e} \right]_y = \frac{d\delta^*}{dx} + (\delta^* - y) \frac{1}{\bar{\rho}_e \bar{u}_e} \frac{d(\bar{\rho}_e \bar{u}_e)}{dx}. \quad (3.4)$$

From equation 3.4 we can immediately draw two alternative conclusions:

— when $y = \delta^*$, we obtain:

$$\left[\frac{\bar{v}}{\bar{u}_e} \right]_{\delta^*} = \frac{d\delta^*}{dx} \quad (3.5)$$

which is a *no slip condition on the displacement body*.

— when $y = 0$, we have:

$$\left[\frac{\bar{v}}{\bar{u}_e} \right]_0 = \frac{1}{\bar{\rho}_e \bar{u}_e} \frac{d}{dx} [\bar{\rho}_e \bar{u}_e \delta^*], \quad (3.6)$$

which corresponds to a condition of *fluid injection at the wall* (this condition is also known as the *transpiration velocity concept*).

When relations 3.5 and 3.6 are used, conditions at the boundary-layer edge $\bar{\rho}_e$, \bar{u}_e are generally identified with inviscid flow quantities \bar{p} , \bar{u} which are computed either on the displacement body or on the wall. There is a certain degree of inconsistency in making this identification which is justified only if the continued inviscid flow remains practically constant in the y -direction. Although this is not true in strong interaction processes, nevertheless the above identification provides a simple way to take into account static pressure variation across the boundary-layer (Le Balleur and Mirande, 1975). This fact is only an empirical observation and a formulation of the “overlapping” problem free of any approximation can be made by redefining boundary-layer integral quantities from the “defect formulation” concept (see Section 3.4 below).

Coupling equations 3.1, 3.5 and 3.6 are in principle equivalent within the boundary-layer approximations. The reality is more subtle and in fact they correspond to different interpretations of the viscous-inviscid interaction problem.

Use of equation 3.1 makes the problem similar to the classical *multi-domain approach* — or “*patching approach*” — in the sense that the two flows are distinct and can be considered as really “existing” on each side of the free boundary. In fact, these streams satisfy different equations (the Euler and Prandtl equations respectively) so that only continuity of quantities can be satisfied at δ ; the derivatives are discontinuous.

Coupling equations 3.5 and 3.6 imply an *overlapping* of the two streams. The boundary-layer flow is no longer contiguous to the inviscid stream and the existence of the boundary-layer is essentially “felt” by the outer flow as an alteration of the inviscid no-slip condition on the body surface. This is particularly true when the coupling condition is written on the wall: then there is no longer a “geometrical” constraint via δ or δ^* between the two flows. The formulation involving an overlapping between the two streams is often termed “*matching*” method and acquires its full significance when the defect formulation is introduced.

Differences between the patching and the matching approaches are immaterial in low subsonic flows and the various coupling relations give nearly identical results. However, in *supersonic* and *transonic* interacting flows, consideration of different coupling equations leads to dramatic change in the behavior of the solution. This problem—which is of the outmost importance when applying the interactive concept to compute shock-wave/boundary-layer interactions—will now be discussed.

3.2.2. — Subcritical and Supercritical Boundary-Layers

The coupling problem will be discussed by considering first the local boundary-layer equations in order to make it clear that this problem is inherent in the boundary-layer approach and is not a consequence of the use of an integral method of solution. In a second part, the problem will be formulated with integral concepts and it will be seen that similar conclusions are then reached.

Local Analysis. — Weinbaum and Garvine (1968) have for the first time established the following equation giving flow deflection $[\theta]_\delta$ at the boundary-layer edge (see also Carrière *et al.*, 1975) :

$$\theta_\delta = B \frac{dp}{dx} + C, \quad (3.7)$$

where:

$$B = -\frac{1}{\gamma p} \int_{\epsilon}^{\delta} \frac{M^2 - 1}{M^2} dy,$$

$$C = -\frac{1}{\gamma p} \int_{\epsilon}^{\delta} \frac{1 + (\gamma - 1) M^2}{M^2} \frac{\partial \tau}{\partial y} dy.$$

In the above expressions, M is the local Mach number in the boundary-layer, p the pressure and γ the ratio of specific heats. It is assumed that θ is zero at the wall. Equation 3.7 is obtained by combination of the boundary-layer equations along with the classical hypothesis: $\partial p / \partial y = 0$.

For a wake flow, the inner limit ϵ can be set equal to zero since velocity is non-zero on the axis $y=0$ (except at a “separation” or “reattachment” station). A difficulty arises in boundary-layer flows since then B and C are singular in the limit $\epsilon \rightarrow 0$ ($M=0$ at $y=0$). However, in turbulent flows, the problem can be circumvented by taking for ϵ the thickness δ of the viscous sublayer, the normal velocity at δ being asymptotically equal to zero to all orders δ^n as shown by Mellor (1972) (see also Section 4.3.1 on analytical methods). An other way to avoid the singularity is to consider a fictitious slip-velocity at the wall equal to the “wake velocity” of the Coles’ composite law. In fact, behaviors to be discussed depend mainly on the more or less important “filling” of the velocity profile. For a turbulent boundary-layer, this filling is essentially represented by the wake component

For a supersonic boundary-layer (or wake), integral B may be either positive or negative, as is intuitively obvious if one considers the change of sign of the integrand at the sonic point of the velocity profile. Drastically different responses of the boundary-layer in a free interaction process correspond to this change in the sign of B . To see this, let us consider a perturbation of equation 3.7 near flat-plate conditions ($dp/dx=0$); then:

$$\theta_\delta - [\theta_\delta]_{FP} = B \frac{dp}{dx}.$$

Consequences:

- if B is *positive*, an increase in θ_δ , i.e., a thickening of the boundary-layer ($\theta \approx d\delta^*/dx$), corresponds to pressure rise. By analogy with one-dimensional perfect fluid theory, the boundary-layer is then said to be *subcritical*, in the sense that it behaves (in an overall a global manner) like a subsonic flow;
- if B is *negative*, an increase in θ_δ is associated with a negative pressure gradient. In this case, the boundary-layer is said to be *supercritical*, since it behaves like a supersonic flow.

The above terminology was introduced in 1952 by Crocco and Lees in their pioneer paper on viscous-inviscid interaction.

A *laminar* boundary-layer is most often subcritical, a supercritical state being encountered only in hypersonic flows or for highly cooled surfaces (in the latter, very low temperature levels close to the wall entail low local speed of sound and accordingly high Mach number; thus B is more likely to be negative). For a *turbulent* boundary-layer, in which the Mach number profile is much fuller, transition from subcritical state to supercritical state occurs approximately for $M_e=1.3$ for a conventional flat-plate profile ($H_i=1.3$). One sees that supercritical behavior is met as soon as the transonic flow régime is reached.

The essential feature of a supercritical state is that the boundary-layer cannot undergo an interaction process with smooth tendency towards separation, i.e., a process in which the pressure p , the thickness δ^* and the shape parameter H_i all increase. Such a behavior is only possible for a subcritical flow. For a supercritical boundary-layer, the onset of an interaction process leading to separation requires a preliminary transition—or *jump*—to subcritical conditions. Various analyses have been proposed to connect a given upstream supercritical state to the associated downstream subcritical state. These jump models have been formulated within the context of integral methods. In a manner similar to normal shock theory, they use a set of equations expressing the conservation of appropriate global quantities across the jump (Crocco, 1954; Klineberg, 1968; Hunter and Reeves, 1971).

We will not comment any further about the “jump” theory, such a discontinuity in the boundary-layer evolution being artificial and physically meaningless. It must be clear that the sub-and supercritical states are not “real” properties of the dissipative layer but are a consequence of the model (inadequate as a result of over simplification) adopted to depict the viscous-inviscid interaction. The subcritical-supercritical behavior which is met when the coupling conditions are written at δ is probably a consequence of the neglect of pressure variation across the boundary-layer. As a matter of fact, in a formulation using coupling at δ , Holden (1969) was able to compute smooth interaction in turbulent supersonic flows (no jump needed), provided that normal pressure gradients were introduced and computed with the help of the integral y -momentum equation (these calculations were made within the context of an integral method).

Le Balleur (1977) has shown that it is possible to write the coupling on the displacement body or at the wall in a manner similar to equation 3.7. By considering a continuation of the inviscid flow below the boundary δ , one can write (if the pressure p is assumed constant across the boundary-layer):

$$\bar{\theta}_\delta - \bar{\theta}_y = -\frac{1}{\gamma \bar{p}} \frac{d\bar{p}}{dx} \int_y^{\delta} \frac{\bar{M}^2 - 1}{\bar{M}^2} dy. \quad (3.8)$$

Within the classical boundary-layer approximations, \bar{M} can be considered as constant and equal to M_e . Combination of equations 3.7 and 3.8 gives:

- for the coupling on the *displacement body* ($y=\delta^*$):

$$\theta_{\delta^*} = B^* \frac{dp}{dx} + C,$$

where:

$$B^* = -\frac{1}{\gamma p} \left[\int_{\epsilon}^{\delta^*} \frac{M^2 - 1}{M^2} dy - \int_{\delta^*}^{\delta} \left(\frac{1}{\bar{M}^2} - \frac{1}{M^2} \right) dy \right].$$

The second integral figuring in B^* is always negative since \bar{M} is always greater than M . The first integral may be positive if the boundary-layer flow remains supersonic below the displacement surface. As a consequence, B^* is less likely to be negative than B (see equation 3.7). In fact, for a flat-plate turbulent boundary-layer ($H_i=1.3$), B^* changes sign near $M_e \approx 2$. One sees that coupling on the displacement surface does not suppress supercritical behavior (in turbulent flows); it only postpones the critical limit to higher Mach numbers.

- for the coupling at the wall ($y=0$):

$$\theta_0 = B_0 \frac{dp}{dx} + C$$

with:

$$B_0 = -\frac{1}{\gamma p} \int_{\epsilon}^{\delta^*} \left(\frac{1}{\bar{M}^2} - \frac{1}{M^2} \right) dy.$$

As is easily seen, B_0 is *always positive* (since \bar{M} is always greater than M). Thus coupling at the wall leads to a formulation of the viscous-inviscid problem in which the boundary-layer *always behaves as a subcritical flow*, whatever the external Mach number may be. There is no longer a need for an artificial jump to initiate an interaction process.

Criticality Within the Context of Integral Methods. – The same above conclusions can also be drawn by consideration of an integral method of solution for the interaction problem. In a general way, the coupling relation (see equations 3.1, 3.5 and 3.6) is expressed by means of an ordinary differential equation involving boundary-layer global characteristics (δ^* , H_i) and the edge velocity (or the edge Mach number). On the other hand, x -wise variations in boundary-layer integral properties are related to change in edge conditions by ordinary differential integral equations generally two in number (see Section 2.2 above). Thus, the interaction process is formulated via a system of three equations for three unknown quantities, namely: a thickness, δ^* for instance, a shape parameter H_i and the velocity (or Mach number) at boundary-layer edge. This system can be written in the condensed form:

$$|A| \cdot \begin{vmatrix} \frac{d\delta^*}{dx} \\ \delta^* \frac{dH_i}{dx} \\ \frac{\bar{u}_e}{u_e} \frac{d\bar{u}_e}{dx} \end{vmatrix} = \begin{vmatrix} C_{f/2} \\ f \\ \theta_y \end{vmatrix} \quad (3.9)$$

with $y=\delta$, δ^* or 0 according to the coupling relation envisaged. Function f is the Entrainment coefficient, or the Shear-Work integral or the Shear Stress integral depending on the “second” equation employed. Coefficients of matrix A depend only on the Mach number M_e and on the *velocity distribution shape parameter*. Denoting by D the determinant of matrix A , and applying Cramer’s rule, system 3.9 leads to a relation of the form:

$$D \frac{1}{\bar{u}_e} \frac{d\bar{u}_e}{dx} = d_1 \theta_y + d_2.$$

One sees that a relation similar to equation 3.7 is obtained in such a way that the same conclusions can be drawn by discussing the sign of D . When equations 3.1 is used, the vanishing of D corresponds exactly to the Crocco-Lees critical point (Crocco and Lees, 1952).

Integration of system 3.9 is not possible at the point where D vanishes, except if regularity conditions are locally satisfied. These conditions are obviously that $d_1 \theta_y + d_2 = 0$ when $D=0$ (It can be shown that if \bar{u}_e is regular, δ^* and H_i are also regular, see Carrière et al., 1975). The critical point corresponds to a saddle-point singularity and is similar to the throat singularity of a one-dimensional perfect fluid flow.

The existence of a critical point (with associated subcritical and supercritical states) has also important repercussions in *boundary-layer calculations using the inverse mode*.

One of the ways to perform an inverse calculation, consists in solving system 3.9 for prescribed θ_y (as we know, see Section 2 above, other inverse procedures are possible). As quoted above, integration of 3.9 is not possible if $D=0$. The diagram shown in Figure 3.1 gives in the plane (H_i , M_e) the locus of the points where D vanishes for the three types of inverse input θ_y . It can be seen that the critical boundaries are not very sensitive to the “second” equation employed (the present calculations have been made with the velocity profiles defined by equation 2.9 in Section 2 above). Concerning an *inverse integral method*, the following conclusions can be drawn for a *turbulent* boundary-layer starting from an initial flat-plate situation:

- if θ_δ is prescribed, supercritical behavior is met as soon as $M_e \approx 1.3$;
- if $\theta_{\delta^*} = \frac{d\delta^*}{dx}$ (i.e. the displacement thickness) is prescribed supercritical behavior appears for $M_e \gtrsim 2$;
- if $\theta_0 = \frac{d}{dx}(\bar{\rho}_e \bar{u}_e \delta^*)/\bar{\rho}_e \bar{u}_e$ (i.e., the “perturbation mass flow”, see Section 2.3.2 above) is prescribed, *there is no risk of “criticity”*: the boundary-layer always responds as a subcritical flow.

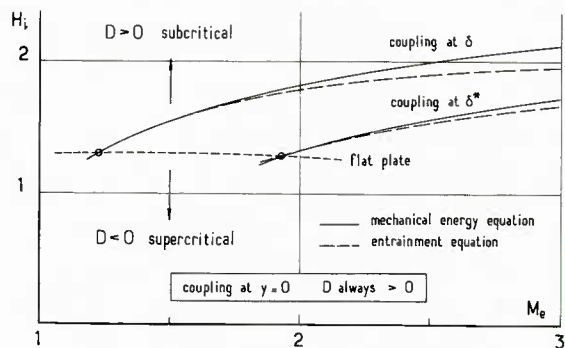


Fig. 3.1 – Integral coupling method – Critical curves.

As shown by numerical experiments, the above conclusions remain valid when the boundary-layer equations are solved with a finite difference method:

Conclusions Concerning the Coupling Formulation. — To summarize the coupling problem in transonic and/or supersonic flows,

— coupling at boundary-layer edge is not recommended (and is now rarely used) for the following reasons:

(i) this technique necessitates the location of the boundary-layer edge, hence difficulties can be met in performing the outer inviscid flow calculation. Furthermore, boundary conditions for the outer field have to be imposed on an ill-defined boundary which moves in the course of the iterative procedure;

(ii) supercritical response appears in the transonic range (for a turbulent régime), leading to severe numerical difficulties. In principle, this problem could be avoided by resorting to higher order boundary-layer formulations but at the cost of a greater complexity in the calculation of the dissipative layers,

— coupling on the displacement body has long been considered as the most natural way to take viscous effects into account. Nevertheless, the displacement surface is changing at every iteration step which complicates the inviscid flow calculation; and supercritical behavior is to be expected for $M_e \gtrsim 2$ (for a turbulent régime);

— coupling at the wall does not suffer from these disadvantages since:

- (i) the effective body geometry “seen” by the inviscid stream remains unchanged during the iterative procedure;
- (ii) the response of the boundary-layer is always subcritical.

However, the use of a coupling equation written at the wall may be questionable as a means of representing viscous effects due to large separated zones. In this case, the displacement body concept seems more appropriate to correctly depict reality. Secondly, when the inviscid flow is computed with the general Euler equations (which is necessary when computing internal flows), a problem arises in the determining of the entropy of the fluid entering into the computation domain when the coupling relation gives a positive mass injection.

In the following Sections, we will mainly consider viscous inviscid calculations in which the dissipative layers remain subcritical, in the sense that no jump has to be introduced. This implies coupling at the wall or on the displacement body for turbulent flows where the Mach number is not too high ($M_e \lesssim 2$).

3.2.3. — Weak and Strong Interactions

In viscous-inviscid interacting flows, one has to distinguish between *weak* and *strong* interaction régimes.

A *weak interaction régime* is said to exist when the flow properties (body pressure distribution, for instance) are essentially imposed by the inviscid solution. This means that there are only small differences between the real (viscous) flow wall pressure distribution and the pressure distribution given by the fully inviscid solution. In this case, the consideration of viscous effects is merely a (small) *correction* to the inviscid solution. In principle, it is not then necessary to iterate the dissipative layers and the perfect fluid calculations. The computation chain is as follows:

(1) Perfect Fluid → (2) Boundary-Layer (direct mode) → (3) Perfect Fluid with corrected boundary conditions at (or near) the wall → Stop.

When the iteration loop is limited to one cycle, the compatibility conditions are not strictly satisfied except the θ_{δ^*} condition (most often, weak interactions are computed with the displacement body concept). However, for a *truly* weak interaction régime, the error on the pressure distribution is very small and, as has been shown by numerical experiments, further iterations do not substantially improve the solution. The weak interaction behavior corresponds to the classical Prandtl boundary-layer concept. In terms of the triple-deck asymptotic theory (see Section 4 below), the hierarchy of the flow tends to the classical direct (i.e., prescribed external pressure field) boundary-layer hierarchy in which the pressure is mainly determined by the outer inviscid region (or upper-deck).

A *strong interaction régime* establishes the moment when the entirely inviscid solution becomes completely unrealistic. This means that this solution comprises regions of very steep pressure gradient and/or pressure discontinuities (shock-waves) which are not compatible with the existence of a thin and attached boundary-layer. In this case, there exists a strong dependence between the viscous and the inviscid parts of the flow, so that it is *strictly necessary* to iterate the calculations of the two regions until a stable and *converged state is reached* (i.e., until all the compatibility conditions are satisfied). The strong interaction régime does not correspond to a breakdown of the boundary-layer concept itself. This is well demonstrated by the triple-deck theory. In fact, it corresponds to a failure of the classical *direct* boundary-layer approach. In terms of the triple-deck theory, there is *no longer a definite hierarchy* between the two flows: with equal importance, the pressure distribution is determined, both by the boundary-layer and the outer inviscid stream.

In the following Sections, the strong interaction problem alone will be envisaged, since it is obviously the only interaction régime pertaining to shock-wave/boundary-layer interaction.

3.3. — The Problem of the Iterative Procedure

3.3.1. — Entirely Supersonic Interactions

The earlier coupling methods were applied to fully supersonic outer flows and, most often, used a coupling condition written at δ (see equation 3.1). In particular, these methods were developed to compute shock/boundary-layer interactions arising at a wedge or when an oblique shock impinges on a wall. The external inviscid flow was generally determined by assuming a Prandtl-Meyer compression which gives a simple and local relation between the flow direction at δ and the pressure gradient $d\rho/dx$ (the tangent-wedge relation was also employed). Use of the Prandtl-Meyer law restricts application of the theory to simple wave flows; i.e., to two-dimensional and initially uniform flows. Such a restriction could be alleviated by using the general Method of Characteristics. In this case, a precise localization of the outer edge of the boundary-layer is essential for the computation of the inviscid stream. On the contrary, the location of δ is without importance when the Prandtl-Meyer law is employed to determine the outer flow (this of course is not true for the evaluation of the deflection [0], induced by the boundary-layer). In these theories, the boundary-layer development was calculated by a variety of techniques: integral, finite difference, Galerkin methods, etc. The laminar as well as the turbulent régimes were both considered.

As the equations describing the outer flow are hyperbolic whereas those applied to the dissipative layer are parabolic in the downstream direction (in separated regions, the FLARE approximation renders the flow parabolic in the downstream direction everywhere), the most immediate method of solution is to use a *downstream marching procedure*. In this procedure, the compatibility conditions (see equations 3.2 and 3.3) are satisfied at each streamwise step so that singularities at separation and/or reattachment are avoided. However, the problem of the interacting boundary-layer envisaged as an *initial value problem is ill-posed*. Some downstream condition is needed to insure unicity of the solution and thus a well-posed problem (see Garvine, 1968; Neyland, 1970; Werle *et al.*, 1973). This downstream condition restores the ellipticity of the real problem which apparently was lost by the use of Prandtl equations.

Handled as an initial value problem, the viscous-inviscid formulation may be summarized in the following terms: for an imposed perturbing agency (i.e., shock strength) and a given boundary-layer initially unperturbed:

— if the flow is *subcritical*, a self-induced destabilization process (H_p , δ^* and p rise at the same time) can be initiated at any abscissa x_0 . The principle of solution consists in iterating on x_0 until the condition prescribed downstream is satisfied (usually, this condition is the return of the solution to a flat plate or weak interaction situation);

— if the dissipative flow is *supercritical*, a self-induced compression can only take place after an initial jump from the supercritical state to the corresponding subcritical state. Now, the proper solution is found by iterating on the abscissa x_0 of the jump until the downstream condition is fulfilled. This condition can be the continuous return to a supercritical situation which requires the passage of the solution through a “throat” where regularity conditions must be satisfied in a manner similar to the behavior of the inviscid flow solution in a converging-diverging nozzle (for more details see Ai, 1970 and Carrière *et al.*, 1975). This throat is in fact the Crocco-Lees critical point (see also Stollery and Hankey, 1970 for a discussion of the problem of subcritical-supercritical boundary-layer).

In fact, there are no fundamental differences between the above two cases since a change in the coupling equation renders a supercritical flow subcritical. The essence of the above methods is the fact that the problem is conceived as a *two-point boundary value problem* which is essentially solved by *shooting techniques*. Such techniques can become tedious and time consuming, especially when large separation bubbles form. Methods belonging to this type have been proposed for laminar flows by Bray *et al.* (1960), Reyhner and Flügge-Lotz (1966), Lees and Reeves (1964), Nielsen *et al.* (1966), Holt (1966), Klineberg and Lees (1969), Alziary de Roquefort (1969), Leblanc *et al.*, (1971), Gautier and Ginoux (1973). The turbulent case has been treated by Alber (1967), Alber and Lees (1968), Todisco and Reeves (1969), Klineberg *et al.* (1972), Aymer de la Chevalerie and Leblanc (1978). (These lists of authours are not exhaustive). Most of these methods employ an integral formulation to compute the dissipative layer. We will not comment any further on these methods which are now rather out-dated and which have been discussed in the preceding AGARDograph on Shock-Wave/Boundary-Layer Interaction. Rather we will focus our attention on new techniques of solution which have been developed in the meantime.

Integration of the interaction equations by a purely downstream marching process is ill posed as an initial value problem in the sense that any error encountered at the initial station will grow exponentially in the x -direction (i.e., will cause a “branching”) and thus will produce a solution unrelated to the correct initial conditions. To overcome this weakness, it is necessary to *specify directly the downstream condition* in terms of some constraint which may be either the pressure level itself or the return of the downstream pressure to its weak interaction value. The *implicit treatment* of the downstream boundary condition results in *sweeping* or *relaxation techniques* in which the computation plane is swept iteratively until convergence is achieved on the wall pressure distribution, for instance. In this relaxation procedure, the downstream boundary condition is *enforced at each iteration step*.

To our knowledge, the first application of this kind of technique was made to laminar flow by Werle and Vatsa (1973). Thereafter, Bertke, Werle and Vatsa (1974) extended the method to turbulent flows (see also Werle *et al.*, 1975).

In these techniques, the coupling is expressed on the displacement body (equation 3.5 of Section 3.2.1 above) and the change in the outer flow pressure via a relation of the form:

$$\frac{dp}{dx} = f \left(\frac{d\theta_s}{dx} + \frac{d^2 \delta^*}{dx^2} \right),$$

where θ_s is the slope of the surface. The above relation may be provided by linear theory, tangent wedge or the unified tangent wedge laws (Cox and Crabtree, 1965). Thus, the boundary-layer x -momentum equation is written in the form:

$$\rho u \frac{\partial u}{\partial x} + \rho v \frac{\partial u}{\partial y} = -f \left(\frac{d\theta_s}{dx} + \frac{d^2 \delta^*}{dx^2} \right) + \frac{\partial}{\partial y} \left[(\mu + \mu_r) \frac{\partial u}{\partial y} \right] \quad (3.10)$$

(we will not consider here the energy equation which does not receive any special treatment). Equation 3.10 can be expressed in the following more condensed form which explicitly displays the influence of the boundary-layer:

$$\frac{\partial}{\partial y} \left[(\mu + \mu_r) \frac{\partial u}{\partial y} \right] + B_1(x, y) \frac{d^2 \delta^*}{dx^2} = B_2(x, y). \quad (3.11)$$

The turbulent viscosity μ_t is modeled by a classical algebraic two-layer description. The boundary-layer equations are integrated by a standard finite difference method (Blottner, 1970) and the viscous-inviscid interaction problem is solved with the following boundary conditions:

— upstream station x_0 :

$$u(x_0, y) \quad \text{and} \quad d\delta^*/dx \quad \text{prescribed},$$

— downstream station:

$$\frac{d\delta^*}{dx} \quad \text{or} \quad \frac{d^2\delta^*}{dx^2} = 0. \quad (3.12)$$

Numerical solution of equation 3.11, along with the prescribed boundary conditions, is accomplished by using Alternating Direction Implicit concepts. It proceeds at two artificial time levels. The first one is from t^n to $t^{n+(1/2)} = t^n + \Delta t/2$:

$$\left\{ \frac{\partial}{\partial y} \left[(\mu + \mu_t) \frac{\partial u}{\partial y} \right] \right\}^{n+(1/2)} + B_1^{n+(1/2)} \left[\left(\frac{d^2 \delta^*}{dx^2} \right)^n - \frac{2}{\Delta t} (\delta^{*(n+(1/2))} - \delta^{*(n)}) \right] = B_2^{n+(1/2)}$$

and the second from $t^{n+(1/2)}$ to $t^{n+1} = t^{n+(1/2)} + \Delta t/2$:

$$\left\{ \frac{\partial}{\partial y} \left[(\mu + \mu_t) \frac{\partial u}{\partial y} \right] \right\}^{n+1} + B_1^{n+(1/2)} \left[\left(\frac{d^2 \delta^*}{dx^2} \right)^{n+1} - \frac{2}{\Delta t} (\delta^{*(n+1)} - \delta^{*(n+(1/2))}) \right] = B_2^{n+(1/2)}. \quad (3.13)$$

Basically, in the first step the viscous properties (i.e., velocity and temperature profiles) are determined; while the second step serves to update the displacement thickness contribution to the inviscid pressure gradient. Equation 3.13 will reduce to a tridiagonal set of algebraic equations in finite difference form which can be solved by the Thomas algorithm, downstream condition 3.12 being taken into account. The time-like march is allowed to proceed until a steady state is achieved.

The first time-step corresponds in fact to a classical *direct mode boundary-layer calculation*, since for this step the pressure—or which is equivalent $d^2 \delta^*/dx^2$ —is prescribed, the streamwise distribution of δ^* being that computed at time level n . Accordingly, a special arrangement of the numerical method has to be introduced to overcome the Goldstein type singularity at separation and reattachment. This point is certainly a weakness of this kind of calculation in which the boundary-layer is always computed in the direct-mode.

A method similar in nature, but without the drawback of the singularities inherent in the direct mode, has been proposed by Aymer de la Chevalerie and Leblanc (1979) for laminar interactions. The method incorporates an inverse finite difference technique for the calculation of the separated boundary-layer. The inverse procedure is worked with the skin friction prescribed, and is a generalization of the method developed by Klineberg and Steger (1974), (see Section 2.3.1 above).

3.3.2. — Mixed Supersonic-Subsonic Flows

3.3.2.1. — Direct, Inverse and Semi-Inverse Methods

Sweeping or relaxation techniques are not essential when the outer flow is entirely supersonic. They only appear as more convenient and probably more efficient than shooting techniques. However, the formulation of the viscous-inviscid interaction problem has to be reconsidered when the outer inviscid flow contains subsonic regions. In this case, it is no longer possible to compute the external stream by a downstream marching method or to use simple formulae to compute the pressure from the local flow angle.

In the mixed supersonic-subsonic situation, computation of the perfect fluid flow requires relaxation or time-marching methods in order to properly take into account the boundary conditions on all the frontiers of the computational domain. In this way it is no longer possible to fulfill the compatibility conditions by a streamwise progression since outer flow quantities at a station x depend on downstream conditions. In fact, the boundary-layer and the external inviscid flow have to be computed separately and in turn according to an iterative process which is repeated until convergence is achieved, i.e., until conditions 3.2-3 are satisfied.

To achieve this goal, various arrangements of the calculation strategy can be envisaged:

(i) *Direct Methods* (see diagram in Fig. 3.2). — The iteration loop starts with given surface boundary conditions (i.e., conditions at or near the body according to equations 3.1, 3.5 or 3.6). These conditions are known from the previous iteration step. An inviscid flow calculation provides a pressure distribution $\bar{p}(x)$ which is then fed into the boundary-layer calculation. This last calculation furnishes new boundary-conditions $\theta(x)$ and the process is repeated. Such an iterative procedure is called a *fixed point iteration*, since at every station there is the following relationship between values of $\theta(x)$ at iterations n and $n+1$:

$$\theta^{n+1}(x) = \mathbb{F}[\theta^n(x)]. \quad (3.14)$$

In the above equation, \mathbb{F} is an operator involving perfect fluid and boundary-layer calculations.

It is clear that an entirely direct method breaks down as soon as separation occurs since the boundary-layer is always computed in the direct mode.

(ii) *Inverse Methods* (see diagram in Fig. 3.2). — Now, both flows are computed by inverse methods. The iteration loop is as follows: for a given pressure distribution $\bar{p}(x)$ (on or near the body surface, according to the coupling relation retained), an inverse inviscid flow calculation gives $\bar{\theta}(x)$ which is, in turn, prescribed to an inverse boundary-layer calculation; hence a new pressure distribution $p(x)$... The inverse fixed point operator is:

$$\bar{p}^{n+1}(x) = \mathbb{G}[\bar{\theta}^n(x)]. \quad (3.15)$$

In fact, the inverse boundary-layer mode is not well suited to weak interaction regions or to accelerating flows (Ardoncau and Alziary de Roquefort, 1980). So that when computing a complete and complex flowfield, (the flow past an airfoil, for example) it is necessary to use alternatively direct and inverse modes. Then, it can become difficult to obtain a smooth transition between regions where the inviscid flow has been calculated either by direct or by inverse methods.

(iii) *Semi-Inverse Methods* (see diagram in Fig. 3.2). In this method, the perfect fluid flow is *always* computed in the *direct mode*, whereas the boundary-layer is computed either in the direct mode, in "well" attached flow regions, or in the inverse mode if separation occurs (or if the dissipative flow is highly destabilized). According to the present procedure, the *same* $\theta(x)$ distribution is fed both in the boundary-layer and in the inviscid flow calculations. Two pressure distributions are thus obtained which coincide when convergence is reached. Here, a new iteration cycle is started by "guessing" a new $\theta(x)$ distribution from the "error" $p(x) - \bar{p}(x)$.

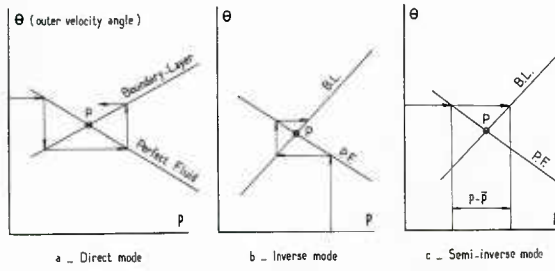


Fig. 3.2 – The various iteration paths in coupling algorithms.

The three above coupling techniques are said to be *explicit* in the sense that the boundary-layer and the inviscid stream are computed in turn, the one after the other. The supersonic methods cited in the preceding Section were in fact *implicit* coupling procedures, since in these methods the two streams were determined simultaneously. In the latter case, use of the Prandtl-Meyer law (or the tangent wedge relation) to find the external pressure makes the implicit formulation very easy. Extension of the implicit procedure to elliptic external flows, with a view to obtaining higher convergence rates, has been proposed by Veldman (1979, 1981). In essence his method is as follows in the case of a strictly incompressible flow: the outer velocity distribution $\bar{u}_e(x)$ is computed by using Cauchy's integral which involves the displacement thickness distribution. This integral constitutes the *interaction law*. Discretization of the interaction law results in an algebraic relation involving δ^* and \bar{u}_e at every grid point i ($i=1, I$) along the body surface. This relation is added to the discretized boundary-layer equations to obtain a system which is solved at each streamwise station x_i (i varying from 1 to I). Due to the fact that the interaction law contains values of δ^* downstream of the computation station x_i (the problem is here elliptic), it is necessary to perform several upstream-downstream sweeps in order to properly account for the ellipticity of the problem. The essential feature of the present method is to use an interaction law (or coupling equation) at iteration number n , and for station x_p , which involves both δ^*_p and \bar{u}_{ei} at the same iteration number.

This is in contrast to:

- direct methods where $\bar{u}_e^{(n)}$ is computed from $\delta^{*(n-1)}$;
- inverse methods where $\delta^{*(n)}$ is computed from $\bar{u}_e^{(n-1)}$.

Such a *quasi-simultaneous* procedure avoids difficulties incurred when either fully direct (as in Werle and Vatsa's method, *see* above) or fully inverse modes are used. We will not comment any further on Veldman's method since its applications have been hitherto restricted to incompressible flows.

3.3.2.2. – Convergence Properties of Direct and Inverse Methods

Fixed Point Methods. – The relationship implicit in equations 3.14 and 3.15 can be viewed conceptually, in simplified form, as representing curves or traces in the $(p-\theta)$ space, such as depicted in Figure 3.3. This graph may also be interpreted as the situation at one particular point of the computation grid along the coupling surface. The two curves represent respectively:

- relation between \bar{p} and θ satisfying the inviscid flow equations;
- relation $p(\theta)$ resulting from boundary-layer calculations.

The intersection point of these two curves is the desired matching point. It is clear that an iteration path based on successive perfect-fluid boundary-layer calculations using simple fixed point iterations, such as those defined by equations 3.14 and 3.15 may be either converging or diverging according to the local shape of the two "response" curves (see diagrams in Fig. 3.3). The classical and well-known method used to insure the convergence of the iteration process or to enhance its convergence rate is to employ underrelaxation.

The process consists in replacing equations 3.14 and 3.15 respectively by:

$$\begin{aligned}\theta^{n+1}(x) &= \theta^n(x) + \omega \{ F[\theta^n(x)] - \theta^n(x) \}, \\ \bar{p}^{n+1}(x) &= \bar{p}^n(x) + \omega \{ G[p^n(x)] - p^n(x) \},\end{aligned}$$

where the underrelaxation coefficient ω is most often determined empirically from trial and error. Effect of underrelaxation in the plane $p-\theta$ is shown in Figure 3.4.

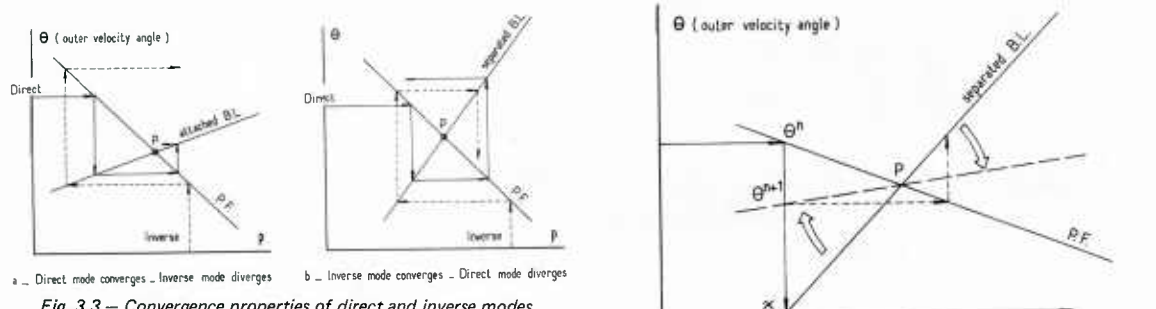


Fig. 3.3 – Convergence properties of direct and inverse modes.

Fig. 3.4 – Effect of underrelaxation on a diverging direct mode calculation.

A rational approach to the stability problem of coupling algorithms was published in 1978 by Le Balleur and has led to important results allowing, in particular, a more rigorous way to define the optimum relaxation coefficient. Basically, Le Balleur's method relies on an approximate, linear, stability analysis (a very similar analysis of this problem has been given by Wigton and Holt, 1983).

Let us first consider the *direct mode* and imagine that a harmonic perturbation $\delta\theta(x, 0) = \varepsilon \exp(i\lambda x)$ is imposed on the converged $\theta^*(x, 0)$ distribution. This distribution is the one for which the outer and the inner flows have been made compatible (i.e., they satisfy equations 3.2-3). Let $\delta\bar{u}(x, 0)$ be the resulting velocity perturbation of the *inviscid flow* (\bar{u} is scaled to some reference velocity, say the velocity at upstream infinity U_∞). $\delta\bar{u}(x, 0)$ is estimated with the help of the linearized small disturbance equation for the perturbation potential $\varphi(x, y)$:

$$(1 - \bar{M}^2) \frac{\partial^2 \varphi}{\partial x^2} + \frac{\partial^2 \varphi}{\partial y^2} = 0,$$

where \bar{M} is the *local unperturbed Mach number*. Knowing that: $\delta\theta = \frac{\partial \varphi}{\partial y}$ and $\delta\bar{u} = \frac{\partial \varphi}{\partial x}$, it can be shown that $\delta\bar{\theta}$ and $\delta\bar{u}$, along the boundary $y=0$ (i.e., on the body surface) are related by:

$$\delta\theta(x, 0) = i\sqrt{1 - \bar{M}^2} \delta\bar{u}(x, 0) \quad (3.16)$$

if the flow is locally *subsonic*,

$$\delta\bar{\theta}(x, 0) = -\sqrt{\bar{M}^2 - 1} \delta\bar{u}(x, 0)$$

if the flow is locally *supersonic*.

Now, let us consider the response of the boundary-layer to the perturbation $\delta\bar{u}(x, 0)$ in the external velocity. This response is given by equation 3.7 (see Section 3.2.2 above) which will be written here in a slightly different form involving velocity instead of pressure:

$$\theta = B' \frac{d\bar{u}}{dx} + C.$$

Hence for the perturbation angle:

$$\delta\theta(x, 0) = i\lambda \tilde{B} \delta\bar{u}(x, 0) \quad \text{where } \tilde{B} = B'/\bar{u}. \quad (3.17)$$

Thus, we arrive at the following relations giving the *response* $\delta\theta(x, 0)$ of the boundary-layer as function of the *perturbation* $\delta\bar{\theta}(x, 0)$ of the converged boundary condition:

$$\begin{aligned} \delta\theta(x, 0) &= \frac{\lambda \tilde{B}}{\beta} \delta\bar{\theta}(x, 0) && \text{if } M < 1, \\ \delta\theta(x, 0) &= -\frac{i\lambda \tilde{B}}{\beta} \delta\bar{\theta}(x, 0) && \text{if } M > 1, \end{aligned}$$

where:

$$\beta = \sqrt{|\bar{M}^2 - 1|}$$

Letting:

$$\mu_D = \frac{\lambda \tilde{B}}{\beta} \quad \text{if } M < 1 \quad \text{or} \quad \mu_I = -\frac{i\lambda \tilde{B}}{\beta} \quad \text{if } M > 1$$

(μ_D is the amplification coefficient of the coupling mechanism), one can see that the classical chain iteration will converge only if $|\mu_D| < 1$, a condition which corresponds to a damping of the oscillations. The restriction $|\mu_D| < 1$ must be satisfied for every wave number λ . If the perturbation is not made up of a simple sinusoid, it can be decomposed into simple harmonics by the Fourier analysis. The condition $|\mu_D(\lambda)| < 1$ must be satisfied for all the wave numbers λ contained in the spectrum of the perturbation. In reality, due to the x -discretization of the computation methods, the numbers λ constitute a finite set of discrete values lying in the range:

$$\frac{\pi}{L} \leq \lambda \leq \frac{\pi}{\Delta x},$$

where Δx is the mesh size and L the length of the computation domain.

A very similar analysis can be made for the *inverse problem* by considering a perturbation $\delta\bar{u}(x, 0)$ of the external velocity. Now, the boundary-layer response is given by:

$$\delta u(x, 0) = \mu_I \delta\bar{u}(x, 0).$$

It is readily verified that μ_D and μ_I are such that:

$$\mu_D \mu_I = 1$$

The above analysis leads to very useful conclusions regarding the convergence properties of the direct and inverse modes:

— in *direct iteration*, a small mesh size (λ_{\max} is large) tends to degrade the convergence properties by increasing the amplification factor $|\mu_D(\lambda_{\max})|$. The converse is true for an inverse iteration: convergence is deteriorated by an enlargement of the computation domain. This latter finding has been confirmed by calculations made by Melnik and Chow (1976);

— in “well” attached flows, \tilde{B} is small (it is recalled that \tilde{B} depends only on the shape of the velocity distribution in the boundary-layer and on the edge Mach number). Consequently, the direct mode is more appropriate for computing these flows. On the other hand, when the boundary-layer is separated or strongly destabilized, \tilde{B} is large and the inverse mode becomes preferable. The above situations are illustrated in Figure 3.3. When the slope at the matching point P of the boundary-layer response curve is small (Fig. 3.3a), i.e., when the flow is attached, the direct mode is more likely to give convergence. On the other hand, when this slope is increased, which corresponds to a destabilized boundary-layer, the inverse mode has a natural tendency to converge (see Fig. 3.3b).

Meauzé and Délery (1983) have developed a coupling method for computing the flow in a transonic channel in which shock/boundary-layer interactions with large separation occur. The aim of this research is the extension of coupling techniques to the prediction of the flow in supersonic axial compressors. Due to the necessity to determine a flow with choking conditions, the outer inviscid stream is computed by solving the full Euler equations with a time marching method (Vivian and Veillot, 1978). This method can be worked out either in the direct mode (i.e., with slip condition on the body surface) or in the inverse mode (i.e., with prescribed pressure along a free boundary, Meauzé, 1980). The turbulent boundary-layer is computed by a direct-inverse finite difference method (Délery and Le Balleur, 1980, see Section 2.3.2). The coupling conditions are written on the *displacement body* in order to satisfy the mass flow conservation in the channel. The iteration procedure can be performed according to the *fully Inverse or Direct modes* or to the *Semi-Inverse mode*.

In situations where the Inverse mode tends to diverge, an underrelaxation coefficient is computed at every grid point situated on the coupling surface. Reasoning is made in the $(\delta^* - M_e)$ plane (the boundary-layer edge Mach number M_e is in fact equivalent to the pressure p of Figure 3.3). Let m_{PF} and m_{BL} be respectively the slopes of the Perfect Fluid and Boundary-Layer response curves at the (desired) matching point P. If in the vicinity of P these response curves are assumed to be rectilinear, it is clear that convergence of the fixed point iteration is insured provided that $m_{PF}/m_{BL} > 1$. In these circumstances, it can be readily demonstrated that the iteration is made to converge by choosing the relaxation coefficient ω in such a way that:

$$\omega < \frac{2m_{PF}}{m_{PF} - m_{BL}}.$$

At every iteration cycle, the slopes m_{PF} and m_{BL} are determined by assuming rectilinear response curves. The perfect-fluid slope is evaluated by considering that locally the inviscid stream is one-dimensional with a Mach number \bar{M}_{PF} equal to the average Mach number of the two-dimensional inviscid flow. Then, by applying the equation for mass flow conservation, one obtains:

$$\frac{d\bar{M}_{PF}}{d\delta^*} = \frac{(1 + (\gamma - 1)/2 \bar{M}_{PF}^2)}{(1 - \bar{M}_{PF}^2)} \frac{\bar{M}_{PF}}{(A - \delta^*)},$$

where A is the cross section of the channel.

The slope m_{BL} relative to the boundary-layer is computed by considering a simplified Von Kármán equation where the skin friction is neglected (in a manner similar to the method used by Carter, see below). This equation is written:

$$\frac{d\theta}{dx} + \theta(H + 2 - M_e^2) \frac{1}{1 + m_e} \frac{1}{M_e} \frac{dM_e}{dx} = 0 \quad \text{where } m_e = \frac{\gamma - 1}{2} M_e^2.$$

By considering the approximate relation $H = H_i + \alpha M_e^2$ where $\alpha = 0.4$, one has:

$$\frac{d\delta^*}{dM_e} = \frac{\delta^*}{M_e} \left[\frac{2\alpha M_e^2}{H} - \frac{1}{1 + m_e} (H + 2 - M_e^2) \right]. \quad (3.18)$$

In the above equation, M_e is the local Mach number at the boundary-layer edge and H is provided by the boundary-layer calculation.

Equation 3.18 is also employed in the Semi-Inverse mode to guess the new δ^* distribution from the mismatch ΔM_e between the perfect-fluid and the boundary-layer calculations (see below).

The Newton Method. — As was suggested by Brune *et al.* (1975) convergence of the coupling iteration can also be achieved by using the *Newton method*. Let us consider a computation grid on the coupling surface where the points are characterized by index i . Any perturbation $\Delta \bar{p}$ of the boundary condition for the inviscid flow will produce changes in pressure $\Delta \bar{p}_i$ at every point i . These changes can be expressed in a linearized form:

$$\{\Delta \bar{p}_i\} = [P_{ij}] \{\Delta \bar{\theta}_j\}, \quad (3.19)$$

where the P_{ij} are the *inviscid flow influence coefficients*.

Similarly, one can write a linearized expression for the changes in boundary-layer deviation θ due to changes in surface pressure p :

$$\{\Delta \theta_i\} = [B_{ij}] \{\Delta p_j\}. \quad (3.20)$$

The situation at iteration number n being defined by: $\{\bar{p}_i\}^n, \{\bar{\theta}_i\}^n, \{p_i\}^n, \{\theta_i\}^n$, the problem is to estimate values of pressure and deviation at iteration $(n+1)$ in such a way that:

$$\begin{aligned} \{\bar{p}_i\}^{n+1} &= \{p_i\}^{n+1}, \\ \{\bar{\theta}_i\}^{n+1} &= \{\theta_i\}^{n+1}. \end{aligned}$$

Thus, we arrive at the following system:

$$\begin{aligned}\{\Delta\bar{p}_i\} &= [P_{ij}]^n \{\Delta\bar{\theta}_j\}, \\ \{\Delta\theta_i\} &= [B_{ij}]^n \{\Delta p_j\}, \\ \{\bar{p}_i\}^n + \{\Delta\bar{p}_i\} &= \{p_i\}^n + \{\Delta p_i\}, \\ \{\bar{\theta}_i\}^n + \{\Delta\bar{\theta}_i\} &= \{\theta_i\}^n + \{\Delta\theta_i\},\end{aligned}$$

which allows, in principle, the calculation of the perturbation values $\{\Delta\bar{p}_i\}$, $\{\Delta\bar{\theta}_i\}$, $\{\Delta p_i\}$ and $\{\Delta\theta_i\}$.

The above process is depicted schematically in Figure 3.5. Conceptually, the perturbation equations 3.19-20 define tangent lines to the inviscid flow and boundary-layer solution curves. In essence, the method is seen to be equivalent to approximating these solution curves by straight lines locally tangent to the starting points and to solving for the point at which these tangent lines intersect.

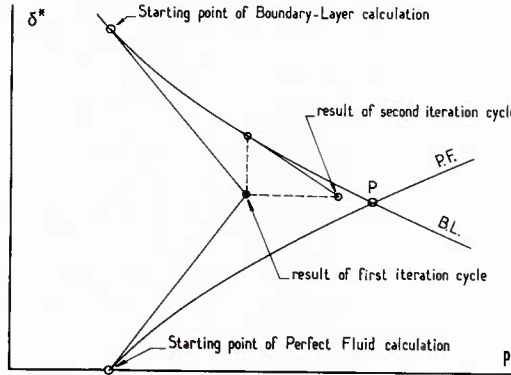


Fig. 3.5 – Newton method for coupling problem
(Brune et al., 1974).

If non-linear effects in P_{ij} and B_{ij} are moderate (i.e., if the solution curves are nearly straight), convergence of the method may be rapid. However, each cycle is very complex since it requires inversion of full matrices. This is why relatively few examples of this approach have been reported for transonic flow calculations (Thiede, 1976).

3.3.2.3. – Semi-Inverse Methods

Fixed Point Methods. – Now the problem is to “guess” a new $\theta(x)$ distribution from the difference (or “error”) in pressure $\Delta p = p(x) - \bar{p}(x)$ in such a way that Δp cancels out at convergence. This kind of iteration procedure was first proposed by Kuhn and Nielsen (1973) in the computation of transonic shock-wave/turbulent boundary-layer interactions. At that time, a rather empirical way to iterate on the $\theta(x)$ distribution was employed. A more rational examination of the convergence properties of the Semi Inverse algorithm can be made by resorting to Le Balleur’s stability analysis.

Let $\theta^*(x, 0)$ and $\bar{u}^*(x, 0) = u(x, 0)$ be the converged values on the coupling boundary and $\theta^n(x, 0)$, $\bar{u}^n(x, 0)$, $u(x, 0)$ the corresponding values at iteration number n (it is recalled that in the Semi-Inverse procedure $\theta^n(x, 0) = \theta^*(x, 0)$, barred quantities being relative to the inviscid flow). Considering the *subsonic case*, the local linear analysis leads to the following relations:

– for the *inviscid flow* (see equation 3.16):

$$\theta^n(x, 0) - \theta^*(x, 0) = \frac{\beta}{\lambda} \left(\frac{1}{\bar{u}^n} \frac{d\bar{u}^n}{dx} - \frac{1}{u^*} \frac{du^*}{dx} \right),$$

– for the *boundary-layer flow* (see equation 3.17):

$$\theta^n(x, 0) - \theta^*(x, 0) = B^* \left(\frac{1}{u^n} \frac{du^n}{dx} - \frac{1}{u^*} \frac{du^*}{dx} \right).$$

Combination of the two above equations gives:

$$\frac{1}{\bar{u}^n} \frac{d\bar{u}^n}{dx} - \frac{1}{u^n} \frac{du^n}{dx} = \left(\frac{\lambda}{\beta} - \frac{1}{B^*} \right) [\theta^n(x, 0) - \theta^*(x, 0)].$$

If convergence is to be achieved at the $(n+1)$ th iteration, we must have: $\bar{\theta}^{n+1}(x, 0) = \theta^*(x, 0)$, hence:

$$\bar{\theta}^{n+1}(x, 0) - \theta^n(x, 0) = \frac{B^* \beta}{\lambda B^* - \beta} \left(\frac{1}{u^n} \frac{du^n}{dx} - \frac{1}{\bar{u}^n} \frac{d\bar{u}^n}{dx} \right). \quad (3.21)$$

For the *supersonic case* a similar calculation gives:

$$\bar{\theta}^{n+1}(x, 0) - \theta^n(x, 0) = \frac{\beta B^{*2}}{\lambda^2 B^{*2} + \beta^2} \left(\frac{1}{u^n} \frac{d^2 u^n}{dx^2} - \frac{1}{\bar{u}^n} \frac{d^2 \bar{u}^n}{dx^2} \right).$$

A relaxation coefficient must generally be introduced and the $(n+1)$ th values are taken to be:

$$\theta^{n+1}(x, 0) = \theta^n(x, 0) + \omega [\bar{\theta}^{n+1}(x, 0) - \theta^n(x, 0)].$$

It is to be noticed that this Semi-Inverse iteration method requires only the knowledge of the error on the *pressure gradient* so that integration of $u(x)$ [or $p(x)$] is not necessary. This property may facilitate a zonal switch between Semi-Inverse iteration which is used in separated regions and Direct iteration which is more appropriate for attached flows.

More recently, Carter (1979, 1981) (see also Whitfield *et al.*, 1981) proposed a rather simple updating procedure which takes the following form when coupling conditions are expressed on the displacement body: the updated displacement thickness $\delta^{*(n+1)}$ is deduced from the mismatch of the viscous and inviscid velocities by:

$$\delta^{*(n+1)} = \delta^{*(n)} \left(\frac{u^n}{\bar{u}^n} \right).$$

The updating procedure including a relaxation coefficient can be written:

$$\delta^{*(n+1)} = \delta^{*(n)} + \omega \delta^{*(n)} \left(\frac{u^n}{\bar{u}^n} - 1 \right). \quad (3.22)$$

A similar expression can be obtained if one considers the simplified Von Kármán equation where the skin friction has been omitted. In this case, one can write:

$$\Delta \delta^* = -(H_i + 2) \frac{\delta^*}{u} \Delta u,$$

thus, if:

$$\begin{cases} \Delta u = \bar{u}^n - u^n, \\ \Delta \delta^* = \delta^{*(n+1)} - \delta^{*(n)}, \end{cases}$$

one gets:

$$\delta^{*(n+1)} = \delta^{*(n)} + (H_i + 2) \delta^{*(n)} \left(\frac{u^n}{\bar{u}^n} - 1 \right). \quad (3.23)$$

Comparison of equations 3.22 and 3.23 shows a close resemblance in relating an increment in u to that in δ^* . Estimation of $\delta^{*(n+1)}$ by equation 3.23 is not in principle entirely rigorous since the momentum integral equation expresses change in u and δ^* in the *streamwise direction*, whereas those in equation 3.23 refer to change between successive iteration cycles. Carter found that overrelaxation could be used in equation 3.22 ($\omega > 1$) to accelerate the convergence of the iteration process. The similarity between equations 3.22 and 3.23 offers an explanation since, even with overrelaxation, it has been observed in these calculations that:

$$\omega < H_i + 2,$$

H_i being always greater than 1.

It can be easily demonstrated that, for subsonic flows, Carter's and Le Balleur's approaches are essentially equivalent. Differentiating equation 3.22 with respect to x gives (after some approximations):

$$\frac{d\delta^{*(n+1)}}{dx} - \frac{d\delta^{*(n)}}{dx} = \omega \delta^{*(n)} \left(\frac{1}{u^n} \frac{du^n}{dx} - \frac{1}{\bar{u}^n} \frac{d\bar{u}^n}{dx} \right).$$

The above equation is identical to equation 3.21 applied to coupling on the displacement body [in this case $\theta(x, 0) = \frac{d\delta^*}{dx}$] provided that:

$$\omega \delta^{*(n)} = \frac{B^* \beta}{\lambda B^* - \beta}.$$

In supersonic or transonic flows, Carter uses coupling on the body surface. As seen in Section 3.2.1, the effect of the boundary-layer is then felt by the outer inviscid flow as mass bleed (positive or negative) along the body surface. In this case, the boundary-layer calculation of the iteration cycle is made by specifying the *perturbation mass flow*: $m = \rho_e u_e \delta^*$ (see Section 2.3.2 about boundary-layer calculation by inverse methods), and the same updating procedure as for coupling on the displacement body is employed which gives:

$$m^{(n+1)} = m^n \frac{u^n}{\bar{u}^n}.$$

Application of the Newton Method. — The Newton iteration method can also be used to enhance convergence of the Semi-Inverse algorithm. Most often, the method is employed in a much simpler form than the initial version proposed by Brune *et al.* (1975) (see above). For example, Gordon and Rom (1981) have devised a matching procedure based on the assumption that the relation between $\{\Delta \bar{p}_i\}$ and $\{\Delta \bar{\theta}_i\}$ and the one between $\{\Delta p_i\}$ and $\{\Delta \theta_i\}$ are two-dimensional. This means that for each station, $\{\Delta \bar{p}_i\}$ depends only on $\{\Delta \bar{\theta}_j\}$ (and not on $\{\Delta \theta_j\}, j \neq i$) and $\{\Delta p_i\}$ depends only on $\{\Delta \theta_i\}$. The procedure consists essentially in keeping only the diagonal of matrices $[P_{ij}]$ and $[B_{ij}]$. The guessed displacement thickness (coupling is expressed on the displacement body) has to be underrelaxed rather strongly to prevent oscillations.

In 1976, Alziary de Roquefort proposed an updating procedure in which only two diagonals in the boundary-layer influence matrix $[B_{ij}]$ (i and $i-1$) were retained. The method worked satisfactorily for laminar shock-wave/boundary-layer interactions.

More recently, Ardoneau (1981, see also Ardoneau, Alziary and Aymer, 1980) published a method which worked efficiently both for (supersonic) laminar and turbulent shock/boundary-layer interaction. Its principle consists in representing the perfect fluid and the boundary-layer sensitivity functions by:

- for the *perfect fluid*:

$$\bar{p}_{i-(1/2)}^{n+1} = \bar{p}_{i-(1/2)}^n + A \bar{p}_\infty (\bar{\theta}^{n+1} - \bar{\theta}^n)_{i-(1/2)}, \quad (3.24)$$

which is the linearized Prandtl-Meyer law:

- for the *boundary-layer*:

$$\left(\frac{dp}{dx} \right)_{i-(1/2)}^{n+1} = \left(\frac{dp}{dx} \right)_{i-(1/2)}^n + S (\bar{\theta}^{n+1} - \bar{\theta}^n)_{i-(1/2)}, \quad (3.25)$$

where the influence coefficient $S = \left(\frac{\partial \text{grad } p}{\partial \theta} \right)_{i-(1/2)}$ is approximated by $\left(\frac{\partial p}{\partial \delta^*} \right)_i$ and estimated numerically.

Discretization of equations 3.24 and 3.25, where \bar{p}^{n+1} is set equal to p^{n+1} , results in a recursive relation allowing the calculation of p^{n+1} . This calculation is started from the most downstream station where the pressure is prescribed as the downstream boundary condition of the viscous-inviscid interaction problem (see Section 3.3.1 above). Thereafter, the updated displacement thickness distribution is computed from 3.24 or 3.25 (in the case where $\theta = \frac{d\delta^*}{dx}$). An underrelaxation of p^{n+1} is required when separation occurs.

3.4. – Higher Order Methods

In the above formulation of the viscous-inviscid interaction problem, it is always tacitly assumed that the classical boundary-layer concept remains valid. According to this concept, the fluid properties in the dissipative layer (velocity, density, etc.) tend towards constant values when $y \rightarrow \infty$, and accordingly, the transverse pressure gradient is assumed to be zero. The limit values are identified with the inviscid flow properties along the coupling surface, which may be the outer edge δ , the displacement body or the solid body itself. This approach leads to some inconsistencies which may be the source of inaccuracies when the external inviscid flow is far from being transversally constant, as is the case in a shock-wave/boundary-layer interaction. Consequently, the pressure can no longer be considered as independent of y inside the boundary-layer. In these circumstances, coupling on the displacement body or on the surface appears as a more or less empirical way to take into account the transverse variation of the pressure. On the other hand, it now seems clear that the assumption $\partial p / \partial y = 0$ is at the origin of the artificial supercritical behavior (see Section 3.2.2 above). Therefore the “classical” formulation leads to an unsatisfactory situation even if the prediction it gives is frequently correct.

In fact, a more rigorous formulation of the viscous-inviscid interaction concept can be made by introducing a “defect formulation” (see Le Balleur, 1982). Basically, this approach consists in considering the difference between the real fluid, with viscous effects near the wall, and the external inviscid fluid continued to the wall. If f designates a real flow property and \bar{f} the corresponding inviscid property, one has:

$$\lim (f - \bar{f}) = 0 \quad y \rightarrow \infty \quad \text{with } f = \{ u, v, p, \rho \}$$

It is possible to write the full Navier-Stokes equations in terms of the difference between viscous and inviscid properties. However, for practical purposes, a simpler form can be obtained by making the same order of magnitude analysis as in Prandtl equations. Then, the following set of equations is obtained:

$$\begin{aligned} \frac{\partial(\rho u - \bar{\rho} \bar{u})}{\partial x} + \frac{\partial(\rho v - \bar{\rho} \bar{v})}{\partial y} &= 0, \\ \frac{\partial(\rho u^2 - \bar{\rho} \bar{u}^2)}{\partial x} + \frac{\partial(\rho uv - \bar{\rho} \bar{u} \bar{v})}{\partial y} &= - \frac{\partial(p - \bar{p})}{\partial x} + \frac{\partial \tau}{\partial y}, \quad 0 = \frac{\partial(p - \bar{p})}{\partial y}. \end{aligned}$$

In the classical (first order) boundary-layer theory, the overbarred quantities are considered as independent of y ; they are now (fictitious) inviscid values which may vary with y . From the above equations, it is possible to derive integral equations very similar to those of the first order theory (see Section 2 above) provided new definitions of the integral thicknesses are introduced. These definitions take into account the variation with y of the local inviscid values:

$$\begin{aligned} \delta^* \rho_e V_e &= \int_0^\infty [\rho u(x, y) - \bar{\rho} \bar{u}(x, y)] dy \quad (V_e^2 = u_e^2 + v_e^2), \\ (\delta^* + \theta) \rho_e V_e^2 &= \int_0^\infty [\rho u^2(x, y) - \bar{\rho} \bar{u}^2(x, y)] dy, \quad \text{etc.} \end{aligned}$$

We will not comment any further about the “Defect Formulation” which is still in the development stage.

It is also possible to improve the representation of viscous effects in high Reynolds number flows by introducing a “splitting” between a viscous component and an inviscid part at the level of the local flow variables themselves (in the viscous-inviscid interactive concept envisaged up to now, the splitting is made between regions). There results what is called a *composite representation* of the pressure or of the velocity field. Such techniques have been proposed by Dodge and Lieber (1977) and by Khosla and Rubin (1982). Further development concerning these relatively new methods would be beyond the scope of the present AGARDograph.

3.5. — Application of Inviscid-Viscous Interactive Methods to Flows Containing Shock-Waves

A large number of calculations based on IVI methods has been published, these methods now being routinely used for practical purposes (see in particular AGARD CP-291, 1980). So in this Section we will only present typical examples calling upon methods which have been discussed in the preceding Sections.

First, we will consider entirely supersonic flows. The first calculations shown in Figure 3.6 were performed by Werle and Vatsa (1974). They are relative to laminar interactions at a compression corner. These results are compared to Navier-Stokes calculations of Carter (1972) and to the well known experiments of Lewis *et al.* (1968). The best agreement—both with Navier-Stokes and measurements—is obtained for a free stream Mach number $M_\infty = 4$ (case *a*). The relatively large discrepancy observed at $M_\infty = 6.06$ (case *b*) cannot be explained.

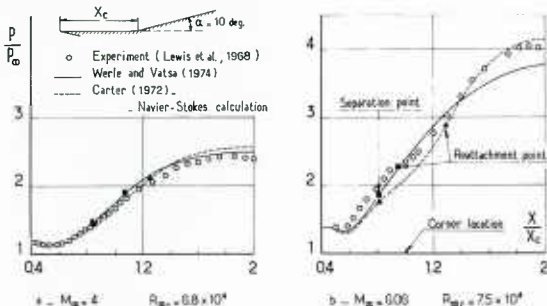


Fig. 3.6 – Ramp flow – Laminar boundary-layer – Inviscid-viscous interactive calculations of Werle and Vatsa (1974)

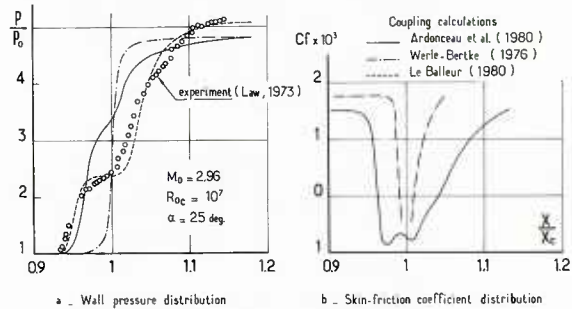


Fig. 3.7 – Ramp flow – Turbulent boundary-layer – Comparison of several coupling calculations.

The following example is a ramp flow in *turbulent* régime. The results presented in Figure 3.7 were obtained by three coupling techniques (Ardoneau *et al.*, 1980; Le Balleur, 1980 and Werle and Bertke, 1976). These calculations are compared to the experimental results of Law (1973) which clearly exhibit the existence of an extended separated zone. In the Ardoneau *et al.* method, the boundary-layer is computed by a finite difference method with the turbulence represented by an equilibrium two-layer model. This can explain the too large an increase in pressure given by this method because—as we know from experimental evidence (see Section 2.9 of Part I)—classical equilibrium turbulence models always overpredict considerably the “stiffness” of the boundary-layer thus leading to too intense pressure gradients. On the other hand the poor performance of the Werle ant Bertke calculation probably comes from the writing of the coupling conditions on the displacement thickness in a situation where the incoming boundary-layer is highly “supercritical” (see Section 3.2.2 above). Another example of application of an IVI method to a supersonic ramp flow in turbulent régime is given in Section 5 dealing with Navier-Stokes calculations.

The forthcoming calculations are relative to transonic airfoil flows. It is clear that such calculations involve many aspects of the coupling problem, for example the modeling of the viscous wake influence. However, a good representation of the shock-wave/boundary-layer interaction(s) is essential to the achievement of a satisfying prediction.

The first example shown in Figure 3.8 is a calculation performed by Tai (1974) in which the boundary-layer is assumed to remain *laminar* down to the profile trailing edge. This boundary-layer has been computed by an integral method using the Mean Flow Kinetic Energy equation (see Section 2.2 above) along with a compressible-incompressible transformation and similar solutions. Coupling conditions are expressed at the boundary-layer outer edge δ which always gives a subcritical response in laminar (except if the wall is highly cooled, see Section 3.2.2 above). Agreement with the experiments of Graham *et al.* (1945) is very good over the major part of the profile. In particular the large shock spreading at the wall which is typical of laminar interactions is well predicted. Agreement is not so satisfactory in the downstream part of the profile, presumably because of possible transition in the experimental case.

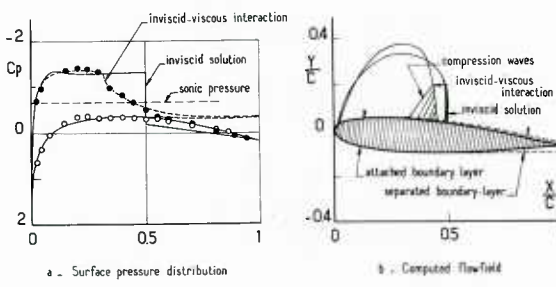


Fig. 3.8 – Transonic airfoil flow – Laminar boundary-layer – Inviscid-viscous interactive calculations of Tai (1974).

In the following examples, the boundary-layer is turbulent over the major part of the airfoil and especially in the shock foot region. Calculations shown in Figures 3.9 and 3.10 concern the RAE 2822 airfoil which was carefully tested by Cook. *et al.* (1979).

In the calculation performed by Melnik *et al.* (1983)—see Figure 3.9 *a*—as also in the one of Le Balleur (1983)—see Figure 3.10 *d*—the outer inviscid flow is computed by solving the full potential equation in conservative form. Coupling conditions are written at the wall according to the transpiration velocity concept. On the other hand in Whitfield *et al.* calculations (1983)—see Figure 3.9 *b*—the inviscid flow is determined from the Euler equations and the transpiration velocity concept is also used (Whitfield *et al.* have also made calculations with coupling on the displacement surface. They found that the results were very close, the difference in shock location being approximately the same as the distance between grid points). In Melnik *et al.*'s calculations, the boundary-layer is computed by the lag-entrainment method (see Section 2.3 above).

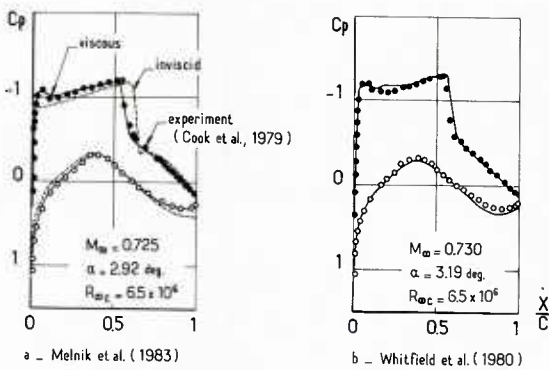


Fig. 3.9 – Transonic airfoil flow – Examples of inviscid-viscous interactive calculations.

To conclude the section on flow past airfoils, Figure 3.10 shows a comparison involving four coupling methods applied to the same flow situation (origin of computations and experiment can be found in the Proceedings of the 1980-1981 AFORS-HTTM Stanford Conference on Complex Turbulent Flows). In the Smith *et al.*'s calculation, the boundary-layer is computed by the already mentioned lag-entrainment method, the inviscid flow being determined from the full potential equation in non conservative form.

Figure 3.11 shows a calculation performed by Carter (1981) on the transonic axisymmetric bump tested by Bachalo and Johnson (1979). Here the boundary-layer is computed by a finite difference technique along with the Cebeci-Smith two-layer algebraic turbulence model (1974). It is seen that a reduction in the "strength" of the wake component of this model ($\alpha=0.0084$ instead of 0.0168) considerably improves the prediction. This effect is in agreement with experimental observations showing that in this kind of strong interaction classical flat-plate models are inadequate (see Section 2.9 of Part I).

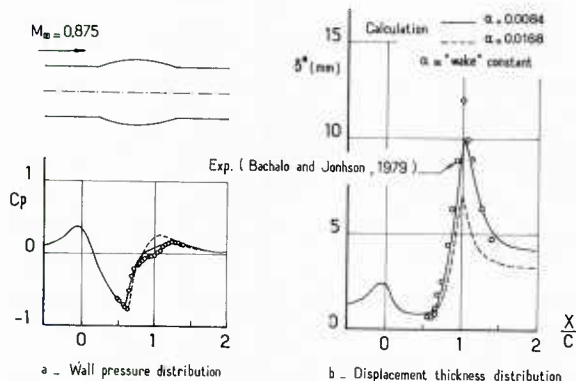


Fig. 3.11 – Transonic interaction over an axisymmetric circular arc bump (coupling calculations of Carter, 1981).

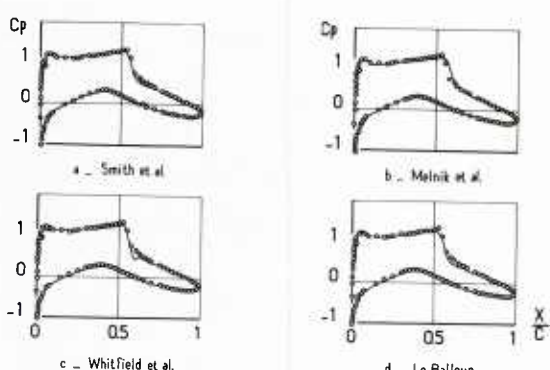


Fig. 3.10 – Transonic flow past an airfoil – Comparison of several coupling calculations (origin of calculations and exp. in the Proc. of the 1980-81 AFOSR-HTTM-Stanford Conference).

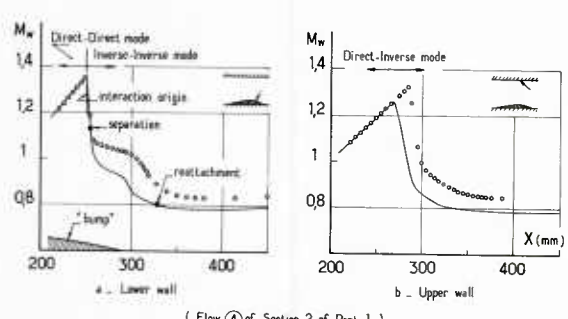


Fig. 3.12 – Shock-wave/boundary-layer interaction in a channel flow – "Wall" Mach number distributions – Inviscid-viscous interactive calculations of Meauzé and Delery (1983).

The two last examples of IVI calculations are relative to *internal flows* at transonic velocities for which viscous effects play an essential role. The first of these examples is relative to the channel flow discussed in great detail in Section 2.8 (Flow 4). In this calculation performed by Meauzé and Délery (1983) the inviscid flow is determined by solving the Euler equations and the boundary-layer is computed by a finite difference method along with an algebraic model based on the mixing length concept (Michel *et al.*, 1972). The geometry of the channel is sketched in Figure 3.12. Its upper wall is made of a flat plate and a long bump is mounted on its lower wall.

In this calculation, the shock-wave/boundary-layer interaction on the lower wall is computed by an Inverse-Inverse technique in which *both* the inviscid flow and the boundary-layer are computed by inverse methods; the interaction on the upper wall being computed by a Semi-Inverse (or Direct-Inverse) method.

The pressure distributions on the two walls are plotted in Figure 3.13, the boundary-layer displacement and momentum thickness being plotted in Figure 3.14. Agreement with experiment is only fair because of the "rusticity" of the employed turbulence model which is known to overpredict pressure rises during such interactions.

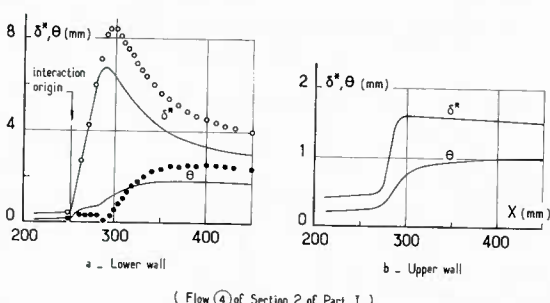


Fig. 3.13 – Shock-wave/boundary-layer interaction in a channel flow – Variations of boundary-layer properties – Inviscid-viscous interactive calculations of Meauzé and Delery (1983).

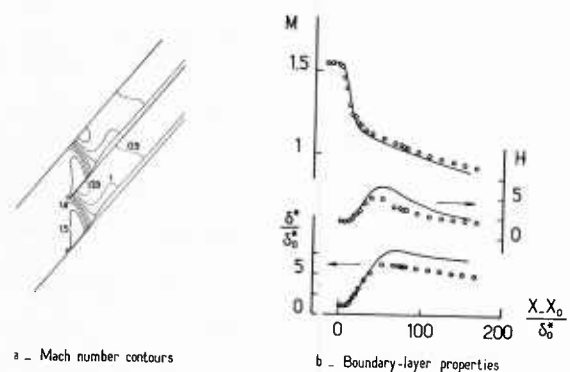


Fig. 3.14 – Shock-wave/boundary-layer interaction in a channel flow – Inviscid-viscous interactive calculations of Calvert (1983).

The second example of channel flow is due to Calvert (1982, 1983). It is relative to the flow in a supersonic cascade. In this calculation the boundary-layer is computed by the lag-entrainment method and both Inverse and Semi-Inverse coupling techniques are also used. The results given in Figure 3.14 are in reasonable agreement with experiment.

To conclude this Section it must be stressed that in making Inviscid-Viscous Interactive calculation in flows containing shock-waves, care should be taken to insure that the grid spacing in the shock foot region is small enough to correctly capture the interaction process (a spacing of the order of the displacement thickness of the incoming boundary-layer is necessary). Such a high mesh refinement can lead to problem of computer storage capacity and to extensive computer time. For this reason, some authors have proposed to represent the shock foot region by a local crude schematization of the interaction zone like the viscous wedge model briefly discussed in Section 2.6.2 of Part I. A more thorough information on this point can be found in the AGARD CP-291 (1981).

3.6. — References

Ai, D. K. (1970): On the Critical Point of the Crocco-Lees Mixing Theory in the Laminar Near Wake. *J. of Engineering Mathematics*, Vol. 4, No. 2, pp. 169-182.

Albert, I. E. (1967): Integral Theory for Turbulent Base Flows at Subsonic and Supersonic Speeds. Ph. D. Thesis, California Institute of Technology.

Alber, I. E. and Lees, L. (1968): Integral Theory for Supersonic Turbulent Base Flow. AIAA Paper 68-101; see also *AIAA Journal*, Vol. 6, No. 7, pp. 1343-1351 (July 1968).

Alziary de Roquefort, T. (1969): Contribution à l'étude de l'interaction et du décollement de la couche limite laminaire avec transfert de chaleur en régime supersonique. Thèse de Docteur ès Sciences Physiques, Université de Poitiers.

Alziary de Roquefort, T. (1976): Couplage fort et couplage faible entre couche limite et écoulement extérieur. 13^e Colloque de l'Association Aéronautique et Astronautique de France, Écully, (Nov. 1976).

Ardonceau, P.; Alziary, T. and Aymer, D. (1980): Calcul de l'interaction onde de choc/couche limite avec décollement. AGARD-CP-291.

Ardonceau, P. L. and Alziary de Roquefort, T. (1980): Direct and Inverse Calculation of Laminar Boundary-Layer Solution. *AIAA Journal*, Vol. 18, No. 11, pp. 1392-1394 (Nov. 1980).

Ardonceau, P. (1981): Étude de l'interaction onde de choc-couche limite supersonique. Thèse de Docteur ès Sciences Physiques, Université de Poitiers.

Aymer de la Chevalerie, D. and Leblanc, R. (1978): Integral Method Improvement for Computation of Transonic Shock-Wave/Turbulent Boundary-Layer Interaction. *AIAA Journal*, Vol. 16, No. 7, pp. 761-763 (July 1978).

Aymer de la Chevalerie, D. and Leblanc, R. (1979): Computation of Strong Interactions in Transonic Flows. Proc. of the Third Conf. on Numerical Methods in Fluid Mechanics, Cologne, 1979, *Notes on Numerical Fluid Mechanics*, Vol. 2, Springer-Verlag.

Bachalo, W. D. and Johnson, D. A. (1979): An Investigation of Transonic Turbulent Boundary-Layer Separation Generated on an Axisymmetric Flow Model. AIAA Paper 79-1479 (July 1979).

Bertke, S. D.; Werle, M. J. and Polak, A. (1974): Finite Difference Solutions for the Interacting Supersonic Turbulent Boundary-Layer Equations, Including Separation Effects. Department of Aerospace Engineering, University of Cincinnati, Cincinnati, Ohio, Report AFL-74-4-9.

Blottner, F. G. (1970): Finite Difference Method of Solution of the Boundary-Layer Equations. *AIAA Journal*, Vol. 8, No. 2, pp. 193-205 (Feb. 1970).

Bray, K. N.; Gadd, G. E. and Woodger, M. (1960): Some Calculations by the Crocco-Lees and Other Methods of Interaction Between Shock-Waves and Laminar Boundary-Layers Including Effects of Heat Transfer and Suction. ARC, Report 21, 834, FM2937.

Brune, G. W.; Rubbert, P. E. and Nark, T. C. (1974): A New Approach to Inviscid Flow Boundary-Layer Matching. AIAA Paper 74-601; see also *AIAA Journal*, Vol. 13, No. 7, pp. 936-938 (July 1975).

Calvert, W. J. (1982): An Inviscid-Viscous Interaction Treatment to Predict the Blade-to-Blade Performance of Axial Compressors with Leading Edge Normal Shock-Waves. ASME Paper 82-GT-135.

Calvert, W. J. (1983): Application of an Inviscid-Viscous Interaction Method to Transonic Compressor Cascades. AGARD-CP-351.

Carrière, P.; Sirieix, M. and Délery, J. (1975): Méthodes de calcul des écoulements turbulents décollés en supersonique. *Progress in Aerospace Sciences*, Vol. 16, No. 4, pp. 385-429.

Carter, J. E. (1972): Numerical Solutions of the Navier-Stokes Equations for the Supersonic Laminar Flow Over a Two-Dimensional Compression Corner. NASA TR-R-385.

Carter, J. E. (1979): A New Boundary-Layer Iteration Technique for Separated Flow. AIAA Paper 79-1450.

Carter, J. E. (1981): Viscous-Inviscid Interaction Analysis of Transonic Turbulent Separated Flow. AIAA Paper 81-1241.

Cebeci, T. and Smith A. M. O. (1974): *Analysis of Turbulent Boundary-Layers*. Academic Press, New York.

Cook, P. H.; McDonald, M. A. and Firmin, M. C. P. (1979): Aerofoil RAE 2822-Pressure Distributions and Boundary-Layer and Wake Measurements. AGARD AR-138, Paper 6.

Cox, R. N. and Crabtree, L. F. (1965): *Elements of Hypersonic Aerodynamics*. The English University Press Ltd., London.

Crocce, L. and Lees, L. (1952): A Mixing Theory for the Interaction Between Dissipative Flows and Nearly Isentropic Streams. JAS, Vol. 19, No. 10, pp. 649-676. (Oct. 1952).

Crocce, L. (1954): Consideration on the Shock/Boundary-Layer Interaction. Proc. Centennial of Brooklyn Poly. Inst.

Délery, J. and Le Balleur, J.-C. (1980): Interaction et couplage entre écoulement de fluide parfait et écoulement visqueux. ONERA RSF No. 4/3073.

Dodge, P. R. and Lieber, L. S. (1977): A Numerical Method for the Solution of Navier-Stokes Equations for a Separated Flow. AIAA Paper 77-170.

Garvine, R. W. (1968): Upstream Influence in Viscous Interaction Problems. The Physics of Fluids, Vol. 11, pp. 1413-1423.

Gautier, B. G. and Ginoux, J. J. (1973): Improvement to Klineberg's Method for the Calculation of Viscous-Inviscid Interactions in Supersonic Flow. AIAA Journal, Vol. 11, No. 9, pp. 1323-1326. (Sept. 1973).

Georgeff, M. P. (1972): A Comparison of Integral Methods for the Prediction of Laminar Boundary-Layer/Shock-Wave Interaction. Imperial College, IC Aero Report 720-1.

Glick, H. S. (1960): Modified Crocco-Lees Mixing Theory for Supersonic Separated and Reattaching Flows. Guggenheim Aeronautical Laboratory, California Institute of Technology, Memorandum No. 53, *see also* JAS, Vol. 29, No. 10, pp. 1238-1244. (Oct. 1962).

Gordon, R. and Rom, J. (1981): Transonic Viscous-Inviscid Interaction Over Airfoils for Separated Laminar and Turbulent Flows. AIAA Journal, Vol. 19, No. 5, pp. 545-552 (May 1981).

Graham, D. J.; Nitzberg, G. E. and Olson, R. N. (1945): A Systematic Investigation of Pressure Distribution at High Speeds Over Five Representative NACA Low-Drag and Conventional Airfoils Sections. NACA Report 832.

Holden, M. S. (1969): Theoretical and Experimental Studies of the Shock-Wave/Boundary-Layer Interaction on Curved Compression Surface. Proc. of the Symposium on Viscous Interaction Phenomena in Supersonic and Hypersonic Flow, Univ. of Dayton Press.

Holt, M. (1966): Separation of Laminar Boundary-Layer Past a Concave Corner. AGARD-CP-4.

Hunter, L. G. and Reeves, B. L. (1971): Results of a Strong Interaction Wake-Like Model of Supersonic Separated and Reattaching Turbulent Flows. AIAA Journal, Vol. 9, No. 4, pp. 703-712 (April 1971).

Khosla, P. K. and Rubin, S. G. (1982): A Composite Velocity for the Compressible Navier-Stokes Equations. AIAA Paper 82-0099.

Klineberg, J. M. (1968): Theory of Laminar Viscous-Inviscid Interactions in Supersonic Flow. Ph. D. Thesis, California Institute of Technology.

Klineberg, J. M. and Lees, L. (1969): Theory of Laminar Viscous-Inviscid Interactions in Supersonic Flow. AIAA Paper 69-7; *see also* AIAA Journal, Vol. 7, No. 12, pp. 2211-2221 (Dec. 1969).

Klineberg, J. M.; Kubota, T. and Lees, L. (1972): Theory of Exhaust-Plume/Boundary-Layer Interactions at Supersonic Speeds. AIAA Journal, Vol. 10, No. 5, pp. 581-588 (Oct. 1972).

Klineberg, J. M. and Steger, J. L. (1974): On Laminar Boundary-Layer Separation. AIAA Paper 74-94.

Kuhn, G. D. and Nielsen, J. N. (1973): Prediction of Turbulent Separated Boundary-Layer. AIAA Paper 73-663.

Law, C. H. (1973): Supersonic Turbulent Boundary-Layer Separation Measurements at Reynolds Numbers of 10^7 to 10^8 . AIAA Paper 73-665; *see also* AIAA Journal, Vol. 12, No. 6, pp. 794-797 (June 1974).

Le Balleur, J.-C. and Mirande, J. (1975): Etude expérimentale et théorique du recollement bidimensionnel turbulent incompressible. AGARD-CP-168.

Le Balleur, J.-C. (1977): Couplage visqueux-non visqueux: analyse du problème incluant décollements et ondes de choc. La Recherche Aérospatiale, No. 1977-6, pp. 349-358. (Déc. 1977).

Le Balleur, J.-C. (1978): Couplage visqueux-non visqueux : méthode numérique et application aux écoulements bidimensionnels transsoniques et supersoniques". La Recherche Aérospatiale, No. 1978-2, pp. 67-76 (March 1978).

Le Balleur, J.-C. (1978): Calculs couplés visqueux-non visqueux incluant décollements et ondes de choc en écoulement bidimensionnel. VKI/AGARD LS-94 on "Three dimensional and Unsteady Separation at high Reynolds Number".

Le Balleur, J.-C. (1980): Calcul des écoulements à forte interaction visqueuse au moyen de méthodes de couplage. AGARD-CP-291.

Le Balleur, J.-C. (1982): Viscid-Inviscid Coupling Calculations for Two and Three Dimensional Flows. VKI LS-1982-6 on "Computational Fluid Dynamics".

Le Balleur, J.-C. (1983): Numerical Viscid-Inviscid Interaction in Steady and Unsteady Flows. 2nd Symposium on Numerical and Physical Aspects of Aerodynamics Flows, Long-Beach (17-20 Jan. 1983).

Leblanc, R.; Horton, H. P. and Ginoux, J. J. (1971): The Calculation of Adiabatic Laminar Boundary-Layer/Shock-Wave Interaction in Axisymmetric Flow. Part II-Hollow-Cylinder-Flare Bodies with Spin. VKI, TN-73.

Lees, L. and Reeves, B. L. (1964): Supersonic Separated and Reattaching Laminar Flows: 1 General Theory and Application to Adiabatic Boundary-Layer/Shock-Wave Interactions. AIAA Paper No. 64-4; *see also* AIAA Journal, Vol. 2, N° 11, pp. 1907-1920 (Nov. 1964).

Lewis, J. E.; Kubota, T. and Lees, L. (1967): Experimental Investigation of Laminar Two-Dimensional Boundary-Layer Separation in a Compression Corner With and Without Cooling. AIAA Paper 67-191; *see also* AIAA Journal, Vol. 6, No. 1, pp. 7-14 (Jan. 1968).

Lighthill, M. J. (1958): On Displacement Thickness. J. Fluid Mech., Vol. 4, Part 2, pp. 383-392.

Lock, R. C. and Firmin, M. C. P. (1981): Survey of Techniques for Estimating Viscous Effects in External Aerodynamics. RAE, Tech. Memo. Aero 1900.

Meauzé, G. (1980): Méthode de calcul inverse pseudo-instationnaire. La Recherche Aérospatiale, No. 1980-1, pp. 23-30 (Jan. 1980).

Meauzé, G. and Délery, J. (1983): Calcul de l'interaction onde de choc-couche limite par emploi de méthodes inverses, AGARD-CP-351.

Mellor, G. L. (1972): The Large Reynolds Number Asymptotic Theory of Turbulent Boundary-Layers. Int. J. Engineering Sc., Vol. 10, pp. 851-873.

Melnik, R. E. and Chow, R. (1976): Asymptotic Theory of Two Dimensional Trailing Edge Flows. NASA SP-347, p. 197.

Melnik, R. E.; Mead, H. R. and Jameson, A. (1983): A Multi-Grid Method for the Computation of Viscid/Inviscid Interaction on Airfoils. AIAA Paper 83-0234.

Michel, R.; Quémard, C. and Durant, R. (1969): Application d'un schéma de longueur de mélange amélioré à l'étude des couches limites d'équilibre. ONERA-N.T. No. 154.

Neyland, V. Ya. (1970): Upstream Propagation of Disturbances in Hypersonic Boundary-Layer Interactions (in Russian). Akad. Nauk. SSSR, Izv. Mekh. Gaza., No. 4, pp. 44-49.

Nielsen, J. N.; Lynes, L. L. and Goodwin, F. K. (1966): Theory of Laminar Separated Flows on Flare Surfaces Including Supersonic Flows with Heating and Cooling. AGARD-CP-4.

Reyhner, T. A. and Flügge-Lotz, I. (1966): The Interaction of a Shock-Wave with a Laminar Boundary-Layer. Division of Engineering Mechanics, Stanford University, TR No. 163.

Stollery, J. L. and Hankey, W. L. (1970): Subcritical and Supercritical Boundary-Layer. AIAA Journal, Vol. 8, No. 7, pp. 1349-1351 (July 1970).

Tai, T. C. (1974). Transonic Laminar Viscous-Inviscid Interaction over Airfoils. AIAA Paper 74-600.

Thiede, P. G. (1976): Prediction Method for Steady Aerodynamics Loading on Airfoils with Separated Transonic Flow. AGARD-CP-204.

Todisco, A. and Reeves, B. L. (1969): Turbulent Boundary-Layer Separation and Reattachment at Supersonic and Hypersonic Speeds. Proc. Symposium on Viscous Interaction Phenomena in Supersonic and Hypersonic Flows, Univ. of Dayton Press, pp. 139-179.

Veldman, A. E. P. (1979): A Numerical Method for the Calculation of Laminar Incompressible, Boundary-Layer with Strong Viscous-Inviscid Interaction. Report NLR TR 79023U.

Veldman, A. E. P. (1981): New, Quasi-Simultaneous Method to Calculate Interacting Boundary-Layers. AIAA Journal, Vol. 19, No. 1, pp. 79-85 (Jan. 1981).

Vivian, H. and Veuillot, J.-P. (1978): Méthodes pseudo-instationnaires pour le calcul d'écoulements transsoniques. Publication ONERA No. 1978-4.

Weinbaum, S. and Garvine, R. W. (1968): An Exact Treatment of the Boundary-Layer Equations Describing the Two-Dimensional Viscous Analogy of the One Dimensional Inviscid Throat. AIAA Paper 68-102.

Werle, M. J.; Hankey, W. L. and Dwoyer, D. L. (1973): Initial Conditions for the Hypersonic Shock/Boundary-Layer Interaction Problem. AIAA Journal, Vol. 11, No. 4, pp. 525-530 (Nov. 1973).

Werle, M. J. and Vatsa, V. N. (1973): Numerical Solution of Interacting Supersonic Boundary-Layer Flows Including Separation Effects. Aerospace Research Laboratories, Wright-Patterson Air Force Base, Ohio, Report 73-0162.

Werle, M. J.; Polak, A.; Vatsa, V. N. and Bertke, S. D. (1975): Finite Difference Solution for Supersonic Separated Flows. AGARD-CP-168.

Werle, M. J. and Vatsa, V. N. (1974): New Method for Supersonic Boundary-Layer Separations. AIAA Journal, Vol. 12, No. 11, pp. 1491-1497 (Nov. 1974).

Werle, M. J. and Bertke, S. D. (1976): Application of an Interacting Boundary-Layer Model to the Supersonic Turbulent Separation Model. Report AFL No. 76-4-21, University of Cincinnati.

Whitfield, D. L.; Swafford, T. W. and Jacocks, J. L. (1981): Calculation of Turbulent Boundary-Layer with Separation and Viscous-Inviscid Interaction. AIAA Journal, Vol. 19, No. 10, pp. 1315-1322 (Oct. 1981).

Whitfield, D. L.; Thomas, J. L.; Jameson, A. and Schmidt, W. (1983): Computation of Transonic Viscous-Inviscid Interacting Flow. 2nd Symposium on Numerical and Physical Aspects of Aerodynamics Flows, Long-Beach (17-20 Jan. 1983).

Wigton, L. B. and Holt, M. (1981): Viscous-Inviscid Interaction in Transonic Flow. AIAA Paper 81-1003.

Proc. of the 1980-1981 AFORS-HTTM Stanford Conference on Complex Turbulent Flows: Comparison of Computation and Experiment. Stanford University (Sept. 14-18, 1981).

Computation of Viscous-Inviscid Interactions, AGARD-FDP Symposium, Colorado-Springs, Colorado, U.S.A. (29 Sept.-1 Oct. 1980); AGARD CP-291 (1981).

4. — ANALYTICAL METHODS OR MULTI-DECK MODELS

4.1. — The Lighthill Multi-Deck Model

The essential features of an interacting boundary-layer were established in 1953 by Lighthill (1950, 1953) who examined the question of upstream propagation in the interaction of an oblique shock-wave with a boundary-layer. Both laminar and turbulent cases were considered. Lighthill recognized that the interaction takes place over a short distance, when compared to a length scale representative of the boundary-layer development, (for instance the boundary-layer thickness). As a consequence, Lighthill showed that the boundary-layer flow develops a two-layer structure comprising (see Fig. 4.1):

— a thick outer-region covering most of the boundary-layer and where the viscous forces can be neglected. In this region, the flow is essentially driven by pressure and inertia forces which become predominant because of the rapid variations in the streamwise direction occurring in the interaction domain. Thus, this part of the flow is considered as an *inviscid rotational stream* (the rotation having been created in the incoming unperturbed boundary-layer).

— a viscous sublayer in contact with the wall. This layer must be introduced since the neglect of viscous forces down to the wall leads to a situation where the flow in the immediate vicinity of the wall is unable to sustain any positive pressure gradient (this point was briefly brought up in Section 1.4 concerning Inviscid Shear Layer Analyses). It is obvious that the zero velocity streamline cannot overcome a pressure rise by a purely inviscid mechanism.

Lighthill proposed a solution to the interaction problem by using a small perturbation approach. For the part of the flow considered as inviscid, he derived what is today a classical equation governing the disturbance pressure field:

$$[1 - M_0^2(y)] \frac{\partial^2 p'}{\partial x^2} - 2 \frac{dM_0(y)/dy}{M_0(y)} \frac{\partial p'}{\partial y} + \frac{\partial^2 p'}{\partial y^2} = 0.$$

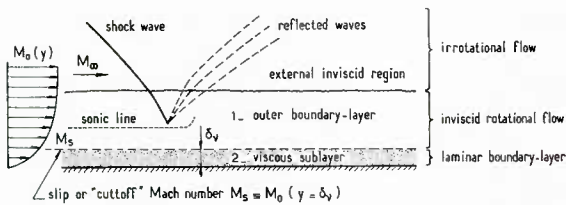


Fig. 4.1 — The Lighthill two-layer model of strong interaction.

In the above equation, $M_0(y)$ is the Mach number distribution in the undisturbed flow which includes the major part of the incoming boundary-layer.

At the outer edge of the boundary-layer ($y = \delta_0$), the solution must match the incoming and reflected disturbances which are assumed to satisfy the linearized supersonic inviscid flow equations.

The tangency condition $v' = 0$ (equivalent to $\frac{\partial p'}{\partial y} = 0$) prescribed at the wall for a boundary-layer flow considered as *wholly inviscid*, would necessarily lead to $\partial p'/\partial x = 0$. Thus, the inner condition for the outer inviscid flow necessitates the consideration of the solution for the *viscous sublayer*.

This *inner region* is here analyzed by considering the density in the sublayer as constant and $\partial p'/\partial y = 0$. The formulation of the perturbation problem leads to an equation for the normal disturbance velocity v' (for more details, see Section 4.3.2.1 below). Lighthill showed that the essential result was that the effect of the sublayer on the outer flow is exactly as if this layer were replaced by a solid wall located at a distance $y^* > 0$. This important finding is analogous to the properties of the displacement thickness in ordinary boundary-layer theory. Now the condition $v' = 0$ for the outer flow is imposed at a distance y^* from the wall where $M_0(y) \neq 0$. The difficulty arising from $M_0 \rightarrow 0$ when $v' = 0$ has been overcome.

We will not give any further details on Lighthill's theory, since its essential principles will be exposed in a more developed form in Section 4.3.2.1 concerning Inger's analysis. We will only add that solutions in the two layers are obtained in closed form by using Fourier's decomposition in the x -direction. These solutions have permitted the establishment of important results governing the *scaling* of the interaction region. Thus, it was shown that in *laminar flows* and for a *supersonic external stream* (which means M_∞ not be too close to unity), the streamwise extent of the interaction Δx scaled to the distance L of the interaction from the leading edge is such that: $\frac{\Delta x}{L} = O(R^{-3/8})$. Here R is the Reynolds number computed with L and external flow unperturbed quantities. This result implies $\Delta x/\delta_0 = O(R^{1/8})$ since $\delta_0/L = O(R^{-1/2})$. The above scaling laws confirm the general order of magnitude of ten boundary-layer thicknesses found experimentally for the distance of upstream influence in laminar interactions without separation.

The considerable reduction in Δx for a turbulent interaction was shown to be partly due to differences in skin friction coefficient (i.e. the initial slope of the velocity profile which measures its resistance to retardation effects) and partly due to differences in the width of the part of the boundary-layer where the Mach number is low (a turbulent profile is much "fuller" than a laminar profile).

The first tendency linked to the shear stress level at the wall is in agreement with the conclusions of the Free Interaction theory which is well verified at low to moderate Reynolds numbers whereas the second finding corroborates the behavior observed at high Reynolds number where the boundary-layer becomes more resistant as its velocity distribution is more "filled" (see Sections 3.6 and 3.7 of Part I).

The cited papers of Lighthill have had a considerable influence on subsequent theoretical research on the shock-wave/boundary-layer interaction problem as well as on the accompanying self-induced separation phenomenon (see below). Let's recall Stewartson's words about one of Lighthill's papers: "In our view, this (final) paper of Lighthill is the key to the whole problem of self-induced separation and any other theory or approximate method which does not build on it is incomplete and cannot provide a full understanding of the phenomenon" (Stewartson and Williams, 1969).

In the following Sections we will first present multi-deck methods for laminar flows by considering in some detail the basic Stewartson and Williams theory for self-induced separation in supersonic flows. In laminar flows, multi-deck theories generally use matched asymptotic expansion methods of solution. In this sense, they are valid in the limit situation where a small parameter ϵ is tending towards zero (in the present case $\epsilon = R^{-1/8}$, thus the limit corresponds to a Reynolds number R tending to infinity). The exception among these theories is the non-asymptotic theory of Tu and Weinbaum (see Section 4.2.2 below).

Multi-deck theories for turbulent flows are reviewed in Section 4.3. These theories use both asymptotic expansion methods and linearized perturbation techniques, the latter being directly inspired from Lighthill's pioneer work.

4.2. — Multi-Deck Theories in Laminar Flows

4.2.1. — Asymptotic Expansion Methods

4.2.1.1. — *Stewartson and Williams' Theory of Self Induced Separation in Supersonic Flows.* In 1969, Lighthill's multi-deck theory was developed into a rational theory for laminar shock-wave/boundary-layer interaction by Stewartson and Williams. These two authors retained the full non-linear boundary-layer equations to describe the sublayer behavior. About at the same time, similar approaches were proposed by Neiland (1970) and Sychev (1972). Such analyses make use of *asymptotic expansion techniques* and focus on the *self induced* separation phenomenon which results, for instance, from impingement of an oblique shock-wave strong enough to induce separation. The problem is conceived as a *Free-Interaction* problem in the sense that it deals with the spontaneous and rapid change of the initially undisturbed boundary-layer velocity profile by interaction with the main stream outside. The Free-Interaction concept, which leads to self-induced separation, was originally introduced by Chapman (1958) to characterize a process by which a boundary-layer departs from its *initially weak interaction régime* as a consequence of some downstream constraint (shock impingement, for example). From a physical standpoint, a simple explanation has been given by Chapman that basically a cycle can be set up in which the growth of the boundary-layer produces an adverse pressure gradient in the outer stream which promotes further growth of the boundary-layer. Thus the interaction is entirely determined by the outer inviscid stream characteristics and the incoming boundary-layer properties. It does not depend on the triggering agent, hence the denomination of *free-interaction* or *self-induced* separation.

The Free Interaction concept is more thoroughly discussed in Section 3.6 of Part 1 by resorting to experimental evidence.

Let us go back to Stewartson and Williams' theory which considers a laminar boundary-layer developing on a flat plate in a supersonic stream. Let L be the distance from the leading edge of the free interaction zone and assume that the Reynolds number: $R = \frac{\rho_\infty U_\infty L}{\mu_\infty}$ is large.

Thus the boundary-layer is well established and its velocity distribution is determined by the Blasius equation suitably generalized to compressible flows.

Following Lighthill's idea, and by using asymptotic expansion arguments, the free interaction zone is shown to develop a *triple deck* structure consisting of (see in Fig. 4.2):

- an *upper-deck* which is the external inviscid stream;
- a *middle-deck* or *main-deck* which comprises most of the boundary-layer;
- a *lower-deck* which is in fact Lighthill's viscous sublayer.

Let us first consider the solution for the *main-deck*, i.e., that part of the flow normally including most of the boundary-layer.

Defining $\epsilon = R^{-1/8}$ as the small parameter, it is shown by asymptotic expansion arguments (see also Lighthill's result in Section 4.1 above) that a consistent approach to the interaction problem impose the following scaling for the main-deck:

- length scale in the x -direction: $\Delta x = O(\epsilon^3)L = O(R^{-3/8})L$;
- length scale in the y -direction: $\Delta y = O(\epsilon^4)L$.

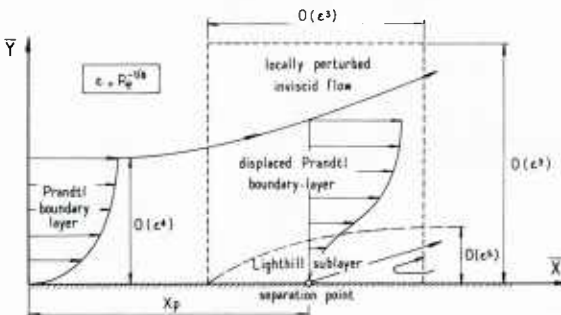


Fig. 4.2 — The triple-deck structure of a free interacting laminar boundary-layer.

In fact Δy is $O(\delta_0)$, δ_0 being the physical thickness of the undisturbed boundary-layer which would exist at $x=L$ in the absence of interaction.

The solution is expressed as a function of the stretched variables:

$$\bar{x} = (x - L)/\epsilon^3 L,$$

$$\bar{y} = y/\epsilon^4 L$$

which are defined in such a way as to be of order unity in the major part of the interacting boundary-layer. The solution has the form:

$$u = U_0(\bar{y}) + \epsilon u_1(\bar{x}, \bar{y}) + \epsilon^2 u_2(\bar{x}, \bar{y}) + \dots, \quad (4.1)$$

$$v = \epsilon^2 v_1(\bar{x}, \bar{y}) + \epsilon^3 v_2(\bar{x}, \bar{y}) + \dots, \quad (4.2)$$

$$p = p_\infty + \epsilon^2 p_2(\bar{x}, \bar{y}) + \dots, \quad (4.3)$$

$$\rho = R_0(\bar{y}) + \epsilon \rho_1(\bar{x}, \bar{y}) + \epsilon^2 \rho_2(\bar{x}, \bar{y}) + \dots \quad (4.4)$$

where all quantities have been made dimensionless by introducing appropriate scales (U_∞ , ρ_∞) and where $U_0(\bar{y})$ is the streamwise velocity profile of the incoming boundary-layer.

At this step, three remarks may be made:

(i) in the absence of interaction we would have: $u = U_0(\bar{y}) + \varepsilon^3 u_3(\bar{x}, \bar{y})$ since in this case $\frac{\partial u}{\partial x} = O(1)$.

Now the streamwise variation of u is much more rapid, because $\frac{\partial u}{\partial x} = O(\varepsilon^{-2})$;

(ii) the expansion for v begins with term $O(\varepsilon^2)$ from the continuity equation. In a “normal” boundary-layer $v = O(R^{-1/2}) = O(\varepsilon^4)$, i.e., is much smaller;

(iii) the expansion for the pressure p omits term $O(\varepsilon)$ for reasons which will be seen later.

Substitution of expansions 4.1 to 4.4 into the full Navier-Stokes equations shows that leading viscous terms are $O(1)$ while the leading inertia term is $O(\varepsilon^{-2})$ in the x -component of the momentum equation. This means that u_1 and u_2 are given by inviscid equations. Similar results are demonstrated for v_1 and v_2 by consideration of the y -component of momentum.

The following equations are obtained for u_1 , v_1 and p_2 (for the sake of simplicity, higher order terms will not be considered here):

$$\begin{aligned} R_0(\bar{y}) U_0(\bar{y}) \frac{\partial u_1}{\partial \bar{x}} + R_0(\bar{y}) v_1 \frac{d U_0(\bar{y})}{d \bar{y}} &= 0, \\ \frac{\partial u_1}{\partial \bar{x}} + \frac{\partial v_1}{\partial \bar{y}} &= 0, \\ \frac{\partial p_2}{\partial \bar{y}} &= 0. \end{aligned}$$

The solutions of the above equations, satisfying $u_1 \rightarrow 0$, $\bar{x} \rightarrow \infty$ are simply:

$$u_1 = A_1(\bar{x}) \frac{d U_0(\bar{y})}{d \bar{y}}, \quad (4.5)$$

$$v_1 = -U_0(\bar{y}) \frac{d A_1(\bar{x})}{d \bar{y}}. \quad (4.6)$$

$A_1(\bar{x})$ is a function, so that $A_1(-\infty) = 0$, which is determined by matching with the upper-deck (external inviscid flow).

If $\bar{y} \rightarrow \infty$, then $u_1 \rightarrow 0$, so that to $O(\varepsilon)$ the main stream is undisturbed. Hence $p_1(\bar{x}, \infty) = 0$ and as $\partial p_1 / \partial \bar{y}$ vanishes in the boundary-layer, then $p_1 \equiv 0$. There is no need to have a term $O(\varepsilon)$ in the expansion for p .

Let us now consider the outer *inviscid irrotational flow* or *upper-deck*. In this flow the length scales in the x and y directions must be comparable. This is true if the flow is frankly supersonic (M_∞ not too close to unity), i.e., if the slope of the characteristics (Mach waves); $(M_\infty^2 - 1)^{-1/2}$ is $O(1)$. In a transonic stream, the vertical and horizontal scales have to be different since then $(M_\infty^2 - 1)^{-1/2}$ tends to infinity (see Section 4.2.1.2 below). For the present situation, the stretched variables in the upper deck are:

$$Y = y/\varepsilon^3 L = \varepsilon \bar{y}, \quad X = \bar{x}.$$

Matching conditions with the main-deck show that the pressure must be of the form (see above):

$$p = p_\infty + \varepsilon^2 P_2(X, Y) + \dots$$

Substitution in the Navier-Stokes equations leads to the well known Prandtl-Glauert equation:

$$(M_\infty^2 - 1) \frac{\partial^2 P_2}{\partial X^2} - \frac{\partial^2 P_2}{\partial Y^2} = 0 \quad (4.7)$$

In the limiting process $\bar{y} \rightarrow \infty$, $Y \rightarrow 0$, $P_2(X, 0) = p_2(X)$.

Using a linearized simple wave equation (derived from equation 4.7) and writing conditions at order ε^2 connecting p_2 and v_1 yields (in the limit $\bar{y} \rightarrow \infty$):

$$\frac{v_1}{U_\infty} = \frac{d A_1}{d \bar{x}} = -\frac{\sqrt{M_\infty^2 - 1}}{\gamma p_\infty M_\infty^2} p_2(\bar{x}), \quad (4.8)$$

Hence:

$$A_1(\bar{x}) = -\frac{\sqrt{M_\infty^2 - 1}}{\gamma p_\infty M_\infty^2} \int_{-\infty}^{\bar{x}} p_2(t) dt,$$

which is the relation that determines $A_1(\bar{x})$.

The solution of the (inviscid) main-deck cannot satisfy the no-slip condition at the wall. This fact is readily seen by considering the $\bar{y} \rightarrow 0$ limit of equations 4.5 and 4.6. Consequently, an *inner-layer* — the so-called *lower-deck* — must be introduced in order to satisfy this condition. The thickness of the lower-deck is a fraction ε of the Blasius' boundary-layer thickness. The characteristic length scales are now:

- $\sim \varepsilon^3 L$ in the x -direction;
- $\sim \varepsilon^5 L$ in the y -direction.

In order to match with the main deck solution, the velocity components u and v are taken to be of the order εU_∞ and $\varepsilon^3 U_\infty$ respectively while the pressure variation is $O(\varepsilon^2 p_\infty)$.

Accordingly, it is demonstrated that the Navier-Stokes equations reduce to *conventional incompressible* boundary-layer equations (for a thermally insulated wall). It is convenient to write:

$$\begin{aligned} y &= \varepsilon^5 ZL, \quad x = L + \varepsilon^3 XL \quad (X = \bar{x}), \\ u &= \varepsilon \tilde{u} U_\infty, \quad v = \varepsilon^3 \tilde{v} U_\infty, \\ p - p_\infty &= \varepsilon^2 p_\infty U_\infty^2 \tilde{p}. \end{aligned}$$

Then, to order ε the equations for the lower-deck are written:

$$\tilde{u} \frac{\partial \tilde{u}}{\partial X} + \tilde{v} \frac{\partial \tilde{u}}{\partial Z} = - \frac{d\tilde{p}}{dX} + \frac{C}{R_0(0)} \frac{\partial^2 \tilde{u}}{\partial Z^2}, \quad (4.9)$$

$$\frac{\partial \tilde{u}}{\partial X} + \frac{\partial \tilde{v}}{\partial Z} = 0. \quad (4.10)$$

(C is the constant of the Chapman viscosity law).

The above system has the following boundary conditions:

(i) $X \rightarrow \infty$ $\tilde{u} = ZU'(0)$ which express the condition that \tilde{u} must join smoothly the undisturbed flow for which:

$$U_0(\bar{y}) = U'_0(0)\bar{y} + O(\bar{y}^4) \quad \left(U'_0 = \frac{dU_0}{d\bar{y}} \right);$$

(ii) $Z \rightarrow \infty$,

$$\tilde{u} - ZU'_0(0) \rightarrow A_1(X) U'_0(0) = - \frac{\sqrt{M_\infty^2 - 1}}{\gamma p_\infty M_\infty^2} \left[\int_{-\infty}^X p_2(t) dt \right] U'_0(0), \quad (4.11)$$

which is the matching condition for the main-deck (see equations 4.1 and 4.5).

(iii) $Z = 0$, $\tilde{u} = \tilde{v} = 0$ which is the no-slip condition at the wall.

Furthermore, it is established that $\tilde{p} = \tilde{p}_3$, i. e., the *pressure is the same as in the main-deck*.

As shown by Stewartson and Williams, the main-deck is *completely passive*. Physically speaking it displaces the streamlines outward in the boundary-layer and simultaneously transmits the pressure perturbation unchanged from the base of the upper-deck to the lower-deck. The stream-tubes divergence in the main-deck is neglected. The solution in the main-deck is simply represented by an outward shift of the Blasius profile.

The function $A_1(x)$ can be interpreted as representing the slip velocity at the base of the main-deck corresponding to the inviscid perturbation of the upstream Blasius' profile by the induced pressure gradient. Alternatively, $A_1(x)$ can be regarded as a displacement thickness (see equation 4.8).

In its final form, the problem is formulated by introducing new dependent and independent variables in such a way that the influence of the flow parameters is rendered explicit. This permits the calculation of a universal Free-Interaction solution in similarity variables. In particular, it is shown that the dimensionless pressure change $\Delta p = (p - p_\infty)/\frac{1}{2} p_\infty U_\infty^2$ in a Free Interaction has the form:

$$\Delta p \sim \frac{\lambda^{1/2} C^{1/4}}{(M_\infty^2 - 1)^{1/4}} R^{-1/4} p_1(x),$$

where $\lambda = 0.332$ results from Blasius' solution. At separation, $p_1(x)$ has a well defined and fixed value which is $O(1)$. Furthermore the theory demonstrates that the dimensionless pressure changes $\Delta p(M_\infty^2 - 1)^{1/4} R^{1/4} \lambda^{-1/2} C^{-1/4}$ must collapse into a single curve when plotted against the dimensionless streamwise distance X_1 defined in Figure 4.3 (In fact, the X_1 co-ordinate used in Figure 4.3 incorporates a modification introduced by Curle (1961) to better represent wall temperature effect, see Section 3.4 of Part I). One sees that the use of these reduced variables leads to a very good correlation of wall pressure distributions measured in ramp-induced separations for very different flow conditions (Lewis *et al.* 1967). Thus the asymptotic theory confirms the similarity laws established by Chapman's introduction of the Free Interaction concept.

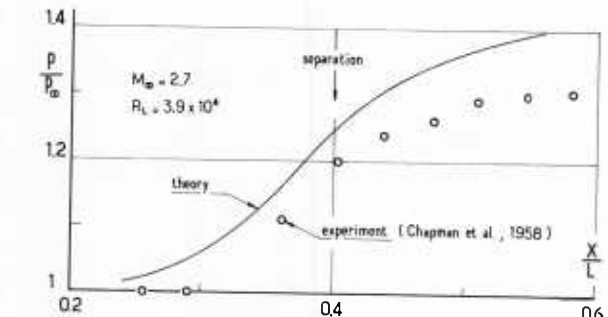
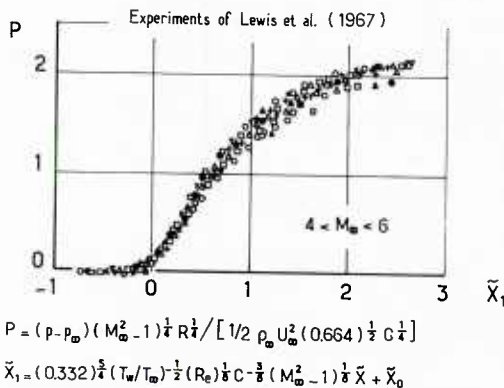


Fig. 4.4 – The Stewartson and Williams theory of laminar self induced separation (Stewartson and Williams, 1969).

Fig. 4.3 – The stewartson and Williams theory of laminar self-induced separation – Wall pressure correlation including Curle's modification. (Stewartson and Williams, 1969).

Applications of the First Order Theory. — In the original work of Stewartson and Williams, the lower-deck equations 4.9-10, along with the boundary conditions, were solved by a finite difference method (Clenshaw, 1966). A stream function $\psi(X, Z)$ was introduced and, by differentiating the governing equations with respect to Z in order to eliminate the pressure term, a fourth order equation for ψ was obtained. The integration was initiated at a distance $X < 0$ by perturbing the trivial solution of the problem $\tilde{u} = ZU'_0(0)$, $\tilde{v} = 0$ and $\tilde{p} = 0$. The outer boundary condition was approximated by a condition at a large finite value of Z . The integration proceeded in the downstream direction, the problem being treated as an *initial value problem*. This method of integration is basically the same as the one described in Section 2.3.2 above. At that time, the published calculations concerned only the self-induced separation region, including the very first part of the reversed flow region, the original calculations did not exhibit instabilities or non-uniqueness downstream of the separation point, which is rather surprising since a purely downstream marching process was used (see Section 2.1 above). In fact, further investigation showed that the stability was illusory (Stewartson, 1974) since a correct treatment of the reversed flow should take downstream conditions into consideration. However, a stable forward marching procedure is possible for cases with small separated flow by using the FLARE approximation in which the term $\tilde{u}\partial\tilde{u}/\partial X$ is neglected whenever $\tilde{u} < 0$ (see Section 2.3.1 above). The ulterior and more convincing numerical experiments of Williams (1975) were made by using the FLARE approximation.

A comparison with experiment of a calculation made by Stewartson and Williams is presented in Figure 4.4. The agreement with experiment is poor presumably because of numerical inaccuracy but also and more certainly because the limit condition $R^{-1/8} \rightarrow 0$ is not satisfied by the present experiments. This point is discussed in what follows.

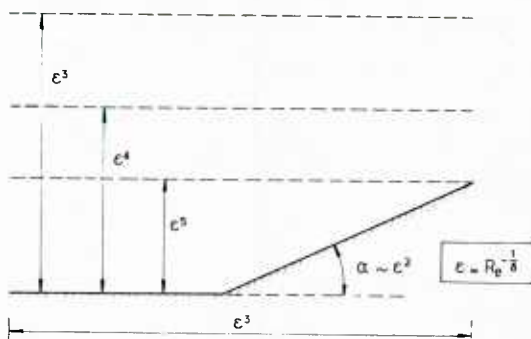


Fig. 4.5 – The triple-deck scaling laws for laminar interaction at a wedge corner

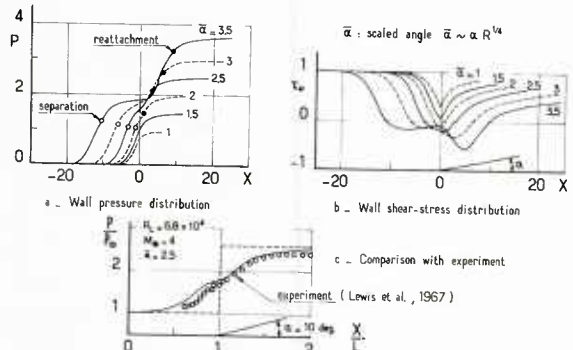


Fig. 4.6 – Application of the triple-deck theory to a laminar corner flow by Rizzetta, Burggraf and Jenson (1978).

In 1978, Rizzetta, Burggraf and Jenson (1978) applied the triple-deck theory to compute the viscous-inviscid interaction produced when a supersonic laminar boundary-layer encounters a corner (compression as well as expansion corners are treated). The method is applied both to supersonic and to hypersonic flows. In the latter case, the pressure-displacement relationship is obtained through the tangent-wedge approximation. It is assumed that the magnitude of the corner angle α is $O(R^{-1/4})$ (see Figure 4.5).

For compression corners (if separation occurs), this limitation ensures that the reattachment is still within the $\Delta x = O(R^{-3/8})$ length scale. In the present problem, uniqueness of the solution is assured by a downstream boundary condition which is prescribed for $X \rightarrow \infty$, after the reattachment point. This condition is simply the matching with the Blasius' solution. The main equation to be solved is derived from equation 4.9 by differentiation with respect to Z , which eliminates the pressure term and leads to an equation for $\tau = \tilde{u}/\partial Z$ (this procedure is similar in nature to the one used by Carter (1975), see Section 2.3.2 above). A modified pressure-displacement interaction condition is derived by twice differentiating the boundary condition 4.11 with respect to X and eliminating the pressure by use of the wall compatibility condition (i.e. $\frac{d\tilde{P}}{dX} = \frac{C}{R_0(0)} \left[\frac{\partial \tau}{\partial Z} \right]_0$).

Thus the problem involves only the strain τ as principal dependent variable. In fact, the problem is formulated as an unsteady problem for τ , time $t=0$. The calculation is initiated at $t=0$ with a uniform boundary-layer flow. It is to be noticed that in this unsteady procedure, the frequently tedious shooting method of ordinary steady approaches is avoided (see Section 3.3 above). To avoid the use of an excessively large computational mesh, the upstream and downstream conditions are replaced by asymptotic expressions valid for $X \rightarrow \pm \infty$ (Stewartson and Williams, 1969; Smith and Stewartson, 1973).

The calculation gives rapidly increasing separated regions when α goes beyond the value α^* for Incipient Separation at the corner [α^* is still $O(R^{-1/4})$]. Consequently, the separation zone moves rapidly upstream and a situation is reached where the pressure plateau and reattachment regions are no longer contained in the $O(R^{-3/8})$ length scale. In this case, a new asymptotic flow structure must be introduced in which the separated free shear-layer, the recirculating zone and the reattachment region have their own scaling.

Examples of calculations performed by Rizzetta *et al.* are shown in Figure 4.6. They are relative to ramp induced interactions for increasing values of the angle α . The results are presented with dimensionless variables that correlate the initial conditions, in particular the Mach number M_∞ . The figure also presents a comparison of the theory with an experimental result obtained by Lewis *et al.* (1967).

An asymptotic theory for extended laminar separation has been developed by Burggraf (1975). The flow model consists basically of three different regions each having their own appropriate length scale (see in Fig. 4.7):

(i) the separation zone, the mathematical structure of which is the one given by Stewartson and Williams (see Section 4.2.1.1 above);

(ii) the shear-layer leaving the separation region; the structure of this shear-layer has been described by Neiland (1971) and more fully by Stewartson and Williams (1973) (see also Stewartson, 1974);

The matching of these three domains permits the calculation of interactions induced by supersonic ramps set at an angle which is greater than the limit value α^* .

Calculations made by Burggraf are presented in Figure 4.8. The first one is relative to separation induced by a forward facing step and the second, to ramp induced separation at $M_\infty = 2.55$. In the second case, agreement with experiment is only moderate.

Very instructive comparisons between the triple-deck theory and the (ordinary) interacting boundary-layer model (see Section 3 above) have been made by Burggraf *et al* (1979). In this work, the triple-deck calculations use the method of Rizzetta, Burggraf and Jenson (1978) whereas interacting boundary-layer calculations employ Werle and Vatsa's method (1974) (see Section 3 above). As we know, the "classical" interacting model considers the boundary-layer as a unique layer for which the *complete* boundary-layer equations are applied. Thus this last model *includes* the asymptotic triple-deck theory.

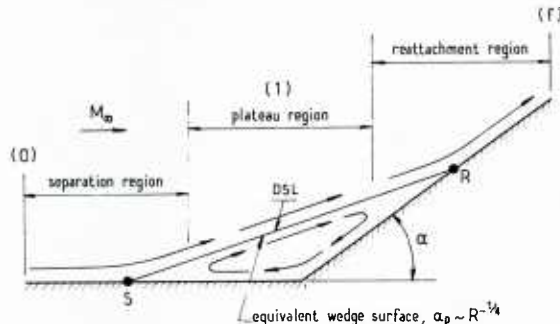


Fig. 4.7 – Flow geometry for interaction with large separation at a wedge corner in laminar flow.

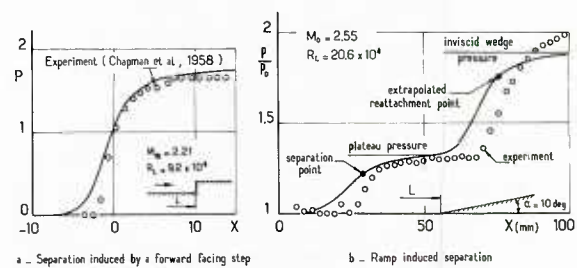


Fig. 4.8 – Application of asymptotic expansion method to extended laminar separation by Burggraf (1975).

In the above mentioned comparisons, the two methods have been applied to the supersonic compression ramp problem. Some of these comparisons are presented in Figure 4.9 which shows that the asymptotic theory indicates the correct qualitative trend but is quantitatively accurate only at very high Reynolds numbers ($R > 10^8$). A cause of inaccuracy at moderate Reynolds numbers ($R \approx 10^4 - 10^6$) may be the ignoring of streamlines divergence in the main-deck (Werle and Vatsa, 1974). The weak point of the asymptotic theory is the fact that it is accurate for *very high Reynolds numbers* ($R \approx 10^9$) for which a laminar régime is very improbable in most usual circumstances where the wall condition is adiabatic (or nearly adiabatic). It is only for extremely cooled walls that transition can be delayed to very high Reynolds numbers.

The triple-deck equations have also been solved by Napolitano, Werle and Davis (1979) by using an Alternating Direction Implicit numerical technique. This technique is similar to the approach used by Werle and Vatsa to solve the supersonic interacting boundary-layer equations (see Section 3.3.1 above). The triple-deck theory is here applied to a flow passing a parabolic hump on a flat plate. The subsonic case is also considered, in which case the pressure-displacement condition is given by a Cauchy integral.

Other improvements of the numerical technique have been proposed by Napolitano and Vacca (1980).

Comparisons of the asymptotic triple-deck theory to numerical solutions of the full Navier-Stokes equations have been made by Hussaini, Baldwin and McCormack (1980). In reality, these calculations were performed essentially to study the accuracy of the numerical schemes employed to solve the Navier-Stokes equations (influence of the grid size); the asymptotic theory was, in fact, used as a test bed. The main conclusion drawn from the comparisons was that the asymptotic scaling laws can be of value for suggesting mesh resolution fine enough to correctly capture the interaction phenomenon.

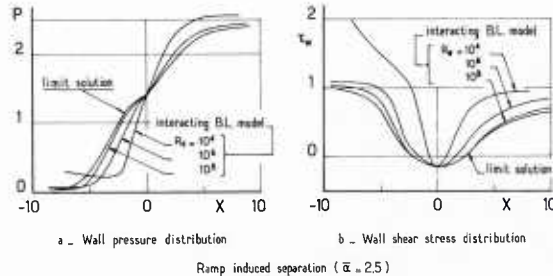


Fig. 4.9 – Comparison between asymptotic model and interacting boundary-layer model (Burggraf *et al.*, 1979).

Applications of the Second-Order Theory. – In the preceding applications of the asymptotic theory, only the leading terms in the expansions were retained. Extension of the method to include second-order terms was made by Brown and Williams (1975). In this case, the solution depends on the thermal conditions at the wall (it is recalled that the inner-layer is incompressible to first-order). Brown and Williams solved the Free Interaction problem for the adiabatic case, but they did not present results for the flowfield inside the separation bubble. A second-order asymptotic solution with separated region was obtained by Ragad and Nayfeh (1978, 1980) for the supersonic flow over a compression corner. Now, as has already been pointed out, the density is no longer constant in the inner-layer and the solution in the main-deck contains four undetermined functions $A_1(\bar{x})$, $A_2(\bar{x})$, $p_2(\bar{x})$ and $p_3(\bar{x})$. Two equations relating these functions are provided by the matching with the upper-deck. Hence, $A_1(\bar{x})$ and $A_2(\bar{x})$ can be expressed in terms of $p_2(\bar{x})$ and $p_3(\bar{x})$. The latter functions are determined from matching with the lower-deck. The basic principle of the method of solution is as follows:

- (i) solving the first-order problem (\tilde{u}_1 , \tilde{v}_1 , \tilde{p}_2);
- (ii) solving the second-order density ($\tilde{\rho}_2$);
- (iii) solving the total solution (\tilde{u} , \tilde{v} , \tilde{p}).

The numerical method employed by Ragad and Nayfeh is similar to the one used by Rizzetta *et al.*, i.e., the problem is formulated for $\tau = \partial \tilde{u} / \partial Z$. The essential difference is in the use of a more accurate discretization scheme [the truncation error is $O(\Delta x^2)$ for the x -derivatives instead of $O(\Delta x)$]. Calculations are made for both adiabatic and non-adiabatic wall conditions. The results obtained are rather disappointing: when compared with Navier-Stokes calculations, the second-order expansion is found to be less accurate than the first-order expansion. According to the authors, the greatest weakness in the matched asymptotic expansion version of the triple-deck theory lies in the expansion of the basic (i.e., undisturbed) boundary-layer flow in powers of the transverse co-ordinate. The stream-tube divergence in the main-deck is likewise probably not negligible for moderate Reynolds numbers since ϵ is then not very small.

4.2.1.2. — The Free Interaction Theory in Transonic Flows. The scaling laws defined in Section 4.2.1.1 fail when the upstream Mach number M_∞ is close to unity and the theory then needs reconsideration. The origin of this failure lies in the use of the linear supersonic theory to relate the pressure and the flow deflection just outside the boundary-layer (see equation 4.7 in Section 4.2.1.1 above). As is well known, the linear theory is not valid when M_∞ is close to one. In fact, according to the transonic small-disturbance theory, the changes in pressure are now of the same order as the two-thirds power of the flow deflection angle. Taking this condition into consideration, Messiter, Feo and Melnik (1971) derived the scaling laws appropriate for transonic flows (see also Stewartson, 1974)

(i) streamwise scale: $\Delta x \sim O(\epsilon^{12/5})L$;

(ii) vertical scales:

— upper-deck: $\Delta y_u \sim O(\epsilon^{8/5})L$;

— main-deck: $\Delta y_m \sim O(\epsilon^4)L$;

— lower-deck: $\Delta y_l \sim O(\epsilon^{24/5})L$.

In the present situation, the vertical and the streamwise length scales in the upper-deck are no longer of the same order: $\Delta y_u / \Delta x \sim O(\epsilon^{-4/5})$; one sees that $\Delta y_u \gg \Delta x$, which is consistent with propagation of disturbances near sonic conditions.

Apart from the change in scaling laws, the flow structure at transonic speeds is basically the same as in supersonic flows: the main-deck still behaves as an inviscid rotational layer which is in fact the inviscid continuation of the Blasius' boundary-layer. Its role is simply to transmit the external pressure field unchanged to the lower-deck. The lower-deck is still represented, to first-order, by the incompressible boundary-layer equation. The major change is in the upper-deck where the transonic small-perturbation equation is now used instead of the linear supersonic theory. As we know, to first-order, the flow in the upper-deck is irrotational. It is thus possible to introduce a velocity potential ϕ which has to satisfy the equation:

$$\frac{\partial^2 \phi}{\partial y_u^2} = \left[K_0 + (\gamma + 1) \frac{\partial \phi}{\partial x} \right] \frac{\partial^2 \phi}{\partial x^2}, \quad (4.12)$$

where the transonic interaction parameter K_0 is of the form:

$$K_0 \sim (M_\infty^2 - 1) \epsilon^{-8/5}.$$

Brilliant and Adamson (1974) have also derived scaling laws for the transonic Free Interaction. The problem considered by these authors concerns the reflection of a weak oblique shock-wave in a transonic flow where the Mach number in the upper-deck always remains greater than one (the case where the shock is normal far from the boundary-layer has been treated by Brilliant, 1971). The shock strength envisaged by Brilliant and Adamson was too weak to induce separation. The problem of a transonic interaction with separation has been solved by Bodonyi and Kluwick (1977). They also restricted themselves to the simpler situation where the outer flow remains entirely supersonic (in this case, equation 4.12 has simple-wave solutions). The lower-deck equations were solved by using a finite difference method with centered differences in the y -direction and backward differences in the x -direction. Instabilities in the reversed flow region were prevented with the help of the FLARE approximation.

4.2.2. — The Tu and Weinbaum Non Asymptotic Triple-Deck Model

In order to avoid the limitations of the asymptotic expansion approach, a *non asymptotic* triple-deck model for laminar supersonic boundary-layer interaction was proposed by Tu and Weinbaum (1976). In this model, the lower-deck is described by the complete boundary-layer equations, including the energy equation (a Prandtl number of unity is assumed). The inner solution has to satisfy the following boundary conditions:

(i) at the wall $u = v = 0$ and prescribed temperature (or absence of heat transfer);

(ii) at the outer edge $\delta = \epsilon \hat{\delta}$: continuous matching both in value and slope with the profile description in the main deck.

Here also, the main-deck is an inviscid rotational fluid with $\partial p / \partial y = 0$, but the stream-tube divergence is taken into account. An integrated pressure/stream-tube area relation is derived which couples the viscous displacement effect at the edge of the inner layer to the interaction pressure imposed by the outgoing wave system of the external flow at the boundary-layer outer edge. This relation, which is also considered in Section 3.2.2, is:

$$\tan \theta_e - \tan \theta_{\hat{\delta}} = - \frac{1}{\gamma p} \frac{dp}{dx} \int_{\hat{\delta}}^{\hat{\delta}} \frac{M^2 - 1}{M^2} dy, \quad (4.13)$$

where θ_e and $\theta_{\hat{\delta}}$ are flow angles at δ and $\hat{\delta}$ respectively. The pressure in the external flow is related to θ_e through the use of the Prandtl-Meyer function $v(M)$, i.e.:

$$\theta_e(x) - \theta_\infty = v(M_\infty) - v(M_e).$$

Thus the external flow is assumed to be a simple wave system, but no linearization is made. Equation 4.13 can be more conveniently expressed with the stream function $\psi(x, y)$:

$$\tan \theta_e - \tan \theta_{\hat{\delta}} = - \frac{R}{\gamma p^2} \frac{dp}{dx} \left(\frac{1}{\gamma R} \right)^{1/2} \int_{\hat{\delta}}^{\hat{\delta}} \frac{M^2(\psi, x) - 1}{M^2(\psi, x)} [T(\psi, x)]^{1/2} d\psi \quad (4.14)$$

(here R is the perfect gas law constant).

The fluid in the main-deck being assumed inviscid, the Mach number and temperature distributions at any streamwise station x can be calculated from known initial profiles and initial pressure p_0 by considering an isentropic evolution from p_0 to p along each streamline (it is recalled that the pressure is assumed to be transversely constant). This kind of calculation is in fact an "Inviscid Shear-Layer Analysis" of the type described in Section 1.4. Consequently, for a specified value of p_0 and initial Mach number profile, the integral on the Right Hand Side of equation 4.14 is only a function of the local interaction pressure p and of the definitions $\hat{\delta}$ and δ of the sublayer and boundary-layer edges.

The viscous sublayer is computed by a Polhausen type method. The distributions are approximated by a fourth-order polynomial for the reduced velocity u/u_{δ} and a third-order polynomial for the reduced stagnation enthalpy S/S_{δ} . The coefficients of these polynomials are determined in a classical way by boundary and compatibility conditions. The remaining unknown thickness δ is computed by integration of the momentum integral equation.

The interacting boundary-layer can be computed by solving the equations appropriate to each layer along with boundary conditions to be satisfied at the wall as well as at their common boundaries. The pressure is obtained through the interaction equation 4.13 connecting the flow at the outer edge of the sublayer and the flow turning angle in the outer inviscid stream. Calculation of shock-wave/boundary-layer interaction in which a downstream condition must be satisfied is made by a shooting technique (see Section 3.3.1 above).

Theoretically, a difficult problem with this kind of method could be the determination of the sublayer thickness δ_0 at the origin of the interaction domain. However, according to the authors' numerical experiments, the choice of δ_0/δ_0 does not greatly affect the results provided that δ_0/δ_0 is not too small and the external Mach number not too high.

The Tu and Weinbaum theory is compared to experiment in Figure 4.10. The first case corresponds to a shock reflection at a free stream Mach number M_∞ equal to 2 (Hakkinen *et al.*, 1959). The second case is a ramp flow with separation at $M_\infty = 6.06$. Agreement with experiment is certainly better than in calculation using asymptotic theory.

The method proposed by Tu and Weinbaum is of course free of certain limitations inherent in the existing asymptotic expansion theories (for example the neglecting of the stream-tube divergence in the main-deck). Nevertheless, from a fundamental point of view (i. e., excluding computation time considerations), the expediency of the present two-layer model is questionable since this model is in fact contained (as well as the asymptotic expansion versions of the triple-deck model) in the "classical" interaction theories which employ finite difference methods for computing the viscous layer (see Section 2.3 above). In these last theories, the complete Prandtl equations are applied to the *entire boundary-layer* so that the exactness of the mathematical model is greater than in the present versions of multi-deck approaches.

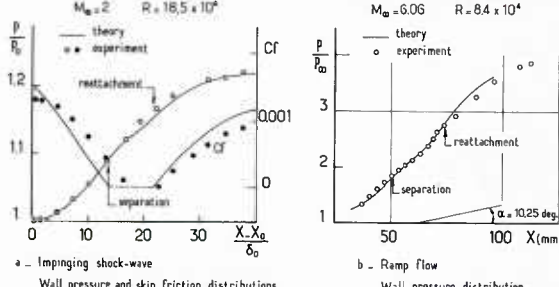


Fig. 4.10 – The Tu and Weinbaum non asymptotic triple-deck model
(Tu and Weinbaum, 1976).

4.3. – Multi-Deck Theories in Turbulent Flow

4.3.1. – Asymptotic Expansion Methods

4.3.1.1. – *The Limiting Processes in Turbulent Flow.* Formal asymptotic methods have also been applied to the shock-wave/boundary-layer interaction problem in turbulent flows. Most of the existing theories consider interaction with normal shock-waves. Recently, Melnik (1980) presented a review of these theories and the conclusions developed in the present Section are largely inspired by his paper (for a general survey of the problem, see also Adamson and Messiter, 1980).

The limiting processes pertaining to the interaction of shock-wave with a turbulent boundary-layer have been clearly established by Melnik and Grossman (1974). The limit conditions must be:

- (i) the shock is weak and nearly normal to the flat plate coincident with the axis $y=0$. This means an upstream Mach number $M_\infty \approx 1$;
- (ii) the Reynolds number is high, so that the boundary-layer velocity profile is "full". This profile can be represented by a conventional form of the law-of-the wake/law-of-the wall (see Section 1.1 of Part I):

$$\frac{u_0(y)}{u_e} = U_0(y) = 1 + \frac{1}{0.41 u_e} \left[\ln \left(\frac{y}{\delta} \right) + \tilde{\pi} w \left(\frac{y}{\delta} \right) \right],$$

where $\tilde{\pi}$ and w are Coles' wake parameter and wake function. A high Reynolds number implies small skin-friction or, small reduced friction velocity u_e/u_e which is the same thing. Thus the large Reynolds number limit is expressed in terms of the small parameter:

$$\varepsilon \equiv \frac{u_e}{u_e} = \frac{u_e}{U_\infty} \approx \sqrt{C_f/2} \quad (\text{weak compressibility effects}).$$

Consequently, the solutions to be found are characterized by the *double limit*:

$$M_\infty \rightarrow 1, \quad \varepsilon \rightarrow 0.$$

The limiting process is in fact more precisely defined by the parameter χ_t such that:

$$\chi_t \equiv \frac{(M_\infty^2 - 1)}{\varepsilon},$$

$(M_\infty^2 - 1)$ being proportional to the shock strength (in the limit $M_\infty \rightarrow 1$), χ_t is a measure of the ratio between the velocity jump across the shock and the velocity defect in the boundary-layer. Various limit cases can be distinguished according to the value of χ_t :

- $M_\infty \rightarrow 1, \varepsilon \rightarrow 0$, in such a way that $\chi_t = O(1)$;
- $M_\infty \rightarrow 1, \varepsilon \rightarrow 0$, in such a way that $\chi_t \rightarrow 0$;
- $M_\infty \rightarrow 1, \varepsilon \rightarrow 0$, in such a way that $\chi_t \rightarrow \infty$.

A fourth situation can be considered in which $M_\infty \neq 1$ (supersonic case) and $\varepsilon \rightarrow 0$; thus:

- $M_\infty \neq 1, \varepsilon \rightarrow 0$, in such a way that $\chi_t \rightarrow \infty$.

The four above limit processes can be interpreted as corresponding to the following flow situations sketched in Figure 4.11;

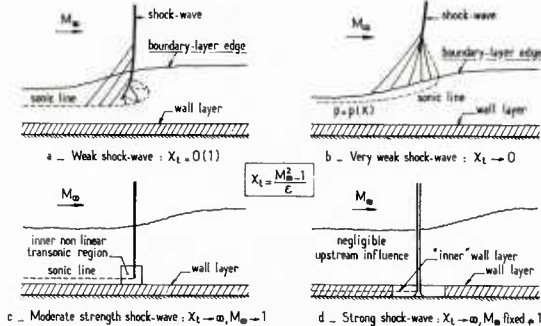


Fig. 4.11 – Turbulent shock-wave/boundary-layer interaction – Flowfield structure variation with shock strength (Melnik, 1980).

(a) *weak shock-wave*: here the velocity change across the boundary-layer is of the same order as the velocity change across the shock-wave. Consequently, as the velocity profile is “full”, the sonic line is in the main part of the boundary-layer. The shock-wave penetrates the boundary-layer and terminates somewhere in the supersonic zone as shown in Figure 4.11 *b*;

(b) *very weak shock-wave*: the Mach number M_∞ is close to one and the defect ε is “large” [compared to $(M_\infty - 1)$]; thus the sonic line is near the outer edge of the boundary-layer. The shock-wave which is weakened by compression waves generated by the boundary-layer thickening does not penetrate into the boundary-layer;

(c) *moderate shock strength*: now the velocity defect is small compared to $(M_\infty - 1)$; in consequence, the sonic line is close to the wall. The shock wave is nearly straight and penetrates deep into the boundary-layer;

(d) *strong shock-wave*: the sonic line is very close to the wall so that the shock penetrates practically the entire boundary-layer and seems to emanate from the wall itself. Such a situation corresponds to supersonic or hypersonic oblique shock-waves. For these cases, a very good description of the flowfield is provided by supersonic inviscid rotational calculations (see Section 1.4 on Inviscid Shear-Layer analyses).

The different theories used to treat cases *a* to *c* are reviewed in the following Sections. Case *a* [weak shock limit, $\chi_t = O(1)$] has been analyzed by Melnik and Grossman (1974, 1975, 1977); case *b* (very weak shock-wave, $\chi_t \rightarrow 0$) by Adamson and Feo (1975); and case *c* (moderate shock strength, $\chi_t \rightarrow \infty$ and $M_\infty \rightarrow 1$) by Adamson and Messiter (1977, 1980; see also Messiter and Adamson, 1978) and Adamson, Liou and Messiter (1980).

4.3.1.2. – Melnik and Grossman’s Theory for Normal Shock-Wave

$$(M_\infty^2 - 1)/\varepsilon = \chi_t \rightarrow O(1).$$

On the basis of formal asymptotic analysis, it can be demonstrated that this limit corresponds to the asymptotic flow structure shown in Figure 4.12. Upstream of the interaction domain, the boundary-layer develops a classical two-layer structure of the law-of-the-wall/law-of-the-wake form. In this region, the thickness δ_0 of the incoming boundary-layer scales with the friction velocity. This means that if L is a characteristic length scale of the upstream region (the distance from the leading edge of an airfoil for instance):

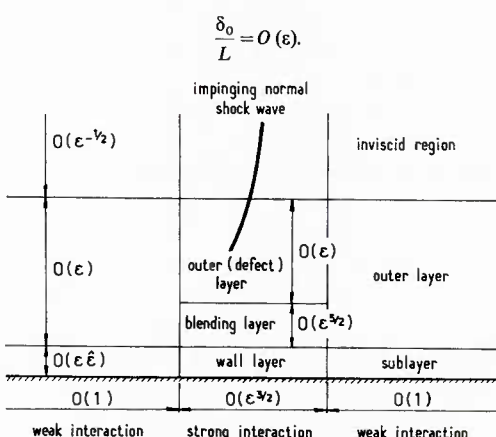


Fig. 4.12 – The Melnik and Grossman theory for weak shock-wave. Asymptotic flowfield structure (Melnik and Grossman, 1974).

The sonic line being well within the boundary-layer, it is assumed that the vertical extent of the interaction is $O(\delta_0)$. It results from consideration of the slope $\tan \alpha = (M_\infty^2 - 1)^{-1/2}$ of the characteristics in the supersonic incoming flow that the streamwise length scale of the (strong) interaction domain is given by [since $\chi_s = O(1)$]:

$$\Delta x = \varepsilon^{1/2} \delta_0 = O(\varepsilon^{3/2}) L. \quad (4.15)$$

As a consequence of this scaling, it can be established that in the interaction region, the boundary-layer develops a three-layer structure consisting of:

(a) an outer inviscid rotational flow, extending over most of the boundary-layer, the length scale of which is: $\Delta y = O(\varepsilon) L$. This layer is called the "main-deck" in triple-deck terminology;

(b) a conventional wall-layer which has to be introduced in order to satisfy the no-slip condition at the wall. This layer is a continuation of the upstream wall-layer, the length scale of which is classically given by:

$$\Delta y = \frac{\mu_{0w}}{\rho_{0w} u_{t0}} = O(\varepsilon \hat{\varepsilon}) L.$$

Following Mellor (1972), $\hat{\varepsilon}$ is defined by:

$$\hat{\varepsilon} = \frac{1}{\varepsilon^2 R} = O(\varepsilon^{-2} e^{-1/\varepsilon}), \quad R = \frac{\rho_\infty U_\infty L}{\mu_\infty},$$

since:

$$\varepsilon = O(\ln R)^{-1},$$

from the skin friction law in the approaching boundary-layer.

By virtue of this scaling, it can be demonstrated that inertia and pressure forces play a negligible role in the wall layer (except near separation conditions) even though the streamwise pressure gradient might be large in the interaction region. A consequence of this finding is that the displacement effect of the wall-layer is negligibly small, so that *the wall-layer cannot significantly influence the solution in the outer inviscid region* (in contrast to Inger's theory, see below).

(c) a blending-layer between the outer and the wall layers. This intermediate layer must be introduced because of the mismatch in both the Reynolds stress and streamwise velocity between the outer and the wall layer solutions (The mismatch results from the "freezing" of the Reynolds stress in the outer region, whereas the Reynolds stress in the wall layer adjusts itself instantaneously to change in skin friction. Thus the two regions cannot overlap.) It can be demonstrated that the vertical velocity in the blending layer is two orders of magnitude less than it is in the outer layer so that the blending layer likewise *does not influence* the outer solution. The vertical scale of the blending-layer is:

$$\Delta y = \varepsilon^{5/2} L.$$

We will now briefly present the methods of solution for each of the three layers.

In the *outer inviscid layer (main-deck)*, the solution is represented by the expansions:

$$U = \frac{u(x, y)}{U_{0e}} = 1 + \varepsilon u_1(\bar{x}, \bar{y}) + \dots,$$

$$V = \frac{v(x, y)}{U_{0e}} = \varepsilon^{3/2} v_1(\bar{x}, \bar{y}) + \dots$$

where the stretched variables \bar{x} and \bar{y} are such that:

$$\bar{x} = \varepsilon^{-3/2} \frac{x}{L}, \quad \bar{y} = \varepsilon^{-1} \frac{y}{L}. \quad (4.16)$$

The undisturbed (or initial) boundary-layer profile is represented by:

$$U_0(y) = 1 + \varepsilon u_0(y),$$

where:

$$u_0(y) = \begin{cases} \frac{1}{0.41} \left[\ln \left(\frac{y}{\delta_0} \right) + \tilde{\pi} w \left(\frac{y}{\delta_0} \right) \right] & \text{if } 0 < y \leq \delta_0 \\ 0 & \text{if } y > \delta_0 \end{cases} \quad (4.17)$$

The perturbation field being irrotational (this can be demonstrated), a disturbance velocity potential ϕ_1 is introduced in such a way that:

$$u_1 = u_0(\bar{y}) + \frac{\partial \phi_1}{\partial \bar{x}}, \quad (4.18)$$

$$v_1 = \partial \phi_1 / \partial \bar{y}. \quad (4.19)$$

Substitution of 4.18 and 4.19 in the Navier-Stokes equations leads to the following equation for ϕ_1 :

$$\left\{ \chi_t + (\gamma + 1) M_{0e}^2 \left[u_0(\bar{y}) + \frac{\partial \phi_1}{\partial \bar{x}} \right] \right\} \frac{\partial^2 \phi_1}{\partial \bar{x}^2} - \frac{\partial^2 \phi_1}{\partial \bar{y}^2} = 0. \quad (4.20)$$

The above equation is in fact similar to the one used by Inger in the outer potential flow region (see Section 4.3.2.1 below) if one replaces $u'/U_{0,e}$ in equation 4.26 by $\varepsilon u_1 = u_0(\bar{y}) + \partial\phi_1/\partial\bar{x}$ and makes the appropriate scaling for x and y (i.e., relations 4.16).

Equation 4.20 is supplemented by boundary conditions imposing that:

- $\frac{\partial\phi_1}{\partial\bar{x}}$ vanish far upstream ($\bar{x} \rightarrow \infty$);
- the solution match the prescribed normal shock conditions for $\bar{y} \rightarrow \infty$, i.e.:

$$\frac{\partial\phi_1}{\partial\bar{x}} = \begin{cases} 0 & \text{for } \bar{x} < 0 \text{ and } \bar{y} \rightarrow \infty, \\ -\frac{2\chi_t}{(\gamma+1)M_{0,e}^2} & \text{for } \bar{x} > 0 \text{ and } \bar{y} \rightarrow \infty. \end{cases}$$

(the origin $x=0$ is located in the plane of the undisturbed normal shock);

- the vertical component $v_1 = \partial\phi_1/\partial\bar{y}$ vanish at the wall. This latter condition results from the conclusion that the wall layer and the blending layer have no displacement effect (see above).

It is to be noticed that $u_0(\bar{y})$ in equation 4.17 tends to infinity when $\bar{y} \rightarrow 0$ (the logarithmic term in equation 4.17 is obviously not valid very near the wall) and a special treatment has to be applied to equation 4.20 in the immediate vicinity of the surface. In fact, the (unphysical) singularity at $\bar{y}=0$ of the representation adopted for the unperturbed velocity profile removes the inadequate behavior at the wall of an entirely inviscid solution (see Section 4.1 above). The physical significance of such an “error compensating” mechanism is certainly questionable.

Thereafter, the pressure disturbance results from the standard small disturbance relationship:

$$p_1 = -\partial\phi_1/\partial x.$$

Equation 4.20, along with the appropriate boundary conditions, is solved by use of the Murman-Cole (1971) non-conservative finite difference method.

The treatment of the blending and wall-layers involves rather complicated algebra so we will restrict ourselves to a presentation of the essential results.

In the *blending-layer*, the independent variables are stretched according to:

$$\bar{x} = \varepsilon^{-3/2}x/L; \quad \bar{y} = \varepsilon^{-5/2}y/L.$$

It can be demonstrated that the inertia and Reynolds stress terms in the streamwise momentum equation are of the same order and the subsequent analysis leads to the following conclusions:

- to second-order, the pressure is constant across the blending layer;
- at transonic speeds, the blending layer is a *parallel* stream (no transverse velocity component) to third-order.

Thus this layer does not influence the outer deck.

The *wall-layer* is treated by introducing the usual scaling:

$$\bar{y} = y^+ = \frac{\rho_w(x)u_r(x)}{\mu_w(x)}, \quad u^+ = \frac{u}{u_r(x)} \quad \text{where } u_r(x) = \sqrt{\frac{\tau_w(x)}{\rho_w(x)}}.$$

$\rho_w(x)$, $\mu_w(x)$ and $u_r(x)$ are *local* wall properties.

The equations describing the wall-layer are:

$$\frac{\tau}{\tau_w} + \frac{\mu}{\mu_w} \frac{\partial u^+}{\partial y^+} = 1 + O(\varepsilon^3), \quad (4.21)$$

from the momentum equation (equation 4.21 expresses the well known property that the total stress, laminar plus turbulent, is constant across the wall layer), and:

$$\frac{\tau}{\tau_w} = \left(\frac{\rho}{\rho_w} \right) \left(0.41 y^+ \frac{\partial u^+}{\partial y^+} \right)^2 D^2(y^+) + O(\varepsilon^3), \quad (4.22)$$

which is a mixing length equation for the Reynolds stress incorporating a damping factor $D(y^+)$. The two above equations 4.21 and 4.22 are supplemented by expressions giving density and molecular viscosity.

It is established that:

- the pressure is constant across the wall layer to *all orders*;
- the v component of velocity is exponentially small: the wall-layer has no influence on the outer solution, as has already been stated.

In order to match the wall-layer to the blending-layer, only the fully turbulent solution of the wall-layer is required. This solution is obtained by dropping the viscous term in equation 4.21 and setting $D=1$ in equation 4.22. It has the familiar form:

$$u^+ = \frac{1}{0.41} \ln y^+ + B(x; \varepsilon),$$

where $B(x; \varepsilon) = B_0 = 5$ in incompressible flows. It is seen that the velocity profile in the wall-layer depends solely on wall properties: $\rho_w(x)$, $\mu_w(x)$, $\tau_w(x)$. These properties result from the wall pressure $p_w(x)$ impressed by the outer layer [$\rho_w(x)$, $\mu_w(x)$] and from the matching of the three layers [$\tau_w(x)$].

To sum up briefly: in the analysis of Melnik and Grossman just presented, the pressure field is defined by a purely inviscid solution which is not influenced by any displacement effects due to the existence of a viscous sublayer. Acting viscous forces are confined within a very thin wall layer which does not interact with the outer flow. This finding is in contradiction with Lighthill's original model.

Calculations performed by Melnik and Grossman are shown in Figure 4.13. They are relative to a transonic interaction inside a circular pipe which was studied experimentally by Gadd (1961). The computed streamwise pressure distributions at increasing distance from the wall are represented in Figure 4.13a. They clearly exhibit the post-shock expansion observed in most transonic flows at a certain distance from the wall (see Section 2.6.1 of Part I). The general flow structure is depicted in Figure 4.13b by the tracing of the shock-wave, the sonic line and the compression waves forming upstream of the shock as a consequence of the interaction mechanism. This tracing is made in the plane of the stretched variables \bar{x} and \bar{y} so that the streamwise scale is dilated by the factor $(M_\infty^2 - 1)^{-1/2}$. A comparison with measured wall pressure distribution is presented in Figure 4.13c.

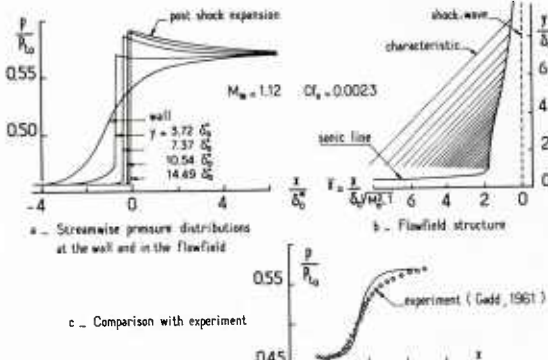


Fig. 4.13 – Application of the melnik and Grossman theory for turbulent interaction (Melnik and Grossman, 1974).

4.3.1.3. – Adamson and Messiter's Theory for Normal Shock-Wave

As already mentioned (see Section 4.3.1.1 above), the case considered by Adamson and Messiter corresponds to moderate shock strength i.e., $M_\infty \rightarrow 1$ and $u_e/u_\infty \rightarrow 0$ in such a way that $\chi_e \rightarrow \infty$. This limiting process means that in the incoming boundary-layer, the sonic line is very close to the wall (because the velocity profile is very "filled"). As a consequence, the shock wave penetrates deep into the boundary-layer.

The flow structure which results from this situation is represented schematically in Figure 4.14. In a classic manner, the flow now comprises an outer inviscid region and a boundary-layer region, the latter being divided into an inviscid rotational part and a viscous near-wall region.

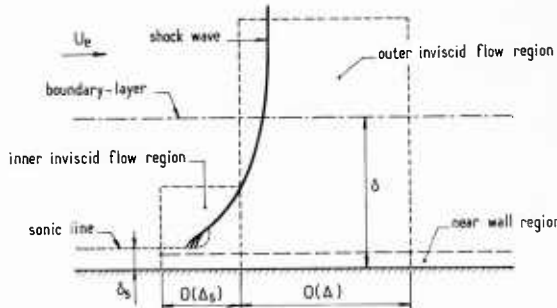


Fig. 4.14 – The Adamson-Messiter-Liou theory for moderate strength shock-wave structure of the inviscid part of the flowfield (Adamson et al., 1980).

The boundary-layer inviscid part must in turn be divided into:

(i) an outer domain which is scaled by the thickness δ_0 of the undisturbed boundary-layer and a corresponding Δx in the x -direction. In this region one sees a normal shock entering the velocity defect part of the boundary-layer;

(ii) an inner region which is scaled by the distance δ_s from the wall of the sonic line in the undisturbed boundary-layer. The streamwise extent of this region is $O(\Delta^* x)$ with $\Delta^* x \ll \Delta x$. Here, the thickening of the subsonic layer, due to upstream influence, produces compression waves in the supersonic part of the flow. These converging waves coalesce to form the shock-wave which becomes progressively normal. Thus, the length scale Δx^* is a measure of the upstream influence of the interaction; Δx^* itself depends on the thickness δ_s of the subsonic part of the incoming boundary-layer. Because in this case $\chi_e \rightarrow \infty$, the sonic line is assumed to be in the logarithmic portion of the velocity profile and, consequently, δ_s is exponentially small compared to δ . It can be demonstrated that the upstream influence $O(\Delta^*)$ is also exponentially small compared to δ_0 .

The near-wall region is excessively thin throughout the interaction domain if separation does not occur. Therefore the conclusions of the analysis given in Section 4.3.1.2 above remain valid. There is no transverse pressure gradient across the viscous region and (to the order considered) there is no displacement effect impressed on the outer inviscid regions, i.e., $v(x, 0) = v_s(x, 0) = 0$ (to the order considered). The pressure field is entirely defined by the behavior of the inviscid flow, consideration of the wall region being necessary only to determine surface properties (the skin friction coefficient, for instance).

First, let us consider the solution for the outer inviscid flow which as we know includes most of the boundary-layer. To the scales δ and Δx of this region, the inner-layer is vanishingly small, and one sees a normal shock entering the boundary-layer which is represented by the velocity defect layer. To order ϵ , the incoming velocity is uniform and the shock is therefore planar. In fact, in the boundary-layer domain of the outer region, there are variations from a uniform incoming velocity so that the shock shape must be corrected in a manner which will be seen later.

In the present Section, the authors' original conventions will be adopted. The velocity is here scaled to the speed of sound in the external upstream flow and the small parameter ϵ is defined by (see in Fig. 4.15):

$$U_{0\epsilon} = 1 + \epsilon,$$

where $U_{0\epsilon}$ is the (reduced) outer flow velocity upstream of the shock-wave. The second small parameter is the dimensionless friction velocity u_t such that: $u_t \ll \epsilon$.

The stretched variables \bar{y} and \bar{x} are defined by:

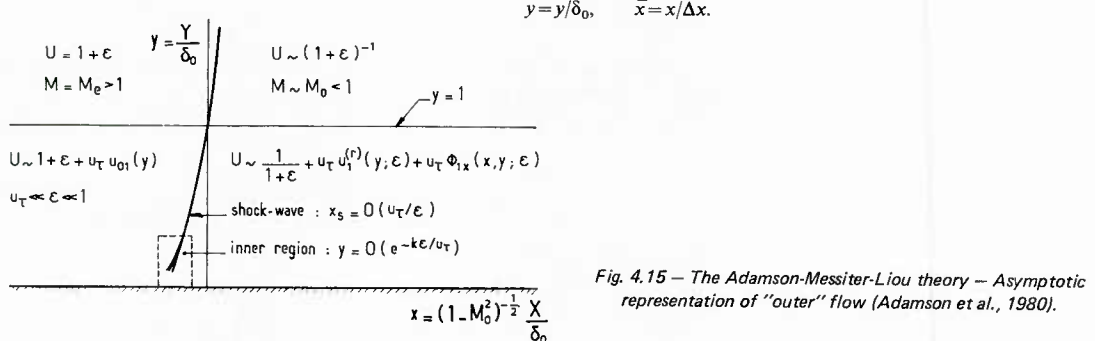


Fig. 4.15 — The Adamson-Messiter-Liou theory — Asymptotic representation of "outer" flow (Adamson et al., 1980).

It is already known (see Section 4.3.1.1 above) that $\delta_0/L = O(u_t)$. Furthermore, asymptotic expansion arguments yield:

$$\Delta x = (\gamma + 1)^{1/2} \epsilon^{1/2} u_t L,$$

which is similar to the scaling given by equation 4.15 ($\gamma + 1$)^{1/2} being $O(1)$.

The upstream velocity field is represented by:

$$\begin{aligned} U &= 1 + \epsilon + u_t u_{01}(\bar{y}) \\ V &= 0 \end{aligned} \quad (4.23)$$

One seeks a downstream solution of the form:

$$\begin{aligned} U &= 1 - \epsilon + u_t u_{01}(\bar{y}) + u_t u_1(\bar{x}, \bar{y}) + \dots \\ V &= (\gamma + 1)^{1/2} \epsilon^{1/2} u_t v_1(\bar{x}, \bar{y}) + \dots \end{aligned} \quad (4.24)$$

plus similar expressions for p , ρ and T . Expression 4.24 satisfies shock jump relations to $O(\epsilon^2)$ in the external flowfield.

Thus, it is assumed that the shock-wave penetrates down to the wall and propagates through an undisturbed upstream flow defined by equation 4.23. The solution to be found is entirely in the subsonic domain and does not comprise any transonic region (since only the flow downstream of the normal shock has to be determined). It can be shown that a potential ϕ_1 exists for the perturbation velocity components $u_1(\bar{x}, \bar{y})$ and $v_1(\bar{x}, \bar{y})$, the governing equation for ϕ_1 being:

$$\frac{\partial^2 \phi_1}{\partial \bar{x}^2} + \frac{\partial^2 \phi_1}{\partial \bar{y}^2} = 0.$$

This means that the Laplace equation holds true downstream of the shock. The boundary conditions of the problem are:

- (i) $\frac{\partial \phi_1}{\partial \bar{y}}(\bar{x}, 0) = 0$, $0 < \bar{x} < \infty$ (no displacement effect of the viscous sublayer);
- (ii) $\lim_{\bar{y} \rightarrow \infty} \frac{\partial \phi_1}{\partial \bar{y}} = 0$, $0 < \bar{x} < \infty$;
- (iii) $\frac{\partial \phi_1}{\partial \bar{x}}(0, \bar{y}) = -2 u_{01}(\bar{y})$, $0 < \bar{y} < \infty$ (shock jump relation);
- (iv) $\lim_{\bar{x} \rightarrow \infty} \frac{\partial \phi_1}{\partial \bar{x}}(\bar{x}, \bar{y}) = 0$, $0 < \bar{y} < \infty$.

A solution can be found by inspection: it consists of a source distribution along $\bar{x} = 0$ (i.e., along the shock-wave) which gives the proper value of $\partial \phi_1 / \partial \bar{x}$ and is symmetric in \bar{y} so that $v_1 = 0$ at $\bar{y} = 0$. The solution for the pressure distribution on the wall is given by:

$$p_w(x) = 1 + \gamma \epsilon - \frac{4 \gamma u_t \bar{x}}{\pi} \int_0^\infty \frac{u_{01}(\eta)}{\bar{x}^2 + \eta^2} d\eta,$$

the integral being along the shock-wave.

It can be seen that the solution for the pressure develops a logarithmic singularity as $\bar{x}, \bar{y} \rightarrow 0$. This singularity is removed by introduction of the inner solution.

As we know, in the inner region the stretched variables are:

$$x^* = x/\Delta^* x, \quad y^* = y/\delta_s.$$

The flow velocity leaving the shock must have variations from sonic value of the same order. Hence, one can write the following asymptotic expansions:

$$U = 1 + u_1 u_1^*(x^*, y^*) + \dots$$

$$V = v_1 v_1^*(x^*, y^*) + \dots$$

(and similar expressions for p , ρ , T).

The scales of the inner layer are found to be:

$$\Delta_x^* = u_1^{1/2} \delta_s, \quad v_1 = u_1^{3/2}.$$

It is seen that the inner region problem is similar to the problem treated by Melnik and Grossman for what they called the main-deck (see Section 4.3.1.2 above), but now the vertical scale is the thickness δ_s of the subsonic part of the boundary-layer instead of the thickness δ_0 of the incoming boundary-layer. Such a similarity is a direct consequence of the fact that δ_0 and δ_s are of the same order in Melnik and Grossman's analysis.

The inner problem (along with proper boundary conditions which include $v_1^* = 0$ at the wall and matching conditions with the outer solution) leads to non-linear equations. Hence, a numerical solution would be called for in general (as was done by Melnik and Grossman). However analytical results can be derived for the form of p_w (and τ_w) at the beginning of the interaction.

As we have seen, the outer solution is determined by assuming that the shock is planar and contained in the plane $x=0$. The exact shock shape is found afterwards from the equation:

$$\frac{d\bar{x}_s}{dy} = \frac{[V]}{[U]},$$

where $\bar{x}_s(y)$ is the shock position at any value of y , and $[U]$ and $[V]$ are the velocity discontinuities across the shock.

To sum up the procedure for the flow considered as inviscid, one can say that the inner solution describes perturbations about the undisturbed boundary-layer flow, while the outer solution describes perturbations about a different boundary-layer flow, downstream of the shock-wave.

The treatment of the viscous part of the flow is like Melnik and Grossman's analysis. Two layers are considered in which the Reynolds stress is modeled by using a mixing length hypothesis including Van Driest's damping factor. These two layers are:

(i) a Reynolds stress sublayer (called the blending-layer by Melnik and Grossman, see above), which is a parallel stream (no vertical component to the order considered);

(ii) a wall layer where the only terms retained are the Reynolds and viscous shear stress terms.

An expression for $\tau_w(x)$ is obtained which shows the correct behavior with a minimum value for τ_w in the course of the interaction. Thereafter it is possible to calculate the corresponding values of R and $M_{e,0}$ for which $(\tau_w)_{\min} = 0$, yielding the condition for Incipient Separation.

As pointed out by Adamson and Messiter (1977), the basic difference in structure of the two kinds of boundary-layers explains the necessity of a three-layer structure for an interaction with a turbulent boundary-layer (i.e., an outer rotational inviscid layer plus two viscous layers: the wall and the blending-layers), as opposed to the two layers required for laminar flows. In laminar régime, a boundary-layer has a one layer structure and so one needs consider only a viscous sublayer. On the other hand, a turbulent boundary-layer has a two-layer structure and so two layers must be considered in the interaction region.

Figure 4.16a shows a computed streamwise pressure distribution outside the boundary-layer for a transonic interaction occurring at a curved wall. Agreement with experiment is relatively good. Mach number at incipient separation vs. Reynolds number for flow over a flat plate is shown in Fig. 4.16b. The rise in shock strength along with Reynolds number is in qualitative agreement with experiment, although the computed limit gives a Mach number too low (see Section 2.7.2 of Part I).

4.3.1.4. — Adamson and Feo's Theory for Oblique Shock-Wave

The problem considered by Adamson and Feo is the interaction between a weak oblique shock-wave and an unseparated turbulent boundary-layer. A solution is looked for in the double limit as the Reynolds number tends to infinity and the Mach number tends to unity. With the same notations as in the previous Section, the two small parameters are defined as:

$$\epsilon = U_{0,e} - 1 \quad \text{and} \quad u_r.$$

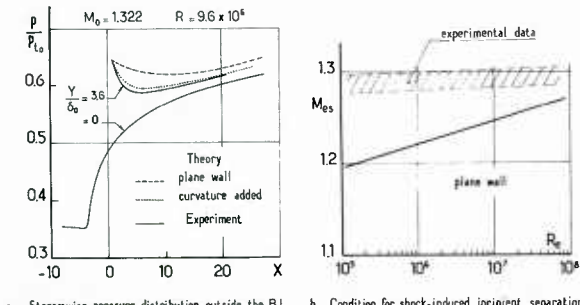


Fig. 4.16 — The Adamson-Messiter-Liou theory — Application to normal shock-wave (Adamson et al., 1980).

b — Condition for shock-induced incipient separation

The limiting process envisaged is $\varepsilon \rightarrow 0$, $u_* \rightarrow 0$ in such a way that $\varepsilon/u_* \rightarrow 0$: this case corresponds to a situation where the sonic line is near the outer edge of the boundary-layer.

Matched asymptotic expansion arguments show that the perturbated flow develops the classical multi-deck structure consisting of:

- (i) an outer transonic non viscous layer, the vertical length scale of which is:

$$\Delta = O(u_*^2 \varepsilon^{-1}) L;$$

(ii) the outermost layer of the boundary-layer which coincides with the velocity defect region. To the order considered, the flow in this region is inviscid. Its vertical length scale is:

$$\Delta y = O(u_*) L \quad \text{or} \quad \Delta y = O(\delta_0) \quad \text{since} \quad u_* = O(\delta_0/L);$$

- (iii) a Reynolds stress layer (or blending-layer) for which:

$$\Delta y = O(u_*^3 \varepsilon^{1/2}) L;$$

- (iv) a wall-layer for which (see Section 4.3.1.2 above):

$$\Delta y = O[u_*^{-1} \exp(-1/u_*)] L.$$

The longitudinal scale Δx is the same for the four layers:

$$\Delta x = O(u_*^2 \varepsilon^{-1/2}) L.$$

Evidently, if $u_* = O(\varepsilon)$, these length scales become identical to the ones introduced in Section 4.3.1.2.

The subsequent analysis of the different zones shows that, to the order considered and for the limiting process envisaged, the static pressure remains transversally constant across the boundary-layer. Furthermore, it is demonstrated that the two inner layers play no role in the interaction mechanism. The progressive pressure rise resulting from the interaction is entirely determined by a coupling between the outer inviscid flow and the velocity defect region of the boundary-layer. This interaction is controlled by the following "coupling relation" (written with dimensionless and stretched variables):

$$v_1 = -\left(\frac{\gamma+1}{\gamma}\right) \frac{dP_1}{dx} \int_0^\infty u_{01} dy. \quad (4.25)$$

In this equation, v_1 is the vertical component of the disturbance velocity at the boundary-layer edge, P_1 is the pressure perturbation and u_{01} represents the velocity defect of the unperturbed incoming velocity profile, i.e.:

$$u_{01} = u_*^{-1} (U - U_{\infty}).$$

It is to be noticed that equation 4.25 is in fact a linearized form of the basic coupling equation discussed in Section 3.2.1.

The solution is thus determined by computing an external inviscid flow which satisfies the following matching (or boundary) conditions, in the limiting process $y_{\text{inner}} \rightarrow \infty$, $y_{\text{outer}} \rightarrow 0$:

- (i) equality of pressure in the two domains;
- (ii) $v_{1 \text{ outer}} = v_{1 \text{ inner}}$ given by equation 4.25.

This method of solution is very similar to the coupling methods presented in Section 3. The wall pressure distribution is in fact calculated by using only the two outer regions and the solution is in reality a *turbulence Free Interaction* solution in the sense of the laminar Free Interaction theory (see Section 4.2.1.1 above).

Adamson and Feo have made numerical applications for situations where the outer flow remains supersonic at all points (in this case the pressure in the outer flow is determined by the Prandtl-Meyer law). The present model yields a solution in which all of the shock induced flow variation occurs upstream of the shock impingement point. Physically speaking this is due to the absence (to the order considered) of displacement effects arising from the inner regions. As shown by equation 4.25, the shape of the velocity distribution (i.e., the velocity defect u_{01}) which contributes to the coupling mechanism with the outer inviscid flow is assumed unaltered by the interaction process. Consequently, the analysis implies that there is not the possibility of a large increase of the boundary-layer thickness through a process in which the velocity distribution is distorted as is the case in a compression. As opposed to the laminar case, the fluid does not turn back towards the wall in the post shock region due to a mechanism in which the pressure continues to rise while the thickness of the boundary-layer decreases as a consequence of the "refilling" of the velocity distribution. The only possible solution is a continuous increase of pressure upstream of the shock impingement point: ahead of the shock, P_1 increases until it reaches a value equal to the final pressure after interaction. Then P_1 rises through the shock and decreases the same amount through the centered expansion fan to insure continuity of pressure.

4.3.2. — Small Perturbations Methods

4.3.2.1. — Inger's Theory for Normal Shock-Wave

The analytical method developed by Inger (see Inger and Mason, 1976; Inger, 1976; Inger, 1980a and 1980b) is in fact a generalization of Lighthill's earlier work (see Section 4.1 above). It consists of a triple-deck model, the equations of which are solved by perturbation techniques. The triple-deck structure is composed of (see in Fig. 4.17):

- (i) an outer inviscid and irrotational flow (the incident shock is assumed weak so that it produces a negligible entropy change);
- (ii) a rotational inviscid boundary-layer flow;
- (iii) a thin shear-disturbance sublayer.

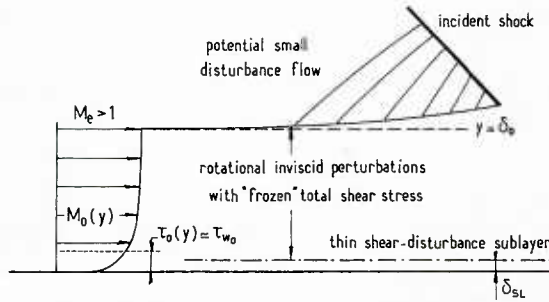


Fig. 4.17 – The Inger flow model for transonic shock-wave/turbulent boundary-layer interaction.

We will now briefly examine the nature of the disturbance flow problem in each of the three basic decks.

Outer potential flow region. — The perturbation velocity components u' , v' and the pressure perturbation p' have to satisfy the following equations:

$$\left[M_{\infty}^2 - 1 + (\gamma + 1) u' \frac{M_{\infty}^2}{U_{\infty}} \right] \frac{\partial u'}{\partial x} = \frac{\partial v'}{\partial y}, \quad (4.26)$$

$$\frac{\partial v'}{\partial x} = \frac{\partial u'}{\partial y}, \quad (4.27)$$

$$\frac{\partial^2 p'}{\partial y^2} + \left[1 - M_{\infty}^2 - 2 \frac{u' M_{\infty}^2}{U_{\infty}} \right] \frac{\partial^2 p'}{\partial x^2} = 0. \quad (4.28)$$

Equation 4.26 results from the continuity equation and assumption of constant entropy; equation 4.27 is the irrotationality condition and equation 4.28 is a combination of the two momentum equations. The third term within the square brackets of equations 4.26 and 4.28 must be retained in the transonic case. Then these equations automatically include the supersonic-subsonic shock jump conditions to this order of approximation. If the term is omitted, equation 4.28 reduces to the familiar Prandtl-Glauert equation.

It is assumed that such a small disturbance solution may be carried out for all x on the upper region $y \geq \delta_0$ where δ_0 is the thickness of the undisturbed boundary-layer. The boundary conditions of the problem are the following:

(i) usual far-field conditions as $y \rightarrow \infty$;

(ii) other conditions are prescribed along the streamline which coincides with the boundary-layer edge. To the same order of approximation, this border is taken to be the edge of the undisturbed boundary-layer of which the thickness δ_0 is considered as constant in the interaction domain. Thus along $y = \delta_0$, both v' and p' are required to be equal to their middle-deck counterparts at $y = \delta_0$.

Middle rotational-disturbance flow deck. — In this part of the flow, the shear stress (turbulent as well as laminar) is considered as “frozen” along each streamline; i.e., disturbances of the viscous forces (not the viscous forces themselves) are ignored. Furthermore, the streamwise changes which would occur if the boundary-layer were not disturbed are neglected. This means that the properties of the undisturbed boundary-layer are assumed functions of y only.

Thus, the disturbance field caused by a weak shock-wave is one of a small perturbation of the incoming non-uniform boundary-layer profile. Such a disturbance field is governed by the equations:

$$\frac{\partial}{\partial y} \left[\frac{v'(x, y)}{U_0(y)} \right] = \frac{1 - M_0^2(y)}{\gamma M_0^2(y)} \frac{\partial(p'/p_0)}{\partial x}, \quad (4.29)$$

$$\frac{\partial u'}{\partial x} = - \frac{\partial p'/\partial x}{p_0 U_0} - \frac{d U_0}{dy} \frac{v'}{U_0}, \quad (4.30)$$

$$\frac{\partial^2 p'}{\partial y^2} - \frac{2}{M_0} \frac{d M_0}{dy} \frac{\partial p'}{\partial y} + \left(1 - M_0^2 - \frac{2 u' M_0^2}{U_0} \right) \frac{\partial^2 p'}{\partial x^2} = 0, \quad (4.31)$$

where $U_0(y)$ and $M_0(y)$ are the velocity and Mach number profiles of the incoming boundary-layer.

The first equation is a result of the particle-isentropic continuity and energy equations; equation 4.30 is the perturbed x -momentum equation; and equation 4.31 is a generalization of Lighthill's well known pressure perturbation equation for non-uniform flow (see Section 4.1 above). The difference lies in the non-linear correction term that accounts for possible transonic effects within the boundary-layer. These effects include the diffracted impinging shock above the sonic level of the incoming boundary-layer profile. Use of equation 4.31 provides an account of any transverse pressure gradient that develops across the interacting boundary-layer.

Equations 4.29 to 4.31 are supplemented by boundary conditions requiring that:

(i) disturbances vanish far upstream (i.e., $x \rightarrow \infty$);

(ii) p' and v' match the outer-flow conditions along $y = \delta_0$;

(iii) v' is equal to zero at a normal distance $y_{w,eff}$ which is determined by the matching with the inner deck solution. It is seen that $y_{w,eff}$ is an effective wall position for the middle deck on which the Mach number is different from zero, since $y_{w,eff} > 0$. As previously established by Lighthill (see Section 4.1 above), this displaced lower boundary removes the singularity which would exist if the $v' = 0$ condition were applied at $y = 0$. The way to determine $y_{w,eff}$ is explained in what follows.

The normal disturbance velocity at δ_0 is given by y -integration of equation 4.29, yielding:

$$\frac{v'(x, \delta_0)}{U_0(y)} = \underbrace{\frac{v'(x, y_{w,eff})}{U_0(y)}}_{=0} + \frac{\partial}{\partial x} \left[\int_{y_{w,eff}}^y \frac{p' - M_0^2(\eta)}{\gamma p_0 M_0^2(\eta)} d\eta \right]$$

The lower limit of the integral represents the inner-deck contribution to the total streamline displacement effect.

The displacement thickness growth $\Delta\delta^*$ along the interaction can be computed from the boundary-layer integral continuity equation. This yields the following formula:

$$\Delta\delta^*(x) = \int_{-\infty}^x \frac{v'(x, \delta_0)}{U_0(\delta_0)} dx + (\delta_0 - \delta_0^*) \left[\frac{M_0^2 - 1}{\gamma p_0 M_0^2} \right] \frac{\partial p'}{\partial x}(x, 0). \quad (4.32)$$

In the above expression, the streamwise pressure gradient is evaluated at the wall, the pressure being here assumed independent of y , which is consistent with the "classical" displacement concept.

The inner shear-disturbance layer. — In the original work of Lighthill, the interaction problem was treated by considering that the inner-layer is entirely contained within the laminar sublayer of the turbulent velocity profile. This simplifying assumption may be incorrect at high Reynolds number where the laminar sublayer tends to be extremely thin. Inger's theory avoids this limitation by taking into account the entire law of the wall which expresses that the total shear stress (i.e., laminar plus turbulent) is constant in the wall region.

The perturbation equations are established within the following (main) hypotheses:

- (i) the influence of density perturbation on the sublayer disturbance flow is neglected (for adiabatic flows, with low to moderate external Mach numbers, the undisturbed and perturbation flow Mach numbers are both quite small within the shear disturbance sublayer).
- (ii) the density is assumed constant, compressibility effects being adequately represented by the Eckert reference temperature method. According to this method, incompressible relations are used with quantities based on wall recovery temperature.
- (iii) due to the extreme thinness of the inner-layer, the normal pressure gradient is neglected.

Under the above assumptions, the disturbance field is governed by the following equations:

— continuity:

$$\frac{\partial u'}{\partial x} + \frac{\partial v'}{\partial y} = 0; \quad (4.33)$$

— momentum:

$$U_0 \frac{\partial u'}{\partial x} + v' \frac{d U_0}{d y} = - \frac{1}{\rho_{0,w}} \frac{d p'_w}{d x} + \frac{\partial}{\partial y} (v_{0,w} + 2\varepsilon_{T_0}) \frac{\partial u'}{\partial y} \quad (4.34)$$

The doubling of the turbulent shear stress disturbance term results from inclusion of the eddy viscosity perturbation.

The eddy viscosity is expressed by the well known relation:

$$\varepsilon_{T_0} = \left\{ 0.41 y \left[1 - \exp \left(- \frac{y}{26 v_{0,w}} \sqrt{\frac{\tau_{0,w}}{\rho_{0,w}}} \right) \right] \right\}^2 \frac{d U_0}{d y}, \quad (4.35)$$

which includes the Van Driest damping factor.

Equations 4.33 and 4.34, along with 4.35 are to be solved subject to the following boundary conditions:

- (i) all disturbances vanish at upstream infinity; i.e. $u'(x, y) = 0$ when $x \rightarrow -\infty$;
- (ii) no-slip condition at the wall; i.e. $u' = v' = 0$ at $y = 0$;
- (iii) at a certain distance δ_{SL} , sufficiently far from the wall, $u'(x, y)$ must tend to the inviscid solution $u'_{inv}(x, y)$ along the bottom of the middle-deck. This latter perturbation $u'_{inv}(x, y)$ is governed by the continuity equation 4.33 plus:

$$U_0 \frac{\partial u'_{inv}}{\partial x} + v'_{inv} \frac{d U_0}{d y} = - \frac{1}{\rho_{0,w}} \frac{d p'_w}{d x}. \quad (4.36)$$

The distance δ_{SL} is defined as the height where the total shear disturbance ($\propto \partial u'/\partial y$) of the inner solution vanishes to a desired accuracy.

For the inner sublayer, the pressure distribution $p_w(x)$ is prescribed. In fact $p_w(x)$ results from the matching with the other decks.

Following Lighthill's idea it proves convenient to derive from 4.33 and 4.34 an equation involving only the normal disturbance velocity field $v'(x, y)$:

$$\frac{\partial}{\partial x} \left(U_0 \frac{\partial^2 v'}{\partial y^2} - v' \frac{d^2 U_0}{\partial y^2} \right) = \frac{\partial^2}{\partial y^2} \left[(v_{0,w} + 2\varepsilon_{T_0}) \frac{\partial^2 v'}{\partial y^2} \right]. \quad (4.37)$$

This equation is to be solved subject to the boundary conditions:

- (i) vanishing of perturbation at downstream infinity;

(ii) at the wall:

$$v'(x, 0) = \frac{\partial v'(x, 0)}{\partial y} = 0;$$

(iii) a third boundary condition is obtained by writing the momentum equation at the wall which leads to:

$$\frac{\partial^3 v'}{\partial y^3} = -\frac{1}{\rho_{0w} v_{0w}} \frac{d^2 p_w}{dx^2};$$

(iv) the fourth boundary condition is the equivalent for v' of condition:

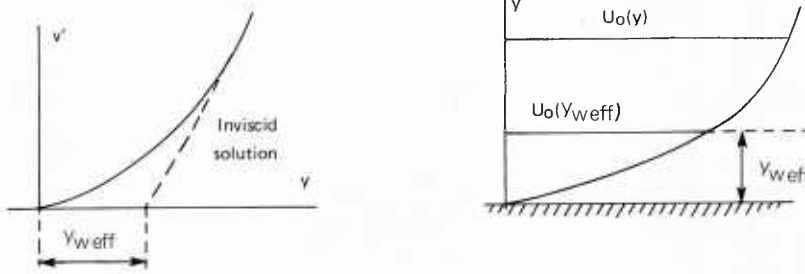
$$\frac{\partial}{\partial x} \left(U_0 \frac{\partial^2 v'_{inv}}{\partial y^2} - v'_{inv} \frac{d^2 U_0}{dy^2} \right) = 0,$$

along with the vanishing of the total disturbance shear, i.e.:

$$\frac{\partial^2 v'}{\partial y^2} = 0.$$

From the solution for $v'(x, y)$ in the inner-deck, it is possible to deduce a boundary condition for the middle-deck in terms of an effective wall position $y_{w,eff} \neq 0$. The distance $y_{w,eff}$ is obtained by "back projection" or more exactly "back extrapolation" of the external inviscid behavior of $v'(x, y)$. This extrapolation is carried out down to the ordinate y where $v'_{inv}(x, y)$ (extrapolated) vanishes. Physically speaking, $y_{w,eff}$ represents the total mass defect height due to the shear stress perturbation field and hence the effective wall position "seen" by the overlying inviscid middle-deck disturbance flow. This process provides the following non-singular boundary condition for the middle deck solution:

$$\frac{\partial p'}{\partial y}(y_{w,eff}) = v'_{inv}(y_{w,eff}) = 0 \quad \text{at} \quad U_0(y_{w,eff} > 0).$$



Once the $v'(x, y)$ field is known, the accompanying streamwise velocity (and hence the disturbance shear stress) may then be found from equation 4.34.

The three sets of equations 4.26-28, 4.29-31, 4.33-37 describing the various decks along with:

- prescribed behavior at infinity,
- wall boundary conditions,
- matching conditions,

constitute a "closed" problem which can be solved by any appropriate method. Following Lighthill's original work, Inger employs a technique of solution involving an x -wise Fourier transform. This procedure leads to rather complicated mathematical expressions which will not be given here.

The original Inger method has been improved upon several times over in order to take into account surface curvature effect (Inger and Sobieczky, 1978), background pressure gradient effect (Panaras and Inger, 1977), suction or blowing effect (Inger and Lee, 1978; Inger, 1979) and also to represent more faithfully shock penetration into the boundary-layer in low transonic flow régime (Inger, 1979). This method has also been incorporated into viscous/inviscid interactive calculations of the flow past transonic airfoils (Stanewsky *et al.*, 1981). Knowing the boundary-layer properties just upstream of the shock (deduced from a "classical" boundary-layer calculation performed from the leading edge), the method permits the calculation of boundary-layer change during the course of the interaction. It is thus possible to deduce from this calculation:

(i) the local evolution of the displacement thickness (see equation 4.32 above). This evolution defines a "viscous ramp" which models the boundary-layer displacement effect as seen by the external non viscous stream;

(ii) the downstream properties of the boundary-layer which are fed as initial conditions into the new "classical" calculation performed downstream of the shock interaction region.

We will now present some applications of Inger's theory which clearly show the specific influence of the essential parameters playing a role in transonic shock-wave/turbulent boundary-layer interactions.

Assessment of the theory is first established by the comparisons with experimental results (Ackeret *et al.*, 1946) shown in Figures 4.18 and 4.19. The wall pressure distributions plotted in Figure 4.18 exhibit the differences occurring between the wall and the boundary-layer edge. In particular, the post-shock expansion (see Section 2.6.1 of Part I) is well predicted by the theory, in spite of some discrepancies with measurements in this part of the field. Also, the rise in the boundary-layer displacement thickness is correctly predicted, as shown in Figure 4.19.

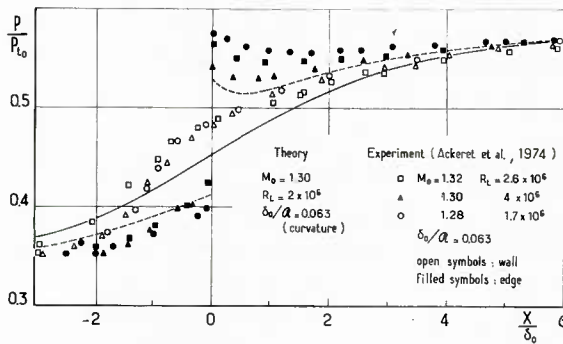


Fig. 4.18 – Application of Inger's flow model – Streamwise pressure distributions (Inger and Sobieczky, 1978).

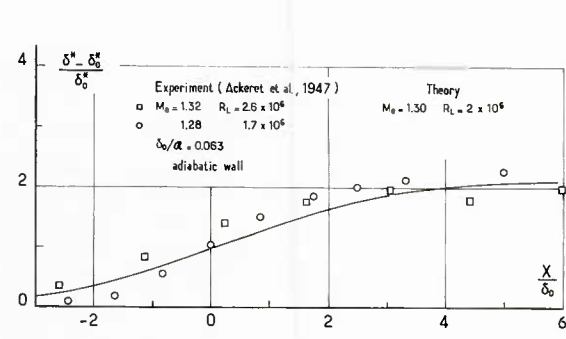


Fig. 4.19 – Application of Inger's flow model. Rise in the boundary-layer displacement thickness (Inger and Sobieczky, 1978).

Figure 4.20 shows a parametric study of shock strength effect for fixed initial shape parameter ($H_{i0} = 1.40$) and Reynolds number ($R_{\delta_0} = 3.5 \times 10^4$). It is clear that an increase in the upstream Mach number provokes a more severe destabilization of the boundary-layer with a higher increase in the displacement thickness and in the shape parameter and a larger dip in the skin-friction distribution which becomes negative for $M_0 = 1.3$. The following figure (Fig. 4.21), shows a parametric study of initial shape parameter effect for fixed upstream Mach number ($M_0 = 1.2$) and Reynolds number ($R_{\delta_0} = 4 \times 10^3$). The present theoretical results are in full agreement with the experimental trends discussed Part I: namely, an increase in H_{i0} (which means a less "filled" incoming profile) entails a greater jump in the boundary-layer thickness and a more important spreading of the pressure rise at the wall. The streamwise evolution of the skin-friction is very characteristic of behavior already discussed in Section 2.7 of Part I devoted to Shock-Induced Incipient Separation in transonic flows. At first when H_{i0} increases, the boundary-layer tends to separate more readily, its profile becoming less "energetic". However, one observes a trend reversal due to the wider spreading of the compression when H_{i0} is high. There results a weakening of the adverse pressure gradient and this effect is such that the boundary-layer is less likely to separate in spite of a less filled velocity distribution.

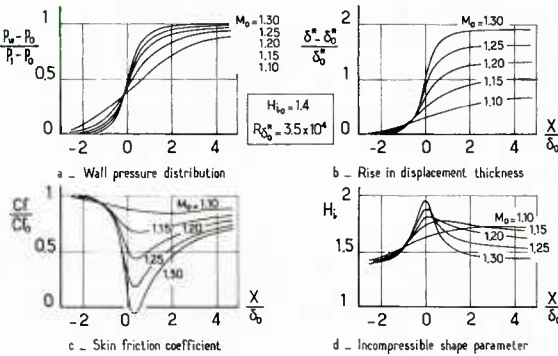


Fig. 4.20 – Application of Inger's flow model – Parametric study of shock strength effect for fixed shape parameter (Inger, 1980).

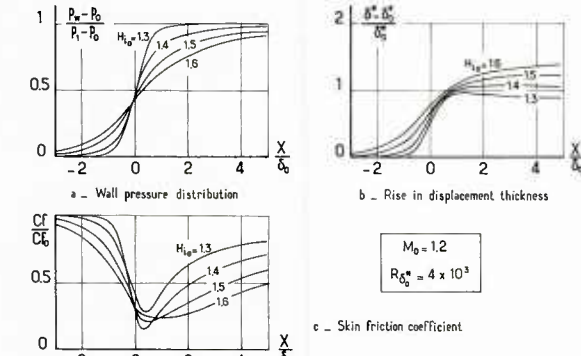


Fig. 4.21 – Application of Inger's flow model – Parametric study of initial shape parameter effect for fixed initial Mach number (Inger, 1980).

The last examples presented here show parametric studies of wall temperature and Reynolds number (see Fig. 4.22). As we already know (see Section 3.75 of Part I), cooling the wall increases the "stiffness" of the boundary-layer which then offers a greater resistance to separation. Of course, heating the wall has the contrary effect. This behavior is clearly demonstrated by the skin-friction distributions represented in Figure 4.22 b. On the other hand, the wall pressure distribution is only slightly affected by thermal conditions at the wall. Moreover, the resistance to separation increases with the Reynolds number as shown in Figure 4.22 c.

Inger's theory has also been employed to determine a limit for Incipient Shock Induced Separation. This limit is computed as a function of the main influence parameters: upstream Mach number M_0 , shape parameter H_{i0} , Reynolds number R_{δ_0} and also wall curvature (Inger, 1981). The validity of the limit thus calculated is discussed in Section 2.7.2 of Part I. Influence of wall temperature on transonic Shock Induced Separation is also discussed in Section 2.7.2 of Part I by resorting to Inger's theory results.

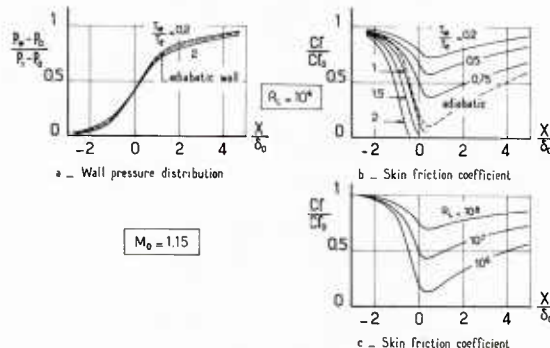


Fig. 4.22 – Application of Inger's flow model – Parametric study of wall temperature and Reynolds number (Inger 1978 b).

4.3.2.2. — Bohning and Zierep's Theory for Normal Shock-Wave (1976 a and b)

The flow model adopted in the present theory is again the triple deck model and the subsequent analysis has much in common with Inger's theory as well as with the basic work of Lighthill.

Schematically, Bohning and Zierep's theory proceeds as follows:

- (i) the *outer-deck* consists of a transonic inviscid flow with a shock-wave becoming normal far from the wall. This flow is computed by a classical method. For curved wall, Oswatitsch and Zierep's method (1960) is employed;
- (ii) in the *main-deck* the viscous forces are neglected. This zone, which comprises most of the boundary-layer, is described by the well known Lighthill perturbation equations for a parallel and rotational inviscid stream. Here, these equations are written in terms of the pressure perturbation p' and the vertical velocity component v' , which gives:

$$\begin{aligned} [1 - M_0^2(y)] \frac{\partial p'}{\partial x} - \rho_0(y) U_0(y) \frac{\partial v'}{\partial y} + \rho_0(y) \frac{d U_0(y)}{dy} v' &= 0, \\ \rho_0(y) U_0(y) \frac{\partial v'}{\partial x} + \frac{\partial p'}{\partial y} &= 0. \end{aligned}$$

The above equations are solved with the following boundary conditions:

- vanishing of vertical disturbance velocity at upstream and downstream infinity;
- prescribed pressure distribution $p'(x)$ along the outer boundary $y = \delta_0$ of the main-deck. This pressure distribution is imparted by the external flow;
- zero vertical velocity on an inner boundary $y = \delta > 0$ which constitutes the outer edge of the viscous sublayer.

Closed form solutions of the above problem are obtained for velocity distributions in the undisturbed boundary-layer that can be approximated by power law functions (these solutions make use of confluent hypergeometric series);

(iii) the *inner viscous layer* is treated by using a simplified boundary-layer formulation in which the flow is considered as a parallel stream. The inner-layer analysis serves mainly to fix the thickness $\hat{\delta}$ which is determined once and for all from the properties of the undisturbed incoming flow. The determination of $\hat{\delta}$ is based on the fact that, in the adopted viscous sublayer analysis, the gradient of wall shear stress $\partial \tau_w / \partial x$ at a fixed position x_0 presents a minimum when $\hat{\delta}$ is being varied. Therefore, the condition $\frac{\partial}{\partial \hat{\delta}} \left[\frac{\partial \tau_w}{\partial x} \right]_{x_0} = 0$ is regarded as a defining equation for $\hat{\delta}$. The scaled inner thickness $\hat{\delta}/\delta_0$ thus determined is a function of the Reynolds number R_δ and of the exponent n of the undisturbed velocity profile representation. This dependence can be represented by the relation:

$$\hat{\delta}/\delta_0 = 1.14 (R_\delta)^{-1/(2+n)} \quad \text{for } 5 \cdot 10^3 \leq R_\delta \leq 5 \cdot 10^5.$$

The overall solution procedure is as follows, $\hat{\delta}/\delta_0$ being known from undisturbed conditions: in the first step, a pressure jump (0th order pressure distribution) is imposed at the outer edge of the boundary-layer. Then the problem for the main-deck is solved. This yields the vertical velocity component v' at the outer edge of the boundary-layer. In the second step, this v' distribution is imposed as a boundary condition for an inviscid external flow calculation which furnishes a new pressure distribution along the main-deck outer edge. This whole procedure can be repeated iteratively until convergence is achieved.

The present flow model has also been used to find the limit for Incipient Shock Induced Separation as a function of: the external Mach number, the Reynolds number and wall curvature (Bohning and Zierep, 1978 and 1981). These predictions are discussed in Section 2.7.2 of Part I

Examples of flow structures computed by Bohning and Zierep are presented in Figure 4.23a which shows tracings of lines of constant density for two cases having the same upstream Mach number but differing by the curvature of the wall. The pattern corresponding to infinite radius of curvature (flat wall) is in good qualitative agreement with interferograms of transonic interactions presented in Section 2.6.1 of Part I. Figure 4.23b shows streamwise pressure distributions at different distances from the wall. The post shock expansion phenomenon is very clearly demonstrated, this effect being enhanced by convex curvature.

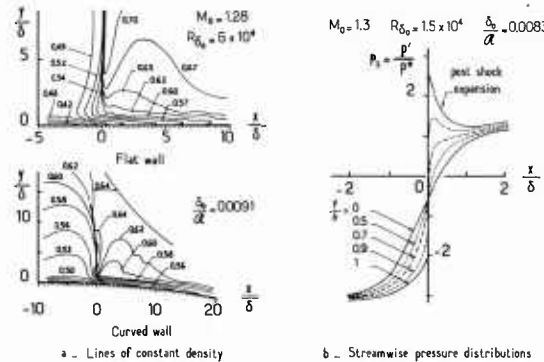


Fig. 4.23 — Application of Bohning and Zierep flow model
(Bohning and Zierep, 1976 a).

4.4. — References

Ackeret, J.; Feldman, F. and Rott, N. (1947). Untersuchungen an Verdichtungsstößen und Grenzschichten in schnell bewegten Gasen. Bericht n° 10 a.d., Inst. für Aerodynamik, ETH, Zürich (1946); see also English translation "Investigation of Compression Shocks and Boundary-Layers in Gases Moving at High Speed". NACA TM-1113.

Adamson, T. C. Jr. and Feo, A. (1975): Interaction Between a Shock-Wave and a Turbulent Boundary-Layer in Transonic Flow. SIAM J. Appl. Math., Vol. 29, pp. 121-145.

Adamson, T. C. Jr. and Messiter, A. F. (1977): Normal Shock-Wave Turbulent Boundary-Layer Interactions in Transonic Flow Near Separation. *Transonic Flow Problems in Turbomachinery*, Hemisphere Publ. Co, pp. 392-413.

Adamson, T. C. Jr.; Liou, M. S. and Messiter, A. F. (1980a): Interaction Between a Normal Shock-Wave and a Turbulent Boundary-Layer at High Transonic Speeds. NASA-CR-3194.

Adamson, T. C. Jr. and Messiter, A. F. (1980b): Simple Approximations for the Asymptotic Description of the Interaction Between a Normal Shock-Wave and a Turbulent Boundary-Layer at Transonic Speeds. AGARD-CP-291.

Adamson, T. C. Jr. and Messiter, A. F. (1980c): Analysis of Two-Dimensional Interactions Between Shock-Waves and Boundary-Layer. in Annual Review of Fluid Mechanics, Vol. 12, pp. 103-138.

Bodonyi, R. J. and Kluwick, A. (1977): Freely Interacting Transonic Boundary-Layer. The Physics of Fluids, Vol. 20, No. 9, pp. 1432-1437.

Bohning, R. and Zierep, J. (1976a): The Normal Shock at a Curved Wall in the Viscous Case. *Symposium Transsonicum II*, pp. 237-243, Springer-Verlag.

Bohning, R. and Zierep, J. (1976b) Der senkrechte Verdichtungsstoss an der gekrümmten Wand unter Berücksichtigung der Reibung. ZAMP, Vol. 27, pp. 225-240.

Bohning, R. and Zierep J. (1978): Bedingung für das Einsetzen der Ablösung der turbulenten Grenzschicht an der gekrümmten Wand mit senkrechtem Verdichtungsstoss. ZAMP, Vol. 29, pp. 190-198.

Bohning, R. and Zierep, J. (1981): Normal Shock/Turbulent Boundary-Layer Interaction at a Curved Wall. AGARD-CP-291.

Brilliant, H. M. (1971): A Theoretical Investigation of the Interaction Between Shock-Waves and Unseparated Boundary-Layers in Transonic Flow. Ph. D. Thesis, Univ. of Michigan, Ann Arbor, Mich.

Brilliant, H. M. and Adamson Jr., T. C. (1974): Shock-Wave/Boundary-Layer Interactions in Laminar Transonic Flow. AIAA Journal, Vol. 12, No. 3, pp. 323-329 (March 1974).

Brown, S. N. and Williams, P. G. (1975): Self-Induced Separation. J. Inst. Maths. Appl., Vol. 16, pp. 175-191.

Burggraf, O. R. (1973): Inviscid Reattachment of a Separated Shear Layer. Proc. 3rd. Int. Conf. on Numerical Methods in Fluid Mech., *Lecture Notes in Physics*, Vol. 18, pp. 39-47, Springer-Verlag.

Burggraf, O. R. (1975): Asymptotic Theory of Separation and Reattachment of a Laminar Boundary-Layer on a Compression Ramp. AGARD-CP-168.

Burggraf, O. R.; Rizzetta, D; Werle, M. J. and Vatsa, V. N. (1979): Effects of Reynolds Number on Laminar Separation of a Supersonic Stream. AIAA Journal, Vol. 17, No. 4, pp. 336-343 (April 1979).

Carter, J. E. (1975): Inverse Solutions for Laminar Boundary-Layer Flows with Separation and Reattachment. NASA TR-R 447.

Chapman, D. R.; Kuehn, D. M. and Larson, H. K. (1958): Investigation on Separated Flows in Supersonic and Subsonic Streams with Emphasis on the Effect of Transition. NACA TR 1356.

Clenshaw, C. W. (1966): Numerical Solutions of Non-Linear Differential Equations. D. Greenspan ed., New York, Wiley.

Curle, N. (1961): The Effect of Heat Transfer on Laminar Boundary-Layer Separation in Supersonic Flow. Aero. Quarterly, Vol. 12 (Nov. 1961).

Gadd, G. E. (1961): Interaction Between Normal Shock-Waves and Turbulent Boundary-Layers. ARC, R. & M. No. 3262.

Hakkinen, R. J.; Greber, I.; Trilling, L. and Abarbanel, S. S. (1959): The Interaction of an Oblique Shock-Wave with a Laminar Boundary-Layer. NASA Memo 2-18-59 W.

Hussaini, M. Y.; Baldwin, B. S. and McCormack, R. W. (1980): Asymptotic Features of Shock-Wave/Boundary-Layer Interaction. AIAA Journal, Vol. 18, No. 8, pp. 1014-1016 (Aug. 1980).

Inger, G. R. and Masson, W. H. (1975): Analytical Theory of Transonic Normal Shock/Turbulent Boundary-Layer Interaction. AIAA Paper 75-831; see also AIAA Journal, Vol. 14, No. 9, pp. 1266-1272 (Sept. 1976).

Inger, G. R. (1976): Analysis of Transonic Shock Interaction with Non-Adiabatic Turbulent Boundary-Layers. AIAA Paper 76-463.

Inger, G. R. (1977): Shock Penetration and Lateral Pressure Gradient Effects on Transonic Viscous Interactions. AIAA Journal, Vol. 15, No. 8, pp. 1198-1200 (Aug. 1977).

Inger, G. R. and Sobieczky, H. (1978): Shock Obliquity Effect on Transonic Shock Boundary-Layer Interaction. ZAMM 58, pp. 333-335.

Inger, G. R. and Zee, S. (1978): Transonic Shock-Wave/Turbulent Boundary-Layer Interaction with Suction or Blowing. Journal of Aircraft, Vol. 15, No. 11, pp. 750-754 (Nov. 1978).

Inger, G. R. (1979): Transonic Shock/Turbulent Boundary-Layer Interaction with Suction and Blowing. AIAA Paper 79-0005.

Inger, G. R. (1980): Upstream Influence and Skin Friction in Non-Separating Shock/Turbulent Boundary-Layer Interactions. AIAA Paper 80-1411; *see also: VPI-Aero-090* (Aug. 1980).

Inger, G. R. (1980): Some Features of a Shock/Turbulent Boundary-Layer Interaction Theory in Transonic Flow Fields. AGARD-CP-291.

Inger, G. R. (1981): Transonic Shock/Turbulent Boundary-Layer Interaction and Incipient Separation on Curved Surfaces. AIAA Paper 81-1244.

Lewis, J. E.; Kubota, T. and Lees, L. (1967): Experimental Investigation of Laminar Two-Dimensional Boundary-Layer Separation in a Compression Corner With and Without Cooling. AIAA Paper 67-191; *see also AIAA Journal*, Vol. 6, No. 1, pp. 7-14 (Jan. 1968).

Lighthill, M. J. (1950): Reflection at a Laminar Boundary-Layer of a Weak Steady Disturbance to a Supersonic Stream Neglecting Viscosity and Heat Conduction. Quart. J. Mech. and Appl. Math. 3, S. 303.

Lighthill, M. J. (1953): On Boundary-Layers Upstream Influence. II Supersonic Flows Without Separation. Proc. Roy. Soc., A 217, pp. 478-507.

Mellor, G. L. (1972): The Large Reynolds Number, Asymptotic Theory of Turbulent Boundary-Layers. Int. J. Eng. Sc., Vol. 10.

Melnik, R. E. and Grossman, B. (1974): Analysis of the Interaction of a Weak Normal Shock-Wave with a Turbulent Boundary-Layer. AIAA Paper 74-598.

Melnik, R. E. and Grossman, B. (1975): Further Developments in an Analysis of the Interaction of a Weak Normal Shock Wave with a Turbulent Boundary-Layer. *Symposium Transsonicum II*, Springer-Verlag, New York, pp. 262-272.

Melnik, R. E. and Grossman, B. (1977): Interactions of Normal Shock-Waves with Turbulent Boundary-Layers at Transonic Speeds. *Transonic Flow Problems in Turbo-Machinery*, Hemisphere Publ. Co, pp. 415-433.

Melnik, R. E. (1980): Turbulent Interactions on Airfoils at Transonic Speeds-Recent Developments. AGARD-CP-291.

Messiter, A. F.; Feo, A. and Melnik, R. E. (1971): Shock-Wave Strength for Separation of a Laminar Boundary-Layer at Transonic Speeds. AIAA Journal, Vol. 9, No. 6, pp. 1197-1198 (June 1971).

Messiter, A. F. and Adamson, T. C. Jr (1978): A Study of the Interaction of a Normal Shock-Wave with a Turbulent Boundary-Layer at Transonic Speeds. *Advanced Technology Airfoil Research*, NASA-CP-2045, Vol. 1.

Murman, E. M. and Cole, J. D. (1971): Calculation of Plane Steady Transonic Flows. AIAA Journal, Vol. 9, No. 1, pp. 114-121 (Jan. 1971).

Napolitano, M.; Werle, M. J. and Davis, R. T. (1979): Numerical Technique for the Triple-Deck Problem. AIAA Journal, Vol. 17, No. 7, pp. 699-705 (July 1979).

Napolitano, M. and Vacca, G. (1980): Toward a Spline Technique for the High Reynolds Number Interaction (Triple-Deck) Problem. AGARD-CP-291.

Neiland, V. Ya. (1970): Upstream Propagation of Disturbances in Hypersonic Boundary-Layer Interactions (In Russian). Izv. Akad. Nauk SSSR, Mekh. Zhidk Gaza, No. 4, pp. 44-49.

Neiland, V. Ya. (1971): Flow Beyond the Separation Point of the Boundary-Layer in a Supersonic Stream. Izv. Akad. Nauk SSSR, Mekh. Zhidk. Gaza, No. 3, pp. 19-24.

Oswatitsch, K. and Zierep, J. (1960): Das Problem des senkrechten Stosses an einer gekrümmten Wand. ZAMM, Vol. 40, pp. 143-144.

Panaras, A. G. and Inger, G. R. (1977): Transonic Normal Shock/Boundary-Layer Interaction in Pressure Gradient Flows. ASME Paper 77-GT-34.

Ragab, S. A. and Nayfeh, A. H. (1978): A Second Order Asymptotic Solution for the Laminar Separation of Supersonic Flows past Compression Ramps. AIAA Paper 78-1132.

Ragab, S. A. and Nayfeh, A. H. (1980): Second Order Asymptotic Solution for Laminar Separation. The Physics of Fluids, Vol. 23, No. 6, pp. 1091-1100.

Rizzetta, D. P.; Burggraf, O. R. and Jenson, R. (1978): Triple-Deck Solutions for Viscous Supersonic and Hypersonic Flow Past Corner. J. Fluid Mech, Vol. 89, Part 3, pp. 535-552.

Smith, F. T. and Stewartson, K. (1973): Plate-Injection Into a Separated Supersonic Laminar Boundary-Layer. J. Fluid Mech, Vol. 58, Part 1, pp. 143-159.

Stanewsky, E.; Nandanan, M. and Inger, G. R. (1981): The Coupling of Shock/Boundary-Layer Interaction Module with a Viscous-Inviscid Computation Method. AGARD-CP-291.

Stewartson, K. and Williams, P. G. (1969): Self-Induced Separation. Proc. Roy. Soc., A 312, pp. 181-206.

Stewartson, K. and Williams, P. G. (1973): Self-Induced Separation. Mathematika 20, pp. 98-108.

Stewartson, K. (1974): Multistructured Boundary-Layers on Flat Plate and Related Bodies. *Advances in Applied Mechanics*, Vol. 14, pp. 145-239. Academic Press.

Sychev, V. Ya. (1972): Concerning Laminar Separation. Izvestiya Akademii Nauk Armyanskoi SSR, Mekh., Zhidk. Gaza, 3, pp. 47-59.

Tu, K. M. and Weinbaum, S. (1976): A Non-Asymptotic Triple-Deck Model for Supersonic Boundary-Layer Interaction. AIAA Journal, Vol. 14, No. 6, pp. 767-775 (June 1976).

Werle, M. J. and Vatsa, V. N. (1974): A New Method for Supersonic Boundary-Layer Separation. *AIAA Journal*, Vol. 12, No. 11, pp. 1491-1497 (Nov. 1974).

Williams, P. G. (1975): A Reverse Flow Computation in the Theory of Self-Induced Separation. *Lecture Notes in Physics*, Vol. 35. Springer-Verlag, New York.

5. — REYNOLDS-AVERAGED NAVIER-STOKES CALCULATION METHODS

5.1. — Introductory Remarks

A potentially powerful approach to predicting turbulent shock wave boundary-layer interactions, including those involving separation is to solve the Reynolds-averaged Navier-Stokes equations. For practical reasons, such an approach is favored over direct simulation of the time-dependent, unaveraged Navier-Stokes equations because the three-dimensional, widely varying scales of turbulence present impossible requirements for even the largest and fastest computers (Chapman, 1981). Consideration of this former approach became possible in the early 1970's when large, fast computers became available. While the technology required to provide adequate engineering solutions is still evolving, techniques have advanced rapidly and matured sufficiently to warrant their consideration in specific practical 2-dimensional applications now and certainly for the more general 3-dimensional applications during this decade. An obvious advantage of such an approach is that the entire viscous and inviscid portions of the flow are captured simultaneously, and the potential exists for focusing directly on turbulence modeling, which is an important pacing item for the successful development of this method and other finite difference methods already discussed. A disadvantage is the long computing time and large storage limitations of current computers, which has hampered attempts to focus directly on turbulence modeling without considering numerical resolution and accuracy. As it now stands, the competing elements of turbulence modeling, numerical resolution, and accuracy must all be considered in any evaluation of our ability to compute flows with strong interactions induced by shock waves (Marvin, 1982). This is particularly true for three-dimensional flows, which are the interesting ones from the viewpoint of practical applications.

Methods for solving the governing equations and various turbulence modeling approaches are reviewed in this section first. Subsequently the physical characteristics of the shock interactions being studied with these methods as derived from experiment are described briefly. More complete descriptions can be found in Part I. Examples of computations are then compared with experiment and in some instances with other methods also discussed previously to provide an assessment of progress.

5.2. — Governing Equations

5.2.1. — The Reynolds-Averaged Navier-Stokes Equations

The time-dependent Navier-Stokes equations, supplemented by mass conservation and suitable gas-law relationships, describe the turbulent motion of a continuum fluid. Solutions to the equations for turbulent flows of practical interest are virtually impossible using today's computers because turbulence is three-dimensional and has an enormous range of length and time scales. The difficulty can be circumvented by rewriting the equations for another set of variables, obtained by suitable averaging. For compressible flows, this has been accomplished by introducing mass-weighted variables, decomposing them into their mean and fluctuating components, and averaging over a time that is long relative to the largest turbulent time-scale (see Rubesin, 1973). The resulting set of equations is commonly referred to as the Reynolds-averaged form of the Navier-Stokes equations.

5.2.2. — The Turbulence Modeling Problem

In the process of deriving the averaged form of the equations physical information on the turbulent motion itself is lost. Furthermore, the formalism results in a new set of equations that has more unknowns, and an equation-closure problem arises. Usually, this is referred to as the turbulence-modeling problem. Introducing supplemental equations for the mean turbulence motion itself obtained by deriving moments of the original equations, does not alleviate the problem, but does help to provide a means to introduce more information on the turbulence. Necessarily then, turbulence modeling becomes an integral, important part of the overall numerical modeling process. A general description of various turbulence modeling concepts used for applications in aerodynamic flows, taken from Marvin (1982) is shown in Table I. Two broad classes are eddy viscosity models and Reynolds stress transport equation models. Features that distinguish models of either class or models within the same class arise through the particular closure technique, i.e., expressing modeled quantities in terms of the mean velocity field or in terms of the mean turbulent field. To date, solutions to the shock interaction problem using the Reynolds-averaged Navier-Stokes equations have invoked the effective viscosity idea of Boussinesq (1877).

EDDY VISCOSITY MODELS $\mu_t \sim (\text{VELOCITY}) (\text{LENGTH})$		STRESS TRANSPORT EQUATION MODELS		
		$\tau_{ij}/k = a_{ij}$	$\tau_{ij} = \tau_{ij}(\bar{u}_n \bar{u}_m, \frac{\partial \bar{u}}{\partial x_j}, k, \epsilon)$	$D\tau_{ij}/Dt = \dots$
0-EQUATION	1-EQUATION	1-EQUATION PLUS UNIVERSAL FUNCTIONS	2-EQUATIONS PLUS ALGEBRAIC RELATION (ASM)	MULTI- EQUATION (RSE)
CLOSURE THRU MEAN-VELOCITY FIELD	CLOSURE THRU MEAN TURBULENT FIELD			

Table I — Turbulence modeling concepts using single-point closure.

5.2.3. — The Equations for Plane Flow

The governing equations in mass-average variables and supplemental equations used in some of the eddy viscosity models are written for plane flow in vector form as follows:

$$\frac{\partial U}{\partial t} + \frac{\partial F}{\partial x} + \frac{\partial G}{\partial y} = H, \quad (5.1)$$

$$U = \begin{bmatrix} \rho \\ \rho u \\ \rho v \\ \rho e \\ \rho k \\ \rho s \end{bmatrix}, \quad F = \begin{bmatrix} \rho u \\ \rho u^2 + \sigma_{xx} \\ \rho uv - \tau_{xy} \\ u(\rho e + \sigma_{xx}) - v \tau_{xy} + q_{tx} \\ \rho uk + q_{ky} \\ \rho us + q_{sx} \end{bmatrix}, \quad G = \begin{bmatrix} \rho v \\ \rho uv - \tau_{xy} \\ \rho v^2 + \sigma_{yx} \\ v(\rho e + \sigma_{yy}) - u \tau_{xy} - q_{ty} \\ \rho vk + q_{ky} \\ \rho vs + q_{sy} \end{bmatrix}, \quad H = \begin{bmatrix} 0 \\ 0 \\ 0 \\ 0 \\ H_k \\ H_s \end{bmatrix}. \quad (5.2)$$

The last two equations are the supplemental equations providing the velocity (k) $^{1/2}$ and length scale s required in higher-order eddy-viscosity models. In the column vectors, q_{Tx} and q_{Ty} are the laminar-plus-turbulent heat-flux vectors; τ_{xx} , τ_{yy} are the laminar-plus-turbulent normal stresses; τ_{xy} is the laminar-plus-turbulent shear stress; and q_{ky} , q_{sx} , and q_{sy} are flux vectors associated with the field variables.

The stress terms and flux vectors are:

$$\begin{aligned}\sigma_{xx} &= p + \frac{2}{3} \rho k - \tau_{xx}, & \tau_{xy} &= \mu_T \left(\frac{\partial u}{\partial y} + \frac{\partial v}{\partial x} \right), \\ \tau_{xx} &= \frac{2}{3} \mu_T \left(2 \frac{\partial u}{\partial x} - \frac{\partial v}{\partial y} \right), & \mu_T &= (\mu + \rho \varepsilon), \\ q_{Tx} &= k_T \frac{\partial T}{\partial x}, & q_{kx} &= -\mu_k \frac{\partial k}{\partial x}, & q_{sx} &= -\mu_x \frac{\partial s}{\partial x}\end{aligned}\quad (5.3)$$

where p is the hydrostatic pressure; $2/3 \rho k$ is the pressure associated with the turbulence; k_T is the thermal conductivity, including the turbulent diffusivity; and $\rho \varepsilon$ is the turbulent eddy viscosity. The functional forms of the source functions H depend on the choice of the turbulence model.

5.3. — Solution Methods and Turbulence Models

5.3.1. — Explicit Methods

Development of methods for solving the mass-weighted form of the Navier-Stokes equations began after MacCormack (1971) used an explicit time-marching scheme to solve the laminar form of the equations. In this second-order-accurate method the equations are discretized and advanced in time such that:

$$U^{n+1} = L(\Delta t) U^n_{i,j}. \quad (5.4)$$

The $L(\Delta t)$ term is replaced by a sequence of time-split, one-dimensional operators, for example,

$$L(\Delta t) = L_x \left(\frac{\Delta t}{2} \right) L_y(\Delta t) L_x \left(\frac{\Delta t}{2} \right), \quad (5.5)$$

where L_x solves the parts of equation (5.1) given by:

$$\frac{\partial U}{\partial t} + \frac{\partial G}{\partial x} = 0$$

and L_y solves that part given by:

$$\frac{\partial U}{\partial t} + \frac{\partial F}{\partial y} = 0. \quad (5.6)$$

The operators are advanced in time to a steady state, if one exists, according to a predictor-corrector sequence of steps. A numerical method stability criterion exists that limits the time-step used to advance the solution. Typically, in high-Reynolds-number turbulent flows the limiting time-step occurs in computational sweeps normal to the surface. It is given by:

$$\Delta t_y \leq \frac{\Delta y}{|v| + c + \{(V_1/\Delta x) + (V_2/\Delta y)\}}, \quad (5.7)$$

where c is the sound speed and V_1 and V_2 represent viscous terms. The Δy step interval has to be very small to resolve the wall region of a turbulent boundary layer, and the permissible time-step presents severe limitations and hence long computing times. Nevertheless, many solutions of shock-separated flows were reported using this method in the mid-1970's.

Zero Equation Turbulence Models. — Given the severe time-step restriction of the method and computer storage limitations, most investigators chose simple zero-equation eddy-viscosity models that use mean-flow information to close the governing equation. These two-layer eddy-viscosity models employed Prandtl's mixing-layer hypothesis in the inner layer,

$$\varepsilon_{inner} = l^2 \left| \frac{\partial u}{\partial y} + \frac{\partial v}{\partial x} \right|,$$

where:

$$\begin{aligned}l &= 0.4 y (1 - \exp^{-y/4}), \\ A &= A^+ \mu_w / (\tau_w / \rho)^{1/2}, \\ A^+ &= 26,\end{aligned}\quad (5.8)$$

In the outer region, either a mixing-length value was chosen, based on some length scale such as boundary-layer thickness, for example,

$$l = l_{max}, \quad (5.9)$$

or Clauser's eddy-viscosity formulation was chosen with an intermittency factor, for example,

$$\varepsilon_{outer} = 0.0168 u_{max} \delta^*/[1 + 5.5(y/\delta)^6], \quad (5.10)$$

where u_{\max} is the maximum velocity achieved in the boundary layer and δ^* is the kinematic displacement thickness. The turbulent heat flux is modeled through a turbulent Prandtl number. To date, this latter aspect of modeling has not been altered. As will be shown later, solutions with these formulations fail to give entirely satisfactory predictions, although they qualitatively reproduce many experimentally observed features. Most of the shortcomings were earlier blamed on turbulence modeling, but not many of the studies reported effects of grid dependence or numerical smoothing which in retrospect may have been as important as the model.

Attempts to Modify Zero Equation Turbulence Models. — Even though computing times were excessive (several hours on a CDC 7600 computer) attempts were made to modify the turbulence model and some improvement in the solutions to complex separated-flow problems was demonstrated. Two approaches are worth noting. One used experimental data to guide modifications to the mixing length constants in the turbulence model (Marvin *et al.*, 1975), and the other attempted to relax the outer eddy viscosity to account for the fact that turbulence does not adjust immediately to rapid changes in the mean flow (Shang *et al.*, 1976; Baldwin and Rose, 1975); for example,

$$\rho\varepsilon = \rho\varepsilon_0 + [\rho\varepsilon_{eq} - \rho\varepsilon_0](1 - \exp^{\alpha(x - x_0/\delta_0)}), \quad (5.11)$$

where $(\rho\varepsilon)_0$ and δ_0 are undisturbed values ahead of the interaction region, $(\rho\varepsilon)_{eq}$ is the usual unmodified value given by equation (10), and α is a relaxation length obtained by a best-fit comparison of final computed results with experiment. It is obvious that both attempts rely heavily on experimental data over a wide range of conditions which limits their generality. However, these studies illustrated the potential of the numerical simulations and encouraged development of faster computing methods and better turbulence models.

At this point, the numerical algorithm development research branched. MacCormack (1976) developed his more efficient explicit hybrid method and Beam and Warming (1978) and Briley and McDonald (1977) developed their implicit schemes. Also, turbulence-modeling improvement studies using higher-order eddy-viscosity models followed in the wake of the hybrid-method development, and improvement studies for algebraic eddy-viscosity models, mostly from a computational compatibility standpoint, followed in the wake of the factored-implicit scheme of Beam and Warming (1978).

5.3.2. — Hybrid Methods

The time-step efficiency of the MacCormack explicit method was improved by combining the advantages of implicit numerical stability with physical insight of the wave-propagating property of the fluid. Conceptually, this was accomplished by further splitting of the y -operator, L_y , into hyperbolic and parabolic parts,

$$L_y(\Delta t) = L_{yh}(\Delta t) L_{yp}(\Delta t). \quad (5.12)$$

The hyperbolic operator contains the convective and pressure terms in the column vector G such that:

$$\frac{\partial U}{\partial t} + \frac{\partial G_h}{\partial y} = 0. \quad (5.13)$$

In the prediction solution to G_h , pressures and velocities are obtained by the method of characteristics in a manner that eliminated the speed of sound from the time-step limit such that:

$$\Delta t_y = \frac{\Delta t}{|v|}. \quad (5.14)$$

Since the finest portion of the mesh is usually confined to the wall-bounded region where v is small, the stability bound of the allowable time-step is much less restrictive than that given by equation (5.7). The corrector step is applied as before. The parabolic operator L_{yp} is treated implicitly and, therefore, unconditionally stable with regard to time advances. The programming for the hybrid method is complicated by the necessity of using characteristics relations in the prediction step for the hyperbolic operator. However, decreases in computing times by an order of magnitude or more relative to the purely explicit method were achieved. Such decreases encouraged some investigators to apply higher-order eddy-viscosity models (e.g., see Viegas and Horstman, 1979), and others to move forward in the computation of three-dimensional flows (e.g., see Hung and MacCormack, 1978).

Higher Order Eddy Viscosity Turbulence Models. — Higher-order eddy-viscosity turbulence models were introduced into the hybrid method by expanding the column vectors to include the turbulent kinetic-energy and length-scale equations in equation (5.2). The one-equation model from Rubesin (1976), two-equation model from Jones and Launder (1971), and the two-equation model from Wilcox and Rubesin (1980) have been examined for a range of different problems. The full equations describing the implementation of these models in the hybrid algorithm are given in Viegas and Horstman (1979). Modeling constants developed for incompressible flows have usually been used but some modifications have also been reported. See Viegas and Horstman (1979) and Liou and Coakley (1981). Authors have reported mixed results, but conclude overall that the higher order models produce improvements.

5.3.3. — Implicit Methods

Concurrently, development of implicit methods was undertaken. For our purposes, the factored-implicit scheme of Beam and Warming (1978) will be briefly described. The method is an extension of their earlier development of an inviscid-flow solver, and, for convenience, the essential elements of the method will be discussed in that context. Time-differencing of equation (5.1), where F and G contain only inviscid terms, is accomplished by the unconditionally stable scheme given by:

$$U^{n+1} = U^n + \frac{\Delta t}{2} \left[\left(\frac{\partial U}{\partial t} \right)^n + \left(\frac{\partial U}{\partial t} \right)^{n+1} \right] + O(\Delta t)^3, \quad (5.15)$$

where:

$$\frac{\partial U}{\partial t} = - \left(\frac{\partial F}{\partial x} + \frac{\partial G}{\partial y} \right).$$

In this form, however, the system of equations is nonlinear and contains a large system of algebraic equations; as a result, the advantage of unconditional stability might not result in solution times significantly smaller than the times for explicit schemes. However, they linearized the equations while maintaining temporal accuracy by a Taylor-series expansion of the nonlinear terms. For example, they let:

$$F^{n+1} = F^n + \left(\frac{\partial F}{\partial U} \right)^n (U^{n+1} - U^n) + O(\Delta t)^2. \quad (5.16)$$

Substituting this expression and a similar one for G , writing the resulting in a delta form $\Delta U^n = U^{n+1} - U^n$, and employing spatial factorization, the final form of the equation was written as:

$$\left(I + \frac{\Delta t}{2} \frac{\partial A^n}{\partial x} \right) \left(I + \frac{\Delta t}{2} \frac{\partial B^n}{\partial y} \right) \Delta U^n = -\Delta t \left(\frac{\partial F}{\partial x} + \frac{\partial G}{\partial y} \right)^n. \quad (5.17)$$

The solution is marched in time to a steady state, if one exists, through a three-step sequence as follows:

$$\begin{aligned} \left(I + \frac{\Delta t}{2} \frac{\partial A^*}{\partial x} \right) \Delta U^* &= -\Delta t \left(\frac{\partial F}{\partial x} + \frac{\partial G}{\partial y} \right)^n, \\ \left(I + \frac{\Delta t}{2} \frac{\partial B^*}{\partial y} \right) \Delta U^n &= \Delta U^*, \\ U^{n+1} &= U^n + \Delta U^n. \end{aligned} \quad (5.18)$$

Results from this procedure compared favorably with those of the hybrid method for the same test problems. Refinements to this method and other implicit solvers have been developed on a continuing basis; see for example, Briley and McDonald (1977) and Coakley (1983). MacCormack (1982) has recently reported a new mixed, explicit-implicit scheme which reduces the computation times and the complex programming problems associated with his hybrid method.

Turbulence Models Used in the Implicit Methods. — Solutions using the implicit scheme developed by Beam and Warming (1978) have usually been obtained by employing zero-equation turbulent models and the thin layer approximation to the full equations; for example, see Baldwin and Lomax (1978). The thin-layer approximation neglects derivatives of the viscous stresses in the flow direction. Baldwin and Lomax (1978) argue that this is computationally acceptable for even large separated flow regions because the accuracy of these derivatives in the discretized form of the full equations is questionable since the aspect ratio of computational cells in the near-wall viscous regions is usually very much less than unity for grids used to resolve turbulent layers. Briley and McDonald (1977), McDonald (1982), and Coakley (1983), however, have employed higher-order, two-equation models and the full equations.

A Modified Zero-Equation Model. — The development of an improved turbulence model was initiated to circumvent a shortcoming of the Clauser outer-eddy-viscosity formulation (equation 5.10), arising because in many instances the inviscid regions in complex flows have a nonuniform velocity field, and determination of the viscous-layer edge needed to evaluate δ^* in the model becomes difficult. The outer eddy viscosity was redefined as:

$$\varepsilon_{\text{outer}} = 0.0168 C_1 F_{\text{wake}} \left[1 + 5.5 \left(\frac{0.3y}{y_{\max}} \right)^6 \right]^{-1}, \quad (5.19)$$

where:

$$F_{\text{wake}} = y_{\max} F_{\max} \quad \text{or} \quad C_{\text{wk}} y_{\max} U_{\text{diff}} / F_{\max} \quad \text{the smaller.} \quad (5.20)$$

The values of F_{\max} and y_{\max} are determined from:

$$F(y) = y \left[\left(\frac{\partial u}{\partial x} - \frac{\partial v}{\partial y} \right)^2 \right]^{1/2} [1 - \exp^{-y^+/A^+}]. \quad (5.21)$$

In wakes, the exponential part of $F(y)$ is set to zero. The F_{\max} is the corresponding value of Y at F_{\max} ; U_{diff} is the difference between the maximum and minimum total velocity at a fixed x -station. The constant C_1 was determined to have a value of 1.6 ensuring that the resulting skin friction computed for a flat plate was equivalent to the value obtained from the original Cebeci-Smith model formulation. In order to have a correct value of eddy viscosity for a far-wake, C_{wk} was taken to be 0.25. For two test problems involving shock-wave interaction, the model gave results that were improved relative to those of the simple two-layer zero-equation model and more or less comparable to those achieved with the relaxation formulation given by equation (11). However, recent studies suggest that a certain degree of caution be exercised in applying this model. It requires modification of constants for Mach number changes, the function $F(y)$ is not always a smoothly varying one, and the choice of F_{\max} is problem-dependent. See for example Deganni and Schiff (1983) and Visbal and Knight (1983).

5.4. — Experimental Requirements

The emergence of these methods for computing complex, turbulent flows places stringent requirements on experiments used to assess their development. In addition to the traditional role of providing basic understanding of the controlling mechanisms, they must also provide guidance for modeling approximations and provide sufficient detail so that accurate checks of computational output can be made. See Kline et al. (1981) and Marvin (1982).

The experimental data used to assess the development of computer codes used to solve the mass-averaged Navier-Stokes equations vary in completeness and accuracy because the flows are complicated by the presences of shock waves or separation or both, and because many investigators used instrumentation techniques that were themselves in developmental stages. Nevertheless, a series of bench-mark experiments can be identified to assist in the process. A number of those available for the problems involving shock boundary layer interactions are cited in Tables II-VII along with citations of studies in which computations are reported. Information is given on test conditions, grid size, and type of turbulence model employed. Grid size alone is not the only criterion for assessing computational resolution, however, because grid stretching and special refinement in regions of rapid flow changes are important techniques commonly used by most investigators. But the size provides some measure for comparison between various computations. Likewise, the eddy viscosity turbulent models listed are only broadly categorized because they usually differ in detail as a result of programming decisions made by the various investigators. Some of the experiments conducted before 1981 are noted in the tables; they were recently reviewed by an independent evaluation committee and ascertained to contain the most comprehensive data sets for code validation (see Kline et al., 1981). There is a continuing need for additional experimental data.

5.5. — Examples of Navier-Stokes Computations

5.5.1. — General Comments

Tables II-VII illustrate the variety of flows that have already been computed with the methods and turbulence models discussed in the previous sections. Due to space limitations of this publication, examples from all the studies cannot be incorporated herein. What we will provide next are some examples, classified according to flow phenomena, which illustrate the essential accomplishments and shortcomings of the computations. The physical characteristics, as deduced from experimental evidence, will be introduced first and then the computations will be compared with experiment (and where possible with other more approximate methods discussed earlier in this paper).

Two broad classes of flows will be discussed: those where the flow field upstream of the interaction is supersonic, where the shock wave position and strength are "fixed" by external means or geometry and where the interaction only weakly affects the entire upstream flow through the elliptic properties of the subsonic regions in the viscous boundary layer (see Tables II-V and VII); and, those where the flow upstream of the shock wave is transonic and where the shock wave position and strength are "free" and they depend on the interaction since it affects a substantial region of the entire flow through the elliptic properties of the inviscid as well as viscous regions of the flow (see Table VI). The latter cases take longer to compute, are more sensitive to boundary conditions, and must be examined even more carefully than the others.

FLOW	EXPERIMENTS	M_∞	$Re \times 10^6$	COMPUTATIONS	GRID x, y, z	MODEL ^a
2-d	HOLDEN (1972) FEDDA AND MURPHY (1973)	8.5 3	22 57	BALDWIN AND McDONALD (1974) BALDWIN AND ROSE (1975) VIEGAS AND HORSTMAN (1979) COAKLEY ET AL (1977) VIEGAS AND HORSTMAN (1982)	40, 32 40, 32 40, 32 40, 32 80, 50	0; 2 0 (MOD.) 0 (MOD.) 0 (MOD.) 0; 1; 2 2
3-d	KUSOY ET AL (1980) ^b	2.2	36	KUSOY ET AL (1980) VIEGAS AND HORSTMAN (1982)	47, 20, 20 47, 20, 20	0 0; 2
3-d	BROSH ET AL (1983)	3	18	BROSH ET AL (1983)	45, 34, 38	0 (MOD.)

^aZERO-, ONE-, AND TWO-EQUATION MODELS

^bSELECTED FOR AFOSR/HTM STANFORD CONFERENCE (KLINE ET AL., 1981)

Table II — Benchmark flows for evaluating Navier-Stokes computations: impinging oblique shock waves.

FLOW	EXPERIMENTS	M_∞	$Re \times 10^6$	COMPUTATIONS	GRID x, y, z	MODEL ^a
3-d	PEAKE (1976) ^b	2	10	HORSTMAN AND HUNG (1978) VIEGAS AND HORSTMAN (1982) HORSTMAN AND HUNG (1978) HORSTMAN AND HUNG (1979) SHANG ET AL (1979)	21, 28, 31 21, 28, 31 21, 28, 31 21, 28, 31 17, 33, 33	0 (MOD.) 0 (MOD.) 0 (MOD.) 0 (MOD.) 0 (MOD.)
3-d	OSKAM ET AL (1976) WEST ET AL (1972)	3 3	5 0.8	"	"	"
3-d	DOLLING AND BOGDONOFF (1962)	3	0.8	HUNG AND KORDULLA (1983)	40, 32, 32	0 (MOD.)

^aZERO-, ONE-, AND TWO-EQUATION MODELS

^bSELECTED FOR AFOSR/HTM STANFORD CONFERENCE (KLINE ET AL., 1981)

Table IV — Benchmark flows for evaluating Navier-Stokes computations: glancing shock waves.

FLOW	EXPERIMENTS	M_∞	$Re \times 10^6$	COMPUTATIONS	GRID x, y, z	MODEL ^a
2-d	COOK (1978) ^b	0.88-0.73	8.5	BAILEY (1982) DEWERT (1982) KORDULLA (1982) MEHTA (1983) COAKLEY (1983)	127, 59 126, 37 108, 32 216, 60 180, 50	0 - EO 0 - EO 0 - EO 0 - EO 2 - EO
NO SEPARATION	SPAIID (1978) ^b	0.8-0.8	2	BAILEY (1982) DEWERT (1982)	127, 59 126, 37	0 - EO 0 - EO
2-d	McDEVITT ET AL (1975, 78) ^b SEGMILLER ET AL (1979) ^b	0.78	4-11 11	McDEVITT ET AL (1978) SEGMILLER ET AL (1979) COAKLEY (1981) HUNG (1982)	78, 35 78, 35 81, 61 127, 59	0 - EO 0 - EO 2 - EO 0 - EO
SEPARATION	JOHNSON (1980) ^b	0.875	13	JOHNSON ET AL (1980) VIEGAS AND HORSTMAN (1982) HORSTMAN AND JOHNSON (1984)	129, 50 129, 50 129, 50	0 - EO 2 - EO 2 - EO 2 - EO

^aZERO-, ONE-, AND TWO-EQUATION MODELS

^bSELECTED FOR AFOSR/HTM STANFORD CONFERENCE (KLINE ET AL., 1981)

Table VI — Benchmark flows for evaluating Navier-Stokes computations: transonic flows.

FLOW	EXPERIMENTS	M_∞	$Re \times 10^6$	COMPUTATIONS	GRID x, y, z	MODEL ^a
2-d	SETTLES ET AL (1978, 1979) ^b	2.8	63-200	HORSTMAN ET AL (1977) VIEGAS AND HORSTMAN (1982) LAW (1974)	60, 32 50, 32 160, 40	0; 1 0; 1; 2 2
3-d	HOLDEN (1972) LAW (1974)	8.7 3	22 10	HUNG (1982) HUNG AND McDONALD (1977) SHANG AND HANKEY (1975) HUNG AND McDONALD (1977)	77, 31 64, 30 63, 31	0; 1 (MOD.) 0; 1 (MOD.) 0; 0 (MOD.)
3-d	TENG AND SETTLES (1982)	2.9	8	SETTLES AND HORSTMAN (1984) HORSTMAN (1984)	40, 35, 20 40, 25, 20	0; 2 2

^aZERO-, ONE-, AND TWO-EQUATION MODELS

^bSELECTED FOR AFOSR/HTM STANFORD CONFERENCE (KLINE ET AL., 1981)

Table III — Benchmark flows for evaluating Navier-Stokes computations: compression corners.

FLOW	EXPERIMENTS	M_∞	$Re \times 10^6$	COMPUTATIONS	GRID x, y, z	MODEL ^a
2-d	SEDDON (1960)	1.5	0.6	VIEGAS AND HORSTMAN (1980) VIEGAS AND HURRISSON (1983) VIEGAS AND HORSTMAN (1979) VIEGAS AND HORSTMAN (1982)	40, 35 20, 35 40, 35 76, 40	0; 1-2 2 0; 1, 2 2
STRAIGHT WALLS	OM ET AL (1982)	1.2-1.5	10-200	McDONALD (1982) OM ET AL (1982)	38, 40 31, 41 170, 40	2 2 2
2-d	DELERY (1963) ^b SALMON ET AL (1981)	1.3-1.6 1.3-1.4	2-4 4	CARRIER ET AL (1981) HORSTMAN (PVT. COMM.) LIOU ET AL (1981)	61, 21 80, 50	0 0; 2 2

^aZERO-, ONE-, AND TWO-EQUATION MODELS

^bSELECTED FOR AFOSR/HTM STANFORD CONFERENCE (KLINE ET AL., 1981)

Table V — Benchmark flows for evaluating Navier-Stokes computations: impinging normal shock waves.

FLOW	EXPERIMENTS	M_∞	$Re \times 10^6$	COMPUTATIONS	GRID x, y, z	MODEL ^a
2-d	SETTLES ET AL (1980)	2.9	0.22	VIEGAS AND HORSTMAN (1982) MCDONALD (1982)	85, 82 61, 40	2 - EO 0 - EO
PLANE SHOCK	KEYS (1977)	6	1.2	TANNAHILL ET AL (1979)	31, 40	0 - EO 0 (MOD.)

^aZERO-, ONE-, AND TWO-EQUATION MODELS

^bSELECTED FOR AFOSR/HTM STANFORD CONFERENCE (KLINE ET AL., 1981)

Table VII — Benchmark flows for evaluating Navier-Stokes computations: reattaching shear layers.

5.5.2. — Impinging Oblique Shock Waves

Physical Characteristics. — Sketches showing the important features of two-dimensional oblique shock-wave interactions are shown in Figure 5.1. For a purely inviscid flow the uniform upstream flow processed by the incoming shock wave is uniformly turned toward the surface and then straightened again by the reflected shock. The corresponding surface-pressure signature is shown. Analytic expressions are available to predict this rather simple situation. The presence of a boundary layer confounds the problem, and the resulting flow-field characteristics depend on the strength of the incoming shock wave.

In the weak interaction, the shock wave penetrates the turbulent boundary layer and turns more steeply toward the surface as it encounters the lower speeds within the viscous layer. It reflects from the viscous layer through a series of compression waves that coalesce into a reflected shock wave. A uniformly increasing surface-pressure signature is found, whose overall rise is nearly equivalent to the inviscid jump.

In the strong interaction, the shock wave also penetrates the viscous layer, but that layer cannot overcome the pressure rise, and separation takes place. The viscous layer is turned above the separation through a series of compression waves that coalesce into what is called a separation shock which is later weakened by expansion waves emanating from the viscous flow accelerating over the separation bubble. Downstream, where the bubble terminates, a series of compression waves coalesce into a reflected shock where the flow aligns itself with the surface. The corresponding surface pressure is characterized by a smooth pressure rise and an inflection region characteristic of separation. Also, it is usually assumed that the separation is closed by a dividing streamline that separates the mass entrained in the region from the outer flow and that a recirculating region is present. In actuality, the turbulence-flow probably leads to unsteadiness within this separated region, but how much influence this has on the mean characteristics is not understood at this time and further study is warranted. Above the separated region an island of very high peak pressure exists near the bifurcation associated with the intersection of the incoming and separation shocks. The extent (scale of the interaction) depends on the boundary layer thickness, flow Reynolds number, and Mach number.

Shock-Capturing Capability of the Numerical Methods. — One of the first considerations in computing such flows is the ability of the computation to resolve shock waves. As reported by Metha and Lomax (1982), the solution methods discussed previously are all capable of capturing shock waves. However, the degree of shock sharpness depends on the numerical method and computational mesh. An example, taken from Coakley (1983), which illustrates what can be achieved with a reasonably good numerical method and a uniform mesh, is shown in Figure 5.2. Pressures along the solid surface and at a location about midway up in the mesh above the surface are shown for the case of an oblique wave inclined at 29° at a free-stream Mach number of 2.9. Similar results would be displayed in pressure distributions normal to the surface as the shock wave was traversed. The mesh used in this example is typical of the mesh dimensions used in the Navier-Stokes codes out in the inviscid regions of the flow. The point to note is that the numerical method requires at least several mesh points to capture the pressure jump associated with the waves. From results such as these, it is easy to deduce that for solutions to the strong-interaction problems, in which separation and reflected-shocks occur, mesh choice will have an influence on how well the flow is modeled and further that a certain amount of shock "smearing" will always occur in practice. What seems to be missing in studies reported in the literature on shock-separated flow problems is an assessment of this effect on the results.

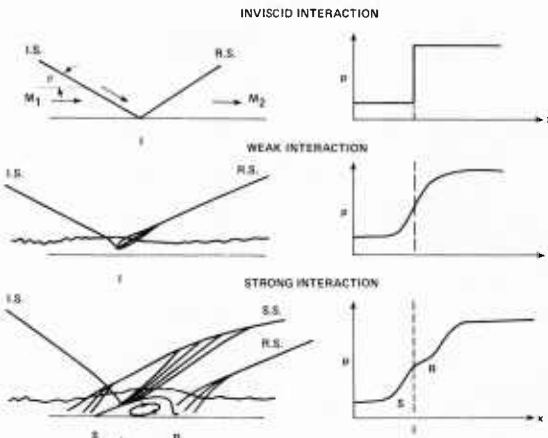


Fig. 1 — Physical characteristics of 2-dimensional oblique shock-wave interaction

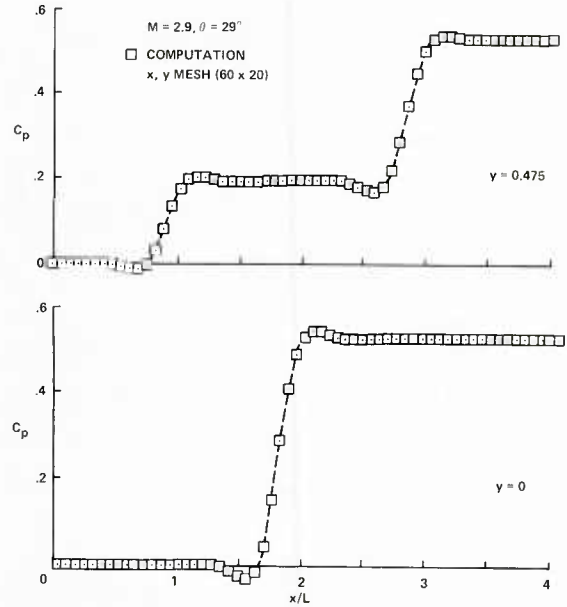
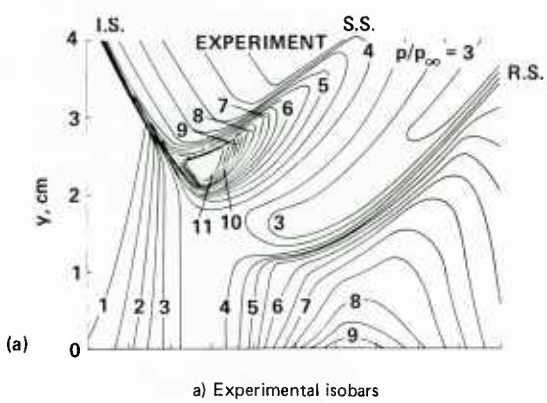


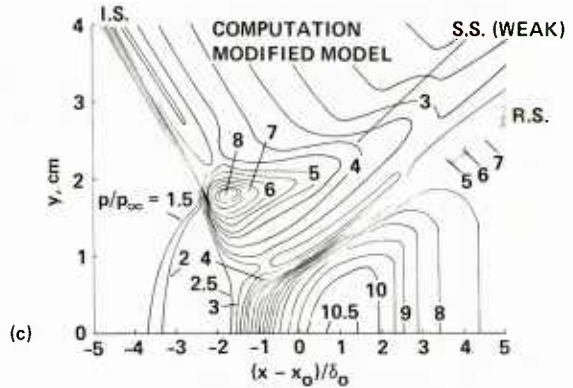
Fig. 2 — Modeling of an inviscid oblique shock-wave interaction.

A Comparison of Computation and Experiment (2-Dimensional). — Many of the first computations of separated turbulent flows were directed toward solving the two-dimensional, strong impinging-shock interaction problem (see Table I). Turbulence modeling was reported to have a strong influence on the results. The bench mark experimental flow of Kussoy and Horstman (1975) was computed with an explicit numerical method and will be used to illustrate how this flow is simulated numerically. The experimental apparatus was axisymmetric and thus eliminated three-dimensional effects now known to be present in other "two-dimensional" experiments.

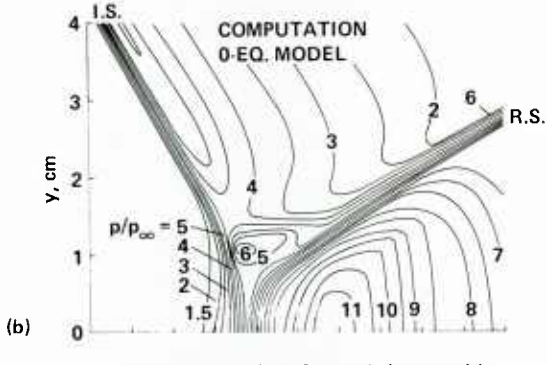
Pressure contours from the experiment and two computations are shown in Figure 5.3. The experimental contours show the presence of the incident-, separation-, and reflected-shock waves as evidenced by the closely spaced contour levels. An island of very high pressure exists above the separation near the intersection of the incident and separation shocks. The computations were made with zero-equation eddy-viscosity models and the equations were solved down to the wall; the 0-equation model consisted of the mixing-length formulation given by equations (5.8) and (5.9), and the modified mixing-length model was determined from data analysis (Marvin *et al.*, 1975). The grid was chosen to allow reasonably accurate shock capture in the outer regions, and in the viscous region a fine mesh was placed near the wall to resolve the turbulent boundary layer. The eddy viscosity from the baseline model is too high in the interaction region and as a consequence the computation only predicts the existence of a reflected shock wave.



a) Experimental isobars



c) Computation using a turbulence model modified by experimental information



b) Computation using a 0-eq. turbulence model

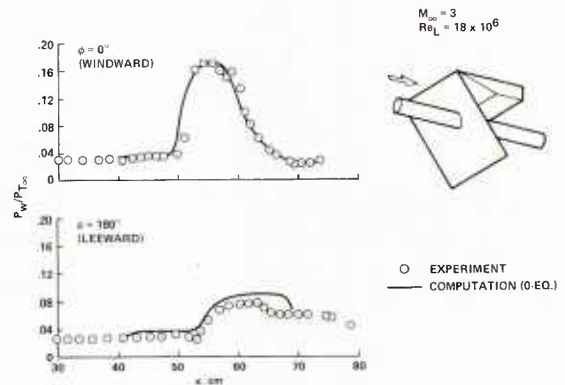


Fig. 3 – Modeling of a strong oblique shock-wave interaction.

Fig. 4 – Modeling of a plane strong oblique shock-wave interacting with a flow-aligned cylinder: surface pressures on windward and leeward planes.

On the other hand, the modified model, which results in lower eddy viscosities, gave a better simulation of the experimental flow. In addition to the reflected shock wave, the presence of a separation shock is evident, but it appears to be weaker and smeared compared with the experiment. This deficiency in the calculations is probably a result of two things: the grid, which is still probably not fine enough to resolve the flow in the region of the island of high pressure, and the modified turbulence model, which still gives a small separation bubble height relative to the experimental one. Surface skin friction and heat transfer were not accurately predicted within the separated zone, although the model modification did improve the results. In this instance, the model modification was experiment-dependent, and, therefore, not extendable to the other conditions of Mach number and Reynolds number.

Although advances in numerical methods that improved computational efficiency provided the opportunity for investigating improvements in turbulence modeling, there has not yet been a significant advance in the ability to predict the flow detail within a separated region. What is known is the zero-equation eddy-viscosity models developed for attached flows must be modified or abandoned in favor of other approaches to provide a physically plausible representation of the flow and that the model must provide some mechanism for altering the effective viscosity in the interaction zone. Two approaches have provided some improvement: modifying the zero-equation model eddy viscosity (Baldwin and Lomax, 1978) and using two-equation eddy-viscosity models (Viegas and Horstman, 1979).

The former approach, which is advantageous from the viewpoint of computational efficiency, has been used extensively in three-dimensional computations in which computer storage and speed make application of higher-order models less attractive.

A Comparison of Computation and Experiment (3-Dimensional). — Results of a recent study by Brosh *et al.* (1983) of a three-dimensional shock interaction are worth examining because they illustrate current limitations. The flow field is sketched in Figure 5.4. A plane shock impinges on a cylinder aligned with free-stream flow. Separation occurs on the windward surface because of shock interaction, and on the leeward surface because, in part, of the cross flow imposed by the windward portion of the free stream being processed by the oblique shock. On the windward plane of symmetry the shock interaction is similar to that depicted in Figure 5.2, but the separation is not closed, and the mean flow within it is not a result of recirculation fed by downstream flow reattachment. (There has been some speculation that such open separations may be modeled appropriately with zero-equation eddy-viscosity models.)

A cursory examination of the computed results using the Baldwin and Lomax (1978) turbulence model indicates that many of the features observed experimentally are simulated, for example, surface-pressure distributions (Fig. 5.4) and the initial separation line. More detailed examination, however, shows deficiencies that result from both turbulence modeling and grid resolution. In Figure 5.5, the windward plane flow field, determined by flow-field surveys, is sketched, and comparisons with static-pressure profiles are shown. Grid resolution in the region outside the viscous zone leads to significant shock smearing, and no separation shock is predicted.

In Figure 5.6, the surface skin-friction directions from the computations are compared with a photograph of oil-flow patterns on a Mylar sheet that had been placed around the cylinder and then “unwrapped” and photographed after the test. On the windward plane ($\phi=0$), a single separated line is predicted, whereas a double separation line is evident in the experiment. It is likely that the deficiencies of the computation are caused by the combination of a poor turbulence model, which gives an effective viscosity that is too high, and poor numerical resolution of the shock system, which causes a local weakening of any shock structure. As the flow proceeds around to the leeward, a single line of separation is predicted, whereas a double line of separation is measured. The turbulence model of Baldwin and Lomax (1978) is unlikely to predict secondary separations without modification and, in addition, the azimuthal grid spacing may have been too coarse. See Deganni and Schiff (1983). Hence grid resolution and turbulence modeling must both be improved before definitive conclusions can be reached on the modeling of three-dimensional, impinging-shock, separated flows.

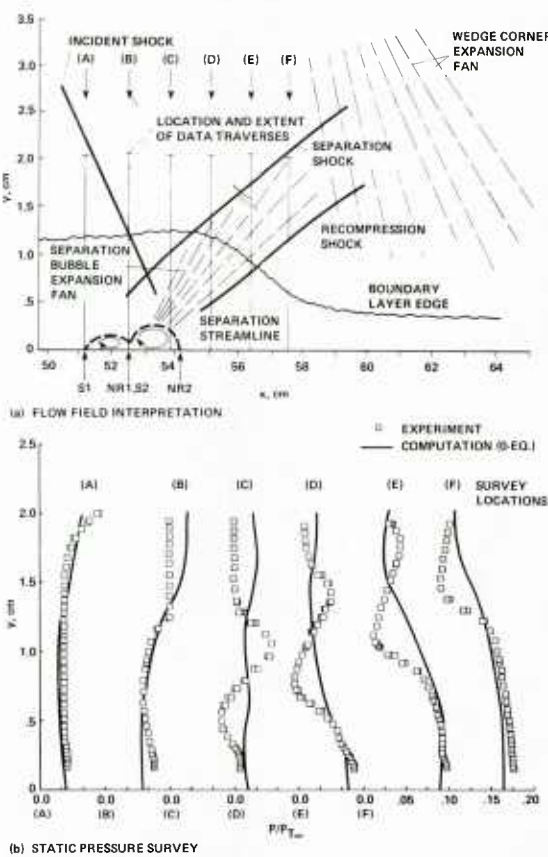


Fig. 5 — Modeling of a plane strong oblique shock-wave interacting with a flow-aligned cylinder: a) Windward symmetry-plane flow field interpretation from experiment; b) Comparison of experimental and computational static pressure surveys in the windward symmetry-plane.

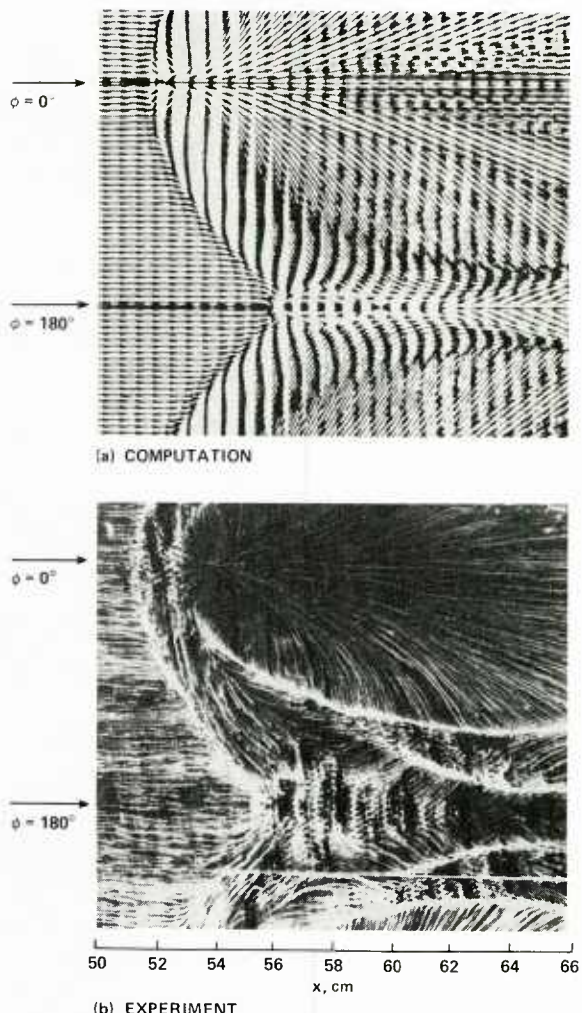


Fig. 6 — Modeling of a plane strong oblique shock-wave interacting with a flow-aligned cylinder: comparison of experimental and computational skin friction lines.

5.5.3. — Supersonic Compression Corner

Physical Characteristics. — The physical characteristics and corresponding wall pressures for a two-dimensional compression corner are sketched in Figure 5.7. For the inviscid flow situation a single shock forms, and the pressure rises abruptly to the level predicted by wedge-flow relations. The presence of a boundary layer complicates the flow, as depicted for two situations, the weak and strong interactions. In the weak interaction, a series of compression waves form within the boundary layer as it encounters the pressure rise and they coalesce with the shock formed in the inviscid flow, which is required to turn the flow in the direction of the ramp. The corresponding pressure rise shows a smoothing of the pressure at the beginning and end of the interaction. For the strong interaction, the boundary layer cannot withstand the pressure rise and it separates. Compression waves that coalesce into a shock wave form near the forward portion of the separation bubble as the outer viscous flow negotiates the pressure rise.

Experimentally, the separation shock-angle is found to be independent of the corner angle. If the separation is large enough and the free-stream Mach number high enough, a second shock will form downstream when the flow over the separated region reattaches and turns in the direction of the ramp. The separation and recompression shocks coalesce with the outer shock wave. The corresponding pressure rise shows inflection over the separated region and the upstream influence is more pronounced than in the weak case. Conceptually, the flow in the closed separated region is divided from the outer flow, and mass is entrained and recirculated through the reattachment process. However, as reported by Dolling and Or (1983), there is experimental evidence of unsteadiness in this process. The characteristic scale of the interaction depends on the boundary-layer thickness and free-stream Mach number.

A Comparison of Computation and Experiment (2-Dimensional). — Computations of corner flows have been reported, as indicated in Table III. Different numerical methods and turbulence models have been employed. A comparison of two of the more recent Navier-Stokes computations with experiment is shown in Figure 5.8. Two cases are shown, one near incipient separation (weak interaction) and one with separation (strong interaction). In one computation, an implicit algorithm and the thin-layer form of the equations were used with the modified zero-equation model of Baldwin and Lomax (1978) which was described earlier. In the other, the MacCormack hybrid algorithm and the full equations were used with the two-equation turbulence model of Wilcox and Rubesin (1980). Metha and Lomax (1982) stated that these different numerical schemes should yield similar results if comparable grids are used and care in carrying out the computation is exercised. Accepting that premise, the differences between these calculations mainly reflect differences owing to turbulence modeling.

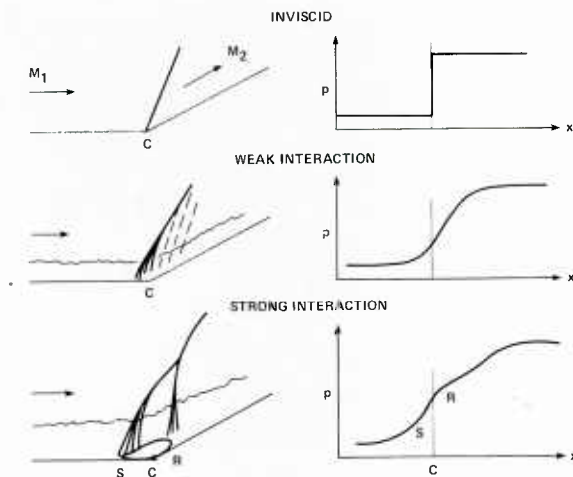


Fig. 7 – Physical characteristics of 2-dimensional compression-corner interactions.

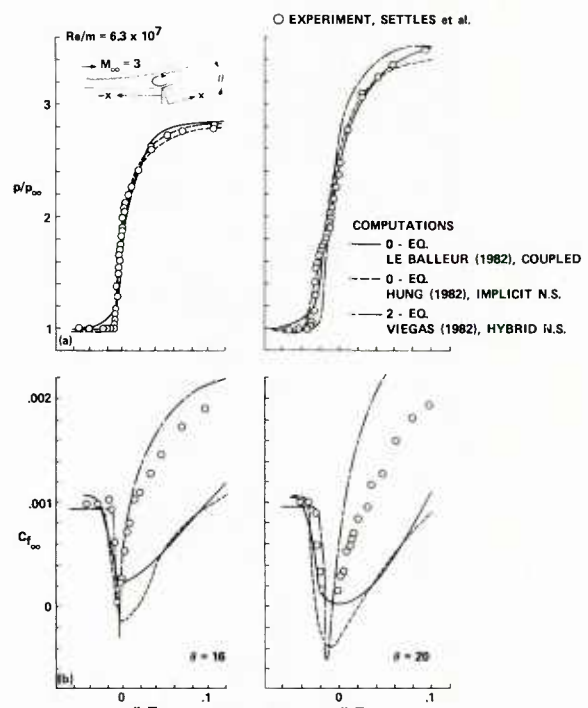


Fig. 8 – Modeling of a compression-corner interaction using different algorithms and different turbulence models: a) Pressure distributions; b) Skin friction distributions.

In both the weak and strong cases, the pressure predicted using either model agree reasonably well with the data, and this reflects the common observation that the pressure rise can be estimated, for engineering purposes, using any of the eddy-viscosity models. However, differences occur in the viscous regions. The modified zero-equation model predicts skin-friction values that are much too low downstream of the weak interaction, and this manifests itself more critically in the strong-interaction case by predicting reattachment too far downstream and velocity profiles that do not compare well with experiment. See also Visbal and Knight (1983). On the other hand, velocity profiles and shape factors in the downstream region are predicted better by the two-equation model, even for the strong-interaction case in which skin friction is somewhat overpredicted (see Marvin, 1982). It is thought that the failure of the two-equation model to predict the skin friction downstream of reattachment resides in the low-Reynolds-number modeling terms developed to allow integration to the wall, but this should be investigated further and in light of the experimental observations on unsteadiness. See Dolling and Or (1983).

Also shown for comparison is the computation of LeBalleur (1982). He used the method described previously in which an inverse integral boundary layer solution including lag entrainment based on the turbulent kinetic energy equation is coupled to an inviscid Prandtl-Meyer outer solution. [LeBalleur (1982) believes the simple inviscid outer solution may be a limitation that should be relaxed in favor of an Euler solution.] This method also reproduces the overall pressure rise through the interaction; but seriously underpredicts the skin friction much in the same fashion as the 0-equation turbulence model solution from the Navier-Stokes implicit solution. This similarity may reflect the inability of 0-equation turbulence modeling to provide adequate simulations of the viscous region of these flows.

The change of separation and reattachment locations with Reynolds number based on boundary layer thickness are compared in Figure 5.9 with the locations from the Navier-Stokes solutions using the 2-equation model. The two distinct data sets were obtained by positioning the corner at two different locations in the facility and the varying Reynolds number by changing the total pressure of the tests. The trend in variation of these locations is predicted although the extent of upstream influence and length of separation are not. Results from the other two computations are not shown because the integral method failed to predict any significant separation and because the Navier-Stokes solution with the 0-equation turbulence model gave reattachment locations that fell out of the range of the graph as can be easily inferred from the skin friction comparison. The latter discrepancy is typical of the Baldwin-Lomax turbulence model as discussed previously.

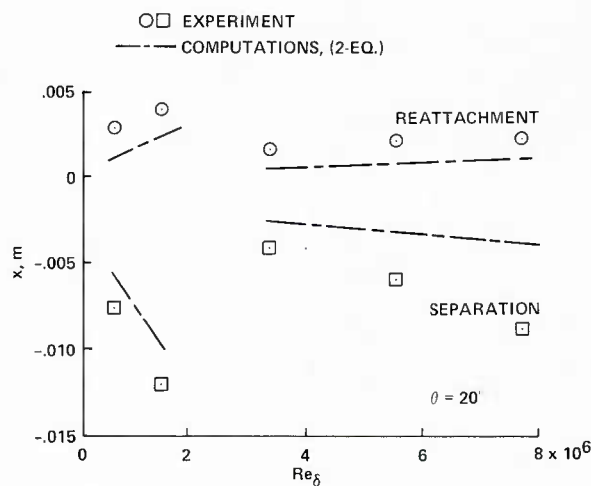


Fig. 9 – Modeling of separation and reattachment points for a compression-corner.

A Comparison of Computation and Experiment (3-Dimensional). — Three-dimensional compression corner flows have also been studied. Teng and Settles (1984) performed a series of experiments which identified two distinct flow regimes depending on the combination of sweep and compression angles. (See the geometry sketch in Table III.) They classified the flows as either having asymptotically cylindrical or conical upstream influence. Typical surface skin friction line topologies are shown in Figure 5.10a and the boundary defining the two regions is shown in Figure 5.10b. Cylindrical symmetry means that the upstream influence line (I) runs parallel to the swept corner line, whereas conical symmetry means that the upstream influence and corner lines belong to a family which have a common origin. Both regimes develop following an initial inception zone near the apex. In subsequent publications by Settles and Horstman (1984) and Horstman (1984) computations from a full 3-dimensional Navier-Stokes code using the implicit-explicit method of MacCormack (1981) were compared with these experiments. Isotropic eddy viscosity models were employed. In that first publication both the 0-equation turbulence model [equations (5.8) and (5.10)] and the 2-equation turbulence model of Jones and Launder (1971) were used and comparisons made for a single flow case with conical influence. As might be expected on the basis of results for 2-D compression corners, the resulting pressure distributions from either turbulence model were essentially indistinguishable and most of the flow features were captured qualitatively with either model. However, the authors indicated a preference for the 2-equation model formulation, mainly on the basis of observations that the upstream influence length was predicted somewhat better, and that the Reynolds number scaling predicted with this model was consistent with experimental observations, and on the knowledge that 2-dimensional compression corners with separation were probably predicted better as shown in the previous section. In the second publication, a parametric study using the 2-equation Jones-Launder turbulence model was made to determine whether the computations could define the boundary between cylindrical and conical influence. The practical implementation of this numerical study was made possible by extending the wall functions developed by Viegas and Rubesin (1983) to 3-dimensional flow and thus eliminating the time consuming task of integrating the model equations to the wall. [Further discussion on the wall function treatment of Viegas and Rubesin (1983) is given in a subsequent section.] Indeed, the resulting computations were successful in predicting the boundary of the two types of flow as shown in Figure 5.10b. Furthermore, combining observations from the experiments and the computations the authors have now established that the boundary is most probably associated with shock detachment and not separation; cylindrical influence associated with attached shock waves and conical associated with detached waves. While the computations are impressive with respect to their ability to predict the qualitative features of the flow and have helped explain some of the experimental observations, deficiencies remain, particularly when separation is present. Grid resolution, flow unsteadiness, and modeling are certainly contributing factors in this regard.

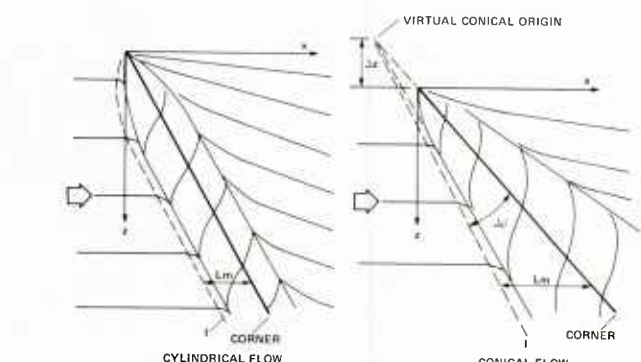
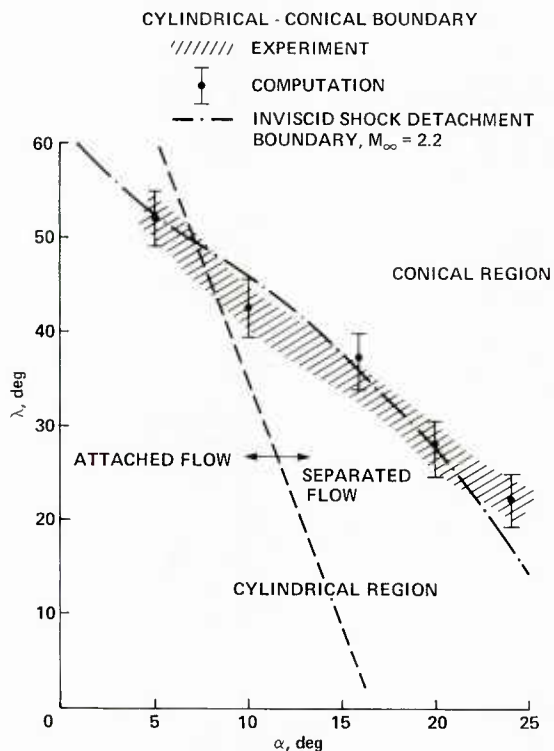


Fig. 10a — Topology of swept compression-corner flow.

Fig. 10b — Comparison of cylindrical-conical boundaries from experiment and computation.

5.5.4. — Glancing Shock Waves

Physical Characteristics. — Some bench mark experiments depicting the essential features of glancing shock flows are available for verifying computations (see Table IV). Geometries for two of these are sketched in Figure 5.11 along with surface skin-friction lines and shock-wave structures which help to describe the general physical characteristics of the flows.

The sharp leading-edge shock generator can result in both weak and strong interactions. In the weak case, the shock interacts with the incoming boundary layer and causes simple flow-turning, with the lower momentum fluid near the wall undergoing larger turning than the higher momentum fluid at the boundary-layer edge. Far from the generator leading edge, the shock pattern formed by the component of the Mach number normal to the shock wave might appear as a weak shock, as sketched in Figure 5.11. In the strong interaction, the boundary layer cannot overcome the pressure gradient, and a separation line forms ahead of the shock wave and a reattachment line forms downstream. Skin-friction lines accompanying such characteristics are sketched in the figure (see Peake and Tobak, 1980). In this case, the component of the Mach number normal to the shock wave is larger, and the interaction is stronger and a shock wave with the characteristic lambda foot emanating from the compression waves forms near the separation line. In contrast to the two-dimensional, normal-shock-wave case, the flow in the separation region is not closed and continued recirculation of the shock-processed fluid does not occur. In this sense, the swept shock flows are probably more steady than the two-dimensional flows. Furthermore, the flow relief owing to the third dimension causes the boundary layers to separate sooner and to have correspondingly larger upstream influence than the two-dimensional flows. The scale of these interactions is determined mainly by the incoming boundary-layer thickness and Mach number.

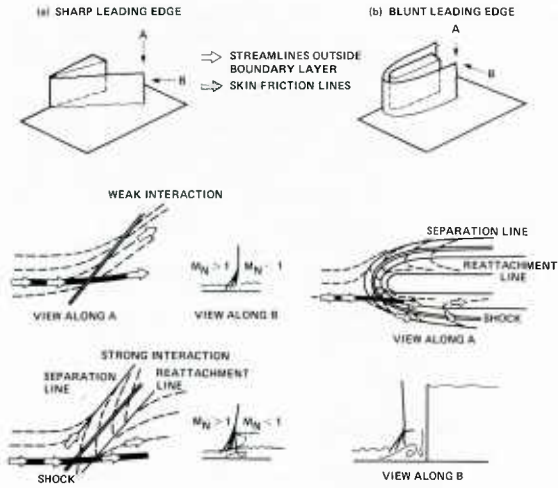


Fig. 11 — Physical characteristics of glancing shock-wave interactions:
a) Sharp leading edge; b) Blunt leading edge.

In the case of the blunt leading edge, a bow shock wave is formed and a strong interaction takes place. Separation and reattachment lines form ahead and downstream of the bow shock wave. A horseshoe vortex forms as a result of the presence of the blunt generating surface and it streams around it. The shock wave in the plane of symmetry can form a lambda foot near the separation line for the strongest interactions and an inviscid shear layer emanates from the bifurcation point. The scale of the interaction is determined by the bluntness of the generator, because the shock standoff position and the horseshoe vortex scale are proportional to it.

A Comparison of Computation and Experiment. — Surprisingly, numerical simulations of these glancing shock-wave flows using rather coarse grids and a simple turbulence model provide adequate predictions of experimental data in contrast to the impinging-shock-wave and corner-flow results discussed in previous sections. To illustrate this point for the sharp-generator case, typical comparisons of computation and experiment are shown in Figures 5, 12-5, 14. The computations by Horstman and Hung (1979) were made with the MacCormack hybrid method along with a two-layer, zero-equation, mixing-length eddy-viscosity model [equations (5.8) and (5.10)], modified by Hung and MacCormack (1978) to account approximately for the flow in the corner formed at the intersection of the generator and the plate.

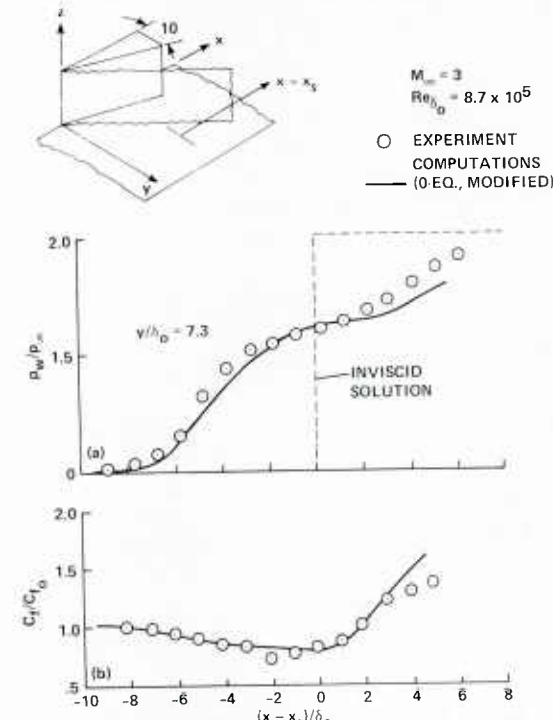


Fig. 12 — Modeling of a glancing shock-wave interaction from a sharp leading-edge wedge: a) Pressures along streamwise direction; b) Skin friction along streamwise direction.

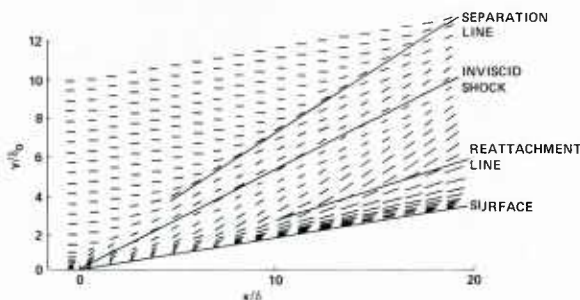


Fig. 14 — Skin-friction line directions computed for a glancing shock wave from a sharp leading-edge wedge.

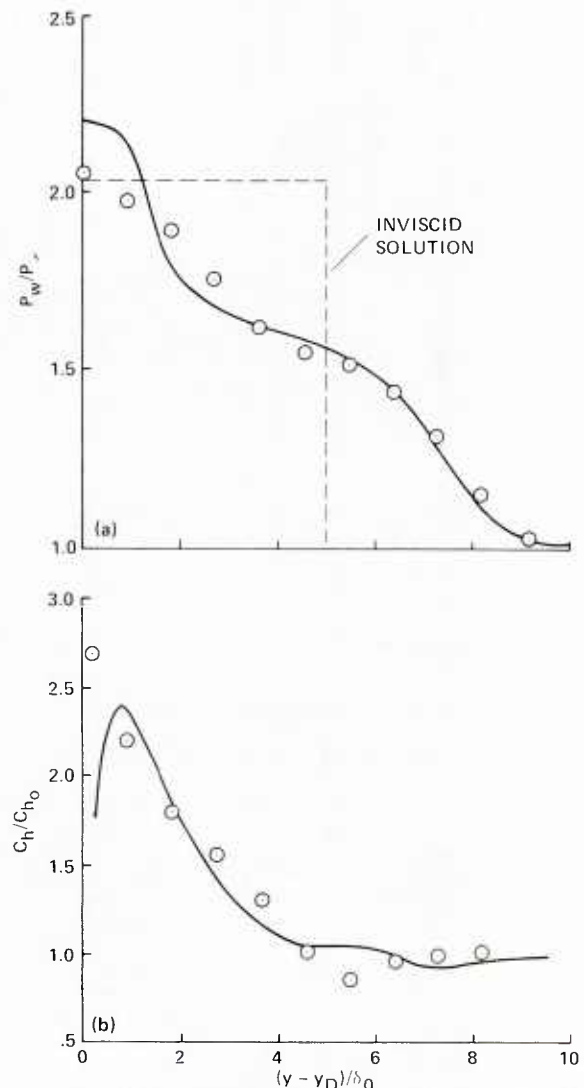


Fig. 13 — Modeling of a glancing shock-wave interaction from a sharp leading-edge wedge: a) Pressure along transverse direction; b) Skin friction along transverse direction.

The axial variations of pressure and skin friction (Fig. 5.12) and the span-wise variation of pressure and heat transfer (Fig. 5.13) agree with the measurements except in the corner where modeling is undoubtedly incorrect. Differences in the axial variations at the farthest downstream location are caused by locating the computational boundary there. Although not shown here, agreement with mean-velocity profiles was also reported. Similarly good comparisons of surface and flow-field quantities have been reported for wedge angles to 12° and Mach numbers to 6.

Surface skin-friction lines from the computations are shown in Figure 5.14. Locations of the main features of this strong-interaction case are noted. The separation and reattachment lines were determined by examining cross-flow velocity vector plots oriented in a plane normal to the center of the vortex formed by the interaction. They correspond closely to the converging and diverging lines usually associated with the separation and reattachment locations (Peake and Tobak, 1980).

Several factors are believed responsible for the good agreement between computations, in which coarse grids and a simple mixing-length turbulent model are used, and experiment. First of all, the normal component of the Mach number is not large and therefore the shock-wave structure is not so difficult to capture. (In the example shown $M_N = 1.3$.) Secondly, the separated-flow region is not closed and highly turbulent fluid is not recirculating. And, as a consequence of the latter, the flow within the separated region is probably more steady than that within a two-dimensional separated region.

The strong interactions resulting from a blunt generator have been recently computed by Hung and Kordulla (1983). The computations were made using a finite-volume version of the newest implicit-explicit method of MacCormack (1982) with the zero-equation turbulence model of Baldwin and Lomax (1978) modified in the same manner as the sharp-generator case to account for the presence of the generator wall. Some example comparisons of these computations with the experimental data of Dolling and Bogdonoff (1982) are shown in Figures 5.15 and 5.16. Surface pressures along the flat plate and along the generator surface are shown. It can be inferred from these comparisons that the scale of the interaction, including its upstream influence on the oncoming flow and its height relative to the oncoming boundary-layer thickness are probably being predicted quite well, although no flow-field data are available to verify such a conclusion.

The predicted particle paths which represent streamlines in the plane of symmetry are shown in Figure 5.17 to illustrate the resolution of the flow-detail within the horseshoe vortex. A secondary vortex formed at the junction between the blunt generator and the plate (see Hung and Kordulla, 1983). The separation region formed by the horseshoe vortex is open and the vortex streams around the blunt generator.

Most of the features observed in oil-flow photographs taken during the experiment also compare favorably, at least qualitatively, with these computations. Again, it may appear surprising that the computations are doing so well, considering the grid resolution and simplicity of the turbulence model. However, the scale of the interaction is set mainly by the blunt leading edge of the generator, in contrast to the two- and three-dimensional, impinging-shock cases (e.g. see Fig. 5.5 and 5.6) in which no physical scale other than boundary-layer thickness is present.

Further study of this blunt generator case is needed to determine whether important quantities, such as heat transfer or skin friction, can be predicted. It should also be mentioned that an unsteady shock-wave structure was found experimentally and that no such unsteadiness was found in the computation.

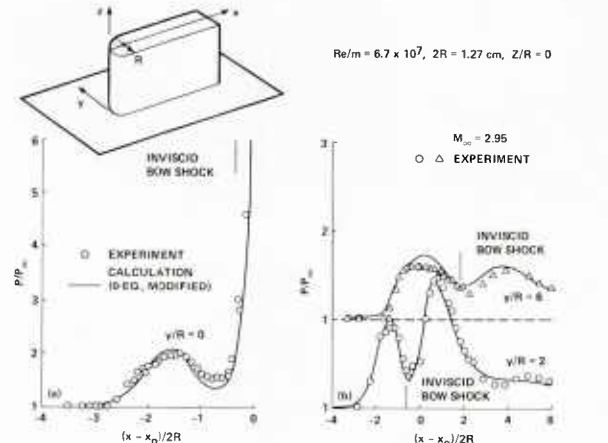


Fig. 15 — Modeling of a glancing shock-wave interaction from a blunt-plate generator: a) Pressures on the flat plate in the plane of symmetry; b) Pressures on the flat plate off the plane of symmetry.

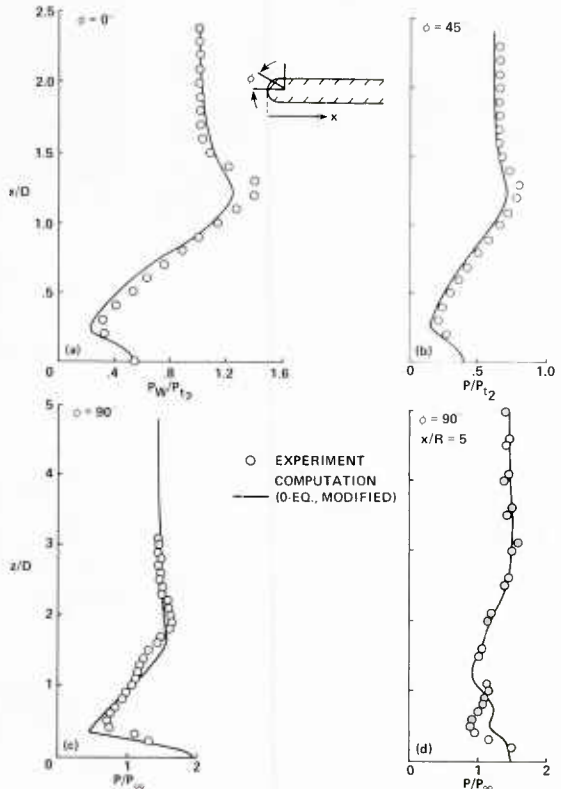


Fig. 16 — Modeling of a glancing shock-wave interaction from a blunt-plate generator: a) Pressures on the blunt-plate generator; $\phi = 0^\circ$; b) $\phi = 45^\circ$; c) $\phi = 90^\circ$; $X/D = 2.5$.

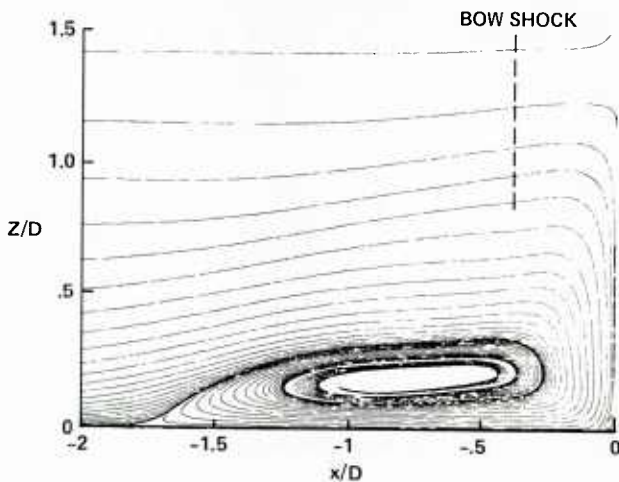


Fig. 17 — Particle paths that depict streamlines in the plane of symmetry ahead of the generator from computations of a glancing shock-wave interaction from a blunt-plate generator.

5.5.5. — Normal-Shock-Wave Interaction

Physical Characteristics. — Some of the physical characteristics are depicted in Figure 5.18. The Schlieren photographs and Mach contours from the two-dimensional experiment of East (1976) are shown. At the lowest Mach number, a weak interaction develops and very little change in the normal-shock-wave structure occurs. A thickening of the subsonic layer takes place during the movement of the viscous-layer from the supersonic to the subsonic regions. A small foot to the normal shock wave appears through a series of weak compression waves. The resulting wall-pressure distribution appears as a smoothing of the inviscid pressure jump, as we have seen previously for the weak-interacting, impinging oblique-shock flows.

Increasing the Mach number strengthens the pressure rise, and eventually the boundary-layer can no longer pass through without separating. The thickening of the viscous layer occurs sooner (farther upstream) and the series of compression waves can eventually coalesce into a distinct oblique, separation shock forming the so-called lambda foot. This oblique shock will intersect the normal shock wave at a bifurcation point. The losses through the normal shock wave are larger than those through the oblique shock wave and, therefore, the static pressure downstream of the normal shock wave is higher than that of the flow downstream of the oblique shock wave and a second rearward-running shock will form at the bifurcation to equalize the disparity.

At the higher Mach numbers, existence of a supersonic "tongue" has been observed (see for example, Kooi, 1978). At the bifurcation point there is a difference in total pressure between the flow processed by the normal and compound shock systems and a shear layer (a discontinuity surface sometimes referred to as a vortex layer) forms. Corresponding surface-pressure distribution will show a steep rise in pressures ahead of separation, a decrease in the pressure gradient over the region of separation, and gradual increase to a level somewhat below the inviscid jump pressure for a normal shock.

A Comparison of Computation and Experiment (Small Separation). — A certain degree of success has been achieved in modeling the moderately strong normal-shock interaction where separation is rather small or nonexistent. A more recent example is illustrated in Figures 5.19 and 5.20. Computations using the MacCormack hybrid method and the two-equation eddy-viscosity model of Wilcox and Rubesin (1980) were reported by Om *et al.* (1982). The grid (Table V) was chosen in order to provide adequate capture of the shock structure and to resolve the near-wall region of the turbulent boundary-layer. In Figure 5.19, pressure-distributions and velocity-profile shape parameters are compared with the experiment reported by Om *et al.* (1982) for a range of Mach number and Reynolds number. The experiment was performed in an axisymmetric test section so that three-dimensional effects could be eliminated; therefore, a high degree of confidence can be placed in the experimental trends that are observed.

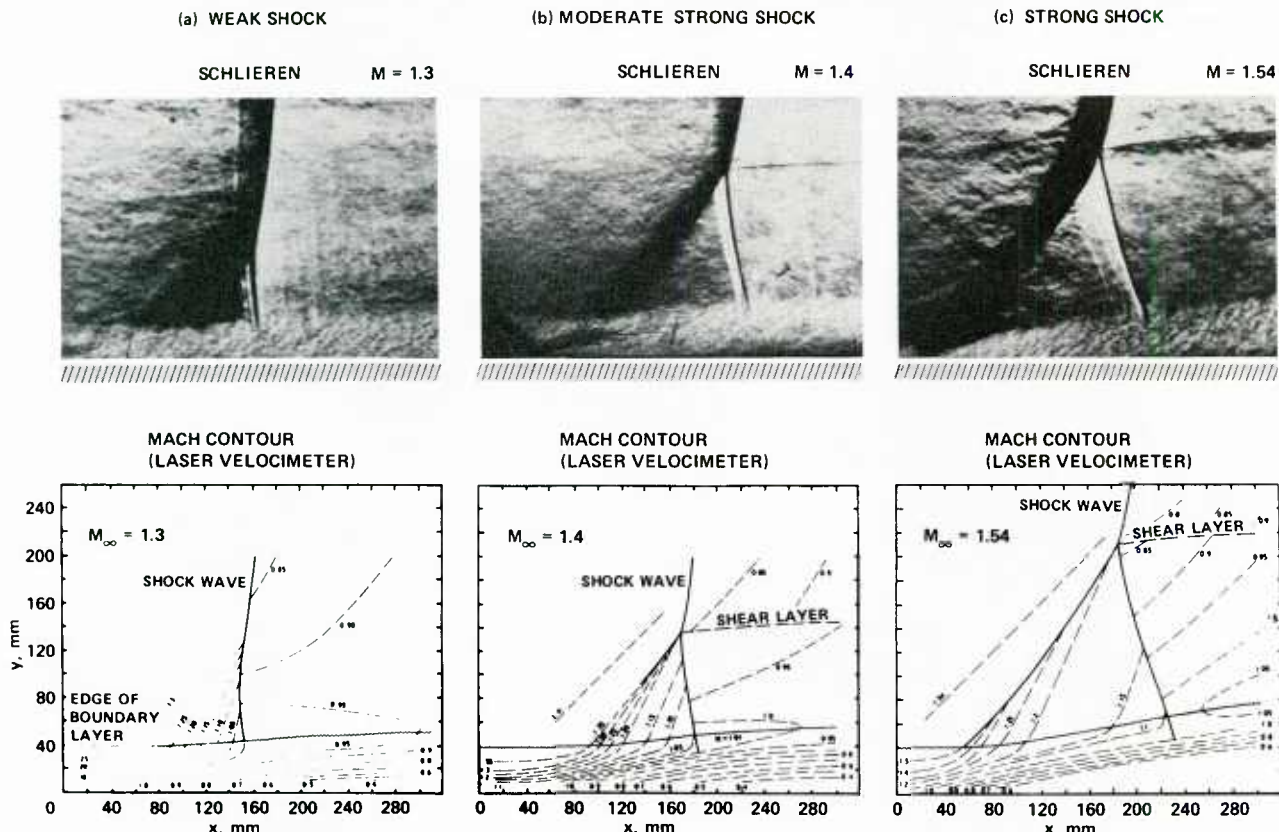


Fig. 18 — Physical characteristics of normal shock-wave interactions: a) Weak shock; b) Moderately strong shock; c) Strong shock.

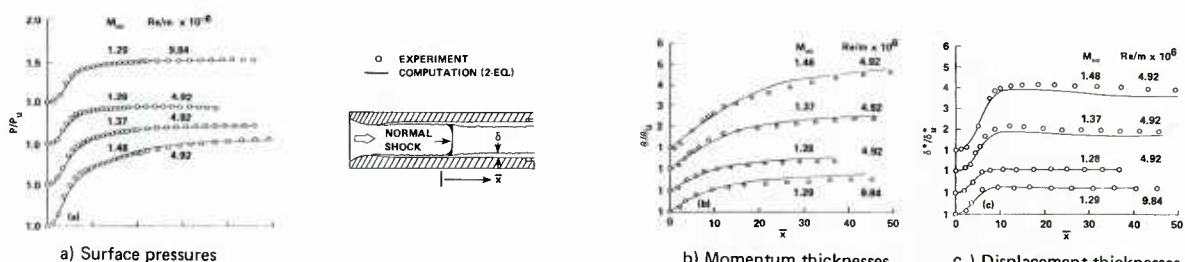
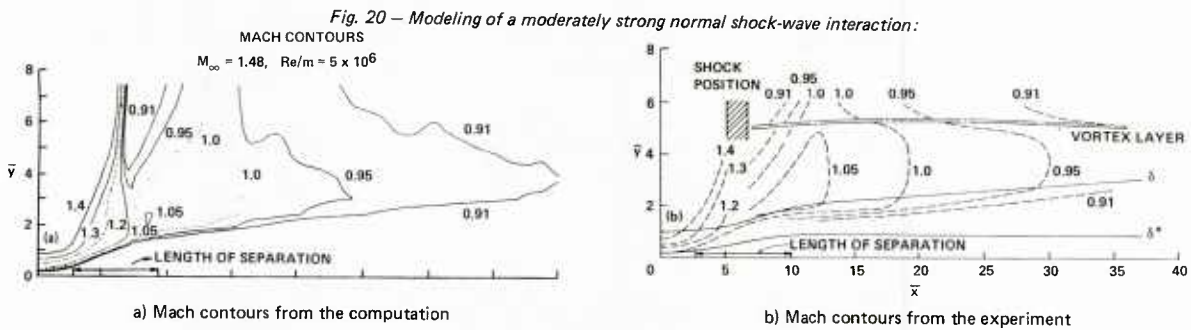


Fig. 19 — Modeling of a moderately strong normal-shock wave interaction for various Mach and Reynolds numbers:



The effects of Mach number and Reynolds number are predicted by the computations, except possibly in the immediate vicinity of the shock at the highest Mach numbers. Mach contours are compared in Figure 5.20 for the highest Mach number case. For the most part the shock structure is also predicted by the computations. The shock is weakened because of viscous-layer thickening near the separation, and a series of compression waves coalesces into the normal shock. A smaller region of supersonic flow is predicted. One would not expect to capture any discontinuity surface in total pressure that would lead to a so-called vortex layer because the grid is too coarse. The extent of separation in the prediction is somewhat smaller than that of the experiment.

Influence of Turbulence Model Selection. — Studies have shown that the turbulence model has an influence on the predictions for these normal shock flows (Viegas and Horstman, 1979). An illustrative example from that study is shown in Figure 5.21. Although the turbulence model has little influence on the prediction of the overall pressure rise, models that use information on the turbulent kinetic energy changes through the shock wave to form the velocity scale of the eddy viscosity provided better estimates of the skin friction and the development of the boundary-layer shape parameters. As reported by Mateer and Viegas (1979), trends with Reynolds number over a wide, practical range are also predicted with those higher-order eddy-viscosity models. However, even these higher-order models have to be applied with caution when wall skin friction or heat transfer is being predicted, because the low-Reynolds-number functions, required when integrating the equation system from a wall boundary out into the flow field have not always been developed adequately.

The reader is referred to a recent paper by Viegas and Rubesin (1983) in which that aspect of higher-order eddy-viscosity modeling for the moderately strong, normal-shock problem is studied. Figure 5.22 summarizes the main points from that study. When integrating from the wall boundary, only the Wilcox-Rubesin model gives skin-friction predictions that compare reasonably well with experiment. (Note the scale change in Figures 5.22 a and b.) In developing this model's low-Reynolds-number functions, particular attention was given to ensure that modeling was adequate for attached, large adverse-pressure-gradient flows.

On the other hand, the model of Jones and Launder (1971), with its original formulation of the low-Reynolds-number terms, and one developed by Chien (1982) to minimize computational stiffness encountered when applying the model of Jones and Launder, do not have the same degree of success. However, they did provide adequate predictions of surface-pressure and velocity-profile shapes. Wall functions were developed by Viegas and Rubesin (1983) for all these models to eliminate the need for integration to the wall. Uniformly successful predictions of the skin friction was achieved with all models, as shown in the second part of Figure 5.22. It is interesting to note that McDonald (1982) also reported predictions of this experimental data. He used an implicit numerical scheme with a different grid along with the Jones and Launder (1971) turbulence model. He employed their low Reynolds number formulation and integrated to the wall. His predicted pressures and skin friction agree with those reported by Viegas and Rubesin (1983) when they used the same model with integration to the wall. It is encouraging that two different numerical methods give essentially the same results using the same turbulence model because more credence can be placed on conclusions regarding the attributes of the various models.

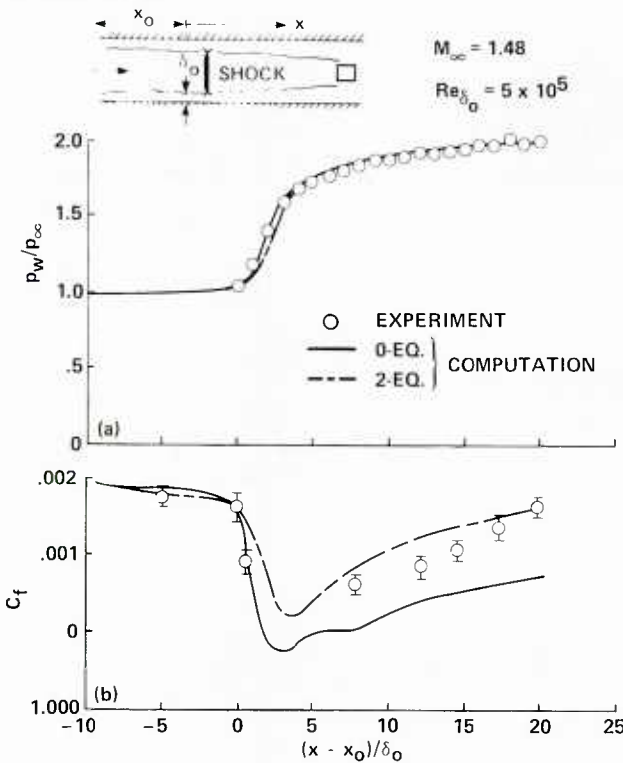


Fig. 21 — Effect of turbulence modeling on moderately strong normal shock-wave interactions: a) Surface pressure; b) Skin friction.

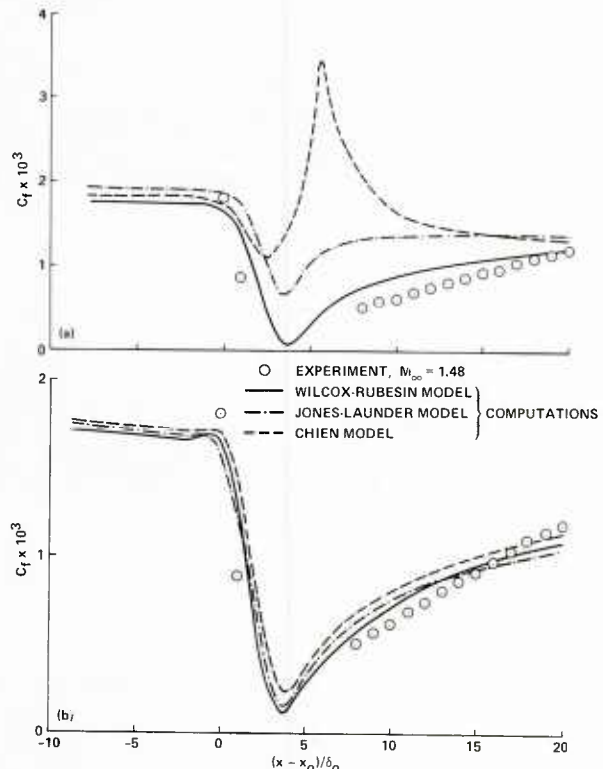


Fig. 22 — Effects of low-Reynolds-number-term treatment in 2-eq. models used to predict moderately strong normal shock-wave interactions: a) Integration to the wall; b) Wall-function treatment.

In addition to developing the wall functions for the two-equation models, the study of Viegas and Rubesin (1983) also showed that the computer code became more robust and converged faster. Together with the savings in grid points near the wall and the advantage of robustness, computational times using wall functions were decreased by nearly one order of magnitude over those using integration to the wall boundary.

A Comparison of Computation and Experiment (Large Separation). — Although the axisymmetric bench mark experimental flows have the advantage of minimizing three-dimensional effects, they are limited to moderately strong interactions because the flow is confined and separation extent is limited. Therefore, one must exercise caution in generalizing these results for two-dimensional situations, in which for the same free-stream Mach number, separation may be considerably larger. In those cases, predictions from computations are not as good. To illustrate this aspect, unpublished computations by C. C. Horstman of the Ames Research Center for the experiment reported by Délery (1983) are presented in the next figures.

In the experiment by Délery, a region of supersonic flow was achieved in an asymmetric channel formed by having a bump on one wall of a rectangular test section. In addition to forming a lambda shock foot, a separated region developed which closed downstream of the junction formed by the bump and the channel wall. Although the flow was choked across the channel, the significant viscous interaction effects only occurred on the bump-wall side. The computations were made using the new implicit-explicit method of MacCormack (1982) along with the two-equation turbulence model of Jones and Launder (1971). Both walls were treated viscously, but the grid resolution was rather coarse on the far wall where interaction effects were small. The equations were integrated to the wall.

An interferogram taken of the flow above the bump-wall is shown in Figure 5.23. Mach contours determined from the interferogram are also shown. They can be compared with the computed contours using two different turbulence models. The unmodified models of Jones and Launder (1971), with the low-Reynolds-number formulation of Chien (1982), predicts a region of separation smaller than that found experimentally. As a result, the shock structure also differs in that the computed lambda foot of the shock is weaker and the zone of supersonic flow smaller. As mentioned previously, the low-Reynolds-number functions of the turbulence model may be affecting these calculations, but at the time they were made, that weakness of this model had not been reported. Horstman made another computation using modification to the model that had provided some improvements in other separated-flow computations (see Horstman, 1983) to see if the correct flow field could be predicted. The results, shown in Figures 5.23 and 5.24, provide a better comparison for the Mach contours and extent of separation and pressure recovery through the interaction. It is worth noting that these flows also have unsteady aspects that may influence our ability to model the separated region.

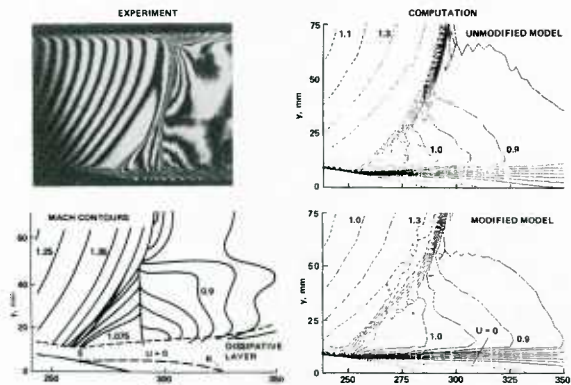


Fig. 23 — Modeling of strong normal shock-wave interactions: comparison of shock structure from experiment and computation.

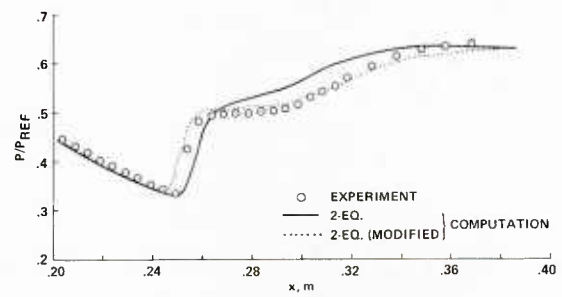


Fig. 24 — Modeling of strong normal shock-wave interactions: surface pressures.

The velocity and turbulence profiles that develop in the shear layer during this strong normal-shock-wave interaction behave like those that develop downstream of a rearward-facing step (Seegmiller *et al.*, 1978; Délery, 1983). They are illustrated and compared with the computations of Horstman in Figure 5.25. In step flow studies (Driver and Seegmiller, 1982; and Driver *et al.*, 1983) which eliminates uncertainties in separation location and the complicating presence of unsteady shocks, were not found to work as well as Reynolds-stress models for predicting the flow within the separated region. The latter models remove the assumption that the stresses respond immediately to changes in the strain rate and therefore constitute a more plausible physical description in the case of strong interactions. The latter models are only now being implemented in compressible Navier-Stokes codes (see Vandromme *et al.*, 1983).

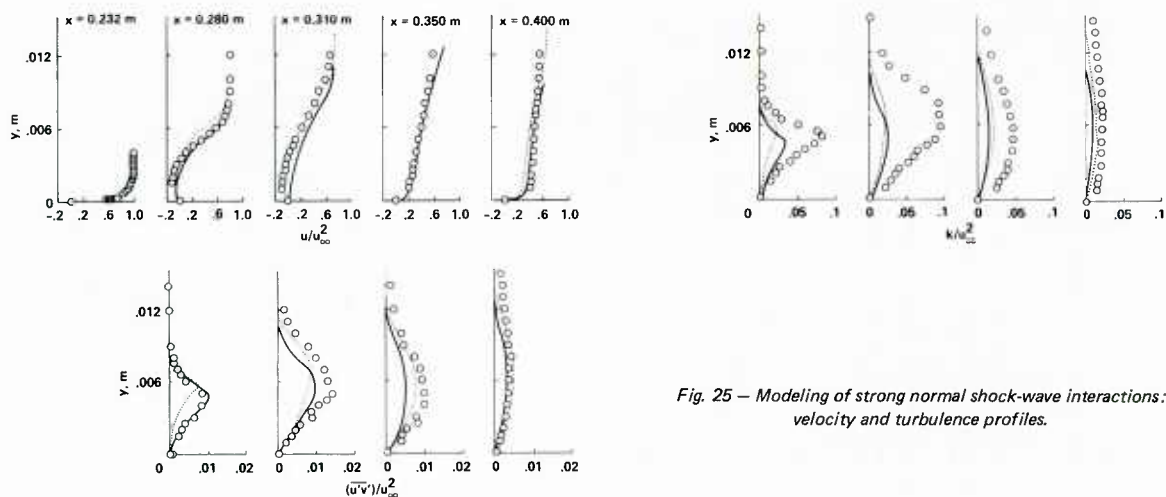


Fig. 25 — Modeling of strong normal shock-wave interactions: velocity and turbulence profiles.

5.5.6. — Transonic Flows with Shock Waves

Physical Characteristics. — The flow field structure in the vicinity of the shock wave formed in transonic flows is essentially the same as that discussed in the previous section and will not be described again here. However, the elliptic character of the transonic flows precludes knowing a priori the shock strength or position even in the inviscid regions of the flow except in very weak interaction cases. Therefore computations must include a larger extent of the flow domain up- and down-stream of the shock wave and other viscous effects away from the vicinity of the shock wave may have a significant influence, e. g., an airfoil near wake.

A Comparison of Computation and Experiment. — Development of computational methods employing the Navier-Stokes equations for airfoils and wings has been under intense development over the past decade. Some of the first computations for a non-lifting airfoil were undertaken by Deiwert and reported in McDevitt *et al.* (1975). The explicit time-marching code of MacCormack was used, grids were coarse, and turbulence modeling was identified as an impediment to accurate solutions for instances where separation was present such as near trailing-edges for subcritical flow and at shock waves for supercritical flow. Computation times were excessive. Since then, more efficient numerical methods have evolved and additional benchmark flows have become available which provide additional opportunities to assess progress. See Table VI. Two examples will be discussed. The flows are two-dimensional and were chosen as test cases for the AFSOR/HTTM-Stanford Conference (Kline *et al.*, 1980, 1982). The first is an airfoil flow without separation. The next is an axisymmetric flow over a circular arc bump where separation forms at the shock wave.

Mehta's Navier-Stokes calculations (1983) of the unseparated airfoil flow are among the most accurate ones known to the authors. A comparison with the experimental pressure distribution is shown in Figure 5.26. Mehta employed the implicit method of Beam and Warming (1978), an O-grid, and used a 0-equation turbulence model. The experimental lift coefficient was matched closely by performing calculations at various angle of attack as recommended by the data evaluators (Kline *et al.*, 1980). As the comparison shows, the solutions are sensitive to grid fineness. Computation and experiment agree only for the finest grid. It was necessary to cluster grid in the vicinity of the shock wave to capture it and resolve the viscous interaction near its foot. Also, he found it necessary to locate his first point away from the wall below a position where $y^+ = 1$ in order to provide skin friction results that were independent of this first grid point position.

Accuracy evaluation, not computational efficiency, was the primary motivation for Mehta's Navier-Stokes computations. Actually, coupling methods which employ integral boundary layer procedures together with potential flow solvers presently provide the best practical methods for predicting unseparated airfoil flows. See for example, Kline *et al.* (1982). However, Coakley (1983) reports accurate results with a coarser grid and convergence within two to three hundred time steps which appears to make the accuracy and computational efficiency of his Navier-Stokes computations competitive with the coupling methods.

A comparison of the airfoil loads from the most recent Navier-Stokes computations and two coupling method computations taken from Kline, *et al.* (1982) are given in the tabulation of Figure 5.27. The upper portion of the table gives the values measured in the experiment and suggested corrected values for interference effects. The coupling method computations and the Navier-Stokes computations of Mehta and Coakley were made by matching the lift coefficient. They predicted the experimental drag to within about 10 drag counts and their angle of attack differed by less than 0.25° with the corrected experimental value. The differences are within the range of experimental accuracy and so the predictions probably represents the best that can be done today for unseparated airfoil flows. The friction drag accounts for less than half of the total and varies little between these methods indicating an insensitivity to differences in turbulence modeling. Coakley (1983) tested the sensitivity of his solutions to turbulence model choice. His results indicate that while the total drag is insensitive to the choice significant differences in the local values of skin friction occur on the airfoil suction side downstream of the shock wave. But there the level of skin friction is small and doesn't contribute much to the total friction drag. Kordulla made his Navier-Stokes calculations at the uncorrected experimental angle of attack and they predict somewhat higher lift, which might be expected. But, the total drag is overpredicted by an amount not expected from the differences in incidence angle. He did not speculate on the causes for this discrepancy. However, far field boundary position may be influencing his results.

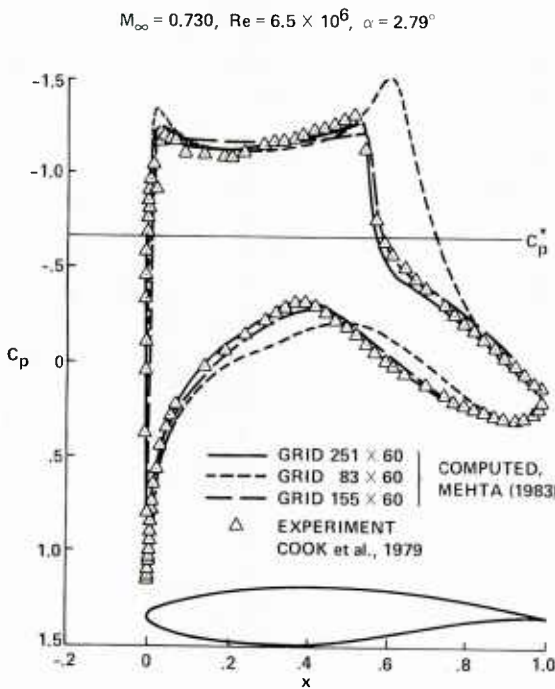
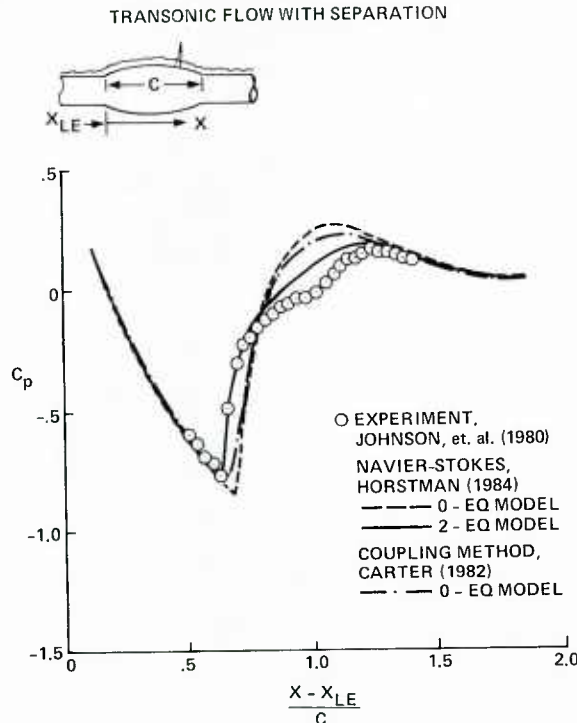


Fig. 26 — A comparison of computation and experiment for the RAE 2822 airfoil with a strong shock wave but no separation.

	M _∞	ANGLE	C _L	C _{Dp}	C _{Df}	C _D	GRID x, y
EXPERIMENT (COOK <i>et al.</i> , 1979)	0.730	3.19	0.803	—	—	0.0168	—
EXPERIMENT CORRECTED DATA	0.730	2.79	0.803	—	—	0.0168	—
COUPLING METHODS							
MELNIK (1982)	0.730	2.54	0.803	0.0100	0.0057	0.0157	0 - 160, 32
LABALLEUR (1982)	0.730	2.79	0.787	0.0111	0.0055	0.0166	0 - 181, 27
0.730	2.85	0.800	0.0119	0.0055	0.0186	0 - 181, 27	
NAVIER STOKES METHODS							
KORDULLA (1982)	0.730	3.19	0.838	—	—	0.0278	C - 216, 60
0.730	3.19	0.838	—	—	—	0.0242	C - 108, 32
MEHTA (1983)	0.730	2.79	0.793	0.0118	0.0059	0.0177	0 - 251, 60
COAKLEY (1983)	0.720	2.50	0.813	0.0118	0.0056	0.0174	C - 180, 50
(VARIATION WITH 2-EQ. TURBULENCE MODEL)	0.730	2.60	0.809	0.0104	0.0065	0.0167	C - 180, 50
0.730	2.60	0.785	0.0096	0.0069	0.0167	0.0167	C - 160, 50

Fig. 27 — Comparison of various methods for calculating airfoil loads with strong shock waves but no separation.

The next example is the transonic, shock-induced separated flow studied experimentally by Johnson *et al.* (1980). The flow developed over a circular arc section which was formed on the outer diameter of a long hollow cylinder whose axis was aligned in the flow direction. The axisymmetric configuration was chosen to eliminate 3-dimensional experimental effects which can be present in airfoil studies. The pressure distribution is compared with several computations in Figure 5.28. The Navier-Stokes computations are taken from Johnson and Horstman (1984) and reflect improvements to their previously reported calculations. The implicit-explicit scheme of MacCormack (1981) was used and two turbulence models were employed: the 0-equation Cebeci-Smith model and the 2-equation Jones-Launder model with terms added to account for curvature effects. Another computation reported by Carter (1982) is also shown. He employed the inverse finite difference boundary-layer procedure discussed previously and coupled it to a fully conservative potential flow solver. The Navier-Stokes and coupling procedure computations that employ the same 0-equation turbulence model agree with one another but not with the data downstream of the shock wave where the flow is separated. The 2-equation model Navier-Stokes solutions agree somewhat better with the experiment downstream of the shock wave, but evidently more improvements in the turbulence model are necessary if the proper pressure plateau is to be predicted. The mean and fluctuating velocity profiles from the 2-equation model solutions are compared with the data at several selected stations in Figure 5.29. Agreement is reasonably good, except just downstream of the shock wave where the shear and turbulent kinetic-energy is overpredicted and turbulence model improvement is needed.



5.5.7. — Unsteady Flows

The time accurate methods described previously can be applied, at least in principle, to unsteady flows. To date, rather successful calculations of some unsteady flows with relatively narrow frequency bands have been undertaken. Readers are referred to a recent summary paper by Deiwert and Bailey (1983) for a detailed discussion. Here we will mention only the essence of the underlying assumptions and give one illustration.

In order to use the time-dependent, mass-averaged form of the equations, the averaging time must be small relative to the aerodynamic time scale of interest, but large relative to the time scale associated with the turbulence. Chapman (1979) compared the known non-dimensional frequency range of many typical aerodynamic flows with those of large scale turbulent eddies for a range of Mach numbers. The results are reproduced in Figure 5.30. The mean frequency of the large scale eddies corresponds to their mean-burst frequency scaled on boundary-layer thickness. It depends weakly on length Reynolds number. All of the unsteady aerodynamic flows noted have characteristic frequencies that are one to two orders of magnitude smaller than those of the large scale eddies. Hence it should be possible to employ the usual steady-flow turbulence models and accurately simulate the time varying aerodynamic changes with the Reynolds-averaged form of the Navier-Stokes equations. These arguments have been used in part to justify the remarkably good results from computations of buffet onset due to shock induced separation [Levy (1978), Levy and Bailey (1981)], aileron buzz [Steger and Bailey (1980)], dynamic stall [Deiwert and Bailey (1983)], and oscillating airfoils [Chyu and Kuwahara (1982)].

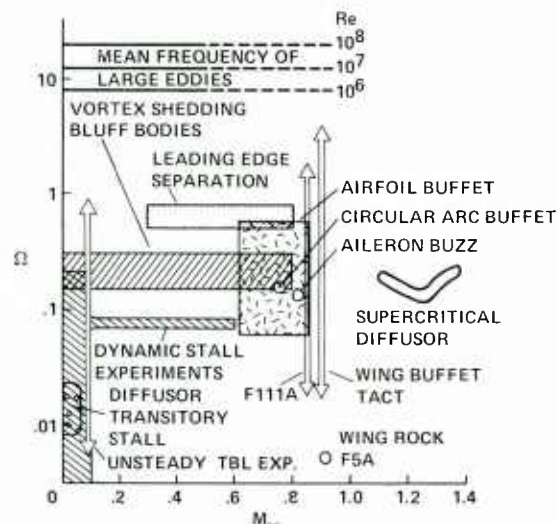


Fig. 30 — Comparison of frequency range of unsteady flows with mean frequency of large-scale turbulent eddies.

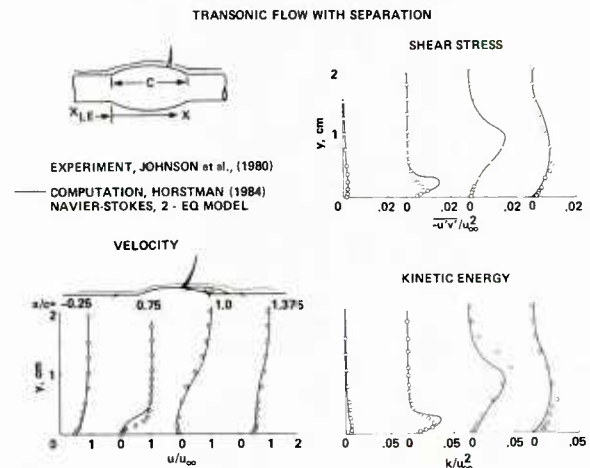


Fig. 29 — A comparison of computation and experiment for a transonic flow with shock-induced separation: velocity and turbulence profiles.

Fig. 28 — A comparison of computation and experiment for a transonic flow with shock-induced separation: Pressure distribution.

To illustrate what has been achieved some of Levy's results are given in Figures 5.31 and 5.32. He computed the flow over an 18% thick biconvex airfoil at zero incidence undergoing self excited periodic oscillations caused by coupling of shock-induced and trailing-edge separation. A comparison of shadowgraphs from the experiment and Mach contours from the computations taken from Seegmiller *et al.* (1978) is shown in Figure 31. The times represent fractions of the dimensionless periodic cycle time of the oscillating flow. Comparisons between the experiment and computations are made at different times to illustrate that the computations reproduce the physical characteristic of the experiment even though the actual frequency of oscillation differed by about 20 percent. A comparison with the surface pressure variation at four different locations on the airfoil is shown in Figure 5.32. The oscillations on the upper and lower surfaces are a half period out of phase with each other. The frequency of oscillation from the computation differs by about 20 percent, but the wave forms and peak pressures compare quite well. Comparisons of velocity profiles in the viscous shear layer also show good agreement. See Marvin *et al.* (1979).

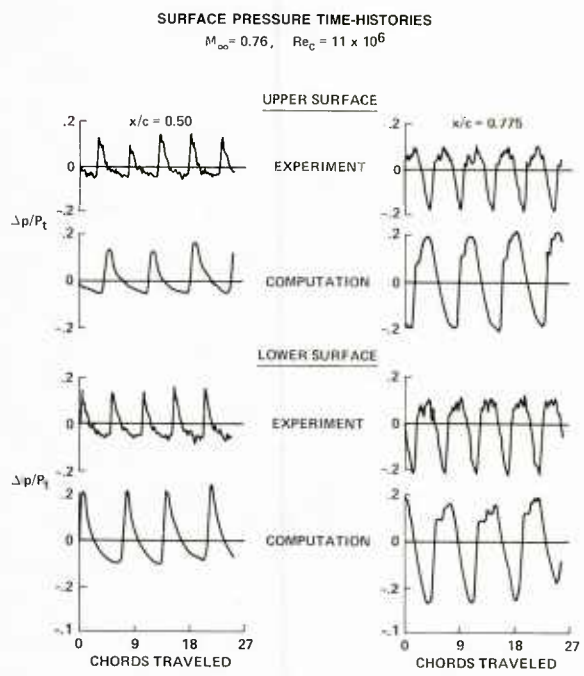
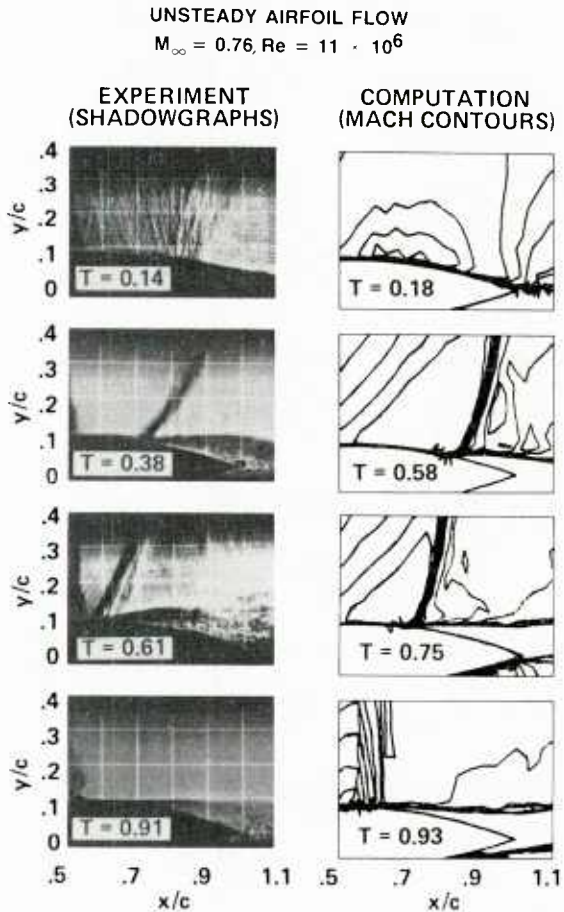


Fig. 32 — Comparison of computation and experiment for an unsteady flow involving shock-induced separation: surface pressure time histories.

Fig. 31 — Comparison of computation and experiment for an unsteady flow involving shock-induced separation: shadowgraphs and computed Mach contours.

5.6. — Concluding Remarks

The mass-averaged Navier-Stokes computer codes in use today are still in their developmental stages. They represent a compromise between the choice of numerical algorithm, grid, and turbulence model. The compromise is dictated by constraints of numerical efficiency and the lack of an adequate turbulence model. Provided that the adequate safeguards are used to ensure numerical resolution, it is apparent that the computations employing eddy-viscosity turbulence models can give a qualitatively good representation of many two- and three-dimensional, complex aerodynamic flows involving shock wave and separation. Although flow details within separated regions cannot be predicted with complete confidence, the solutions can now provide a bridge for connecting computations on either side of embedded separated regions.

Of the work remaining in developing these codes into predictive tools, proper physical modeling remains paramount. The challenges of better numerical accuracy and resolution along with better turbulence modeling are areas for further exploration. With regard to the latter, it is clear that some distinct advantages are gained by employing higher-order turbulence models. For example, they provide unambiguous, albeit approximate, determinations of the length and velocity scales needed to define an effective viscosity, and they provide inherent means to allow turbulence to adjust itself appropriately to rapid changes in the mean flow. Whether they can be improved to provide completely adequate modeling or whether they must give way to Reynolds stress modeling is a debatable issue, the resolution of which requires additional study.

More has to be done to determine the causes and effect of flow unsteadiness in shock wave interactions and its importance in modeling both two- and three-dimensional flows. And, more has to be done experimentally to define flow field structures and critical parameters, to gain further understanding of modeling, and to provide well-documented bench mark tests against which progress can be gauged.

5.7. — References

Bailey, H. E. (1982): The 1980-81 AFSOR/HTTM-Stanford Conference on Complex Turbulent Flows: Comparison of Computation and Experiment, Vol. III. Comparison of Computation with Experiment and Computers Summary Reports. S. J. Kline, B. J. Cantwell and G. M. Lilley, eds., pp. 1303-1304.

Baldwin, B. S. and MacCormack, R. W. (1974): Numerical Solution of a Strong Shock Wave With a Hypersonic Turbulent Boundary-Layer. AIAA Paper 74-558, Palo Alto, Calif.

Baldwin, B. S. and Rose, W. C. (1975): Calculations of Shock-Separated Turbulent Boundary-Layers. NASA SP-347.

Baldwin, B. S. and Lomax, H. (1978): Thin Layer Approximation and Algebraic Model for Separated Turbulent Flows. AIAA Paper 78-257, Huntsville, Ala.

Bannink, W. J. and Nebbeling, C. (1978): Measurement of the Supersonic Flow Field Past a Slender Cone at High Angles of Attack. High Angle of Attack Aerodynamics, AGARD CP-247, Paper 22.

Beam, R. M. and Warming, R. F. (1978): An Implicit Factored Scheme for the Compressible Navier-Stokes Equations. AIAA Journal, Vol. 16, No. 4, pp. 393-402.

Briley, W. R. and McDonald, H. (1977): Solution of the Multidimensional Compressible Navier-Stokes Equations by a Generalized Implicit Method. J. Comput. Phys., Vol. 24, No. 4, p. 372.

Brosh, A.; Kussoy, M. K. and Hung, C. M. (1983): An Experimental and Numerical Investigation of the Impingement of an Oblique Shock Wave on a Body of Revolution. AIAA Paper 83-1757, Danvers, Mass.

Cambier, L.; Ghazzi, W.; Veuillot, J. P. and Viviand, H. (1981): Une approche par domaines pour le calcul d'écoulements compressibles. 5^e Coll. Int. sur les Méthodes de Calcul Scientifique et Technique, INRIA, TP-ONERA No. 1981-143.

Carter, J. E. and Vasta, V. N. (1982): Analysis of Separated Boundary-Layer Flows, Proceedings of the 8th International Conference on Numerical Methods in Fluid Dynamics, June 1982, Aachen, W. Germany.

Chapman, D. R. (1979): Dryden Lectureship in Research, Computational Aerodynamics Development and Outlook. AIAA Journal, Vol. 17, No. 12, pp. 1293-1313.

Chapman, D. R. (1981): Trends and Pacing Items in Computational Aerodynamics. Seventh International Conference on Numerical Methods in Fluid Dynamics, Lecture Notes in Physics, Springer-Verlag.

Chien, K.-Y. (1982): Predictions of Channel Boundary-Layer Flows with a Low-Reynolds-Number Turbulence Model. AIAA Journal, Vol. 20, No. 1, pp. 33-38.

Chyu, W. J. and Kawahara, K. (1982): Computations of Transonic Flow over an Oscillating Airfoil with Shock-Induced Separation. AIAA Paper 82-350 (Jun. 1982).

Coakley, T. J., Viegas, J. R. and Horstman, C. C. (1977): Evaluation of Turbulence Models for Three Primary Types of Shock Separated Boundary-Layers. AIAA Paper 77-692, Albuquerque, N. Mex.

Coakley, T. J. (1981): Numerical Method for Gas Dynamics Combining Characteristics and Conservation Concepts. AIAA Paper 81-1257, Palo Alto, CA.

Coakley, T. J. (1983): Turbulence Modeling Methods for the Compressible Navier-Stokes Equations. AIAA Paper 83-1958, Danvers, MA (Jul. 1983).

Coakley, T. J. (1983): Implicit Upwind Methods for the Compressible Navier-Stokes Equations. AIAA Paper 83-1953, Danvers, Mass.

Degani, D. and Schiff, L. B. (1983): Computation of Supersonic Viscous Flows Around Pointed Bodies at Large Incidence. AIAA Paper 83-0034, Reno, Nev.

Deiwert, G. S. (1982): The 1980-81 AFSOR/HTTM-Stanford Conference on Complex Turbulent Flows: Comparison of Computation and Experiment, Vol. III. Comparison of Computation with Experiment and Computers Summary Reports. S. J. Kline, B. J. Cantwell and G. M. Lilley, eds., pp. 1337-134 .

Deiwert, G. S. and Bailey, H. E. (1983): Time Dependent Finite-Difference Simulation of Unsteady Interactive Flows. Second Symposium on Numerical and Physical Aspects of Aerodynamic Flows, 17-20 January, California State University, Long Beach, California.

Déléry, J. M. (1983): Experimental Investigation of Turbulent Properties in Transonic Shock/Boundary-Layer Interaction. AIAA Journal, Vol. 21, No. 2, pp. 180-185.

Dolling, D. S. and Or, C. T. (1983): Unsteadiness of Shock Wave Structure in Attached and Separated Compression Ramp Flow Fields. AIAA Paper 83-1715, Danvers, Mass.

Dolling, D. S. and Bogdonoff, S. M. (1982): Blunt Fin-Induced Shock Wave/Turbulent Boundary-Layer Interaction. AIAA Journal, Vol. 20, No. 12, pp. 1674-1680.

Driver, D. M. and Seegmiller, H. L. (1982): Features of a Reattaching Turbulent Shear Layer Subject to an Adverse Pressure Gradient. AIAA Paper 82-1029.

Driver, D. M., Seegmiller, H. L. and Marvin, J. G. (1983): Unsteady Behavior of a Reattaching Shear Layer. AIAA Paper 83-1712, Danvers, Mass.

East, L. F. (1976): The Application of a Laser Anemometer to the Investigation of Shock-Wave Boundary-Layer Interactions. AGARD Conference Proceedings No. 193 on Applications of Non-Intrusive Instrumentation in Fluid Flow Research, Paper 5.

Holden, M. S. (1972): Shock Wave-Turbulent Boundary-Layer Interaction in Hypersonic Flow. AIAA Paper 72-74, San Diego, Calif.

Horstman, C. C.; Settles, G. S.; Vas, I. E.; Bogdonoff, S. M. and Hung, C. M. (1977): Reynolds Number Effects on Shock Wave Turbulent Boundary-Layer Interaction. AIAA Journal, Vol. 15, No. 8, pp. 1152-1158.

Horstman, C. C. and Hung, C. M. (1979): Computation of Three Dimensional Turbulent Separated Flows at Supersonic Speeds. AIAA Paper 79-002, New Orleans, La.

Horstman, C. C. (1983): Numerical Simulation of Turbulent Trailing Edge Flows. Second Symposium on Numerical and Physical Aspects of Aerodynamic Flows, Long Beach, Calif.

Horstman, C. C. and Johnson, D. A. (1984): Prediction of Transonic Separated Flows, Accepted as a TN for the AIAA Journal; to be published in 1984.

Horstman, C. C. (1984): A Computational Study of Complex Three-Dimensional Compressible Turbulent Flow Fields. AIAA Paper 84-1556, Snowmass, CO.

Hung, C. M. and MacCormack, R. W. (1977): Numerical Simulation of Supersonic and Hypersonic Turbulent Compression Corner Flows. AIAA Journal, Vol. 15, No. 3, pp. 410-416.

Hung, C. M. and MacCormack, R. W. (1978): A Numerical Solution of Three-Dimensional Shock Wave and Turbulent Boundary-Layer Interaction. AIAA Journal, Vol. 16, pp. 1090-1096.

Hung, C. M. (1982): The 1980-81 AFSOR/HTTM-Stanford Conference on Complex Turbulent Flows: Comparison of Computation and Experiment. Vol. III. Comparison of Computation with Experiment and Computers Summary Reports. S. J. Kline, B. J. Cantwell and G. M. Lilley, eds., pp. 1372-1374.

Hung, C. M. and Kordulla, W. (1983): A Time Split Finite Volume Algorithm for Three-Dimensional Flow Field Simulations. AIAA Paper 83-1957, Danvers, Mass.

Johnson, D. A.; Horstman, C. C. and Bachalo, W. D. (1980): A Comprehensive Comparison between Experiment and Prediction for a Transonic Turbulent Separated Flow. AIAA Paper 80-1407, Snowmass, CO.

Jones, W. P. and Launder, B. E. (1971): The Prediction of Laminarization with a Two-Equation Model of Turbulence. International Journal of Heat and Mass Transfer, Vol. 15, Pergamon Press.

Kayser, L. D. and Sturek, W. B. (1978): Experimental Measurements in the Turbulent Boundary-Layer of a Yawed, Spinning Ogive-Cylinder Body of Revolution at $M=3$. Part II. Data Tabulation. ARBRL-MR-02813, U.S. Army Ballistic Research Laboratory, ARRADCOM, Aberdeen Proving Ground, Md.

Keys, J. W. (1977): Correlation of Turbulent Shear Layer Attachment Peak Heating Near Mach 6. AIAA Journal, Vol. 15, No. 12, pp. 1821-1823.

Kline, S. J.; Cantwell, B. J. and Lilley, G. M., eds. (1981): The 1980-81 AFSOR/HTTM-Stanford Conference on Complex Turbulent Flows: Comparison of Computation and Experiment. Vol. I. Objectives, Evaluation of Data, Specifications of Test Cases, Discussion, and Position Papers. Published and Distributed by Thermosciences Div., Mechanical Engineering Department, Stanford U., Stanford, Calif.

Kooi, J. W. (1978): Influence of Free-Stream Mach Number on Transonic Normal Shock Wave/Turbulent Boundary-Layer Interaction. NLR MD 78013 U.

Kordulla, W. and MacCormack, R. W. (1982): Transonic-Flow Computation Using an Explicit-Implicit Method. Proceedings of the 8th International Conference on Numerical Methods in Fluid Dynamics, Aachen, West Germany, June 1982.

Kussoy, M. I. and Horstman, C. C. (1975): An Experimental Documentation of a Hypersonic Shock-Wave Turbulent Boundary-Layer Interaction Flow-With and Without Separation. NASA TM X-62, 412.

Kussoy, M. I., Horstman, C. C. and Viegas, J. R. (1980): An Experimental and Numerical Investigation of a 3-D Shock Separated Turbulent Boundary-Layer. AIAA Journal, Vol. 18, No. 12, pp. 1477-1484.

Law, C. H. (1974): Supersonic Turbulent Boundary-Layer Separation. AIAA Journal, Vol. 12, No. 6, pp. 794-797.

LeBalleur, J. C. (1981): The 1980-81 AFSOR/HTTM-Stanford Conference on Complex Turbulent Flows: Comparison of Computation and Experiment. Vol. III. Comparison of Computation with Experiment and Computers Summary Reports. S. J. Kline, B. J. Cantwell and G. M. Lilley, eds., pp. 1411-1417.

Levy, L. L., Jr. (1978): Experimental and Computational Steady and Unsteady Transonic Flows About a Thick Airfoil. AIAA Journal, Vol. 16, No. 6, pp. 564-572.

Levy, L. L., Jr. and Bailey, H. E. (1981): Computation of Airfoil Buffet Boundaries. AIAA Journal, Vol. 19, No. 10, pp. 1488-1490.

Liou, M. S.; Coakley, T. J. and Bergman, M. Y. (1981): Numerical Simulation of Transonic Flow in Diffusers. AIAA Paper 81-1632, Palo Alto, Calif.

MacCormack, R. W. (1971): Numerical Solution of the Interaction of a Shock Wave with a Laminar Boundary-Layer. Lecture Notes in Physics, Vol. 8, Springer-Verlag, pp. 151-163.

MacCormack, R. W. (1976): An Efficient Numerical Method for Solving the Time-Dependent Compressible Navier-Stokes Equations at High Reynolds Number. NASA TM X-73, 129.

MacCormack, R. W. (1982): A Numerical Method for Solving the Equations of Compressible Viscous Flow. AIAA Journal, Vol. 20, No. 9, pp. 1275-1281.

McDonald, H. (1982): The 1980-81 AFSOR/HTTM-Stanford Conference on Complex Turbulent Flows: Comparison of Computation and Experiment. Vol. III. Comparison of Computation with Experiment and Computers Summary Reports. S. J. Kline; B. J. Cantwell and G. M. Lilley eds., pp. 1424-1427.

McRae, D. S.; Peake, D. J. and Fisher, D. F. (1980): A Computational and Experimental Study of High Reynolds Number Viscous/Inviscid Interaction about a Cone at High Angle of Attack. AIAA Paper 80-1422, Snowmass, Colo.

Marvin, J. G.; Horstman, C. C.; Rubesin, M. W.; Coakley, T. J. and Kussoy, M. I. (1975): An Experimental and Numerical Investigation of Shock-Wave-Induced Turbulent Boundary-Layer Separation at Hypersonic Speeds. AGARD-CCP 168.

Marvin, J. G. (1980): Advancing Computational Aerodynamics through Wind-Tunnel Experimentation. AGARD Fluid Dynamics Panel Meeting on Integration of Computers and Wind Tunnel Testing, Chattanooga, Tenn., Sept. 24-25.

Marvin, J. G.; Levy, L. L., Jr. and Seegmiller, H. L. (1980): On turbulence Modeling for Unsteady Transonic Flows; AIAA Journal, Vol. 18, No. 5, pp. 489-496 (May 1980).

Marvin, J. G. (1983): Turbulence Modeling for Computational Aerodynamics. AIAA Journal, Vol. 21, No. 7, pp. 941-955 (July 1983).

Mateer, G. G.; Brosh, A. and Viegas, J. R. (1976): A Normal Shock-Wave Turbulent Boundary-Layer Interaction at Transonic Speeds. AIAA Paper 76-161, Washington, D.C.

Mateer, G. G. and Viegas, J. R. (1979): Effect of Mach and Reynolds Numbers on a Normal Shock/Turbulence Boundary-Layer Interaction. AIAA Paper 79-1502, Williamsburg, Va.

McDevitt, J. B.; Levy, L. L., Jr. and Deiwert, G. S. (1976): Transonic Flow About a Thick Circular-Arc Airfoil. AIAA Journal, Vol. 14, No. 5, pp. 606-613 (May 1976).

Mehta, V. and Lomax, H. (1982): Reynolds-Averaged Navier-Stokes Computations of Transonic Aerodynamics. Progress in Astronautics and Aerodynamics, Vol. 82, D. Nixon ed., published by AIAA, New York, N.Y., pp. 297-375.

Mehta, V. (1983): Reynolds-Averaged Navier-Stokes Computations of Transonic Flows Around Airfoils. Paper presented at the Second Symposium on Numerical and Physical Aspects of Aerodynamic Flows, California State University, Long Beach, CA, 17-20 January 1983.

Om, D.; Childs, M. E. and Viegas, J. R. (1982): An Experimental Investigation and a Numerical Prediction of a Transonic Normal Shock Wave/Turbulent Boundary-Layer Interaction. AIAA Paper 82-0990, St. Louis, Mo.

Oskam, B.; Bogdonoff, S. M. and Vas, I. E. (1975): Study of Three-Dimensional Flow Fields Generated by the Interaction of a Skewed Shock Wave with a Turbulent Boundary-Layer. AFFDL-TR 75-21, Air Force Flight Dynamics Laboratory.

Peake, D. J. (1976): Three Dimensional Swept Shock/Turbulent Boundary-Layer Separation with Control of Air Injection. Aeronautical Report L. R., 592, National Research Council, Canada.

Peake, D. J. and Tobak, M. (1980): Three Dimensional Interaction and Vortical Flows with Emphasis on High Speeds. NASA TM-81169.

Rainbird, W. J. (1968): Turbulent Boundary-Layer Growth and Separation on a Yawed Cone. AIAA Journal, Vol. 6, p. 2410. (See also AGARD CP 30, 1968.)

Rakich, J. V.; Davis, R. T. and Barnett, M. (1982): Simulation of Large Turbulent Structures with the Parabolic Navier-Stokes Equations. Eighth International Conference on Numerical Methods in Fluid Dynamics, Aachen, W. Germany.

Ramaprian, B. R.; Patel, V. C. and Sastry, M. S. (1981): Turbulence Wake Development Behind Streamlined Bodies. IIHR Report 231, Iowa Institute of Hydraulic Research, U. of Iowa, Iowa City, Iowa.

Redda, D. C. and Murphy, J. D. (1973): Shock Wave Turbulent Boundary-Layer Interaction in Rectangular Channels. Part II. The Influence of Sidewall Boundary-Layers on Incipient Separation and Scale of Interaction. AIAA Journal, Vol. 11, No. 10, pp. 1367-1368.

Rubesin, M. W. (1976): A One-Equation Model of Turbulence for Use with the Compressible Navier-Stokes Equations. NASA TM X-73128.

Rubesin, M. W. and Rose, W. C. (1973): The Turbulent Mean Flow Reynolds-Stress and Heat Flux Equations in Mass-Averaged Dependent Variables. NASA TM X-62, 248.

Salmon, J. T.; Bogar, T. J. and Sejben, M. (1981): Laser Velocimeter Measurements in Unsteady, Separated, Transonic Diffuser Flows. AIAA Paper 81-1197, Palo Alto, Calif.

Schiff, L. B. and Steger, J. L. (1980): Numerical Simulation of Steady Supersonic Viscous Flows. AIAA Journal, Vol. 18, No. 12, pp. 1421-1430 (Dec.).

Schiff, L. B. and Sturek, W. B. (1980): Numerical Simulation of Steady Supersonic Flow over an Ogive-Cylinder/Boattail Body. AIAA Paper 80-0066, Pasadena, Calif.

Seddon, J. (1960): The Flow Produced by Interaction of a Turbulent Boundary-Layer with a Normal Shock Wave of Strength Sufficient to Cause Separation. Aeronautical Research Council Reports and Memoranda No. 3502 (Mar. 1960).

Seegmiller, H. L.; Marvin, J. G. and Levy, L. L., Jr. (1978): Steady and Unsteady Transonic Flows. AIAA Journal, Vol. 16, No. 12, pp. 1262-1270.

Settles, G. S.; Vas, I. E. and Bogdonoff, S. M. (1976): Details of a Shock-Separated Turbulent Boundary-Layer at a Compression Corner. AIAA Journal, Vol. 14, pp. 1709-1715.

Settles, G. S.; Fitzpatrick, T. J. and Bogdonoff, S. M. (1979): Detailed Study of Attached and Separated Compression Corner Flow Fields in High Reynolds Number Supersonic Flow. AIAA Journal, Vol. 15, No. 4, pp. 1152-1158.

Settles, G. S.; Baca, B. K.; Williams, D. R. and Bogdonoff, S. M. (1980): A Study of Reattachment of a Free Shear Layer in Compressible Turbulent Flow. AIAA Paper 80-1408, Snowmass, CO.

Settles, G. S. and Teng, H. Y. (1984): Cylindrical and Conical Upstream Regimes of 3-D Shock/Turbulent Boundary-Layer Interactions. AIAA Journal, Vol. 22, No. 2, pp. 194-200.

Shang, J. S. and Hankey, W. L., Jr. (1975): Numerical Solution of the Navier-Stokes Equations for a Compression Ramp. AIAA Journal, Vol. 13, No. 10, pp. 1368-1374.

Shang, J. S.; Hankey, W. L., Jr. and Law, H. C. (1976): Numerical Simulation of Shock-Wave-Turbulent Boundary-Layer Interaction. AIAA Journal, Vol. 14, No. 10, p. 1451.

Shang, J. S.; Hankey, W. L. and Petty, J. S. (1979): Three-Dimensional Supersonic Interacting Turbulent Flow along a Corner. AIAA Journal, Vol. 10, No. 5, pp. 652-656.

Sindir, M. (1982): Numerical Study of Separating and Reattaching Flows in a Backward-Facing Step Geometry. Ph. D. dissertation, Mechanical Engineering Department, U. of California at Davis, Davis, Calif.

Steger, J. L. and Bailey, H. E. (1980): Calculation of Transonic Aileron Buzz. AIAA Journal, Vol. 18, No. 3, pp. 249-255.

Tannehill, J. G., Vigneron, Y. C., and Rakich, J. V. (1979): Numerical Solution of Two-Dimensional Turbulent Blunt Body Flows with an Impinging Shock. AIAA Journal, Vol. 17, No. 12, pp. 1289-1290 (Dec. 1978).

Teng, H. Y. and Settles, G. S. (1982): Cylindrical and Conical Upstream Influence Regimes of 3-D Shock/Turbulent Boundary-Layer Interactions. AIAA Paper 82-0987, St. Louis, Mo.

Viegas, J. R. and Horstman, C. C. (1979): Comparison of Multiequation Turbulence Models for Several Shock Boundary-Layer Interaction Flows. AIAA Journal, Vol. 17, No. 8, pp. 811-820.

Viegas, J. R. and Horstman, C. C. (1982): The 1980-81 AFSOR/HTTM-Stanford Conference on Complex Turbulent Flows: Comparison of Computation and Experiment. Vol. III. Comparison of Computation with Experiment and Computers Summary Reports. S. J. Kline; B. J. Cantwell and G. M. Lilley eds., pp. 1535-1539.

Viegas, J. R. and Rubesin, M. W. (1983): Wall Function Boundary Conditions in the Solution of the Navier-Stokes Equations for Complex Turbulent Flows. AIAA Paper 83-1694, Danvers, Mass.

Visbal, M. and Knight, D. (1983): Evaluation of the Baldwin-Lomax Turbulence Model for Two-Dimensional Shock-Wave Boundary-Layer Interactions. AIAA Paper 83-1697, Danvers, Mass.

Viswanath, P. R.; Cleary, J. W.; Seegmiller, H. L. and Horstman, C. C. (1980): Trailing Edge Flows at High Reynolds Number. AIAA Journal, Vol. 18, No. 9, pp. 1959-1965.

Viswanath, P. R. and Brown, J. L. (1982): Separated Trailing-Edge Flow at a Transonic Mach Number. AIAA Paper 82-0348, Orlando, Fla.

West, J. E. and Korkegi, R. H. (1972): Supersonic Interaction in the Corner of Intersecting Wedges and High Reynolds Number. AIAA Journal, Vol. 10, No. 5, pp. 652-656.

Wilcox, D. C. and Rubesin, M. W. (1980): Progress in Turbulence Modeling for Complex Flow Fields Including the Effects of Compressibility. NASA TP-1517.

ACKNOWLEDGEMENTS

The senior author would like to thank Mr. Claude Copy for preparing and executing the illustrations of his text and Mrs Lesly Bry for revising and correcting his manuscript.

He would also like to express his gratitude to the Documentation and Edition Department of ONERA for his help in the collection of documents and for the task of typing and preparing the final camera ready text.

<p>AGARDograph No.280 Advisory Group for Aerospace Research for Development, NATO TURBULENT SHOCK-WAVE/BOUNDARY-LAYER INTERACTION by J.Delery, J.G.Marvin and edited by Prof. E.Reshotko Published February 1986 224 pages</p> <p>This AGARDograph presents a comprehensive, up-to-date review of the shock-wave boundary-layer interaction problem. A detailed physical description of the phenomena for transonic and supersonic speed regimes is given based on experimental observations, correlations, and theoretical concepts. Approaches for solving the problem are then reviewed in depth. Specifically, these include: global</p> <p style="text-align: center;">P.T.O</p>	<p>AGARD-AG-280</p> <p>Aerodynamic characteristics Shock waves Boundary layer Transonic flow Supersonic flow Data processing</p>	<p>AGARDograph No.280 Advisory Group for Aerospace Research for Development, NATO TURBULENT SHOCK-WAVE/BOUNDARY-LAYER INTERACTION by J.Delery, J.G.Marvin and edited by Prof. E.Reshotko Published February 1986 224 pages</p> <p>This AGARDograph presents a comprehensive, up-to-date review of the shock-wave boundary-layer interaction problem. A detailed physical description of the phenomena for transonic and supersonic speed regimes is given based on experimental observations, correlations, and theoretical concepts. Approaches for solving the problem are then reviewed in depth. Specifically, these include: global</p> <p style="text-align: center;">P.T.O</p>	<p>AGARD-AG-280</p> <p>Aerodynamic characteristics Shock waves Boundary layer Transonic flow Supersonic flow Data processing</p>
<p>AGARDograph No.280 Advisory Group for Aerospace Research for Development, NATO TURBULENT SHOCK-WAVE/BOUNDARY-LAYER INTERACTION by J.Delery, J.G.Marvin and edited by Prof. E.Reshotko Published February 1986 224 pages</p> <p>This AGARDograph presents a comprehensive, up-to-date review of the shock-wave boundary-layer interaction problem. A detailed physical description of the phenomena for transonic and supersonic speed regimes is given based on experimental observations, correlations, and theoretical concepts. Approaches for solving the problem are then reviewed in depth. Specifically, these include: global</p> <p style="text-align: center;">P.T.O</p>	<p>AGARD-AG-280</p> <p>Aerodynamic characteristics Shock waves Boundary layer Transonic flow Supersonic flow Data processing</p>	<p>AGARDograph No.280 Advisory Group for Aerospace Research for Development, NATO TURBULENT SHOCK-WAVE/BOUNDARY-LAYER INTERACTION by J.Delery, J.G.Marvin and edited by Prof. E.Reshotko Published February 1986 224 pages</p> <p>This AGARDograph presents a comprehensive, up-to-date review of the shock-wave boundary-layer interaction problem. A detailed physical description of the phenomena for transonic and supersonic speed regimes is given based on experimental observations, correlations, and theoretical concepts. Approaches for solving the problem are then reviewed in depth. Specifically, these include: global</p> <p style="text-align: center;">P.T.O</p>	<p>AGARD-AG-280</p> <p>Aerodynamic characteristics Shock waves Boundary layer Transonic flow Supersonic flow Data processing</p>

methods developed to predict sudden changes in boundary-layer properties; integral or finite-difference methods developed to predict the continuous evolution of a boundary-layer encountering a pressure field induced by a shock wave; coupling methods to predict entire flow fields; analytical methods such as multi-deck techniques; and finite-difference methods for solving the time-dependent Reynolds-averaged Navier-Stokes equations used to predict the development of entire flow fields. Examples are presented to illustrate the status of the various methods and some discussion is devoted to delineating their advantages and shortcomings. Reference citations for the wide variety of subject material are provided for readers interested in further study.

This AGARDograph has been produced at the request of the Fluid Dynamics Panel of AGARD.

ISBN 92-835-1519-6

methods developed to predict sudden changes in boundary-layer properties; integral or finite-difference methods developed to predict the continuous evolution of a boundary-layer encountering a pressure field induced by a shock wave; coupling methods to predict entire flow fields; analytical methods such as multi-deck techniques; and finite-difference methods for solving the time-dependent Reynolds-averaged Navier-Stokes equations used to predict the development of entire flow fields. Examples are presented to illustrate the status of the various methods and some discussion is devoted to delineating their advantages and shortcomings. Reference citations for the wide variety of subject material are provided for readers interested in further study.

This AGARDograph has been produced at the request of the Fluid Dynamics Panel of AGARD.

ISBN 92-835-1519-6

methods developed to predict sudden changes in boundary-layer properties; integral or finite-difference methods developed to predict the continuous evolution of a boundary-layer encountering a pressure field induced by a shock wave; coupling methods to predict entire flow fields; analytical methods such as multi-deck techniques; and finite-difference methods for solving the time-dependent Reynolds-averaged Navier-Stokes equations used to predict the development of entire flow fields. Examples are presented to illustrate the status of the various methods and some discussion is devoted to delineating their advantages and shortcomings. Reference citations for the wide variety of subject material are provided for readers interested in further study.

This AGARDograph has been produced at the request of the Fluid Dynamics Panel of AGARD.

ISBN 92-835-1519-6

methods developed to predict sudden changes in boundary-layer properties; integral or finite-difference methods developed to predict the continuous evolution of a boundary-layer encountering a pressure field induced by a shock wave; coupling methods to predict entire flow fields; analytical methods such as multi-deck techniques; and finite-difference methods for solving the time-dependent Reynolds-averaged Navier-Stokes equations used to predict the development of entire flow fields. Examples are presented to illustrate the status of the various methods and some discussion is devoted to delineating their advantages and shortcomings. Reference citations for the wide variety of subject material are provided for readers interested in further study.

This AGARDograph has been produced at the request of the Fluid Dynamics Panel of AGARD.

ISBN 92-835-1519-6

U224158

AGARD

NATO OTAN

7 RUE ANCELLE • 92200 NEUILLY-SUR-SEINE
FRANCE

Telephone (1) 47.45.08.10 · Telex 610176

**DISTRIBUTION OF UNCLASSIFIED
AGARD PUBLICATIONS**

AGARD does NOT hold stocks of AGARD publications at the above address for general distribution. Initial distribution of AGARD publications is made to AGARD Member Nations through the following National Distribution Centres. Further copies are sometimes available from these Centres, but if not may be purchased in Microfiche or Photocopy form from the Purchase Agencies listed below.

NATIONAL DISTRIBUTION CENTRES

BELGIUM



National Aeronautics and Space Administration

Washington, D.C. 20546

SPECIAL FOURTH CLASS MAIL BOOK

ITALY

Aeronautica Militare



Postage and Fees Paid
National Aeronautics and Space Administration
NASA-451

Official Business
Penalty for Private Use \$300

Corrispondenze all'AGARD

AGARD
Library, NLR

Research Establishment

Coordinator to AGARD
Programs

GREECE

Hellenic Air Force General Staff
Research and Development Directorate
Holargos, Athens

ICELAND

Director of Aviation
c/o Flugrad
Reykjavik

TURKEY

Department of Research and Development (ARGE)
Ministry of National Defence, Ankara

UNITED KINGDOM

Defence Research Information Centre
Station Square House
St Mary Cray
Orpington, Kent BR5 3RE

UNITED STATES

National Aeronautics and Space Administration (NASA)
Langley Research Center
M/S 180
Hampton, Virginia 23665

THE UNITED STATES NATIONAL DISTRIBUTION CENTRE (NASA) DOES NOT HOLD STOCKS OF AGARD PUBLICATIONS, AND APPLICATIONS FOR COPIES SHOULD BE MADE DIRECT TO THE NATIONAL TECHNICAL INFORMATION SERVICE (NTIS) AT THE ADDRESS BELOW.

PURCHASE AGENCIES

Microfiche or Photocopy

National Technical Information Service (NTIS)
5285 Port Royal Road
Springfield
Virginia 22161, USA

Microfiche

ESA/Information Retrieval Service
European Space Agency
10, rue Mario Nikis
75015 Paris, France

Microfiche or Photocopy

British Library Lending Division
Boston Spa, Wetherby
West Yorkshire LS23 7BQ
England

Requests for microfiche or photocopies of AGARD documents should include the AGARD serial number, title, author or editor, and publication date. Requests to NTIS should include the NASA accession report number. Full bibliographical references and abstracts of AGARD publications are given in the following journals:

Scientific and Technical Aerospace Reports (STAR)
published by NASA Scientific and Technical
Information Branch
NASA Headquarters (NIT-40)
Washington D.C. 20546, USA

Government Reports Announcements (GRA)
published by the National Technical
Information Services, Springfield
Virginia 22161, USA



Printed by Specialised Printing Services Limited
40 Chigwell Lane, Loughton, Essex IG10 3TZ

ISBN 92-835-1519-6